EPTT 2014

SÃO LEOPOLDO - RS

Anais da 9ª Escola de Primavera de Transição e Turbulência

Universidade do Vale do Rio dos Sinos - UNISINOS
São Leopoldo, 22 a 26 de setembro de 2014
www.abcm.org.br/eptt2014

EPTT 2014

Caros colegas Professores, Pesquisadores e Alunos

É com imenso prazer que disponibilizamos *on-line* os Anais da IX Escola de Primavera de Transição e Turbulência – EPTT 2014, contendo na íntegra os artigos submetidos e aprovados para apresentação durante o evento.

A EPTT 2014 ocorre em São Leopoldo, no campus da Universidade do Vale do Rio dos Sinos – UNISINOS, entre os dias 22 e 26 de setembro de 2014. Esta é a 9ª edição deste evento já tradicional na agenda da ABCM e que reúne os fluidodinamicistas brasileiros e estrangeiros, especialmente nossos vizinhos da América do Sul, que têm comparecido com a apresentação de vários artigos. Durante os cinco dias do evento são apresentadas palestras do mais alto nível, para as quais foram convidados eminentes pesquisadores nacionais e internacionais.

Agradecemos a todos que enviaram seus trabalhos, apresentados nas seções de pôsteres do evento. Agradecemos também ao comitê científico pela revisão dos artigos submetidos.

Um agradecimento especial deve ser feito às agências, instituições e empresas que apoiaram este evento, tornando possível a sua realização.

Cordialmente

Comitê organizador da IX EPTT

EPTT 2014
22 a 26 de setembro de 2014 - UNISINOS

PROMOÇÃO: Associação Brasileira de Engenharia e Ciências Mecânicas ± ABCM

Comitê Organizador:

Alexandre Vagtinski de Paula
Conrad Yuan Yuen Lee
Flávia S. F. Zinani
Maria Luiza Sperb Indrusiak
Rejane de Césaro Oliveski

Comitê Científico

Alexandre Vagtinski de Paula
Alex Mendonça Bimbato
Conrad Yuan Yuen Lee
Erick de Moraes Franklin
Flávia S. F. Zinani
Juliana Braga Rodrigues Loureiro
Leandro Franco de Souza
Luiz Eduardo Bittencourt Sampaio
Marcelo Souza de Castro
Sandi Itamar Schafer de Souza

Patrocinadores:

ÍNDICE
em ordem alfabética

DIRECT NUMERICAL SIMULATION OF BI-DISPERSE PARTICLE-LADEN GRAVITY CURRENTS

E. P. Francisco, L. F. R. Espath, J. H. Silvestrini

DOUBLE MIXING LAYER LINEAR STABILITY ANALYSIS

O. M. R. de Souza, L. S. B. Alves, M. T. de Mendonça

EFFECT OF THICKNESS RATIO ON THE STABILITY OF MIXING LAYERS WITH A WAKE COMPONENT

M. S. Soares, F. F. Filho, M. T. Mendonça

ESTUDO DE TURBULÊNCIA GERADA POR OGT OBSERVADA POR PIV

A. P. S. D. Vieira, W. N. L. Roma

ESTUDO EXPERIMENTAL DO EFEITO AEROACÚSTICO DE UMA EXCRESCÊNCIA BIDIMENSIONAL NA COVA DO ESLATE

F. R. do Amaral, D. S. Souza, C. C. P. Junior, J. C. Serrano, M. Blanco, M. A. F. de Medeiros

EXPERIMENTAL STUDY OF WIND FEATURES IN THE ALCÂNTARA SPACE LAUNCH CENTER

A. C. Avelar. A. F. Faria, F. L. C. Brasileiro, G. Fisch

FLAT PLATE TURBULENT FLOW SIMULATIONS USING A CORRELATION-BASED TRANSITION MODEL

G. L. O. Halila, E. D. V. Bigarella, J. L. F. Azevedo

INFLUENCE OF RADIATION ON TURBULENCE IN A 2D AXISYMMETRIC TURBULENT FLAME SIMULATION

F. R. Centeno, E. D. dos Santos, C. V. da Silva, F. H. R. França

LINEAR GÖRTLER INSTABILITY DEVELOPMENT IN THE PRESENCE OF PRESSURE VARIATIONS

J. K. Rogenski, L. E. de Souza, J. M. Floryan

MODELAGEM COMPUTACIONAL DA ESTEIRA AERODINÂMICA DE TURBINAS EÓLICAS BASEADA EM SUMIDOURO DE QUANTIDADE DE MOVIMENTO

M. L. Lovatto, A. P. Petry

NUMERICAL MODELLING OF SWIRLING FLOW IN A COMBUSTION CHAMBER

J. L. P. Anapolski, T. C. Hayashi

NUMERICAL STUDY OF NON-REACTIVE TURBULENT JET FLOW WITH COMBINED CONVECTIVE AND RADIATIVE HEAT TRANSFER IN OPTICALLY THIN PARTICIPANT MEDIUM
E. D dos Santos, F. R. Centeno, L. A. O. Rocha, A. P. Petry, F. H. R. França

ON THE DIFFERENT RELAXATION TIME SCALES IN THE COMPRESSIBLE HEAT TRANSFER WITHIN A SUPERCRITICAL FLUID
L. S. B. Alves

ON THE TURBULENCE MODULATION BY PARTICLES IN CONFINED GAS-SOLID FLOWS
J. Utzig, F. J. de Souza, H. F. Meier

SIMULAÇÃO NUMÉRICA DE ESCOAMENTOS ESTRATIFICADOS POR PARTÍCULAS EM SUSPENSÃO E SALINIDADE
F. N. Schuch, L. C. Pinto, J. H. Silvestrini

STABILITY OF O2/H2 BINARY MIXING LAYERS: EFFECT OF TEMPERATURE GRADIENTS, COMPRESSIBILITY AND THREE-DIMENSIONALITY
L. M. Fernandes, R. B. Freitas, M. T. Mendonça

VERIFICATION AND VALIDATION OF A HIGH-ORDER LAMINAR-TURBULENT NUMERICAL CODE
P. Sartori, L. A. Petri, L. F. de Souza

ANÁLISE NUMÉRICA DO ESCOAMENTO TURBULENTO EM MATRIZES TUBULARES COM AFUNILAMENTO

Paulo Sergio Berving Zdanski, paulo.zdanski@udesc.br [1]
Fernando André Lindroth Dauner, Fernando_dauner1@hotmail.com[1]
Douglas Pauli, dougpauli0@gmail.com[1]
Maico Jeremias da Silva, maicojs@weg.net[1]
[1]Departamento de Engenharia Mecânica, Centro de Ciências Tecnológicas – CCT, Universidade do Estado de Santa Catarina – UDESC, Cep.: 89223-100 - Joinville - SC

Resumo. *Este trabalho teve como objetivo determinar através de uma metodologia numérica/experimental os fatores que influenciam a transferência de calor em uma matriz tubular (com 6 cilindros) imersa em um escoamento turbulento cruzado. Nesta etapa os dados obtidos experimentalmente (fluxo de calor na superfície dos cilindros, temperatura e velocidade do ar na entrada do domínio) foram utilizados como condições de contorno para a simulação numérica do problema, sendo que para esta análise foi empregado o Software comercial Ansys CFX®. Os aspectos estudados neste trabalho foram: a velocidade de incidência do escoamento e o posicionamento dos cilindros na matriz tubular. Os principais resultados obtidos indicaram uma influência considerável do afunilamento da matriz tubular bem como do número de Reynolds na transferência de calor por convecção forçada.*

1. INTRODUÇÃO

O problema da convecção forçada visa analisar a troca de calor associada com o escoamento de um fluido, podendo ser tanto para o resfriamento como aquecimento de um equipamento/produto. Estes problemas são amplamente estudados e empregados na indústria, desde processos de secagem de produtos (onde também é estudado o transporte de matéria), como por exemplo, o processo de secagem de madeira, até processos de refrigeração de motores de combustão interna. Uma das principais aplicações da convecção forçada na indústria é no projeto de trocadores de calor, sendo este estudo complexo e dispendioso para a aplicação exclusiva de uma metodologia experimental, de forma que a simulação computacional vem ganhando espaço e sendo disseminada tanto na indústria como na área de pesquisa.

É possível constatar na literatura recente uma grande quantidade de publicações na análise de sistemas térmicos compostos de matrizes tubulares (Khan, 2004; Khan et al., 2006; Mandhani et al., 2002; Wilson e Bassiouny, 2000; Huang et al., 2009; Ay et al.,2002). Uma pequena síntese das análises realizadas nestes trabalhos é apresentada na sequência. (i) Khan et al (2006) analisaram a influência do posicionamento e, também, do espaçamento dos tubos numa matriz tubular; (ii) Em outro trabalho, Khan (2004) também realizou uma comparação entre diversas equações obtidas empiricamente para estimativa da troca de calor convectiva em uma matriz tubular; (iii) Mandhani et al. (2002) realizaram um estudo sobre a influência da variação da porosidade de uma matriz tubular na troca de calor em sistemas térmicos; (iv) Wilson e Bassiouny (2000) estudaram a troca de calor e a perda de carga em uma matriz tubular alternada com duas fileiras; (v) Huang et al. (2009) analisaram experimentalmente a troca de calor convectiva para uma matriz tubular aletada, variando o espaçamento das aletas para arranjos alinhadas e alternados; (vi) Ay et al. (2002) apresentaram um estudo experimental onde foi avaliado a variação de temperatura e a troca de calor em uma matriz tubular, utilizando para tanto, a técnica de termografia de infravermelho.

Neste trabalho o foco principal foi a realização de uma simulação numérica do escoamento cruzado de ar para um novo arranjo de matriz tubular (denominado matriz tubular afunilada). Para a execução das simulações foi empregado o *Software* comercial Ansys CFX® em uma abordagem tipo *RANS* para o escoamento turbulento médio. Alguns resultados experimentais também foram utilizados para confiar mais credibilidade nas simulações. Os principais resultados obtidos indicaram que o afunilamento da matriz tubular resultou em um incremento da troca de calor convectiva (especialmente na faixa de alto Reynolds) quando comparada ao caso do arranjo clássico com tubos alinhados.

2. FORMULAÇÃO TEÓRICA

2.1. EQUAÇÕES DE GOVERNO

Neste trabalho foram utilizadas as equações de Navier-Stokes com média de Reynolds - *RANS* (*Reynolds-averaged Navier-Stokes Equations*) – para a solução do problema convectivo. Para um escoamento turbulento médio e incompressível, as equações do modelo resultam em,

$$\frac{\partial}{\partial t}(\rho\bar{u}_i) + \frac{\partial}{\partial x_j}\left(\rho\bar{u}_j\bar{u}_i\right) = -\frac{\partial}{\partial x_i}(p_e) + \frac{\partial}{\partial x_j}\left(2\mu_e\bar{s}_{ji}\right) \quad (1)$$

$$\frac{\partial}{\partial t}\left(\rho c_p\bar{T}\right) + \frac{\partial}{\partial x_i}\left(\rho c_p\bar{u}_i\bar{T}\right) = \frac{\partial}{\partial x_i}\left[\kappa_e\frac{\partial\bar{T}}{\partial x_i}\right] \quad (2)$$

$$\frac{\partial}{\partial x_i}(\bar{u}_i) = 0 \quad (3)$$

onde μ_e e k_e são definidos como coeficientes efetivos, $\mu+\mu_t$ e $k+k_t$. Para determinar os valores de μ_t e k_t, utilizou-se o modelo de turbulência κ-ε padrão para altos números de Reynolds (Launder e Spalding, 1974; Wilcox, 1998). As variáveis presentes no equacionamento para este modelo são a energia cinética turbulenta, κ, e a taxa de dissipação de energia cinética por unidade de massa, ε. Como se trata de um modelo clássico, não será apresentado o equacionamento desta metodologia neste documento.

2.2. MÉTODO NUMÉRICO

O esquema numérico utilizado pelo *Software* comercial Ansys CFX® é composto pelo método de volumes finitos baseado em elementos (*EBFVM*), sendo que este modelo é brevemente discutido em Maliska (2004) e descrito mais detalhadamente em Rezende (2008). Vale salientar que através deste método é possível se valer das principais vantagens de cada abordagem que são: a natureza conservativa dos volumes finitos e a liberdade geométrica do método dos elementos finitos. Desta forma, é possibilitada a utilização de malhas não estruturadas sem perder as características conservativas do método de volumes finitos. É importante destacar que a estratégia de acoplamento pressão-velocidade utilizada no *software* comercial corresponde ao esquema clássico proposto por Rhie e Chow (1983) para arranjos de malha co-localizadas.

2.3. CONDIÇÕES DE CONTORNO

Para a realização da simulação do escoamento é necessária a especificação das condições de contorno apropriadas, na entrada e saída do domínio, bem como nas superfícies dos cilindros (ver Fig. 1). Devido ao fato do *software* realizar somente simulações em âmbito tridimensional, é necessário utilizar um domínio com espessura unitária, aplicando sobre as paredes a condição de simetria, determinando que o gradiente das propriedades na direção normal à parede é igual ao gradiente na outra face

$$\left.\frac{\partial\varphi}{\partial\boldsymbol{n}}\right|_{s1} = \left.\frac{\partial\varphi}{\partial\boldsymbol{n}}\right|_{s2}, \quad (4)$$

onde *S1* e *S2* são as superfícies de simetria, *n* é a direção normal à superfície e φ é uma propriedade qualquer. A condição de entrada foi definida pelas Eqs. (5) e (6),

$$V_{entrada} = V_{ar} \quad (5)$$

$$T_{entrada} = T_{ar} \quad (6)$$

nas quais, V_{ar} é a velocidade do ar e T_{ar} a temperatura do ar (Temperatura ambiente). As paredes superior e inferior foram consideradas adiabáticas, não apresentando troca de calor na sua superfície. Na saída do domínio foi especificada a pressão estática relativa, sendo definido um valor nulo. Na superfície dos cilindros foi utilizada a condição de parede com troca de calor, sendo especificado o fluxo térmico, relação esta dada pela Eq. (7) na qual o sub-índice *w* indica a parede,

$$Q''_w = Q''_{cilindro} \quad (7)$$

3. RESULTADOS E DISCUSSÕES

Este trabalho é composto de duas etapas, sendo que na primeira foi realizado um teste de validação do *software* comercial Ansys CFX®, através da simulação da troca de calor sobre uma matriz tubular alinhada sobre a qual incide um escoamento cruzado de ar, sendo comparados os resultados obtidos com dados empíricos da literatura (Incropera et al., 2008). A seguir, foi estudado o escoamento em uma matriz tubular com afunilamento identificando as tendências na troca de calor por convecção para este arranjo. Um esquema para a matriz afunilada pode ser visualizado na Fig. 1, onde um novo parâmetro *S* (fator de afunilamento) foi incorporado.

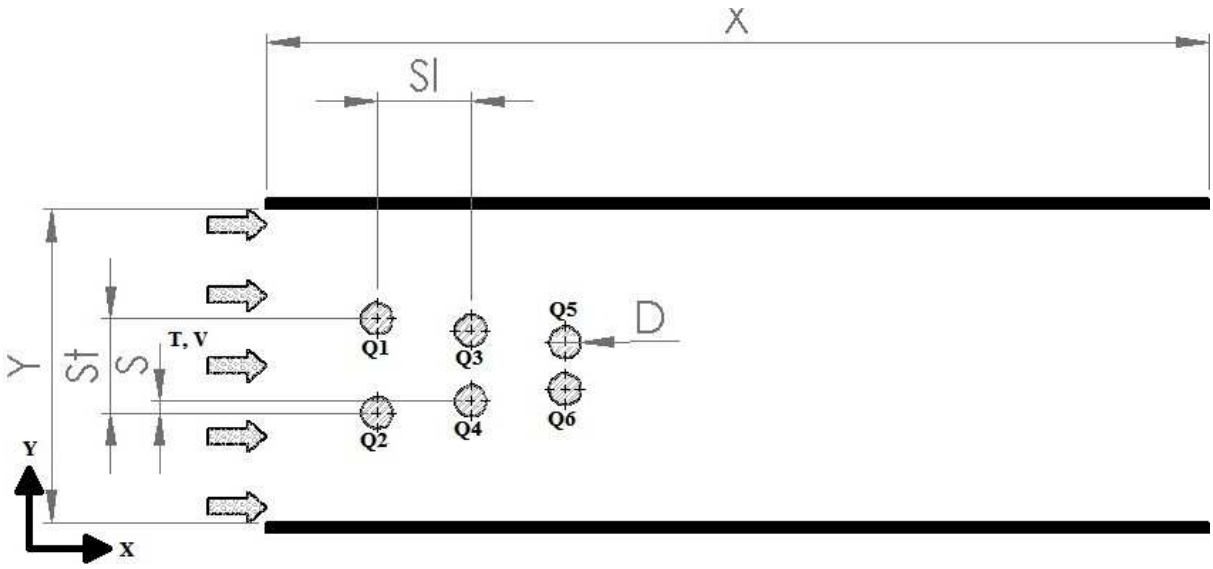

Figura 1. Esquema de uma matriz tubular afunilada com as dimensões utilizadas.

3.1. VALIDAÇÃO PARA UMA MATRIZ ALINHADA

Para uma matriz tubular alinhada (*S=0* – ver Fig. 1), o número de Nusselt médio do conjunto pode ser determinado pela equação empírica de Grimison (Incropera et al., 2008), a saber,

$$Nu_D = 1.13*C1*C2*Re^{m}_{D,máx.}Pr^{1/3} \tag{8}$$

onde Nu_D é o valor de Nusselt médio para a matriz tubular, *C1*, C2 e *m* são constantes que dependem dos valores de S_l, S_t e do número de fileiras da matriz, *Pr* é o número de Prandtl e $Re_{D,máx.}$ é o valor máximo do número de Reynolds na matriz, ou seja, o valor de Reynolds para a máxima velocidade do escoamento. Os valores de *C1* e *m* são apresentados na Tab. 1, enquanto o valor de *C2* é dado na Tab. 2 (Incropera et al., 2008).

Tabela 1. Valor das constantes *C1* e *m* para a Eq. (8).

$S_t/D = 3$ e $S_l/D = 3$	
C1	*M*
0.286	*0.608*

Tabela 2. Valor de *C2* para a Eq. (8).

3 fileiras
0.87

É importante salientar que todas as propriedades do fluido utilizadas para o cálculo do número de Reynolds são estimadas utilizando a temperatura de filme,

$$T_f = (T_w+T_\infty)/2 \tag{9}$$

na qual T_f é a temperatura de filme, T_w a temperatura da parede e T_∞ é a temperatura da corrente livre de ar, que neste trabalho é a temperatura de entrada do ar T_{ar}.

Para a execução da simulação numérica desta geometria foram utilizadas as condições de contorno que estão representadas nas Tabs. 3 e 4 a seguir. Na Tab. 3 são apresentados os valores de propriedades que permaneceram inalterados durante as simulações, sendo importante destacar que os fluxos de calor especificados como condições de contorno nas superfícies dos cilindros da matriz foram obtidos através de medições experimentais (o mesmo arranjo de tubos foi testado experimentalmente em um túnel de vento). Por outro lado, na Tab. 4 são fornecidos os parâmetros variáveis da simulação na entrada do domínio, a saber, a velocidade e a energia cinética turbulenta (que corresponde a 10 % da energia cinética do escoamento incidente). Finalmente, vale destacar que a malha que a malha computacional utilizada na discretização do domínio contém 170000 nós.

Tabela 3. Condições de contorno fixas.

Propriedades	Símbolo	Valor
Temperatura de entrada do ar [K]	T_{ar}	292.85
Dissipação de energia cinética por unidade de massa [m^2/s^3]	ε	392
Pressão relativa na saída [Pa]	$P_{est,rel.}$	0
Resíduo	δ	0.00001
Fluxo de calor no cilindro 1 [W/m^2]	$Q1'_w$	20505.30
Fluxo de calor no cilindro 2 [W/m^2]	$Q2'_w$	22415.15
Fluxo de calor no cilindro 3 [W/m^2]	$Q3'_w$	19259.49
Fluxo de calor no cilindro 4 [W/m^2]	$Q4'_w$	20824.25
Fluxo de calor no cilindro 5 [W/m^2]	$Q5'_w$	22378.35
Fluxo de calor no cilindro 6 [W/m^2]	$Q6'_w$	22750.46

Tabela 4. Condições de contorno variáveis para uma matriz alinhada

Velocidade [m/s]	Energia cinética turbulenta [m^2/s^2]
18.00	16.20
15.00	11.25
12.00	7.20
6.50	2.11
6.00	1.80
5.30	1.40
4.50	1.01
4.00	0.80

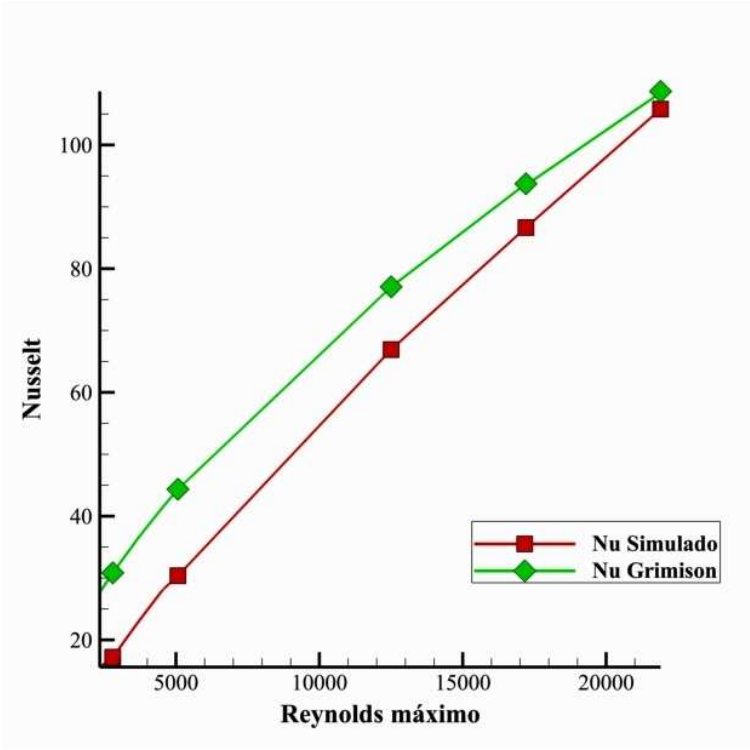

Figura 2. Comparação entre os resultados simulados e a equação empírica.

Na Fig. 2 é exposta a comparação entre os valores obtidos utilizando o *Software* comercial ANSYS CFX® e os valores obtidos através da Eq. (8). Inicialmente, é possível verificar que para valores de Reynolds baixos (<10000) o erro é mais significativo do que para valores maiores de Reynolds (>10000). Este comportamento era esperado uma vez que o modelo de turbulência empregado não apresenta um desempenho adequado para escoamentos de baixo Reynolds (Wilcox, 1998). O erro percentual entre as curvas é calculado partindo da seguinte equação (ver Tab. 5)

$$\Delta\%_{Grimison} = (Nu - Nu_{Grimison})*100/Nu_{Grimison} \quad (10)$$

na qual Nu é o número de Nusselt para a simulação, $Nu_{Grimison}$ é o Nusselt dado pela equação empírica e $\Delta\%_{Grimison}$ é a diferença percentual entre as curvas. Ao analisarem-se os resultados da Tab. 5 é importante destacar que as equações empíricas podem apresentar erros da ordem de até 20 % (Incropera et al., 2008). Desta forma, é possível verificar que para escoamentos com velocidade de incidência mais alta sobre a matriz (acima de 10 m/s), os valores das diferenças ficaram abaixo de 20 %, enquanto que para a faixa de velocidades menores o erro foi superior a 30 %.

Tabela 5. Diferença percentual entre os valores do número de Nusselt empírico e simulado.

Velocidade [m/s]	$\Delta\%_{Grimison}$ [%]
18.00	-2.64
15.00	7.56
12.00	-13.16
6.50	-31.50
6.00	-32.18
5.30	-37.15
4.50	-44.22
4.00	-43.70

3.2. ESTUDO DE MATRIZES TUBULARES AFUNILADAS

Nesta etapa realizaram-se simulações para uma matriz tubular afunilada, onde o fator de desalinhamento, S/D, apresentou valores iguais a 3/16 e 6/16 (ver Fig. 1). Como não foram encontrados resultados na literatura para esta geometria, os resultados da simulação foram comparados com dados obtidos experimentalmente em ensaios com túnel de vento. As condições de contorno fixas utilizadas nas simulações foram as mesmas do caso de uma matriz alinhada (ver Tab. 3), sendo a velocidade e a energia cinética turbulenta na entrada especificadas conforme valores apresentados na Tab. 6. Neste ponto é importante salientar que os ensaios experimentais foram realizados em um túnel de vento de sucção com circuito aberto na faixa de velocidades entre 3.8 – 6.25 m/s. O nível de turbulência na seção de testes do túnel é menor que 1 %, sendo a não-uniformidade média do perfil de velocidades em torno de 2 %. Como o escopo principal deste artigo é uma análise numérica, não serão apresentados os detalhes da metodologia experimental utilizada. Entretanto, vale destacar que a incerteza experimental para as medições do número de Nusselt foi em torno de ±4 %. Maiores detalhes sobre a metodologia experimental utilizada podem ser encontrados em Zdanski et al. (2012, 2013).

Tabela 6. Velocidade e energia cinética turbulenta na entrada da matriz tubular afunilada

S/D = 3/16			S/D = 6/16		
Velocidade [m/s]	κ [m^2/s^2]	Velocidade máxima [m/s]	Velocidade [m/s]	κ [m^2/s^2]	Velocidade máxima [m/s]
18.00	16.20	29.87	18.00	16.20	29.91
15.00	11.25	25.46	15.00	11.25	25.45
12.00	7.20	21.31	12.00	7.20	21.13
6.25	1.96	11.45	5.90	1.74	11.42
5.80	1.68	10.73	5.55	1.54	10.80
5.05	1.28	9.50	4.80	1.15	9.45
4.40	0.97	8.40	4.10	0.84	8.18
3.80	0.72	7.36	3.60	0.65	7.29

Analisando a Fig. 3 é possível realizar a comparação dos resultados obtidos usando a simulação numérica com os resultados obtidos experimentalmente. Esta comparação é dividida em dois gráficos, a saber: no primeiro são mostrados os valores obtidos experimentalmente e numericamente e, no segundo são mostradas as mesmas curvas, porém após a realização de uma regressão linear (os resultados experimentais foram extrapolados para uma faixa de Reynolds mais elevada). Esta regressão foi realizada com o auxílio do *Software* comercial Microsoft Excel 2010®, sendo as equações para as retas das distribuições numérica e experimental dadas pelas Eqs. (11) e (12),

$$Nu_D = 4.814*10^{-3}Re_{D,máx.} + 6.4432, \quad (11)$$

$$Nu_D = 4.41*10^{-3}Re_{D,máx.} + 16.6647. \quad (12)$$

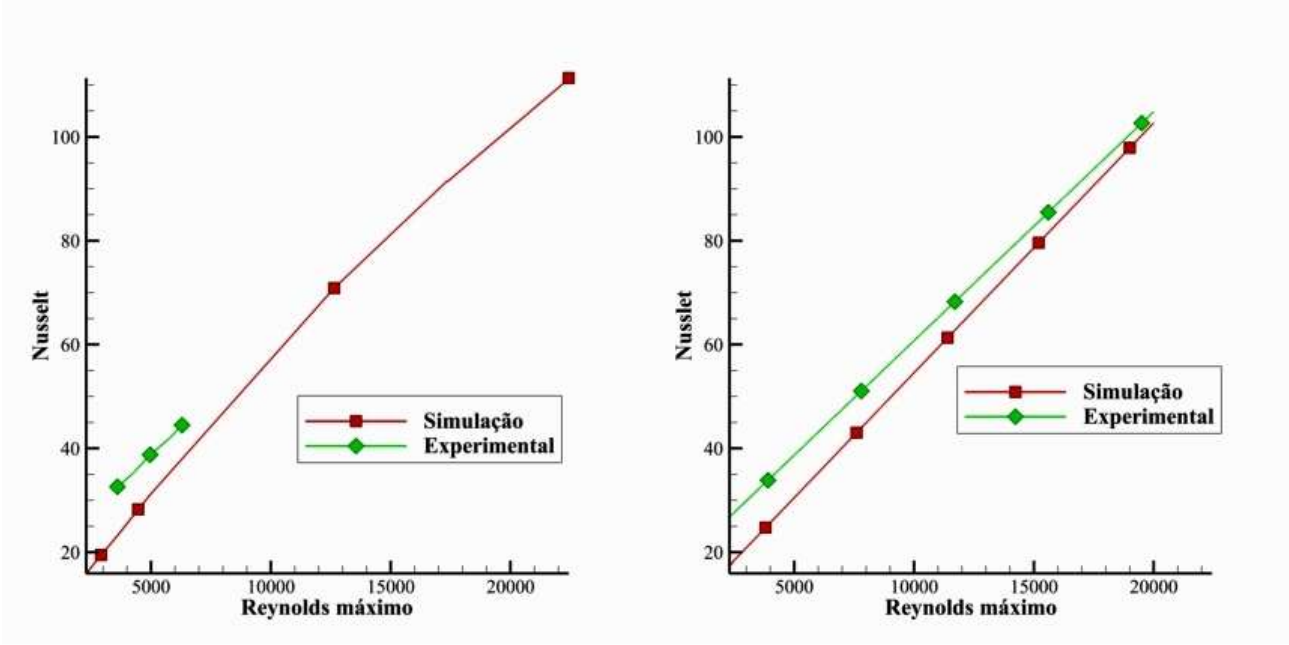

Figura 3. Comparação entre o resultado experimental e a simulação para um fator de afunilamento de 3/16.

Analisando a Fig. 3 é possível perceber que o resultado obtido através da simulação apresentou algumas discrepâncias quando comparado com o resultado experimental. As diferenças percentuais obtidas utilizando as Eqs. (11) e (12) para o cálculo do valor de Nusselt, tendo como base o valor experimental, são apresentados na Tab. 7. Neste ponto é importante salientar que a curva numérica apresenta uma boa concordância com a tendência da curva experimental extrapolada na faixa de alto Reynolds (nesta faixa não foram executados experimentos por limitações no aparato experimental). Desta forma, apesar de não serem confirmados experimentalmente na faixa para alto Reynolds (>10000), fica como conclusão que a simulação numérica pode ser empregada com um intervalo de confiança médio de aproximadamente 10 % na análise deste novo tipo de arranjo de matrizes tubulares (com afunilamento).

Tabela 7. Diferença percentual entre os resultados experimentais e simulados

Reynolds máximo	$\Delta\%_{exp}$
5000	-21.1845
10000	-10.1729
15000	-5.0251
20000	-2.0422

Finalmente, na Fig. 4 são apresentadas as curvas para as três configurações estudadas, a saber: S/D=0/16, S/D=3/16 e S/D=6/16. Inicialmente é possível verificar que, para a faixa de baixos valores de Reynolds, Re<10000, o fator de afunilamento não apresentou uma influência significativa sobre a troca de calor convectiva na matriz (expressa pelo número de Nusselt). Porém, para valores de Reynolds superiores a 15000, este fator passou a apresentar uma influência considerável sobre a troca de calor da matriz (houve um incremento do número de Nusselt à medida que se aumentou o fator de afunilamento).

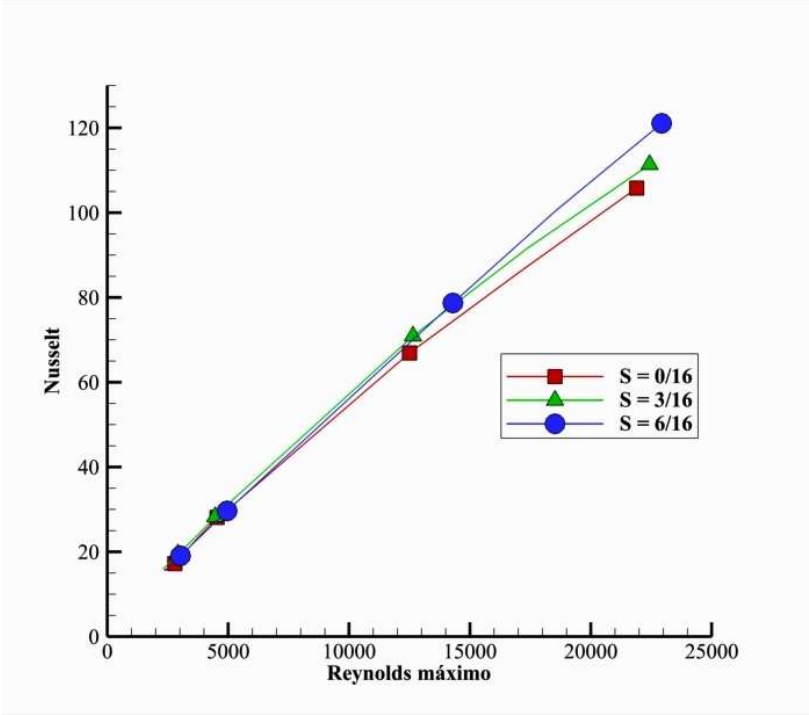

Figura 4. Influência do fator de afunilamento no número de Nusselt

A seguir, na Tab. 8, são expostos os valores dos incrementos percentuais no número de Nusselt para as matrizes afuniladas em relação à matriz alinhada (S/D = 0/16). Observa-se que para baixos valores de Reynolds os ganhos na troca de calor apresentaram valores pequenos (< 5 %), sendo que para valores mais elevados de Reynolds foram obtidos ganhos de quase 10% em relação à disposição original dos tubos (máximo incremento foi para o caso de S/D=6/16 e Reynolds de 20000). Visualiza-se também que, para o fator de afunilamento de 3/16, o ganho permaneceu aproximadamente constante ao longo de todo o intervalo de simulação, apresentando uma variação de aproximadamente 1 %.

Tabela 8. Aumento percentual do número de Nusselt para matrizes afuniladas em relação a uma matriz alinhada.

Reynolds máximo	$\Delta\%_{3/16}$	$\Delta\%_{6/16}$
5000	4.0174	-0.7274
10000	4.7252	2.7799
15000	4.9229	6.3444
20000	3.8878	9.4245

Com o intuito de estudar melhor os motivos deste aumento na troca de calor, foram comparados os perfis verticais (direção Y – ver Fig. 1) da energia cinética turbulenta (κ) para os diferentes fatores de afunilamento nas posições frontais e tangentes a montante dos cilindros em cada uma das três fileiras (a seção avaliada passa pelo ponto de estagnação frontal de cada cilindro). Estas comparações podem ser visualizadas na Fig. 5, sendo importante destacar que estes resultados foram extraídos para uma simulação com velocidade de entrada igual a 12 m/s.

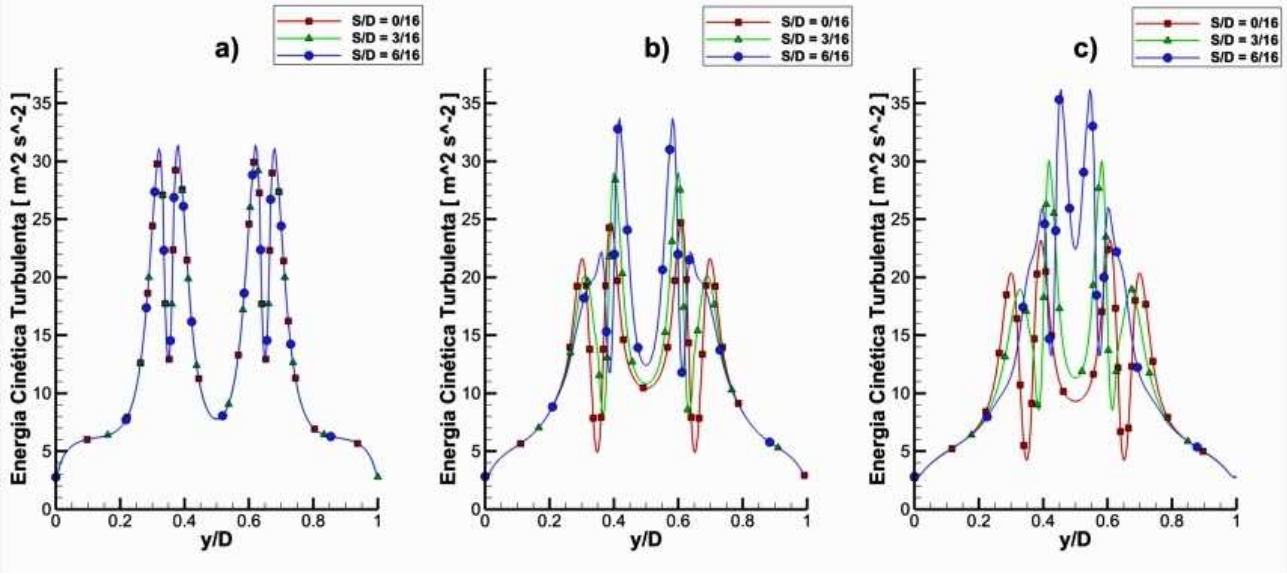

Figura 5. Perfis de energia cinética turbulenta para, a) primeira fileira, b) segunda fileira, c) terceira fileira.

Analisando a Fig. 5 é possível constatar que ao aumentar-se o fator de afunilamento, a energia cinética turbulenta apresentou picos mais elevados (em relação à matriz alinhada). Observa-se também que este aumento foi mais considerável na seção tangente aos cilindros da terceira fileira (provavelmente devido à interferência das outras duas fileiras sobre o escoamento incidente nesta última fileira). Desta forma, como conclusão desta análise fica evidente que o incremento no número de Nusselt para o caso S/D = 6/16 na faixa de alto Reynolds é devido ao incremento do mecanismo da produção de turbulência (expresso na Fig. 5 através dos perfis da energia cinética das flutuações turbulentas).

4. CONCLUSÃO

Neste trabalho foi inicialmente realizado um estudo de validação computacional onde foram comparados os resultados obtidos numericamente com correlações empíricas da literatura, bem como com dados obtidos experimentalmente. Estas comparações tiveram como objetivo dar credibilidade aos resultados numéricos obtidos através do *Software* comercial Ansys CFX®.

Num segundo momento, foram efetuadas simulações com o objetivo de verificar os efeitos do afunilamento de uma matriz tubular sobre a troca de calor convectiva do conjunto (principalmente verificar quais fatores que apresentariam as maiores influências nesta troca de calor). As principais variáveis estudadas nesta segunda etapa do trabalho foram: a velocidade do escoamento incidente e o fator de afunilamento da matriz tubular (parâmetro este definido como sendo S/D). Sendo assim, as principais conclusões obtidas após a realização desta pesquisa foram:

(i) O fator de afunilamento apresentou uma influência significativa na troca de calor global da matriz tubular, principalmente em situações onde os valores de Reynolds são mais elevados, com incrementos de até 10 % para um número de Reynolds igual a 20000.

(ii) Foi constatado, também, que a energia cinética turbulenta apresentou picos mais intensos com o incremento do fator de afunilamento da matriz; Portanto, existe a evidência de que o incremento na troca de calor convectiva da matriz (na faixa de alto Reynolds) foi devido a intensificação do mecanismo de produção de turbulência.

5. AGRADECIMENTOS

O autor Paulo Sergio Berving Zdanski agradece ao CNPq pelo auxílio financeiro à pesquisa recebido (processo 470581/2012-3). Os autores Fernando André Lindroth Dauner e Douglas Pauli agradecem ao CNPq pelo auxílio financeiro recebido através das bolsas PIBIC/CNPq.

6. REFERÊNCIAS BIBLIOGRÁFICAS

AY, H.; JANG, J. Y.; YEH, J. Local Heat transfer measurements of plate finned-tube heat exchangers by infrared thermography, Int. J of Heat and Mass Transfer 45 (2002) 4069-4078.

HUANG, C.; YUAN, I.; AY, H. An experimental study in determining the local heat transfer coefficients for the plate finned-tube heat exchangers, Int. J. of Heat and Mass Transfer 52 (2009) 4883-4893.

INCROPERA, F. P.; DE WITT, D. P.; BERGMAN, T. L.; LAVINE, A. S. Fundamentos da Transferência de Calor e Massa. 6ª edição. LTC, 2008.

KHAN, W. A., Modeling of Fluid Flow and Heat Transfer for Optimization of Pin-Fin Heat Sinks, Ph.D. Thesis, University of Waterloo, Canada, 2004.

KHAN, W. A.; CULHAM, J. R.; YOVANOVICH, M. M. Convection heat transfer from tube banks in crossflow: Analytical approach, Int. J. Heat and Mass Transfer 49 (2006) 4831 – 4838

LAUNDER, B. E.; SPALDING, D. B. The Numerical Computation of Turbulent Flows. Computer Methods in Applied Mechanics and Engineering, v.3, p.269-289. 1974.

MANDHANI, V. K.; CHHABRA, R. P.; ESWARAN, V. Forced Convection heat transfer in tube banks in cross flow, Chemical Engineering Science 57 (2002) 379-391.

MALISKA, Clovis R. Transferência de calor e mecânica dos fluidos computacional. 2. ed. rev. e ampl. Rio de Janeiro: Livros Técnicos e Científicos, 2004, 453 p.

REZENDE, R. V. P. Modelagem Matemática e Desenvolvimento de Metodologia Computacional para a Simulação Numérica do Escoamento Bifásico de Ar e Ferro-Gusa em Canal de Corrida de Alto-Forno, 2008. Tese de mestrado, UFSC, Florianópolis.

RHIE, C. M.; CHOW, W. L. Numerical Study of the Flow Past an Airfoil with Trailing-Edge Separation. AIAA Journal, v. 21, n.11 (1983) 1525-153.

WILCOX, D. C. Turbulence Modeling for CFD. La Canãda: DCW Industries, 1998. 460 p.

ZDANSKI, P. S. B.; BUBLITZ, A. E.; CORREA, C. N. Análise experimental da influência de promotores de turbulência na troca de calor por convecção forçada em escoamentos transversais sobre cilindros, In: VII Congresso Nacional de Engenharia Mecânica - CONEM2012, 2012, São Luis – MA.

ZDANSKI, P. S. B.; BUBLITZ, A. E.; CORREA, C. N. An experimental study of the convective heat transfer enhancement: applications of turbulence promoters, Engenharia Térmica 12 (2) (2013) 3-7.

WILSON, A. S.; BASSIOUNY, M. K. Modeling of heat transfer for flow across tube banks, Chemical Engineering and Processing 39 (2000) 1-14.

7. DIREITOS AUTORAIS

EFFECT OF THICKNESS RATIO ON THE STABILITY OF MIXING LAYERS WITH A WAKE COMPONENT

Mariana dos Santos Soares, mariana.s.oares@hotmail.com
Universidade Federal de Itajubá - Campus Itajubá, MG, Brazil

Fernando Fachini Filho, fachini@lcp.inpe.br
Instituto Nacional de Pesquisas Espaciais, INPE/LCP, São Cachoeira Paulista, SP, Brazil

Marcio T. Mendonca, marciomtm@iae.cta.br
Instituto de Aeronáutica e Espaço, IAE/APA, São José dos Campos, SP, Brazil

Abstract.
The present investigation is part of a study on the stability of complex mixing layers whose long term objective is the understanding of combustion stability. Compressible, binary mixing layers linear stability, with and without jet and wake components are been studied considering variable properties base flows. Besides the local normal mode stability analysis, compressible mixing layers are also been addressed through direct numerical simulations in order to elucidate the flow topology due to initial stage stability development. Those studies show that a wake component has a considerable effect on the development of the Kelvin-Helmholtz instability, both in terms of growth rates and vorticity distribution. In this study the effect of wake on the stability of the mixing layer is further considered. The influence of the ratio parameter R_δ between the wake thickness and the mixing layer thickness and the wake deficit amplitude R_W are studied. Preliminary results show that for small wake deficit amplitude and R_δ greater than 1 the base flow is more complex in the shear layer region, increasing the instability of the flow. For R_δ less than 1, the wake spreads the velocity gradients and the resulting shear layer is more stable than shear layers with higher R_δ, but still more unstable than the mixing layer due to the presence of other inflectional points in the base flow velocity profile. The present study considers incompressible stability analysis of a base flow given by a combination of hyperbolic tangent and hyperbolic secant velocity profiles.

Keywords: *mixing layer, inviscid hydrodynamic stability, normal modes stability analysis, wake stability*

1. INTRODUCTION

The present investigation is part of a study on the stability of complex mixing layers whose long term objective is the understanding of combustion stability. Compressible, binary mixing layers, with and without jet and wake components are been studied considering variable properties base flows (Salemi and Mendonca, 2008; Mendonça, 2010; Freitas *et al.* , 2014; Mendonca, 2014). Besides the local normal mode stability analysis, compressible mixing layers are also been addressed through direct numerical simulations in order to elucidate the flow topology due to initial stage stability development (Manco and Mendonca, 2014). Those studies show that a wake component has a considerable effect on the development of the Kelvin-Helmholtz instability, both in terms of growth rates and vorticity distribution.

The stability of mixing layers modified by a wake have already been addressed by other research groups, such as the early work of Zhuang (1995) who showed the destabilizing effect of the wake component. Gennaro and Medeiros (2008) also studied the effect of a wake component on the stability of mixing layers and proposed a different scaling in order to explain differences found on previous investigations. Recently Shin (2011) addressed the problem of a mixing layer modified by a wake and compared the effect of density stratification on the stability of the complex mixing layer plus wake and concluded that sinuous modes are more unstable than varicose modes when the fast stream has a higher density.

Figure 1 from Manco and Mendonca (2014) DNS simulations compares the vorticity distribution for a hyperbolic tangent mixing layer velocity profile and the mixing layer profile with a wake component. It shows that the wake component destabilizes the mixing layer and changes the flow topology, which enhances the mixing between the fast and slow streams.

In this study the effect of wake on the stability of the mixing layer is further considered. The ratio parameter R_δ between the wake thickness and the mixing layer thickness, and the wake deficit amplitude R_W are considered as illustrated in Fig. 2. Preliminary results show that for small wake deficit amplitude and R_δ greater than 1 the base flow is more complex in the shear layer region, increasing the instability of the flow. For R_δ less than 1, the wake spreads the velocity gradients and the resulting shear layer is more stable than those for R_δ higher or equal to 1. This study considers incompressible stability analysis of a base flow given by a combination of hyperbolic tangent and hyperbolic secant velocity profiles.

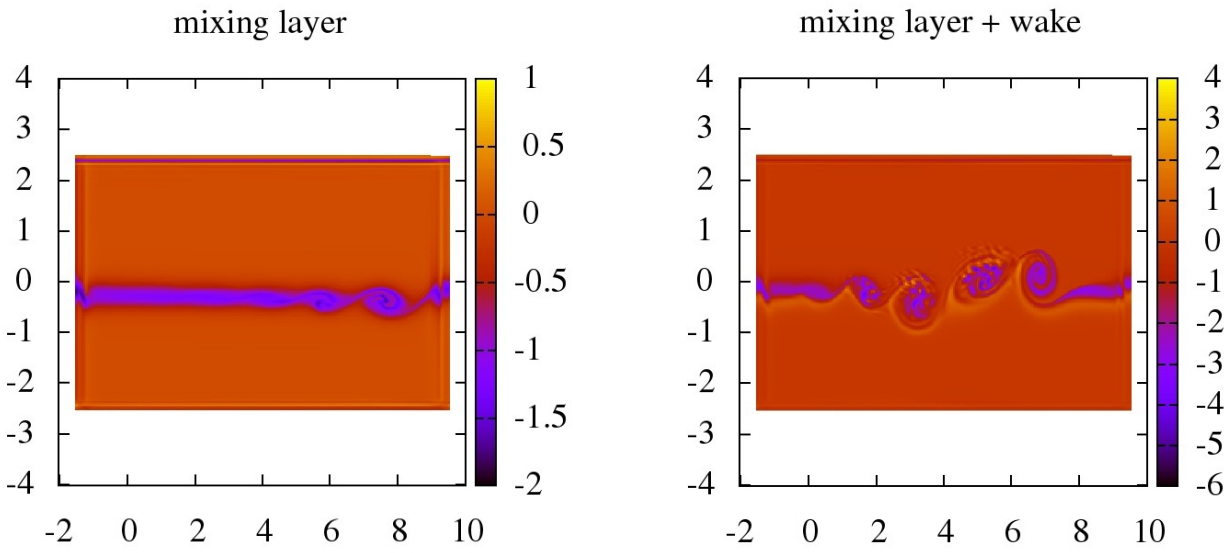

Figure 1. Vorticity distribution.

(a) large wake deficit (b) small wake deficit

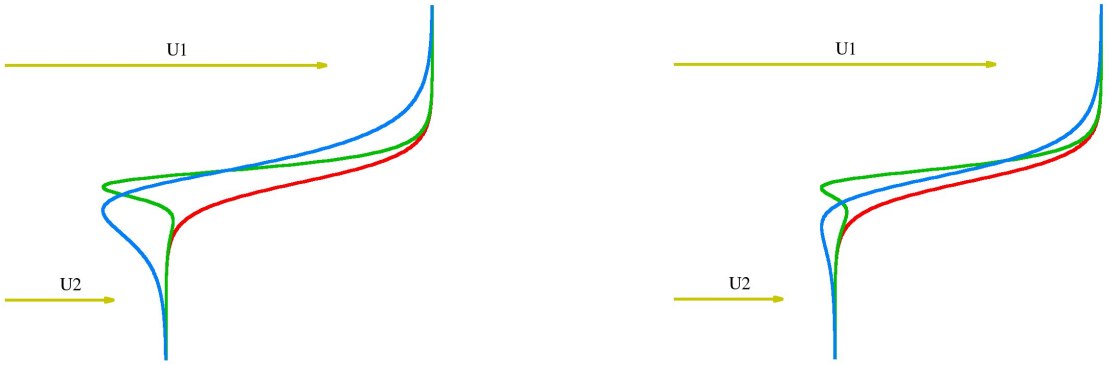

Figure 2. Base flow velocity distributions. Different thickness ratios and wake deficits.

2. FORMULATION AND METHODOLOGY

The base flow velocity is given by a combination of hyperbolic tangent mixing layer U_{m} and hyperbolic secant wake U_{w} velocity profiles. The amplitude of the wake component is controlled by the parameter R_{w} while the thickness ratio between mixing layer and wake is controlled by R_δ. The parameter R_{mis} controls the misalignment between the mixing layer and the wake component. The base flow is nondimensionalized by the upstream velocity U_1 and a slow stream velocity of $.5U_1$ is taken such that the velocity ratio results $\beta_U = .5$.

$$U_{\mathrm{m}} = .5\left[(1+\beta_U) + (1-\beta_U)\tanh(\eta)\right] \tag{1}$$

$$U_{\mathrm{w}} = 1 - \tanh\left[R_\delta\left(\eta - R_{\mathrm{mis}}\right)\right]\tanh\left[R_\delta\left(\eta - R_{\mathrm{mis}}\right)\right] \tag{2}$$

$$U(\eta) = U_{\mathrm{m}} - R_{\mathrm{w}}U_{\mathrm{w}} \tag{3}$$

Three different thickness ratios and three different wake amplitudes are considered. The wake component amplitudes R_{w} are chosen such that the resulting velocity profile minimum amplitudes u_{min} are 0.45, 0.40 and 0.35. The lower the minimum velocity the stronger the wake deficit. Table 1 shows the wake amplitudes R_{w} for the three different wake thicknesses ratios R_δ and the three different base flow minimum amplitudes. The resulting profiles are shown in Fig. 3.

A second experiment considers the case when the center of the mixing layer and the center of the wake component are misaligned. For this second experiment the thickness ratio is fixed at $R_\delta = 1$ and four different values of R_{mis} are considered, $R_{\mathrm{mis}} = -5, -2, +2$ and $+5$. The wake component velocity deficit R_{w} of 20% is taken, resulting in the base flow profiles shown in Fig. 4

The spatial stability of these base flows is investigate through a linear, local, normal mode inviscid analysis where the eigenvector v, frequencies ω and streamwise wavenumbers α result from the solution of the incompressible Rayleight

Table 1. Base flow thickness and amplitude ratios. Wake amplitude R_{W} as a function of u_{min} and R_δ.

		u_{min} .45	.40	.35
	0.5	0.1235	0.1990	0.2663
R_δ	1.	0.2329	0.2975	0.3561
	1.5	0.2736	0.3283	0.3815

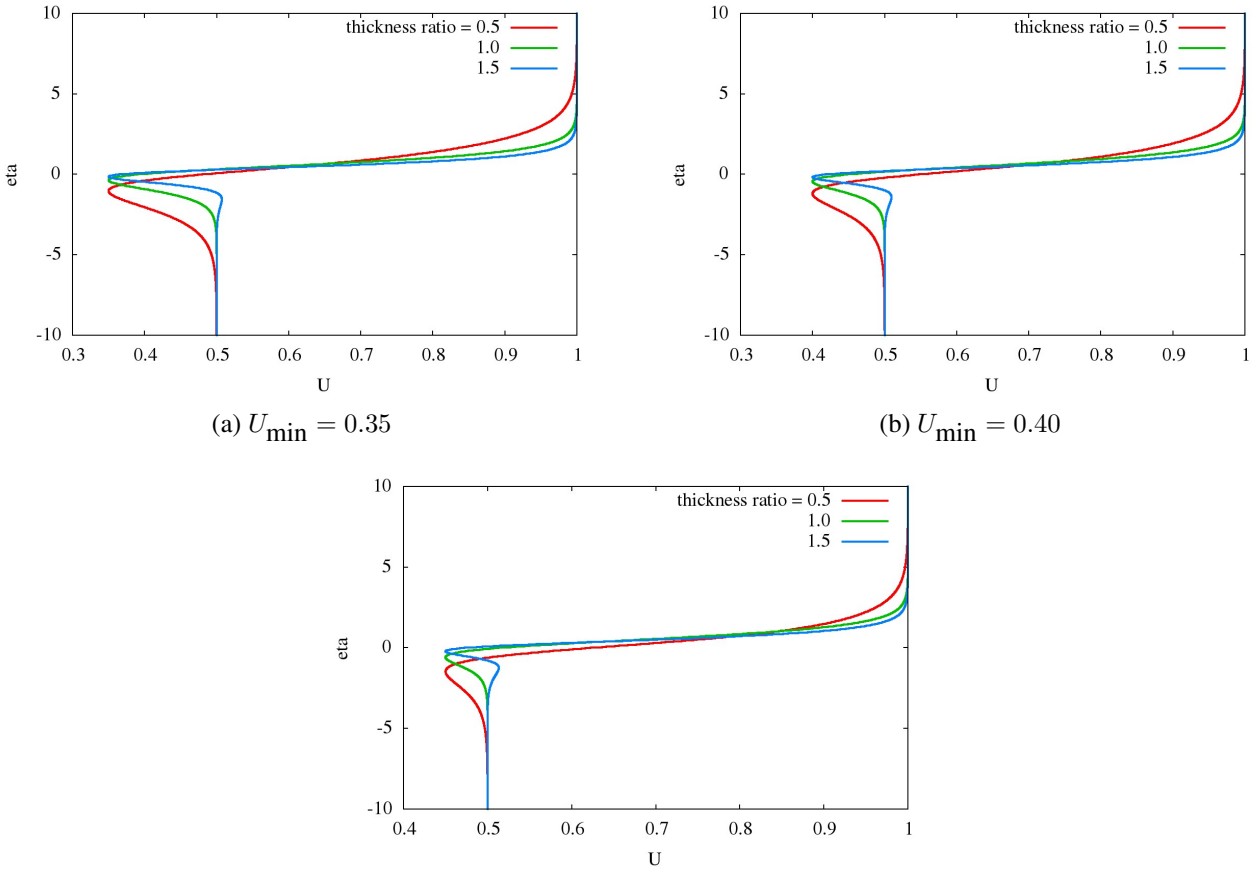

(a) $U_{\mathrm{min}} = 0.35$

(b) $U_{\mathrm{min}} = 0.40$

(c) $U_{\mathrm{min}} = 0.45$

Figure 3. Base flow velocity profiles for the conditions of Tab. 1.

equation.

$$(\alpha U - \omega)\left(v'' - \alpha^2 v\right) - U'' v = 0, \tag{4}$$

which, written in terms of χ (similar to the Gropengeiser variable for compressible flow stability analysis (Gropengeiser, 1970)).

$$\chi = \frac{i\alpha p}{v}, \tag{5}$$

the Rayleigh equation results in the following first order ordinary differential equation

$$\chi' = \alpha^2 (U - c) - \frac{\chi(\chi + U')}{(U - c)}, \tag{6}$$

with boundary conditions at $\pm\infty$, where $U' = 0$,

$$\chi(y \to \pm\infty) = \mp\alpha (U - c)\,. \tag{7}$$

Where U' and v' are the first derivatives of the base flow streamwise velocity U and disturbance normal velocity eigenvalue v.

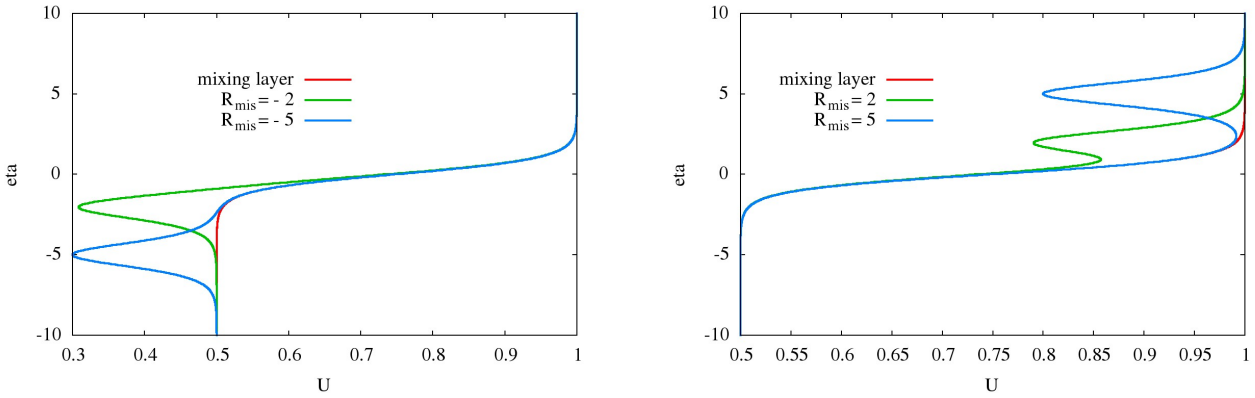

Figure 4. Base flow velocity profiles for the test cases with wake component misalignment.

3. RESULTS

Figures 5 to 7 show the growth rate versus frequency for the three different thickness ratio R_δ tested ($R_\delta = 0.5, 1.0$and1.5. In each figure a comparison is presented showing the effect of the magnitude of the wake component. As the wake deficit increases the minimum base flow velocity decreases and the maximum amplification rate increases for all three thickness ratios. For the thickness ratio of $R_\delta = 0.5$ the range of unstable frequencies is reduced, but the other thickness ratios the range of unstable frequencies are not so sensitive to the wake component and the frequency corresponding to the highest growth rate does not change.

Figures 8 to 10 show the same results but presenting a direct comparison between different thickness ratios for a given wake component. As the wake component gets thinner the flow becomes more and more unstable, both in terms of the maximum growth rate as in terms of the range of unstable frequencies. This result is summarized in Fig. 11 that shows the highest growth rate as a function of thickness ratio for the three different wake component amplitudes. Reducing the thickness of the wake component results in stronger velocity gradients at the inflectional point on the base flow profile, which explains the higher growth rates observed.

As also observed by previous investigations (Zhuang and Dimotakis, 1995; Gennaro and Medeiros, 2008; Shin, 2011), the wake component introduces other unstable modes, but here only the more unstable modes are shown. The other modes have growth rates that are at least one order of magnitude lower that the ones presented here.

When there is a misalignment between the mixing layer and the wake, as shown if Fig. 4 the stability characteristics change as presented in Figs. 12 and 13. Displacing the wake downward, if the misalignment is such that there is still interference between the mixing layer and the wake ($R_{\text{mis}} = 2$), the maximum growth rate is about the same as that of the aligned shear layers but with a reduce range of unstable frequencies. Displacing the wake upwards ($R_{\text{mis}} = -2$) results in a more stable flow with about the same stability limits (growth rate and range of unstable frequencies) as the mixing layer.

When the misalignment result in a base flow velocity profile where the mixing layer shear region does not get distorted by the wake ($R_{\text{mis}} = \pm 5$) the dominant instability mode is the mixing layer mode as shown in Fig. 13.

4. CONCLUSIONS

In this study the effect of a wake component on the stability of a mixing layer for different wake component thicknesses and velocity deficit has been investigated. The results show that the wake component destabilizes the mixing layer and the thinner the wake thickness the higher the resulting growth rates. The range of unstable frequencies also increase with decreasing wake thickness. These results are associated with the higher velocity gradients on the base flow velocity inflection points. When the mixing layer and the wake are misaligned but still interfering the stability characteristics change depending on the wake component displacement. When the misalignment is such that the mixing layer and the wake do not interfere the dominant mode is the mixing layer mode. These results will be extended to compressible and binary mixing layers.

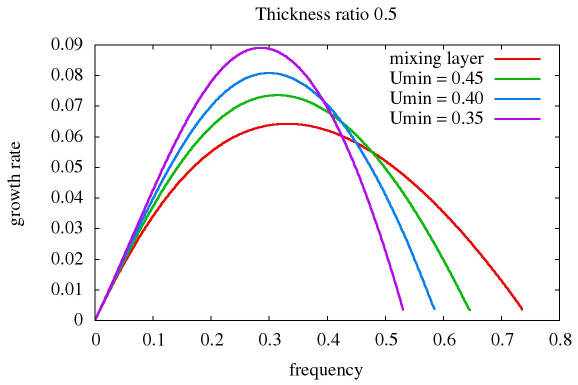

Figure 5. Growth rate versus frequency, $R_\delta = 0.5$.

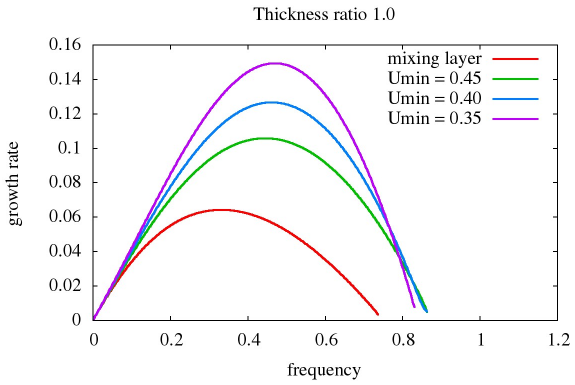

Figure 6. Growth rate versus frequency, $R_\delta = 1.0$.

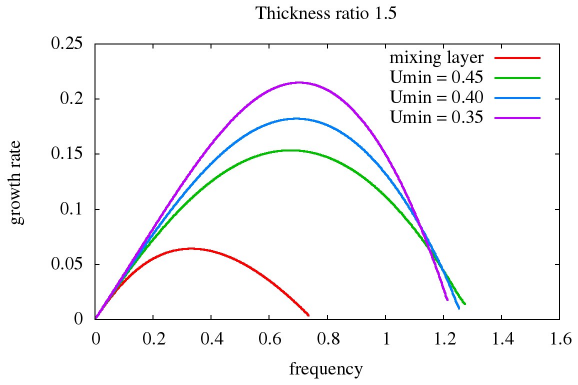

Figure 7. Growth rate versus frequency, $R_\delta = 1.5$.

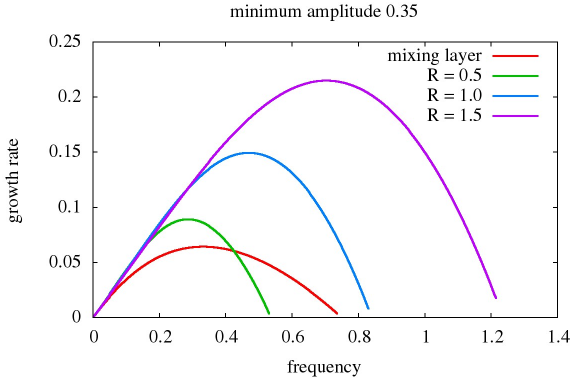

Figure 8. Growth rate versus frequency, $u_{\text{min}} = 0.35$.

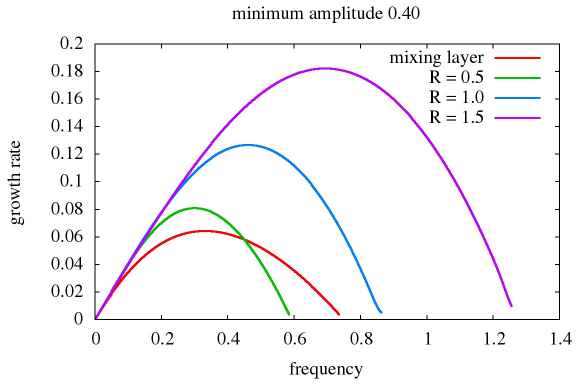

Figure 9. Growth rate versus frequency, $u_{\text{min}} = 0.40$.

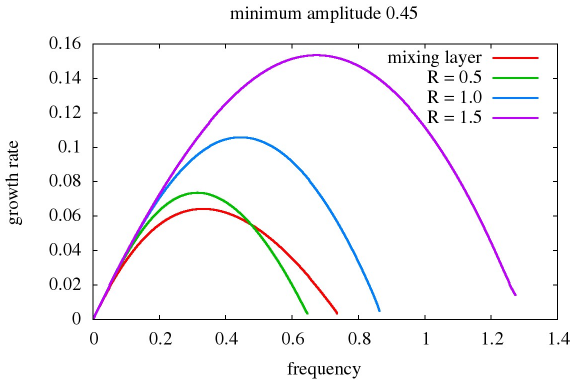

Figure 10. Growth rate versus frequency, $u_{\text{min}} = 0.45$.

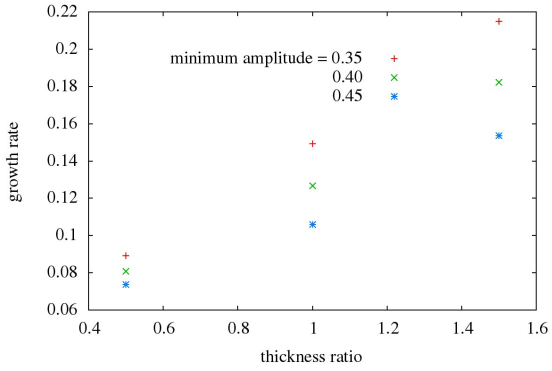

Figure 11. Maximum growth rate versus thickness ratio for different base flow minimum velocity.

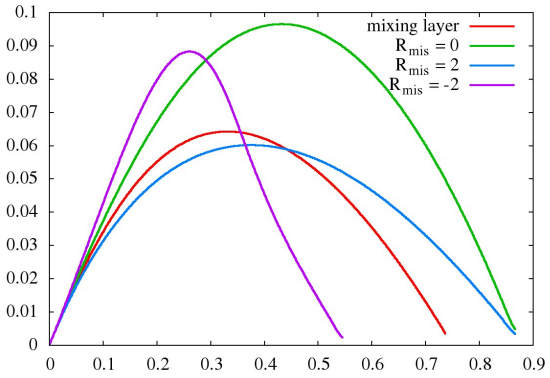

Figure 12. Growth rate versus frequency, $R_{\text{mis}} = \pm 2$.

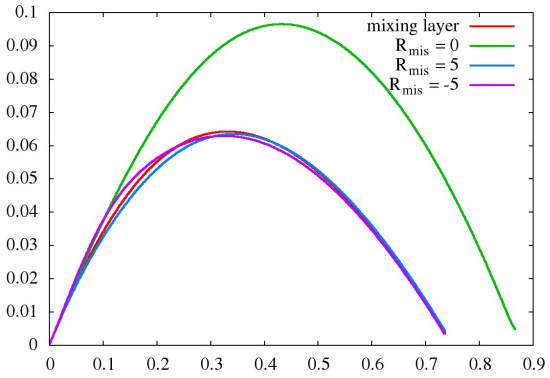

Figure 13. Growth rate versus frequency, $R_{\text{mis}} = \pm 5$.

5. ACKNOWLEDGEMENTS

The authors would like to acknowledge the financial support from CNPQ through Grant 129719/2013-7, and from FAPESP through Grant 2014/14584-7.

6. REFERENCES

Freitas, R. B., Fernandes, L. M., and Mendonca, M. T. 2014. Three-dimensional disturbances on binary mixing layers modified by jets and wakes. *In: IUTAM Symp. on Laminar-Turbulent Transition*. submitted.

Gennaro, E. M., and Medeiros, M. A. F. 2008. Numerical and Theoretical Investigation of the Asymmetry Effects in a Wake Profile. *Pages 1–10 of: Brazilian School of Transition and Turbulence*. ABCM.

Gropengeiser, H. 1970. *Study on the stability of boundary layers and compressible fluids*. Tech. rept. Report TT F-12786. NASA.

Manco, J. A. A., and Mendonca, M. T. 2014. Direct Numerical Simulation of Binary Free Shear Layer Hydrodynamic Stability. *In: IUTAM Symp. on Laminar-Turbulent Transition*. submitted.

Mendonça, M. T. 2010. Cooled gas turbine blade trailing edge flow analysis. *Pages 1–9 of: 13th Brazilian Congress of Engineering and Thermal Sciences - ENCIT 2010*.

Mendonca, M. T. 2014. Linear Stability Analysis of Binary Compressible Mixing Layers Modified By a Jet or a Wake Deficit. *Pages 1–13 of: 52nd AIAA Aerospace Sciences Meeting and Exhibit*.

Salemi, L., and Mendonca, M. T. 2008. Spatial and Temporal Linear Stability Analysis of Binary Compressible Shear Layer. *Pages 1–23 of: AIAA 38th Fluid Dynamics Conference*. AIAA paper 2008-3841.

Shin, D. S. 2011. Stability analysis of reacting mixing layers with density gradient and wake deficit. *Journal of Mechanical Science and Technology*, **25**(3), 683–688.

Zhuang, M., and Dimotakis, P. E. 1995. Instability of wake-dominated compressible mixing layers. *Physics of Fluids*, **10**, 2489–2495.

7. Responsibility notice

The author(s) is (are) the only responsible for the printed material included in this paper

8. APPENDIX

8.1 Modified Rayleigh Equation

Decomposing the instantaneous flow variables into a base component Φ_b and a disturbance component ϕ_d and searching for normal mode solutions to the incompressible disturbance equations (mass, x momentum and y momentum)

$$\Phi_b(y) + \phi_d(x, y, t) = \Phi_b(y) + \phi(y) \exp\left(i\alpha x - i\omega t\right),$$

the following equations result

$$i\alpha u + v' = 0 \qquad \text{such that} \quad \rightarrow \qquad u = \frac{iv'}{\alpha},$$

$$i\alpha(U-c)u + U'v + i\alpha p = 0,$$

$$i\alpha(U-c)v + p' = 0,$$

where, for a given variable ϕ, $\phi' = d\phi/dy$.

Using the first equation to eliminate u from the second and defining (Gropengeiser, 1970)

$$\chi = \frac{i\alpha p}{v} \qquad \text{such that} \quad \rightarrow \qquad p = -\frac{i\chi v}{\alpha}, \quad \text{and} \quad p' = -\frac{i}{\alpha}(\chi' v + \chi v'),$$

results

$$-(U-c)v' + U'v + \chi v = 0,$$

or in terms of v

$$v = \frac{(u-c)v'}{(U' + \chi)}.$$

Given p' above inserted into the y momentum equation results

$$i\alpha(U-c)v - \frac{i}{\alpha}\chi' v - \frac{i}{\alpha}\chi v' = 0.$$

Inserting v from the expression above into this last version of the y momentum equation, results

$$\alpha^2(U-c)^2 - \chi'(U-c) - \chi(\chi + U') = 0,$$

or rearranging

$$\chi' = \alpha^2(U-c) - \frac{\chi(\chi + U')}{(U-c)}.$$

Which is the final version of the stability equation used in this work.

VERIFICATION AND VALIDATION OF A HIGH-ORDER LAMINAR-TURBULENT NUMERICAL CODE

Patrícia Sartori, psartori26@gmail.com
Larissa Alves Petri, lariss@gmail.com
Leandro Franco de Souza, lefraso@gmail.com
Institute of Mathematical and Computer Sciences, University of São Paulo. São Carlos-SP, Brazil.

Abstract. *The verification of a numerical code is carried out using the Method of Manufactured Solutions. Numerical results from the Direct Numerical Simulation code are also compared in a boundary layer over an airfoil with experimental and Linear Stability Theory results. Characteristics from the boundary layer, as displacement thickness, momentum thickness and shape factor, are taken into consideration. Comparisons considering the amplitude of the velocity disturbance caused by two-dimensional Tollmien-Schlichting waves are also made. The results shows that the DNS code is verified and validated.*

Keywords: *Boundary Layer Flow, High-Order Compact Finite Differences, Direct Numerical Simulation, Verification and Validation, Method of Manufactured Solutions*

1. INTRODUCTION

The numerical studies aiming the simulation of boundary layer flows has been the focus of many researchers in CFD. Due to the great importance of these numerical predictions for practical applications, the credibility of mathematical models and numerical methods is a factor that should be investigated. Validation and Verification is the field of study that provides different techniques to quantify how reliable is a simulation code.

The no-slip condition on a solid body reduces the velocities of the outer flow to zero on the surface. This reduction generates large velocity gradients in a thin layer adjacent to the surface of the body. This layer is the boundary layer, in which strong viscous effects exist (Currie, 2003). The boundary layer is directly affected by the outer flow (Reed et al., 1996; White, 2006). The presence of a favorable pressure gradient causes the outer flow to accelerate and stabilizes the boundary layer flow. On the other hand, the presence of an adverse pressure gradient decelerates the outer flow and increases the instability of the boundary layer. An increasing instability leads to transition to turbulence and predicting the location of the transition point is still a challenge. Experimental and numerical studies are being used to explain and predict this phenomenon.

In this paper, the results carried out by a Direct Numerical Simulation (DNS) code are verified through the Method of Manufactured Solutions (MMS). This is the most efficient method for verification of codes. The basic idea is producing a solution and transforming the original set of governing equations into a set of similar equations where the exact solution is available. In this sense, this paper presents a verification study of the DNS code using MMS.

A comparison of the amplification rate of Tollmien-Schlichting waves in a boundary layer to Linear Stability Theory (LST) and to experimental results were also used to verify and validate the code. Small disturbances produce Tollmien-Schlichting (TS) waves in the flow. The growth or decay of this waves indicates if the flow is stable or unstable. According to LST, when the amplitudes of these waves are small, they can grow until certain point (neutral curve) and start to decay. Based on this, TS waves were introduced in the flow, in order to study the disturbance caused by them in the velocity profile. The amplitude of the disturbance in the streamwise direction was also compared between experimental, LST and numerical results with the aim of verifying and validating the DNS code.

The governing equations are the incompressible Navier-Stokes equations written in vorticity-velocity formulation. The numerical method adopted is based on high-order finite difference approximations for the discretization of the streamwise and wall-normal spatial derivatives. In the spanwise direction a spectral method based on Fast Fourier Transformation is applied. The time integration is carried out by a fourth-order Runge-Kutta scheme.

2. FORMULATION

In this section the governing equations are presented.

2.1 Governing equations

The governing equations are the Navier-Stokes equations written in orthogonal coordinates for incompressible flow with constant viscosity. The non-dimensional equations are considered for the results presented in this research. The

non-dimensionalization is made based on the Reynolds number, given by:

$$Re = \frac{\tilde{U}_\infty \tilde{L}}{\tilde{\nu}}, \tag{1}$$

where $\tilde{U}_\infty$ is the reference velocity, $\tilde{L}$ is the reference length and $\tilde{\nu}$ is the kinematic viscosity. The reference velocity is the free stream velocity and the reference length is a distance from the leading edge.

The non-dimensional variables are written as:

$$\begin{aligned} &x = \frac{\tilde{x}}{\tilde{L}}; \quad y = \frac{\tilde{y}\sqrt{Re}}{\tilde{L}}; \quad z = \frac{\tilde{z}}{\tilde{L}}; \quad u = \frac{\tilde{u}}{\tilde{U}_\infty}; \quad v = \frac{\tilde{v}\sqrt{Re}}{\tilde{U}_\infty}; \quad w = \frac{\tilde{w}}{\tilde{U}_\infty}; \\ &\omega_x = \frac{\tilde{w}_x \tilde{L}}{\tilde{U}_\infty \sqrt{Re}}; \quad \omega_y = \frac{\tilde{w}_y \tilde{L}}{\tilde{U}_\infty}; \quad \omega_z = \frac{\tilde{w}_z \tilde{L}}{\tilde{U}_\infty \sqrt{Re}}; \quad t = \frac{\tilde{t}\tilde{U}_\infty}{\tilde{L}}, \end{aligned} \tag{2}$$

where the variables with a tilde denote dimensional variables; x, y and z are the spatial coordinates, in streamwise, normal and spanwise directions, respectively; u, v and w are the velocity components in each direction; ω_x, ω_y and ω_z are the vorticity components in each direction; and t is the time.

The vorticity can be defined as the negative curl of the velocity vector and the vorticity component in each direction can be written as:

$$\omega_x = \frac{1}{Re}\frac{\partial v}{\partial z} - \frac{\partial w}{\partial y}, \tag{3}$$

$$\omega_y = \frac{\partial w}{\partial x} - \frac{\partial u}{\partial z}, \tag{4}$$

$$\omega_z = \frac{\partial u}{\partial y} - \frac{1}{Re}\frac{\partial v}{\partial x}. \tag{5}$$

Using the fact that both velocity and vorticity fields are solenoidal, one can obtain the following vorticity transport equation in each direction:

$$\frac{\partial \omega_x}{\partial t} + \frac{\partial a}{\partial y} - \frac{\partial b}{\partial z} = \nabla^2 \omega_x, \tag{6}$$

$$\frac{\partial \omega_y}{\partial t} + \frac{\partial c}{\partial z} - \frac{\partial a}{\partial x} = \nabla^2 \omega_y, \tag{7}$$

$$\frac{\partial \omega_z}{\partial t} + \frac{\partial b}{\partial x} - \frac{\partial c}{\partial y} = \nabla^2 \omega_z, \tag{8}$$

where

$$a = v\omega_x - u\omega_y, \tag{9}$$

$$b = u\omega_z - w\omega_x, \tag{10}$$

$$c = w\omega_y - v\omega_z, \tag{11}$$

are the nonlinear terms resulting from convection, vortex stretching and vortex bending. The Laplace operator is:

$$\nabla^2 = \frac{1}{Re}\left(\frac{\partial^2}{\partial x^2} + \frac{\partial^2}{\partial z^2}\right) + \frac{\partial^2}{\partial y^2}. \tag{12}$$

The continuity equation is given by:

$$\frac{\partial u}{\partial x} + \frac{\partial v}{\partial y} + \frac{\partial w}{\partial z} = 0. \tag{13}$$

Taking the definition of the vorticity and the mass conservation equation, one can obtain Poisson-type equations for each velocity component:

$$\frac{\partial^2 u}{\partial x^2} + \frac{\partial^2 u}{\partial z^2} = -\frac{\partial \omega_y}{\partial z} - \frac{\partial^2 v}{\partial x \partial y}, \tag{14}$$

$$\nabla^2 v = -\frac{\partial \omega_z}{\partial x} + \frac{\partial \omega_x}{\partial z}, \tag{15}$$

$$\frac{\partial^2 w}{\partial x^2} + \frac{\partial^2 w}{\partial z^2} = \frac{\partial \omega_y}{\partial x} - \frac{\partial^2 v}{\partial y \partial z}. \tag{16}$$

The set of Eqs. (6)-(8) and (14)-(16) describes the flow being simulated and will be solved in the integration domain defined in the next section.

2.2 Reference system and integration domain

The reference system considered for the numerical procedure is shown in Fig. 1. The x-axis lies on the surface, in the streamwise direction and its zero position is a certain distance from the leading edge. The y-axis is normal to the surface and its coordinate is zero at the surface, and assume positive values within the boundary layer. The z-axis is in the spanwise direction, parallel to the leading edge, and is oriented so that the resulting system is right-handed.

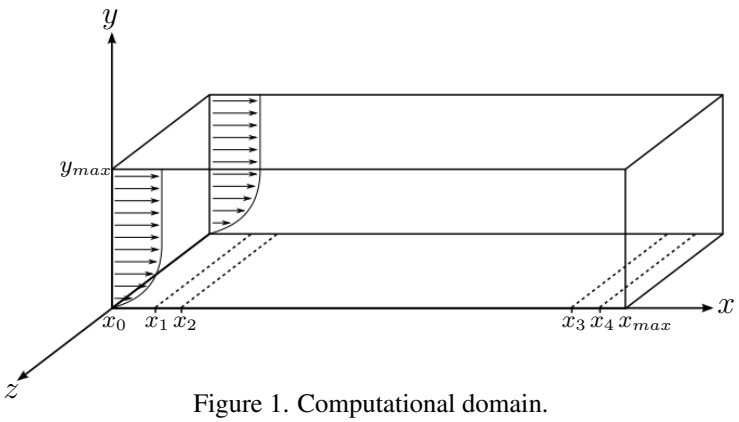

Figure 1. Computational domain.

In the streamwise direction the domain goes from x_0, a certain distance from the leading edge, to x_{max}. In the normal direction, the domain starts at the surface ($y = 0$) and ends in y_{max}. y_{max} is large enough to guarantee that the vorticity components are zero at the boundary. In the spanwise direction the flow is considered periodic and the domain starts at $z = 0$ and ends at $z = \lambda_z$, where λ_z is the fundamental wavelength in z direction.

The disturbance strip is located between points x_1 and x_2. These disturbances are introduced by mass suction and blowing. Points x_0 and x_1, and x_3 and x_4 determine the relaminarization zones. These zones are used to avoid numerical reflexions of the disturbances at the inflow and outflow boundaries, respectively.

2.3 Baseflow

To initiate the numerical simulation, a baseflow should be calculated, and its computation can be carried out considering a two-dimensional domain. This is not necessary for the MMS tests, as the initial condition is given by the manufactured solution.

First of all, a Falkner-Skan (FS) equation is solved, considering the experimental data as boundary condition. This solution is used as initial condition for the baseflow simulation. The baseflow simulation removes simplification errors from the Falkner-Skan equations.

The two-dimensional equations for the baseflow are:

$$\frac{\partial \omega_{z_b}}{\partial t} + \frac{\partial (u_b \omega_{z_b})}{\partial x} + \frac{\partial (v_b \omega_{z_b})}{\partial y} = \frac{1}{Re}\frac{\partial^2 \omega_{z_b}}{\partial x^2} + \frac{\partial^2 \omega_{z_b}}{\partial y^2}, \tag{17}$$

$$\frac{1}{Re}\frac{\partial^2 v_b}{\partial x^2} + \frac{\partial^2 v_b}{\partial y^2} = -\frac{\partial \omega_{z_b}}{\partial x}, \tag{18}$$

$$\frac{\partial v_b}{\partial y} = -\frac{\partial u_b}{\partial x}. \tag{19}$$

The code that solves the baseflow equations has the same structure as the one used to solve the three-dimensional problem, without the disturbances. For the baseflow simulation, the code is executed until it reaches the steady state, i.e. until the differences in the vorticity values between two consecutive time steps were smaller than 10^{-9}.

3. NUMERICAL METHOD

The equations presented above are discretized by high-order finite differences schemes and spectral approximations for the spatial derivatives. A fourth-order four-step Runge-Kutta method is used for the temporal discretization.

3.1 Discretization of field equations

As the physical phenomena involve a large number of scales in time and space, the numerical code needs to have non-dissipative and non-dispersive characteristics to represent all the relevant scales. For this reason, a numerical integrator

of Runge-Kutta type with 4^{th}-order precision is used. Moreover, the spatial derivatives are calculated using high-order compact finite difference methods in x and y directions and spectral method in the z direction.

As the phenomenon under investigation is concentrated near the surface, a large amount of points is necessary in this region. With the aim of reducing the total amount of points, a grid stretching is used in the normal direction (Babucke and Kloker, 2009). The coefficient matrices for the derivative calculation and for the Poisson equation solution, suggested by (Linnick and Fasel, 2005), were used.

3.2 Spectral method

The flow is assumed to be periodic in the spanwise direction. Therefore, the flow field can be expanded in Fourier series with K spanwise Fourier modes, as follows:

$$g(x,y,z,t) = \sum_{k=0}^{K} G_k(x,y,t) e^{(-i\beta_k z)}, \tag{20}$$

where

$$g = \{u, v, w, \omega_x, \omega_y, \omega_z, a, b, c, f_x, f_y, f_z\} \tag{21}$$

represents the variables in the physical space;

$$G_k = \{U_k, V_k, W_k, \Omega_{x_k}, \Omega_{y_k}, \Omega_{z_k}, A_k, B_k, C_k, F_{x_k}, F_{y_k}, F_{z_k}\} \tag{22}$$

represents the variables in the Fourier space; β is the spanwise wavenumber, given by $\beta_k = \dfrac{2\pi k}{\lambda_z}$; λ_z is the spanwise wavelength of the fundamental spanwise Fourier mode; $i = \sqrt{-1}$; and k is the Fourier mode, that ranges from 0 to K.

Note that G_k may be fully complex, i.e., non-symmetric three-dimensional disturbance fields can be computed. The nonlinear terms are computed pseudospectrally, i.e. by transformation of all flow variables to physical space, computing the nonlinear terms at consecutive spanwise stations, and transforming the products back to Fourier space.

The substitution the Fourier transforms (Eq. (20)) in the vorticity transport equations (Eq. (6) – Eq. (8)) and in the velocity Poisson equations (Eq. (14) – Eq. (16)) yields the governing equations in the Fourier space, for each Fourier mode k:

$$\frac{\partial \Omega_{x_k}}{\partial t} + \frac{\partial A_k}{\partial y} + \beta_k B_k = \nabla_k^2 \Omega_{x_k}, \tag{23}$$

$$\frac{\partial \Omega_{y_k}}{\partial t} - \beta_k C_k - \frac{\partial A_k}{\partial x} = \nabla_k^2 \Omega_{y_k}, \tag{24}$$

$$\frac{\partial \Omega_{z_k}}{\partial t} + \frac{\partial B_k}{\partial x} - \frac{\partial C_k}{\partial y} = \nabla_k^2 \Omega_{z_k}, \tag{25}$$

$$\frac{\partial^2 U_k}{\partial x^2} - \beta_k^2 U_k = \beta_k \Omega_{y_k} - \frac{\partial^2 V_k}{\partial x \partial y}, \tag{26}$$

$$\nabla^2 V_k = -\frac{\partial \Omega_{z_k}}{\partial x} - \beta_k \Omega_{x_k}, \tag{27}$$

$$\frac{\partial^2 W_k}{\partial x^2} - \beta_k^2 W_k = \frac{\partial \Omega_{y_k}}{\partial x} + \beta_k \frac{\partial V_k}{\partial y}, \tag{28}$$

where

$$\nabla_k^2 = \left[\frac{1}{Re} \left(\frac{\partial^2}{\partial x^2} - \beta_k^2 \right) + \frac{\partial^2}{\partial y^2} \right]. \tag{29}$$

The time derivatives in the vorticity transport equations are discretized with the fourth-order Runge-Kutta integration scheme of Xu and Wang (2006). The spatial derivatives are calculated using a high-order compact finite difference schemes (Lele, 1992; Kloker, 1998; Souza, 2003; Souza et al., 2005). The V-Poisson equation (Eq. (27)) is solved using a multigrid Full Approximation Scheme (FAS) (Stüben and Trottenberg, 1981). A V-cycle with 4 grids is implemented. The code is parallelized, using domain decomposition in the streamwise direction.

3.3 Boundary conditions

At the wall ($y = 0$), a no-slip condition is imposed for the streamwise (U_k) and the spanwise (W_k) velocity components. The wall-normal velocity component (V_k) is specified at the suction and blowing strip, where the disturbances are introduced. Away from the disturbance region this velocity component is set to zero. The function used for the wall-normal velocity at the disturbance generator strip is:

$$V_k(x, 0, t) = A f_p(x) \sin(\omega_{t_k} t + \theta_k) \qquad \text{for} \qquad x_1 \leq x \leq x_2, \tag{30}$$

where A and θ_k are real constants chosen to adjust the amplitude and phase of the disturbance, and ω_{t_k} is the dimensionless frequency. The function $f_p(x)$ is of ninth-order and ensures that the discontinuities at $y = 0$ in the vertical velocity component, its first and second derivatives are avoided at the edges of the suction and blowing region.

At the inflow boundary ($x = x_0$), the velocity and vorticity components are specified based on the Falkner-Skan boundary layer solution. At the outflow boundary ($x = x_{max}$), the second derivatives with respect to the streamwise direction of the velocity and vorticity components are set to zero. At the upper boundary ($y = y_{max}$) the flow is considered non rotational. This is satisfied by setting all vorticity components and their derivatives to zero. The wall-normal velocity component at the upper boundary is settled according to the condition:

$$\frac{\partial V_k}{\partial y}|_{x, y_{max}, t} = -\frac{\alpha^*}{\sqrt{Re}} V_k(x, y_{max}, t), \tag{31}$$

where $\alpha^* = \sqrt{\alpha^2 + k^2\beta^2}$.

In addition, at the wall ($y = 0$), the condition $\dfrac{\partial V_k}{\partial y} = 0$ is imposed in the solution of the Poisson equation (Eq. (26)), to ensure mass conservation. The equations used for evaluating the vorticity components at the wall are:

$$\frac{\partial^2 \Omega_{x_k}}{\partial x^2} - \beta_k^2 \Omega_{x_k} = -\frac{\partial^2 \Omega_{y_k}}{\partial x \partial y} - \beta_k \nabla_k^2 V_k, \tag{32}$$

$$\frac{\partial \Omega_{z_k}}{\partial x} = \beta_k \Omega_{x_k} - \nabla_k^2 V_k. \tag{33}$$

3.4 Relaminarization

A damping zone near the outflow boundary is defined in which all disturbances are gradually damped down to zero (Kloker and Konzelmann, 1993) so that reflections in the outflow boundary are avoided. The basic idea is to multiply the vorticity components by a ramp function $f_1(x)$ after each sub-step of the integration method. Using this technique, the vorticity components are taken as:

$$\Omega_k(x, y, t) = f_1(x) \Omega_k^*(x, y, t), \tag{34}$$

where $\Omega_k^*(x, y, t)$ is the disturbance vorticity component that results from the Runge-Kutta integration and $f_1(x)$ is a ramp function that goes from 1 to 0. The implemented function is:

$$f_1(x) = f_1(\epsilon) = (1 - \epsilon^{50})^4 e^{-\frac{\epsilon^4}{10}}, \tag{35}$$

where

$$\epsilon = \frac{x - x_3}{x_4 - x_3} \qquad \text{for} \qquad x_3 \leq x \leq x_4. \tag{36}$$

To ensure good numerical results and efficiency a minimum distance between x_3 and x_4 and between x_4 and the end of the domain x_{max} had to be studied. In the present study, 100 points between x_3 and x_4 and 40 points between x_4 and x_{max} were considered.

Another buffer domain, located near the inflow boundary is also implemented in the code. Meitz (1996) adopted a fifth-order polynomial, and a similar function is used in the present model:

$$f_2(x) = f_2(\epsilon) = 6\epsilon^5 - 15\epsilon^4 + 10\epsilon^3 \tag{37}$$

where

$$\epsilon = \frac{x - x_0}{x_1 - x_0} \qquad \text{for} \qquad x_0 \leq x \leq x_1. \tag{38}$$

All vorticity components are multiplied by this function in this region.

4. VERIFICATION X VALIDATION

The words "verification" and "validation" have different meanings in CFD. There are two phrases that are widely used in the literature (Roache, 1998; Oberkampf and Trucano, 2002) to explain this difference:

- Verification: *Are we solving the equations right?*
- Validation: *Are we solving the right equations?*

According to Roache (1997) and Oberkampf and Trucano (2002), validation is related to the capacity of the model to represent the physical problem, i.e. the numerical code must solve the correct equations representing the physical problem. Moreover, the verification relates to the correct implementation of the model in a computational code, in other words, to solve properly the equations that describes the model.

In the next section, the verification of the DNS code is presented through comparisons with MMS and LST results, and its validation is shown by means of comparisons between experimental and numerical results.

5. RESULTS

In this section, the verification of the numerical code by means of the MMS is presented. The overall convergence order obtained for the velocity and vorticity components are also shown.

The validation of the DNS code is shown, by means of comparisons between experimental and numerical results. In Sec. 5.2 boundary layer characteristics are compared and in Sec. 5.3 the variation of the amplitude of the streamwise velocity disturbance, caused by Tollmien-Schlichting (TS) waves in the boundary layer, are presented.

The experimental results were performed in the laminar wind tunnel of the Institute of Aerodynamics and Gas Dynamics (IAG) of the University of Stuttgart (Plogmann et al., 2012).

5.1 Method of Manufactured Solutions - MMS

The method of manufactured solutions is the most efficient method for code verification and has been widely used in the scientific community (Roache, 1998; Salari and Knupp, 2000; Roy, 2005; Eça et al., 2007).

In principle, it is not necessary that the manufactured solution satisfies the Partial Differential Equations (PDE). Instead, after the generation of the manufactured solution for all the unknown variables of the problem, they must be inserted into the original PDE so that all derivatives can be calculated analytically. Then, the original PDE is rearranged and the terms in excess are grouped into a source term that must be placed on the right side of the equation. As a result, the creation of a modified problem in which the solution is known allow the comparison between the exact and numerical solutions.

Initially a manufactured solution was proposed for the boundary layer code, in which a term with exponential decay in the wall normal direction was introduced. The results have shown that the term with exponential decay is responsible to reduce the formal overall order of the numerical method. Then, only trigonometric and polynomial functions were used to generate the manufactured solution.

The manufactured solutions proposed are:

$$u = -\sin(\alpha x)\sin(\alpha z)P'(y), \tag{39}$$

$$v = \alpha\cos(\alpha x)\cos(\alpha z)P(y), \tag{40}$$

$$w = -\cos(\alpha x)\cos(\alpha z)P'(y) - \cos(\alpha x)\sin(\alpha z)P'(y), \tag{41}$$

with the polynomial $P(y)$ given by:

$$P(y) = \frac{y^5}{b^4} - \frac{y^4}{b^3} - \frac{y^3}{b^2} + \frac{y^2}{b}, \qquad b = dy(j_{max} - 1), \tag{42}$$

where dy and j_{max} the grid spacing and the maximum number of points in the normal direction, respectively. The vorticity components are computed analytically through Eqs. (3) – (5). It is worth mentioning that the velocity components satisfy the continuity equation.

The simulations were carried out using different amounts of points and grid spacing to get the overall order. This order was checked using L_1, L_2 and L_∞ error norms for the velocity and vorticity components. The order of accuracy is given by:

$$p \approx \frac{\log\left(\frac{||E_h||}{||E_{\frac{h}{2}}||}\right)}{\log r}, \tag{43}$$

where h is the grid spacing and $r = \dfrac{h}{\frac{h}{2}}$ is the grid refinement factor.

For the MMS simulation was considered the domain of Fig. 1, with dimensions $12.8 \times 12.8 \times 6.086$. The Reynolds number was $Re = 322,326$ and 11 Fourier modes were used (considering 32 points in the pysical space).

First of all, 4 meshes without stretching were considered: 65×65, 129×129, 257×257 and 513×513. In Tab. 1 the norm of the error and the convergence order obtained with these meshes are shown. The results obtained for DNS code verification showed that the overall order for the velocity components are between 2.9 and 4.7. The analysis of the vorticity components showed results between 3 and 5.5.

Table 1. Error norm and convergence order for velocity and vorticity components calculated with MMS.

Mesh	Variable	Norm L_1	Order	Norm L_2	Order	Norm L_∞	Order
65×65	u_x	1.80×10^{-7}	-	9.07×10^{-7}	-	2.98×10^{-5}	-
	u_y	3.32×10^{-7}	-	1.32×10^{-6}	-	1.08×10^{-5}	-
	u_z	1.67×10^{-7}	-	8.52×10^{-7}	-	3.12×10^{-5}	-
	ω_x	2.85×10^{-8}	-	2.35×10^{-7}	-	1.11×10^{-5}	-
	ω_y	1.14×10^{-7}	-	1.57×10^{-6}	-	6.29×10^{-5}	-
	ω_z	6.97×10^{-8}	-	5.59×10^{-7}	-	1.20×10^{-5}	-
129×129	u_x	6.65×10^{-9}	4.76	7.39×10^{-8}	3.62	3.90×10^{-6}	2.93
	u_y	2.02×10^{-8}	4.03	8.55×10^{-8}	3.95	7.95×10^{-7}	3.76
	u_z	6.42×10^{-9}	4.70	6.88×10^{-8}	3.63	4.06×10^{-6}	2.94
	ω_x	1.29×10^{-9}	4.47	1.76×10^{-8}	3.74	1.04×10^{-6}	3.43
	ω_y	2.42×10^{-9}	5.56	3.75×10^{-8}	5.39	2.07×10^{-6}	4.93
	ω_z	1.66×10^{-9}	5.39	1.99×10^{-8}	4.81	1.11×10^{-6}	3.44
257×257	u_x	4.09×10^{-10}	4.02	6.81×10^{-9}	3.44	5.01×10^{-7}	2.96
	u_y	1.39×10^{-9}	3.87	6.08×10^{-9}	3.81	9.41×10^{-8}	3.08
	u_z	3.97×10^{-10}	4.02	6.29×10^{-9}	3.45	5.15×10^{-7}	2.98
	ω_x	7.71×10^{-11}	4.06	1.48×10^{-9}	3.57	1.26×10^{-7}	3.04
	ω_y	8.09×10^{-11}	4.90	8.65×10^{-10}	5.44	6.40×10^{-8}	5.02
	ω_z	6.14×10^{-11}	4.76	1.30×10^{-9}	3.94	1.26×10^{-7}	3.13
513×513	u_x	3.49×10^{-11}	3.55	6.37×10^{-10}	3.42	6.34×10^{-8}	2.98
	u_y	1.03×10^{-10}	3.76	5.07×10^{-10}	3.58	1.14×10^{-8}	3.04
	u_z	3.39×10^{-11}	3.55	5.87×10^{-10}	3.42	6.49×10^{-8}	2.99
	ω_x	5.51×10^{-12}	3.81	1.30×10^{-10}	3.52	1.56×10^{-8}	3.02
	ω_y	5.07×10^{-12}	4.00	3.07×10^{-11}	4.82	1.90×10^{-9}	5.08
	ω_z	3.57×10^{-12}	4.10	1.09×10^{-10}	3.58	1.54×10^{-8}	3.03

A second test, considering meshes with stretching in the normal direction was made. Each mesh has a different stretching value to ensure that the points coincide among them, in order to enable the calculation of the error. The meshes and its stretching are given in Tab. 2. The results obtained with the meshes of Tab. 2 are presented in Tab. 3. The convergence order for the velocity components are between 2.6 and 3.4, and for the vorticity components are between 2.5 and 5.

Table 2. Amount of points for each mesh and its stretching.

Points in x direction	Points in y direction	Stretching
65	33	1.0406
129	65	1.0201
257	129	1.01
513	257	1.005

In both cases the decay of the error can be noticed. It also can be seen that the use of stretching in the normal direction reduces the overall order of the numerical code. However, this fact occurs near the upper boundary and, in the case of boundary layer studies, the main physical phenomena occurs close to the wall. For this reason, there is no influence of these errors in the problem under investigation.

5.2 Baseflow characteristics

The formation of the boundary layer is analyzed in this section comparing some boundary layer characteristics. The characteristics considered here are the following: streamwise velocity component at the boundary layer edge, displacement thickness, momentum thickness and shape factor.

Table 3. Error norm and convergence order for velocity and vorticity components calculated with MMS.

Mesh	Variable	Norm L_1	Order	Norm L_2	Order	Norm L_∞	Order
65×33	u_x	3.61×10^{-6}	-	5.35×10^{-5}	-	1.53×10^{-3}	-
	u_y	2.10×10^{-6}	-	2.11×10^{-5}	-	5.81×10^{-4}	-
	u_z	3.36×10^{-6}	-	5.27×10^{-5}	-	1.61×10^{-3}	-
	ω_x	1.21×10^{-6}	-	1.64×10^{-5}	-	5.18×10^{-4}	-
	ω_y	2.41×10^{-7}	-	1.95×10^{-6}	-	6.19×10^{-5}	-
	ω_z	1.54×10^{-6}	-	1.76×10^{-5}	-	3.55×10^{-4}	-
129×65	u_x	3.31×10^{-7}	3.45	6.41×10^{-6}	3.06	2.47×10^{-4}	2.63
	u_y	2.28×10^{-7}	3.20	2.78×10^{-6}	2.93	8.69×10^{-5}	2.74
	u_z	3.10×10^{-7}	3.44	6.14×10^{-6}	3.10	2.59×10^{-4}	2.63
	ω_x	5.09×10^{-8}	4.57	7.67×10^{-7}	4.42	3.18×10^{-5}	4.02
	ω_y	2.00×10^{-8}	3.59	1.77×10^{-7}	3.46	4.39×10^{-6}	3.82
	ω_z	4.65×10^{-8}	5.05	6.98×10^{-7}	4.66	2.11×10^{-5}	4.07
257×129	u_x	3.01×10^{-8}	3.46	6.66×10^{-7}	3.27	3.47×10^{-5}	2.83
	u_y	2.59×10^{-8}	3.14	3.49×10^{-7}	2.99	1.18×10^{-5}	2.88
	u_z	2.86×10^{-8}	3.44	6.27×10^{-7}	3.29	3.63×10^{-5}	2.84
	ω_x	2.92×10^{-9}	4.12	4.02×10^{-8}	4.26	1.51×10^{-6}	4.39
	ω_y	2.21×10^{-9}	3.18	2.15×10^{-8}	3.04	7.39×10^{-7}	2.57
	ω_z	1.55×10^{-9}	4.91	2.46×10^{-8}	4.83	1.25×10^{-6}	4.08
513×257	u_x	2.92×10^{-9}	3.37	6.60×10^{-8}	3.34	4.60×10^{-6}	2.92
	u_y	2.99×10^{-9}	3.11	4.25×10^{-8}	3.04	1.54×10^{-6}	2.94
	u_z	2.80×10^{-9}	3.35	6.17×10^{-8}	3.35	4.80×10^{-6}	2.92
	ω_x	2.61×10^{-10}	3.48	3.55×10^{-9}	3.50	1.63×10^{-7}	3.22
	ω_y	2.57×10^{-10}	3.10	2.61×10^{-9}	3.04	1.30×10^{-7}	2.50
	ω_z	1.15×10^{-10}	3.75	1.54×10^{-9}	4.00	1.50×10^{-7}	3.06

The integral boundary layer characteristics are defined by:

- displacement thickness:

$$\delta_1 = \int_{y=0}^{\infty} \left(1 - \frac{u}{\tilde{U}_\infty}\right) dy; \tag{44}$$

- momentum thickness:

$$\delta_2 = \frac{u}{\tilde{U}_\infty} \int_{y=0}^{\infty} \left(1 - \frac{u}{\tilde{U}_\infty}\right) dy; \tag{45}$$

- shape factor:

$$H_{12} = \frac{\delta_1}{\delta_2}. \tag{46}$$

In the 2D-DNS code the following parameters were considered: velocity scale $\tilde{U}_{\infty,x_0} = 27.935$m/s , where $\tilde{U}_{\infty,x_0} = \tilde{U}_\infty|_{x_0}$, i. e., $\tilde{U}_\infty$ at the initial point of the domain; length scale $\tilde{L} = 0.18$m; kinematic viscosity $\tilde{\nu} = 1.56 \times 10^{-5}$m^2/s; domain size $1,177 \times 177$ points in streamwise and wall-normal directions; respectively; grid space $dx = 3.125 \times 10^{-3}$ and $dy_0 = 1.8 \times 10^{-4}$ in streamwise and wall-normal directions, respectively, with stretching of mesh in wall-normal direction of 1%.

For the comparison, three results are presented: experimental, theoretical boundary layer profile, and 2D-DNS. The theoretical boundary layer profile uses the finite difference scheme given by Cebeci and Smith (1974). Figure 2 shows the baseflow characteristics for decelerated flow. The streamwise coordinate is non-dimensionalized by the roughness diameter $d_r = 20mm$.

It is possible to see that all numerical results are close to the experimental and theoretical ones. Good agreements were obtained in the velocity profiles and boundary layer integral parameters. This results show that the 2D-DNS code was capable to simulate the flow in agreement with the experimental results. This fact allowed the validation of this code.

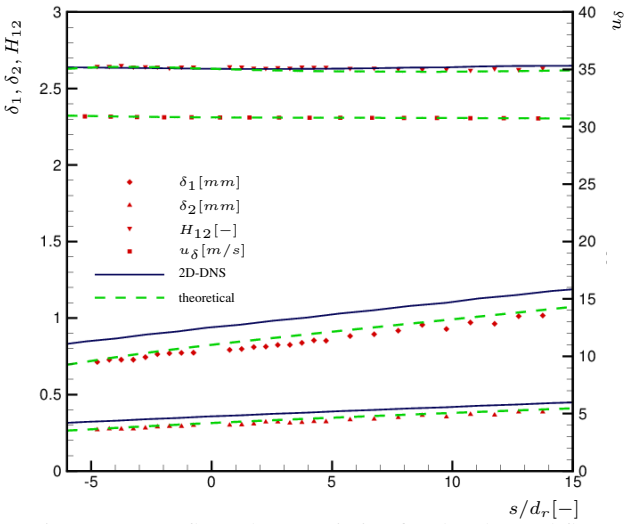

Figure 2. Baseflow characteristics for decelerated flow.

5.3 Downstream development of modal amplitudes

After validating the code for a boundary layer flow, a linear stability test was made. For this test, disturbances with an infinitesimal amplitude were introduced via mass suction and blowing in the region located between x_1 and x_2 (see Fig. 1). These disturbances produce TS waves in the velocity field. The spatial evolution of these waves are measured and compared to LST and experimental results. The amplitude of the TS waves is small enough to neglect the nonlinear products.

The variation in the amplitude of the maximum value of the disturbance of the streamwise velocity component u over the wall-normal direction y, is defined as:

$$amp = \max_y(u'(1,0)), \tag{47}$$

where u' is the disturbance of the velocity.

The parameters used for the 3D-DNS code are the same as those for the 2D-DNS code, with wavelength in spanwise direction $\lambda_z = 0.4$m. Three frequencies were considered: $F = 396$Hz, 549Hz and 701Hz. Figure 3 shows the variation in the amplitude of the disturbance u' in streamwise direction for these cases.

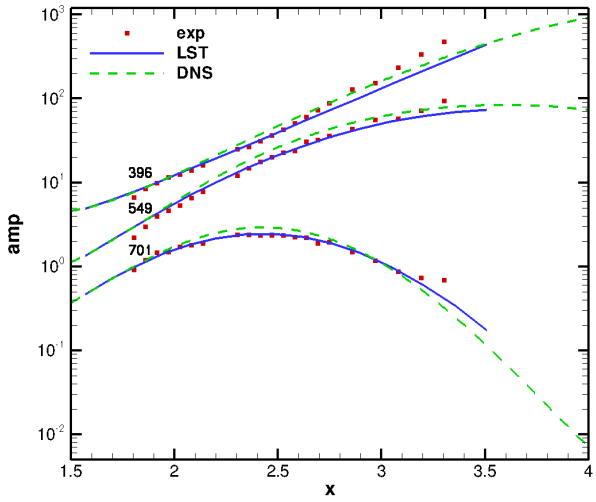

Figure 3. Amplitude of perturbation of the streamwise velocity component (amp - in log scale) in streamwise direction x for the flow with adverse pressure gradient, with frequencies $F = 396$Hz, 549Hz and 701Hz.

It can be noticed that the 3D-DNS numerical results agree with both the experimental and the LST code results. With these comparisons it is possible to say that the code is capable of simulating the spatial development of TS waves properly.

6. CONCLUSION

The MMS results showed that the numerical code has an overall order of at least 2.5. The results also show that experimental data and numerical solution are in good agreement in the formation of the boundary layer. Experimental, LST and numerical results also agree in the development of Tolmmien–Schlichting waves in a boundary layer. In this sense, the DNS code can be considered verified and validated.

7. ACKNOWLEDGEMENTS

The authors acknowledge Benjamin Plogmann and Werner Würz for providing the experimental results and assistance in the analysis of the comparisons.

The authors also acknowledge the financial support received from FAPESP under grants 2010/00880-2, 2011/00647-9, 2011/19215-1 and 2012/25121-2.

8. REFERENCES

Babucke, A. and Kloker, M.J., 2009. "Accuracy analysis of finite-difference methods on non-uniform grids". Technical report, Institut für Aerodynamik und Gasdynamik.

Cebeci, T. and Smith, A.M.O., 1974. "Analysis of turbulent boundary layers". Academic Press, Inc.

Currie, I.G., 2003. "Fundamental Mechanics of Fluids". Marcel Dekker, Inc.

Eça, L., Hoekstra, M., Hay, A. and Pelletier, D., 2007. "Verification of RANS solvers with manufactured solutions". Engineering with Computers, Vol. 23, pp. 253–270.

Kloker, M. and Konzelmann, U., 1993. "Outflow boundary conditions for spacial Navier-Stokes simulations of transition boundary layers". AIAA Journal, Vol. 31, pp. 620–628.

Kloker, M.J., 1998. "A robust high-resolution split-type compact FD-scheme for spatial direct numerical simulation of boundary-layer transition". Applied Scientific Research, Vol. 59, No. 4, pp. 353–377.

Lele, S.K., 1992. "Compact finite difference schemes with spectral-like resolution". Journal of Computational Physics, Vol. 103, pp. 16–42.

Linnick, M.N. and Fasel, H.F., 2005. "A high-order immersed interface method for simulating unsteady incompressible flows on irregular domains". Journal of Computational Physics, Vol. 204, pp. 157–192.

Meitz, H.L., 1996. "Numerical investigation of suction in a transitional flat-plate boundary layer". Ph.D. thesis, University of Arizona.

Oberkampf, W.L. and Trucano, T.G., 2002. "Verification and validation in computational fluid dynamics". Progress in Aerospace Sciences, Vol. 38, pp. 209–272.

Plogmann, B., Würz, W. and Krämer, E., 2012. "Interaction of a three-dimensional roughness element with a TS-wave near an airfoil leading edge". In Procedings of the 16th International Conference on Methods of Aerophysical Research. Kazan, Russia.

Reed, H.L., Saric, W.S. and Arnal, D., 1996. "Linear stability theory applied to boundary layers". Annual Review of Fluid Mechanics, Vol. 28, pp. 389–428.

Roache, P.J., 1997. "Quantification of uncertainty in computational fluid dynamics". Annual Review of Fluid Mechanics, Vol. 29, pp. 123–160.

Roache, P.J., 1998. "Verification of codes and calculations". AIAA Journal, Vol. 36, pp. 696–702.

Roy, C.J., 2005. "Review of code and solution verification procedures for computational simulation". Journal of Computational Physics, Vol. 205, pp. 131–156.

Salari, K. and Knupp, P., 2000. "Code verification by the Method of Manufactured Solutions". Technical report, Sandia National Laboratories.

Souza, L.F., Mendonça, M.T. and Medeiros, M.A.F., 2005. "The advantages of using high-order finite differences schemes in laminar-turbulent transition studies". International Journal for Numerical Methods in Fluids, Vol. 48, pp. 565–582.

Souza, L.F.d., 2003. "Instabilidade centrífuga e transição para turbulência em escoamentos laminares sobre superfícies côncavas". Ph.D. thesis, Instituto Tecnológico de Aeronáutica.

Stüben, K. and Trottenberg, U., 1981. "Nonlinear multigrid methods, the full approximation scheme", Köln-Porz, chapter 5, pp. 58–71. Lecture Notes in Mathematics.

White, F.M., 2006. "Viscous Fluid Flow". McGraw-Hill.

Xu, S. and Wang, Z.J., 2006. "An immersed interface method for simulating the interaction of a fluid with moving boundaries". Journal of Computational Physics, Vol. 216, pp. 454–493.

9. Responsibility notice

The authors are the only responsible for the printed material included in this paper.

Stability of O2/H2 Binary Mixing Layers: Effect of Temperature Gradients, Compressibility and Three-dimensionality

Leandro Marochio Fernandes, leandro.mfernandes@ifes.edu.br
Instituto Federal de Educação, Ciência e Tecnologia do Espírito Santo, Unidade Cachoeiro de Itapemirim - IFES, ES, Brazil

Romulo Bessi Freitas, romulodnj@hotmail.com
Universidade Federal Fluminense, Laboratório de Mecânica Teórica e Aplicada, Niteroi, RJ, Brazil

Marcio T. Mendonca, marciomtm@iae.cta.br
Instituto de Aeronáutica e Espaço, Divisão de Propulsão Aeronáutica, DCTA/IAE/APA, São José dos Campos, SP, Brazil

Abstract.
The present investigation considers the stability of binary O2/H2 mixing layers of compressible base flows. The effect of strong temperature gradients across the mixing layer is considered. The base flow is computed either based on a hyperbolic tangent velocity and mass fraction profile and Crocco-Busemann relation of temperature, or on the solution of the parabolic boundary layer equations for the compressible, binary, variable properties mixing layer. The inviscid stability of these base flows are investigated through the solution of the compressible Rayleigh equations. The results show a significant difference between the hyperbolic tangent base flow results and the results for the based flow computed with the boundary layer equations.

Keywords: *mixing layer, inviscid hydrodynamic stability, normal modes stability analysis*

1. INTRODUCTION

The stability of mixing layers has been used extensively as a model problem relevant to combustion processes in propulsion devices in order to understand the parameters that affect the mixing between fuel and oxidizer. Combustion efficiency, flame stability, thermo-acoustic coupling and pollutant emissions are some of the relevant characteristics of combustion devices that depend on the proper mixing of reactants.

In the late nineties and early 2000 the problems of binary and reactive compressible mixing layers have been address and the main characteristics of such flows identified (Shin and Ferziger, 1991; Kennedy and Gatski, 1994; Kozusko *et al.* , 1996; Day *et al.* , 1998; Fedioun and Lardjane, 2005; Na *et al.* , 2006; Salemi and Mendonca, 2008; Caillol, 2009), among others. The stability of a reacting mixing layer using a base flow given by canonical hyperbolic tangent velocity profiles or the solution of the compressible boundary layer equations with variable properties and chemical reaction have been considered. Most of these works either consider constant properties of Prandtl and Lewis number equal to unit in order to simplify the solutions. A more detailed base flow computation would have to account for the fact that viscosity, heat diffusivity and other properties vary across the mixing layer both due to species concentration and temperature simultaneously.

The aim of the present investigation is to extend the work presented by Salemi and Mendonca (2008) for the stability of binary mixing layers in the compressible regime. Instead of computing the base flow through a similarity, constant properties formulation, the base flow is computed with a variable properties binary mixing layer, boundary layer code, taking into consideration the effect of species concentration and temperature gradients. This work addresses the question about the effect of large temperature gradients across the mixing layer for two and three-dimensional disturbances in compressible flow.

2. FORMULATION AND METHODOLOGY

In this section the governing equations are presented. The stability of the base flow is analysed using the compressible version of the Rayleigh equation. The base flow velocity, temperature and density profiles are computed with a boundary layer code marching from a initial position x_0, downstream of the splitter plate to a position down stream two times x_0.

2.1 Base Flow Equations

The two-dimensional, compressible, binary mixing layer base flow boundary layer equations are presented in this section (Anderson, 2000; Mendonca, 2014). The equations are nondimensionalized by the fast stream properties and the distance from the virtual plate trailing edge x_0 as length scale. The pressure is considered constant across the layer, consistent with the boundary layer approximation. The continuity equation (Eq. 1), the momentum conservation equation in the x direction (Eq. 2), the momentum conservation equation in the y direction (Eq. 3), the energy conservation

equation (Eq. 4), the species conservation equation (Eq. 5) and the perfect gas equation of state (Eq. 6) are presented below.

$$\frac{\partial(\rho u)}{\partial x}+\frac{\partial(\rho v)}{\partial y}=0, \tag{1}$$

$$\rho u\frac{\partial u}{\partial x}+\rho v\frac{\partial u}{\partial y}=\frac{1}{Re}\frac{\partial}{\partial y}\left(\mu\frac{\partial u}{\partial y}\right), \tag{2}$$

$$\frac{\partial p}{\partial y}=0, \tag{3}$$

$$\rho u\frac{\partial T}{\partial x}+\rho v\frac{\partial T}{\partial y}=\frac{1}{RePr}\frac{1}{c_p}\frac{\partial}{\partial y}\left(k\frac{\partial T}{\partial y}\right)+\frac{(\gamma-1)Ma^2}{Re}\frac{\mu}{c_p}\left(\frac{\partial u}{\partial y}\right)^2, \tag{4}$$

$$\rho u\frac{\partial s_1}{\partial x}+\rho v\frac{\partial s_1}{\partial y}=\frac{1}{ReLePr}\frac{\partial}{\partial y}\left(\rho\mathcal{D}_{12}\frac{\partial s_1}{\partial y}\right), \tag{5}$$

$$1=\rho RT, \tag{6}$$

The nondimensional numbers are Reynolds, Mach, Prandtl and Lewis numbers.

$$Re=\frac{\rho_1 U_1 x_0}{\mu_1},\quad Ma=\frac{U_1}{\sqrt{\gamma R_1 T_1}},\quad Pr=\frac{\mu_1 c_{p_1}}{k_1},\quad \text{and}\quad Le=\frac{k_1}{\rho_1 c_{p_1}\mathcal{D}_{12}}, \tag{7}$$

where, ρ is the density, u and v are the velocity components in the streamwise and normal directions, p is the pressure, μ is the dynamic viscosity, k is the thermal conductivity, T the temperature, c_p the specific heat at constant pressure, R the gas constant s_1 the mass fraction of the fast stream component, γ is the specific heat ratio and $\mathcal{D}_{12}$ the mass diffusivity coefficient.

The nondimensional mixture properties vary across the mixing layer according to the species concentration and temperature as given below. The equation of state is used to calculate the density as a function of the mixture temperature T and mass fractions s_1 and s_2.

$$1=\rho R_u T\left(s_1 W_1+S_2 W_2\right). \tag{8}$$

The gas constant and specific heat at constant pressure are,

$$R=s_1+R_{\text{ratio}}(1-s_1),\qquad c_p=s_1+c_{p_{\text{ratio}}}(1-s_1). \tag{9}$$

The dynamic viscosity is,

$$\mu=\frac{X_1\mu_1}{X_1+X_2\phi_{12}}+\frac{X_2\mu_2}{X_2+X_1\phi_{21}},\qquad \phi_{12}=\frac{\left[1+(\mu_1/\mu_2)^{1/2}\left(\mathcal{M}_2/\mathcal{M}_1\right)^{1/4}\right]^2}{\left[8\left(1+\mathcal{M}_1/\mathcal{M}_2\right)\right]^{1/2}},\qquad \phi_{21}=\phi_{12}\frac{\mu_1}{\mu_2}\frac{\mathcal{M}_1}{\mathcal{M}_2} \tag{10}$$

The thermal conductivity is,

$$k=\frac{X_1 k_1}{X_1+X_2\phi_{12}}+\frac{X_2 k_2}{X_2+X_1\phi_{21}},\qquad \phi_{12}=\frac{\left[1+(k_1/k_2)^{1/2}\left(\mathcal{M}_2/\mathcal{M}_1\right)^{1/4}\right]^2}{\left[8\left(1+\mathcal{M}_1/\mathcal{M}_2\right)\right]^{1/2}},\qquad \phi_{21}=\phi_{12}\frac{k_1}{k_2}\frac{\mathcal{M}_1}{\mathcal{M}_2} \tag{11}$$

where $\mathcal{M}$ is the molar mass of a given species, X_i the molar fraction of species i, the underscore "ratio" indicates the fast to low stream properties ratio and R_u is the universal gas constant.

The boundary conditions for velocity, temperature, density and mass fraction are 1 at the fast stream side and $\beta_u = U_{\text{ratio}} = U2/U1$, $\beta_T = T_{\text{ratio}} = T2/T1$, $\rho_{\text{ratio}} = \rho_2/\rho_1$ and $s_{\text{ratio}} = s_2/s_1$ at the slow stream side.

2.2 Linear disturbance equations

The compressible free shear layer local, normal modes, inviscid instability is investigated using the Rayleigh equation written in terms of the Gropengiesser variable given by the χ function (Gropengiesser, 1970; Salemi and Mendonca, 2008; Mendonca, 2014).

$$\chi=\frac{i\alpha\hat{p}}{\gamma_1 Ma_1^2\hat{v}},\qquad \frac{d\chi}{dy}=\frac{\alpha^2\left(\bar{u}-\omega/\alpha\right)}{R\overline{T}}-\chi\left[\frac{\chi G+\left(d\bar{u}/dy\right)}{\left(\bar{u}-\omega/\alpha\right)}\right], \tag{12}$$

with the following boundary condition:

$$\chi\left(y \to \pm\infty\right) = \mp\frac{\alpha\left(\bar{u} - \omega/\alpha\right)}{\sqrt{G\bar{R}\bar{\bar{T}}}}, \qquad G = \frac{\alpha^2 + \beta^2}{\bar{\rho}\alpha^2} - Ma_1^2\frac{\gamma_1}{\gamma}\frac{\left(\alpha\bar{u} - \omega\right)^2}{\alpha^2}. \tag{13}$$

where the variables identified with a hat $\hat{\phi}$ are the eigenfunctions of the dependent variables of the flow, α_r is the wave number in the x direction, α_i is the spatial growth rate, β is the wave number in the z direction and ω is the angular frequency of the disturbance.

3. RESULTS

Results in terms of growth rate as a function of Mach number and temperature ratios for different values of spanwise wave numbers are shown in this section. Section 3.1 discusses mean flow and stability results for the hyperbolic tangent canonical base flow profiles and Sec. 3.2 disccuses the mean flow and stability results for the boundary layer base flow profiles.

Table 1 show the range of Mach numbers and spanwise wave numbers for the temperature ratios considered in this study. The temperature ratio β_T varies from 0.25 to 4.0 in steps of 0.25.

Table 1. Range of Mach number Ma and spanwise wave numbers β.

Ma	0.001	0.25	0.5	0.75	1.0	1.25
β	0.0	0.2	0.4	0.6		

3.1 Hyperbolic Tangent Canonical Base Flow

Prior to investigate the more realistic binary mixing layer base flow provided by the boundary layer code a study of the effect of temperature ratio $\beta_T = T_2/T_1$ is conducted in this section considering the canonical hyperbolic tangent velocity and mass fraction profile with a Crocco-Busemann temperature distribution.

First, the main characteristics of the base flow are highlighted in Sec. 3.1.1. Then, the usual stability diagram in terms of growth rate α_i versus angular frequency ω is presented for two selected conditions as sample results which is similar to the stability diagram for other conditions (Sec. 3.1.2). In Sec. 3.1.3 the largest growth rate observed on the stability diagram for each flow condition is plotted as a function of Mach number and spanwise wave number for different temperature ratios.

3.1.1 Base Flow Characteristics

Figure 1 shows the mixing layer velocity profile for the velocity ratio $\beta_U = 0.5$ used in this study. The Temperature profiles for different temperature ratios β_T are shown in Figs. 2 to 4 for Mach number $Ma = 1.25$. Other values of Mach number have similar temperature distributions, but the small kinetic heating observed for the higher Mach number when $\beta_T = 1$ is accordingly lower for lower Mach numbers. The kinetic heating is overshadowed by the temperature ratio for $\beta_T \neq 1$. The temperature profile change very little with Mach number and the effect of compressibility observed on the stability of the mixing layer is thus associated with the compressible Rayleigh equation itself (Eq. 12).

3.1.2 Growth Rate Versus ω

Typical results for the variation of growth rate versus angular frequency are presented in Figs. 5 and 6. They show the amplification rates and the range of unstable frequencies for $Ma = 0.25$ and $\beta = 0.2$, and for $Ma = 1.0$ and $\beta = 0.4$. The different curves correspond to different temperature ratio $\beta_T = T_2/T_1$. The stability curves for other conditions are similar. For low Mach number and three-dimensional disturbances the growth rate changes mostly at the lowest temperature ratio. For two-dimensional disturbances ($\beta = 0$) the growth rate is not a strong function of the temperature ratio and the frequency corresponding to the largest growth rate does not change with β_t.

In the following section (3.1.3) for each Mach number Ma and each spanwise wave number β the largest growth rate obtained from the stability diagrams (such as Figs. 5 and 6) will be plotted as a function of the temperature ratio β_T.

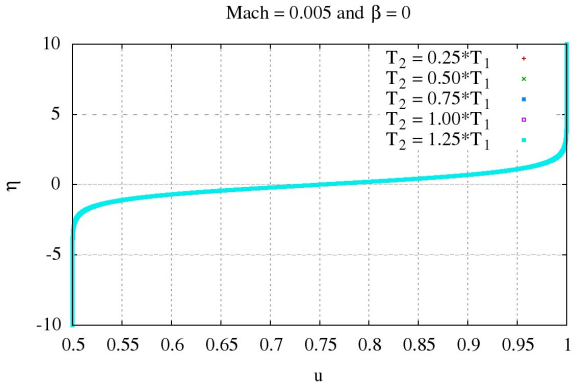

Figure 1. Base flow velocity profile.

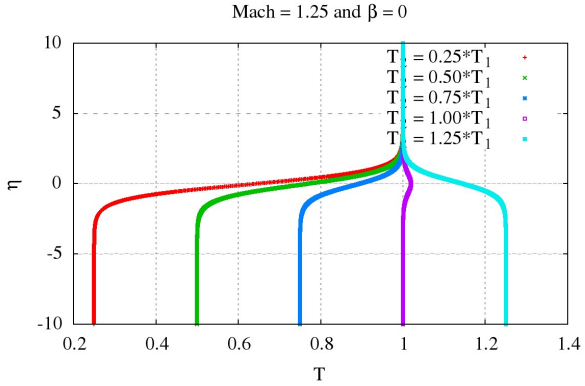

Figure 2. Base flow temperature distribution for different temperature ratios and $Ma = 1.25$. $.25 < \beta_T < 1.25$.

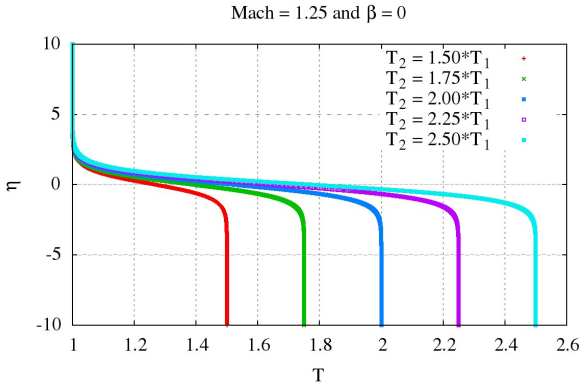

Figure 3. Base flow temperature distribution for different temperature ratios and $Ma = 1.25$. $1.5 < \beta_T < 2.5$.

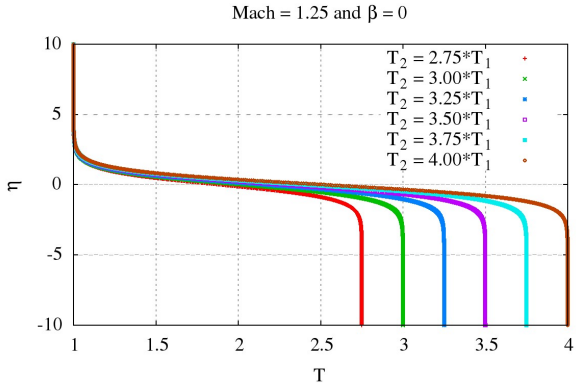

Figure 4. Base flow temperature distribution for different temperature ratios and $Ma = 1.25$. $2.75 < \beta_T < 4$.

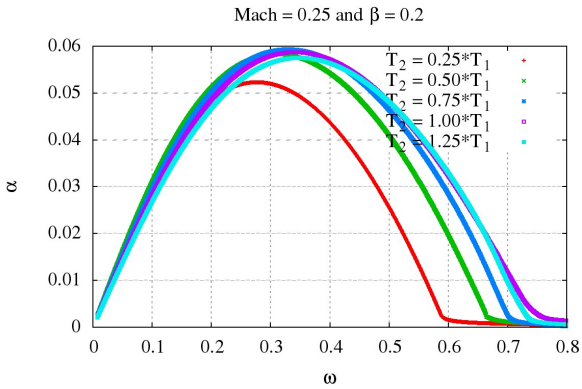

Figure 5. Growth rate versus angular frequency for $Ma = 0.25$ and $\beta = 0.2$.

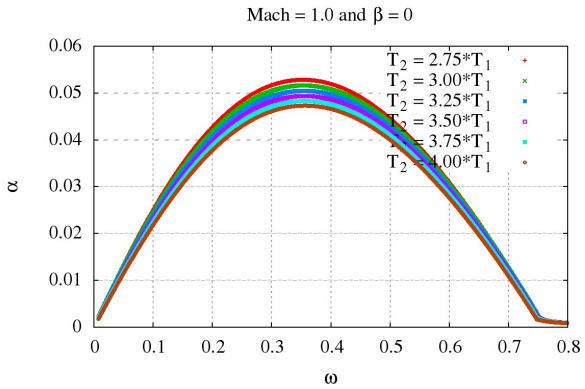

Figure 6. Growth rate versus angular frequency for $Ma = 1.$ and $\beta = 0.0$.

3.1.3 Largest Growth rate versus β and Ma

Based on the stability curves, the variation of the larges growth rate with Ma number and spanwise wave number β are presented in this section in Figs 7 through 12. Each figure shows the variation of the largest growth rate for different temperature ratios $\beta_T = T_2/T_1$ and different spanwise wave number β. As expected, the spanwise wave number has a significant effect on the largest growth rate, while the effect of the temperature ratio β_T is not as strong. The strongest growth rate corresponds to a temperature ratio of the order of $\beta_T = 0.75$, regardless of the wave number and Mach number. As the temperature ratio increases the largest growth rate changes little with β_T since the temperature gradient at the inflection point on the temperature distribution shown in Fig 4 does not vary significantly either.

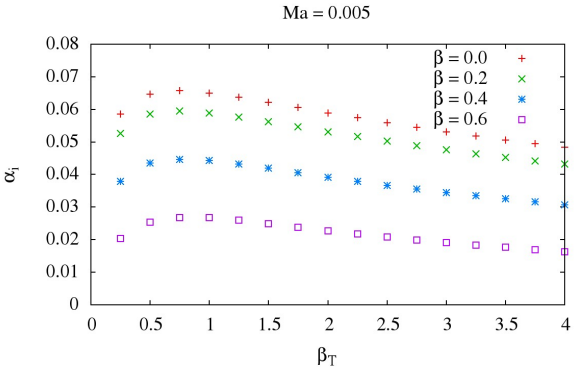

Figure 7. Largest growth rate as a function of the temperature gradient $\beta_T = T_2/T_1$ for different spanwise wave numbers at $Ma = 0.005$

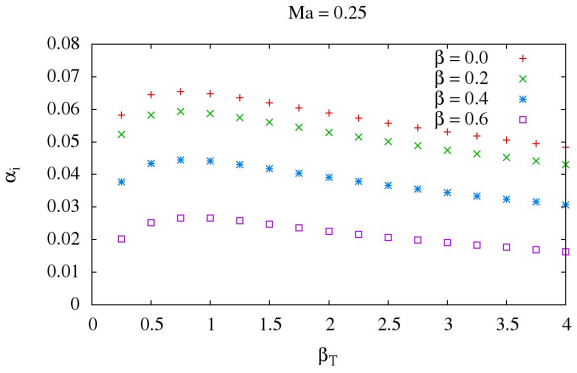

Figure 8. Largest growth rate as a function of the temperature gradient $\beta_T = T_2/T_1$ for different spanwise wave numbers at $Ma = 0.25$

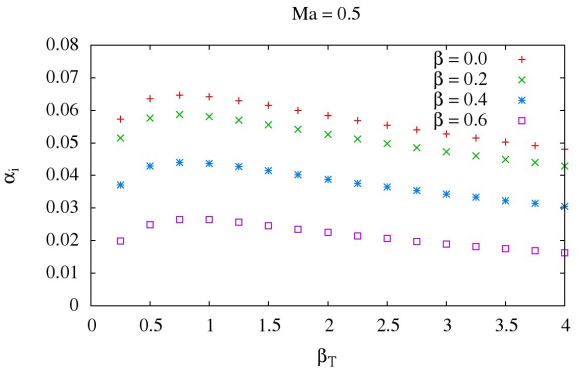

Figure 9. Largest growth rate as a function of the temperature gradient $\beta_T = T_2/T_1$ for different spanwise wave numbers at $Ma = 0.5$

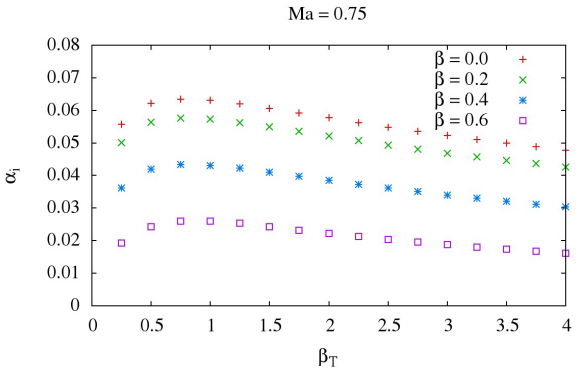

Figure 10. Largest growth rate as a function of the temperature gradient $\beta_T = T_2/T_1$ for different spanwise wave numbers at $Ma = 0.75$

The same results are presented again in Figs. 13 through 16 in order to highlight the effect of the Ma number for a given spanwise wave number. For a given spanwise wave number β the largest growth rates α_i do not have a strong dependence on the Mach number, The dependence on the spanwise wave number shown above is much stronger. This is a consequence of the observation made earlier that the base flow temperature varies little with Mach number and is associated with a small kinetic heating for the range of Mach numbers considered in this study.

Close to the lowest temperature ratios ($\beta_T = 0.25$ to 0.75) the largest growth rates have a greater variation with Ma, but as the temperature ratios increase the compressibility effect seems to be reduced even further. That must be associated with the temperature gradient at the inflection point on the temperature distribution.

3.2 Boundary Layer Profiles Base Flow

In this section stability results are presented for base flow properties distributions given by the solution of a boundary layer equations for the binary O2/H2 mixing layer. In Sec. 3.2.1 the base flow velocity, temperature and mass fraction distribution are presented for different values of Mach number Ma and temperature ratios β_T. Then the stability characteristics of these base flow profiles are discussed in Sec. 3.2.2 . The same flow conditions presented in Tab. 1 are considered again.

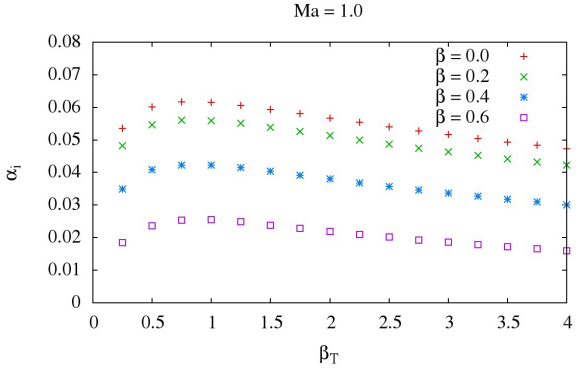

Figure 11. Largest growth rate as a function of the temperature gradient $\beta_T = T_2/T_1$ for different spanwise wave numbers at $Ma = 1.0$

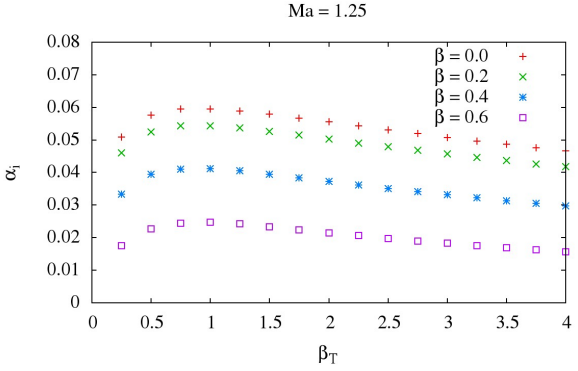

Figure 12. Largest growth rate as a function of the temperature gradient $\beta_T = T_2/T_1$ for different spanwise wave numbers at $Ma = 1.25$

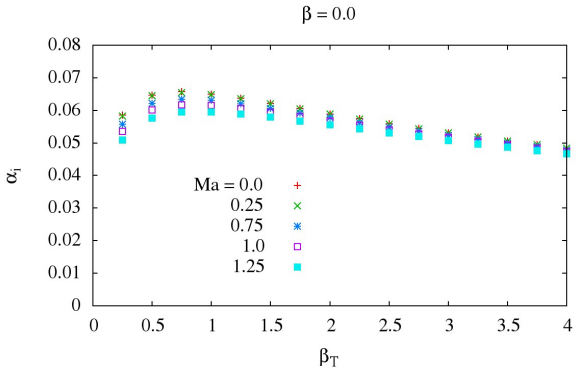

Figure 13. Largest growth rate as a function of the temperature gradient $\beta_T = T_2/T_1$ for different Ma numbers at $\beta = 0.0$

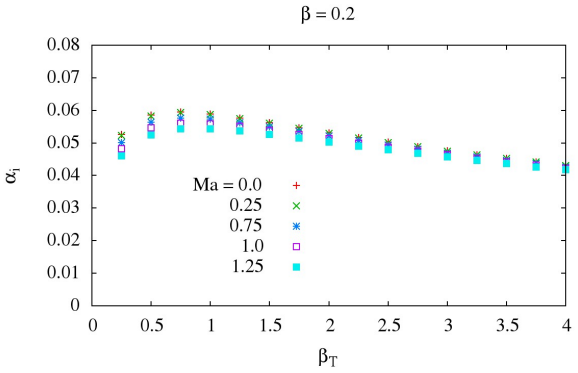

Figure 14. Largest growth rate as a function of the temperature gradient $\beta_T = T_2/T_1$ for different Ma numbers at $\beta = 0.2$

3.2.1 Binary Mixing Layer Base Flow Profiles

A sample of the base flow properties computed with the compressible, variable properties parabolic equations solver is presented in Figs. 17 through 21. Other combinations of β_T and Mach number follow similar trends and are not shown. Fig. 17 shows the effect of compressibility when the temperature ratio is $\beta_T = 0.25$. Other temperature ratios show a hyperbolic tangent like profile without the bump around $\eta = 0$ which is due to viscous heating. Note that the density distribution does not quite follow the hyperbolic tangent profile due to the simultaneous dependence on temperature and species mass fraction. The velocity profile shown in Fig. 18 is not a typical hyperbolic tangent profile for the same reason. The O2 layer is much more uniform than the lower H2 layer due to mass and viscous diffusion across the mixing layer. This have a significant effect on the stability of the mixing layer as already observed by Mendonca (2014).

Sample temperature profiles for different temperature ratios are shown in Figs. 19 and 20. When β_T is 0.75 or 1.0 the kinetic heating is clearly seen. For other values of temperature gradient, due to the temperature variation and due to the low values of Mach number considered, the kinetic heating is not of major influence. Again, the O2 layer has a much more uniform temperature distribution than the H2 layer.

Mass fraction profiles are shown in Figs. 22 and 21 where one can see that the compressibility does not have a strong influence on the species distribution. As the temperature ratio increase the mass fraction becomes strongly asymmetric with a much more uniform concentration of O2 in the upper layer and a slow transition to H2 in the lower layer. This is due to the mass, momentum and heat diffusion properties of the two gases.

3.2.2 Binary Mixing Layer Stability Results

Only some typical stability diagram results are presented in the following figures in order to illustrate the main conclusions. Other combinations of Ma and β that follow the same trends and are not shown but are available from the authors.

In general, for increasing β_T the most unstable growth rate is reduced and the range of unstable frequencies increase

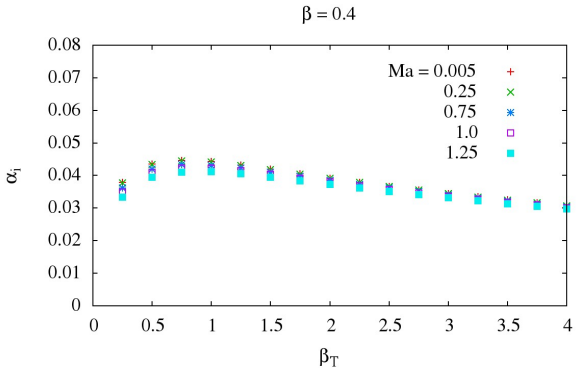

Figure 15. Largest growth rate as a function of the temperature gradient $\beta_T = T_2/T_1$ for different Ma numbers at $\beta = 0.4$

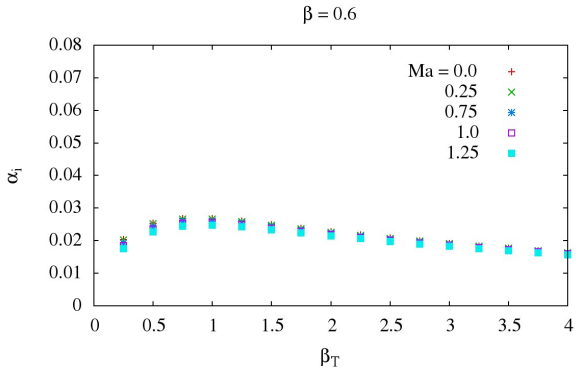

Figure 16. Largest growth rate as a function of the temperature gradient $\beta_T = T_2/T_1$ for different Ma numbers at $\beta = 0.6$

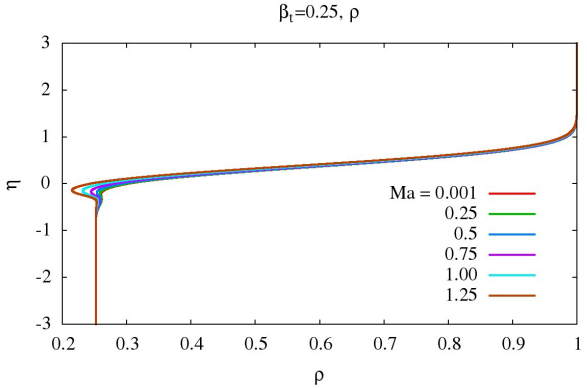

Figure 17. density profile for $\beta_T = 0.25$.

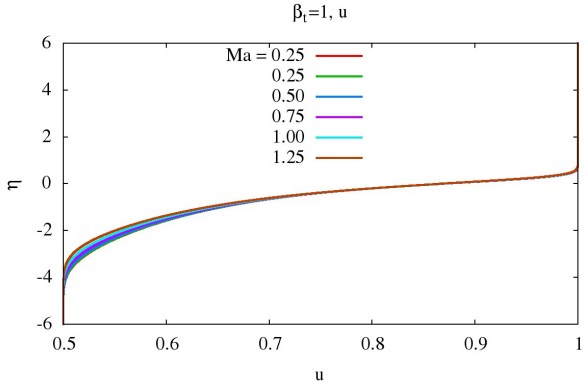

Figure 18. Velocity profile for $\beta_T = 1$.

as shown in Fig 23. As expected, comparing Figs. 23 and 24 it is possible to see that increasing the Mach the base flow becomes more stable. This conclusion is valid for any β_T.

As the spanwise wave number increase to $\beta = 0.4$ the growth rate of the $\beta_T = 0.25$ ceases to be dominant (Fig. 25) and as the flow becomes more compressible it is actually lower than the growth rate of other temperature ratios (Fig. 26). In this cases the largest growth rate for different β_T are about the same and only starts to reduce for $\beta_T \geq 2.0$. In any case, when the temperature of the slow H2 stream at the bottom is four times the temperature of the fast O2 stream at the top, the instability is much weaker than in other conditions.

The same trend observed for $\beta = 0.4$ is also observed increasing β to 0.6, where the $\beta_T = 0.25$ case is further stabilized with respect to other temperature ratios as seen if Figs 27 and 28. Besides this strong effect on the stability of the $\beta_T = 0.25$ condition, three-dimensionality has a stabilizing effect on all temperature ratios considered in this study.

Compared to the results for the canonical hyperbolic tangent base flow profiles, the stability of the base flow computed with the boundary layer code is much more sensitive to the temperature gradient, both in terms of the largest amplification rate α_i and in terms of the frequency of this largest α_i which is shifted to higher values as β_T increases. Note that no quantitative comparison between growth rates for the hyperbolic tangent and boundary layer profile should be attempted, since no care was taken to ensure similar vorticity thickness between profiles.

3.2.3 Largest Growth Rates

Figures 29 through 34 show the largest growth rate variation with the temperature ratio β_T for different spanwise wave numbers β and different Mach numbers. Regardless of Mach number, the stronger growth rate is two-dimensional and the lower H2 layer is cooler than the upper O2 layer. Increasing three-dimensionality of the disturbances the strongest growth shifts to the temperature ratio β_T in the range of $0.5 \leq \beta_T \leq 0.75$. This is in contrast with the results from the canonical hyperbolic tangent base flow profiles, where the strongest growth as always close to $\beta_T = 0.75$ regardless of the spanwise wave number. As the temperature ratio increases the maximum growth rate becomes less dependent on the three-dimensionality of the disturbances (β). The results show the expected behaviour of decreased instability with increasing compressibility.

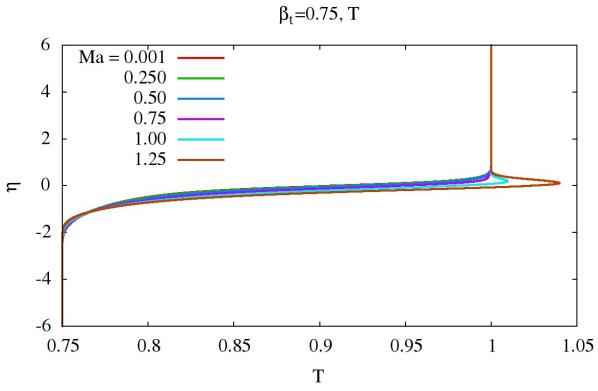

Figure 19. Temperature profile for $\beta_T = 0.75$.

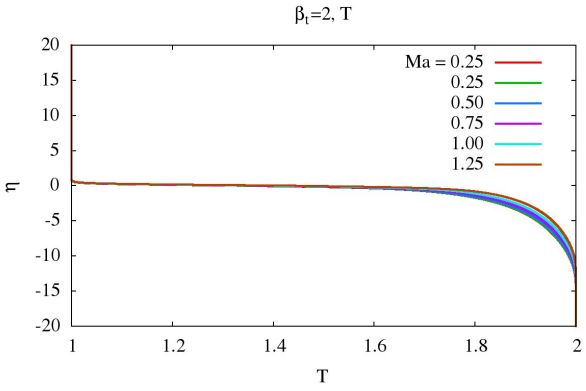

Figure 20. Temperature profile for $\beta_T = 2$.

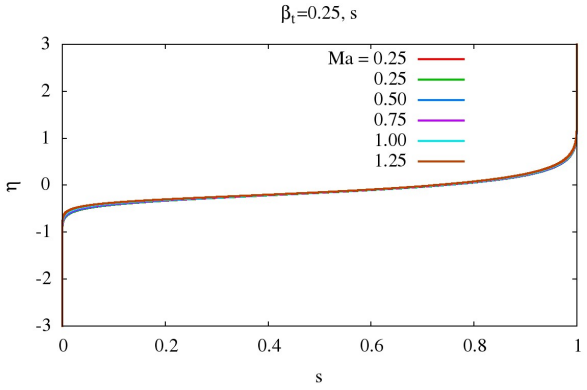

Figure 21. Mass fraction profile for $\beta_T = 0.25$.

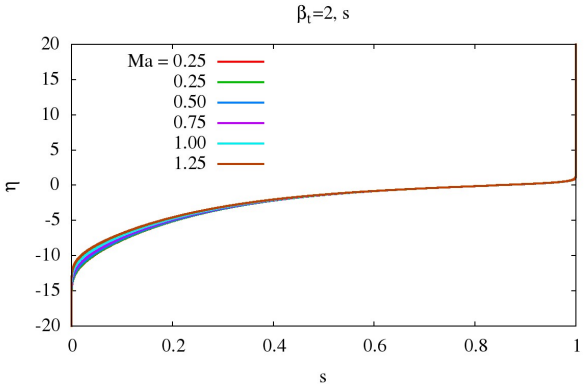

Figure 22. Mass fraction profile for $\beta_T = 2$.

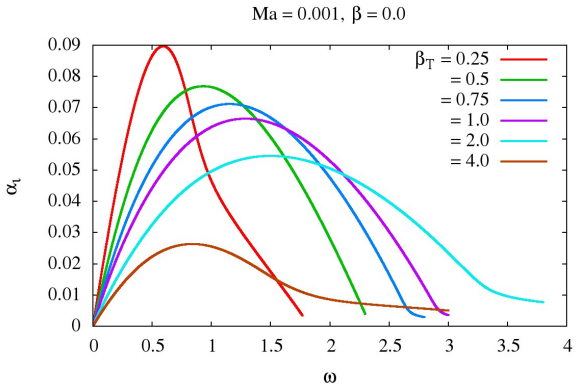

Figure 23. $Ma = 0.001$, $\beta = 0$.

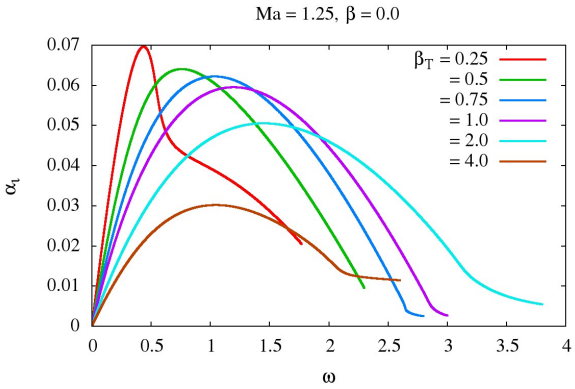

Figure 24. $Ma = 1.25$, $\beta = 0$.

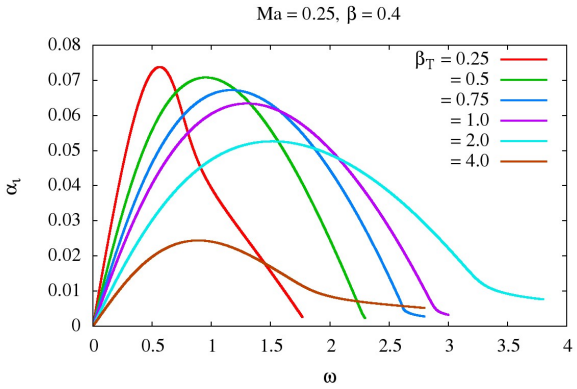

Figure 25. $Ma = 0.25$, $\beta = 0.4$

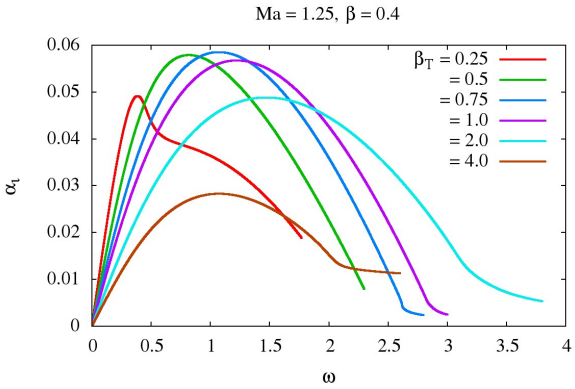

Figure 26. $Ma = 1.25$, $\beta = 0.4$

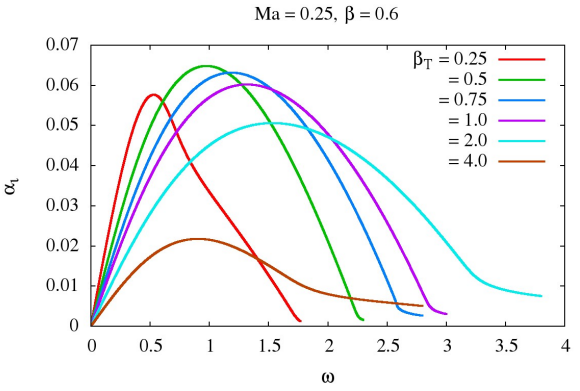

Figure 27. $Ma = 0.25$, $\beta = 0.6$

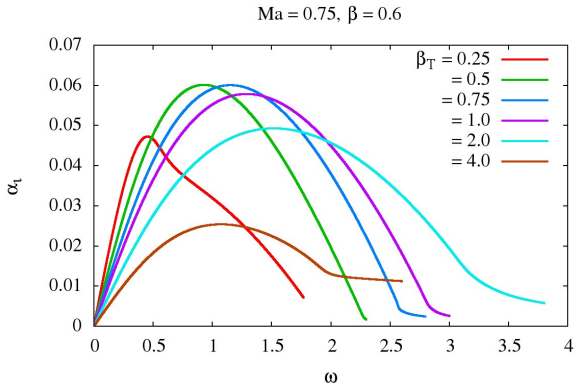

Figure 28. $Ma = 0.75$, $\beta = 0.6$

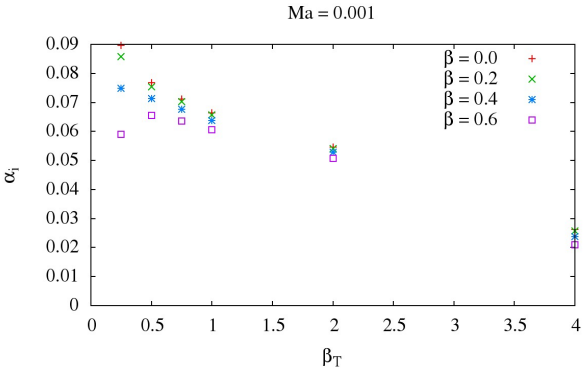

Figure 29. $Ma = 0.001$

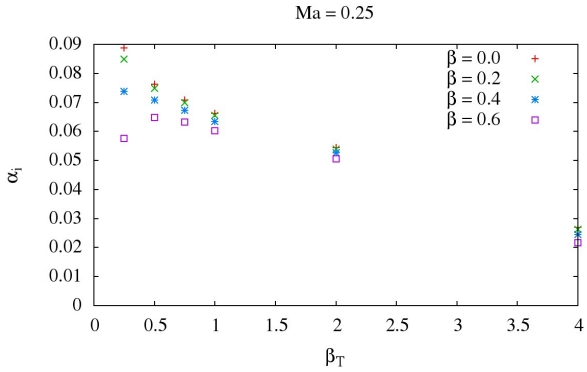

Figure 30. $Ma = 0.25$

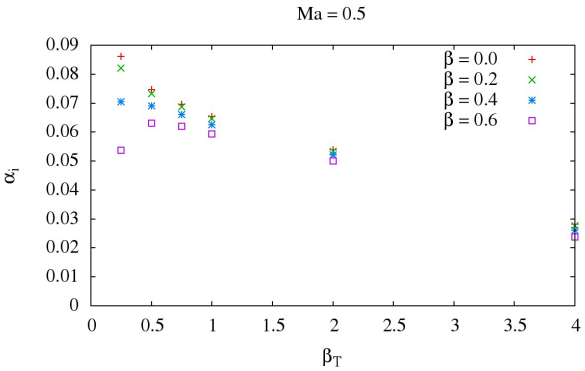

Figure 31. $Ma = 0.5$

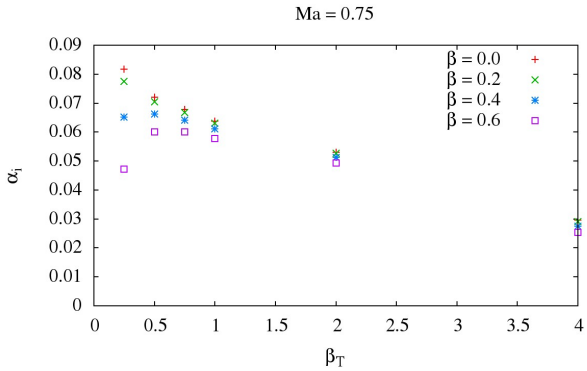

Figure 32. $Ma = 0.75$

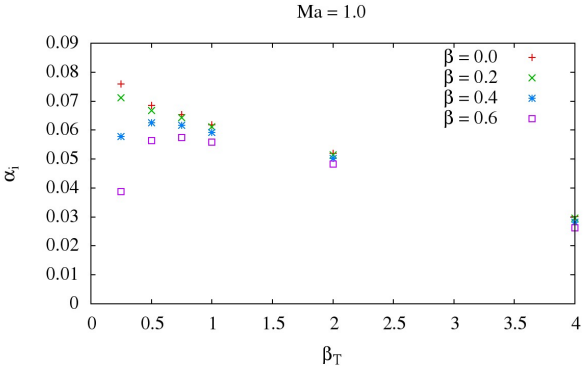

Figure 33. $Ma = 1.$

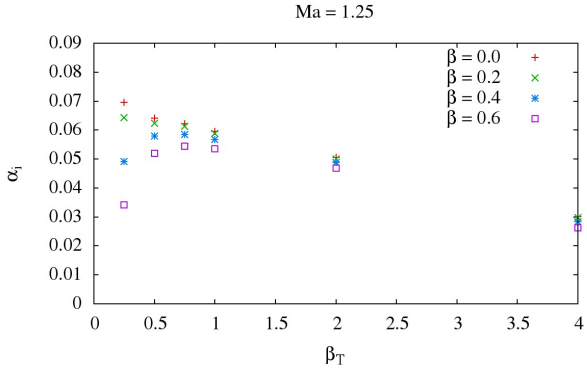

Figure 34. $Ma = 1.25$

4. CONCLUSIONS

Results for single species and binary species mixing layer for compressible flows were investigated for a range of Mach numbers, spanwise wave numbers and temperature ratios $\beta_T = T_2/T_1$. The base flow was computed either with a hyperbolic tangent velocity and mass fraction profile and temperature profile given by a Crocco-Busemann relation, and with the solution of the parabolic, compressible, variable properties, binary boundary layer code.

For the conditions tested the growth rate drops with compressibility and three-dimensionality of the disturbance. For the canonical base flow profiles the largest growth rate is found to occur at the temperature ratio of $\beta_T = 0.75$, and at higher temperature ratios the largest growth rate still show a strong dependence on the spanwise wave number. On the other hand for the more detailed boundary layer base flow profiles, the larges growth rate corresponds to the lower temperature ratio for two-dimensional disturbances, but shifts to temperature ratios of the order of 0.5 for three-dimensional disturbances. When the more realistic boundary layer profile are considered for the base flow, increasing the temperature ratio the growth rates are less dependent on the three-dimensionality of the disturbance, a behaviour that was not observed on the hyperbolic tangent base flow profiles.

5. REFERENCES

Anderson, J. D. 2000. *Hypersonic and High Temperature Gas Dynamics*. General Interest. AIAA.

Caillol, P. 2009. Absolute and convective instabilities of an inviscid compressible mixing layer:Theory and applications. *Physics of Fluids*, **21**, 104101–1–104101–17.

Day, M. J., Mansour, N. N., and Reynolds, W. C. 1998. The structure of the compressible reacting mixing layer: Insights from linear stability analysis. *Physics of Fluids*, **10**(4), 993–1007.

Fedioun, Ivan, and Lardjane, Nicolas. 2005. Temporal linear stability analysis of three-dimensional compressible binary shear layers. *AIAA Journal*, **43**(1), 111–123.

Gropengiesser, H. 1970. *Study on the stability of boundary layers in compressible fluids*. Tech. rept. NASA TT F-12. National Aeronautics and Space Administration – NASA.

Kennedy, C. A., and Gatski, T. B. 1994. Self-similar supersonic variable-density shear layers in binary systems. *Physics of Fluids*, **6**(2), 662–673.

Kozusko, F., Grosch, C. E., Jackson, T. L., Kennedy, Christopher A., and Gatski, Thomas B. 1996. The structure of a variable property, compressible mixing layers in binary gas mixtures. *Physics of Fluids*, **8**(7), 1945–1953.

Mendonca, M. T. 2014. Linear Stability Analysis of Binary Compressible Mixing Layers Modified By a Jet or a Wake Deficit. *Pages 1–13 of: 52nd AIAA Aerospace Sciences Meeting and Exhibit*.

Na, Y., S., Lee, and Shin, D. S. 2006. Linear Stability Analysis of the Reacting Shear Flow. *Journal of Mechanical Science and Technology*, **20**(8), 1309–1320.

Salemi, L., and Mendonca, M. T. 2008. Spatial and Temporal Linear Stability Analysis of Binary Compressible Shear Layer. *Pages 1–23 of: AIAA 38th Fluid Dynamics Conference*. AIAA paper 2008-3841.

Shin, D. S., and Ferziger, J. H. 1991. Linear stability of the reacting mixing layer. *AIAA Journal*, **29**(10), 1634–1642.

6. Responsibility notice

The author(s) is (are) the only responsible for the printed material included in this paper

ANALYSIS OF DIFFERENT TURBULENCE MODELS CONSIDERING JET INSTABILITY FOR DISCHARGE COEFFICIENT PREDICTION IN INTERNAL COMBUSTION ENGINE

Soriano, B S, soriano@mecanica.ufrgs.br
Vielmo, H A, vielmoh@mecanica.ufrgs.br
Mechanical Engineering Department, Federal University of Rio Grande do Sul
Rua Sarmento Leite, 425, CEP 90050-170, Porto Alegre, RS, Brazil

Rech, C, charlesrech@uol.com.br
Automotive Mechanical Engineering Department, Lutheran University of Brazil
Av. Farroupilha, 8001, CEP , 92425-900, Canoas, RS, Brazil

Abstract. *A well know method to characterize intake systems of internal combustion engines (ICE) is based on steady flow tests, with fixed pressure drops across the system at different valve lifts. This means to consider only the average flow, even that there is an inherent transient, caused by the complex geometry. This paper presents a comparison of different numerical methodologies to solve the C_D in the intake system of an ICE. In this way, the k-ε standard and the SST k-ω Turbulence Models were utilized. With the k-ε standard model it was possible to obtain the average flow, but the SST k-ω requires the transient solution, in order to satisfy the convergence criteria in the numerical solution, as a consequence of the instable jet generated after the flow passes through the valve. The numerical results were compared with experimental data obtained by the authors with the same boundary conditions. The C_D results revealed a good agreement among both turbulence models, however, the SST k-ω presented a better approximation of the experimental data. Regarding the velocity fields, a notably difference between the models is obtained, with the k-ε standard model revealing a smoother field, if compared with the SST k-ω turbulence model.*

1. INTRODUCTION

The discharge coefficient in an internal combustion engine (*ICE*) is studied computationally to assess the capability of Computational Fluid Dynamics (*CFD*) in assisting experimental calibration and to develop better intake shapes. Valves and ports play an important role in the design of internal combustion engines, and influence their performance in the period they are open (Winterbone and Pearson, 1999) The steady flow data are representative of the dynamic flow behavior of the valve in an operating engine. The pressure upstream of the valve varies significantly during the intake process. However, it has been shown that over the normal engine speed range, steady flow discharge coefficient results can be used to predict dynamics performance with reasonable precision (Heywood, 1988). Due to the curvature of the intake geometry, the high gradients in the valve region and the large scale of the Reynolds number, the flow computation in *ICE* becomes a big challenge for the turbulence models. Moreover, the flow in the valve exit generates a highly turbulent conical jet that separates from the valve seat, producing shear layers with large velocity gradients. (Heywood, 1988). When the jet reaches the wall, it deflects the major portion of the jet toward the piston, however, a substantial fraction flows upward toward the cylinder head (Bicen et al, 1985). The well prediction of this kind of free shear flow is a big challenge for the turbulence models (Wilcox, 2000).

During the last years more numerical simulations have been done regarding the discharge coefficient focusing in directed intake port types, including comparisons with experimental measurements (Bianchi et al, 2002, 2003; Paul and Ganesan, 2010; Rech et al, 2010), With the growing availability of turbulent models and computational resources, many works make comparisons, regarding their capacity of reproduce experimental data and CPU time demanding.

Kaario et al (2003) compared the *k-ε RNG* (k-ε Renormalization Group) turbulence model with the one-equation subgrid scale model, incompressible and isothermal *LES* approach (Large Eddy Simulation). This particularized form of the LES model used was able to capture more flow's complex structures than the *k-ε RNG* model, but remains the CPU large time demand problem. Vielmo et al (2008) analyzed the numerical methodology applied on discharge coefficient simulation of a Diesel intake system with experimental results. They utilized two different *CFD* codes, Star_CD and Fluent, and two different turbulence models: *k-ε* standard and *k-ε RNG*. The results with the best accuracy were obtained with Star_CD software and *k-ε RNG* model. Although, the results with the Fluent are coherent if compared with the experimental data, the difference was 6%. Martins et al. (2009) with Fluent software and *k-ε RNG* turbulence model developed an intake system with high swirl generation for a small engine in order to promote rapid combustion. Accordingly, many works were done utilizing the group of *k-ε* turbulence model and this study area lacks for more accurately models.

It is important observe that all these computations are performed utilizing the steady state regime, because all the boundary conditions are permanent. However, since the interaction between the valve and the flow generates an instable jet, the steady-state solution may not describe all the reality of the phenomenon. The objective of this paper is the analysis of different turbulence models to predict the intake system's discharge coefficient of an internal combustion engine. The numerical results were compared with experimental measurements in the engine with the valve stopped in a certain gap.

2. THE DISCHARGE COEFFICIENT

The mass flow rate through a poppet valve is usually described by the equation for compressible flow through a flow restriction (Heywood, 1988). The Eq. (1) relates the actual mass flow rate through the intake valve to the isentropic mass flow rate.

$$C_D = \frac{\dot{m}}{A\frac{p_o}{(RT_o)^{1/2}}\left(\frac{p_{out}}{p_o}\right)^{1/\gamma}\left\{\frac{2\gamma}{\gamma-1}\left[1-\left(\frac{p_{out}}{p_o}\right)^{\gamma-1/\gamma}\right]\right\}^{1/2}} \quad (1)$$

where $\dot{m}$ is obtained from the numerical solution, or experimentally. R is the gas (air) constant, T_o the stagnation (inlet) absolute temperature and γ the specific heat ratio. The variable A, that represents the valve flow area, is treated considering the valve lift, seat angle, inner and outer diameter as described for Blair (1999).

A global coefficient is obtaining by integration along the crankshaft angle, as follows (Vielmo et al., 2008):

$$C_{D\_Global} = \frac{\int_{IVO}^{IVC} C_D \, d\theta}{IVC - IVO} \quad (2)$$

where θ is a crankshaft angular position, IVO is the intake valve angle opening and IVC is the intake valve angle closing.

3. MATHEMATICAL FORMULATION

In order to solve a turbulent flow, the Reynolds averaging is applied in the Navier-Stokes equation by means of a decomposition of the instantaneous velocity in a mean (time-averaged) and fluctuation component. So, the velocity field in the turbulent flow is described by the mass and momentum conservation equations (Navier-Stokes), in their transient, compressible form as Eq.(3) and (4).

In Cartesian tensor notation, according Fluent (2014), the mass conservation is

$$\frac{\partial \rho}{\partial t} + \frac{\partial}{\partial x_i}(\rho u_i) = 0 \quad (3)$$

and the momentum

$$\frac{\partial(\rho u_i)}{\partial t} + \frac{\partial(\rho u_i u_j)}{\partial x_i} = -\frac{\partial p}{\partial x_i} + \frac{\partial}{\partial x_j}\left[\mu\left(\frac{\partial u_i}{\partial x_j} + \frac{\partial u_j}{\partial x_i} - \frac{2}{3}\delta_{ij}\frac{\partial u_l}{\partial x_l}\right)\right] + \frac{\partial}{\partial x_j}\left(-\overline{\rho u_i' u_j'}\right) \quad (4)$$

The Eq.(3) and Eq.(4) are called the Reynolds Averaged Navier-Stokes (*RANS*) equation. They have the same general form of the instantaneous equations, however the solution of the variables represent a time averaged value. The turbulence effect is described by the additional term that appears in the standard Navier-Stokes equation. This additional term $-\overline{\rho u_i' u_j'}$, named Reynolds stress, cause a mathematical inconsistency by adding more variable than equations. In this way, the Reynolds stress needs to be modeled in order to solve the mathematical system. Each model depends on the assumption made to represent the physical phenomena. The models presented in this paper employ the Boussinesq hypothesis to relate the Reynolds stress to the mean velocity gradients as presented in Eq.(5).

$$-\overline{\rho u_i' u_j'} = \mu_t S_{ij} - \frac{2}{3}\left(\mu_t \frac{\partial \mu_k}{\partial x_k} + \rho k\right)\delta_{ij} \quad (5)$$

where μ_t is the turbulent viscosity, k is the turbulent kinetic energy ($k = \frac{\overline{u_1' u_j'}}{2}$) and S_{ij} is the mean strain rate. The turbulent viscosity is not a fluid property, but a physical property of the flow, that varies point by point and with the flow (Deschamps, 1998). Thus, the μ_t is modelled by an equation that depends on the utilized model. The models are presented in the sequence of the paper.

3.1 Governing Equations for the *k-ε* Standard Turbulence Model

The well-known k-ε turbulence model was proposed by Launder and Spanding (1974). The model is based on transport equations for the turbulent kinetic energy (k) and the turbulent dissipation rate (ε).

$$\frac{\partial(\rho k)}{\partial t} + \frac{\partial(\rho k u_i)}{\partial x_i} = \frac{\partial}{\partial x_j}\left[\left(\mu + \frac{\mu_t}{\sigma_k}\right)\frac{\partial k}{\partial x_j}\right] + G_k + G_b - \rho\varepsilon - Y_M + S_k \quad (6)$$

$$\frac{\partial(\rho \varepsilon)}{\partial t} + \frac{\partial(\rho \varepsilon u_i)}{\partial x_i} = \frac{\partial}{\partial x_j}\left[\left(\mu + \frac{\mu_t}{\sigma_\varepsilon}\right)\frac{\partial \varepsilon}{\partial x_j}\right] + C_{1\varepsilon}\frac{\varepsilon}{k}(G_k + C_{3\varepsilon} G_b) - C_{2\varepsilon}\rho\frac{\varepsilon^2}{k} + S_\varepsilon \quad (7)$$

In these equations, G_k represents the generation of turbulence kinetic energy due to the mean velocity gradients, *Gb* is the generation of turbulence kinetic energy due to buoyancy, Y_M represent the contribution of the fluctuating dilatation in compressible turbulence to the overall dissipation rate, $C_{1\varepsilon}$, $C_{2\varepsilon}$ and $C_{3\varepsilon}$ are constants, σ_k and σ_ε are the Prandtl number for k and ε respectively and S_k e S_ε are source terms. All the models constants are presented in Launder and Spalding (1974).

The turbulent viscosity is calculated by the relation of the k and ε.

$$\mu_t = \frac{C_\mu \rho k^2}{\varepsilon} \tag{8}$$

where ρ is the fluid density and C_μ a constant of the model.

The standard k-ε model is not completely adequate for flows with curved streamlines (Deschamps, 1998), however, the robustness, economy, and reasonable accuracy for a wide range of turbulent flows explain its popularity in industrial flow and heat transfer simulations (Fluent, 2014).

3.2 Governing Equations for the SST K-ω Turbulence Model

The standard k-ω model proposed by Wilcox (1988), differs from the standard k-ε due to the better prediction of flow with adverse pressure gradient and the near the wall region. Comparing with the Direct Numerical Simulation (*DNS*) results, the specific dissipation rate (ω) obtained good agreement when integrated until the wall (Wilcox, 2000). One of the weak points of the standard k-ω model is the sensitivity of the solution in the free stream region (Fluent, 2014). Due to utilize the good prediction of the k-ε model in the free stream and standard k-ω model near the wall, Menter (1993) proposed a model that combine both models depending on the region of the flow. This combination is made utilizing a blending function (F).

The specific dissipation rate is defined as $\omega = \varepsilon / C_\mu k$, and the general form of the turbulent kinetic energy is

$$\frac{\partial(\rho k)}{\partial t} + \frac{\partial(\rho k u_i)}{\partial x_i} = \frac{\partial}{\partial x_j}\left[\left(\mu + \frac{\mu_t}{\sigma_k}\right)\frac{\partial k}{\partial x_j}\right] + \widetilde{G_k} - Y_k + S_k \tag{9}$$

and specific dissipation rate is

$$\frac{\partial(\rho \omega)}{\partial t} + \frac{\partial(\rho \omega u_i)}{\partial x_i} = \frac{\partial}{\partial x_j}\left[\left(\mu + \frac{\mu_t}{\sigma_\varepsilon}\right)\frac{\partial \omega}{\partial x_j}\right] + G_\omega - Y_\omega + D_\omega + S_\omega \tag{10}$$

where. $\widetilde{G_k}$ represents the generation of turbulence kinetic energy due to the mean velocity gradients, G_ω represents the generation of ω, Γ_k and Γ_ω represent the effective diffusivity of k and ω respectively. Y_k and Y_ω represent the dissipation of k and ω due to turbulence, D_ω represent the cross-diffusion term, S_k and S_ω the source terms.

The turbulent viscosity is computed according to Eq.(11)

$$\mu_t = \frac{\rho k}{\omega} \frac{1}{max\left[\frac{1}{\alpha^*}, \frac{S F_2}{a_1 \omega}\right]} \tag{11}$$

where F_2 is a blending function, S a strain rate, α^* a damping coefficient.

4. NUMERICAL METHODOLOGY

The numerical solution was performed with FLUENT Finite Volumes CFD code, using k-ε standard and *SST* k-ω turbulence. The boundary condition at the inlet was atmospheric pressure and at outlet the desired experimental suction pressure, as can be seen in Fig.1. The mass air flow was solved for the same intake valve lift of the experimental methodology. For all cases the temperature was 296 K, the wall treated as adiabatic, turbulence intensity I = 0.05, and length scale l = 0.014 m, as a consequence of the flow and geometrical characteristics. The convergence criteria used for residuals was 10^{-5} and all computations were performed in double precision. In the k-ε standard model the flow near wall was computed with the High-Reynolds approach (standard wall function). The *SST* k-ω model enabled the hybrid treatment near the wall and was utilized in the solution. The hybrid wall treatment blends the High-Reynolds approach and the Low-Reynolds solution depending on the mesh refinement near the wall. For both cases the pressure-velocity coupling is solved through the SIMPLE algorithm and the differencing scheme was second order upwind.

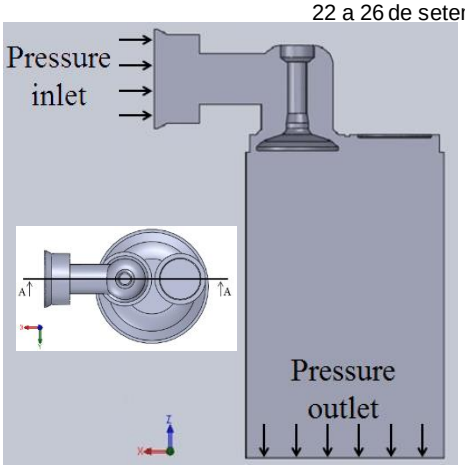

Fig. 1 – Cut A-A in the domain with the boundary conditions

Owing to the poor prediction of flows with high curvature, the k-ε model can converge the solution in the steady-state configuration, so the cases with this model were computed with the temporal term disabled. It is important to point that computations with k-ε model were not tested in transient state because the residual criterion could be achieved in steady state regime. However, the studied phenomena have an intrinsic time variation due to the jet instability after the valve gap and its recirculation. So the *SST* k-ω model can't solve the flow in a steady state regime and computations for this model were performed in transient configuration.

Regarding the mesh, all ones were generated with ICEM (ANSYS) software using unstructured tetrahedral cells with three prism layers of 0.3 mm of thickness and a height ratio of 1.2. A mesh independence study was performed for each model utilized, taking as parameter the mass flow rate in the outlet boundary.

4.1 Mesh independence study for k-ε Standard Turbulence Model

For the mesh independence study the case taken was the 10 kPa of suction pressure and 2.5 mm of valve lift. All meshes were generated with the same number of prism layers and thickness. After ten simulations with different volume numbers, it was chosen about 750,000 cells in the domain. As can be seen in Fig.3, after this value, the parameter varied only 0.5%.

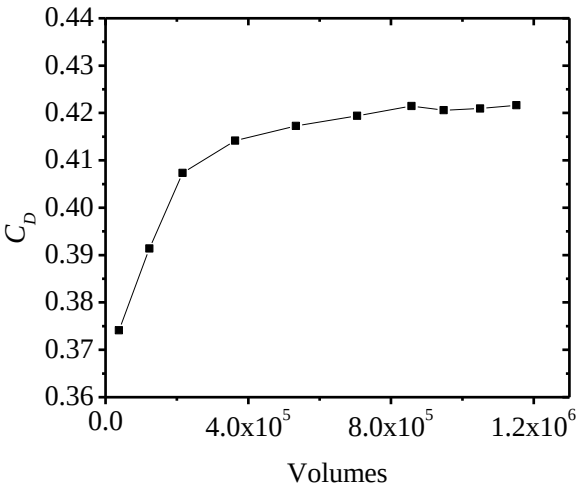

Fig.2 – Mesh independence study for k-ε Standard Model

4.2 Mesh independence study for SST k-ω Turbulence Model

The case taken was the 10 kPa of suction pressure and 1 mm of valve lift. These simulations have a temporal variation, therefore the results of mass flow rate were obtained as a time-averaged of ten emitted vortexes. First of all, the spatial mesh independence study was performed with an appropriate time-step (Δt) that can converge the solution. The Fig.3(a) shows the discharge coefficient of each mesh utilized. According to the figure, the mesh with about 1,500,000 volumes had an error minor than 1%, and was adopted in the temporal mesh independence study. Five time-steps were analyzed and, as can be seen in the Fig.3(b), for all Δt utilized, the solution varied less than 0.2%. So, the time-step selected was the 10^{-5} s.

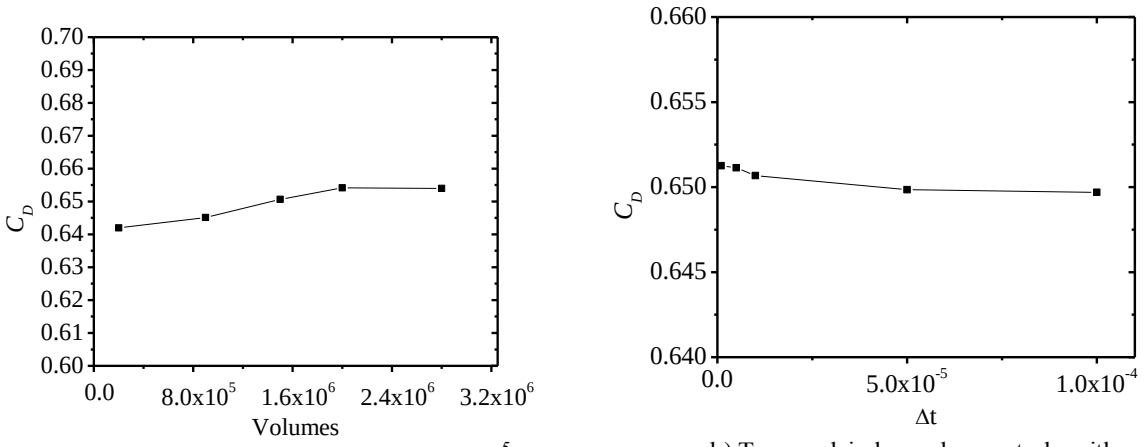

a) Spatial independence study with $\Delta t = 10^{-5}$ s

b) Temporal independence study with 1,500,000 volumes

Fig.3 - Mesh independence study for *SST k-ω* Turbulence Model

The Fig.4 shows the mesh cut plane A-A adopted for each model, where the left was utilized for the *SST k-ω* and the right for the *k-ε* Standard. In *ICE*, the intake flow is the minimum area for the flow, so, owing to this characteristic, a mesh density with the half size of the global mesh was utilized in this region. A good mesh quality could be achieved in all domain.

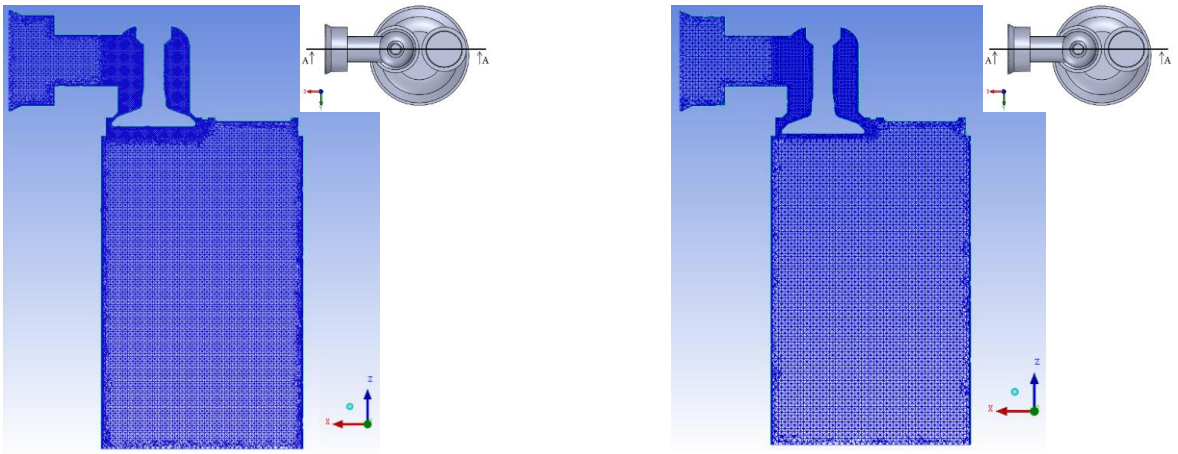

a) *SST k-ω* turbulence model

b) *k-ε* Standard turbulence model

Fig.4 – Mesh utilized in each case

5. EXPERIMENTAL METHODOLOGY

Measurements were made in the intake system of a standard single cylinder four stroke Honda GX35 engine (specifications in the Table 1).

Table 1. Specifications of the engine (Honda, 2014)

Bore x Stroke [mm]	39 x 30
IVO/IVC [BTDC/ATDC]	25.41/66.21
Displacement [cm^3]	35.8
Maximum valve lift [mm]	2.82
Intake air system	Naturally aspirated
Compression ratio	8:1

In order to generate the flow in the intake system the piston was removed, and an electrical fan controlled by a voltage variator was put at end of the cylinder, providing a known suction pressure. The Fig.5 shows the scheme of the developed test rig. It was set three different suction pressures: 10 kPa, 8 kPa and 6 kPa. This pressure downstream of the valve was monitored with a piezoresistive transducer MPX4115AP (Freescale, 2010). For each suction pressure, the intake valve was opened at: 1 mm, 2 mm, 2.5 mm. The valve lift was measured with a length gauge with an accuracy of ± 0.2 µm (Heidenhain MT 25, 2012).

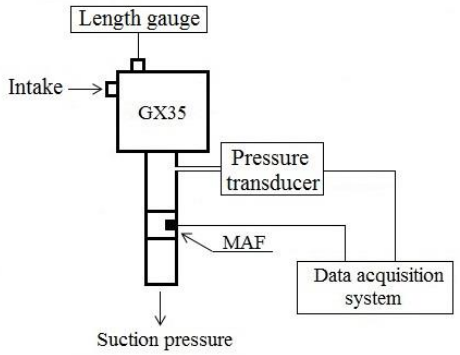

Fig.5 – The test rig

The carburetor system was removed, and the mass flow measured below the intake valve with an automotive hot film anemometer (Bosch, 2010; Beckwith et al, 1993). (Only part of the air-mass flow is registered by the sensor element. The total air mass flowing through the measuring tube is determined by means of calibration, known as the characteristic-curve of the sensor (Bosch, 2010). The characteristic-curve, relating output voltage of the hot film anemometer and the air mass flow, was taken by an orifice plate, according ABNT standard (NBR ISO 5167-1, 1994). The hot film anemometer was connected to a data acquisition board National Instruments 6221 (NI, 2012). With the supply of the LabVIEW software (LV, 2008), the measurements were done with a 2,000 samples per second. The "steady" results were obtained with an average of one minute of measurement.

The intake valve opening was measured as a function of crankshaft angle in order to calculate the C_{D_Global}. The angular position of the crankshaft was measured by a rotary encoder, with a resolution of 0.175 degree (Autonics, 2012), and the lift with the same length gauge previously described. Table 2 presents the angular interval corresponding to each intake valve lift utilized to calculate the global discharge coefficient.

Table 2. Angular interval corresponding to each intake valve lift

Intake valve lift [mm]	Angular interval $\Delta\theta$ [degrees]
1.000	41.967
2.000	30.059
2.500	21.929

An uncertainty study was performed to estimate the total uncertainty of the mass flow measurement system. The utilized method was the propagation of uncertainty, according Kline and McClintock (1953). By this way, the total obtained uncertainty or the system is 4% (Soriano, 2012).

6. RESULTS

The discharge coefficient of the intake system of an internal combustion engine was obtained through computational three-dimensional calculation utilizing *k-ε* Standard and *SST k-ω* turbulence models. In order to compare the model's results, the same simulated cases were measured in a test rig developed by the authors.

The Fig.6 presents the experimental and numerical C_D results for the three valve lift utilized. The vertical line centered in the experimental result denotes the uncertainty of the test rig. According to the Fig.4, both turbulence models presented good results when compared with the measurement, however, for lower valve lifts the *SST k-ω* achieved better results, as expected. The biggest deviation of the *SST k-ω* was in the higher valve lift, but it is still close to the experimental result. Regarding the *k-ε* model, although not perfectly adequate for this physical situation, for a global parameter as the C_D its use can be accepted, taking into the account its lower computational cost and industrial popularity.

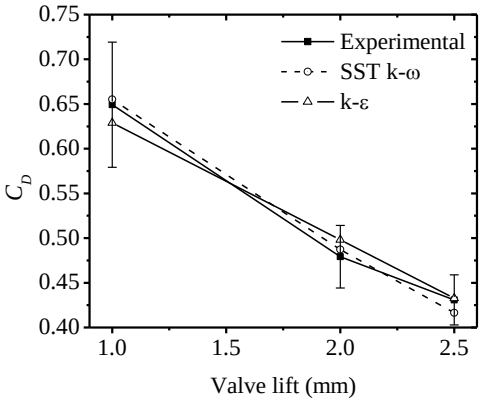

Fig.6 – C_D for each valve lift

The Fig.7 shows the results of C_{D_GLOBAL}, for the three applied methodologies. Although the flow in the studied cases had a wide range of Reynolds number, and in some regions a relaminarization occurs, both turbulence models presented a good agreement with experimental results. However, the *SST k-ω* is the model that presented better results compared with the experimental data.

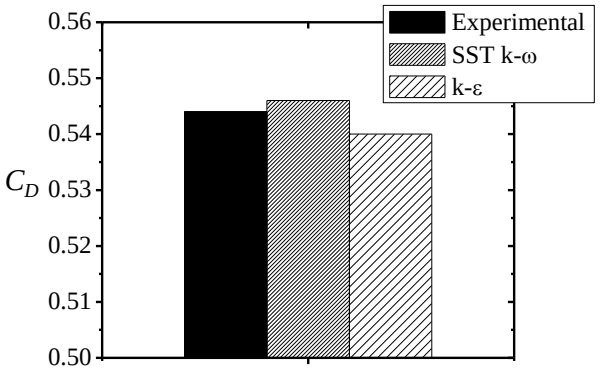

Fig.7 – C_{D_GLOBAL} of the three methodologies applied

The Fig.8 shows the velocity contours in a section plane A-A in the center of the valve, for a lift of 2.5 mm. The *SST k-ω* model oscillates the jet in the valve exit, so, for comparison, it was taken an instant of time that the jet was similar to the *k-ε* model. According to the results, there is a discrepancy in the velocity field regarding the turbulence model. The difference starts upstream of the valve. When the flow hits the valve stem, a stagnation point is established, and it behaves like a flow around a cylinder. So, in the right side of the valve stem, the *SST k-ω* model predicts a higher velocity due to a different prediction of the recirculating flow in this region. The difference persists inside the cylinder, where in this instant of time the *SST k-ω* computes a bigger jet.

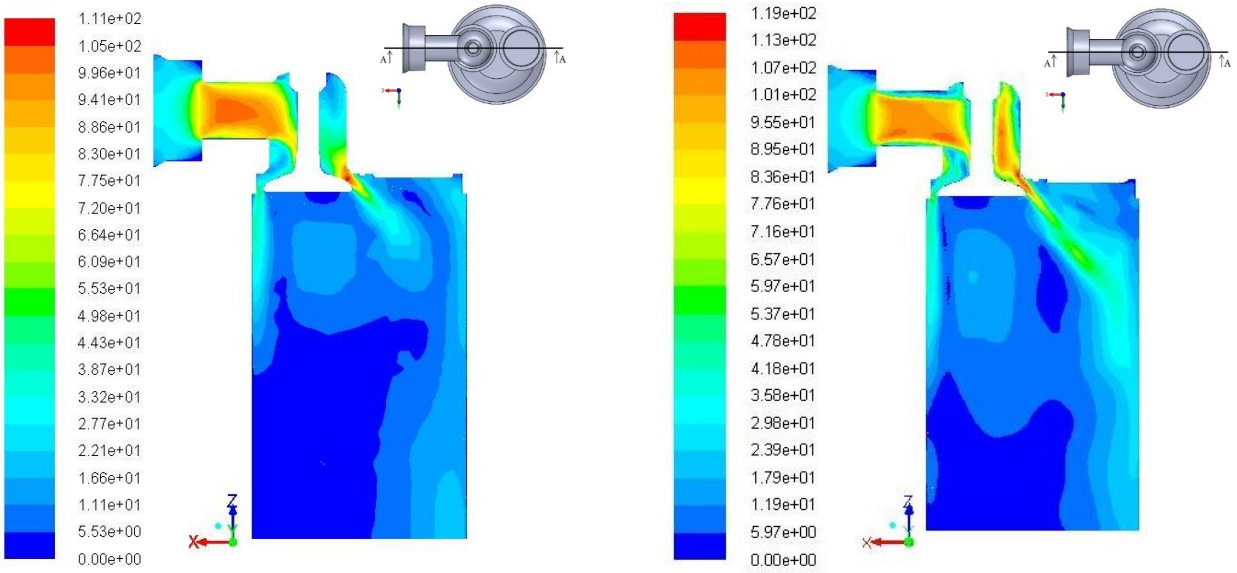

a) k-ε Standard turbulence model b) SST k-ω turbulence model

Fig.8 – Contours of velocity in the section A-A for 2.5 mm of valve lift [m/s]

7. CONCLUSION

The steady flow through the intake system of an *ICE* was solved with FLUENT Finite Volumes *CFD* code, applying the *k-ε* standard and *SST k-ω* turbulence model. The numerical results were compared in terms of C_D, for three different valve lifts, with experimental results using an automotive hot film anemometer sensor, calibrated through an orifice plate.

The studied phenomena have an intrinsic time variation due to the jet instability after the valve gap. In the case of the *SST k-ω* model, the flow could not be computed in a steady state regime. So, for this model, computations were performed in transient configuration and the results of mass flow rate obtained as a time-averaged of ten emitted vortexes. On the other hand, the *k-ε* model permits the convergence of the solution in the steady-state configuration, because it's poorly prediction of this type of flow. Nevertheless, both numerical results revealed a good agreement with the experimental data, taking into account its uncertainty. For lower valve lifts the SST k-ω achieved better results, as expected. Additionally, the worst result of this model is still in the experimental uncertainty range. Regarding the *k-ε* standard model, all results are in the experimental uncertainty range too. This model is not perfectly adequate for this

physical situation, however, referring to a global quantity as the C_D, its use can be accepted, taking into the account its lower computational cost and industrial popularity.

Considering the velocity fields, a difference between the models results is seemed for the region of the duct upstream the valve gap, where a recirculation region is present.

Concluding, for the well prediction of the flow simulation in internal combustion engines, the SST k-ω turbulence model is more appropriated. This result is achieved because the engine ducts have a high curvature and a separating region downstream the valve, which adds more complexity for the studied phenomenon.

8. REFERENCES

ANSYS FLUENT. Theory Guide, 2014.

Associação Brasileira de Normas Técnicas. NBR ISO 5167-1: Medição de vazão de fluidos por meio de instrumentos de pressão – Parte 1: Placas de orifício, bocais e tubos de Venturi instalados em seção transversal circular de condutos forçados. Rio de Janeiro, 1994.

Autonics rotary encoder (incremental type), 2012, "E40S-6-2048-6-L-5 manual". http://autonics.thomasnet.com/Asset/E40S,HB,E80H%20manual.pdf

Beckwith, T. G.; Marangoni, R. D.; Leinhard, J.H. "Mechanical Measurements", 5. ed., 1993.

Bianchi, G.M., Fontanesi, S., 2003, "On the Applications of Low-Reynolds Cubic k-ε Turbulence Models in 3D Simulations of ICE Intake Flows". SAE Paper No 2003-01-0003.

Bianchi, G.M., Cantore, G. and Fontanesi, S., 2002, "Turbulence Modeling in CFD Simulation of ICE Intake Flows: The Discharge Coefficient Prediction". SAE Paper No 2002-01-1118.

Bicen, A.; Vafidis, C.; Whitelaw, J. H. Steady and unsteady airflow through the intake valve of a reciprocating engine. ASME Trans., J. Fluids Engng, vol. 107, pp. 413-420, 1985.

Blair, G. P., Design and Simulation of Four Stroke Engines. SAE International, 1999.

Bosch, 2010 "Hot-film air-mass meter, type HFM 2" model 0 280 218 002 http://apps.bosch.com.au/motorsport/downloads/sensors_airmass.pdf.

Deschamps, C. J. . Modelos Algébricos e Diferenciais. In: A.P.S. Freire, P.P.M. Menut e S. Jian. (Org.). I Transição e Turbulência. Rio de Janeiro / RJ: ABCM. 1998, v. 1, p. 99-155.

Freescale semiconductor. Integrated silicon pressure sensor on-chip signal conditioned, temperature compensated and calibrated, 2010. http://www.freescale.com/files/sensors/doc/data_sheet/MPX5050.pdf

Heywood, J.B. 1988, Internal Combustion Engines. McGrawHill Inc.

High-accuracy length gauges, 2012, "HEIDENHAIN-METRO MT25", https://www.valuetronics.com/Manuals/HEIDENHAIN_MT12-MT25B.pdf.

Honda Engines GX35, 2012, "model-detail/gx35" http://engines.honda.com/models/model-detail/gx35.

Kaario, O.; Pokela, H.; Kjaldman, L.; Tiainen, J.; Larmi, M. LES and RNG Turbulence Modeling in DI Diesel Engines, SAE paper N°. 2003-01-1069, 2003.

Kline, S. J.; McClintock, F. A. Describing uncertainties in single-sample experiments. Mech. Engr. 75:3-8, 1953.

Labview, 2008 "User guide" National Instruments.

Launder, B.E.; Spalding, D.B. The Numerical Computation of Turbulent Flows, Comp. Meth. in Appl. Mech. and Eng., 3, PP. 269-289, 1974.

Martins, J.; Teixeira, S; Coene, S. "Design of an inlet track of a small I.C. engine for swirl enhancement", 20th International Congress of Mechanical Engineering, Gramado – RS. Proceedings of COBEM 2009, Rio de Janeiro, RJ: ABCM, 2009.

Menter, F.R. Zonal Two Equation k-ω Turbulence Models for Aerodynamic Flows, Proc. 24th Fluid Dynamics Conf., Orlando, Florida, USA, 6-9 July, AIAA Journal 93-2906, 1993.

National instruments, 2012, "NI PCI-6221". http://sine.ni.com/nips/cds/print/p/lang/en/nid/14132.

Rech, C., 2010, "Análise Numérica e Experimental do Escoamento em Motores de Combustão Interna." Tese (Doutorado em Engenharia Mecânica) – Programa de Pós-Graduação em Engenharia Mecânica, Universidade do Rio Grande do Sul. Porto Alegre.

Soriano, B. S. Investigação Númerica E Experimental Do Coeficiente De Descarga Em Motor De Combustão Interna. Trabalho de conclusão de curso – Ulbra, 2012.

Vielmo, H. A.; Rech, C.; Baratta, M.; Catania, A.E.; Pesce, F.C.; Spessa, E. "Comparisons Between Steady State Analyses of a High Swirl-Generating Helical Intake Port for Diesel Engines", 12th Brazilian Congress of Thermal Engineering and Sciences, Belo Horizonte - MG. Proceedings of ENCIT, Rio de Janeiro, RJ: ABCM, 2008.

Wilcox, D.C. Reassessment of the Scale-Determining Equation for Advanced Turbulence Models, AIAA Journal. Vol. 26, Nov., pp. 1299-1310, 1988.

Wilcox, D.C. Turbulence Modeling for CFD, 2nd edition, DCW Industries, Inc. La Cañada, California, 2000.

3. ACKNOWLEDGEMENTS

Soriano, B S thanks the Capes for the master's grant, and Vielmo H A thanks CNPq for research grant 303823/2012-7.

5. RESPONSIBILITY NOTICE

The authors are the only responsible for the printed material included in this paper.

Analysis of the influence of synthetic inlet turbulence on the prediction of reactive flow fields

João Marcelo Vedovoto, jmvedovoto@mecanica.ufu.br
Aristeu da Silveira Neto, aristeus@mecanica.ufu.br
School of Mechanical Engineering, Federal University of Uberlândia, Uberlândia-MG, 38400-902 Brazil
Luis Fernando Figueira da Silva, luisfer@esp.puc-rio.br
Department of Mechanical Engineering, Pontifícia Universidade Católica do Rio de Janeiro, Rio de Janeiro-RJ, 22453-900 Brazil
Arnaud Mura, arnaud.mura@isae-ensma.fr
Institut Pprime, UPR3346 CNRS, ENSMA and University of Poitiers, BP40109 - 86961, Poitiers, France

Time-resolved numerical simulations, such as Large Eddy Simulations (LES), have the capability of simulating the unsteady dynamic of large scale energetic structures of turbulent velocity fields. However, they are known to be sensitive to inflow conditions so that modelling of the inflow boundary conditions may become a crucial ingredient of the computational model. The present work reports Large Eddy Simulations of reactive turbulent channel flows of premixed propane/air mixtures. The principal aim of this study is to investigate the sensitivity of the flow dynamics and mixing to inflow conditions. The analysis undoubtedly confirms that the mean velocity and turbulence kinetic energy profiles at the inflow significantly affects the computational flowfield. It is also found that, even with properly set mean velocity and turbulence kinetic energy profiles as available from experimental data flowfields still remain extremely sensitive to the choice of the synthetic turbulence model retained.

1. Introduction

It is well known that a subject of great importance for fluid flow numerical simulations is the prescription of correct and realistic boundary conditions. For outflow conditions, it appears that the use of a buffer zone (BODONY, 2006) or an advective boundary condition (ORLANSKI, 1976), or even a combination of both, may adequately describe several flow conditions of practical interest. The specification of inflow boundary conditions may also raise several issues. For steady Reynolds Averaged Navier Stokes (RANS) simulations, simple analytical or experimental profiles are retained for mean velocity components and turbulent characteristics. For LES or Direct Numerical Simulations (DNS), however, the inflow data should consist of an unsteady fluctuating velocity signal representative of the turbulent velocity field at the inlet.

There are several ways to remedy this situation, and the existing methods belong to two principal categories: *(i) recycling methods*, in which some sort of turbulent flow is pre-computed, prior to the main calculation, and subsequently introduced at the domain inlet, and *(ii) synthetic turbulence methods*, in which some form of random fluctuation is generated, modulated according to experimental data, and combined with mean inflow. Other appealing strategies have been introduced in the literature, some of them are based on Fourier techniques, and others rely on the Proper Orthogonal Decomposition (POD) introduced by Lumley (1967), see for instance Druault et al. (2004).

The present manuscript is organized as follows: first a brief description of recycling methods is provided. Further, synthetic turbulence generators are presented, and the four methods retained in the present work are detailed: (i) the *white noise*, (ii) the method proposed by Klein, Sadiki and Janicka (2003), (iii) the *Random Flow Generator - RFG* introduced by Smirnov, Shi and Celik (2001) and (iv) the *Synthetic Eddy Method - SEM* of Jarrin et al. (2009). The synthetic turbulence generators have been implemented in a low Mach number Navier-Stokes solver, the main features of which are presented, including a brief description of both mathematical and numerical aspects. Finally, the paper ends with the application of the above-mentioned synthetic turbulence generators to the numerical simulation of high speed non-reactive and reactive turbulent mixing layers, which were experimentally studied by Moreau and Boutier (1977), see also Magre et al. (1988).

2. Literature review

The specification of realistic turbulent inflow boundary conditions remains a challenging issue for both LES and DNS. A review of some of the existent methods that deal with such turbulent inlet conditions is provided below.

2.1 Recycling methods

The most accurate method to specify turbulent fluctuations for either LES or DNS would be to run a suitable precursor simulation with the purpose of providing the main simulation with accurate boundary conditions. However, such a procedure has been used only when the turbulence at the inlet can be regarded as a fully developed or a spatially developing boundary layer and in the absence of feedback mechanisms. In these cases periodic boundary conditions in the mean flow direction can be applied to the precursor simulation. In general, the simulation of the precursor flow is initialized with a mean velocity profile perturbed with a few unstable Fourier modes. Instantaneous velocity fluctuations in a plane positioned at a fixed streamwise location are extracted from the precursor simulation and prescribed at the inlet of the main simulation at each time step.

In practice, periodic boundary conditions can only be used to generate inflow conditions for homogeneous flows in the streamwise direction, which restricts their applications to simple fully developed flows. In the present work, we focused our developments searching for a general approach for generating inlet turbulent conditions, hence the resort to synthetic turbulence generators.

2.2 Synthetic turbulence generators

Methods that do not rely on a precursor simulation, or re-scaling of a database obtained from a precursor simulation, synthesize inflow conditions using some sort of stochastic procedure. These procedures use random number generators to build a fluctuating velocity signal similar to those observed in turbulent flows. This is possible based on the assumption that a turbulent flow can be approximated from a set of low order statistics, such as mean velocity, turbulent kinetic energy, Reynolds stresses, two-point or two-time correlations. However, it is worth emphasizing that the resulting synthesized signals remain only a crude approximation of turbulence. From a statistical point of view, some crucial quantities, such as the dissipation rate, the turbulent transport or the pressure-strain term that appears in the Reynolds stresses balance are often not well reproduced. The dynamics of the turbulent eddies are not perfectly recovered, and the synthesized flow may undergo a transition to turbulence. Therefore, synthesized turbulence can have a structure that significantly differs from that of the real flow fields (JARRIN et al., 2009).

2.2.1 White noise based synthetic turbulence generators

The most straightforward approach to build synthetic fluctuations is to generate a set of independent random numbers between zero and unity which can *mimic* the turbulence intensity at the inlet. Indeed, if the turbulent kinetic energy level k is known, it can be used to scale a random signal $\mathcal{R}_{u_i}$ with zero mean and unity variance. Thus, the fluctuations exhibit the correct level of turbulent kinetic energy, which yields $u_i = \widetilde{u}_i + \mathcal{R}_{u_i}\sqrt{2k/3}$, where $\mathcal{R}_{u_i}$ is taken from independent random variables for each velocity component at each instant and location on the computational inlet plane. This procedure generates an isotropic random signal that reproduces both the mean velocity and turbulent kinetic energy levels. However, the signal generated does not present any two-point nor two-time correlations. The white noised based random fluctuations have their energy sprectrum uniformly spread over all wave numbers and, as already stated above, this energy will be quickly dissipated downstream of the inlet boundary. A more valuable approach for generating synthetic turbulence consists in creating bins of random data, which can then be processed using digital filters, so that the resulting set of processed data will display desired statistical properties, such as spatial and temporal correlations (LUND, 1998; KLEIN; SADIKI; JANICKA, 2003).

2.2.2 Digital filters based synthetic turbulence generators

Klein, Sadiki and Janicka (2003) proposed a digital filtering procedure to remedy the lack of large-scale correlation in the inflow data generated from the above method. In one dimension the velocity signal $u'(j)$ at a point j is defined as a convolution or a digital linear non-recursive filtering, $u'(j) = \sum_{k=-N}^{N} b_k \mathcal{R}_{j+k}$, where $\mathcal{R}_{j+k}$ is a series of random data generated at point $(j+k)$ with $\overline{\mathcal{R}}_m = 0$, $\overline{\mathcal{R}_m \mathcal{R}_m} = 1$ and b_k are the filter coefficients. The integer number N is related to the size of the filter support.

Following Klein, Sadiki and Janicka (2003), it is possible to generate a large amount of data, store and convect it through the inflow plane by applying Taylor's hypothesis. However, for the applications considered here, the inflow data will be generated on-the-fly.

It should be noted that the main parameters retained to evaluate this method are the choice of the length scales, which

are directly connected to the filter support size, and the dimensions of the control volume. Thus, a given value of the characteristic length scale may be reproduced by correctly choosing the filter support size as well as the control volumes dimensions. However, as will be shown below, the length scales and, consequently, the filter support size strongly impact on the computational cost of the method. Finally, since a fixed computational grid is used here to assess the different turbulent inflow generators, the parameters retained to evaluate the method of Klein, Sadiki and Janicka (2003) will be the support size, only.

2.2.3 Synthetic turbulence generators based on Fourier techniques

To the authors best knowledge, Kraichnan (1970) was the first to use a Fourier decomposition to generate a synthetic fluctuating turbulent flow field. In Kraichnan's early work, the flow is initialized with a three-dimensional homogeneous and isotropic synthetic velocity field to study the diffusion of a passive scalar. Since velocity fluctuations are homogeneous in the three dimensions, they can be decomposed in the Fourier space, $\mathbf{u}'(\mathbf{x}) = \sum_{\mathbf{k}} \hat{\mathbf{u}}'_{\mathbf{k}} e^{-i\mathbf{k}.\mathbf{x}}$, where $\mathbf{k}$ is a three-dimensional wave number vector. Each complex Fourier coefficient $\hat{\mathbf{u}}'_{\mathbf{k}}$ defines an amplitude evaluated from a prescribed isotropic three-dimensional energy spectrum $E(|\mathbf{k}|)$ and a random phase $\theta_{\mathbf{k}}$, taken uniformly in the $[0, 2\pi]$ interval (ROGALLO, 1981). The synthesized velocity field is thus given by $\mathbf{u}'(\mathbf{x}) = \sum_{\mathbf{k}} \sqrt{E(|\mathbf{k}|)} e^{-i(\mathbf{k}.\mathbf{x}+\theta_{\mathbf{k}})}$. Several adaptations of Kraichnan's method were proposed throughout the years. Among them,important developments can be found in Lee, Lele and Moin (1992) and Le, Moin and Kim (1997). More recently, Smirnov, Shi and Celik (2001) modified the method of Le, Moin and Kim (1997) in such a manner that it becomes possible to obtain a turbulent velocity field by requiring statistical information only. The method of Smirnov, Shi and Celik (2001) is capable of synthesizing non-homogeneous turbulence within a general framework. It relies on the Fourier decomposition, with Fourier coefficients computed from spectral data based on local turbulent time and length scales obtained at different locations across the flow. This method, called *Random Flow Generation - RFG*, differs from the original proposal of Lee, Lele and Moin (1992) since it does not use of Fourier transforms. It is based on scaling and coordinates transformation operations only, which, on non-uniform grids, are much more efficient.
It is worth noting that this procedure requires specifying the characteristic integral length and time scales of turbulence, and the correlation tensor R_{ij} of the flow. These quantities can be obtained from experimental data, but some of them may also be approximated from preliminary RANS simulations.

2.2.4 Synthetic eddy method - SEM

The synthetic eddy method (SEM), proposed by Jarrin et al. (2009), is based on the decomposition of the turbulent flow field into stochastic coherent structures. The corresponding eddy-structures are generated at the computational domain inlet plane and defined thanks to a shape-function $f_\sigma(x)$, which is intended to embrace turbulence spatial and temporal characteristics.

The synthetic eddy method can be introduced by using a one-dimensional scheme, in which the velocity component is generated within the range $[a, b]$. The shape-function of each turbulent spot features a compact support in $[-\sigma, \sigma]$, a position x_i, a length scale σ and is assigned a signal ϵ_i. In other words, the contribution $u^{(i)}(x)$ of a turbulent spot i to the velocity field, is defined as $u^{(i)}(x) = \epsilon_i f_\sigma(x - x_i)$, with a location x_i randomly chosen within the range $[a-\sigma, b+\sigma]$ and where ϵ_i denotes a random step of value -1 or $+1$. The synthetic eddies are generated in an interval larger than $[a, b]$. This larger interval guarantees that the inlet points are surrounded by eddies. Finally, the resulting velocity field $u(x)$ at any location will be the sum of the contributions of all synthetic eddies located in the domain, $u(x) = \sum_{i=1}^{N} \epsilon_i f_\sigma(x - x_i)/\sqrt{N}$, where N denotes the total number of synthetic eddies. The final velocity field u_i is then obtained from the above synthetic fluctuating velocity field u'_j, the velocity mean profile $\bar{u}_i$, and the Cholesky's decomposition a_{ij} of the Reynolds stress tensor: $u_i = \bar{u}_i + a_{ij} u'_j$.

3. Computational model

The mathematical and computational framework retained to proceed with the numerical simulation is now briefly presented. The interested reader may find a detailed presentation elsewhere (VEDOVOTO et al., 2011). A hybrid approach in which the LES methodology is coupled with the transport of the scalar probability density function (PDF) is retained to describe the reactive cases. The method involves the numerical solution of partial differential equations (LES solver) together with stochastic differential equations (PDF solver). From the LES approach the Eulerian filtered variables are evaluated while stochastic differential equations (SDE) are solved using Lagrangian notional particles to simulate the

modelled transport equation of the scalar PDF (POPE, 1985; COLUCCI et al., 1998). The latter yields the one-point, one-time statistics of subgrid-scale scalar fluctuations and thus provides the LES solver with the corresponding filtered chemical reaction rate.

3.1 Set of filtered equations

The following simplifying assumptions are used: (a) fluid is considered as Newtonian, (b) body forces, heat transport by radiation, Soret and Dufour effects are not addressed, (c) the model is developed for low Mach number flows, (d) we consider unity Lewis number values and equal molecular diffusion coefficients for all species, (e) heat losses are neglected. The mathematical model considers multi-species variable-density reactive flows, in which the primary transported variables are the density ρ, the three velocity components u_i, the specific enthalpy h and the mass fractions Y_k of the K chemical species $(k = 1, \ldots, K)$, the balance equations are:

$$\frac{\partial \overline{\rho}}{\partial t} + \frac{\partial \overline{\rho}\,\widetilde{u}_j}{\partial x_j} = 0, \tag{1}$$

$$\frac{\partial \overline{\rho}\,\widetilde{u}_i}{\partial t} + \frac{\partial \overline{\rho}\,\widetilde{u}_j\,\widetilde{u}_i}{\partial x_j} = \frac{\partial \overline{T}_{ij}}{\partial x_j} - \frac{\partial \tau_{ij}^{SGS}}{\partial x_j}, \tag{2}$$

$$\frac{\partial \overline{\rho}\,\widetilde{\phi}_\alpha}{\partial t} + \frac{\partial \overline{\rho}\,\widetilde{u}_j\,\widetilde{\phi}_\alpha}{\partial x_j} = \frac{\partial \overline{Q}_{\alpha,j}}{\partial x_j} - \frac{\partial Q_{\alpha,j}^{SGS}}{\partial x_j} + \overline{S}_\alpha, \tag{3}$$

where the variable ϕ_α denotes the mass fraction of a chemical species or the enthalpy of the mixture, $(x_i, i = 1, 2, 3)$ are the spatial coordinate, and t is the time. $T_{ij} = \tau_{ij} - p\,\delta_{ij}$ is the tensor of mechanical constraints including both a deviatoric (shear stresses τ_{ij}) and a spheric (pressure $p\,\delta_{ij}$) contribution, while $Q_{\alpha,j}$ denotes the component of the molecular diffusion flux of the scalar α in the direction j. In the above expression, $\tau_{ij}^{SGS} = (\overline{\rho u_i u_j} - \overline{\rho}\,\widetilde{u}_i\,\widetilde{u}_j)$ is the subgrid scale (SGS) stress tensor and $Q_{\alpha,j}^{SGS} = \left(\overline{\rho u_i \phi_\alpha} - \overline{\rho}\,\widetilde{u}_i\,\widetilde{\phi}_\alpha\right)$ represents the SGS scalar flux components, respectively. Finally, the last term in the RHS of Eq. (3), i.e. $\overline{S}_\alpha$, denotes the filtered reaction rate. The above system is completed by an equation of state: $P = P_0(t) + p(\mathbf{x}, t)$, with $P_0(t)$ the thermodynamic pressure.

The unresolved momentum fluxes are expressed according to the Boussinesq assumption,

$$\tau_{ij}^{SGS} - \delta_{ij}\tau_{kk}^{SGS}/3 = 2\mu_{SGS}\left(\widetilde{S}_{ij} - \delta_{ij}\widetilde{S}_{kk}/3\right) \tag{4}$$

where μ_{SGS} is the subgrid scale viscosity, and $\widetilde{S}_{ij} = (\partial\widetilde{u}_i/\partial x_j + \partial\widetilde{u}_j/\partial x_i)/2$ is the strain rate tensor of the resolved field (FERZIGER; PERIC, 1996). The eddy viscosity μ_{SGS} is obtained from the Smagorinsky closure, i.e., assuming that the small scales are in equilibrium, so that energy production and dissipation are in balance, which yields, $\mu_{SGS} = 2\bar{\rho}(C_s\Delta)^2|\widetilde{S}| = 2\bar{\rho}(C_s\Delta)^2\left(2\widetilde{S}_{ij}\widetilde{S}_{ij}\right)^{1/2}$, where C_s denotes the Smagorinsky constant. It is known that this closure can be excessively dissipative, especially near the walls, which is corrected herein by using a van Driest damping function (FERZIGER; PERIC, 1996). Finally, the SGS scalar flux is represented with a gradient law, $Q_{\alpha,j} = -\bar{\rho}\Gamma_{SGS}\partial\widetilde{\phi}_\alpha/\partial x_j$, where $\widetilde{\phi}_\alpha$ is the resolved scalar field and Γ_{SGS} denotes the subgrid diffusion coefficient evaluated from $\Gamma_{SGS} = 2\bar{\rho}(C_s\Delta)^2|\widetilde{S}|/Sc_{SGS}$ with Sc_{SGS} a subgrid scale turbulent Schmidt number.

3.2 Lagrangian Monte Carlo approach

The Lagrangian Monte Carlo approach offers the most classical framework to deal with the above PDF transport equation (POPE, 1985; FOX, 2003). In this approach, the joint scalar PDF is represented by an ensemble of notional particles (FOX, 2003), which evolve according to equivalent stochastic differential equations (SDE). A general framework to construct SDEs that are equivalent to the PDF transport equation is provided by Gardiner (2009).

In the present context, the SDEs that describe the trajectory of the particles in the physical space, $\mathbf{x}$, and in the sample space of the scalar field, Ψ, can be written as:

$$d\mathbf{x} = \left[\tilde{\mathbf{u}}(\mathbf{x}, t) + \frac{\partial \Gamma_{SGS}}{\partial x_i}\right] dt + \sqrt{2\Gamma_{SGS}}\, d\mathbf{W}(t), \tag{5}$$

$$d\Psi = \left[-\Omega_m\left(\Psi - \langle\Phi\rangle\right) + S(\Psi)/\rho(\Psi)\right] dt \tag{6}$$

where $\mathbf{W}(t)$ denotes the Wiener process, associated with a gaussian random variable featuring zero mean value and a variance dt (FOX, 2003), $\Omega_m = C_\omega(\Gamma + \Gamma_{sgs})/\Delta^2$ denotes the turbulent mixing frequency, with $C_\omega = 2.0$ the mechanical to scalar time scale ratio (RAMAN, 2004). The evolution of each notional particle occurs according to statistically independent increments $d\mathbf{W}(t)$, with a subgrid scale diffusion coefficient evaluated from the LES solver. The possible restrictions associated with the use of such an approach have been extensively discussed by Haworth (2010).

3.3 Numerical model

The essential features of the solver that has been used to conduct the numerical simulations are now presented and the reader may refer to (VEDOVOTO et al., 2011) for further details.

3.3.1 Navier-Stokes equations (NSE) solver

The numerical method is based on a three-dimensional, conservative, staggered, finite-volume discretization. In the present work, a fully implicit scheme is retained, which requires the numerical resolution of a large algebraic system; the MSIP - Modified Strongly Implicit Procedure (SCHNEIDER; ZEDAN, 1981) is retained to this purpose.

In the low Mach number flows under consideration, the density is solely determined by the temperature and thermodynamic pressure fields P_0. The energy equation plays the role of an additional constraint on the velocity field, which is enforced by the dynamic pressure. This constraint acts onto the velocity field divergence, and it is related to the total derivative of the density, see Vedovoto et al. (2011). Once the pressure correction is evaluated, the velocity field can be updated. The present numerical simulations are conducted with a central difference scheme (CDS) to represent the spatial derivatives. Time integration is performed using the backward difference scheme (BDF) with a CFL number value set to 0.5. Further information about the available discretization procedures, as well as the verification of the numerical code developed can be found in Vedovoto et al. (2011).

3.3.2 Stochastic differential equations (SDE) solver

The Lagrangian stochastic particles move through the physical space independently of each other. They are assigned spatial coordinates and represent mass. Due to the stochastic nature of motion, the number of particles present in a given elementary volume changes in time. In order to prevent particle accumulations in computational cells, and to keep small computational cells from running empty, particles are ascribed a relative weight and are periodically sampled (ZHANG; HAWORTH, 2004). Following Pope (1985), the SDEs are discretized resorting to a fractional step method. In the next sections we proceed with the analysis of the different turbulent inflow generators by conducting the LES of the experimental test case of Moreau and coworkers. In a first step of the analysis, the corresponding wall bounded turbulent mixing layer flows is investigated in non reactive conditions and then attention is focused on the high-speed turbulent and reactive mixing layer.

4. Numerical simulations of a wall bounded turbulent mixing layer flow

The influence of the synthetic turbulence generators is studied via three-dimensional numerical simulations of a high speed mixing layer. The obtained results are compared with the experimental data provided by Moreau and Boutier (1977). The computational domain is a three-dimensional box with dimensions $(800 \times 100 \times 100)$ mm^3, discretized with a finite volume mesh featuring $320 \times 100 \times 100$ cells in the x_1, x_2 and x_3 directions, respectively. Since the numerical code developed has the capability of performing distributed computing, the computational domain is divided into 40 subdomains. No-slip boundary conditions are imposed in the x_2 and x_3 directions. An advective boundary condition is used at the outflow. The Smagorinsky model is used with $C_s = 0.18$, and the Van-Driest damping function is applied at the walls. The Reynolds number, based on the initial width of the mixing layer, $\delta_m = 5$ mm, the mean velocity difference between the two inlet streams $U_r = 97.5$ m/s and the value of the kinematic viscosity of air at 600 K is $Re = 3075$.

To perform the comparative analysis, the white noise synthetic turbulence generator is considered with fluctuation levels of 20% and 10% imposed on the streamwise and transverse velocity components respectively. For the simulations conducted with the method of Klein, Sadiki and Janicka (2003) the size of the filter support is set to 10, whereas $1,000$ Fourier modes are retained for the simulations based on the method of Smirnov, Shi and Celik (2001). For the simulation carried out using the method of Jarrin et al. (2009), $10k$ eddies are used.

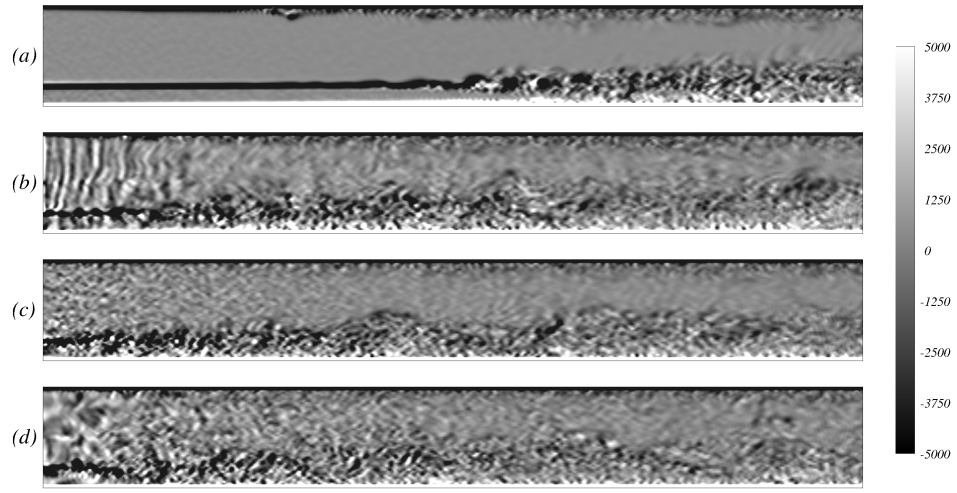

Figure 1. Component in x_2-direction of the vorticity as obtained from the simulations carried out with the method: (a) white noise, (b) Klein, Sadiki and Janicka (2003), (c) RFG of Smirnov, Shi and Celik (2001), and (d) SEM of Jarrin et al. (2009).

Figure (1), which depicts the vorticity component along direction x_2, also provides a valuable insight into the behavior of the Smagorinsky model. It is commonly agreed that the Smagorinsky model is highly dissipative. This is one of the reasons that also explains why the white noise generator signal imposed at the inlet may be rapidly destroyed. However, provided that a more elaborated method is retained to generate the inflow turbulence, Fig. (1) confirms that a signal featuring large scales introduced in the domain is not so quickly dissipated, even when the Smagorinsky model is used.

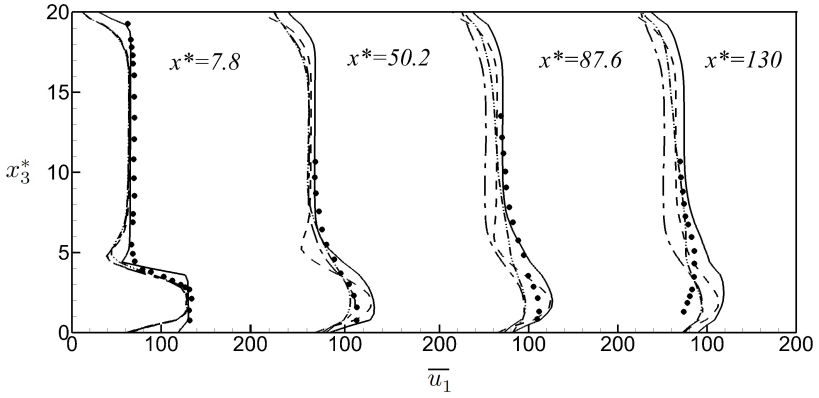

Figure 2. Mean longitudinal velocity profiles. (•): Moreau and Boutier (1977); RFG of Smirnov, Shi and Celik (2001) (- - -); Klein, Sadiki and Janicka (2003) $(- \cdot -)$; white noise $(- \cdot \cdot -)$; SEM of Jarrin et al. (2009) (——).

In order to assess quantitatively the methods implemented, Fig. (2) displays comparisons of the averaged u_1-component of the velocity with experimental data at four distinct locations in the computational domain, for $x_2^* = 10$. The results confirm that the different methods provide an acceptable representation of the mean velocity field when compared with experimental data. However the need for an improved turbulent inflow generator becomes clear to reproduce the levels of velocity fluctuations. Indeed, it can be seen in Fig. (3) that the superimposition of white noise on the mean velocity is unable to recover the experimental data in the first half of the computational domain along the x_1-direction. In contrast, the results obtained with the methods of Klein, Sadiki and Janicka (2003), Smirnov, Shi and Celik (2001), and Jarrin et al. (2009) display a more satisfactory level of agreement with experimental data at the same location.

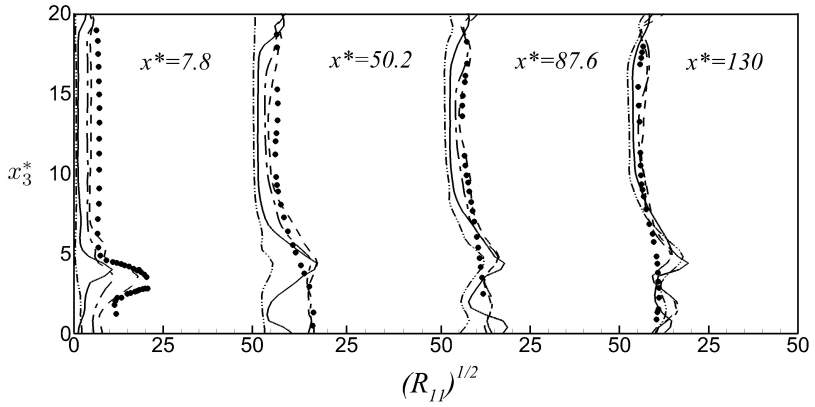

Figure 3. $\sqrt{R_{11}}$ stress tensor component. (•): Moreau and Boutier (1977); RFG of Smirnov, Shi and Celik (2001) (- - -); Klein, Sadiki and Janicka (2003) $(- \cdot -)$; white noise $(- \cdot\cdot -)$; SEM of Jarrin et al. (2009) (——).

From the computational cost point of view, it is clear that the better quality of the results obtained with the methods of Klein, Sadiki and Janicka (2003), Smirnov, Shi and Celik (2001) and Jarrin et al. (2009) require longer CPU times than that associated with the simple superimposition of a white noise on the mean inlet velocity. However, for the present test case, the simulations conducted with the methods of Klein, Sadiki and Janicka (2003) and Smirnov, Shi and Celik (2001) correspond to approximately the same computational cost, i.e., about 40% more than that associated with the white noise methodology, for the former, and 35% for the latter. The cost associated with the numerical simulations conducted with the SEM is 55% higher than that conducted with the white noise. The methods of Klein, Sadiki and Janicka (2003) and Smirnov, Shi and Celik (2001), therefore, appear as particularly attractive. Nevertheless, there are two crucial differences between the methods of Klein, Sadiki and Janicka (2003) and Smirnov, Shi and Celik (2001). The first does not yield temporal correlations, only spatial correlations are guaranteed. Moreover, the method of Smirnov, Shi and Celik (2001) generates a divergence-free velocity field at the inlet.

5. Reactive flows simulations

Although there is already some literature available to describe the influence of realistic turbulent inflow data prescription on non-reactive flows (TABOR; BABA-AHMADI, 2010), such an analysis of the turbulent inflow data effects is much less common for turbulent reactive flows. In this last subsection, a set of two-dimensional reactive flow simulations is conducted to evidence such effects. The computational domain is a three-dimensional box with dimensions $(800 \times 2 \times 100)$ mm^3. It is discretized with a mesh of $320 \times 1 \times 100$ control volumes in the x_1, x_2 and x_3-direction, respectively. Periodicity and no-slip boundary conditions are imposed along x_2 the x_3-directions respectively. The computational domain is divided into 8 parallel regions. The other parameters remain the same as those retained for non reactive cases. Concerning the turbulent inlet generators, for the reactive flow simulations we retain the set-up of the non-reactive simulations.

For the simulation conducted with the white noise, a fluctuation level of 20% is imposed on the streamwise velocity component, while fluctuations of 10% are set for the cross stream velocity component. For the simulations performed with the method of Klein, Sadiki and Janicka (2003) the filter support size is set to 10, while one thousand $(1,000)$ Fourier modes are used for the simulations based on the method of Smirnov, Shi and Celik (2001). Ten thousands $(10k)$ eddies are considered in the simulation conducted with the Synthetic Eddy Method of Jarrin et al. (2009). Magre et al. (1988) have provided a large amount of experimental data gathered in the geometry previously used by Moreau and Boutier (1977) for different flow conditions.

To proceed with the mathematical modelling of the chemical source term, we retain a single step, global, and irreversible reaction that involves the progress variable, i.e., a normalized temperature defined by $c \equiv (T - T_u)/(T_b - T_u)$ where the subscripts u and b denote fresh reactants and fully burned gases conditions respectively. The corresponding chemical reaction rate is given by $S(c) = A_\alpha \rho \dot{\mathcal{S}}$, where the pre-exponential constant can be calculated as $A_\alpha = \Lambda S_L^2/[\alpha \exp(-\beta/\alpha)]$ and $\dot{\mathcal{S}} = (1-c)\exp[-\beta(1-c)/(1-\alpha(1-c))]$ Williams (1985). In the previous expressions, α denotes a normalized temperature factor $\alpha = (T_b - T_u)/T_b$ and the reduced activation energy is $\beta = \alpha(T_a/T_b)$, where

$T_a = E_a/R$ is the activation temperature, E_a is the activation energy and R is the universal constant of gases. Here, we set $E_a = 8,000J/mole$, which is a value representative of CH_4-air combustion. The DVODE algorithm of Byrne and Dean (1993) is employed to perform the numerical integration of the chemical reaction rate.

The initial and boundary condition for the mean value of the progress variable at $x_1^* = 0$, are set with a hyperbolic profile, separating the streams of gases from the auxiliary burner ($c_q = 1$; $T_b = 2000$ K) and of the main duct ($c_p = 0$; $T_u = 560$ K). Concerning the Monte Carlo simulation, 50 particles per control volume are used and the Milstein scheme is employed for the numerical integration of the system of SDEs.

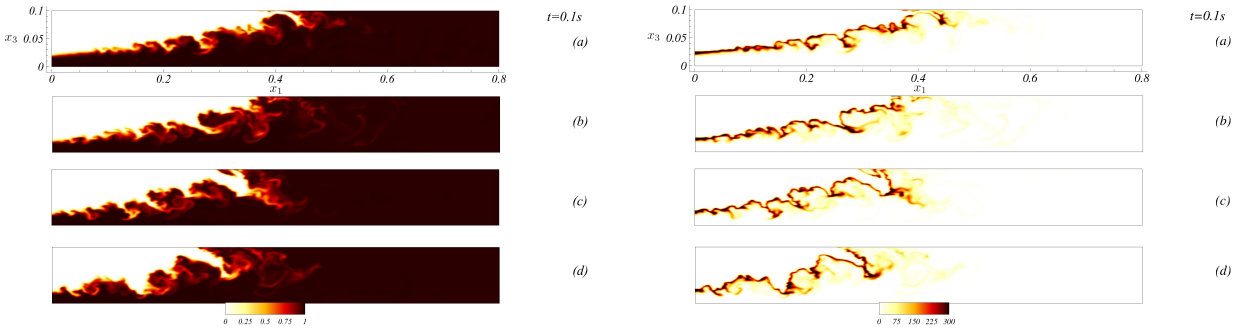

Figure 4. Instantaneous fields of chemical reaction progress variable c - top, and chemical reaction rate $S(c)$ - bottom. The subfigures (a), (b), (c), and (d) display results of simulations with the respective inlet boundary condition methods: white noise; Klein, Sadiki and Janicka (2003), RFG of Smirnov, Shi and Celik (2001) and SEM of Jarrin et al. (2009)

Figure (4) shows instantaneous fields of the chemical reaction progress variable c and the filtered chemical reaction rate $S(c)$ for the present set of numerical simulations. The method of turbulent inflow data generation clearly influences the shear layer spreading rate as well as the position of the instantaneous filtered flame front. For instance, if we consider the subfigure (a) of Fig. (4), the longitudinal span of the turbulent flame front obtained with the white noise is larger than the one obtained using the other three methods.

Concerning the influence of the inlet boundary condition, we observe in Fig. (5) that accounting for a fluctuation spectrum always gives rise to a shorter and thicker flame brush. The length of the 2D flame brush, based on the location of the iso-line $\langle c \rangle = 0.9$ in the x_1 direction, is found to be 560 mm for the simulation carried out with the superimposition of a white noise, while for the methods of Klein, Sadiki and Janicka (2003), Smirnov, Shi and Celik (2001) and Jarrin et al. (2009) the lengths are 543, 497 and 414 mm respectively.

Finally, an interesting point that can be evidenced from the present investigation is to determine how the choice of the method of generation of turbulent inflow data may affect the representation of the flame-turbulence interaction. To this purpose, we recall the definition of the Damköhler number, $Da = \tau_t/\tau_c$, which is the ratio of the characteristic turbulent time scale, τ_t and the chemical time scale, τ_c. This number is one of the quantities that characterizes how turbulence interacts with chemical reactions. It should be noted that the different synthetic turbulence generators may lead to different Damköhler number values.

Indeed, the characteristic time of turbulence is strongly affected by the different methods retained to generate inflow data. Considering the white noise technique, we observed that the fluctuations lie in the range $1 - 20$ m/s, whereas using the methods of Smirnov, Shi and Celik (2001), Klein, Sadiki and Janicka (2003) and Jarrin et al. (2009), the maximum value of fluctuations downstream of the flame brush are about 60, 40 and 70 m/s respectively. Given the grid size and the computational domain retained in the present study, which provide a minimum length of the control volumes of 1 mm, the turbulent characteristic times for the white noise superimposition, the method of Klein, Sadiki and Janicka (2003), the method of Smirnov, Shi and Celik (2001), and the Synthetic Eddy Method are $50\,\mu s$, $16\,\mu s$, $25\,\mu s$ and $14\,\mu s$, respectively. For the cases simulated in the present work, the Damköhler number value is found to be 0.11 for the white noise. For the simulations performed with the methods of Klein, Sadiki and Janicka (2003), Smirnov, Shi and Celik (2001) and Jarrin et al. (2009), the Damköhler number is 0.033, 0.055 and 0.03, respectively which clearly confirms how the results of turbulent reactive flow simulations may be sensitive to the methodology used to generate synthetic turbulence at inlet boundary conditions.

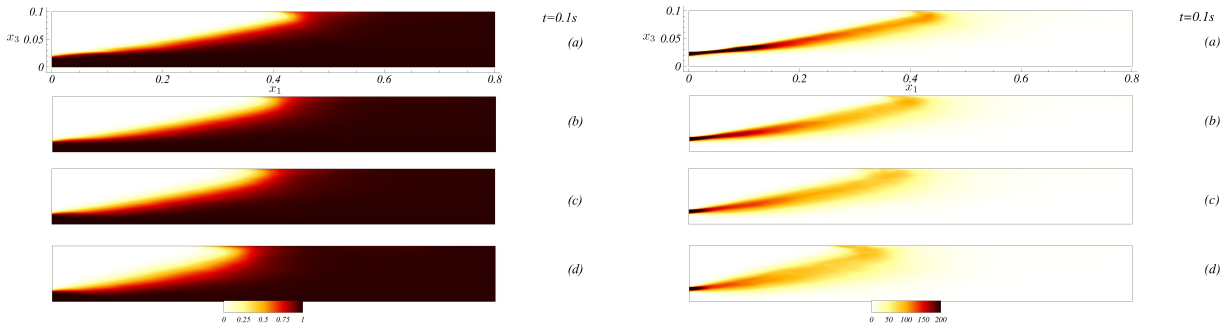

Figure 5. Averaged fields of chemical reaction progress variable c - top, and chemical reaction rate $S(c)$ - bottom. The subfigures (a), (b), (c), and (d) are results of simulations with the respective inlet boundary condition methods: white noise ; Klein, Sadiki and Janicka (2003), RFG of Smirnov, Shi and Celik (2001) and SEM of Jarrin et al. (2009)

6. Conclusion

Large Eddy Simulations of both reactive and non reactive turbulent channel flows of methane/air mixtures have been conducted with special emphasis placed on the influence of turbulent inlet Boundary Conditions. The analysis undoubtedly confirms the sensitivity of the obtained results to the choice of the synthetic turbulence generator retained at the inlet of the computational domain. The computational results of the corresponding LES are investigated in details and the quality of the agreement with experimental data is found to be significantly improved by resorting to elaborated synthetic turbulence generators that account for the large scale dynamics and coherence. The results obtained for reactive flow conditions also clearly emphasize the influence of the retained model on the chemical rate statistics, which confirms the importance of this issue for the LES of turbulent reactive flows. From the computational cost point of view, the methods of Klein, Sadiki and Janicka (2003), Smirnov, Shi and Celik (2001) and Jarrin et al. (2009) require longer CPU time than the method associated with the simple superimposition of a white noise on the mean velocity inlet profile. For the present applications, the additional CPU costs lie between 35% for the method of Smirnov, Shi and Celik (2001), and 55% for the method of Klein, Sadiki and Janicka (2003), which remains moderate considering the potential improvements that may be obtained from their use.

7. Acknowledgements

These results have been obtained as a part of the PhD thesis of J.M. Vedovoto and have been presented at the Eighth International Symposium on Turbulence and Shear Flow Phenomena (TSFP-8) held in August 2013 in Poitiers (France). The authors would like to thanks $Capes$, $FAPEMIG$, $CNPq$ and $Petrobras$ for financial support.

8. REFERENCES

References

BODONY, D. Analysis of sponge zones for computational fluid mechanics. *Journal of Computational Physics*, v. 212, n. 2, p. 681–702, mar. 2006.

BYRNE, G. D.; DEAN, A. M. The numerical solution of some kinetics models with vode and chemkin ii. *Computers & Chemistry*, v. 17, n. 3, p. 297 – 302, 1993.

COLUCCI, P. J.; JABERI, F. a.; GIVI, P.; POPE, S. B. Filtered density function for large eddy simulation of turbulent reacting flows. *Physics of Fluids*, v. 10, n. 2, p. 499, 1998.

DRUAULT, P.; LARDEAU, S.; BONNET, J. P.; COIFFET, F.; DELVILLE, J.; LAMBALLAIS, E.; LARGEAU, J. F.; PERRET, L. Generation of three-dimensional turbulent inlet conditions for large-eddy simulation. *AIAA Journal*, v. 42, p. 447–456, 2004.

FERZIGER, J.; PERIC, M. *Computational methods for fluid dynamics*. [S.l.]: Springer, 1996.

FOX, R. O. *Computational models for turbulent reacting flows*. [S.l.]: Cambridge University Press, 2003.

GARDINER, C. *Stochastic methods: a handbook for the natural and social sciences*. [S.l.]: Springer, 2009. 447 p.

HAWORTH, D. Progress in probability density function methods for turbulent reacting flows. *Progress in Energy and Combustion Science*, Elsevier Ltd, v. 36, n. 2, p. 168–259, abr. 2010.

JARRIN, N.; PROSSER, R.; URIBE, J.-C.; BENHAMADOUCHE, S.; LAURENCE, D. Reconstruction of turbulent fluctuations for hybrid RANS/LES simulations using a Synthetic-Eddy Method. *International Journal of Heat and*

Fluid Flow, Elsevier Inc., v. 30, n. 3, p. 435–442, jun. 2009.
KLEIN, M.; SADIKI, A.; JANICKA, J. A digital filter based generation of inflow data for spatially developing direct numerical or large eddy simulations. *Journal of Compututational Physics*, Academic Press Professional, Inc., San Diego, CA, USA, v. 186, p. 652–665, April 2003.
KRAICHNAN, R. H. Diffusion by a random velocity field. *Physics of Fluids*, v. 13, n. 1, p. 22–31, 1970.
LE, H.; MOIN, P.; KIM, J. Direct numerical simulation of turbulent flow over a backward-facing step. *Journal of Fluid Mechanics*, Cambridge Univ Press, v. 330, p. 349–374, 1997.
LEE, S.; LELE, S. K.; MOIN, P. Simulation of spatially evolving turbulence and the applicability of taylor's hypothesis in compressible flow. *Physics Of Fluids A Fluid Dynamics*, v. 4, n. May 1991, p. 1521–1530, 1992.
LUMLEY, J. L. The structure of inhomogeneous turbulence. In: YAGLOM, A. M.; TATARSKI, V. I. (Ed.). *Atmospheric turbulence and wave propagation*. Moscow: Nauka, 1967. p. 166–178.
LUND, T. Generation of turbulent inflow data for spatially-developing boundary layer simulations. *Journal of Computational Physics*, v. 140, n. 2, p. 233–258, mar. 1998.
MAGRE, P.; MOREAU, P.; COLLIN, G.; BORGHI, R.; PÉALAT, M. Further studies by cars of premixed turbulent combustion in a high velocity flow. *Combustion and Flame*, v. 71, n. 2, p. 147 – 168, 1988.
MOREAU, P.; BOUTIER, A. Laser velocimeter measurements in a turbulent flame. *Symposium (International) on Combustion*, v. 16, n. 1, p. 1747 – 1756, 1977.
ORLANSKI, I. A simple boundary condition for unbounded hyperbolic flows. *Journal of Computational Physics*, v. 21, n. 3, p. 251 – 269, 1976.
POPE, S. B. Pdf methods for turbulent reactive flows. *Progress in Energy and Combustion Science*, Elsevier, v. 11, n. 2, p. 119–192, 1985.
RAMAN, V. Hybrid finite-volume/transported PDF simulations of a partially premixed methane-air flame. *Combustion and Flame*, v. 136, n. 3, p. 327–350, fev. 2004.
ROGALLO, R. S. Numerical experiments in homogeneous turbulence. *Nasa Technical Memorandum*, v. 81, n. 81835, 1981.
SCHNEIDER, G. E.; ZEDAN, M. A modified strongly implicit procedure for the numerical solution of field problems. *Numerical Heat Transfer*, v. 4, p. 1–19, mar. 1981.
SMIRNOV, A.; SHI, S.; CELIK, I. Random flow generation technique for large eddy simulations and particle-dynamics modeling. *Journal of Fluids Engineering*, v. 123, p. 359–371, 2001.
TABOR, G.; BABA-AHMADI, M. Inlet conditions for large eddy simulation: A review. *Computers & Fluids*, v. 39, n. 4, p. 553–567, 2010.
VEDOVOTO, J. M.; NETO, A. da S.; MURA, A.; SILVA, L. F. Figueira da. Application of the method of manufactured solutions to the verification of a pressure-based finite-volume numerical scheme. *Computers & Fluids*, v. 51, n. 1, p. 85 – 99, 2011.
WILLIAMS, F. A. *Combustion theory*. [S.l.]: The Benjamin/Cummings Publishing Company, Inc., 2nd ed., 1985.
ZHANG, Y. Z.; HAWORTH, D. C. A general mass consistency algorithm for hybrid particle/finite-volume pdf methods. *Journal of Computational Physics*, v. 194, n. 1, p. 156 – 193, 2004.

9. Responsibility notice

The author(s) is (are) the only responsible for the printed material included in this paper

ANÁLISIS EXPERIMENTAL DE PROCESOS DE DIFUSIÓN DE GASES CONTAMINANTES EN LA ATMÓSFERA EN UN TUNEL DE VIENTO

Gisela M. Alvarez y Alvarez, giselaalvarezyalvarez@yahoo.com.ar
Adrián R. Wittwer, a_wittwer@yahoo.es
Laboratorio de Aerodinámica, Facultad de Ingeniería, Universidad Nacional del Nordeste, Av. Las Heras 727, Resistencia, Chaco, Argentina
Acir M. Loredo-Souza, acir@ufrgs.br
Laboratório de Aerodinâmica das Construções, Túnel de Vento, Universidade Federal do Rio Grande do Sul, Av. Bento Gonçalves 9500, Porto Alegre, Brasil.
Edith B. Camaño Schettini, bcamano@iph.ufrgs.br
Departamento de Hidromecânica e Hidrologia, Instituto de Pesquisas Hidráulicas, Universidade Federal do Rio Grande do Sul, Av. Bento Gonçalves 9500, Porto Alegre, Brasil.

Abstract. *El objeto de presente trabajo es el estudio de problemas de dispersión de contaminantes en la atmósfera en túneles de viento. El empleo de un modelo a escala reducida brinda la posibilidad de analizar el proceso de dispersión en modelos complejos, donde intervienen una mayor cantidad de variables debido a la presencia de edificaciones de gran altura o topografía complejas. Además, permite el estudio de varias situaciones y alternativas para el diseño de la fuente emisora. La simulación del proceso de dispersión de contaminantes en el túnel de viento requiere de dos conjuntos de criterios de semejanza, el primero establece que el escurrimiento dentro del túnel de viento sea semejante al viento natural en la capa limite atmosférica y el segundo que las características de la fuente entre el modelo y prototipo sean semejantes. Los objetivos de este trabajo son; el estudio de criterios de semejanza del escurrimiento atmosférico y de la fuente de emisión para conseguir reproducir el proceso de dispersión, y realizar una primera aproximación al estudio experimental de este fenómeno. En primer lugar se presentan los resultados obtenidos de un estudio de visualización de un proceso de dispersión realizado en el túnel de viento de la Facultad de Ingeniería de la UNNE, empleando humo como trazador y tres velocidades de operación. Se realiza el estudio de la pluma simulada a partir del procesamiento digital de las imágenes obtenidas durante el ensayo. Se analiza además el levantamiento de la pluma comparando las mediciones realizadas con valores teóricos.*
Finalmente se presentan resultados preliminares de experimentos realizados para evaluar el campo de concentración para una fuente de emisión de un gas muy liviano utilizando un modelo a escala reducida. Estas pruebas fueron realizadas en el túnel de viento del Laboratorio de Aerodinâmica das Construções de la UFRGS.
Los resultados obtenidos en este trabajo contribuirán en gran medida al perfeccionamiento de técnicas de visualización, que como se describió tienen la ventaja de ser más sencillas económicas de realizar que los estudios de campo. Por otro lado, en estudios de este tipo, un primer análisis cualitativo significa una optimización de los posteriores ensayos de medición puntual de concentraciones.

1. INTRODUCCIÓN

Los contaminantes del aire son sustancias que cuando están presentes en la atmósfera afectan de manera adversa la salud de humanos, animales plantas, dañan materiales o generan molestias en la vida cotidiana. En los últimos años ha crecido el interés en este tema debido a los innumerables efectos que ocasiona sobre la vida en el planeta. Eliminar estas acciones sería una medida tan drástica que alteraría los estándares de vida actual, por lo cual se opta por un mayor estudio del fenómeno y por un planteo de soluciones que tiendan a controlar las emisiones que se realicen a la atmósfera (Noel de Nevers, 2000).

Los efectos que los contaminantes tengan sobre la salud humana dependerán del tiempo de exposición, concentración del contaminante y de la edad y estado de salud de la persona. Los animales, la vegetación, también son susceptibles a los efectos de los contaminantes del aire, como así también algunos materiales en los que ocasiona un deterioro acelerado.

El control de las emisiones muchas veces se hace sin contar con herramientas que permitan evaluar los procesos de dispersión de gases y determinar los niveles de concentración de los contaminantes, y otras veces no se realiza. En este contexto, el desarrollo de experimentos y modelos que permitan evaluar los procesos de dispersión de contaminantes descargados en la atmósfera se torna importante.

La simulación matemática o experimental de un fenómeno tan complejo como es la dispersión atmosférica constituye un instrumento útil al momento de planificar o adoptar medidas correctoras en instalaciones determinadas.

El transporte y la difusión turbulenta de contaminantes atmosféricos, los efectos del viento en edificios y estructuras y la modificación del viento en áreas urbanas por la presencia de edificios, pueden ser considerarse problemas a la Ingeniería de Vientos. Para el análisis de estos problemas, esta rama de la Ingeniería utiliza principalmente mediciones a escala natural, ensayos en túneles de viento de capa límite y simulación numérica.

En particular, el proceso de difusión y transporte de contaminantes depende de las condiciones meteorológicas de la capa límite atmosférica y es controlado por las fluctuaciones de velocidad y dirección del viento. La estabilidad atmosférica, la topografía de la zona y la rugosidad superficial del terreno tienen gran influencia sobre la extensión necesaria para que las emisiones sean diluidas por el viento.

El túnel de viento de capa límite permite estudios experimentales sobre modelos a escala reducida que reproducen las características de la turbulencia en la capa límite atmosférica, y también es factible modelar fuentes de emisión.

Los estudios de campo para la determinación de la dispersión atmosférica son difíciles de controlar y costosos. Las teorías de difusión permiten estudiar algunos problemas, pero las soluciones analíticas son complicadas o imposibles de realizar. Por este motivo el desarrollo de métodos de estudio de esta problemática en túneles de viento resulta una herramienta útil que puede tener una variedad de aplicaciones. En este marco, un túnel de viento de capa límite se torna una herramienta importante para el análisis de problemas de difusión turbulenta.

Para realizar los estudios de dispersión en túneles de viento se requiere de la implementación de una adecuada técnica de simulación del escurrimiento del aire de la capa límite atmosférica y, posteriormente, simular la fuente y el proceso de emisión.

Simular la capa límite atmosférica en un túnel de viento consiste en desarrollar un modelo físico del flujo turbulento atmosférico de manera tal que los parámetros que lo caracterizan se reproduzcan lo más fielmente posible dentro del túnel. Esta técnica permite representar las condiciones que se darían en la realidad empleando modelos a escala reducida. Una adecuada simulación de la capa límite atmosférica requiere de la reproducción del comportamiento del flujo de los vientos naturales dentro de la misma, lo cual implica lograr una reproducción apropiada de la distribución de la velocidad media en función de la altura y de parámetros turbulentos.

Este trabajo se centra en el análisis de los criterios de semejanza necesarios para el estudio de procesos de dispersión de gases en un túnel de viento. con el objeto de realizar una primera aproximación del estudio experimental de este fenómeno se presentan; resultados obtenidos de ensayos de visualización de flujos realizados en el túnel de viento TV2 del Laboratorio de Aerodinámica de la Facultad de ingeniería de la Universidad Nacional; y algunos resultados preliminares de medición del campo de concentración en procesos de dispersión de gases para una fuente de emisión puntual realizados en el túnel de viento del Laboratorio de Aerodinámica de las Construcciones, de la Universidad Federal do Rio Grande do Sul.

2. MODELADO DE LA CAPA LÍMITE ATMOSFÉRICA

Según Isyumov y Tanaka (1980) la simulación de una pluma de dispersión en un túnel de viento requiere de un modelado representativo de las características de la capa límite atmosférica y de las propiedades dinámicas y térmicas de la pluma. Un modelado riguroso de la capa límite atmosférica requiere de la semejanza geométrica, la semejanza del campo de flujo, y la igualdad de los números adimensionales de Reynolds (Re), Richardson (Ri), Rossby (Ro), Prandtl (Pr) y Eckert (Ec).

La semejanza geométrica implica el modelado del entorno, incluyendo la rugosidad del terreno, relieve topográfico y temperatura de la superficie, El modelado del campo de flujo, contempla la semejanza de las velocidades medias y turbulentas y la temperatura de estratificación. La semejanza exacta es imposible de lograr en escalas reducidas, por lo que se plantean hipótesis con el objeto de lograr una semejanza aproximada.

La semejanza del número de Richardson está ligada a la semejanza de la estabilidad atmosférica. Para una simulación de atmósfera neutra como la realizada en este trabajo el número de Richardson puede ser ignorado. La semejanza en el número de Prandtl se satisface siempre que el fluido con que se trabaje sea aire; y la igualdad del número de Eckert es de pequeña importancia en flujo compresible. El número de Rossby no es considerado debido a que la fuerza de Coriolis no puede ser simulada en túneles de viento. La semejanza del número de Reynolds se logra manteniendo las condiciones turbulentas en el flujo simulado.

La simulación aproximada del flujo, es representativa del viento natural para condiciones atmosférica neutralmente estable y levemente inestable. Esta condición resulta adecuada para el estudio de dispersión de plumas desde chimeneas altas (Isyumov y Tanaka, 1980).

3. MODELADO DE LA PLUMA

Una vez establecida la simulación de la capa límite atmosférica en el túnel de viento, los requerimientos de semejanza para el modelado del levantamiento de la pluma y su dispersión requiere de la semejanza de parámetros adimensionales referidos a las características de la chimenea y de la pluma. Para el modelado exacto del comportamiento de la pluma de emisión se debe verificar (Isyumov y Tanaka, 1980): la semejanza geométrica de la fuente, y la igualdad de los siguientes parámetros adimensionales; el número de Froude, la relación de densidad de la emisión y la del aire, la relación entre la velocidad de salida de la emisión y la velocidad del flujo atmosférico, y finalmente la igualdad del número de Reynolds. Esta semejanza completa tampoco puede realizarse, y al igual que sucede con la simulación de la capa límite atmosférica se debe aplicar el criterio de semejanza a algunos parámetros, buscando una semejanza aproximada (Poreh & Kacherginsky, 1981). Las simplificaciones propuestas son variadas y dependerán del caso a estudiar. Para simular la elevación de la pluma y la dispersión es importante que el número de Reynolds del flujo que sale de la chimenea se lo suficientemente grande, como para despreciar su efecto como así también el del número de Prandtl y el número de Schmidt. Además, la mayoría de los autores (Poreh & Kacherginsky, 1981) concuerdan que el efecto de la densidad en la simulación no es crítico y podría ocasionar como máximo el desplazamiento del origen virtual de la pluma en unos pocos diámetros de la chimenea. Melbourne y también Isumov et al propusieron que la semejanza de la elevación de una pluma se logra manteniendo la igualdad de un parámetro de flotación, un parámetro relacionado a la cantidad de movimiento del efluente, y la escala geométrica de la chimenea (Ec.1) (Poreh & Kacherginsky, 1981).

$$\lambda\left(\frac{\rho_a U^2}{\Delta\rho g L}\right)=1 \quad ; \quad \lambda\left(\frac{\rho_s W_s^2}{\rho_a U^2}\right)=1 \quad ; \quad \lambda\left(\frac{d}{L}\right)=1 \tag{1}$$

Skinner y Ludwig también emplean el parámetro adimensional de cantidad de movimiento, que aparece en la Ec. (1), pero modificaron el parámetro de flotabilidad. Plantean que la pluma a sotavento es dominada por la flotabilidad, y sugieren que el parámetro de semejanza adecuado para describirla es la relación entre la cantidad de movimiento de la corriente y la cantidad de movimiento de flotabilidad en un pequeño volumen Δv, que asumen que es igual a $(1-Cs)\rho_a U^2/Cs(\rho_a-\rho_s)L$, donde Cs es la concentración del gas emitido por la chimenea. Además, asumiendo que a una distancia alejada de la fuente a sotavento $Cs << 1$ y que Cs es directamente proporcional a la velocidad del efluente al salir de la chimenea W_s e inversamente proporcional a la velocidad del viento U, el parámetro de flotabilidad puede aproximarse con $\rho_a U^3/(\Delta\rho g L W)$. Finalmente, los parámetros para realizar una semejanza aproximada del proceso de dispersión serían los citados en la Ec. (2).

$$\lambda\left(\frac{\rho_a U^3}{\Delta\rho g L W_s}\right)=1 \quad ; \quad \lambda\left(\frac{\rho_s W_s^2}{\rho_a U^2}\right)=1 \quad ; \quad \lambda\left(\frac{d}{L}\right)=1 \tag{2}$$

3. ENSAYOS DE VISUALIZACIÓN

El estudio de la pluma simulada se puede realizar captando una serie de fotografías del proceso y realizando posteriormente un procesamiento digital de las imágenes obtenidas. Estudios de este tipo se han realizado en distintas partes del mundo con resultados satisfactorios como por los obtenidos por White y Stein (1990) que determinaron la dispersión a sotavento producida por una chimenea de altura variable en un edificio, empleando humo con trazador y grabando con una video cámara el ensayo, para luego procesar las imágenes adquiridas. Gerdes y Olivari (1999) también emplearon la técnica de visualización del flujo, midiendo la intensidad píxel a píxel de imágenes captadas con una cámara en el análisis de fenómenos de dispersión en cañones urbanos.

En este trabajo se buscó aplicar en el túnel de viento, TV2, de la UNNE, una técnica de visualización para el análisis de las concentraciones en una pluma, determinando las modificaciones que se necesitan implementar para mejorar los resultados obtenidos, para ello se examinó el comportamiento y la configuración de la pluma obtenida para diferentes números de Reynolds. La concentración del contaminante fue medida empleando humo como trazador y obteniendo fotografías del proceso; seguidamente estas imágenes fueron procesadas digitalmente.

Los experimentos se realizaron túnel de viento (TV2) de la Universidad Nacional del Nordeste, Argentina (Alvarez y Alvarez y Wittwer, 2004). Es un túnel de circuito abierto cuya longitud total es de 7,50 m, su cámara de ensayos consiste en un conducto de sección cuadrada de 0,48 m de lado y de 4,45 m de longitud. La máxima velocidad del flujo en el canal vacío es aproximadamente 18 m/seg y emplea un ventilador centrífugo accionado por un motor trifásico de 1450 rpm y 10 CV de potencia.

La simulación de la capa límite atmosférica se efectúo empleando elementos de rugosidad y dispositivos de mezcla apropiados para reproducir una capa límite neutralmente estable de espesor parcial. En la Figura 1 se pueden ver los elementos de rugosidad y las agujas que permitieron simular la capa límite superficial correspondiente a un terreno de la categoría IV de la norma NBR-6123/1988, equivalente a una categoría de exposición B del reglamento argentino CIRSOC 102. El análisis de la capa límite simulada fue presentada en trabajos previos (Alvarez y Alvarez y Wittwer, 2006).

Para la realización del ensayo se empleó humo producido por un generador que utiliza un líquido a base de glicerina, la velocidad de salida del humo fue aproximadamente 14,3 m/seg. La fuente del contaminante fue representada mediante un conducto metálico de 1,02 cm de diámetro interno y 10 cm de alto, ubicado en el centro de la cámara. Se prestó especial cuidado a la iluminación de la pluma, tratando que solo un haz lineal de luz la intercepte. Las imágenes fueron captadas por una cámara digital y luego trasferidas a un ordenador.

3. 1. RESULTADOS EN ENSAYOS DE VISUALIZACIÓN

En una primera instancia se efectuó el ensayo a la máxima velocidad posible en el canal, 18 m/seg, en esta ocasión el número de Reynolds con respecto a la altura del canal fue de Re =5,7 $x10^5$ y con respecto al diámetro de la chimenea $1,2x10^4$. A continuación, se redujo la velocidad alcanzando el valor de 9,82 m/seg en la mitad de la altura de la cámara de ensayo y alcanzándose un número de Reynolds de $3,1x10^5$ y $6,7x10^3$ con respecto a la altura del canal y al diámetro de la pluma, respectivamente. Finalmente, se obtuvo la configuración de la pluma para una velocidad de 1,83 m/seg determinada en la mitad de la altura de la cámara de ensayo con un consiguiente número de Reynolds de $5,8x10^4$ con recto a la altura del canal y de $1,2x10^3$ con respeto al diámetro de la chimenea. En la Figura 2 se aprecia la configuración de la pluma para los tres casos citados.

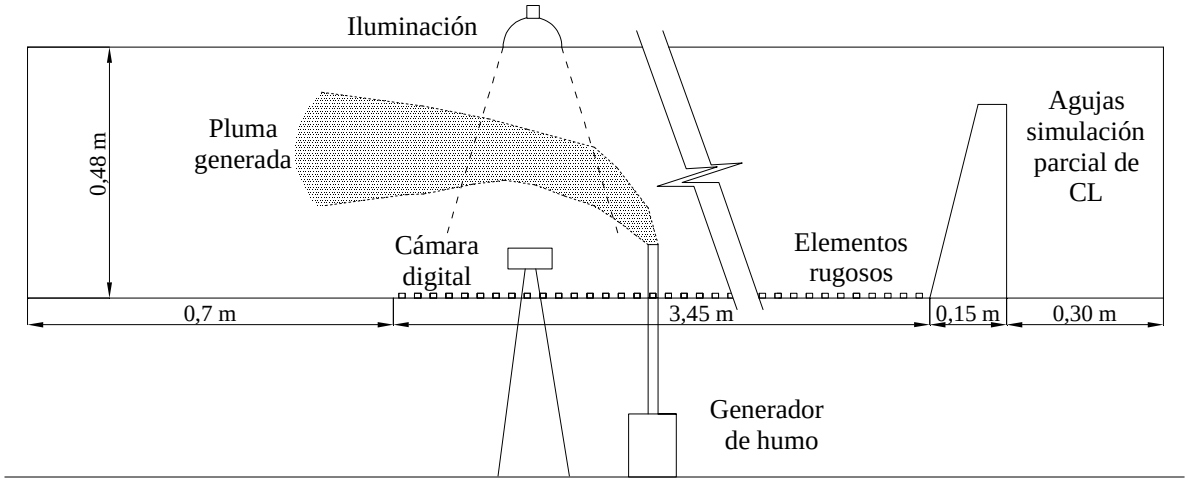

Figura 1. Disposición del instrumental durante el ensayo.

Figura 2. Pluma de dispersión en la cámara del túnel de viento, correspondiente a Re= $5{,}7x10^5$, Re= $3{,}1{,}x10^5$, Re= $5{,}8x10^4$.

Las imágenes captadas con la cámara fueron de alta resolución, para que permitieran su posterior procesamiento. El mismo consistió en superponer a la fotografía una malla, y realizar una valoración en función de la intensidad del color que tuviese cada cuadro, comparando con un patrón realizado. El patrón empleado en la comparación, se determinó asignando el menor y mayor valor, a la menor y mayor intensidad encontrada en la imagen, respectivamente.

A continuación, se procedió al trazado, cada 0,1 m, de los perfiles longitudinales de concentración, en función de los valores asignados a cada cuadro de la malla. En la Figura 3 se aprecia el resultado del procesamiento correspondiente al ensayo realizado a una velocidad de 1,83 m/seg. Únicamente fueron procesados los resultados correspondientes a la menor velocidad y No. de Reynolds, porque es la situación en que mejor se puede visualizar el proceso de difusión.

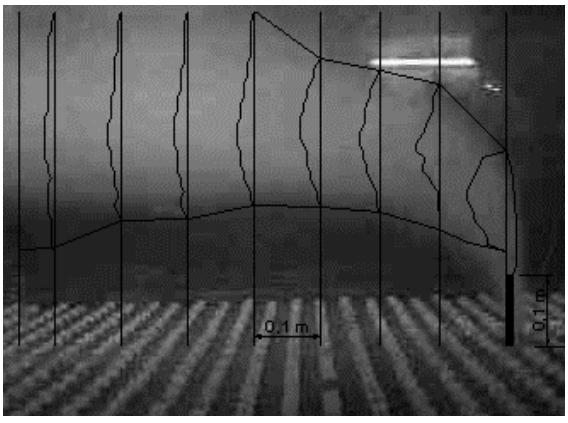

Figura 3. Desarrollo de la pluma en túnel, correspondiente una velocidad de 1,83 m/seg.

En la discusión cualitativa del comportamiento de la pluma y su dependencia de la estabilidad atmosférica, frecuentemente se mencionan tres modelos básicos; ondulado, el que ocurre cuando la temperatura disminuye rápidamente con la altura (gradiente es inestable); cónico, si disminuye poco o es constante con la altura (en condiciones aproximadamente neutrales) y abanico, si aumenta con la altura (inversión).

También se mencionan tres modelos intermedios; el de elevación, que ocurre cuando la chimenea se extiende a través de la inversión de superficie con una capa inestable arriba; fumigación y confinado que ocurren cuando una capa de superficie inestable o neutral está limitada por una inversión arriba de la altura de la chimenea.

El levantamiento de la pluma por encima de la altura de la chimenea depende de factores meteorológicos y de la emisión; entre los meteorológicos se tiene a la velocidad del viento U, la temperatura del aire T_a, el gradiente vertical de la velocidad, la presión atmosférica p y la estabilidad atmosférica. Y los factores de emisión que influyen son la velocidad del efluente al salir de la chimenea W_s, su temperatura T_s y el diámetro interior de la chimenea d. La mayoría de las fórmulas para determinar el levantamiento de la pluma Δh, son empíricas debido a la complejidad de las relaciones entre las variables, como por ejemplo la ecuación de Holland Ec. (3) la cual fue desarrollada a partir de datos experimentales.

$$\Delta h\,(m) = \frac{W_s\,(m/seg).d\,(m)}{U\left(m/seg\right)}\left(1{,}5 + 2{,}68.10^{-3}.p\;(hPa).d(m).\frac{T_s(^o\,K) - T_a\,(^o\,K)}{T_s\,(^o\,K)}\right) \tag{3}$$

En la Tabla 1, se expresan los valores de levantamiento de pluma hallados en los ensayos, en función de las distintas velocidades, junto con los determinados empleando la expresión de Holland.

Tabla1. Comparación de valores de la elevación de la pluma calculadas con la expresión de Holland y determinadas experimentalmente.

U (m/seg)	$U/\,W_s$	Δh teórica (m)	Δh experimental (m)
18,00	1,26	0,012	0,012
9,57	0,67	0,023	0,021
1,83	0,13	0,121	0,188

La determinación del levantamiento de la pluma es necesario para el cálculo de la altura efectiva de la chimenea, ésta se obtiene de la suma de la altura real de la chimenea más el levantamiento Δh de la pluma. Esta altura interviene en las expresiones de los modelos matemáticos de difusión, como es el caso del modelo de Gauss.

4. MEDICIONES DEL CAMPO DE CONCENTRACIÓN

Las mediciones de concentraciones fueron realizadas en el túnel de viento “Prof. Joaquim Blessmann” del Laboratorio de Aerodinámica de las Construcciones, de la Universidad Federal do Rio Grande do Sul. Para este ensayo se empleó una simulación de capa límite neutralmente estable correspondiente a un terreno suburbanos con un exponente de la ley potencial α = 0,23 y una escala geométrica de 1:300. Para el modelado de la capa límite se emplearon en forma conjunta elementos de rugosidad dispuestos en el piso del túnel, barrera y dispositivos de mezcla (Wittwer et al.,2003).

La altura de la fuente de emisión modelada tiene una altura de 250 mm y 17 mm de diámetro, representando en la escala natural a una chimenea de aproximadamente 75 m de altura y 5 m de diámetro (Fig. 4). El gas trazador emitido desde la fuente fue emitido helio puro. La emisión se realizó con caudales y fueron analizados dos casos diferentes; el caso 1 con una velocidad del escurrimiento a la altura de la chimenea U = 2,3 m/s y una velocidad de la emisión Ws = 1,26 m/s, y el caso 2 con U = 0,7 m/s y Ws = 0,56 m/s. En la tabla 2 se resumen las velocidades y los parámetros adimensionales que permiten caracterizar cada caso (relación de velocidades, cantidad de movimiento y número de Froude densimétrico).

Figura 4. Fuente de emisión y elementos de simulación de la capa límite.

Tabla 2. Parámetros característicos de los experimentos.

Casos	U (m/s)	W_s (m/s)	$\frac{W_s}{U}$	$\frac{\rho_s W_s^2}{\rho_a U^2}$	$\frac{\rho_a U^3}{(\rho_s - \rho_a) d\, g\, W_s}$
1	2,3	1,26	0,56	0,043	52,632
2	0,7	0,80	0,80	0,089	3,559

Para la medición de las concentraciones, se utilizó un anemómetro de hilo caliente con una sonda aspirante que permite medir valores medios y flotantes. En cada punto de medición fue obtenido un registro con una frecuencia de adquisición de 1024 Hz y 60 segundos de duración.

4. 1. RESULTADOS

En la Figura 5, se muestran los perfiles verticales de concentración másica de helio, $masa_{He}/(masa_{aire} + masa_{He})$, determinados a sotavento de la chimenea. Las distancias x1 y x2 indican la posición en que fueron obtenidos los perfiles para los casos 1 y 2, respectivamente, con relación a la chimenea. Son considerables las diferencias de los perfiles obtenidos en cada caso para el valor medio y para el valor RMS.

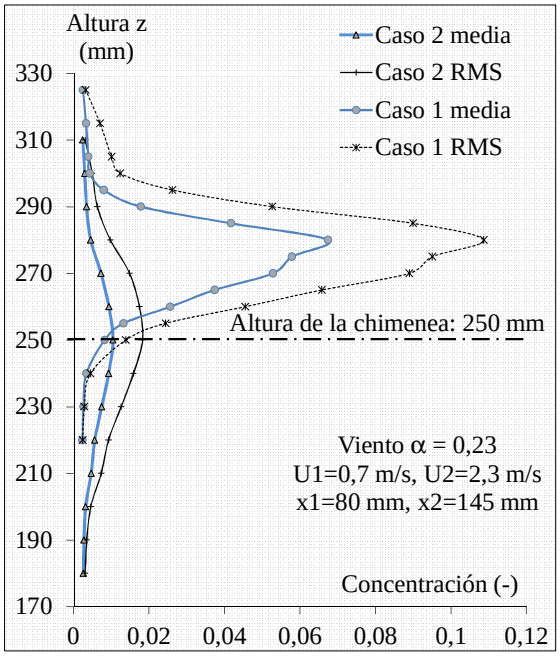

Figura 5. Perfiles de concentración de las plumas de emisión.

Para el caso 1, se presentan los registros de las concentraciones fluctuantes, en forma parcial (5 segundos) en dos puntos de medición; en la posición central de la pluma y en el extremo superior (en los bordes de la pluma). Los valores pico tienen el misma orden de magnitud, tanto que el proceso es altamente intermitente en el extremo de la pluma y de baja intermitencia en el centro de la pluma. Este comportamiento del campo de concentraciones es semejante al obtenido por Cheung & Melbourne (2000).

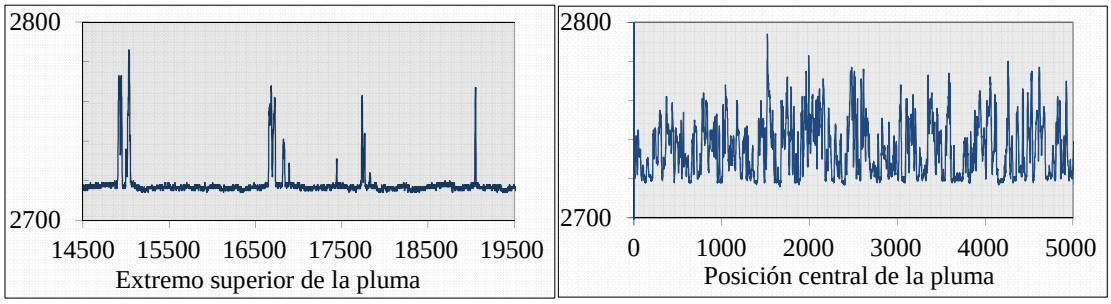

Figura 6. Registros de las concentraciones fluctuantes.

5. DISCUSIÓN DE RESULTADOS Y CONCLUSIONES

El ensayo de visualización de la dispersión de la pluma permitió hacer un análisis cualitativo y cuantitativo de las imágenes fotográficas. En la Figura 2, se aprecian las modificaciones generadas en la pluma simulada al variar el número de Reynolds. Se ve que únicamente para números de Reynolds bajos se produce un levantamiento significativo de la pluma.

Como el ensayo fue realizado en condiciones de estabilidad neutra la pluma debería adaptarse al modelo cónico, si se analizan las configuraciones de la pluma para los tres casos analizados (Fig. 2) se puede apreciar que la adaptación de la pluma a este modelo es correcta. En el ensayo realizado a una velocidad de 1,83 m/seg se produce en primer lugar un levantamiento de la pluma, pero a continuación, ésta tiende rápidamente a adoptar una forma cónica.

En la comparación efectuada en la Tabla 1 se aprecia claramente que el levantamiento de las plumas generadas a distintas velocidades será mayor cuanto menor sea la velocidad y se ve que en los dos primeros casos la situación simulada concuerda con los valores calculados con la expresión (3). La disparidad que se presenta en el tercer caso entre el valor teórico y el experimental de Δh puede atribuirse a las condiciones de realización del ensayo. Es necesario señalar que la técnica empleada tiene sus limitaciones, ya que la iluminación y adquisición de imágenes, en principio, deben mejorarse. Debe apuntarse a generar un haz de luz uniforme que intercepte a la pluma linealmente, y esta no debe provenir de una fuente de luz puntual como la empleada en el ensayo que puede verse en la Fig. 1. También se puede mejorar la toma de las fotografías si estas se hacen de acuerdo a una secuencia y siempre desde la misma posición, cuidando que sombras o luces exteriores alteren la imagen, como sucede en el tercer caso de la Fig. 2.

Con respecto a los resultados obtenidos del análisis de los campos de concentración en la región próxima a una fuente de emisión de un gas muy liviano, se observa que los dos casos analizados representan situaciones casi extremas. En el caso 1, se tiene una situación en la cual los efectos inerciales del escurrimiento incidente prevalecen sobre los efectos de empuje de la propia emisión; y en el segundo caso, son evidentes los efectos del empuje del gas emitido, en la elevación de la pluma, y la menor dilución en la concentración del gas. La intermitencia en las concentraciones será analizada a continuación utilizando distribuciones de probabilidad. Los resultados preliminares presentados son ejemplos de los múltiples perfiles verticales y horizontales que ya fueron medidos, y que permitirán una caracterización más general del proceso de dispersión.

Los resultados obtenidos en este trabajo contribuirán al perfeccionamiento de técnicas de visualización, que como se describió tienen la ventaja de ser más sencillas económicas de realizar que los estudios de campo. Por otro lado, en estudios de este tipo, un primer análisis cualitativo significa una optimización de los posteriores ensayos de medición puntual de concentraciones.

4. REFERENCES

Alvarez y Alvarez, Gisela M., Wittwer, Adrián R., 2004. “Estudio de escurrimientos turbulentos de capa límite en un túnel de viento de circuito abierto”, Anais da 4a Escola de Primavera de Transição e Turbulência - EPTT 2004, Associação Brasileira de Engenharia e Ciências Mecânicas - ABCM, Porto Alegre, RS.

Alvarez y Alvarez, Gisela M., Wittwer, Adrián R., 2006. “Análisis de los parámetros del perfil de viento en la CL simulada en un túnel de viento”, Anais da 5a Escola de Primavera de Transição e Turbulência - EPTT 2006, Paper ETT-06-0007, Associação Brasileira de Engenharia e Ciências Mecânicas - ABCM, Rio de Janeiro, Brasil.

Cheung, J., Melbourne, W., 2000. “Probability distribution of dispersion from a model plume in turbulent wind”, J.Wind Eng. Ind. Aerodyn. 87, 271-285.

De Nevers, N.,1998, “Air pollution control engineering”, McGraw-Hill.

Gerdes, F, Olivari, D, 1999, “Analysis of pollutant dispersion in an urban street canyon”, Journal of Wind Engineering and Industrial Aerodynamics, vol. 82, pp. 105-125.

Isymov, N., Tanaka, H. ,1980, “Wind tunnel modelling of stack gas dispersion – Difficulties and aproximations”, Wind Engineering, Proceedings of the fifth International Conference, Fort Collins, Colorado, USA, Ed. by J. E. Cermak, Pergamon Press Ltd.

Poreh, M. and A. Kacherginsky, 1981. “Simulation of Plume Rise in Small Wind-Tunnel Models”. Journal of Wind Engineering and Industrial Aerodynamics, Vol. 7, pp. 1-14.

White, B. y Stein, W., 1990, “Wind tunnel studies of variable stack heights for a low – profile building”, Journal of Wind Engineering and Industrial Aerodynamics, vol. 36, pp. 675-687.

Wittwer, A. R., Loredo-Souza, A. M., Camaño Schettini, E. B., 2003. “Modelagem do vento atmosférico para estudos de dispersão em túnel de vento”, Ciência & Natura–III Workshop Brasileiro de Micrometeorologia, 217-220.

5. RESPONSIBILITY NOTICE

Los autores son los únicos responsables por el material impreso incluido en esta publicación.

LINEAR GÖRTLER INSTABILITY DEVELOPMENT IN THE PRESENCE OF PRESSURE VARIATIONS

J. K. Rogenski, josuelkr@gmail.com
L. F. de Souza, lefraso@icmc.usp.br
Institute of Mathematical and Computer Sciences, University of São Paulo, São Carlos-SP, Brazil

J. M. Floryan, mfloryan@eng.uwo.ca
Department of Mechanical and Materials Engineering, The University of Western Ontario, London-ON, Canada

Abstract.

The effects of pressure gradient variations on the development of the Görtler instability are investigated. A linear Direct Numerical Simulation code in vorticity-velocity formulation is used. The flow is decomposed in steady and perturbation parts. Periodicity in the spanwise direction is assumed in agreement with experimental observations. The time derivative is integrated using the classical fourth-order Runge-Kutta method. High-order, compact, finite-difference schemes are applied to discretize the spatial derivatives in the streamwise and wall normal directions. A spectral method is used to discretize the spatial derivative in the spanwise direction. The Poisson equation is solved by a multigrid technique. The use of the Message Passing Interface library is adopted for code parallelization. The results obtained show that variations in the pressure distribution under investigation are not very effective to control Görtler vortices development.
Keywords: *Görtler vortices, pressure gradient, laminar-turbulent transition, Direct Numerical Simulation*

1. INTRODUCTION

The influence of geometry parameters in flow stability analyses has been frequently discussed due to its applicability in industry. By playing with different geometry configurations one may reduce drag in an aircraft's wing or increase the efficiency of a mixing process.

It is well known that in boundary layer flows over concave geometries the instability mechanism is inviscid and it is generated by imbalances between the centrifugal force and normal to the wall pressure gradient (Saric, 1994; Floryan, 1991). This instability mechanism generates streamwise vortices. The vortices are historically named as Görtler vortices. The instability is represented by counter-rotating streamwise pair of vortices with spanwise periodicity. Theoretical analysis establishes an instability criterion based on a dimensionless parameter defined as

$$Go = Re_\delta \sqrt{\frac{\delta}{R}}, \tag{1}$$

where Re_δ is the Reynolds number based on the boundary layer reference length δ and R is the radius of the wall. Go is here called Görtler number.

Following Görtler much has been done in the transition field aimed to understand the curvature effect and its interaction with other geometry parameters. Specifically one can choose the pressure as a possible parameter of influence. Linear local and nonlocal studies focused on the pressure gradient influence are provided by Goulpie et al. (1996). Moreover some nonlinear studies are discussed by Matsson (2008).

In this sense the purpose of the present paper is to investigate the influence of pressure variations on the control of Görtler instability. In Section 2 are written down the system of equations and boundary conditions. Numerical procedures are described in Sec. 3. Some verification tests are described in Sec. 4. Results and main considerations are provided in Sec. 5. Section 6 provides final considerations.

2. FORMULATION

It is considered the motion of an incompressible, isothermal and Newtonian fluid flow on concave geometries. Defining the vorticity as the opposite of the curl of the velocity vector the dimensionless governing equations in vorticity-velocity formulation are expressed as

$$\frac{\partial(\widetilde{\omega}_x\widetilde{v}-\widetilde{\omega}_y\widetilde{u})}{\partial y} - \frac{\partial(\widetilde{\omega}_z\widetilde{u}-\widetilde{\omega}_x\widetilde{w})}{\partial z} + \frac{Go^2}{\sqrt{Re}}\frac{\partial\widetilde{u}^2}{\partial z} = \frac{1}{Re}\nabla^2\widetilde{\omega}_x, \tag{2}$$

$$\frac{\partial(\widetilde{\omega}_y\widetilde{w}-\widetilde{\omega}_z\widetilde{v})}{\partial z} - \frac{\partial(\widetilde{\omega}_x\widetilde{v}-\widetilde{\omega}_y\widetilde{u})}{\partial x} = \frac{1}{Re}\nabla^2\widetilde{\omega}_y, \tag{3}$$

$$\frac{\partial(\widetilde{\omega}_z\widetilde{u}-\widetilde{\omega}_x\widetilde{w})}{\partial x}-\frac{\partial(\widetilde{\omega}_y\widetilde{w}-\widetilde{\omega}_z\widetilde{v})}{\partial y}-\frac{Go^2}{\sqrt{Re}}\frac{\partial\widetilde{u}^2}{\partial x} = \frac{1}{Re}\nabla^2\widetilde{\omega}_z, \tag{4}$$

where $\widetilde{\omega}_x$, $\widetilde{\omega}_y$ and $\widetilde{\omega}_z$ are the vorticity vector components in streamwise (x), normal to wall (y) and spanwise (z) directions respectively. $\widetilde{u}$, $\widetilde{v}$ and $\widetilde{w}$ are the velocity vector components in the x, y and z directions.

The reference length is a characteristic plate length L and the reference velocity U_∞ is the freestream velocity. The Reynolds number is given by $Re = U_\infty L/\nu$, where ν is the kinematic viscosity. Following the order of magnitude analyses provided by Floryan and Saric (1982) the terms $Go^2\frac{\partial\widetilde{u}^2}{\partial x}/(\sqrt{Re})$ and $Go^2\frac{\partial\widetilde{u}^2}{\partial z}/(\sqrt{Re})$ are the remaining curvature terms.

The continuity equation is given by

$$\frac{\partial\widetilde{u}}{\partial x}+\frac{\partial\widetilde{v}}{\partial y}+\frac{\partial\widetilde{w}}{\partial z}=0. \tag{5}$$

Using the vorticity definition and the Eq. (5) one can obtain the following Poisson equations for each velocity component:

$$\frac{\partial^2\widetilde{u}}{\partial x^2}+\frac{\partial^2\widetilde{u}}{\partial z^2} = -\frac{\partial\widetilde{\omega}_y}{\partial z}-\frac{\partial^2\widetilde{v}}{\partial x\partial y}, \tag{6}$$

$$\frac{\partial^2\widetilde{v}}{\partial x^2}+\frac{\partial^2\widetilde{v}}{\partial y^2}+\frac{\partial^2\widetilde{v}}{\partial z^2} = -\frac{\partial\widetilde{\omega}_z}{\partial x}+\frac{\partial\widetilde{\omega}_x}{\partial z}, \tag{7}$$

$$\frac{\partial^2\widetilde{w}}{\partial x^2}+\frac{\partial^2\widetilde{w}}{\partial z^2} = -\frac{\partial\widetilde{\omega}_y}{\partial x}-\frac{\partial^2\widetilde{v}}{\partial y\partial z}. \tag{8}$$

A solution for the system of equation represented by a generic function $\widetilde{f}=\{\widetilde{u},\widetilde{v},\widetilde{z},\widetilde{\omega}_x,\widetilde{\omega}_y,\widetilde{\omega}_z\}$ is rewritten as

$$\widetilde{f}=f_b+f, \tag{9}$$

where f_b is the base and f is the perturbation part of the function. $\widetilde{f}$ represent the global vorticity and velocity variables. Here the baseflow is considered steady and bidimensional.

A system of equations is obtained by introducing the Eq. (9) in Eq. (2)-(4) and (6)-(8), and then subtracting the baseflow. Thus,

$$\frac{\partial a}{\partial y}-\frac{\partial b}{\partial z}+\frac{Go^2}{\sqrt{Re}h}\frac{\partial d}{\partial z} = \frac{1}{Re}\nabla^2\omega_x, \tag{10}$$

$$\frac{\partial c}{\partial z}-\frac{\partial a}{\partial x} = \frac{1}{Re}\nabla^2\omega_y, \tag{11}$$

$$\frac{\partial b}{\partial x}-\frac{\partial c}{\partial y}-\frac{Go^2}{\sqrt{Re}h}\frac{\partial d}{\partial x} = \frac{1}{Re}\nabla^2\omega_z, \tag{12}$$

$$\frac{\partial^2 u}{\partial x^2}+\frac{\partial^2 u}{\partial z^2} = -\frac{\partial\omega_y}{\partial z}-\frac{\partial^2 v}{\partial x\partial y}, \tag{13}$$

$$\frac{\partial^2 v}{\partial x^2}+\frac{\partial^2 v}{\partial y^2}+\frac{\partial^2 v}{\partial z^2} = -\frac{\partial\omega_z}{\partial x}+\frac{\partial\omega_x}{\partial z}, \tag{14}$$

$$\frac{\partial^2 w}{\partial x^2}+\frac{\partial^2 w}{\partial z^2} = \frac{\partial\omega_y}{\partial x}-\frac{\partial^2 v}{\partial y\partial z}, \tag{15}$$

where the nonlinear terms a, b, c and d are:

$$a = \omega_x(v_b+v)-\omega_y(u_b+u), \tag{16}$$

$$b = (\omega_{z_b}+\omega_z)(u_b+u)-\omega_x w, \tag{17}$$

$$c = \omega_y w-(\omega_{z_b}+\omega_z)(v_b+v), \tag{18}$$

$$d = 2u_b u+u^2. \tag{19}$$

Figure 1. Sketch of the simulation domain for each Fourier mode. Buffer regions are represented by rectangles in gray color. Suction and blowing region (regarding just the fundamental mode) is represented by the dashed rectangle.

Regarding the boundary conditions, at the upper boundary the flow is assumed to be nonrotational. At the wall, the streamwise and normal to the wall velocity components are zero by the no-slip condition. At the outflow boundary the second derivative of the velocity and vorticity components are set to zero. Inflow boundary and baseflow are specified based on Falkner-Skan similar solutions (Schlichting, 1979).

3. NUMERICAL METHOD

Justified by experimental evidences it is assumed periodicity in the spanwise direction. All the variables can be written as combination of K Fourier modes as

$$f(x,y,z,t) = \sum_{k=0}^{K} F_k(x,y,t)e^{-i\gamma_k z} \tag{20}$$

where f a variable, i is the imaginary unit, k is a Fourier mode and γ_k is the wavenumber in the spanwise direction. The wavenumber is defined as

$$\gamma_k = \frac{2\pi k}{\lambda_z},$$

where λ_z is the spanwise wave length of the fundamental Fourier mode.

The Eq. (10)-(15) is expressed (for each k Fourier mode) by:

$$\frac{\partial A_k}{\partial y} + i\beta_k B_k - \frac{Go^2}{\sqrt{Re}}\frac{i\beta_k(D_k^2)}{h} = \frac{1}{Re}\nabla_k^2\Omega_{x_k}, \tag{21}$$

$$-i\beta_k C_k - \frac{\partial A_k}{\partial x} = \frac{1}{Re}\nabla_k^2\Omega_{y_k}, \tag{22}$$

$$\frac{\partial B_k}{\partial x} + \frac{\partial C_k}{\partial y} - \frac{Go^2}{\sqrt{Re}h}\frac{\partial(D_k^2)}{\partial x} = \frac{1}{Re}\nabla_k^2\Omega_{z_k}, \tag{23}$$

$$\frac{\partial^2 U_k}{\partial x^2} - \beta_k^2 U_k = i\beta_k\Omega_{y_k} - \frac{\partial^2 V_k}{\partial x\partial y}, \tag{24}$$

$$\frac{\partial^2 V_k}{\partial x^2} + \frac{\partial^2 V_k}{\partial y^2} - \beta_k^2 V_k = -\frac{\partial\Omega_{z_k}}{\partial x} - i\beta_k\Omega_{x_k}, \tag{25}$$

$$\frac{\partial^2 W_k}{\partial x^2} - \beta_k^2 W_k = \frac{\partial\Omega_{y_k}}{\partial x} + i\beta_k\frac{\partial V_k}{\partial y}, \tag{26}$$

where $\nabla_k^2 = \left(\frac{\partial^2}{\partial x^2} + \frac{\partial^2}{\partial y^2} - \beta_k^2\right)$.

For each Fourier mode the Eq. (21) to (26) are solved in a domain represented by Fig. 1. Inflow and outflow regions are represented by the points $x = x_0$ and $x = x_{max}$.

Vortices are generated by a suction and blowing at the wall. The suction and blowing region is located between x_2 and x_3. In the regions from x_0 to x_1 and from x_4 and x_5 buffer zones are included in order to avoid reflections.

A pseudo-temporal technique is applied aimed to solve the transport of vorticity equations. A 4^{th} order Runge-Kutta method is applied for that purpose. Spatial derivatives are calculated using high order compact finite difference schemes (Souza et al., 2005; Lele, 1992). The V–Poisson equation (25) is solved by the use of the Full Approximation Scheme(FAS) multigrid method.

The large amount of points necessary to obtain acceptable results in a physical way justify the use of a parallel strategy. A domain decomposition strategy in the streamwise direction is adopted. The physical domain is partitioning into n equal parts. There is an overlap region and communications points are conveniently placed. The Message Passing Interface(MPI) library is used for the message-passing process. It is also applied a stretching technique in the normal direction.

The baseflow solution is represented by boundary layers approximations based on bidimensional Navier-Stokes solution (Falkner-Skan similar solution).

4. VERIFICATION

Based on the assumption that the dimensional spanwise Görtler wavenumber (λ_z) is constant, the global wavenumber parameter defined as

$$\Lambda_0 = \frac{U_\infty \lambda_z}{\nu}\sqrt{\frac{\lambda_z}{R}} \tag{27}$$

can be used to characterized the vortices. In the previous equation U_∞ is the potential velocity at L.

Otherwise specified all simulations adopt physical parameters presented by Tab. 1. It is also imposed the global Görtler number (Go) and the global characteristic wavelength (Λ_0) at L. The characteristic length L, the Re number and the spanwise wavenumber are calculated straightforward.

Table 1. Adopted physical values

R	$9\ m$
ν	$1.59 \times 10^{-5}\ m^2.s^{-1}$
U_∞	$5\ m.s^{-1}$

The Görtler number is taken equal 1. It is considered 985 points in the streamwise direction with step size $dx = 7.5 \times 10^{-2}$. 137 points are taken in the wall normal direction with first step size $dy_0 = 2.0 \times 10^{-3}$ and stretching factor of 1%. Linear simulations require just 2 Fourier modes. Inflow starts at $x_0 = 1$. Buffer zones are defined by $x_1 = 1$, $x_2 = 1.2$, $x_4 = 69.6$ and $x_5 = 72.6$. The suction and blowing region is defined between $x_2 = 2.4$ and $x_3 = 4.2$. For that set of parameters the code shows to be grid-independent.

4.1 Agreement with literature results

Based on experiments of Tandiono et al. (2008, 2009), Schrader et al. (2011) reports spatial DNS of the Görtler flow over concave walls for different geometry configurations. Linear results are compared with ones provide by the present code for a Görtler boundary layer with wavelength parameter $\Lambda_0 = 250$.

Some calculations are necessary to express the variables of Schrader et al. (2011) in terms of local Go_δ. Considering the list of physical parameters represented by Tab. 2 one can associate the authors initial $Re_{\delta_0} = 198.36$ with the approximate value of the initial position ($x_0 = 2.071 \times 10^{-1}\ m$).

Table 2. Physical parameters extract from Tandiono et al. (2008, 2009)

R	$1\ m$
U_∞	$2.85\ m.s^{-1}$
ν	$1.5 \times 10^{-5}\ m^2.s^{-1}$
λ	$12\ mm$

Following Schrader et al. (2011) we represent the streamwise evolution of disturbances by the wall-normal maximum of spanwise root-mean-square of the velocity vector components. Figure 2 provides a qualitative comparison for a Görtler flow with $\Lambda_0 = 250$. The maximum of the RMS-metric for each velocity component are plotted as a function of local Go_δ. Square symbols represent literature results and full lines represent our DNS results. One can notice good agreement for all the three metrics in the region of interest. Effects of the buffer zones and transient can be noticed in a neighbourhood of the inflow and outflow regions.

5. RESULTS AND DISCUSSION

Some linear tests have been done to investigate the influence of pressure variations in the control of Görtler vortices.

In this paper results based on geometry configurations for two Falkner-Skan parameters ($\beta = -0.15$ and $\beta = 0.25$) and two constant pressure gradients ($dp/dx = 0.003$ and $dp/dx = -0.01$) are compared for a range of spanwise wavelengths

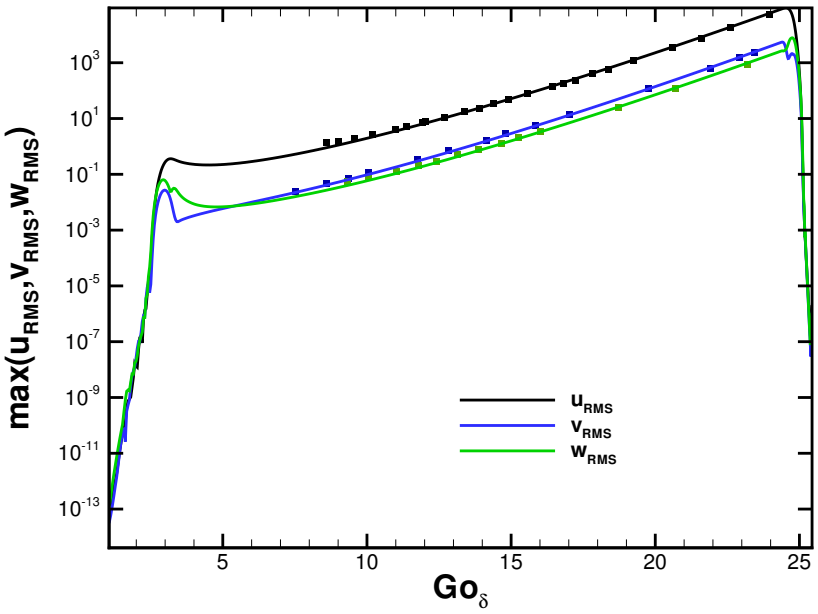

Figure 2. Linear comparison with $\Lambda_0 = 250$ based on literature results provided by Schrader et al. (2011). Square symbols represent literature results. Full lines represent the result provided by our numerical code.

aimed to identify zones of maximum amplification rate. Neutral case ($dp/dx = 0$) simulations are used as reference for comparison. Results are normalized by the dimensionless position $x = 15.1$.

Figure 3 describes variations of the most dangerous Λ_0 as a function of the dimensionless position x. For the cases under consideration the higher the boundary layer thickness, the higher the most dangerous wavenumber parameter. This can be supported based on the facts that (a) the maximum Λ_0 increases as a function of the streamwise direction and (b) adverse pressure configurations ($\beta = -0.15$ and $dp/dx = 0.003$) have bigger maximums compared with neutral and favorable ($\beta = 0.25$ and $dp/dx = -0.01$) ones.

Figure 4 shows the maximum u_{RMS} metric for the Falkner-Skan configurations. Just $max(\Lambda_0)$ limits for each case are considered. In the figure numbers follow by the letter A (adverse, $\beta = -0.15$), N (neutral, $\beta = 0$) or F (favorable, $\beta = 0.25$) identify different Λ_0 vortice configurations.

For the cases under consideration the pressure gradient does not affect the development of Görtler vortices significantly. Close to the inflow region the tests support the conclusions of Goulpie et al. (1996) in which an adverse pressure gradient is more effective in destabilizing the flow. However in a region further downstream the favorable pressure gradient shows to be more unstable. The most unstable case in the linear region is $\beta = -0.15$ with $\Lambda_0 = 250$ (full line with label 250_A).

A similar behavior can be observed in the cases characterized by constant pressure gradient. For constant pressure gradient tests results are provided by Fig. 5. Letter A in the figure represents $dp/dx = 0.003$, letter N denotes $dp/dx = 0$ and letter F, $dp/dx = -0.01$.

6. CONCLUSIONS

In linear simulations pressure gradient distributions different from the neutral case are not a very significant geometry parameter aimed to flow control. At the region where the linear approximation is physically acceptable an adverse pressure gradient is more unstable than a neutral or a favorable pressure one.

7. ACKNOWLEDGEMENTS

Josuel acknowledges Márcio Teixeira Mendonca for gainful discussions. Josuel is supported by São Paulo Research Foundation (FAPESP) grants #2011/08010-0 and #2013/00553-0.

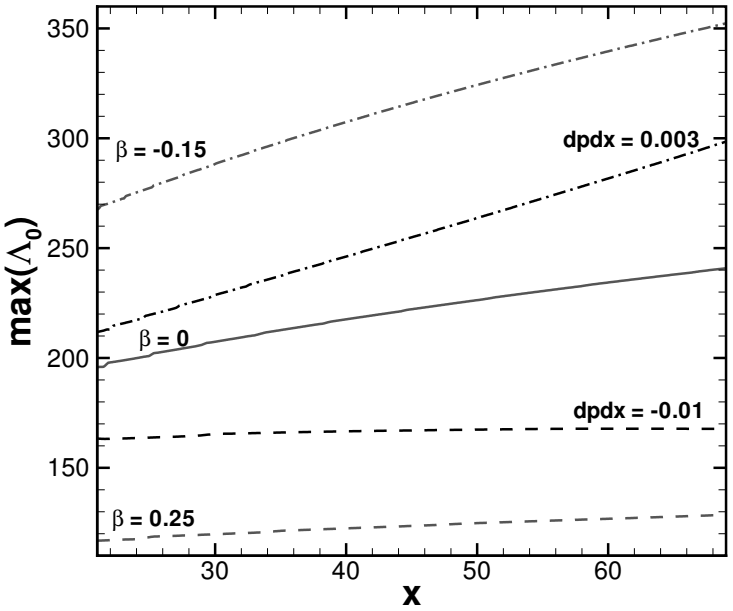

Figure 3. Most dangerous wavenumber parameter as a function of the streamwise position for different geometry configurations.

8. REFERENCES

Floryan, J.M., 1991. "On the Görtler instability in boundary layers". Prog. Aerospace Sci., Vol. 28, pp. 235–271.

Floryan, J.M. and Saric, W., 1982. "Stability of Görtler vortices in boundary layers". AIAA J., Vol. 20, No. 3, pp. 316–324.

Goulpie, P., Klingmann, B.G.B. and Bottaro, A., 1996. "Görtler vortices in boundary layers with streamwise pressure gradient: Linear theory". Phys. Fluids, Vol. 8, pp. 451–459.

Lele, S.K., 1992. "Compact finite difference schemes with spectral-like resolution". Journal of Computational Physics, Vol. 103, pp. 16–42.

Matsson, O.J.E., 2008. "Görtler vortices in falkner-skan with suction and blowing". Int. J. Num. Meth. Fluids, Vol. 56, pp. 257–277.

Saric, W., 1994. "Görtler vortices". Annu. Rev. Fluid Mech., Vol. 26, pp. 379–409.

Schlichting, H., 1979. "Boundary Layer Theory". McGraw-Hill.

Schrader, L., Brandt, L. and Saki, T.A., 2011. "Receptivity, instability and breakdown of Görtler flow". J. Fluid Mech., Vol. 682, pp. 362–396.

Souza, L.F., Mendonça, M.T. and Medeiros, M.A.F., 2005. "The advantages of using high-order finite differences schemes in laminar-turbulent transition studies". International Journal for Numerical Methods in Fluids, Vol. 48, pp. 565–582.

Tandiono, S., Winoto, H. and Shah, D.A., 2008. "On the linear and nonlinear developtment of Görtler vortices". Phys. Fluids, Vol. 20.

Tandiono, S., Winoto, H. and Shah, D.A., 2009. "Wall shear stress in Görtler vortex boundary layer flow". Phys. Fluids, Vol. 21.

9. Responsibility notice

The authors are the only responsible for the printed material included in this paper.

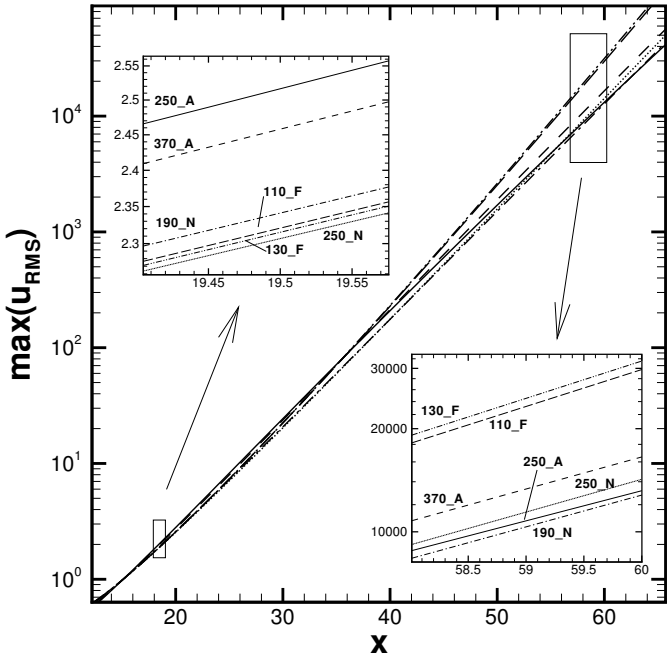

Figure 4. Evolution of the $max(u_{RMS})$ metric for three Falkner-Skan parameters as a function of x.

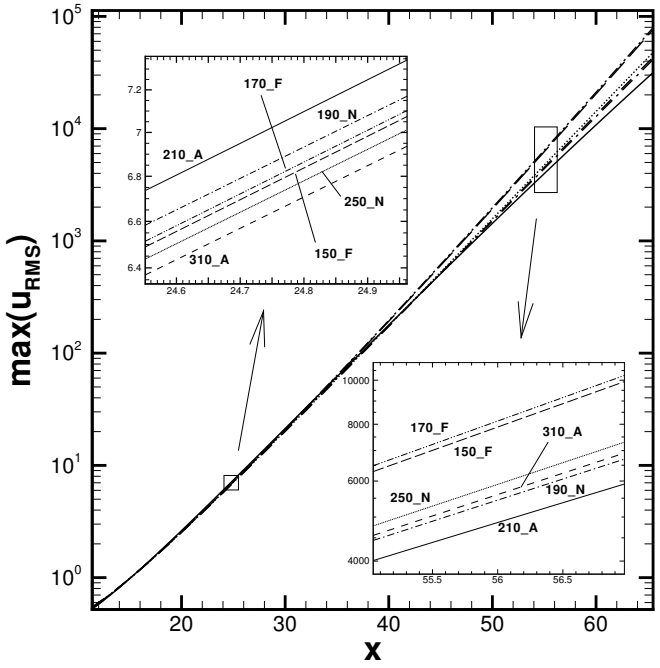

Figure 5. Evolution of the $max(u_{RMS})$ metric for three constant pressure gradient distributions as a function of x.

FLAT PLATE TURBULENT FLOW SIMULATIONS USING A CORRELATION-BASED TRANSITION MODEL

Gustavo Luiz Olichevis Halila, gustavohalila@gmail.com
Instituto Tecnológico de Aeronáutica, 12228-903 São José dos Campos, SP, Brazil

Enda Dimitri Vieira Bigarella, enda.bigarella@embraer.com.br
Embraer S.A., 12227-901 São José dos Campos, SP, Brazil

João Luiz F. Azevedo, joaoluiz.azevedo@gmail.com
Instituto de Aeronáutica e Espaço, 12228-903 São José dos Campos, SP, Brazil

Abstract. *A correlation-based transition model is tested against two different zero pressure gradient flat plate test cases. Special attention is dedicated to analyze how simulation setup impacts the results. Calculations are performed with the CFD++ finite volume solver. The compressible preconditioned Navier-Stokes equations are considered. Turbulence closure is achieved with the SST model. This turbulence model is augmented by a transition model based on two additional transport equations, one for the intermittency and another for the momentum thickness Reynolds number. Flow parameters, such as freestream turbulence intensity and turbulence length scale, have important effects on transition onset and extent of the transition region. Mesh refinement, y^+ dependence and number of time steps for convergence are numerical parameters also considered. Different limiter formulations and reconstruction polynomials, nodal and centroidal bases, have also been investigated. It is observed that the transition model is robust and the results are not sensitive to numerical settings. On the other hand, the dimensionless wall distance, y^+, has significant impact in the computational results. Skin friction and velocity profiles are presented and used for validation of the present computations. Good agreement with the experimental data is observed.*

1. INTRODUCTION

Stability analysis in fluid flows plays an important role in many engineering applications. In the aerospace industry, the nature of the fluid flow, *e.g.*, laminar or turbulent, has a direct impact on drag and, hence, on overall flight efficiency. Additionally, heat and mass transfer are equally influenced by the nature of the flow. These aspects of industrial situations, in which an accurate prediction of transition might be extremely important, have led to several studies on possible modifications to existing turbulence models such that they would be able to predict the transition onset and extent [1]. These studies have looked at viscous modifications and a more recent approach takes into account correlation-based transition models built upon local variables. The model presented by Langtry and Menter [2] is herein adopted and further studied against experimental data. Some other attempts have been made, such as the three-equation eddy-viscosity model by Walters and Cokljat [3] or the single-point $k - k_\ell - \omega$ model discussed in Ref. [4], for which simulations were carried out by Fürst [5]. At present, it is clear that transition modeling is an active research area.

If one considers the physical basis for transition, several mechanisms are recognized as the starting point for a full turbulent flow. Unstable Tollmien-Shclichting waves are, generally, the prevailing mechanism for natural transition in airplanes. Crossflow effects are an important transition mechanism in swept wings. Bypass transition occurs when linear transition steps are bypassed by means of boundary layer nonlinear disturbances due to high levels of turbulence in the freestream. RANS turbulence models are based on a time-averaging procedure, which corresponds to a low-pass filter. As a result, only an average frequency is seen by the model and, therefore, important spectral information is lost. For example, Tollmien-Schlichting waves are not detected by RANS turbulence models. The natural approach to overcome such difficulty is, typically, the development an extra model for the transitional region and its integration into the original turbulence closure.

In order to simulate transition phenomena, some specific methods have been developed in the last decades. Low Reynolds number models have the idea of avoiding a mismatch between turbulence and transition models by considering low-Reynolds number phenomena in a single model. This approach makes the necessary assumption that the applications are restricted to broadband transition-triggering disturbances. Additionally, they typically suffer from a close interaction of the transition prediction capability and the viscous sublayer modeling, which can prevent an independent calibration of either phenomena [6, 7]. Low Reynolds number models are only applicable to bypass transition, what clearly reduces their range of application.

Another methodology available for evaluating transitional flows is the e^N technique. Based on linear stability theory, this method assumes parallel flow in order to calculate the growth of the disturbance amplitude from the boundary layer neutral point to the transition location [8, 9]. It is considered a semi-empirical method, because the N factor depends on wind tunnel or flight test calibration. The transition is assumed to start when the factor e^N exceeds the limiting value of

N. Transition due to nonlinear effects, such as high freestream turbulence levels, cannot be predicted by the e^N method, because it uses linear stability theory.

Empirical correlations are the next step into the transition modeling capability. The first attempts were performed by Abu-Ghannam and Shaw [10], Mayle [11] and Suzen et al. [12]. In general, the transition momentum thickness Reynolds number is correlated to local variables such as the pressure gradient along the wall-normal direction and the freestream turbulence intensity. The growth of Tollmien-Schlichting waves, crossflow-induced instabilities, roughness effects and bypass transition are different transition mechanisms, which, hence, demand distinct correlations. Standard correlation-based methodologies present several technical challenges. The onset of transition is described as the point in space where the momentum-thickness Reynolds number, Re_θ, exceeds a threshold value. The calculation of Re_θ is performed by integration until the edge of the boundary layer. In aerodynamic applications, in which boundary layer effects are typically combined with wall-curvature issues, the edge of the boundary layer is not well defined. Additionally, the need for performing simulations based on unstructured grids in parallelized CFD codes poses extra challenges. In fact, unstructured meshes do not have easily identified wall-normal grid lines. As a result, the integration of boundary layer global parameters is difficult. These issues make standard correlation-based models not compatible with modern CFD codes.

Unlike other approaches, the correlation-based transition model presented in Ref. [2] does not require non-local information. The strain-rate Reynolds number [13] is a key factor for assuring the code locality. It is a local variable and it is defined as

$$Re_v = \frac{\rho y^2}{\mu}\frac{\partial u}{\partial y} = \frac{\rho y^2}{\mu} S \,, \tag{1}$$

where y is the distance from the nearest wall, μ is the dynamic molecular viscosity coefficient, ρ is the density and S is the absolute strain rate. In a physical standpoint, the term $y^2 S$ is responsible for the growth of disturbances inside the boundary layer, whereas $\nu = \mu/\rho$ represents damping of such disturbances [14, 15]. As stated by Menter and Langtry [2], the strain-rate Reynolds number has its maximum value inside the boundary layer related to the momentum thickness Reynolds number according to the expression

$$Re_\theta = \frac{\max(Re_v)}{2.193} \,. \tag{2}$$

The approach just described has proven to be superior than the use of low-Reynolds number models. However, an independent calibration of both viscous sublayer damping and transition prediction is not possible. For solving such inconvenient, Langtry and Menter [16, 17, 18] propose a new model where two additional transport equations are employed to estimate transition onset and extent. This is possible thanks to the combination of the strain-rate Reynolds number with experimental transition correlations. In addition, viscous sublayer damping and transition prediction are independent. A first transport equation based on the intermittency allows for an estimation of the extent of the transition region. Transition onset is triggered by the momentum thickness Reynolds number transport equation. The SST turbulence model [19] is coupled to the intermittency transport equation, which turns on the term responsible for producing the turbulent kinetic energy downstream of the transition onset point. The proposed transport equations do not attempt to model the physics of the transition process, but they form a framework for the implementation of correlation-based models into general-purpose CFD methods. Therefore, the term Local Correlation-Based Transition Model (LCTM) [2] is used in order to distinguish the present model formulation from physics-based transport modeling.

Numerical simulations included in the present work are performed with the CFD++ finite volume solver, version 11.1. The present paper is organized as follows. Section 2.consists of an overview of the governing equations and the $\gamma - Re_\theta$ transition model. Section 3.presents the numerical results for two flat plate test cases and Section 4.concludes the present paper with some final remarks.

2. THEORETICAL FORMULATION

2.1 Governing equations

The unsteady motion of a viscous and compressible fluid is represented by the Navier-Stokes equations. In a conservative form, these equations are written as

$$\begin{aligned} \frac{\partial \rho}{\partial t} + \frac{\partial(\rho u_j)}{\partial x_j} &= 0 \\ \frac{\partial(\rho u_i)}{\partial t} + \frac{\partial(\rho u_i u_j)}{\partial x_j} + \frac{\partial p}{\partial x_i} - \frac{\partial \tau_{ij}}{\partial x_j} &= 0 \\ \frac{\partial e}{\partial t} + \frac{\partial}{\partial x_j}\left[(e+p)u_j - \tau_{ij}u_i + q_{H_j}\right] &= 0 \end{aligned} \tag{3}$$

where $\mathbf{v} = \{u, v, w\}$ is the vector of velocities in the Cartesian coordinate system and ρ stands for the density. The equations above do not form a closed system and, therefore, additional constitutive relations are required. The total energy per unit volume, e, is defined as

$$e = \rho \left[e_i + \frac{1}{2}(u^2 + v^2 + w^2) \right] \tag{4}$$

The internal energy, e_i, is expressed as

$$e_i = C_v T \tag{5}$$

where C_v is the gas specific heat at constant volume. The state equation for a perfect gas can be written as

$$p = (\gamma - 1) \left[e - \frac{1}{2}\rho(u^2 + v^2 + w^2) \right] \tag{6}$$

where p is the static pressure. The heat flux vector, $\mathbf{q}_H$, is obtained from the Fourier law for heat conduction as

$$\mathbf{q}_H = -\kappa \nabla T \tag{7}$$

$$\kappa = \frac{C_p \mu}{Pr} \tag{8}$$

For a Newtonian fluid, the components of the viscous tensor are expressed as

$$\tau_{ij} = \mu \left(\frac{\partial u_i}{\partial x_j} + \frac{\partial u_j}{\partial x_i} \right) - \frac{2}{3}\mu \frac{\partial u_k}{\partial x_k} \delta_{ij} \tag{9}$$

where δ_{ij} is the Kronecker delta.

2.2 Transition model

The Langtry-Menter [2] correlation-based transition model is composed of two additional transport equations. The transport equation for the intermittency reads

$$\frac{\partial(\rho\gamma)}{\partial t} + \frac{\partial(\rho u_j \gamma)}{\partial x_j} = P_\gamma - E_\gamma + \frac{\partial}{\partial x_j} \left[\left(\mu + \frac{\mu_t}{\sigma_f} \right) \frac{\partial \gamma}{\partial x_j} \right] \tag{10}$$

The intermittency equation allows for the estimation of the extent of the transition region since the intermittency represents the probability of a fluid cell to be turbulent. Transition onset, on the other hand, is triggered by the momentum thickness Reynolds number transport equation which can be written as

$$\frac{\partial(\rho \tilde{Re}_{\theta t})}{\partial t} + \frac{\partial(\rho u_j \tilde{Re}_{\theta t})}{\partial x_j} = P_{\theta_t} + \frac{\partial}{\partial x_j} \left[\sigma_{\theta t}(\mu + \mu_t) \frac{\partial \tilde{Re}_{\theta t}}{\partial x_j} \right] \tag{11}$$

The empirical correlations that complete the model can be found in the literature [2]. The interaction between the transition model and the SST turbulence model is performed by a modified kinetic energy production term, $\tilde{P}_k$, as

$$\frac{\partial(\rho k)}{\partial t} + \frac{\partial(\rho u_j k)}{\partial x_j} = \tilde{P}_k - \tilde{D}_k + \frac{\partial}{\partial x_j} \left[(\mu + \sigma_k \mu_t) \frac{\partial k}{\partial x_j} \right] \tag{12}$$

$$\tilde{P}_k = \gamma_{\text{eff}} P_k \tag{13}$$

3. TEST CASES AND RESULTS

3.1 Definition of test cases

The test cases for zero-pressure flat plate are introduced in this section. The forthcoming results have been computed using the European Research Community on Flow Turbulence and Combustion (ERCOFTAC) T3 flat plate, cases A and B, as test bed. The ERCOFTAC T3 flat plate cases were specially designed to validate numerical procedures for the calculation of transition phenomena. The experimental results are available in the literature [20]. Both cases have a zero pressure gradient boundary layer, with different freestream turbulence intensity (FSTI) levels, which are above 1%. This is relevant because 1% of FSTI corresponds to bypass transition. Table 1 presents important experimental data for testing the transition model. Both A and B cases share the same geometry, *i.e.*, a $1,500$ mm long flat plate with a small leading

Table 1: Experimental data for the ERCOFTAC T3A and T3B flat plate test cases.

Test Case	U_0 [m/s]	FSTI at Leading Edge (%)	Density [kg/m^3]	Dynamic Viscosity [kg/(m.s)]
T3A	5.4	3	1.2	1.8 $\times 10^5$
T3B	9.4	6	1.2	1.8 $\times 10^5$

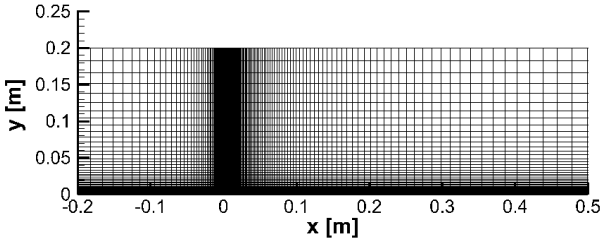

Figure 1: Representative computational mesh for the T3 test cases.

edge radius of 0.75 mm. In order to control the circulation around the flat plate and, hence, ensure an attached flow, a trailing edge flap is used. Since no data concerning this trailing edge flap could be found and Ref. [21] states that the experimental data is free of separated flow, the rounded leading edge, the 0.5 deg. angle of attack and the trailing edge flap were not considered in the numerical simulations in the present work. Therefore, a simple flat plate is used here and a representative computational mesh is shown in Fig. 1.

Three different meshes are tested. The coarsest one has $11,000$ cells and the finest one has $42,000$ control volumes. An intermediate mesh with $22,000$ cells, which is actually shown in Fig. 1, is also created. The best practices for the use of the SST model together with the present transition model [15] recommend the use of y^+ values smaller than 1. The computational domain and the boundary conditions are as follows. Inflow/outflow characteristic-based boundary conditions are specified at the left, right and top boundaries. At the bottom boundary, the first 200 mm are defined as an inviscid wall, or as a symmetry condition. The remainder of the bottom boundary comprises the plate itself and, hence, viscous wall boundary conditions are specified. All simulations in the present work perform integration to the wall or, in other words, no wall functions are used.

The simulations are performed considering the compressible preconditioned Navier-Stokes equations, which is one of the options offered by the CFD++ finite volume solver, version 11.1.. An implicit steady approach is chosen, given the test case characteristics. In most of the simulations, the CFD++ nodal based reconstruction polynomials are used, although centroidal base reconstruction polynomials are also considered for verifying the model robustness to numerical settings. Furthermore, both *minmod* and van Albada limiters [22] are used in the simulations and their results are compared. Clearly, however, as one should expect, the limiter choice has no effect in the present results, since low speed flows are considered here.

3.2 T3A test case

The first of the ERCOFTAC test cases, addressed here, is the T3A flat plate case. Freestream speed is 5.4 m/s and the leading edge freestream turbulence intensity is 3%. Grid refinement is investigated by means of the three aforementioned meshes. It is clear that the intermediate mesh, with $22,000$ cells, is refine enough to study the flat plate bypass transition case here addressed. Figure 2 presents friction coefficient results for the three meshes, together with the experimental data.

The nondimensional wall distance, y^+, has important effects on the model behavior. As specified in the literature [15], values smaller than 1 must be used to assure that the model works properly. Herein, three values of y^+ are tested, 0.6, 1.3 and 2.7, as illustrated in Fig. 3. The first cell heights are, respectively, 5.6×10^{-6} m, 1.5×10^{-5} m and 4.5×10^{-5} m. The results clearly indicate that the model has a dependency on the wall dimensionless distance, y^+. The use of $y^+ = 0.6$ yields the best results and shows that employing values smaller than 1 is necessary for an adequate model performance. Solution convergence is addressed by performing simulations with 1000 and 3000 time steps, as shown in Fig. 4. The results show that the skin friction coefficient is already converged after 1000 iterations. Therefore, these tests are indicating that the use of a mesh with $22,000$ cells, $y^+ = 0.6$ and 1000 time steps yield results in good agreement with the experimental data. Therefore, the forthcoming simulations have used this numerical set up as the standard for grid refinement and number of time steps.

The turbulent length scale, L, has a direct impact on transition onset and extent of transition. According to Yang and Voke [23], the value for the turbulent length scale for the T3A test case is $L = 12$ mm. These authors performed DNS

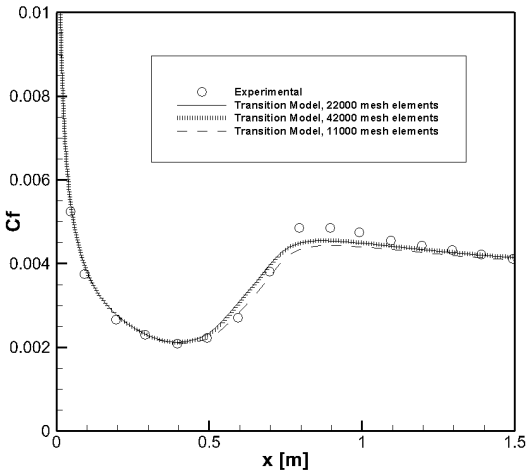

Figure 2: Mesh refinement effect on the skin friction coefficient.

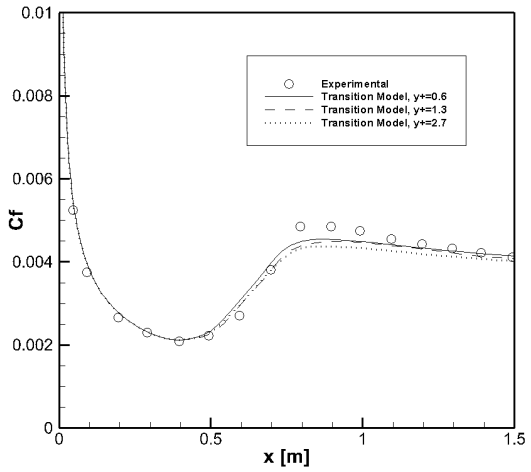

Figure 3: Dimensionless wall distance, y^+, effect on the skin friction coefficient.

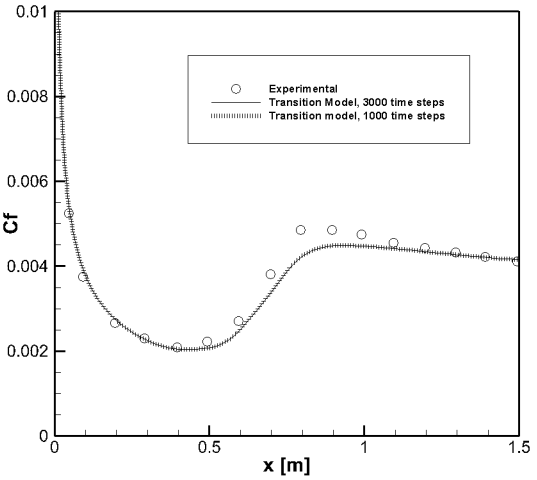

Figure 4: Effect of solution convergence on the skin friction.

calculations for the present configuration. In order to verify the model ability to respond to variations in the turbulent length scale, which is linked to the μ_t/μ ratio, values of L ranging from 5 to 30 mm are used in the present calculations. The results for the skin friction coefficient for such tests are shown in Fig. 5. The results are in accordance with the

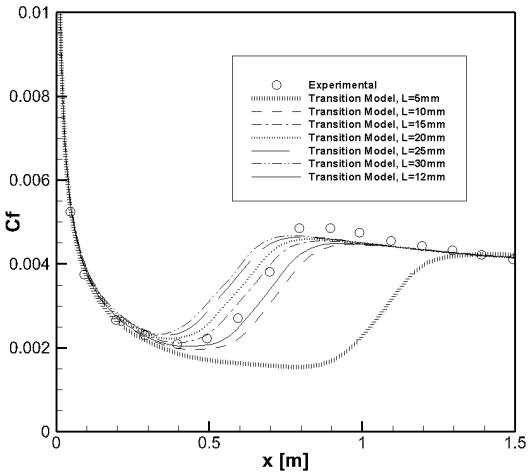

Figure 5: Skin friction coefficient dependency on freestream turbulence length scale.

problem physics, that is, a larger L moves the transition onset upstream and decreases the extent of the transition region. Although the DNS calculations in Ref. [23] have indicated that $L = 12$ mm, the present results are indicating that the best fit of the experimental data is obtained for RANS simulations with $L = 15$ mm. Of course, this might be dependent on the choice of turbulence closure and of transition model. In general, the skin friction coefficient in the turbulent region of the boundary layer is underpredicted by the present model, regardless of the value of turbulent length scale used.

The influence of numerical settings is further investigated by performing two additional simulations, namely with nodal base polynomials and minmod limiter, and with centroidal base polynomials and the van Albada (continuous) limiter. The results of such tests are presented in Fig. 6. The model is robust with regard to numerical settings and both

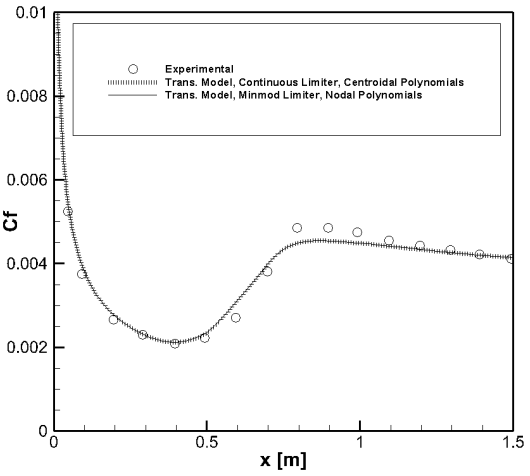

Figure 6: Skin friction coefficient dependency on numerical settings.

numerical schemes yield similar results for the skin friction coefficient. Another interesting evaluation for the transition model can be performed by observing the velocity profiles. Two streamwise stations are used to analyse such profiles, namely one at $x = 45$ mm and another at $x = 1,295$ mm from the leading edge. Experimental data show that the flow is laminar at the first station but it is turbulent at the latter. The velocity profile results are shown in Fig. 7. The numerical results are clearly in accordance with the experimental data, showing a laminar profile near the leading edge of the flat plate and a turbulent profile further downstream. The velocity profile in the laminar region is very well predicted by the simulation, whereas the turbulent profile does not reach the same agreement. Furthermore, it seems that the computed boundary layer thickness for the turbulent region is somewhat smaller than the experimental one.

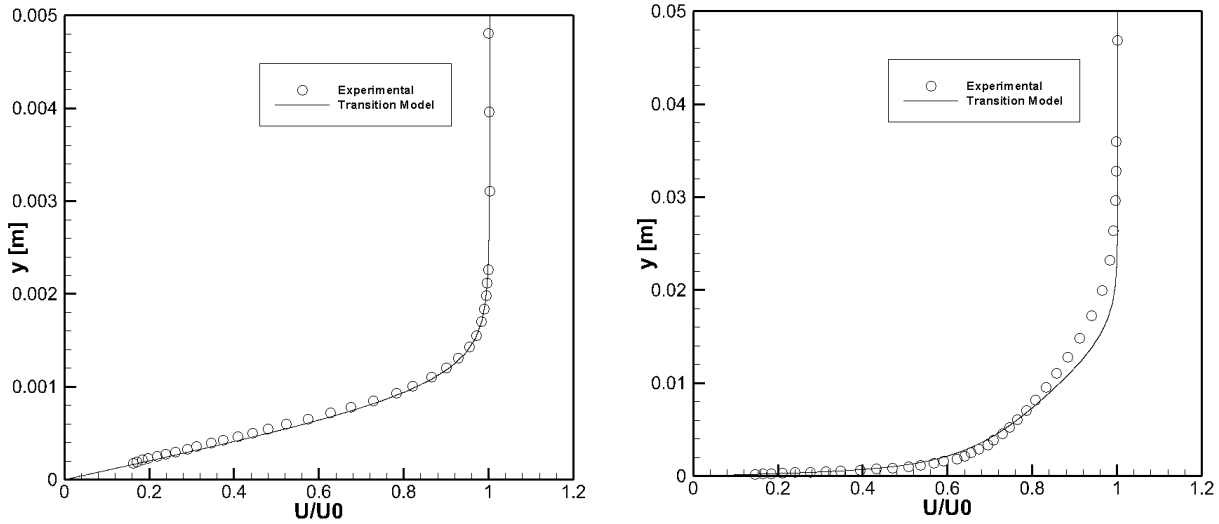

(a) $x = 45$ mm (b) $x = 1,295$ mm

Figure 7: Velocity profiles at two stations along the flat plate; x is measured from the leading edge.

3.3 T3B test case

For this test case, freestream speed is 9.4 m/s and the leading edge freestream turbulence intensity is 6%. Since the freestream turbulence intensity and freestream speed are larger than those for the T3A test case, transition onset is expected to move upstream and the extent of the transition region should be smaller than the corresponding results obtained for the previous test case. Solution convergence is, again, verified by performing simulations with 1000 and 3000 time steps, as shown in Fig. 8. As in the previous case, it is clear that 1000 time steps are sufficient to obtain convergence of the skin

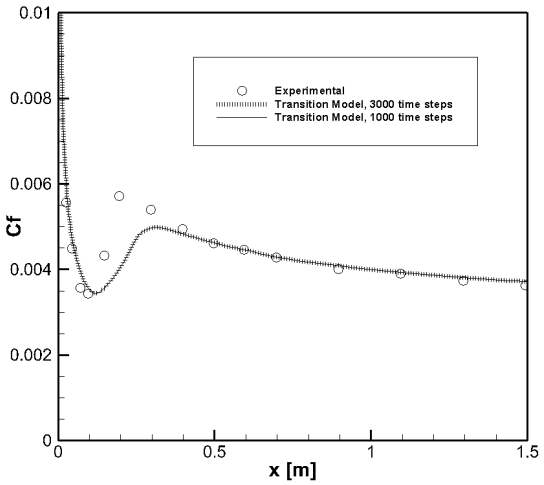

Figure 8: Effect of solution convergence on the skin friction for the T3B test case.

friction coefficient.

The sensitivity of the skin friction coefficient to the turbulence length scale can be observed in Fig. 9. Considering the results obtained for the T3A test case, similar behavior, concerning the onset of transition and extent of the transition region, is observed in the present test case. An increase in the turbulence length scale yields an upstream motion of the transition onset and a decrease in the extent of the transition region. DNS calculations by Yang and Voke [23] have indicated that, for the T3B test case, the value for the turbulent length scale is $L = 13.5$ mm. Figure 9 is indicating that such value of turbulence length scale does not yield good agreement of the calculated skin friction coefficient with experiment in the transition region. However, since the present computational results have a tendency of exaggerating

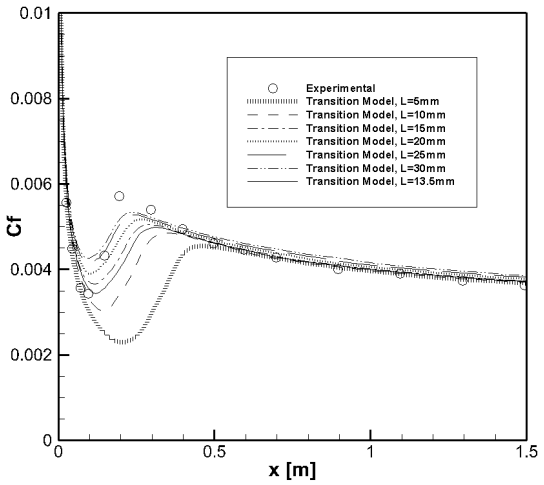

Figure 9: Skin friction dependency on turbulence length scale for the T3B test case.

the variation in C_f in the transition region, there is no value of L that would actually fit the experimental data adequately throughout the transition region in the present simulations.

As discussed, the present computational skin friction coefficient is underpredicted for $L = 13.5$ mm in the transition region. Moreover, the extent of the transition region is overpredicted for this value of turbulence length scale. However, a comparison of the values of freestream eddy viscosity specified in the present calculations with those reported in Ref. [15] indicates that our simulations are using fairly smaller values of the μ_t/μ ratio at the flow entrance boundary. The cited reference uses $\mu_t/\mu = 100$, whereas the present calculations use $\mu_t/\mu = 56$, for instance, when $L = 13.5$ mm. Clearly, values of μ_t/μ and L are related, and $\mu_t/\mu = 100$ corresponds to a value of $L = 25$ mm. Therefore, such observations can explain why the results in Ref. [15], and also our results for $L = 25$ mm, have such overprediction of C_f in the transition region.

The present test case is assuming a freestream turbulence intensity which is twice that used in the T3A test case. This higher value of FSTI has moved the transition onset much closer to the flat plate leading edge, as expected. Moreover, the larger FSTI value yields a transition region which is smaller that that observed in the previous test case, as one should also expect. Finally, Fig. 10 presents boundary layer velocity profiles for two streamwise stations along the flat plate, namely at $x = 45$ mm and $x = 1,295$ mm from the leading edge, as in the previous case. Furthermore, as in the T3A test case, experimental data indicates that the boundary layer at $x = 45$ mm is laminar, whereas it is turbulent at $x = 1,295$ mm. The numerical results are clearly in accordance with the experimental data, showing a laminar profile near the plate leading edge and a turbulent profile at the downstream station. The results in Fig. 10 also indicate that the increase in the freestream turbulence intensity makes the velocity profile at $x = 45$ mm sharper than the one observed at the same station for the previous test case, but it is still laminar. It is also interesting that one obtains a better agreement between the computational results and the experimental data for the velocity profile at $x = 1,295$ mm in the present test case.

4. CONCLUDING REMARKS

In the present paper, the Langtry-Menter transition model is investigated by simulating two ERCOFTAC flat plate test cases, namely the T3A and T3B cases. A brief review of some recent CFD transition models indicates some weaknesses present in previous approaches, especially in what concerns their applications to unstructured grid CFD simulations. An overview of the Langtry-Menter model is provided and some of its important aspects are highlighted. The model is free of non-local variables, which makes it appropriate for daily industrial CFD applications.

The model sensitivity to freestream turbulence intensity and turbulence length scale is investigated in the paper. As one should expect, an increase in the turbulence length scale moves the transition onset upstream and reduces the extent of the transition region. Similarly, an increase in freestream turbulence intensity also yield the same behavior for transition onset and length of the transition region. Mesh refinement and dimensionless distance to the wall, y^+, are evaluated in order to understand how the grid may affect the model performance. The results show that one must use $y^+ \leq 1$, since values larger than 1 may lead to a slight underprediction for the skin friction coefficient in the upstream portion of the turbulent boundary layer region.

The present paper also addressed the effect of some numerical settings of the CFD++ code. For instance, the use of both nodal and centroidal base reconstruction polynomials was tested, as well as the use of the van Albada and *minmod* limiters. The results are essentially independent of such numerical parameters. It is correct to state that, in general, good

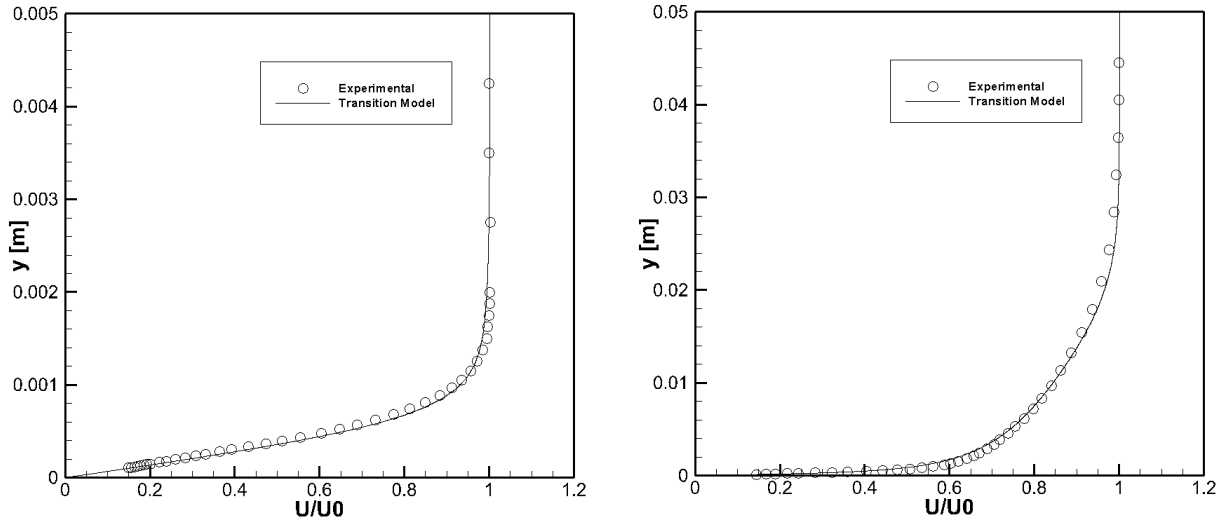

(a) $x = 45$ mm

(b) $x = 1,295$ mm

Figure 10: Velocity profiles at two stations along the flat plate for case T3B; x is measured from the leading edge.

agreement with experimental data is observed in the present calculations. It is true that such behavior might be explained by the fact that the T3 test cases were considered in the calibration of the empirical correlations present in the transition model here adopted.

5. ACKNOWLEDGMENTS

The authors gratefully acknowledge the partial support for this research provided by Conselho Nacional de Desenvolvimento Científico e Tecnológico, CNPq, under the Research Grant No. 309985/2013-7. The authors are also indebted to the partial financial support received from Fundação de Amparo à Pesquisa do Estado de São Paulo, FAPESP, under Grant No. 2013/07375-0.

6. REFERENCES

Wilcox, D. C., "Simulation of Transition with a Two-Equation Turbulence Model," *AIAA Journal*, Vol. 32, No. 2, Feb. 1994, pp. 247–255.

Langtry, R. B. and Menter, F. R., "Correlation-Based Transition Modeling for Unstructured Parallelized Computational Fluid Dynamics Codes," *AIAA Journal*, Vol. 47, No. 12, Dec. 2009, pp. 2894–2906.

Walters, D. K. and Cokljat, D., "A Three-Equation Eddy-Viscosity Model for Reynolds-Averaged Navier-Stokes Simulations of Transitional Flows," *Journal of Fluids Engineering*, Vol. 130, Dec. 2008, pp. 1–13.

Schlichting, H. and Gersten, K., *Boundary-Layer Theory*, Springer, Boston, 2003.

Fürst, J., "Numerical Simulation of Transitional Flows with Laminar Kinetic Energy," *Engineering Mechanics*, Vol. 20, No. 5, 2013, pp. 379–388.

Savill, A. M., "Some Recent Progress in the Turbulence Modeling of By-pass Transition," In *Near-Wall Turbulent Flows*, Elsevier, 1993.

Savill, A. M., *One-Point Closures Applied to Transition, Turbulence and Transition Modeling*, M. Hallbäck et al., eds., Kluwer, 1996.

Smith, A. M. O. and Gamberoni, N., "Transition, Pressure Gradient and Stability Theory," Douglas Aircraft Company Report ES 26388, Douglas Aircraft Company, 1956.

van Ingen, J. L., "A Suggested Semi-Empirical Method for the Calculation of the Boundary Layer Transition Region," Univ. Delft Report VTH-74, University of Delft, Delft, The Nederlands, 1956.

Abu-Ghannam, B. J. and Shaw, R., "Natural Transition of Boundary Layers – The Effects of Turbulence, Pressure Gradient and Flow History," *Journal of Mechanical Engineering Science*, Vol. 22, No. 5, 1980, pp. 213–228.

Mayle, R. E., "The Role of Laminar-Turbulent Transition in Gas Turbine Engines," *ASME Journal of Turbomachinery*, Vol. 113, 1991, pp. 509–537.

Suzen, Y. B., Huang, P. G., Hultgren, L. S., and Ashpis, D. E., "Predictions of Separated and Transitional Boundary-

Layers Under Low-Pressure Turbine Airfoil Conditions Using an Intermittency Transport Equation," *Journal of Turbomachinery*, Vol. 125, No. 3, Jul. 2003, pp. 455–464.

Driest, E. and Blumer, C., "Boundary Layer Transition: Freestream Turbulence and Pressure Gradient Effects," *AIAA Journal*, Vol. 1, No. 6, 1963, pp. 1303–1306.

Langtry, R. B. and Menter, F. R., "Transition Modeling for General CFD Applications in Aeronautics," AIAA Paper No. 2005-522*, 43rd AIAA Aerospace Sciences Meeting and Exhibit*, Reno, NV, Jan. 2005.

Langtry, R. B., *A Correlation-Based Transition Modeling using Local Variables for Unstructured Parallelized CFD Codes*, Ph.D. Thesis, Universitat Stuttgart, Stuttgart, Germany, 2006.

Menter, F. R., Esch, T., S., and Kubacki, "Transition Modeling Based on Local Variables," *5th International Symposium on Turbulence Modeling and Measurements*, Spain, 2002.

Menter, F. R., Langtry, R. B., Likki, S. R., Suzen, Y. B., Huang, P., and Volker, S., "A Correlation Based Transition Model Using Local Variables. Part 1: Model Formulation," *ASME TURBO EXPO 2004*, ASME Paper No. 22004-53452, Vienna, Austria, 2004.

Langtry, R., Menter, F. R., Likki, S. R., Suzen, Y. B., Huang, P., and Volker, S., "A Correlation Based Transition Model Using Local Variables. Part 2: Test Cases and Industrial Applications," *ASME TURBO EXPO 2004*, ASME Paper No. 22004-53452, Vienna, Austria, 2004.

Menter, F. R., "Two-Equation Eddy Viscosity Turbulence Models for Engineering Applications," *AIAA Journal*, Vol. 32, No. 8, Feb. 1994, pp. 1598–1605.

Roach, P. E. and Brierley, D. H., "The Influence of a Turbulent Free-Stream on Zero Pressure Gradient Transitional Boundary Layer Development. Part I: Test Cases T3A and T3B," *ERCOFTAC Workshop*, Cambridge University Press, Lausanne, Switzerland, March 1990.

Savill, A. M., "Synthesis of T3 Test Case Predictions," *ERCOFTAC Workshop*, Cambridge University Press, Lausanne, Switzerland, March 1990.

Hirsh, C., *Numerical Computation of Internal and External Flows. 2. Computational Methods for Inviscd and Viscous Flows*, Wiley, New York, 1990.

Yang, Z. and Voke., P., "Numerical Simulation of Boundary Layer Transition in the Presence of Free-Stream Turbulence," *ERCOFTAC Workshop*, Cambridge University Press, Lausanne, Switzerland, March 1990.

7. Responsibility notice

The authors are the only responsible for the printed material included in this paper

ESTUDO EXPERIMENTAL DO EFEITO AEROACÚSTICO DE UMA EXCRESCÊNCIA BIDIMENSIONAL NA COVA DO ESLATE

Filipe Ramos do Amaral, framaral@usp.br[1]
Daniel Sampaio Souza, dss_em@yahoo.com.br[1]
Carlos do Carmo Pagani Junior, paganni@sc.usp.br[1]
Juan Carlos Serrano, jcserrano@unipamplona.edu.co[2]
Manuela Blanco, manuelavblanco1@gmail.com[3]
Marcello Augusto Faraco de Medeiros, marcello@sc.usp.br[1]
[1]Universidade de São Paulo, Escola de Engenharia de São Carlos, Departamento de Engenharia Aeronáutica – Av. Trabalhador São Carlense, 400, São Carlos/SP, CEP 13566-590.
[2]Universidad de Pamplona, Programa Ingeniería Mecánica – Km 1 via Bucaramanga, Pamplona, Colombia.
[3]Universidade Federal de São Carlos, Centro de Ciências Exatas e Tecnologia, Departamento de Física – Rodovia Washington Luís, Km 235, São Carlos/SP, CEP 13565-905.

Resumo. *O presente trabalho refere-se a um estudo aeroacústico experimental do dispositivo hipersustentador denominado eslate sob a presença de excrescências instaladas no interior de sua cova. O eslate é um elemento posicionado no bordo de ataque do perfil aerodinâmico e possibilita a aeronave se manter em voo com uma menor velocidade, de maneira a permitir procedimentos de pouso e decolagem mais seguros e uma pista menor para ambas as operações. O estudo contempla o aerofólio denominado MDA 30P30N, com excrescências presentes em diferentes posições na cova do eslate, ao longo de toda a envergadura do elemento, para diferentes de ângulos de ataque e velocidades de escoamento. Os experimentos foram realizados em um túnel de vento de seção e circuito fechados. O pós-processamento dos dados aeroacústicos adquiridos nos ensaios realizados, de forma a caracterizar o ruído a partir de espectros de frequência e mapas para localização e determinação da intensidade das fontes sonoras, foi efetivado com códigos in-house de beamforming e DAMAS. Os resultados obtidos para excrescências de seção transversal quadrada e em quatro posições distintas na cova do eslate, revelam que a posição do selo possui grande impacto no ruído de eslate, alterando significativamente o espectro em frequência.*

Palavras-chave*: aeroacústica, dispositivos hipersustentadores, ruído de eslate, beamforming, DAMAS.*

1. INTRODUÇÃO

Os dispositivos de hipersustentação são sistemas aerodinâmicos acoplados à aeronave capazes de aumentar a sustentação em certas condições de voo, tais como decolagem e pouso. Como consequência, a velocidade de estol é reduzida consideravelmente, sendo a aeronave capaz de efetuar um voo mais lento (e seguro) nos momentos de pouso e decolagem. Com o desenvolvimento dos motores *turbofan*, a partir da década de *70*, a contribuição dos trens-de-pouso e dos dispositivos de hipersustentação, como eslate e flape, tornou-se significativa em condições de aproximação e aterrissagem.

Existe um aumento no ruído aeroacústico devido à presença dos dispositivos hipersustentadores. Dobrzynski (2010) afirma que, para uma mesma velocidade, uma asa com dispositivos de hipersustentação estendidos é cerca de *10* [dB] mais ruidosa do que quando comparada com a mesma asa em condição de cruzeiro (com os elementos hipersustentadores recolhidos). O eslate possui um ruído de fonte menos intenso por unidade de área em comparação com o ruído de ponta de flape. Entretanto, na contribuição total, o ruído de flape é menos importante quando comparado com o eslate, pois este último apresenta uma fonte estendida em linha, ao longo da envergadura. Em aeronaves de médio porte, tais como aeronaves regionais, a razão entre a envergadura da asa e as demais dimensões características dos componentes da fuselagem da aeronave é muito maior do que àquela observada em aviões de grande porte, daí então a importância do entendimento dos mecanismos de geração de ruído em eslate para aeronaves regionais.

O eslate é um dispositivo hipersustentador localizado a montante do bordo de ataque do elemento principal da asa. Seu formato geométrico possui uma cavidade (cova), devido ao espaçamento existente entre ele e o elemento principal da asa, e uma cúspide em sua superfície inferior, de forma que, quando recolhido, as características aerodinâmicas do perfil em condição de cruzeiro sejam minimamente afetadas. A Fig. (1) mostra o esquema de um eslate, incluindo um típico escoamento ao redor deste componente, e a representação das linhas de corrente baseadas na média temporal do escoamento. A camada limite no intradorso do eslate é forçada a separar na cúspide por um forte gradiente adverso de pressão. Essa separação forma uma camada de mistura que representa uma fronteira entre o escoamento acelerado, entre o eslate e o elemento principal, e o escoamento lento da bolha, dentro da cova do eslate. O perfil de velocidade da camada de mistura confere a esta uma condição de instabilidade, ou seja, ela amplifica pequenas perturbações, levando à formação de vórtices discretos que crescem e se emparelham à medida que são convectados em direção ao ponto de recolamento na parede da cova. Simulações numéricas e experimentos de túnel de vento demonstram que o tamanho da bolha de separação na cova do eslate reduz à medida que se aumenta o ângulo de ataque do aerofólio e que o há uma oscilação do ponto de recolamento, (Dobrzynski e Pott-Pollenske, 2001). Após o recolamento, parte dos vórtices da camada de mistura são ejetados através da folga entre o eslate e o elemento principal e a outra parte adentra a bolha de separação, e fica presa dentro dela, recirculando, o que acaba por introduzir perturbações no estágio inicial da camada de mistura, próximo à cúspide.

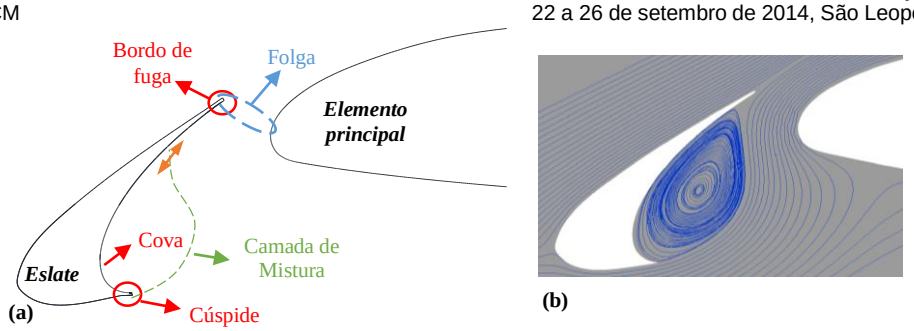

Figura 1 – Desenho esquemático de um eslate. (a) Principais pontos de referência e (b) campo de escoamento típico ao redor de um eslate, apresentando as linhas de corrente para um ângulo de ataque de *4* [°], retirado de Souza (2012).

Medições aeroacústicas em perfis hipersustentadores são de difícil realização com modelos de testes em escala real, devido à indisponibilidade de túneis de vento acústicos com tamanho apropriado. Por outro lado, modelos de testes em escala reduzida raramente reproduzem o regime observado em condições operacionais, o que pode induzir o surgimento de mecanismos de geração de ruído atípicos, de acordo com Dobrzynski et al. (2008). Ensaios com modelos completos, em túneis de vento de larga escala, são muito caros para serem utilizados com o intuito de pesquisar os complexos mecanismos de geração de ruído. Dobrzynski (2010) afirma que geralmente este tipo de pesquisa é conduzido em modelos de asas bidimensionais em escala, empregando túneis de vento menores. Com o túnel de vento devidamente adaptado para medições aeroacústicas e utilizando-se de uma matriz (antena ou *array*) de microfones, torna-se possível quantificar os níveis de som propagado, bem como a identificar as regiões das fontes de ruído.

Uma representação esquemática do espectro de ruído gerado pelo eslate é apresentada na Fig. (2). Conforme Imamura et al. (2009) descreve em seus trabalhos, o ruído de eslate pode ser dividido em três componentes. A primeira componente é de banda larga (BB – *broadband*), sendo esta a fonte principal de ruído de eslate, entretanto seu mecanismo de geração ainda não é completamente entendido. A segunda componente é a de múltiplos picos tonais (*multiple tonal peaks* – MTP). Muitos estudos têm sido feitos à respeito desta componente, tal como pode ser observado em Kolb et al. (2007), Dobrzynski et al. (1998), Dobrzynski e Pott-Pollenske (2001) e Kaepernick, Koop e Ehrenfried (2005). Estes picos não são harmônicos de um modo fundamental, a provável causa do aparecimento desta componente é um mecanismo de retroalimentação, conforme Kolb et al. (2007) explora em seu trabalho, porém seu mecanismo de geração de ruído também não é completamente entendido. A terceira componente, o pico tonal de alta frequência (*high frequency tone* – HT), é emitida pelo bordo de fuga do eslate. Sua frequência dominante é consistente com o fenômeno de desprendimento de vórtices em bordos de fuga, (Khorrami, Berkman e Choudhari, 2000) e (Choudhari et al., 2002).

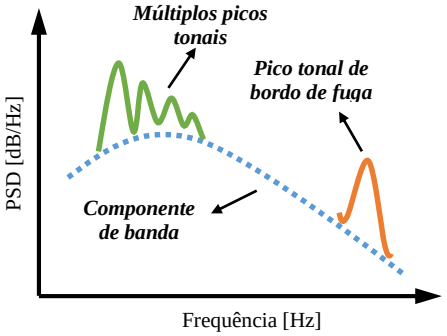

Figura 2 – Espectro típico de ruído de eslate.

O processamento de sinais, *beamforming* convencional e *DAMAS*, faz parte da etapa de pós-processamento dos dados. A técnica de *beamforming* aplicada à acústica é bastante utilizada para o mapeamento de fontes de ruído. Para este trabalho foi utilizado um código *in-house* de *beamforming*, contendo o método de deconvolução *DAMAS*.

Aeronaves reais apresentam diversos elementos na cova do eslate, tal como mecanismos de deflexão, tubos do sistema anti-gelo e selos que isolam a cova e evitam o contato direto do eslate com o elemento principal em condição de cruzeiro. A maioria dos estudos dedicados ao ruído gerado pelo eslate consideram geometrias idealizadas, sem a presença destes detalhes geométricos na cova do eslate, por exemplo. O objetivo deste trabalho refere-se à caracterização de ruído de eslate sob a presença de excrescências no formato de selos em sua cova, conforme a Fig. (3). Nesta figura é mostrado um selo na cova do eslate bem como uma representação do gabarito utilizado para posicionar os selos. Os resultados experimentais são fundamentados na base de dados obtida com a campanha *2014-1* de ensaios aeroacústicos do projeto Aeronave Silenciosa, uma cooperação entre EMBRAER e universidades. Foram feitas medições aeroacústicas e aerodinâmicas para diversas de velocidades de escoamento livre, ângulos de ataque, geometrias e posições de selos na cova do eslate. Os resultados apresentados consistem em espectros de ruído e mapas de *beamforming* gerados a partir de um algoritmo de deconvolução *DAMAS in-house*.

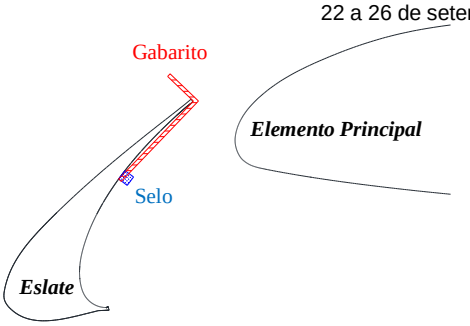

Figura 3 – Detalhe do perfil hipersustentador *MDA 30P30N* bidimensional contendo um selo quadrado posicionado na cova do eslate.

A estrutura deste artigo está organizada como descrito a seguir. A seção 2 traz a metodologia utilizada, relatando a estrutura (modelo, equipamentos, sistemas, etc.) empregada nos ensaios, os procedimentos experimentais adotados e uma breve descrição sobre as técnicas de *beamforming* e *DAMAS*. Já a terceira seção apresenta os resultados e discussões para a configuração padrão (sem a presença dos selos) e para os selos de seção transversal quadrada em determinadas posições da cova. Por fim, a quarta seção mostra as conclusões obtidas a partir do estudo realizado.

2. METODOLOGIA

O modelo utilizado nos ensaios foi confeccionado basicamente em alumínio, a partir de uma geometria de aerofólio nomeada *MDA 30P30N*, sendo este um perfil hipersustentador para o qual as cordas do eslate e do flape correspondem, respectivamente, a *15* [%] e *30* [%] da corda do aerofólio em condição de cruzeiro (com os elementos de hipersustentação, flape e eslate, recolhidos). No modelo ensaiado, a corda em condição de cruzeiro é de *0,5* [m]. Na configuração padrão, as deflexões do flape e do eslate são de *30* [°], o *gap* e *overlap* do flape são, respectivamente, *1,27* [%] e *0,25* [%] (valores relativos à corda em condição de cruzeiro), e o *gap* e *overlap* do eslate são, respectivamente, *2,95* [%] e *-2,50* [%] (valores relativos à corda do perfil em condição de cruzeiro). O comprimento ao longo do *span* (envergadura) para o eslate, elemento principal e flape é de *1,3* [m]. A Fig. (4) apresenta o perfil do aerofólio estendido e recolhido, bem como o modelo instalado na câmara de ensaios do túnel de vento *LAE-1*.

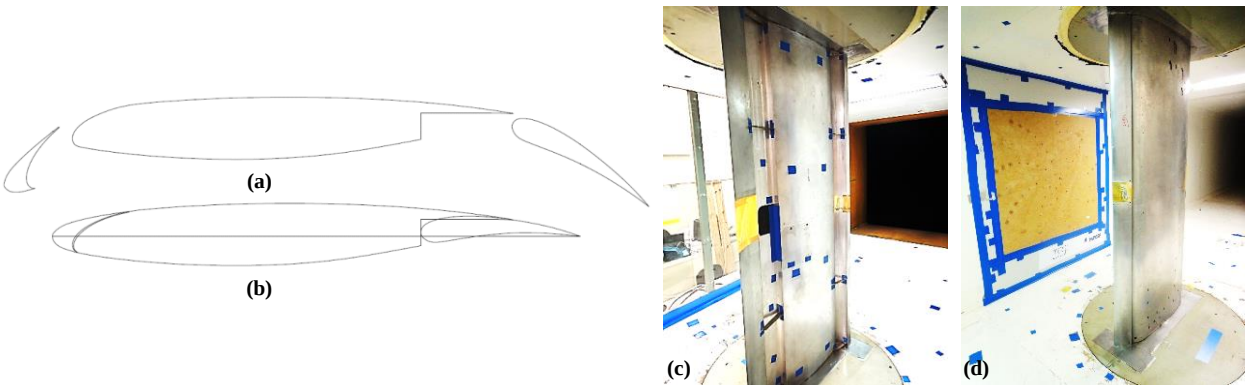

Figura 4 – *MDA 30P30N*. (a) perfil com flape e eslate estendidos, (b) perfil em condição de cruzeiro, com flape e eslate recolhidos (detalhe para a linha de corda), (c) e (d) modelo na câmara de ensaios.

Os selos possuem seção transversal quadrada, de aresta *3* [mm], e estão presentes ao longo de toda a envergadura do eslate, localizados em sua cova e com posição medida a partir do bordo de fuga do eslate. A Fig. (5) mostra a vista do intradorso do modelo, com detalhe para o eslate, na qual é possível visualizar os selos posicionados na cova do eslate. Ao todo são quatro posições medidas a partir do bordo de fuga do eslate: *8* [mm], *17,5* [mm], *30,5* [mm] e *45* [mm].

O túnel de vento utilizado nos ensaios é subsônico, de seção e circuito fechados e está localizado no Laboratório de Aerodinâmica (LAE) da Escola de Engenharia de São Carlos (USP-EESC) e é denominado *LAE-1*. A seção de testes é retangular, possuindo *1,30* [m] de altura, *1,67* [m] de largura e *3* [m] de comprimento útil e está envolta em uma câmara plena, que isola a área de medições do ambiente externo. O ventilador axial de *8* pás é propelido por um motor de *115* [HP], de corrente alternada, é controlado por um inversor de frequência. A razão de contração é de *1:8*, a faixa de velocidades está entre *10* [m/s] e *45* [m/s] e o nível de turbulência é cerca de *0,25* [%]. Este túnel de vento foi originalmente projetado para ensaios aerodinâmicos, sendo posteriormente adaptado para experimentos aeroacústicos, sendo que a metodologia adotada reduziu marginalmente o ruído de fundo do túnel sem alteração significativa em suas características aerodinâmicas, conforme pode ser observado em Santana et al. (2010).

Figura 5 – Vista do intradorso do modelo contendo os selos na cova do eslate. Posições: (a) *8* [mm], (b) *17,5* [mm], (c) *30,5* [mm] e (d) *45* [mm].

O sistema de aquisição de dados inclui uma antena com *62* microfones, montada em um painel na parede do túnel voltada para o intradorso do aerofólio. Esta antena foi projetada na forma de uma espiral logarítmica de múltiplos braços e de maneira a permitir variadas configurações, tais como maior ou menor número de microfones. Os microfones da antena são do tipo *GRAS 40BD ¼* [pol]. Eles possuem uma faixa de frequência útil maior que *20* [kHz] e faixa dinâmica de *135* [dB]. O restante do sistema de aquisição de dados é baseado no *hardware* da *National Instruments*. Maiores detalhes sobre o sistema de aquisição de dados utilizado podem ser encontrados em Pagani Jr, Costa e Medeiros (2011).

Os ensaios foram realizados com o aerofólio em ângulos de ataque de *2* [°], *4* [°], *6* [°], *8* [°] e *10* [°] e velocidade de escoamento de *24* [m/s], *27* [m/s], *31* [m/s] e *34* [m/s], para o caso de referência, e *31* [m/s] e *34* [m/s] para os casos com selos na cova do eslate. Foi utilizado um sistema de sucção da camada limite na *turntable* da seção de testes do túnel de vento, de forma a atenuar efeitos de tridimensionalidade que ocorrem no escoamento ao redor do modelo.

A técnica de *beamforming* é comumente utilizada para mapear fontes acústicas a partir do processamento das medições realizadas com uma antena de microfones. Esta técnica permite a separação de fontes concorrentes sobre um modelo de testes e a estimativa do nível de ruído emitido por cada distribuição de fontes pela simples integração de níveis discretos de pressão sonora, conforme Sarradj (2012). A resolução de um algoritmo de *beamforming* define a sua capacidade em distinguir ondas incidentes de direções próximas umas das outras. Para uma distância focal finita, a resolução é a mínima distância entre duas fontes que permite separá-las. A presença de lóbulos laterais (*side lobes*) causa a interferência de ondas incidentes de outras direções que não a de foco na avaliação da direção principal e isso resultará em picos ou fontes falsas no mapa direcional. Um sistema de *beamforming* eficiente pode ser caracterizado por um reduzido nível máximo de lóbulos laterais, medido em relação ao lóbulo principal (*main lobe*). O desempenho de um sistema de *beamforming* é largamente dependente da geometria da antena, uma vez que ela define a sua função de forma, conforme constatam Brooks e Humphreys (2006).

O algoritmo de *beamforming* utilizado neste trabalho assume a propagação de ondas esféricas em condição de campo livre, com origem em uma distribuição de fontes pontuais descorrelacionadas, do tipo monopolo. O princípio do *beamforming* envolve o algoritmo básico de atraso e soma (*delay-and-sum*), estando este descrito em Christensen e Hald (2004). Um plano de varredura, encerrando uma malha discreta contendo N pontos, é definido ao redor da região da fonte de ruído. Um código de *beamforming* combina as matrizes de correlação espectral dos sinais medidos pelos microfones, *Cross-Spectral Matrix* (*CSM*) e os vetores direção, *steering vector*s (estando estes associados com o ponto n da malha), focando sucessivamente a antena de microfones em cada ponto da malha, de forma a obter uma estimativa da amplitude das fontes e sua distribuição aparente, (Mueller et al., 2002).

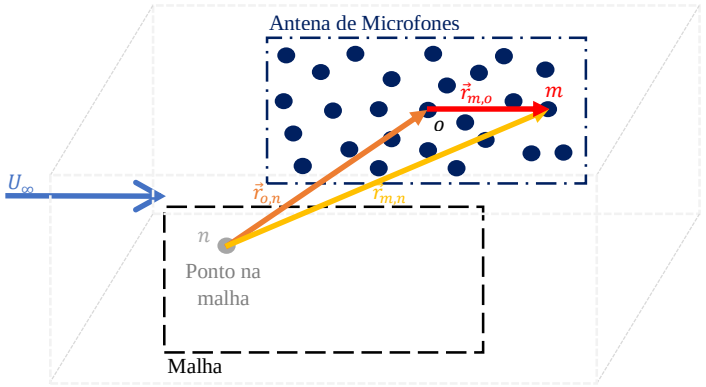

Figura 6 – Desenho esquemático dos referenciais utilizados para formulação de *beamforming* convencional.

A Fig. (6) exibe, esquematicamente, os referenciais utilizados para a formulação de *beamforming* deste trabalho, bem como a malha de escaneamento, encerrando a região de interesse em que supostamente se encontram as fontes, e a antena de microfones. A posição n é um ponto na malha a ser varrida à procura da fonte sonora, onde $1 \leq n \leq N$; o é a posição de referência ou de origem (para este trabalho, o centro da antena) e m é a posição do m-ésimo microfone, onde $1 \leq m \leq M$, sendo M o número total de microfones ativos da antena.

A expressão da Eq. (1) mostra uma formulação geral para *beamforming* convencional no domínio da frequência bastante encontrada na literatura, tal como em Sarradj (2012). Espera-se de um algoritmo de *beamforming* que a resposta máxima (pico), ocorra quando o ponto focal na malha (n) coincida com a posição real da fonte.

$$b(\vec{r}_{o,n}, \omega) = \boldsymbol{h}^{\dagger}(\vec{r}_{m,n}, \omega)\, \langle \boldsymbol{p}(\vec{r}_{m,o}, \omega)\, \boldsymbol{p}^{\dagger}(\vec{r}_{m,o}, \omega) \rangle\, \boldsymbol{h}(\vec{r}_{m,n}, \omega) \qquad 1$$

Nesta formulação, b é um escalar e denota a estimativa espectral do nível de pressão sonora à frequência angular ω (onde $\omega = 2.\pi.f$), no ponto focal n (sendo o vetor posição dado por $\vec{r}_{o,n}$) em relação à uma referência, ou origem, dada por o. O vetor $\boldsymbol{p}$ contém as estimativas espectrais dos níveis de pressão sonora, sendo escrito como a transformadas de *Fourier* dos sinais adquiridos pelos microfones de vetor posição $\vec{r}_{m,o}$. Já o vetor $\boldsymbol{h}$ contém os *steering vectors*, ou vetores direção, sendo estes funções de transferência normalizadas utilizadas para modelar a propagação de uma onda acústica entre o ponto na malha em relação à referência, $\vec{r}_{o,n}$, e os microfones da antena, $\vec{r}_{m,n}$. O operador hermitiano é dado pelo símbolo †, e o símbolo $\langle ... \rangle$ denota o valor esperado de uma medida.

Os resultados de *beamforming* apresentados de maneira tradicional, geram mapas acústicos a partir dos resultados obtidos com as medições da antena. Estes não necessariamente representam a distribuição de fontes, devido ao resultado desta operação estar convolvida com o padrão de resposta da própria antena (*point spread function - psf*), entre outros parâmetros. No método *DAMAS*, apresentado por Brooks e Humphreys (2006), o objetivo é que as quantidades desejadas, tais como os níveis de pressão sonora e distribuição das fontes, sejam extraídas de forma independente das características de forma da antena de microfones. Assume-se a existência de um número *N* de fontes estatisticamente independentes, cada uma em posição diferente. Assim, é construído um sistema linear determinado por *N* incógnitas, de forma a relacionar o campo espacial de pontos do *beamforming* convencional com a equivalente distribuição de fontes na mesma localização de pontos, sendo que a distribuição de fontes é resolvida de forma iterativa. Desta maneira, o problema é escrito como:

$$\boldsymbol{b} = A.\boldsymbol{X} \qquad 2$$

A Eq. (2) representa um sistema linear de equações, relacionando o campo espacial de pontos com o *beamforming* proveniente da resposta da antena, $\boldsymbol{b}$, e sua equivalente distribuição de fontes, $\boldsymbol{X}$, na mesma localização dos pontos do *beamforming*. Neste sistema linear de equações da Eq. (2), a matriz A é quadrada, de ordem N, e não-singular. Justamente por ser mal condicionada, sua solução de maneira $\boldsymbol{X} = A^{-1}.\boldsymbol{b}$ é imprecisa. Bons resultados são obtidos utilizando um método iterativo de *Gauss-Seidel* adaptado, no qual é aplicada a restrição de que os valores X_n (componentes do vetor $\boldsymbol{X}$) devem ser positivos para cada iteração.

Alguns parâmetros a serem adotados são muito importantes para o bom funcionamento e convergência do algoritmo *DAMAS*, tais como o espaçamento entre os pontos na malha que encerra a região de interesse, as dimensões da malha, e etc. Estes parâmetros podem ser verificados em Brooks e Humphreys (2006). Maiores detalhes sobre o método numérico utilizado, bem como o completo desenvolvimento das equações, análises de desempenho e validação dos códigos de *beamforming* convencional e *DAMAS*, podem ser encontrados em Pagani Jr (2014), Sarradj (2012) e Mueller et al. (2002).

3. RESULTADOS E DISCUSSÕES

O eslate apresenta, de maneira ideal, uma fonte de ruído distribuída linearmente ao longo de sua envergadura, sendo que o nível de pressão sonora medido pela antena é estimado através da soma dos níveis discretos (integração) em um subdomínio da malha no qual encontram-se as fontes de interesse. A região de integração (região de interesse ou *region of interest – ROI*) pode ser escolhida com base na localização espacial das fontes presentes nos mapas de *beamforming* para as frequências analisadas. No caso do eslate, as fontes de baixa frequência se mostram irregularmente distribuídas nos mapas de *beamforming*, sendo difícil a determinação de uma região de interesse adequada. Já para médias e altas frequências, as fontes se mostram bem distribuídas ao longo da envergadura do eslate. A região de integração deve ser definida de maneira a representar uma boa amostragem da distribuição de fontes ao longo da envergadura do eslate e excluir fontes espúrias. Esta região deveria representar, idealmente, uma distribuição bidimensional de fontes, excluindo eventuais fontes tridimensionais, tais como aquelas geradas na junção entre o modelo e a mesa giratória (*turntable*).

Para este trabalho, adotaram-se os parâmetros referentes à malha estudados por Pagani Jr (2014), onde se verificou a independência dos resultados para diferentes condições operacionais do aerofólio, tais como ângulos de ataque, velocidades de escoamento e entre outros. Também são apresentados estudos de independência em relação à resolução em frequência, ao número de pontos da malha, ao tamanho e à posição espacial da malha, ao tempo de aquisição e à região de interesse a ser aplicada. Em um breve resumo, a malha utilizada neste trabalho possui dimensões mínimas de *1,4* [m] de altura (na direção do eixo *y*) por *0,3* [m] de largura (na direção do eixo *x*), estando centrada em um ponto localizado à *0,34* [m] de distância horizontal (em relação ao eixo x) do ponto de referência (sendo este o centro da antena de microfones). Para a faixa de ângulos de ataque e ângulo de deflexão do eslate abordados neste trabalho, a posição central do eslate em relação ao eixo *x* varia muito pouco, de forma que um ponto distante de *0,34* [m] em relação à origem (centro da antena, no eixo *x*), representa bem a posição central do eslate para os casos analisados. A região de interesse possui *0,8* [m] na direção da envergadura do modelo por *0,18* [m] na direção da corda do modelo, estando centrada na malha. Estes valores foram definidos após análise conjunta dos espectros de ruído, dos mapas de *beamforming* e da posição do modelo no túnel de vento, conforme Pagani Jr (2014). A Fig. (7) expõe esquematicamente as posições e tamanhos da malha (retângulo azul) e da região de interesse (retângulo cinza) em relação ao modelo e à antena de microfones e o esquema da região de interesse no intradorso do modelo.

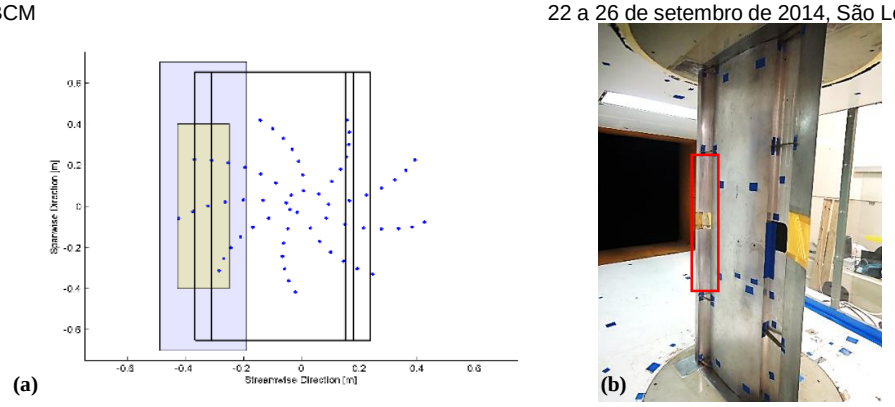

Figura 7 – (a) Malha (dimensões mínimas) e região de interesse (ou de integração) utilizadas para este trabalho e (b) esquema da região de interesse no intradorso do modelo.

As duas figuras seguintes apresentam o espectro de frequências para o caso padrão, sem a presença dos selos na cova do eslate. É possível observar claramente as três componentes de ruído: múltiplos picos tonais de baixa frequência, banda larga e pico de alta frequência, vindo de encontro com os trabalhos encontrados na literatura, tais como os de Imamura et al. (2009), Ura et al. (2010) e Dobrzynski e Pott-Pollenske (2001).

Na Fig. (8) são exibidos os espectros para as velocidades (U) de *27* e *34* [m/s] e ângulos de ataque (AoA) de *2* à *10* [°]. Nota-se que quanto menor o ângulo de ataque, maior a intensidade do ruído e mais salientes os picos tonais de baixa frequência, sendo que a frequência de ocorrência dos picos varia ligeiramente conforme o ângulo de ataque analisado. O pico tonal de alta frequência acontece em frequências tão maiores quanto maior o ângulo de ataque.

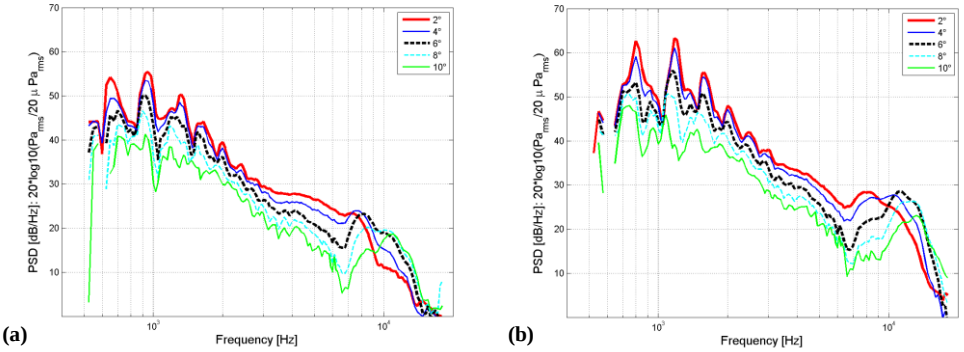

Figura 8 - Espectro e frequências para o caso padrão, AoA de *2* [°] a *10* [°]. (a) U *27* [m/s] e (b) U *34* [m/s].

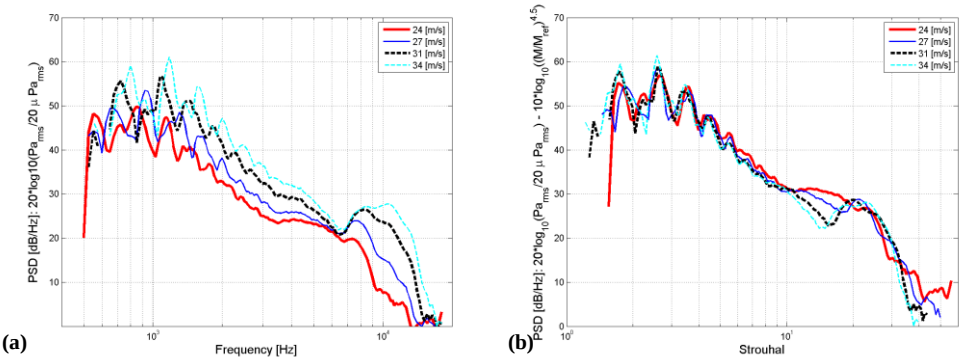

Figura 9 – Espectro de frequências para o caso padrão. U de *24* à *34* [m/s]. (a) AoA *4* [°] e (b) AoA *4* [°] e colapsos em *Mach* e *Strouhal*.

A Fig. (9) mostra os espectros de ruído de eslate para ângulo de ataque de *4* [°] e velocidades entre *24* e *34* [m/s]. Nesta figura observa-se a dependência da intensidade do ruído com a velocidade do escoamento (quanto maior a velocidade, maior a intensidade). Também é apresentado o escalonamento das curvas com o número de *Mach* para potência de *4,5*, conforme Dobrzynski e Pott-Pollenske (2001), e com o número de *Strouhal*, baseado na corda do eslate e na velocidade do escoamento livre. Os picos tonais, tanto de baixa quanto de alta frequência, são deslocados para frequências maiores conforme a velocidade do escoamento aumenta. Existe um bom colapso no escalonamento com o número de *Mach* elevado à potência de *4,5* e normalizado por um *Mach* de referência, tal que $M_{ref} = 0{,}1$, e para *Strouhal* compreendido entre *2* e *10*. Observa-se ainda que o pico de amplitude do espectro gira em torno de $St = 2$ (quando baseado na corda do eslate e na velocidade do escoamento livre), estando em acordo com os resultados apontados por (Imamura et al., 2009).

Os próximos dados são referentes aos selos instalados na cova do eslate, ao longo de sua envergadura, possuindo seção transversal quadrada com *3* [mm] de aresta cada.

Na Fig. (10) são exibidos os espectros de frequência para a velocidade de escoamento de *34* [m/s] e ângulos de ataque

de *2*, *4*, *8* e *10* [°], comparando o caso padrão, sem a presença de selos, com os casos em que há a presença dos selos.

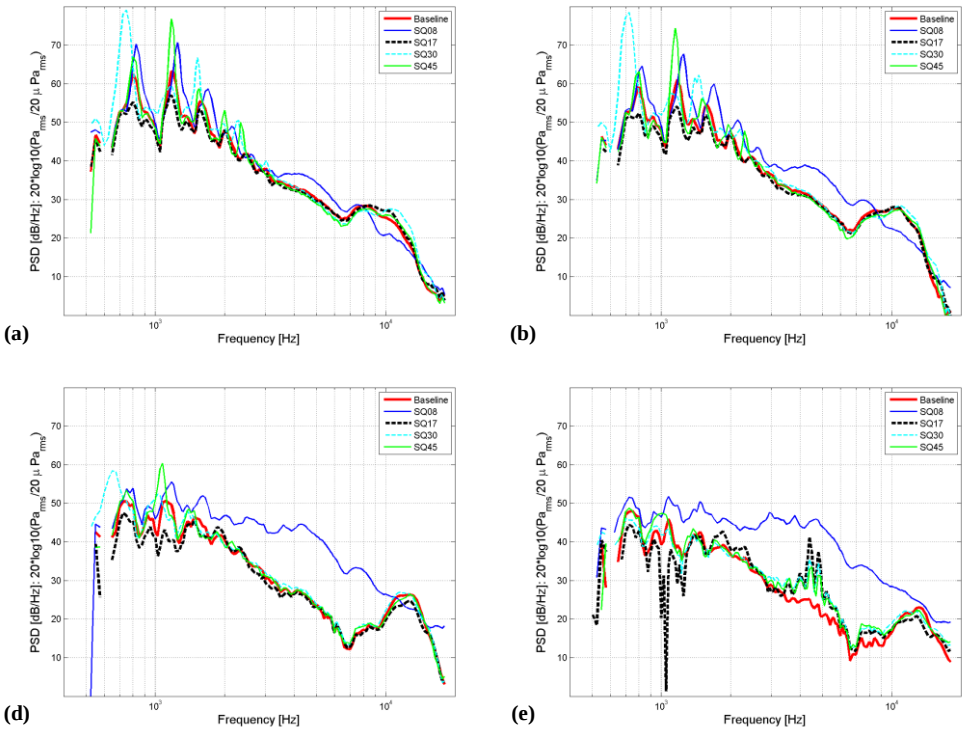

Figura 10 – Comparação entre os casos padrão e com a presença de selos para U *34* [m/s]. (a) AoA *2* [°], (b) AoA *4* [°], (c) AoA *8* [°] e (d) AoA *10* [°].

Quanto ao primeiro pico tonal de baixa frequência, atenta-se que este é mais pronunciado para o caso com o selo posicionado à 30 [mm] do bordo de fuga do eslate para ângulos de ataque entre *2* e *8* [°], chegando a ser *20* [dB] mais intenso em relação ao caso padrão (quando o ângulo de ataque é de *4* [°]). Nota-se também que a frequência de ocorrência deste pico é menor para o caso de *30* [mm], e nos demais casos a ocorrência deste pico é apenas ligeiramente diferente, girando em torno dos *800* [Hz] para ângulo de ataque de *2* [°], por exemplo. O segundo pico tonal é melhor pronunciado quando o selo está à *45* [mm] do bordo de fuga do eslate, sendo a exceção feita quando o ângulo de ataque é de *10* [°]. Para este pico, a frequência de ocorrência é menos similar para os diferentes casos analisados. Quanto maior o ângulo de ataque, mais distantes em frequência estes picos se encontram, porém oscilam em torno de *1200* [Hz]. Quando o ângulo de ataque é de *4* [°], o segundo pico tonal do caso *45* [mm] é cerca de *15* [dB] mais intenso em relação ao caso padrão. Por fim, o terceiro pico tonal é mais ruidoso no caso com o selo em *30* [mm], para ângulos de ataque de *2* à *6* [°], sendo que para *8* e *10* [°] o caso de *8* [mm] se sobressai. Sua frequência de aparição difere significativamente com a posição dos selos e o ângulo de ataque, sendo os mais próximos os casos padrão, *17,5* e *45* [mm], nas proximidades de *1500* [Hz]. Para ângulo de ataque de *4* [°], o selo na posição de *30* [mm] é cerca de *8* [dB] mais intenso do que o caso padrão.

A componente de banda larga se apresenta bem comportada, com as curvas colapsando bem para os casos padrão, *17,5*, *30* e *45* [mm] entre os ângulos de ataque de *2* [°] e *8* [°]. Quando o ângulo de ataque é de *10* [°] ocorre a presença de dois picos tonais na faixa de frequência compreendida entre *3,5* e *6* [kHz]. Os selos mais distantes do bordo de fuga do eslate apresentam menor intensidade nestes picos (estes fenômenos ainda precisam ser melhor compreendidos). O caso com o selo posicionado à *8* [mm] mostra um comportamento peculiar, com a componente de banda larga se sobressaindo em intensidade em relação aos demais casos para todos os ângulos de ataque. Para ângulos de *8* e *10* [°], o espectro é quase que inteiramente de banda larga, porém apresentando alguns tonais ao longo do espectro. Quando *10* [°] de ângulo de ataque, todo o espectro de frequências é dominado pelo caso de *8* [mm], sendo que para *8* [kHz] a diferença de intensidade do ruído em relação ao caso padrão chega à *25* [dB].

No que diz respeito ao pico tonal de alta frequência, este decresce ligeiramente, em intensidade, conforme o ângulo de ataque avança. Com exceção do caso com o selo posicionado à *8* [mm] do bordo de fuga, os demais praticamente colapsam em intensidade e frequência para todos os casos em cada ângulo de ataque, apresentando apenas uma ligeira diferença. Quanto maior o ângulo de ataque, maior a frequência de ocorrência desta componente. Já para o caso de selo em *8* [mm], o pico tonal de alta frequência também existe, porém ocorrem em frequências menores que as dos demais casos, com exceção para ângulo de ataque de *2* [°] (quando em todos os casos praticamente existe um colapso). Outro fato curioso é que neste caso a frequência de ocorrência do pico tonal de alta frequência praticamente não se altera com o aumento do ângulo de ataque, mantendo-se em torno de *7,5* [kHz]. Importante destacar que o pico mais ruidoso é sempre o do caso *8* [mm], chegando a diferença em intensidade, chegando à cerca de *10* [dB], em relação ao caso padrão, quando o ângulo de ataque é de *10* [°].

A Fig. (11) exibe os espectros de frequência para os selos acima citados, para velocidade do escoamento livre em *34* [m/s] e ângulos de ataque entre *2* e *10* [°].

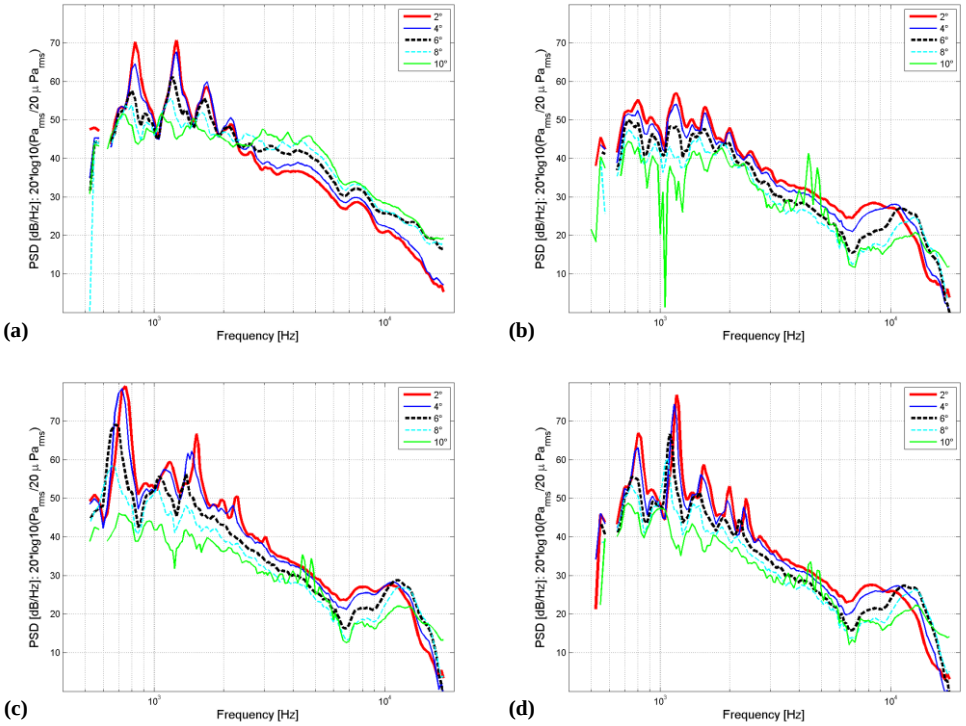

Figura 10 – Espectros de frequência para U *34* [m/s]. Posições relativas ao bordo de fuga do eslate: (a) *8* [mm], (b) *17,5* [mm], (c) *30* [mm] e (d) *45* [mm].

No selo posicionado a *8* [mm] do bordo de fuga do eslate, nota-se que a intensidade do segundo pico tonal é ligeiramente maior do que a do primeiro e do terceiro picos, porém, para o ângulo de ataque de *2* [°], o primeiro e o segundo pico tonais praticamente se equivalem em intensidade. Para efeitos de comparação com o caso de referência, utilizando o ângulo de ataque de *2* [°] e o primeiro pico tonal, este é cerca de *8* [dB] mais ruidoso para selo à *8* [mm]. O selo posicionado a *17,5* [mm] do bordo de fuga do eslate, é o que possui as menores intensidades dos picos tonais de baixa frequência, em comparação com os demais casos. Para ângulos de ataque de *2* e *4* [°], o segundo pico tonal possui maior intensidade, porém com o primeiro e terceiro picos com intensidade comparável. Já para os ângulos de ataque de *6* e *8* [°], o primeiro pico possui a maior intensidade, entretanto o segundo e terceiro picos também possuem intensidade comparável, não havendo um grande destaque. O primeiro pico tonal, para ângulo de ataque de *2* [°], chega a ser *8* [dB] menos ruidoso em relação ao caso de referência. Com o selo posicionado à *30* [mm] do bordo de fuga do eslate, o primeiro pico tonal mostra-se pronunciado em relação aos demais (com exceção para o ângulo de ataque de *10* [°]), podendo ser cerca de *17* [dB] mais intenso do que o caso padrão, para ângulos de ataque de *2*, *4* e *6* [°]. O próximo pico tonal de maior intensidade é o terceiro. Já para o caso com o selo posicionado a *45* [mm] do bordo de fuga do eslate, o segundo pico tonal se destaca em relação aos demais (também com exceção para o ângulo de ataque de *10* [°]). Para ângulos de ataque de *2*, *4* e *6* [°], este pico pode ser *13* [dB] mais intenso em relação ao caso de referência. Em todos os casos é perceptível que a intensidade do ruído, em quase todo o espectro de frequências, diminui conforme o ângulo de ataque avança.

Quanto à componente de banda larga, para o selo posicionado à *8* [mm] do bordo de fuga, esta possui maior intensidade do que as dos demais casos, sendo que para ângulo de ataque de 10 [°] o espectro de frequências é quase que totalmente de banda larga. Para os selos posicionados a *17,5*, *30* e *45* [mm], nota-se que a componente de banda larga para ângulo de ataque de 10 [°] é caracterizada por possuir dois picos tonais entre *4* e *5* [kHz], sendo que sua intensidade diminui conforme o selo é deslocado no sentido da cúspide do eslate.

No caso de *8* [mm] praticamente não há pico tonal de alta frequência. Para os demais casos, o tonal de alta frequência já é mais evidente e o comportamento global dos espectros está mais em acordo com o caso padrão.

A Fig. (12) exibe os mapas de deconvolução *DAMAS* para algumas frequências selecionadas, tais como os três primeiros picos tonais de baixa frequência, Figs. (12a), (12b) e (12c) respectivamente, o pico tonal de alta frequência, Fig. (12d), e uma frequência que esteja na parcela de banda larga dos espectros, Fig. (12e). Nota-se nos mapas a antena de microfones (círculos azuis), o eslate (retângulo de borda preta), bem como a região de interesse (ou de integração), e os níveis de ruído. A faixa dinâmica exibida nos mapas é de *12* [dB]. Não há grande diferença na posição e no formato das fontes nos mapas *DAMAS* para os selos em diferentes posições e para o caso padrão. Verifica-se que no primeiro pico tonal há a presença de duas fontes localizadas sobre o eslate, bem definidas, nas extremidades da região de interesse. No segundo pico é possível observar três fontes, nas extremidades e no centro da região de interesse, enquanto que no terceiro pico já se observa um padrão de distribuição das fontes. Para o pico tonal de alta frequência e para a frequência de banda larga, constata-se uma fonte em linha ao longo de toda a envergadura do eslate na região analisada.

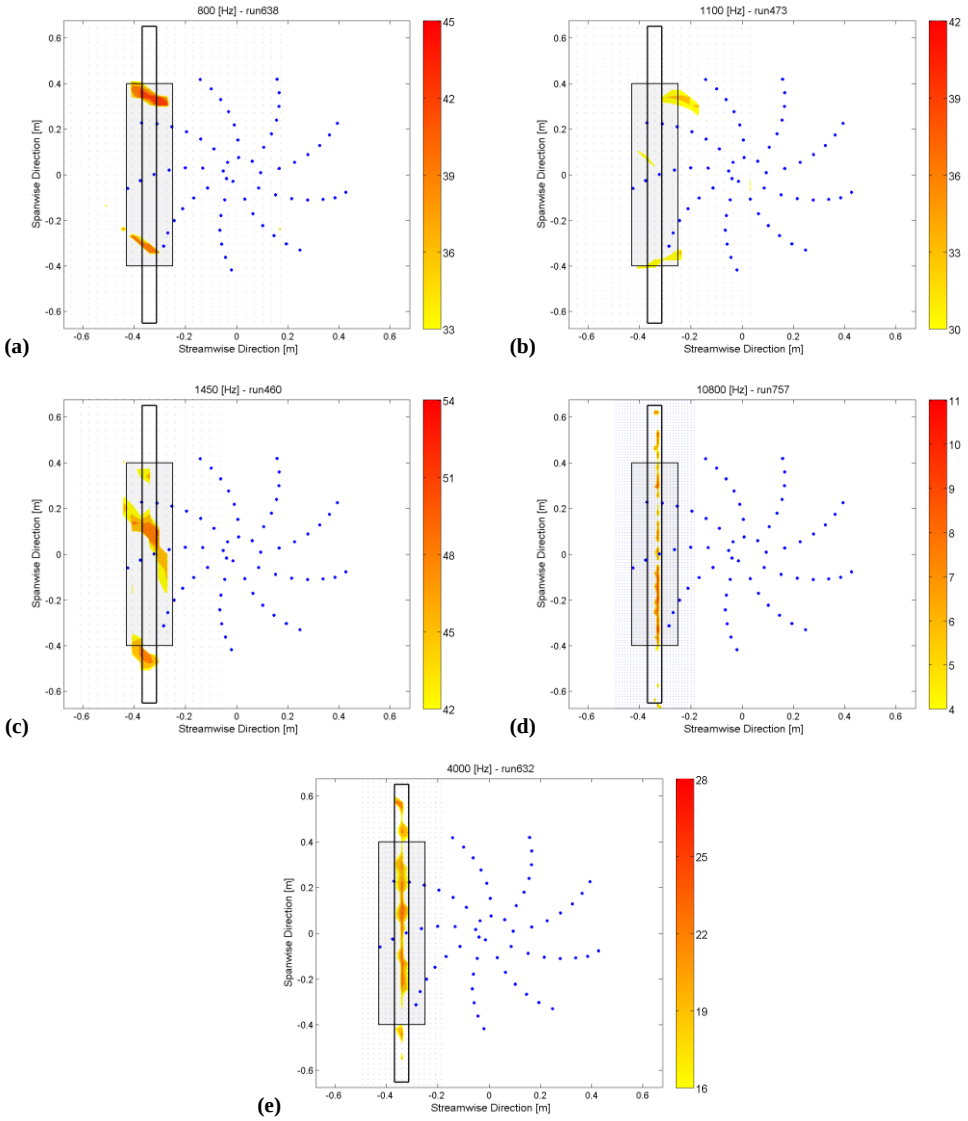

Figura 12 – Mapas *DAMAS* para os casos com selos na cova do eslate. (a) *800* [Hz], selo à *8* [mm], U *34* [m/s] e AoA *8* [°], (b) *1100* [Hz], selo à *17,5* [mm], U *34* [m/s] e AoA *8* [°], (c) *1450* [Hz], selo à *30,5* [mm], U *34* [m/s] e AoA *4* [°], (d) *10800* [Hz], selo à *45* [mm], U *34* [m/s] e AoA *4* [°] e (e) *4000* [Hz], selo à *17,5* [mm], U *31* [m/s] e AoA *6* [°].

4. CONCLUSÃO

A partir dos dados levantados no presente estudo, verifica-se que os selos têm grande influência no espectro de frequências do eslate, tornando o ruído mais ou menos intenso, conforme a posição do selo, deslocando ligeiramente a posição dos picos tonais e, na posição de *8* [mm], modificando completamente o espectro de frequências. Os mapas de *beamforming* também são alterados, porém mantém as características das fontes semelhantes ao caso padrão. Em suma, é possível afirmar que o selo de posição *17,5* [mm] reduz a intensidade de ruído para praticamente todas as frequências, velocidades de escoamento e ângulos de ataque analisados (com exceção do ângulo de *10* [°], para médias frequências em diante), enquanto que os selos nas demais posições ora intensificam o primeiro tonal de baixa frequência, ora intensificam o segundo tonal de baixa frequência, e por vezes ainda modificam a componente de banda larga do espectro.

5. REFERÊNCIAS BIBLIOGRÁFICAS

BANDLE, L. et al. **On Detrimental Effects of Excrescences on the Slat Noise**. 18th AIAA/CEAS Aeroacoustics Conference (33rd AIAA Aeroacoustics Conference): American Institute of Aeronautics and Astronautics 2012.

BROOKS, T. F.; HUMPHREYS, W. M. A deconvolution approach for the mapping of acoustic sources (DAMAS) determined from phased microphone arrays. **Journal of Sound and Vibration,** v. 294, n. 4-5, p. 856-879, Jul 2006. ISSN 0022-460X. Disponível em: < <Go to ISI>://WOS:000238359200011 >.

CHOUDHARI, M. M. et al. Aeroacoustic experiments in the Langley low-turbulence pressure tunnel. **NASA TM,** v. 211432, p. 1-46, 2002

CHRISTENSEN, J. J.; HALD, J. **Technical Review: Beamforming**. Naerum, Denmark, p.54. 2004

DOBRZYNSKI, W. Almost 40 Years of Airframe Noise Research: What Did We Achieve? **Journal of Aircraft,** v. 47, n. 2, p. 353-367, Mar-Apr 2010. ISSN 0021-8669. Disponível em: < <Go to ISI>://WOS:000276565300001 >.

DOBRZYNSKI, W. et al. Research at DLR towards airframe noise prediction and reduction. **Aerospace Science and Technology,** v. 12, n. 1, p. 80-90, Jan 2008. ISSN 1270-9638. Disponível em: < <Go to ISI>://WOS:000254099600008 >.

_____. **Airframe noise studies on wings with deployed high-lift devices**. 4th AIAA/CEAS Aeroacoustics Conference: American Institute of Aeronautics and Astronautics 1998.

DOBRZYNSKI, W.; POTT-POLLENSKE, M. **Slat noise source studies for farfield noise prediction**. 7th AIAA/CEAS Aeroacoustics Conference and Exhibit: American Institute of Aeronautics and Astronautics 2001.

IMAMURA, T. et al. **A Far-field Noise and Near-field Unsteadiness of a Simplified High-lift-configuration Model (Slat)**. 47th AIAA Aerospace Sciences Meeting including The New Horizons Forum and Aerospace Exposition: American Institute of Aeronautics and Astronautics 2009.

KAEPERNICK, K.; KOOP, L.; EHRENFRIED, K. **Investigation of the Unsteady Flow Field Inside a Leading Edge Slat Cove**. 11th AIAA/CEAS Aeroacoustics Conference: American Institute of Aeronautics and Astronautics 2005.

KHORRAMI, M. R.; BERKMAN, M. E.; CHOUDHARI, M. Unsteady Flow Computations of a Slat with a Blunt Trailing Edge. **AIAA Journal,** v. 38, n. 11, p. 2050-2058, 2000/11/01 2000. ISSN 0001-1452. Disponível em: < http://dx.doi.org/10.2514/2.892 >. Acesso em: 2014/03/27.

KOLB, A. et al. **Aeroacoustic Wind Tunnel Measurements on a 2D High-Lift Configuration**. 13th AIAA/CEAS Aeroacoustics Conference (28th AIAA Aeroacoustics Conference): American Institute of Aeronautics and Astronautics 2007.

MUELLER, T. J. et al. **Aeroacoustic Measurements**. Berlin: Springer, 2002.

PAGANI JR, C. D. C. **Mapeamento de Fontes Aeroacústicas de um Eslate em Túnel de Vento de Seção Fechada Utilizando Beamforming com Deconvolução DAMAS**. 2014. (Tese submetida (Doutorado em Aeronaves)). Engenharia Mecânica, Escola de Engenharia de São Carlos, Universidade de São Paulo, São Carlos, SP.

PAGANI JR, C. D. C.; COSTA, L.; MEDEIROS, M. A. F. **A study to investigate wind tunnel background noise for the purpose of aeroacoustic beamforming**. 21st Brazilian Congress of Mechanical Engineering (COBEM 2011). Natal, RN, Brazil: ABCM 2011.

SANTANA, L. D. et al. **The update process and characterization of the Sao Paulo University wind-tunnel for aeroacoustics testing**. 27th International Congress of the Aeronautical Sciences (ICAS 2010). Nice, France 2010.

SARRADJ, E. Three-Dimensional Acoustic Source Mapping with Different Beamforming Steering Vector Formulations. **Advances in Acoustics and Vibration,** v. 2012, p. 12, 2012. Disponível em: < http://dx.doi.org/10.1155/2012/292695 >.

SOUZA, D. S. **Simulação numérica de ruído de eslate em configurações práticas usando um código comercial**. 2012. (Dissertação (Mestrado em Aeronaves)). Escola de Engenharia de São Carlos, Universidade de São Paulo, São Carlos, SP.

URA, H. et al. **Airframe noise measurements by using a simplified high-lift model**. ICAS2010 - 27th International Congress of the Aeronautical Sciences**:** 11 p. 2010.

6. RESPONSABILIDADE AUTORAL

Os autores são os únicos responsáveis pelo conteúdo deste trabalho.

A COMPARISON OF LES MODELS AND THE EFFECT OF SUBGRID SCALE MODELS

Laís Corrêa, lacorrea@icmc.usp.br
Instituto de Ciências Matemáticas e de Computação - ICMC/USP, Av. Trabalhador São-carlense, 400 - Centro, 13566-590 - São Carlos - SP, Brazil

Gilmar Mompean, gilmar.mompean@polytech-lille.fr
Université des Sciences et Technologies de Lille - Polytech'Lille, Cité Scientifique - Av. Paul Langevin, 59650 - Villeneuve-d'Ascq, France

Fabrício Simeoni de Sousa, fsimeoni@icmc.usp.br
Instituto de Ciências Matemáticas e de Computação - ICMC/USP, Av. Trabalhador São-carlense, 400 - Centro, 13566-590 - São Carlos - SP, Brazil

Abstract. *In this work, we show that a appropriate choice of the subgrid scale model is very important in turbulent large eddy simulations (LES). For this purpose, we presents a comparison of three different LES models, namely, LES with Smagorinsky, LES with dynamic subgrid scale models, and ILES (Implicit LES) model.*

1. INTRODUCTION

When solving the Direct Numerical Simulation (or DNS) simulation of Navier-Stokes equations for high Reynolds number flows strategy calculates the entire turbulent energy spectrum by solving all turbulent motions, being a impractical strategy for high Reynolds number flows in terms of computational cost. In this sense, one of the first approach developed was RANS (Reynolds-average Navier-Stokes), in which all turbulent fluid dynamic effects are replaced by a suitable model. A more recent and reliable approach for turbulent flow is LES, which solves directly the large-scale turbulent spectrum and employ modeling only for the small structures. This strategy is based on the separation of turbulent scales by a filter function, which removes the components of the small (subgrid) scales.

To provide a closure for the Navier-Stokes equations in LES, a subgrid scale (SGS) stress model is employed. In this work, we use SGS models based on an eddy viscosity assumption, namely, Smagorinsky (1963) and dynamic models (Germano *et al.*, 1991). A another strategy applied in this work to model the subgrid stress is the ILES model (Grinstein and Drikakis, 2007), where no subgrid modeling is used, i.e., the eddy viscosity is considered null. The influence of the unresolved scales on the resolved ones is accounted for by the numerical dissipation of the convective scheme applyed in the discretization of the momentum equation.

In this sense, we present here a comparison of the three LES models mencioned previously, which are applied in turbulent simulations of the channel flow at $Re_\tau = 395$: 1) LES with Smagorinsky model; 2) LES with dynamic model; 3) ILES. The results are compared with channel flow DNS data presented by Laurent (2011).

2. MATHEMATICAL SETTING

We consider the dimensionless incompressible filtered Navier-Stokes equations given by

$$\frac{\partial \overline{u_i}}{\partial t} + \frac{\partial}{\partial x_j}\left(\overline{u_i}\,\overline{u_j}\right) = -\frac{\partial \overline{p}}{\partial x_i} + \frac{1}{\mathrm{Re}_b}\frac{\partial^2 \overline{u_i}}{\partial x_j^2} - \frac{\partial \tau_{ij}}{\partial x_j}, \tag{1}$$

$$\frac{\partial \overline{u_i}}{\partial x_i} = 0, \tag{2}$$

where $\overline{u_i}$ is the filtered instantaneous velocity field, $\overline{p}$ is the pressure, $\mathrm{Re}_b = U_b h/\nu$ is the Reynolds number, being U_b the bulk velocity and h the channel half-height.

Moreover, τ_{ij} is the SGS stress tensor (subfilter stress), given by

$$\tau_{ij} = \overline{u_i u_j} - \overline{u_i}\,\overline{u_j}. \tag{3}$$

To provide a closure for the system formed by equations (1)-(2), the SGS models are presented in the next section, which are applied to approach the SGS stress tensor based on an eddy viscosity assumption.

2.1 SGS models

These models are employed to provide a closure for the filtered Navier-Stokes equations, modeling the turbulent small scales. For this, the SGS stress was described by the Boussinesq model, as a function of the turbulent viscosity ν_t:

$$\tau_{ij} = -2\nu_t \overline{S_{ij}} + \frac{1}{3}\tau_{kk}\delta_{ij}. \tag{4}$$

According to Erlebacher *et al.* (1992), in this work, the effect of the term τ_{kk} is negligible. In the next susbsections, we describe the Smagorinsky and dynamic SGS models.

2.1.1 Smagorinsky model

According to Smagorinsky (1963), considering the local equilibrium hypothesis for the small scales, the subgrid turbulent stress production ($\wp$) may be equal to the dissipation (ε), where

$$\wp = -\overline{u_i' u_j'}\,\overline{S_{ij}} = 2\nu_t \overline{S_{ij}}\,\overline{S_{ij}}, \tag{5}$$

$$\varepsilon = -c_1(\overline{u_i' u_j'})^{\frac{3}{2}}/\Delta, \tag{6}$$

being $(\overline{u_i' u_j'})^{\frac{1}{2}}$ and Δ the velocity and subgrid length scales, respectively. Supposing that the turbulent viscosity is proportional to these two scales, it can be written as

$$\nu_t = c_1 \Delta(\overline{u_i' u_j'}). \tag{7}$$

After some manipulation of eqs. (5), (6) and (7), we obtain

$$\nu_t = (C_S \cdot \Delta)^2 \cdot |\overline{S}|, \tag{8}$$

where $|\overline{S}| = \sqrt{2\overline{S_{ij}}\,\overline{S_{ij}}}$, and C_S is the Smagorinsky constant. The value $C_S = 0.18$ was obtained analytically by Lilly (1967), however this value was further questioned. Deardorff (1970) considered $C_S = 0.1$ in channel flow simulations, because the value calculated by Lilly caused damping of the turbulence large scales. Still, tests made by Mason and Callen (1986) showed that the value $C_S = 0.2$ produced good results for a fine grid. However, Piomeli *et al.* (1988) presented $C_S \simeq 0.1$ as the optimal value using finer grids than Mason and Callen. In short, the literature considers the Smagorinsky constant between the values 0.1 and 0.22.

Considering that the model provides a constant value, several modifications in the Smagorinsky subgrid model have been developed in the literature, since it is not possible to capture a variety of phenomena with a single constant. Furthermore, the Smagorinsky model is not capable of capturing the backscatter phenomenon (energy flux from small to large scales).

To fix this problem, Van Driest (1956) proposed to compute the turbulent viscosity as

$$\nu_t = (C_S \cdot f \cdot \Delta)^2 \cdot |\overline{S}|, \tag{9}$$

where f is a damping function, given by

$$f = 1 - \exp\left(\frac{y^+}{25}\right)^2, \tag{10}$$

and y^+ is the normal wall distance. According to Krajnović (2011), if a damping function is used, wall effects are partially taken into account by "damping" length scale $l = C_S \cdot \Delta$ near the walls.

2.1.2 Dynamic model

Other subgrid models are developed, however the most popular in the literature is the Dynamic Subgrid Model (DSM) of Germano *et al.* (1991). Considering the filtering process given by

$$\overline{u}(x,t) = \int_V u(x',t)\overline{G}(x-x')dx', \tag{11}$$

where $\overline{G}$ is a filter function (grid filter), they introduce the test filter function $\widetilde{G}$, which represents a second filtering process in the form

$$\widetilde{u}(x) = \int_V u(x',t)\widetilde{G}(x-x')dx', \tag{12}$$

where the characteristic length of the test filter is larger than the grid filter. Furthermore, one can note that $\widetilde{\overline{G}} = \widetilde{G}\,\overline{G}$.

As previously seen, when the filter $\overline{G}$ is applied to the Navier-Stokes equations, one obtain

$$\frac{\partial \overline{u_i}}{\partial t} + \frac{\partial}{\partial x_j}\left(\overline{u_i}\,\overline{u_j}\right) = -\frac{1}{\rho_0}\frac{\partial \overline{p}}{\partial x_i} + \frac{1}{\mathrm{Re}_b}\frac{\partial^2 \overline{u_i}}{\partial x_j^2} - \frac{\partial \tau_{ij}}{\partial x_j}, \tag{13}$$

where τ_{ij} represents the SGS stress, that needs to be modeled, given by

$$\tau_{ij} = \overline{u_i u_j} - \overline{u_i}\,\overline{u_j}. \tag{14}$$

Applying the filter $\widetilde{G}$ to eq. (13), the filtered momentum equation becomes

$$\frac{\partial \widetilde{\overline{u_i}}}{\partial t} + \frac{\partial}{\partial x_j}\left(\widetilde{\overline{u_i}}\,\widetilde{\overline{u_j}}\right) = -\frac{1}{\rho_0}\frac{\partial \widetilde{\overline{p}}}{\partial x_i} + \frac{1}{\mathrm{Re}_b}\frac{\partial^2 \widetilde{\overline{u_i}}}{\partial x_j^2} - \frac{\partial T_{ij}}{\partial x_j}, \tag{15}$$

and now the subgrid stress of the $\widetilde{\overline{u}}$ field is given by

$$T_{ij} = \widetilde{\overline{u_i u_j}} - \widetilde{\overline{u_i}}\,\widetilde{\overline{u_j}}. \tag{16}$$

The resolved turbulent stress (also called global Leonard stress), which corresponds to the test filter applied to the field $\overline{u}$, is given by

$$\pounds_{ij} = \widetilde{\overline{u_i}\,\overline{u_j}} - \widetilde{\overline{u_i}}\,\widetilde{\overline{u_j}}. \tag{17}$$

The stress τ_{ij}, T_{ij} and $\pounds_{ij}$ defined, respectively, in the eqs. (14), (16) and (17), are algebraically related by

$$\pounds_{ij} = T_{ij} - \widetilde{\tau_{ij}}, \tag{18}$$

where $\widetilde{\tau_{ij}}$ is obtained applying the test filter to eq. (14). This relation is known by Germano identity, which gives the stress $\pounds_{ij}$ explicitly, since stresses T_{ij} and $\widetilde{\tau_{ij}}$ are modeled. Using the Boussinesq hypothesis, we can write

$$\widetilde{\tau_{ij}} - \frac{1}{3}\widetilde{\tau_{kk}}\delta_{ij} = -2C\Delta^2\widetilde{A_{ij}}, \tag{19}$$

with $A_{ij} = |\overline{S}|\,\overline{S_{ij}}$. The stress T_{ij} can also be analagously determined by:

$$T_{ij} - \frac{1}{3}T_{kk}\delta_{ij} = -2C\widetilde{\Delta}B_{ij}, \tag{20}$$

where $B_{ij} = |\widetilde{\overline{S}}|\,\widetilde{\overline{S_{ij}}}$, $C = C_S^2$ and $\widetilde{\Delta}$ the size grid of the test filter (in general, $\widetilde{\Delta} = 2\cdot\Delta$ is adopted, according to Lesieur, 1996). The variables $|\widetilde{\overline{S}}|$ and $\widetilde{\overline{S_{ij}}}$ are analogous to the quantities $|\overline{S}|$ and $\overline{S_{ij}}$ obtained from the filtered field $\widetilde{\overline{u}}$. Subtracting $\widetilde{\tau_{ij}}$ from T_{ij}, we have

$$\pounds_{ij} - \frac{1}{3}\pounds_{kk}\delta_{ij} = -2C\widetilde{\Delta}B_{ij} + 2C\Delta^2\widetilde{A_{ij}}, \tag{21}$$

or still,

$$\pounds_{ij} - \frac{1}{3}\pounds_{kk}\delta_{ij} = -2CM_{ij}, \tag{22}$$

where

$$M_{ij} = \widetilde{\Delta}B_{ij} - \Delta^2\widetilde{A_{ij}}. \tag{23}$$

In order to determine the value of C, two alternatives are presented in the literature. The first was proposed by Germano *et al.* (1991), that was obtained multiplying both members of eq. (22) by $\overline{S_{ij}}$. Since we are considering incompressible flows, we have $\overline{S_{ii}} = 0$, so that constant C can be calculate by

$$C = -\frac{1}{2}\cdot\frac{\pounds_{ij}\,\overline{S_{ij}}}{M_{ij}\,\overline{S_{ij}}}. \tag{24}$$

This allows C to be determined dynamically, and consequently, we denote it as C_S, as a function of space and time. However, when performing DNS tests for the channel flow, Germano (1991) showed that the denominator of eq. (24) can become very small, allowing numerical instabilities. To remove these instabilities, Lilly (1992) computed C using a least squares approach, by defining Q as the error, which is written as

$$Q = \left(\pounds_{ij} - \frac{1}{3}\pounds_{kk}\delta_{ij} + 2CM_{ij}\right)^2. \tag{25}$$

By taking $\partial Q/\partial C = 0$ and performing some algebraic manipulations, we finally obtain

$$C = -\frac{1}{2}\cdot\frac{\pounds_{ij}\,M_{ij}}{M_{ij}^2}. \tag{26}$$

2.2 ILES model

One of the more recents LES approaches is the implicit LES, which has recently achieved great acceptance in the research area (see Georgiadis *et al.*, 2010). In this strategy, no subgrid modeling is used, i.e., the eddy viscosity is considered zero. The influence of the unresolved scales on the resolved ones is accounted for by the numerical dissipation of the convective scheme applied in the discretization of the momentum equation. This model depends on numerical computations to obtain the turbulent energy dissipation, which is lost because the small structures are not being resolved.

The term "implicit large eddy simulation" was originally used by Visbal *et al.* (2003) to describe approaches that are based in numerical methods to provide turbulent energy dissipation instead of using an explicit SGS model. The essential characteristic of ILES is that the numerical dissipation mimics sufficiently well the physical process of turbulent vortices dissipation. To apply this model to simulate LES, it is enough to set the Smagorinsky constant $C_S = 0$ in the SGS model.

One of the problems in using this strategy is the lack of knowledge on how the numerical scheme solves turbulent structures, especially those closest to the cutoff scale. In this sense, to obtain success in the application of numerical scheme, is very important to have some information about the method. For example, Grinstein and Fureby (2002) found that a key component with dissipative nature is the upwind strategy for the construction of the numerical flows, which provides a virtually all implicit dissipation. However, applying low-order numerical schemes using coarse meshes to simulate problems at high Reynolds numbers probably will not capture many small structures.

According to Drikakis (2009), there are two categories of ILES related of the numerical resolution:

– The first one considers that mesh and numerical methods must be combined in such way that the numerical viscosity does not influence in the resolution of the large scales, which should be completely resolved. Still, the numerical dissipation of the scheme should not influence the numerical resolution of the problem. For this, one should know well the limitations and requirements of the numerical scheme.

– The second category of ILES often appear in complex industrial flows, where the application of LES is very common. In this case, both large and small scales are not well separated. For this, the numerical method should influence the dissipation of large scales, such that separation occurs.

3. NUMERICAL METHOD

The discretization is based on finite volume method for spatial discretizations and explicit projection method for pressure segregation. The equations are integrated and the Gauss theorem is used to transform the volume integral in transverse flux at the facets of the control volume. Due to the choice of a staggered grid, the velocities $\overline{u_i}$ are calculated in cells facets, while other variables are calculated at cell centers. The filtered Navier-Stokes equations in x, y and z directions are discretized at $(i+\frac{1}{2}, j, k)$, $(i, j+\frac{1}{2}, k)$ and $(i, j, k+\frac{1}{2})$, respectively. The continuity equation is discretized at position (i, j, k). The spatial derivates are approximated by second order central differences, while temporal derivates are approximated by explicit Euler scheme. The diffusive terms and pressure gradients are discretized by second order central difference. For the convective terms, the 3rd order QUICK scheme is applied.

4. RESULTS

For a comparison of the LES models studied here, we performed the rectangular channel flow, with Reynolds number $\mathrm{Re}_\tau = 395$, corresponding to a bulk Reynolds number $\mathrm{Re}_b = 6800$. A mesh of $151 \times 65 \times 65$ computational cells was used in a $25m \times 2m \times 4m$ domain. The time step used was $\delta t = 0.001h/U_b$. For the initial conditions, the DNS data (Laurent, 2011) of instantaneous velocity fields was applied. Also the no-slip boundary condition was used for the rigid surfaces. In the streamwise direction, periodic boundary condition was applied.

Figure 1 presents the streamwise velocity u^+ as a function of the normal distance to the wall y^+. The models presented in this work were simulated and compared with the DNS results, showing a good agreement. As expected, the Smagorinsky model is dissipative, while the dynamic and ILES models present a similar and best profile, as compared to DNS results.

Figures 2 and 3 show selected components of the Reynolds stress, R_{xx} and R_{yy}, compared to DNS data. The Smagorinsky model is very dissipative for this property too, while the other models show similar profiles in both figures. For the component R_{xx} of the Reynolds stress, the dynamic model show results closest of the DNS profile, however, for the component R_{yy}, the ILES model presents best profile.

To show the influence of the eddy viscosity in LES simulations, Fig. 4 displays a comparison of eddy viscosity profiles provided by SGS models. According to Temmerman *et al.* (2003), the theoretical wall-asymptotic behaviour for the eddy viscosity is cubic in y^+, represented by the straight line in Fig. 4. Also it is important to observe that the greater importance of the eddy viscosity is in the buffer region ($10 < y^+ < 20$), and not in the logarithmic region, because the SGS transport is a small portion of the resolved transport in this region. Considering this, we can concluded from this figure, as expected, that the dynamic model presents best results for eddy viscosity, considering that its profile is closest of the y^{+3} in the buffer region.

Figure 5 shows the temporal evolution of the streamwise velocity. From this profile, it is possible to clearly see the dissipation provided by the Smagorinsky model. The other models presented good velocity variation until time $t = 250s$, a time long enough that allows the fluid to travel 10 channel lengths, obtaining a stable turbulent profile.

We depicted in Fig. 6 a z-plane velocity profile, showing the turbulent behavior at the centerline of the channel.

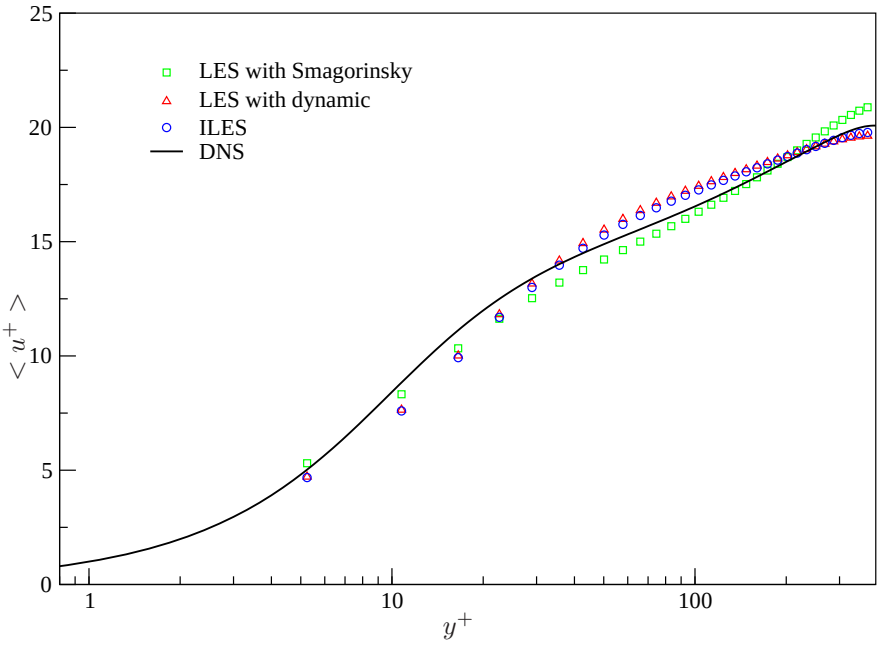

Figure 1. Streamwise velocity u^+ as a function of the normal distance to the wall y^+.

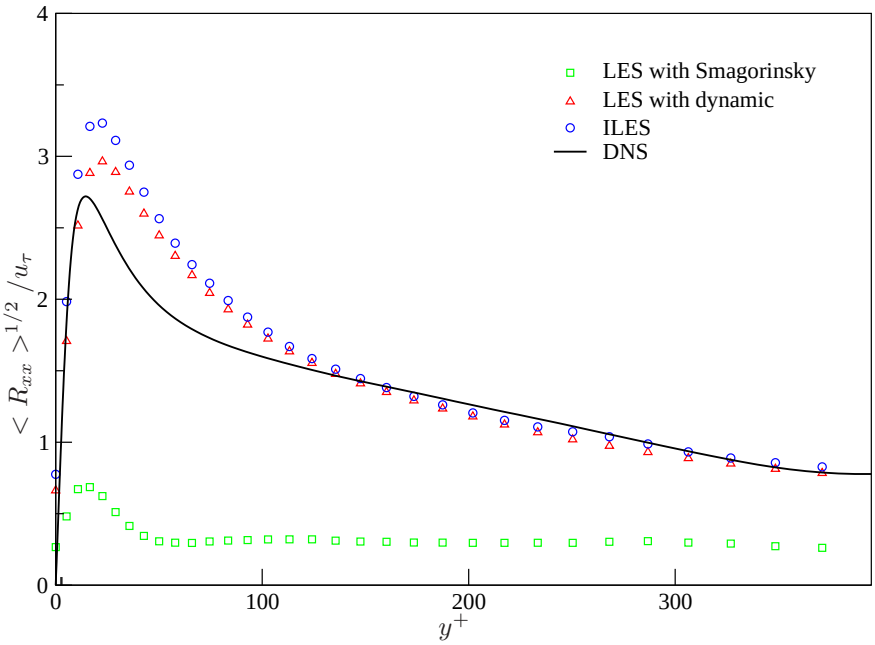

Figure 2. Reynolds stress: comparison of LES and DNS results.

5. CONCLUSIONS

We presented a comparison of three different LES models, namely, LES with Smagorinsky model, LES with dynamic subgrid scale model, and ILES model. As expected, the Smagorinsky model proved to be highly dissipative, while the other models showed a similar profile and in agreement with DNS results. However, in general, we can concluded that

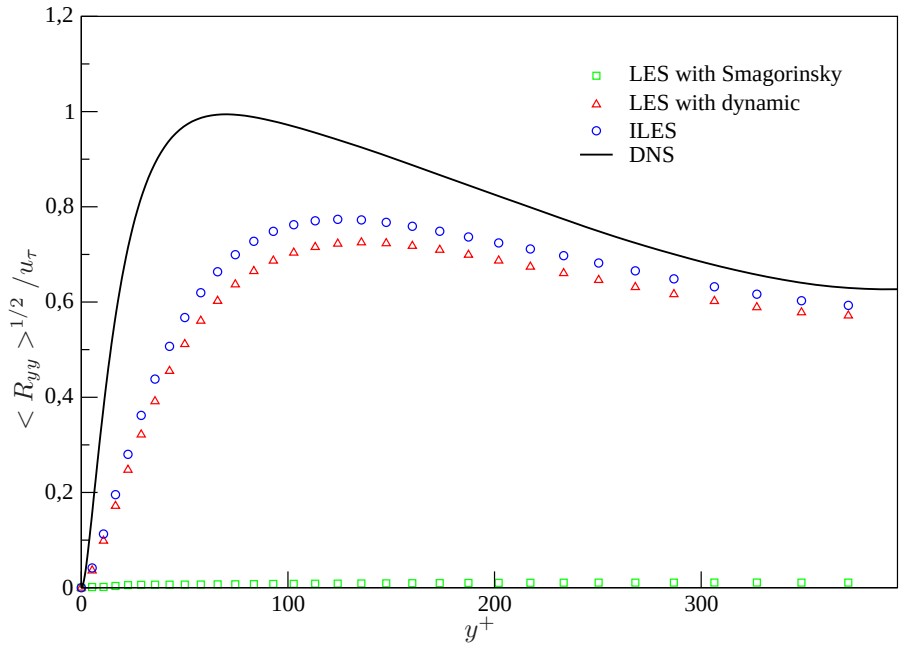

Figure 3. Reynolds stress: comparison of LES and DNS results.

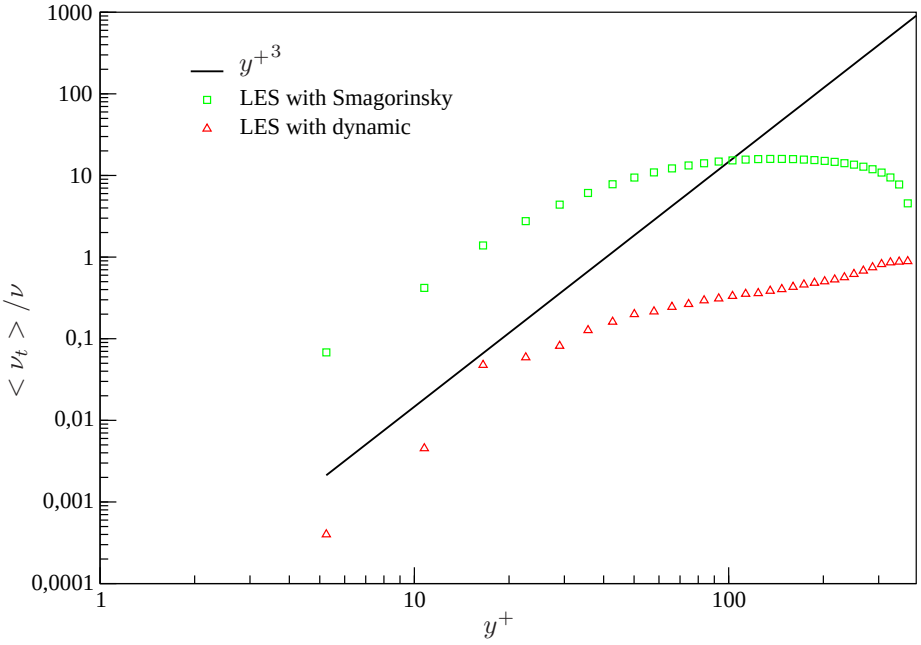

Figure 4. Eddy viscosity sensivity of SGS models.

the ILES model is a better choice for this type of simulation, considering that this model is computationally cheaper than LES with dynamic SGS model.

6. ACKNOWLEDGEMENTS

We gratefully acknowledge the support provided by FAPESP (Grants 2010/16865-2 and 2012/17827-2).

7. REFERENCES

Deardorff, J.W., 1970, “A numerical study of three-dimensional turbulent channel flow at large Reynolds numbers”, Journal of Fluid Mechanics, Vol.41, pp. 453-480.

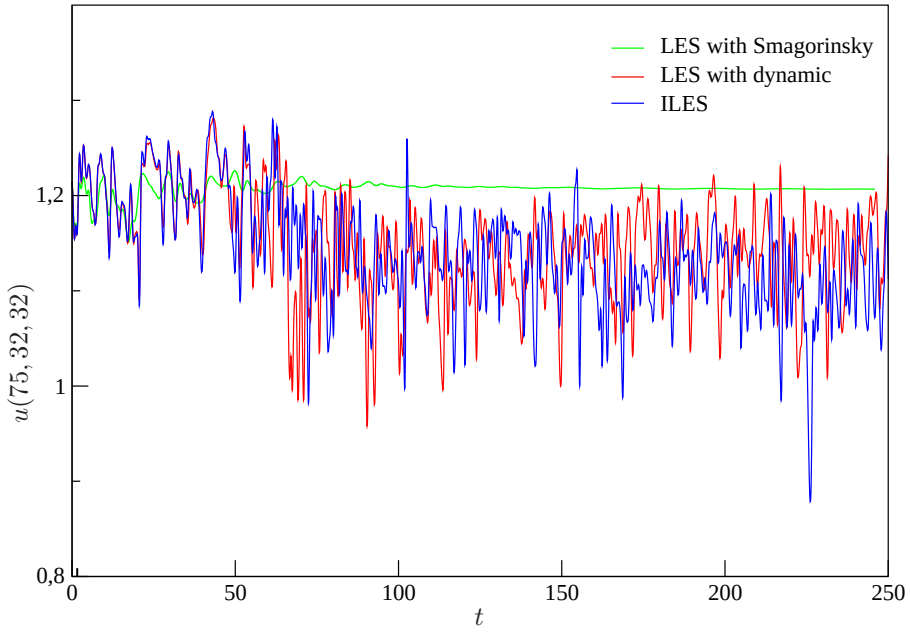

Figure 5. Temporal evolution of the longitudinal velocity at position $(75, 32, 32)$.

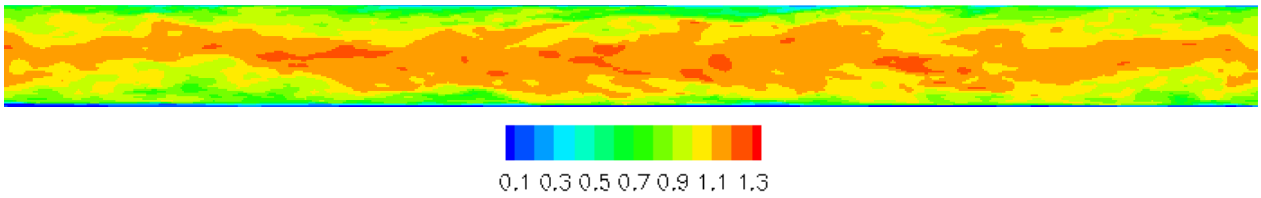

Figure 6. z-plane velocity profile in the channel middle position.

Drikakis, D., Hahn, M., Mosedale, A. and Thornber, B., 2009, “Large eddy simulation using high-resolution and high-order methods”, Phil. Trans. R. Soc., Vol.367, pp. 1985-2997.

Erlebacher, G., Hussaini, M., Speziale, C. and Zang, T., 1992, “Toward the large eddy simulation of compressible turbulent flow”, Journal of Fluid Mechanics, Vol.238, pp. 155-185.

Georgiadis, N. J., Rizzetta, D. P. and Fureby, C., 2010, “Large-Eddy Simulation: current capabilities, recommended tractices, and future research”, AIAA Journal, Vol.48, pp. 1772-1784.

Germano, M., Piomelli, U., Moin, P. and Cabot, W.H., 1991, “A dynamic subgrid-scale eddy viscosity model”, Physics of Fluids, Vol. 3, pp. 1760-1765.

Grinstein, F.F. and Drikakis, D., 2007, “Computing turbulent flow dynamics with implicit large eddy simulation”, Journal of Fluids in Engineering, Vol.129, pp. 1481-1482.

Grinstein, F.F. and Fureby, C., 2002, “Large eddy simulation of high Reynolds-number wall-bounded shear flows”, CA: Academic Press Professional Inc., San Diego.

Krajnović, S., 2011, “Flow around a tall finite cylinder explored by large eddy simulation”, Journal of Fluid Mechanics, pp. 1-24.

Laurent, T., 2011, “DNS of Newtonian and Non-Newtonian Turbulent Channel Flows”, http://lthais.plil.fr/.

Lesieur, M. and MÃl’tais, O., 1996, “New trends in large-eddy simulations of turbulence”, Annu. Rev. Fluid. Mech., Vol.28, pp. 45-82.

Lilly, D.K., 1992, “A proposed modification of the Germano sub-grid scale closure method”, Physics of Fluids, Vol.4, pp. 633-635.

Mason, P.J. and Callen, N.S., 1986, “On the magnitude of the subgrid-scale eddy coefficient in large-eddy simulations of turbulent channel flow”, Journal of Fluid Mechanics, Vol.162, pp. 439.

Piomelli, U., Moin, P. and Ferziger, J.H., 1988, “Model consistency in large eddy simulations of turbulent channel flows”, Physics of Fluids, Vol.31, pp. 1884-1891.

Smagorinsky, J., 1963, “General circulation experiments with primitive equation”, Mon. Weather Rev., Vol.91, pp. 99-164.
Temmerman, L., Leschziner, M.A., Mellen, C.P. and Fröhlich, J., 2003, “Investigation of wall-function approximations and subgrid-scale models in large eddy simulation of separated flow in a channel with streamwise periodic constrictions”, International Journal of Heat and Fluid Flow, Vol.24, pp. 157âĂŞ180.
Van Driest, E.R., 1956, “On turbulent flow near a wall”, J. Aero Sci., Vol.23, pp. 1007-1011.
Visbal, M.R., Morgan, P.E. and Rizzetta, D.P., 2003, “An Implicit LES Approach Based on High-Order Compact Differencing and Filtering Schemes”, AIAA Journal, pp. 2003-4098.

8. Responsibility notice

The authors are the only responsible for the printed material included in this paper.

DOUBLE MIXING LAYER LINEAR STABILITY ANALYSIS

Oberdan Miguel Rodrigues de Souza, oberdanmiguel@gmail.com
Pontifícia Universidade Católica do Rio de Janeiro, Rio de Janeiro, RJ, 22451-900, Brazil

Leonardo Santos de Brito Alves, Ph.D., leonardo.alves@gmail.com
Universidade Federal Fluminense, Centro Tecnológico, Escola de Engenharia, Niteroi, RJ, 24210-240, Brazil

Marcio Teixeira de Mendonça, Ph.D., marcio_tm@yahoo.com
Comando Geral de Tecnologia Aeroespacial, Instituto de Aeronáutica e Espaço, São José dos Campos, SP, 12228-904, Brazil

Abstract.
The main goal of this work is to perform a linear stability analysis of double mixing layers. By a double mixing layer it is meant a free shear layer composed of two parallel mixing layers separated by a distance δ. This type of flow field is a model for coaxial jets and is present in many technological applications, ranging from aerospace to environmental engineering. Nevertheless, the motivation for this work are the coaxial jets used by injection systems of liquid rocket engines. In order to carry out the investigation, two codes were developed, one to solve the similar boundary layer equations for the base flow and another for the inviscid stability equation. To generate the double mixing layer profile two single mixing layers are added using matched asymptotic expansions. Only incompressible flows were considered in the present study. However, the codes are capable of simulating compressible flow effects controlled by the Mach number, temperature and mass fraction differences. The external layer was considered either faster or slower than the internal one. Despite the fact that only one mode is found in a single mixing-layer, three modes were discovered for the double mixing-layer. Finally, evidence for an instability transition was found when the distance between layers decreases below a critical value.

Keywords: *hydrodynamic stability, Kelvin-Helmholtz stability, binary mixing layer*

1. INTRODUCTION

Thermal and hydrodynamic instabilities are found in many problems in fluid mechanics, such as in mixing layers, jets, wakes and boundary layers. They are present in many applications in mechanical and aerospace engineering as well as in environmental engineering. In propulsive systems they can be found in turbojets, ramjets and scramjets, both in subsonic and supersonic regimes and have a significant effect on component performance. Flame stability, mixing of reactants, emissions and component cooling are directly affected by hydrodynamic stability conditions.

The mixing layer is strongly unstable and sensitive to acoustic excitation. One of the grate challenges faced by designers is to avoid that the unsteady flow and noise resonate with the combustor natural frequencies, leading to its destruction. The present study aims at mapping the instability regions associated with the double mixing layer in order to aid the design of the fuel injection system and of the combustion chamber to avoid acoustic resonance.

The experimental works by (Leyva *et al.* , 2007) and (Rodriguez *et al.* , 2008) motivated the present work. The experiments considered coaxial jets excited by high intensity acoustic disturbances in order to investigate the effects on combustion stability. Those studies considered the subcritic and supercritic transition effects on the coaxial injector shown in Fig. 1. This type of injector is found in the J-2 type engines used on the Saturn V rocket, on the RS-24 space shuttle main engine and on the Ariane 5 Vulcan engine. The coaxial injector work with both liquid and gaseous oxidyzers (O_2, H_2 O_2, N_2O_2, etc) in the inner stream and gaseous fuel (H_2, kerosene, $C_{12}H_{26}$, etc) in the outer stream.

In the present work the results presented by (Salemi, 2006) for the single mixing layer are extended to consider double mixing layers. The double mixing layer profile composed of two single mixing layers separated by a distance δ represents better the shear layer studied in by (Leyva *et al.* , 2007) and (Rodriguez *et al.* , 2008).

The single mixing layer shown in Fig. 2 results from the interaction of two parallel streams where small disturbances evolve into spanwise vortices that transition the laminar flow to a turbulent regime. The double mixing layer in cartesian coordinates is an approximation of a free jet in cylindrical coordinates when the thickness of the shear layer is thin compared to the jet radius. It is formed by two regions, where for the first region U_1 is the upper layer velocity and $U_2 < U_1$ is the middle layer velocity. The second region U_2 is the middle layer velocity and U_3 is the lower layer velocity. The two velocity ratios present are $\beta_{u21} = \frac{U_2}{U_1}$ and $\beta_{u31} = \frac{U_3}{U_1}$, as shown in Fig. 3.

Besides the extension of the results from (Salemi, 2006), the present investigation also proposes the use of matched asymptotic expansions of simple mixing layers in order to obtain the base flow. The methodology to matched two simple mixing layers is presented in Sec. 4. This approach is proposed due to the fact that the stability analysis is strongly sensitive to discontinuity in the base flow profiles or on its derivatives and the matched asymptotic expansion provides a better base flow profile than just superposed profiles used in previous works.

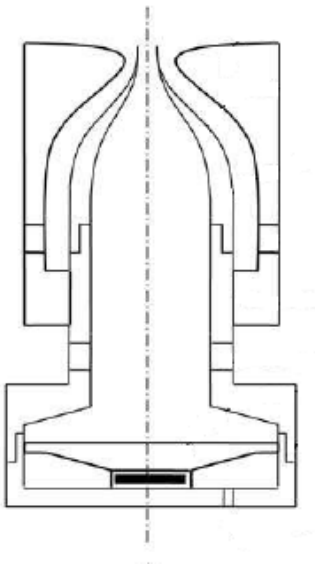

Figure 1. Coaxial injector.

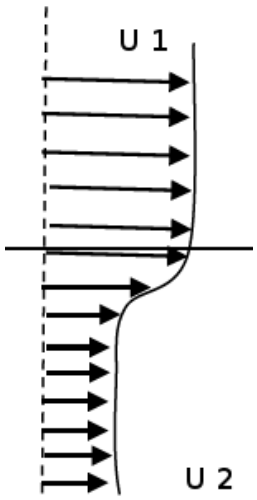

Figure 2. Single mixing layer.

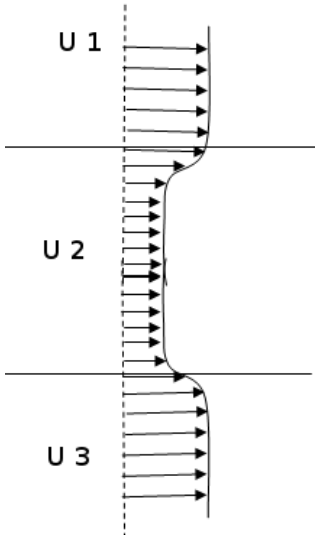

Figure 3. double mixing layer.

2. FORMULATION

The linear stability analysis considers the stability of small disturbances on a given base flow. For the present study the base flow is computed from the boundary layer equations written in similarity variables. For the disturbances, inviscid normal mode solutions are sought leading to a compressible, binary version of the Rayleigh equation.

2.1 Base Flow

For the steady, laminar, two dimensional, compressible base flow of a perfect gas, without chemical reaction, the usual boundary layer approximations are considered, leading to the following equations (Anderson, 2000) in Cartesian coordinates x, y for the velocity u, v, pressure p, density ρ, enthalpy h and mass fraction Y:
continuity

$$\frac{\partial(\rho u)}{\partial x} + \frac{\partial(\rho v)}{\partial y} = 0, \tag{1}$$

x and y momentum

$$\rho u \frac{\partial u}{\partial x} + \rho v \frac{\partial u}{\partial y} = -\frac{\partial p}{\partial x} + \frac{\partial}{\partial y}\left(\mu \frac{\partial u}{\partial y}\right), \qquad \frac{\partial p}{\partial y} = 0, \tag{2}$$

energy

$$\rho u\frac{\partial h}{\partial x}+\rho v\frac{\partial h}{\partial y}=\frac{\partial}{\partial y}\left[\rho\mathcal{D}_{12}\left(h_{gas_1}\frac{\partial Y_{gas_1}}{\partial y}+h_{gas_2}\frac{\partial Y_{gas_2}}{\partial y}\right)\right]+\frac{\partial}{\partial y}\left(\kappa\frac{\partial T}{\partial y}\right)+u\frac{\partial p}{\partial x}+\mu\left(\frac{\partial u}{\partial y}\right)^2, \tag{3}$$

mass fraction and equation of state

$$\rho u\frac{\partial Y_1}{\partial x}+\rho v\frac{\partial Y_1}{\partial y}=\frac{\partial}{\partial y}\left(\rho\mathcal{D}_{12}\frac{\partial Y_1}{\partial y}\right),\qquad p=\rho RT, \tag{4}$$

where $\mathcal{D}_{12}$ is the mass diffusion coefficient, κ is the gas mixture conductivity, μ is the dynamic viscosity, T is the absolute temperature and R the gas constant.

Applying the Levy-Less similarity transformation (Less, 1956; Levy, 1954) to the above boundary layer equations

$$\xi=\int_0^x\rho_1u_1\mu_1dx,\qquad \eta=\frac{u_1}{\sqrt{2\xi}}\int_0^y\rho dy, \tag{5}$$

where ρ_1, u_1 and μ_1 are the density, velocity and viscosity coefficient for the upper layer, and, defining the velocity f', enthalpy g, and mass fraction s as

$$\frac{\partial f}{\partial\eta}=f'=\frac{u}{U_1},\qquad g=\frac{h}{h_1},\qquad s_1=Y_1. \tag{6}$$

the following system of ordinary differential equations result (Anderson, 2000)

$$f'''+\frac{ff''}{\mathcal{C}}=0,\qquad g''+\frac{Pr}{\mathcal{C}}fg'+\frac{PrU_1^2}{h_1}(f'')^2=0,\qquad s''+\frac{LePr}{\mathcal{C}}fs'=0, \tag{7}$$

where $\mathcal{C}$ is the Chapman-Rubesin parameter, Pr is the mixture Prandtl number and Le is the Lewis number

$$\mathcal{C}=\frac{\rho\mu}{\rho_1\mu_1},\qquad Pr=\frac{\mu c_p}{\kappa},\qquad Le=\frac{\kappa}{\rho c_p}\mathcal{D}_{12}. \tag{8}$$

The boundary conditions for the upper layer are

$$f(0)=0,\qquad f'(+\infty)\to1,\qquad f'(-\infty)\to\beta_{u21}, \tag{9}$$

$$g(+\infty)\to1,\qquad g(-\infty)\to\beta_{h21}, \tag{10}$$

$$s(+\infty)\to1,\qquad s(-\infty)\to0. \tag{11}$$

And for the lower layer

$$f(0)=0,\qquad f'(+\infty)\to\beta_{u21},\qquad f'(-\infty)\to\beta_{u_31}, \tag{12}$$

$$g(+\infty)\to\beta_{h21},\qquad g(-\infty)\to\beta_{h31}, \tag{13}$$

$$s(+\infty)\to0,\qquad s(-\infty)\to1, \tag{14}$$

The system of ordinary differential equations for the base flow similarity solution is solved through a shooting method.

2.2 Matching The Base Flow Mixing layers

The double mixing layer velocity, temperature and other profiles will be constructed using matched asymptotic expansions of simple mixing layer profiles U_a and U_b (Alves, 2006; Cole, 1968). The double mixing layer velocity profile will be composed as follows:

$$U_{ab}=U_a(\frac{y}{\delta}-\frac{\delta}{2})+U_b(\frac{y}{\delta}+\frac{\delta}{2})-W, \tag{15}$$

where δ is the distance between the different layers and W is the matching velocity at the central layer. Figure 4 shows the matching process for a double mixing layer profile.

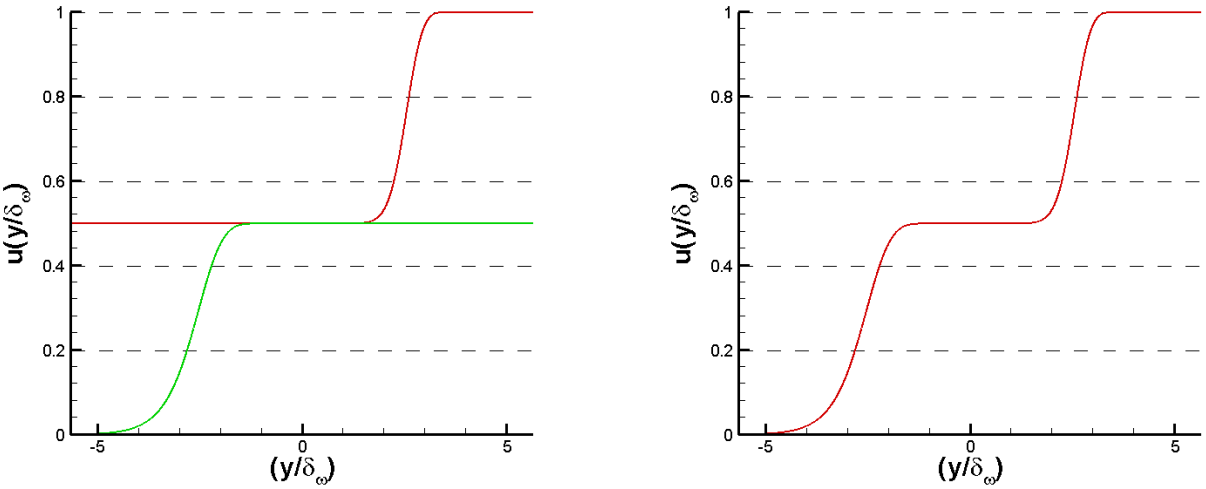

Figure 4. Velocity profile matching for $\beta_{u21} = 1/2$, $\beta_{u31} = 0$, $\beta_{T31} = \beta_{T21} = 1$ and $\delta/2 = 4.5$.

2.3 Stability Equations

The free shear layer base flow is subject to inviscid instability described by the evolution of small disturbances. Normal modes solutions are sought for the disturbance in the velocity component u' with complex amplitude $\hat{u}$, complex streamwise wave number and spatial growth rate $\alpha = \alpha_r + i\alpha_i$, spanwise wavenumber β and frequency ω.

$$u'(x, y, z, t) = \Re[\hat{u}(y) \exp(i\alpha x + i\beta z - i\omega t)]. \tag{16}$$

Upon substitution of u' (and similar expressions for the other variables) on the Euler equations and linearization, an eigenvalue problem results, and using the transformation proposed by (Gropengiesser, 1970)

$$\chi = \frac{i\alpha\hat{p}}{\gamma_1 Ma_1^2 \hat{v}}, \tag{17}$$

the equivalent of the Rayleigh equation for compressible, inviscid stability analysis is obtained.

$$\frac{d\chi}{dy} = \frac{\alpha^2(\bar{u} - \omega/\alpha)}{R\overline{T}} - \chi\left[\frac{\chi G + (d\bar{u}/dy)}{(\bar{u} - \omega/\alpha)}\right], \tag{18}$$

$$G = \frac{\alpha^2 + \beta^2}{\bar{\rho}\alpha^2} - Ma_1^2 \frac{\gamma_1}{\gamma} \frac{(\alpha\bar{u} - \omega)^2}{\alpha^2}. \tag{19}$$

where Ma_1 is the Mach number of the upper stream.

The boundary condition at $y \to \pm\infty$ are (Salemi and MENDONÇA, 2008):

$$\chi(y \to \pm\infty) = \mp \frac{\alpha(\bar{u} - \omega/\alpha)}{\sqrt{GR\overline{\overline{T}}}}. \tag{20}$$

3. RESULTS AND DISCUSSIONS

The following results consider only the stability of double mixing layers of a single fluid on all streams in order to search for additional instability modes. All simulations consider the base flow in the incompressible regime ($Ma_1 = 0.01$), with $\mathcal{C} = Pr = Le = 1$, $\beta_{u31} = 0$ and uniform temperature distribution, $\beta_{T31} = \beta_{T21} = 1$.

The effect of the velocity ratio β_{u21} on the stability of the shear layer is shown in Fig. 5. The base flow is shown on the right (with $\delta/2 = 4.5$) and the amplification curves on the left. Due to the existence of two inflection points in the velocity profiles, two instability modes are found. The lower the value of β_{u21} the closer are the two instability modes, but for increasing velocity ratio they become distinct, with one mode with a much higher maximum amplification rate and another mode with a wider range of unstable frequencies. When $\beta_{u21} = 1$ or 0 a single mixing layer is recovered and a single mode is found

Figure 6 show results for the condition where the external stream is slower than the central stream, as shown on the left. Again, two modes are found, one with a stronger growth rate and another with a wider range of unstable frequencies. The

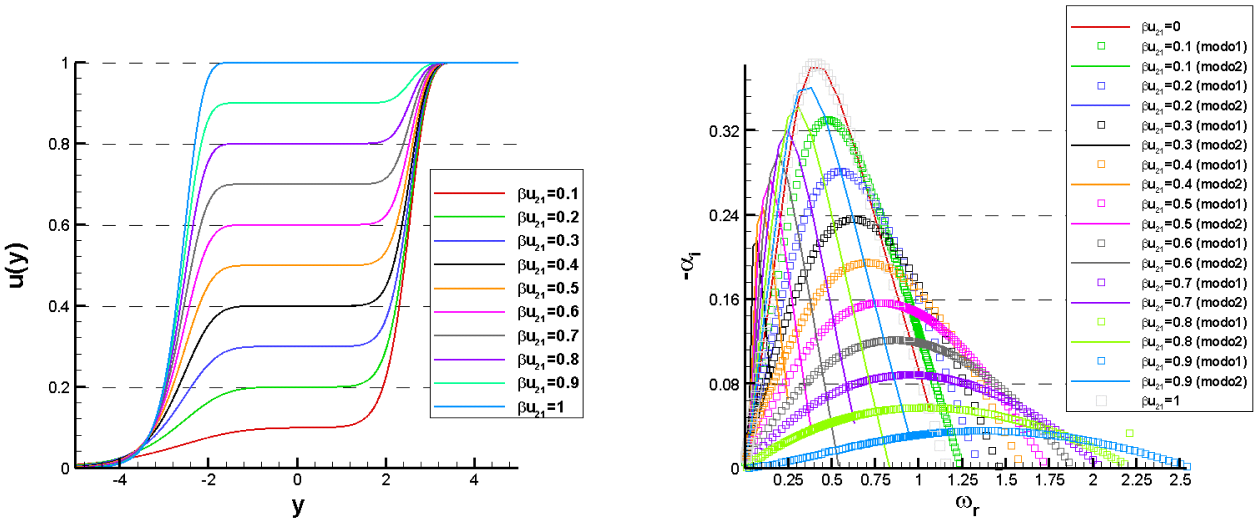

Figure 5. Shear layer and amplification rates variation with $0.1 \leq \beta_{u21} \leq 1$.

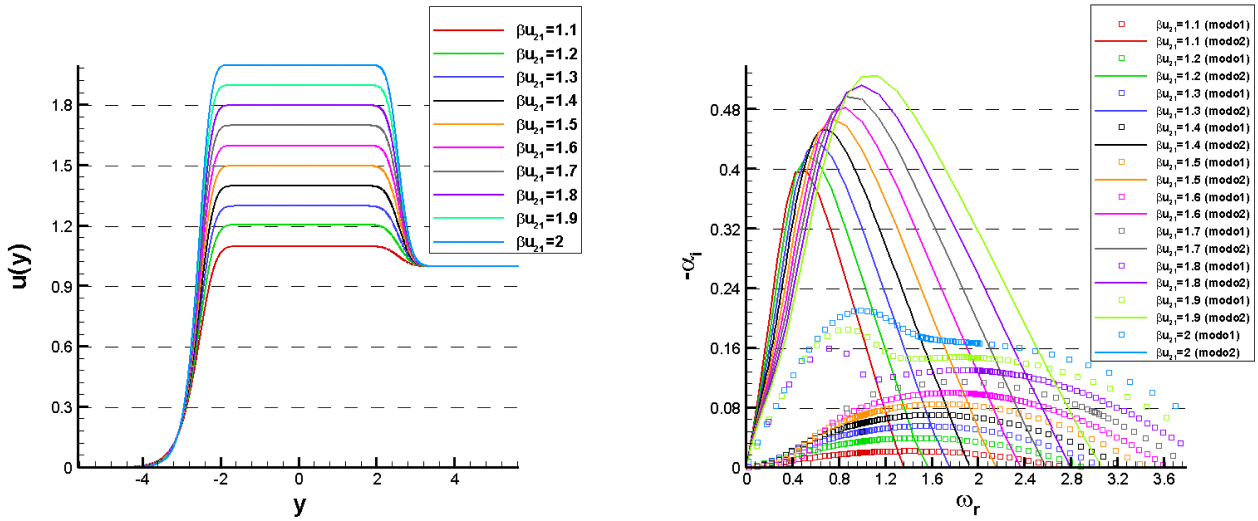

Figure 6. Shear layer and amplification rates variation with $1.1 \leq \beta_{u21} \leq 2$.

least unstable mode shows a strange behaviour around $\beta_{u21} = 1.7$ that needs further investigations. The wavenumbers for the above cases are shown in Fig. 7.

A third mode was found with a significant amplification rate for the range of $.6 \leq \beta_{u21} \leq .9$ as shown in Fig. 8. The range of unstable frequencies does not start at zero, which shows that these are not Kelvin-Helmholtz modes.

The following results consider the condition when de distance δ between the two mixing layers is reduced. Two values of β_{u21} are considered, 0.5 and 1.5. The base flows considered for $\beta_{u21} = 0.5$ is shown in Fig. 9. Similar results are encountered as before with two instability modes. But for $\delta \leq 1.$ a significant change is observed since only one mode was found. This suggests that a minimal distance between mixing layers is necessary for two modes to exist.

Increasing β_{u21} to 1.5 results in the base flow profiles shown in Fig. 10. In this case no minimum distance was found

that resulted in a single instability mode. Again a stronger mode and a mode with wider unstable frequency range are found.

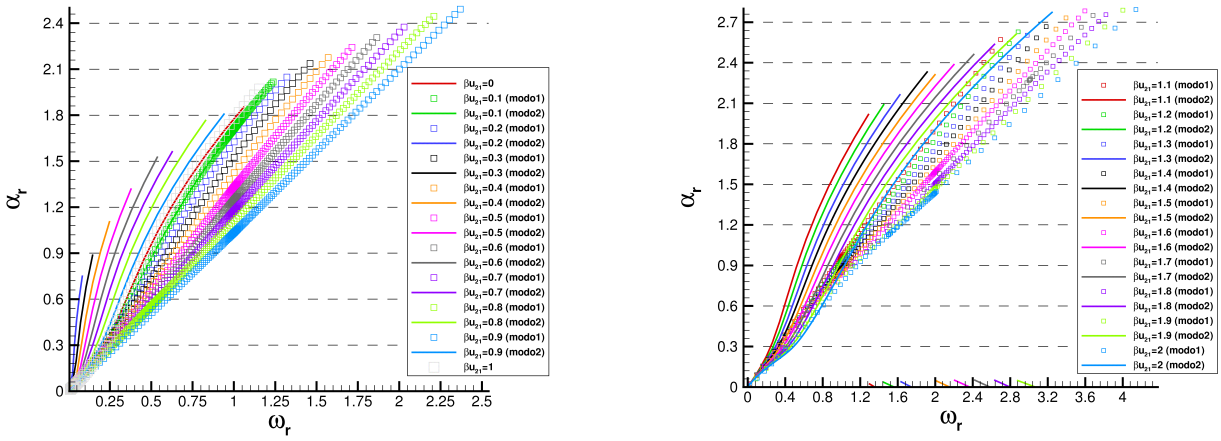

Figure 7. Wave numbers with varying β_{u21} for the conditions of the previous figures.

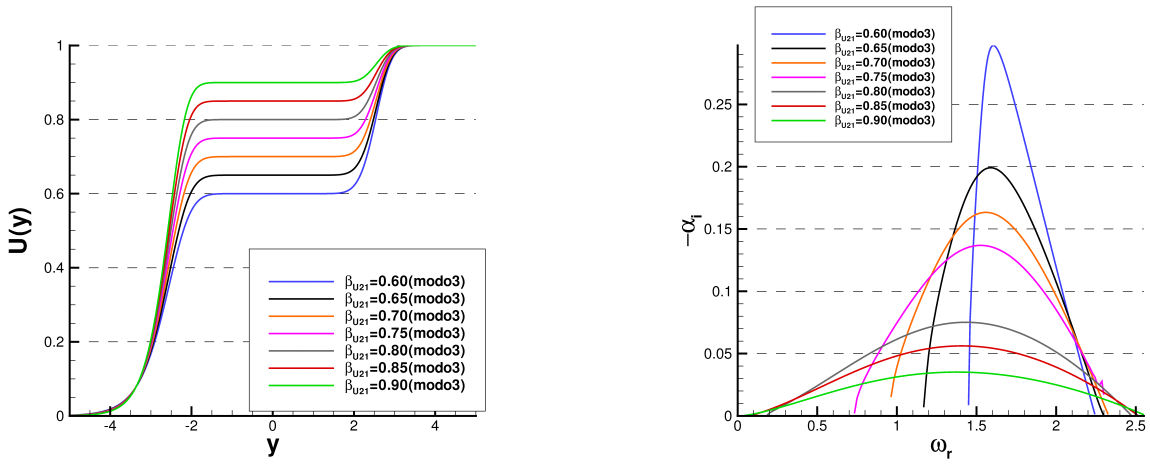

Figure 8. Third instability mode found for the base flow shown on the left.

4. CONCLUSIONS

A methodology based on matched asymptotic expansion was used to construct a double mixing layer profile which is subject to an inviscid stability analysis. This complex free-shear layer is a model for coaxial jets present in the injector of combustion devices used in aerospace propulsion systems. The stability analysis showed the existence of at least two modes, and a third mode was also found for some flow conditions. Further investigations are necessary to investigate the nature of these third mode. Compressibility and binary gas systems will be considered in future work.

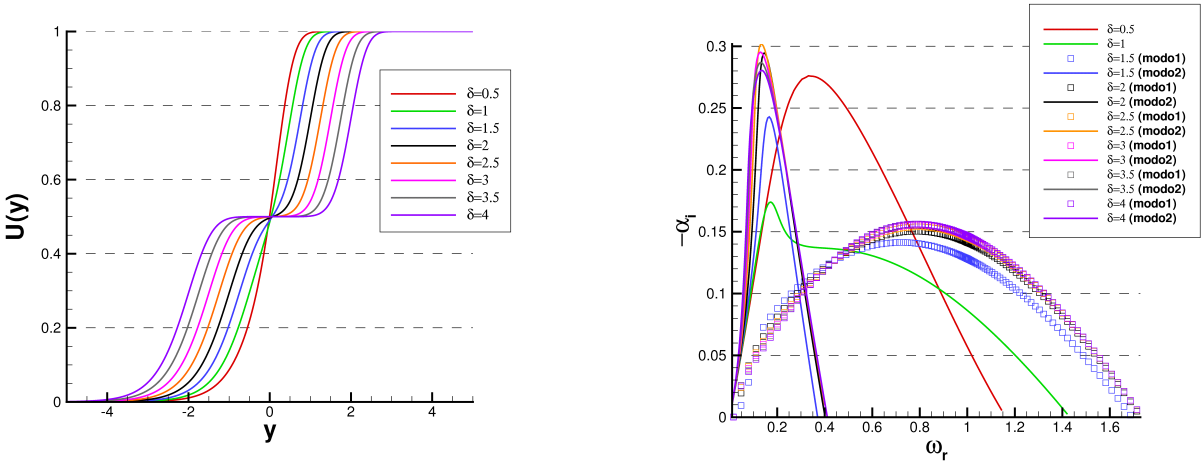

Figure 9. Base flow and stability diagram for $\beta_{u21} = 0.5$ and varying δ.

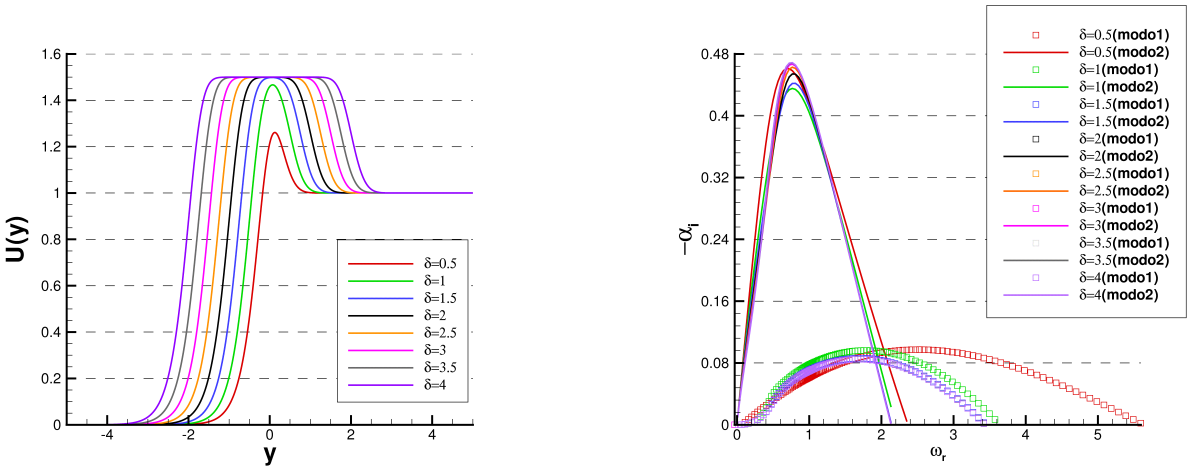

Figure 10. Base flow and stability diagram for $\beta_{u21} = 1.5$ and varying δ.

5. ACKNOWLEDGEMENTS

The authors would like to acknowledge the financial support from CNPq.

6. REFERENCES

Alves, Leonardo S. de B. 2006 (March). *Transverse Jet Shear-Layer Instabilities: Linear Stability Analysis and Numerical Simulations*. Ph.D. thesis, University of California, Los Angeles.

Anderson, J. D. 2000. *Hypersonic and High Temperature Gas Dynamics*. AIAA.

Cole, J.D. 1968. *Perturbation Methods in Applied Mathematics*. Massachusetts: Blaisdell Publishing Company.

Gropengiesser, H. 1970. Study on the stability of boundary layers in compressible fluids. *National Aeronautics and Space Administration-NASA*, **F-12**.

Less, L. 1956. Laminar Heart Transfer over Blunt-Nosed Bodies at Hypersonic Flight Speeds. *Jet Propulsion*, **26**(7), 259–269.

Levy, S. 1954. Effect of Large TemperatChages(Including Viscous Heating)Upon Laminar Boundary Layers With Variable Free-Stream Velocity. *Journal of Aeronautical Sciences*, **21**(7), 459–474.

Leyva, I. A., Chehroudi, B., and Talley, D. 2007. Dark core analysis of coaxial injectors at sub-, near-, and supercritical pressures in a transverse acoustic field. *AIAA Journal*, **43**.

Rodriguez, J. I., Leyva, I. A., Chehroudi, B., and Talley, D. 2008. Results on Subcritical One-Phase Coaxial Jet Spread Angles and Subcritical to Supercritical Acoustically-Forced Coaxial Jet Dark Core Lengths. *AIAA Journal*, **44**.

Salemi, L. C., and MENDONÇA, M. T. 2008. Spatial and Temporal Linear Stability Analysis of Binary Compressible Shear Layer. *AIAA Journal*, 2008–3841.

Salemi, Leonardo da Costa. 2006. *Análise de Estabilidade Linear de Camada de Mistura Laminar Compressível Binária*. M.Phil. thesis, Instituto Nacional de Pesquisas Espaciais, Cachoeira Paulista.

7. RESPONSIBILITY NOTICE

The authors are the only responsible for the printed material included in this paper

MODELAGEM COMPUTACIONAL DA ESTEIRA AERODINÂMICA DE TURBINAS EÓLICAS BASEADA EM SUMIDOURO DE QUANTIDADE DE MOVIMENTO

Marco Leonardelli Lovatto, marco.lovatto@ste-pdi.com.br
STE Pesquisa e Desenvolvimento – R. Faria Santos, 47 / 404 – Porto Alegre, RS, Brasil.

Adriane Prisco Petry, adrianep@mecanica.ufrgs.br
Universidade Federal do Rio Grande do Sul – Dep. de Engenharia Mecânica – R. Sarmento Leite, 425 – Porto Alegre, RS, Brasil.

Resumo. *Empregando CFD (Dinâmica dos Fluidos Computacional), este estudo propõe um novo modelo para simular a esteira aerodinâmica de turbinas eólicas de eixo horizontal, bem como a magnitude e direção da velocidade do vento incidente sobre cada máquina, sem a necessidade de modificar a discretização do domínio para diferentes direções de vento global. Esta nova metodologia baseia-se no modelo de disco atuador descrito por Burton* et al. *(2001), substituindo o disco por uma região volumétrica esférica, dentro da qual um sumidouro de quantidade de movimento é distribuído, representando a energia extraída do escoamento pelo aerogerador. O modelo tradicional baseia-se no conhecimento prévio da velocidade de vento incidente sobre a máquina, no que diz respeito à sua magnitude e direção, enquanto o modelo desenvolvido é capaz de determinar tanto a magnitude quanto a direção da velocidade incidente por meio de um cálculo iterativo simples interno a cada iteração do modelo fluidodinâmico. Os resultados obtidos são muito satisfatórios e promissores para o cálculo de parques eólicos, pois é possível alterar as direções do vento global sem modificar a discretização do domínio. Esta característica é especialmente adequada para aplicação em parques eólicos sobre terrenos complexos onde, para uma mesma magnitude e direção de vento global, o vento local pode tomar direções e velocidades variadas. As aplicações estudadas neste trabalho, no entanto, ainda apresentam resultados e fatores de correção dependentes do software utilizado.*

Palavras-chave. *energia eólica, CFD, disco atuador, quantidade de movimento.*

1. INTRODUÇÃO

A avaliação do potencial de produção energética previsto para um parque eólico em fase de projeto envolve a modelagem da esteira aerodinâmica dos aerogeradores, em outras palavras, da redução de energia cinética do vento após este atravessar o plano de rotação da turbina. Essa esteira, chamada pela comunidade de energia eólica de sombra aerodinâmica, pode incidir sobre máquinas adjacentes e, portanto, afetar sua produção de energia elétrica.

O foco da presente pesquisa são as turbinas eólicas de eixo horizontal. Em projetos de pesquisa, é possível utilizar a Dinâmica dos Fluidos Computacional (CFD) para simular a geometria completa do rotor em rotação e obter a esteira. Contudo, esta abordagem tem um custo computacional muito elevado, conduzindo à necessidade de modelar a esteira sem calcular o rotor. Para isto, existem modelos analíticos ou semi-analíticos, baseados em dados empíricos, muito empregados em programas comerciais de projeto de parques eólicos. Entretanto, tais modelos têm limitações, principalmente quanto ao conhecimento da magnitude da velocidade de vento incidente sobre cada máquina. Também, no caso dos modelos hoje utilizados em conjunto com CFD, a malha utilizada na discretização do domínio precisa ser modificada para lidar com as diferentes direções do vento incidente e, logo, da esteira.

2. OBJETIVO

Para contornar as limitações descritas, é proposto um novo modelo para simulação de esteira fundamentado no modelo de disco atuador descrito por Burton *et al.* (2001), sendo tal disco uma representação numérica do aerogerador por meio de uma superfície ou volume virtual que tem a função de extrair energia do escoamento.

O novo modelo consiste não mais na utilização de um disco atuador, mas sim de uma esfera atuadora. Essa abordagem tem como objetivo sua utilização na simulação numérica de parques eólicos sem modificar a discretização do domínio, considerando:

- A necessidade de realizar testes numéricos com ventos vindos de diversas direções.
- A necessidade de se fazer cálculos sobre terrenos complexos onde, para uma mesma magnitude e direção de vento global, o vento local pode tomar direções e velocidades variadas.
- A influência direta da esteira de uma máquina sobre outra máquina.

3. REVISÃO BIBLIOGRÁFICA

Estudos recentes em aerodinâmica de turbinas eólicas têm mostrado grande interesse na reprodução por CFD (Sezer-Uzol e Long, 2006; Ribeiro, 2012; Fleck, 2012) de resultados obtidos experimentalmente (Hand *et al.*, 2001), aproveitando-se do considerável aumento do poder computacional na última década. Outro foco, porém, tem sido a comparação de resultados de esteira obtidos por modelos analíticos e semi-analíticos já existentes com os obtidos pela simulação de um rotor completo por CFD, a exemplo de Wenzel (2010).

Burton *et al.*(2001) descreve um modelo de esteira baseado num disco atuador, aplicado em conjunto com CFD por

Calaf *et al.* (2010) e Norris *et al.* (2010). Entretanto, a abordagem utilizada por esses autores consiste na fixação de um parâmetro que, na realidade, não é constante, conforme descrito na Seção 5.1.

Todas as referências citadas utilizam vento incidente de magnitude e direção constantes, enquanto que o presente estudo propõe um modelo que avalia as variáveis envolvidas na modelagem, incluindo a magnitude e direção da velocidade de vento incidente sobre cada máquina.

4. FUNDAMENTAÇÃO TEÓRICA

Um aerogerador é uma turbina que converte a energia cinética do vento em energia elétrica, de forma que a velocidade à jusante do aparato é menor que à montante (Burton *et al.*, 2001). Como a massa se conserva e não se comprime, o resultado é um tubo de corrente de maior diâmetro à jusante, conforme mostra a Fig. 1a, sendo um tubo de corrente uma fronteira imaginária do escoamento através da qual não há fluxo de massa, dentro da qual a vazão mássica é constante. A esteira aerodinâmica, ou sombra aerodinâmica, é a região interna ao tubo de corrente e à jusante do rotor. A zona externa ao tubo é dita região de *corrente livre*.

A Fig. 1b apresenta, de forma genérica e qualitativa, o comportamento da pressão e da velocidade de vento através do plano de rotação das pás. A energia mecânica do ar disponível numa unidade de volume pode ser definida pela soma da pressão estática (termodinâmica) com a pressão dinâmica, e sua taxa em relação ao tempo é chamada de *potência aerodinâmica*. A diferença entre a potência aerodinâmica disponível à jusante da turbina e a existente à montante é a potência extraída pela máquina.

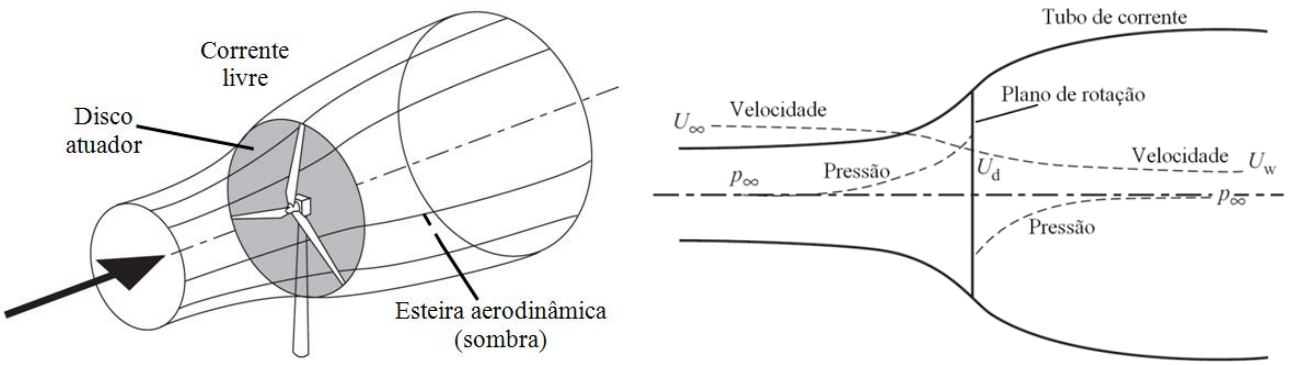

(a) (b)

Figura 1. (a) Tubo de corrente representativo do escoamento através de uma turbina eólica de eixo horizontal e (b) variação da pressão e da velocidade. Adaptados de Burton *et al.* (2001).

Disco atuador é a superfície ou o volume virtual representativos do plano de rotação das pás e que tem como função extrair energia do vento. O propósito do uso da teoria do disco atuador em simulações numéricas de parques eólicos é modelar a esteira gerada pelo aerogerador para um vento incidente de magnitude U_∞ e direção conhecida, sem a necessidade de modelar o escoamento sobre a geometria completa do rotor de cada turbina eólica. Essa esteira, por sua vez, irá influenciar na velocidade de vento incidente sobre máquinas adjacentes.

Além das forças atuantes no plano de rotação, que contribuem para o torque, o vento também produz uma força de arrasto sobre o rotor, na direção perpendicular a esse plano, chamada pela comunidade de energia eólica de força de empuxo. Por reação, a turbina gera a mesma força sobre o ar, no sentido contrário ao do vento incidente, promovendo uma redução da velocidade de corrente livre U_∞, ou uma redução da energia cinética à jusante do rotor (lado esquerdo da Fig. 1b). Como a energia mecânica se conserva antes do disco, esta redução da velocidade à jusante ocorre juntamente com um aumento da pressão na mesma região.

A energia extraída do vento pelo rotor – e convertida em trabalho de eixo – é energia termodinâmica. Essa extração da energia do vento se manifesta por meio de uma rápida queda de pressão, sabendo-se que a pressão de um fluido é a sua energia termodinâmica por unidade de volume. O ar, que ao atravessar o rotor já tinha uma velocidade reduzida (U_d), agora tem também uma pressão reduzida.

A pressão do ar na esteira (lado direito da Fig. 1b) tende a aumentar novamente para equilíbrio com a pressão atmosférica (p_∞). Como a energia mecânica do ar volta a se conservar nessa região, o aumento de pressão ocorre em detrimento de uma diminuição adicional da energia cinética e, portanto, de velocidade do vento.

Não havendo turbulência e nem viscosidade (hipótese teórica ideal da Fig. 1b) a velocidade do vento na esteira manter-se-ia constante e igual a U_w logo após o equilíbrio de pressão. Entretanto, a hipótese de escoamento invíscido da Fig. 1b não é mais válida na região da esteira. Como mostrado na Fig. 2, a viscosidade e a turbulência geram uma camada de cisalhamento, transferindo quantidade de movimento da região de corrente livre para dentro da esteira. A consequência é uma recuperação gradual da velocidade média do vento na esteira e, logo, da energia cinética.

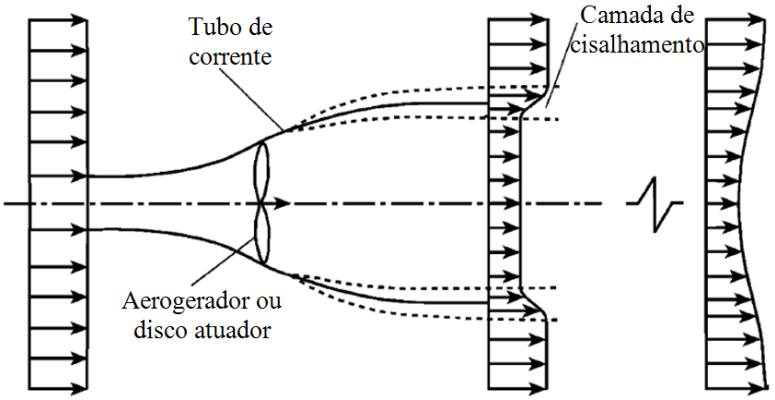

Figura 2. Representação esquemática da recuperação de velocidade na esteira devida à viscosidade e turbulência. Adaptado de Gómez-Elvira *et al.* (2005).

O valor da potência aerodinâmica do ar extraída pelo disco atuador depende do conhecimento do empuxo (somatório das forças perpendiculares ao plano de rotação). O empuxo pode ser imposto computacionalmente por meio da imposição de um salto de pressão através de uma superfície ou por meio de um sumidouro de quantidade de movimento dentro de uma região volumétrica. A escolha de um ou de outro é dependente das capacidades de modelagem de fenômenos oferecidas pelo software utilizado.

O desafio é descobrir o valor do empuxo para cada velocidade de vento incidente U_∞. O modelo do disco atuador atende a este desafio e o raciocínio é descrito abaixo, adaptado de Burton *et al.* (2001).

A potência elétrica (P_{ele}) pode ser dada pela Eq. (1):

$$P_{ele} = \eta P_{ext} \tag{1}$$

onde P_{ext} é a potência extraída e η é a eficiência da máquina, que depende do modelo de aerogerador, das condições de vento, torque e rotação.

A potência extraída pode ser dada pela Eq. (2):

$$P_{ext} = F U_d \tag{2}$$

onde U_d é a velocidade do vento que atravessa o disco e F é a força de empuxo, que pode ser calculada por:

$$F = \Delta U \dot{m} \tag{3a}$$

onde ΔU é a variação de velocidade do vento antes e depois do rotor e $\dot{m}$ a vazão mássica de ar através do rotor. Ou seja,

$$F = (U_\infty - U_w)\rho A_d U_d \tag{3b}$$

onde U_∞ é a velocidade de corrente livre do vento incidente, U_w a velocidade teórica do vento na esteira, ρ a massa específica do ar e A_d a área varrida pelo rotor.

Burton *et al.* (2001) define U_d como

$$U_d = U_\infty(1 - a) \tag{4}$$

onde a é chamado de fator de indução axial, sempre entre 0 e 1. Essa equação é uma hipótese para o modelo, a qual diz que U_d é igual a U_∞ subtraída de aU_∞.

Das Eqs. (3b) e (4) tem-se que:

$$F = (U_\infty - U_w)\rho A_d U_\infty(1 - a) \tag{5}$$

Aplicando a equação de Bernoulli antes e depois do plano de rotação (nas duas regiões onde a energia se conserva), Burton *et al.* (2001), prova que:

$$F = \frac{1}{2}\rho({U_\infty}^2 - {U_w}^2)A_d \tag{6}$$

Então, igualando as Eqs. (5) e (6), chega-se a:

$$U_w = (1 - 2a)U_\infty \tag{7}$$

Finalmente, as Eqs. (5) e (7) fornecem a equação fundamental para a o cálculo da força de empuxo e modelagem da

$$F = 2\rho A_d {U_\infty}^2 a(1-a) \tag{8}$$

Daí, das Eqs. (2), (4) e (8), temos que:

$$P_{ext} = 2\rho A_d {U_\infty}^3 a(1-a)^2 \tag{9}$$

Mesmo conhecendo-se U_∞, o fator de indução axial (a) ainda precisa ser determinado. Isso é feito por meio da definição de *coeficiente de potência* utilizado por Burton *et al.* (2001):

$$C_p = \frac{P_{ext}}{P_\infty} \tag{10}$$

Então, das Eqs. (9) e (10), e dado que $P_\infty = \frac{1}{2}\rho {U_\infty}^3 A_d$, tem-se:

$$C_p = 4a(1-a)^2 \tag{11}$$

A Eq. (11) é de terceiro grau, interessando-nos apenas o intervalo $0 < a < 1$, que fornece $C_p > 0$ (vide Fig. 3). O valor máximo possível para C_p ocorre quando sua derivada em relação a a é nula, que ocorre para $a = 1/3$, resultando num $C_p = \frac{16}{27} = 0{,}593$. Tal valor de C_p é conhecido como máximo de Betz, e significa que, teoricamente, nenhuma turbina eólica seria capaz de extrair mais de 59,3% da potência aerodinâmica incidente disponível. De fato, nenhum aerogerador conseguiu ultrapassar esse limite até a presente data.

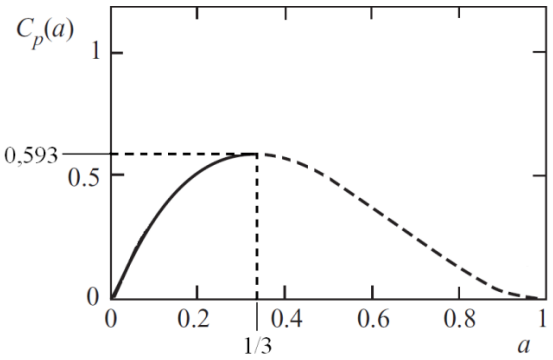

Figura 3. Coeficiente de potência (C_p) em função do fator de indução axial (a). O máximo de Betz ($Cp = 0{,}593$) ocorre para $a = 1/3$. Adaptado de Burton *et al.* (2001).

Ressalta-se que o propósito do modelo de disco atuador não é determinar a potência elétrica extraída pela máquina para um vento incidente conhecido, e sim determinar a *potência aerodinâmica que a máquina extrai do vento*, com o objetivo de avaliar o comportamento da esteira. Tal modelagem depende do cálculo de F pela Eq. (8), que depende do conhecimento de U_∞ e a.

5. MODELAGEM

5.1. Limitações do modelo tradicional de disco atuador

O estudo numérico do potencial eólico de um parque em fase de projeto envolve a necessidade do cálculo de ventos vindos de diferentes setores da rosa dos ventos. Diferentes direções de U_∞ significam ângulos diferentes dos discos atuadores em seus eixos verticais. Para aplicações de CFD, a alteração do ângulo do disco significa a necessidade de modificar a malha utilizada na discretização. Isso implica uma nova malha para cada nova direção de vento, elevando os custos computacionais ou de trabalho humano.

Mesmo quando o disco e a malha estão adaptados à direção do vento, a esteira de uma máquina pode estar gerando sombra sobre outra máquina adjacente, onde a velocidade de vento incidente acaba sendo inferior àquela de corrente livre. Isso faz com que U_∞ para máquinas sob o efeito de esteira de turbinas próximas seja desconhecida.

O valor de U_∞ é utilizado na Eq. (8) para o cálculo de F. A metodologia usualmente empregada para determinação de U_∞, como mostram Calaf *et al.* (2010) e Norris *et al.* (2010), tem-se restringido à obtenção de U_d como sendo a velocidade média que atravessa o disco atuador, seguida do cálculo de U_∞ pela Eq. (4) e usando-se um valor constante para a, normalmente igual a 0,25. Uma abordagem mais direta poderia ser o monitoramento da velocidade U_∞ por meio de um ponto localizado à montante do disco atuador.

No entanto, além do fator de indução axial a não ser constante na realidade, a utilização de um ponto de monitoramento para determinar a magnitude de U_∞ é uma abordagem que carece de precisão, especialmente para parques eólicos sobre terrenos complexos. Este ponto não garante a captura da velocidade média real que realmente

incide sobre a área do rotor, principalmente quando existe influência parcial da esteira de uma máquina próxima.

5.2. O modelo de esfera atuadora

Com o propósito de contornar essas limitações do modelo de disco atuador tradicional, é proposta uma nova abordagem, através de uma *esfera* atuadora representante da máquina, inspirada nas discussões dentro da STE Pesquisa e Desenvolvimento, sob financiamento do Conselho Nacional de Desenvolvimento de Pesquisa (CNPq) no contexto dos editais de inovação RHAE (Recursos Humanos para Áreas Estratégicas).

O modelo proposto tem como objetivos:

- Substituir o disco por uma esfera, eliminando a necessidade de modificar o ângulo de um disco para cada direção de vento incidente e a consequente modificação da malha.
- Calcular corretamente os valores de U_∞ e a antes do cálculo de F.

A abordagem apresentada, com uso de CFD, envolve o acoplamento de dois grupos principais e independentes de equações, ou dois modelos trabalhando em conjunto:

- Modelo fluidodinâmico.
- Modelo de esfera atuadora.

O modelo fluidodinâmico envolve a análise do escoamento turbulento através das equações de conservação de massa, princípio da quantidade de movimento com médias de Reynolds (RANS) e modelo de turbulência k-ω SST. Estas equações são resolvidas pelos softwares de CFD utilizados, ANSYS CFX 13.0 e ANSYS Fluent 13.0, e não foram alteradas ao longo do trabalho, sendo descritas na monografia do autor (Lovatto, 2013) e também nas documentações ANSYS Inc. (2009) e ANSYS Inc. (2010).

O ANSYS CFX 13.0, software onde o modelo de esfera atuadora foi testado, é capaz de obter a magnitude da velocidade média dentro de um volume esférico de mesmo diâmetro do rotor. Essa velocidade média, comprovadamente igual à U_d, tem componentes u, v e w relativas às coordenadas espaciais, que também podem ser determinadas. O sumidouro de quantidade de movimento, distribuído no volume esférico, pode ser decomposto em componentes espaciais que respeitam a direção do vento obtida pelas componentes de U_d. Isso torna o modelo de esfera atuadora capaz de lidar com ventos vindos de qualquer direção, sem a necessidade de mudar o ângulo de um disco e modificar a malha para cada direção de vento incidente.

Os dados de entrada fundamentais para a utilização do modelo de esfera atuadora são a *curva de potência* do aerogerador (P_{ele} em função de U_∞), a eficiência η e a área ou o diâmetro do rotor. Os fabricantes de turbinas eólicas seriam capazes de fornecer todos os dados, embora a eficiência η não seja uma informação atualmente disponível no mercado. Portanto, num primeiro momento, η deveria ser estimado de maneira arbitrária. Assim, na presente pesquisa, como dado de entrada escolheu-se trabalhar diretamente com a curva de *coeficiente* de potência, $C_p = f(U_\infty)$. A área ou o diâmetro do rotor servem de base para o tamanho da esfera que, neste trabalho, terá um diâmetro ligeiramente maior que o do rotor e uma seção máxima de área A_d.

O modelo de esfera atuadora começa com a leitura de U_d como sendo a magnitude da velocidade média dentro da esfera, segundo a Eq. (12).

$$U_d = \frac{\iiint_{esfera} |U| \, dV}{V_{esfera}} \tag{12}$$

No início do cálculo, U_d será igual à velocidade com a qual o domínio fluido foi inicializado, e seu valor é atribuído a U_∞ como chute inicial. Em seguida, segue-se o cálculo iterativo descrito a seguir:

1. Determina-se C_p a partir de U_∞ por meio de uma tabela representativa da curva de coeficiente de potência, $C_p = f(U_\infty)$.
2. Obtém-se a a partir de C_p por meio de uma tabela construída com a Eq. (11).
3. Atualiza-se U_∞ pela Eq. (4).

Para cada iteração espacial das equações do modelo fluidodinâmico, os três passos acima se repetem num processo iterativo interno até a convergência de C_p, a e U_∞. Testes apresentados por Lovatto (2013) mostram convergência de C_p, a e U_∞ em 10^{-4} após seis iterações. Finalmente, calcula-se a magnitude do empuxo F pela Eq. (8), que é a taxa de variação da quantidade de movimento extraída pelo sumidouro (ANSYS Inc., 2010) distribuído dentro da esfera.

Essa magnitude do empuxo precisa ser dividida em componentes espaciais correspondentes às componentes de U_d. Com essa finalidade, para cada uma das direções x, y e z do espaço, o empuxo é multiplicado pelos fatores multiplicadores $\bar{u}^*$, $\bar{v}^*$ e $\bar{w}^*$, das Eqs. (13), abaixo. Tais fatores são as componentes espaciais da velocidade média na esfera ($\bar{u}$, $\bar{v}$ e $\bar{w}$) adimensionalizadas pela magnitude da velocidade média na esfera, igual a U_d.

$$\bar{u}^* = \frac{\bar{u}}{U_d} \tag{13a}$$

$$\bar{v}^* = \frac{\bar{v}}{U_d} \tag{13b}$$

$$\bar{w}^* = \frac{\bar{w}}{U_d} \tag{13c}$$

O sumidouro de quantidade de movimento reflete-se no cálculo com um aumento da pressão à montante e diminuição à jusante, o que leva a uma redução da velocidade U_d, que atravessa a esfera. Na iteração espacial seguinte do modelo fluidodinâmico, o valor de U_d será atualizado. O novo U_d de cada iteração do modelo fluidodinâmico é utilizado no passo 3 das iterações do modelo de esfera atuadora. Segue-se, então, um novo processo iterativo da esfera atuadora antes da próxima iteração espacial do modelo fluidodinâmico.

Portanto, a convergência final dos cálculos nessa metodologia ocorre por meio da convergência do modelo de esfera atuadora *para cada iteração* do modelo fluidodinâmico, junto com a convergência posterior do modelo fluidodinâmico.

6. VALIDAÇÃO DO MODELO DE ESFERA ATUADORA

O estudo do modelo de esfera atuadora foi realizado em seis etapas. Na primeira, a geometria virtual completa de um aerogerador em rotação foi simulada com a finalidade de se obter a força de empuxo. Esta força foi utilizada como referência nas etapas seguintes. Testando-se o modelo por partes, foi possível rastrear os possíveis pontos fracos com maior facilidade e aplicar as correções necessárias.

6.1. Empuxo e esteira de rotor completo em rotação sob vento incidente de 7m/s

6.1.1. Descrição do problema do rotor completo em rotação

Num primeiro momento, foi calculado, por CFD, um rotor em rotação sob vento incidente, com a finalidade de determinar a força de empuxo (F) e o comportamento da velocidade média do vento em diversas seções da esteira. O propósito é usar o valor calculado da força de empuxo como valor de entrada na Etapa 2. A Etapa 2 é o primeiro teste do modelo de esfera atuadora, com a finalidade de analisar se o comportamento da esteira é semelhante.

O rotor calculado por CFD reproduz um dos testes reais (Hand *et al.*, 2001) efetuados em túnel de vento pelo *National Renewable Energy Laboratory* (NREL) sobre uma turbina eólica de eixo horizontal com rotor de 10m de diâmetro, composto por um cubo (parte central) e duas pás com ângulo de passo de 0°. O aparelho é dotado de um motor-gerador, que mantém a velocidade de rotação constante. Para o cálculo CFD, as condições de teste foram com vento de corrente livre incidente forçado (U_f) a 7m/s e rotação do rotor a 72rpm. Como o objeto de estudo é a esteira aerodinâmica provocada exclusivamente pelo rotor, as outras estruturas presentes na máquina real, como a torre, não foram reproduzidas na geometria virtual.

A Fig. 4 mostra as geometrias virtuais do rotor (a) e do túnel de vento virtual (b). A geometria do rotor foi modelada por Fleck (2012) a partir dos dados de Hand *et al.* (2001). O rotor está dentro de um volume esférico (Fig. 4a) onde são utilizados modelos de fluido rotativo (ANSYS Inc., 2009). Esse volume será chamado de *domínio rotativo*, o qual está dentro de um *domínio estático* (Fig. 4b) por onde escoa o vento de corrente livre forçado, U_f, igual a 7m/s.

A superfície esférica é uma interface virtual entre o domínio estático e o domínio rotativo, e não deve interferir no escoamento, pois não é uma parede real. Entretanto, para o cálculo utilizando o ANSYS CFX, houve problemas de continuidade da solução nessa interface (Lovatto, 2013). Por essa razão, este caso foi recalculado no ANSYS Fluent.

É importante salientar que tal problema não foi motivo suficiente para fazer uma migração completa de ferramenta, do CFX para o Fluent, para as etapas seguintes. Embora o rotor completo tenha sido calculado no Fluent, os testes do modelo de esfera atuadora foram feitos no CFX. O motivo é que o Fluent exige um código escrito em linguagem C para programar o modelo de esfera atuadora. Esse código significaria habilidades e complexidade adicionais para um primeiro teste do modelo; enquanto isso, o CFX permite a inserção de expressões de forma interativa, gráfica, intuitiva e simples. Embora a troca de software de uma etapa para a outra não seja a abordagem científica correta, ela foi considerada inevitável para os primeiros passos de compreensão do novo modelo proposto.

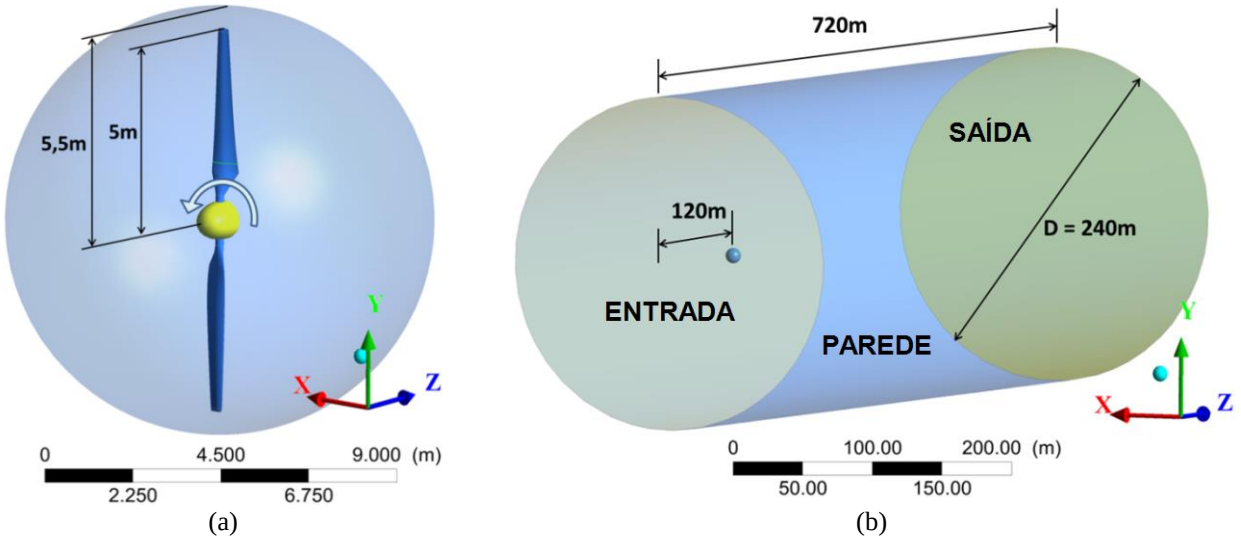

(a) (b)

Figura 4. (a) Rotor e seu sentido de rotação, dentro de um domínio rotativo; e (b) domínio estático por onde escoa o vento de corrente livre.

A malha foi criada no software ANSYS ICEM e é mostrada por Lovatto (2013). Somam-se 6,8 milhões de volumes tetraédricos – e prismáticos na região de camada-limite –, onde o menor índice de qualidade é 0,16, e menos de 0,002% destes elementos têm qualidade inferior a 0,25. Lovatto (2013) também disponibiliza os parâmetros de simulação numérica utilizados no ANSYS Fluent.

6.1.2. Resultados do rotor completo em rotação

Para o cálculo da camada limite, o modelo de turbulência utilizado, k-ω SST, exige um y^+ próximo de 1 e inferior a 4. A Fig. 5 mostra que o campo de y^+ ficou dentro do intervalo esperado. Na mesma figura, a linha vertical representa uma seção de pá a 30% do raio do rotor, de onde foi obtida a curva de coeficiente de pressão[1] (C_{pr}), apresentada na Fig. 6. A curva azul representa os resultados obtidos por este estudo em comparação com os dados experimentais de Hand *et al.* (2001), e com os resultados numéricos de outros autores (Sezer-Uzol e Long, 2006; Ribeiro, 2012).

O empuxo (F) é o somatório das forças – sobre as pás e o cubo – na direção z positivo, resultando 1255N. Dados adicionais, como a força e torque em cada pá e em outras direções, são apresentados por Lovatto (2013).

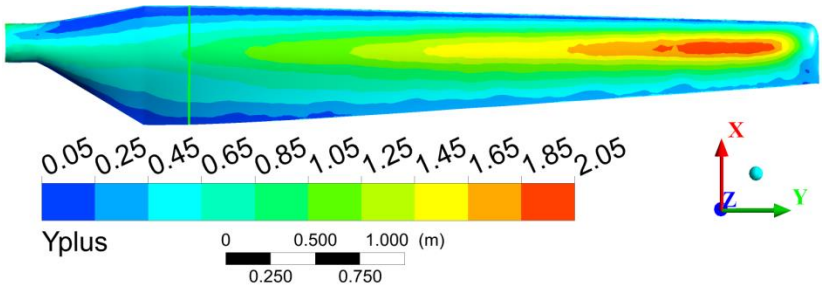

Figura 5. Campo de y^+ sobre o intradorso da pá superior.

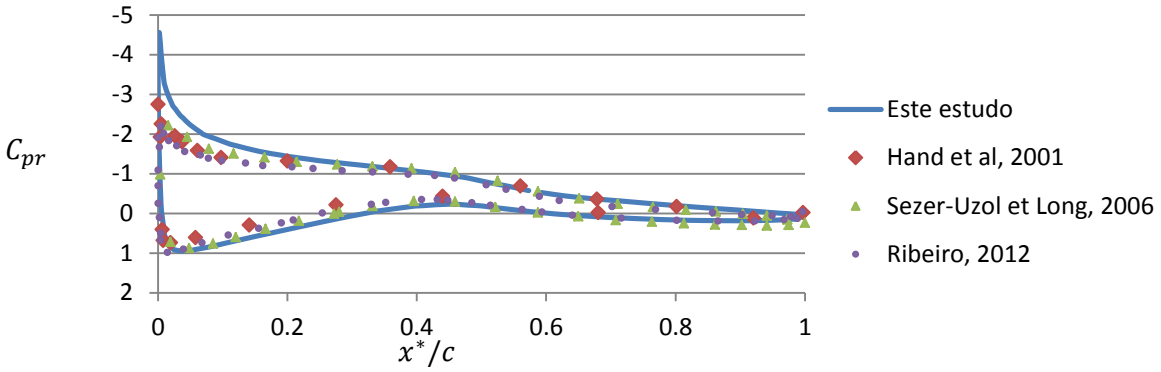

Figura 6. Coeficiente de pressão (C_{pr}) em função da distância a partir do bordo de ataque da pá (x^*) adimensionalizada pela corda (c) numa seção a 30% do raio do rotor.

Os resultados numéricos obtidos para o coeficiente de pressão são coerentes. Embora não tenham completa aderência com os resultados experimentais de teste em túnel de vento (Hand *et al.*, 2001), este afastamento não representa uma limitação considerando a proposta deste estudo: analisar a esteira obtida por CFD com o empuxo obtido por CFD, não com o empuxo real. Na próxima etapa, o empuxo calculado numericamente (1255N) é imposto dentro do domínio esférico sem o rotor por meio de uma taxa de variação da quantidade de movimento distribuída neste domínio, e espera-se que a mesma esteira seja reproduzida. O objetivo desta pesquisa é a comparação entre duas esteiras aerodinâmicas obtidas por CFD: aquela resultante da presença do rotor em rotação e aquela resultante de um sumidouro de quantidade de movimento *equivalente* ao empuxo sobre o rotor em rotação.

A esteira resultante é apresentada na curva verde contínua da Fig. 7, juntamente com os resultados de esteira obtidos pela imposição do empuxo de 1255N por meio de um sumidouro de quantidade de movimento no volume da esfera, para malhas de densidades diferentes.

6.2. Imposição do empuxo no domínio esférico por meio de um sumidouro de quantidade de movimento

6.2.1. Descrição do problema do sumidouro de quantidade de movimento no domínio esférico

Nesta etapa, o rotor foi removido do cálculo. Migrando para o ANSYS CFX pelos motivos expostos na Seção 6.1.1, agora o empuxo F, igual a 1255N, foi imposto como taxa de variação (negativa) da quantidade de movimento dentro do volume esférico vazio. Com exceção da ausência do rotor, a geometria foi mantida inalterada. As condições físicas

[1] O sub-índice pr substitui o tradicional p com a finalidade de não confundir com o coeficiente de potência, C_p. A maneira pela qual C_{pr} foi calculado é mostrada por Lovatto (2013).

também não mudaram, embora os parâmetros que representam tais condições físicas, bem como os parâmetros numéricos, tenham mudado devido à mudança de software, e são apresentados por Lovatto (2013).

Devido à retirada do rotor, a malha acaba sendo simplificada na região da esfera, reduzindo-se drasticamente o número de nós de cálculo.

O mesmo caso foi calculado em seis malhas de densidades diferentes na região da esfera e da esteira, com a finalidade de escolher a densidade que mais fielmente reproduz a esteira resultante do rotor completo. O tamanho inicial dos volumes foi de 3,7m, seguindo-se uma razão de refinamento de 1,3 até a malha mais refinada, com tamanho dos volumes de 1,0m, sendo este igual ao refinamento da esteira no caso do rotor completo.

Tanto para o rotor completo quanto para as etapas de teste do modelo de esfera atuadora, a esteira é calculada sobre o eixo z (eixo paralelo ao vento e que passa pelo centro da esfera). Foram definidas diversas seções circulares normais ao eixo z, de mesmo diâmetro da esfera, sobre diversas posições ao longo do eixo z. O valor médio de w (componente da velocidade paralela ao eixo z) foi calculado em cada uma dessas seções. Chama-se tal velocidade de $\overline{w_s}$ (velocidade w média na seção).

6.2.2. Resultados do sumidouro de quantidade de movimento no domínio esférico

A esteira (valor de $\overline{w_s}$ ao longo do eixo z) resultante de cada malha é mostrada na Fig. 7, juntamente com a esteira do rotor completo obtida na Etapa 1. Lovatto (2013) disponibiliza os perfis de pressão, obtidos da mesma maneira.

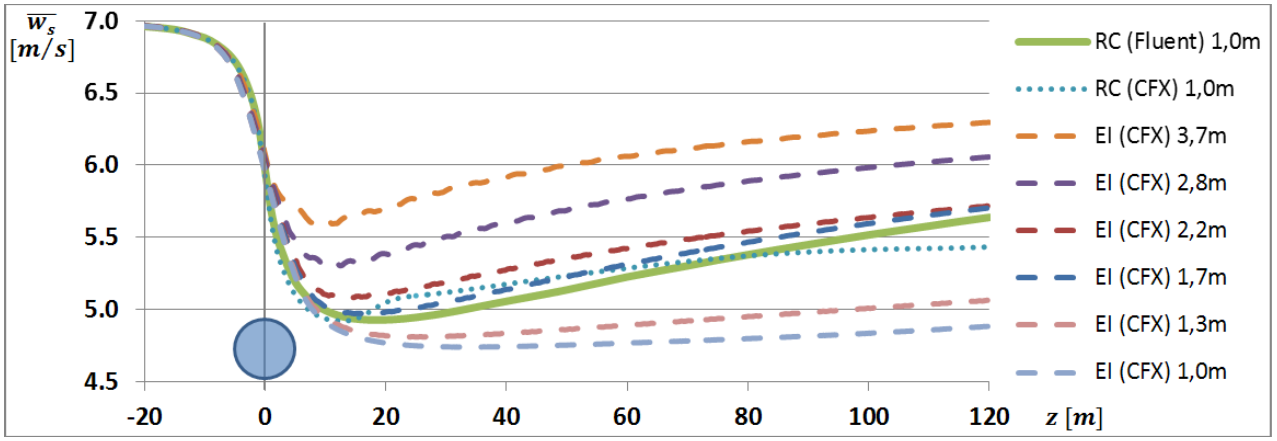

Figura 7. Perfis de esteira obtidos pelo cálculo do rotor completo (RC, linha verde contínua) no Fluent e no CFX e pelo cálculo com empuxo imposto (EI, linhas tracejadas) no CFX sobre malhas com volumes de tamanhos diferentes. O círculo azul representa a dimensão e posição da esfera sobre o eixo z.

Os resultados apresentados na Fig. 7 mostram que não há independência de malha com o refinamento na região da esteira. Inclusive, a esteira obtida por empuxo imposto na malha com volumes de 1,0m é visivelmente superestimada (maior queda de velocidade) em relação à esteira obtida pelo rotor completo, cujo tamanho dos volumes, nessa região, é o mesmo. Malhas grosseiras subestimam a esteira (menor queda de velocidade) devido ao excesso de difusão numérica.

Para dar continuidade aos testes do modelo de esfera atuadora propriamente dito, foi escolhida a malha com volumes de 1,7m na esteira, cujos resultados foram os mais próximos do rotor completo.

Mesmo com o empuxo F não sendo calculado pelo modelo, mas imposto em 1255N, as equações utilizadas no modelo acusam $C_p\left(U_f = 7\,m/s\right) = 0{,}38996$. Então, para testar o modelo com o empuxo não imposto, foi utilizado como dado de entrada uma curva arbitrária $C_p = f(U_\infty)$ tal que $C_p\left(U_\infty = U_f = 7\,m/s\right) = 0{,}38996$.

6.3. Teste do modelo de esfera atuadora para vento incidente forçado a 7m/s

Em seguida, o modelo de esfera atuadora foi testado sem se impor F, mas na sua capacidade de reproduzir os valores esperados de U_∞, C_p, a e F (as incógnitas do modelo) para o caso-teste de $U_f = 7\,m/s$. Após a convergência do modelo fluidodinâmico, espera-se que o modelo de esfera atuadora ofereça como saída $U_\infty = U_f = 7\,m/s$, $C_p(U_\infty) = 0{,}38996$, $a\left(C_p\right) = 0{,}1283$ e $F = 1255N$.

Para que os resultados fossem satisfatórios com 100% de acerto, os testes possibilitaram a determinação de fatores multiplicadores de a e U_∞, conforme as Eqs. (14) e (15).

$$a^* = 1{,}04a \tag{14}$$

$$U_\infty{}^* = 1{,}0197U_\infty \tag{15}$$

onde a^* e $U_\infty{}^*$ são os valores corrigidos de a e U_∞ após a convergência do processo iterativo descrito na Seção 5.2. Finalmente, o valor de C_p obtido pelo processo iterativo também é corrigido para que seja função de $U_\infty{}^*$ (corrigido) ao invés de U_∞, ou seja, definiu-se $C_p{}^* = f(U_\infty{}^*)$, obtido pela curva de coeficiente de potência. Essas correções oferecem 100% de acerto para o valor esperado das quatro incógnitas do modelo de esfera atuadora e resulta no mesmo perfil de

esteira do caso com empuxo imposto, validando o modelo para o caso-teste de vento incidente forçado $U_f = 7m/s$, no software ANSYS CFX com malha tetraédrica de 1,7m de resolução.

6.4. Teste do modelo de esfera atuadora para diferentes velocidades de vento incidente forçado

Com o propósito de testar o modelo de esfera atuadora para velocidades incidentes forçadas diferentes de 7m/s, foram impostos na entrada do domínio os valores de 2, 3, 5, 8, 13 e 21 m/s para U_f, arbitrários e pertencentes à série de Fibonacci. Como os fatores de correção descritos na Seção 6.3 foram calibrados para $U_f = 7m/s$, é natural esperar que os valores finais tenham certo nível de erro para outras velocidades, mas que seja tolerável.

Como resultado dos testes para diferentes velocidades, o erro da velocidade de vento incidente calculada corrigida, $U_\infty{}^*$, relativo à velocidade incidente forçada, U_f, não passa de 2%, como verificado por Lovatto (2013). A Fig. 8a mostra a igualdade entre os valores de velocidade forçada (U_f) e calculada corrigida ($U_\infty{}^*$). A curva do coeficiente de potência arbitrária utilizada para os testes é apresentada na Fig. 8b, juntamente com os pontos ($U_\infty{}^*$, $C_p{}^*$) resultantes dos cálculos para os diferentes U_f testados. Lovatto (2013) mostra que a maioria dos erros são inferiores a 5%.

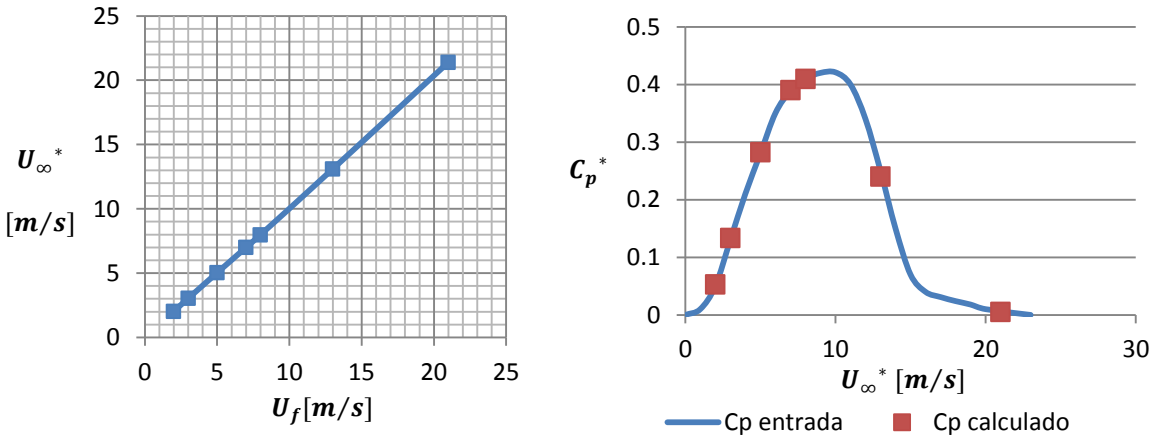

(a) (b)

Figura 8. (a) Igualdade entre os valores de velocidade incidente forçada no domínio (U_f) e a velocidade incidente calculada e corrigida pelo modelo ($U_\infty{}^*$); e (b) a consequente sobreposição dos pontos ($U_\infty{}^*$, $C_p{}^*$) calculados pelo modelo sobre a curva de coeficiente de potência da máquina, arbitrária.

Dado que $P_\infty{}^* = \frac{1}{2}\rho {U_\infty{}^*}^3 A_d$ é a potência aerodinâmica disponível incidente sobre a máquina, com $C_p{}^*$ pode-se calcular, pela Eq. (10), a potência aerodinâmica que cada máquina extraiu (P_{ext}), bem como a potência elétrica (P_{ele}) pela Eq. (1), caso a eficiência η seja conhecida.

6.5. Modificação da direção do vento sobre esferas adjacentes

A última etapa deste estudo foi referente à capacidade do modelo de trabalhar com mais de uma esfera no domínio de cálculo, bem como à capacidade de lidar com ventos de diferentes direções.

A Fig. 9a ilustra bem as esteiras geradas por duas esferas espaçadas de quatro diâmetros uma da outra, sob um vento incidente forçado de 7m/s vindo de quatro direções diferentes. Alguns resultados para cada esfera do caso IV são mostrados na Tab. 1.

A Fig. 9b mostra o perfil de velocidade $\overline{w_s}$ para o caso IV da Fig. 9a. Nota-se claramente que a queda de velocidade na região da esfera à direita é menor que a da esfera à esquerda. Isso ocorre porque a potência extraída é menor, afinal a velocidade média incidente é menor.

Tabela 1. Resultados para a esfera da esquerda e da direita no caso IV da Fig. 9a.

Esfera	$U_\infty{}^*[m/s]$	$C_p{}^*$	$U_d[m/s]$	$F[N]$	$P_{ext}[W]$
Esquerda	7,0350	0,39067	6,0269	1273	7672
Direita	5,8797	0,34158	5,1672	750	3876

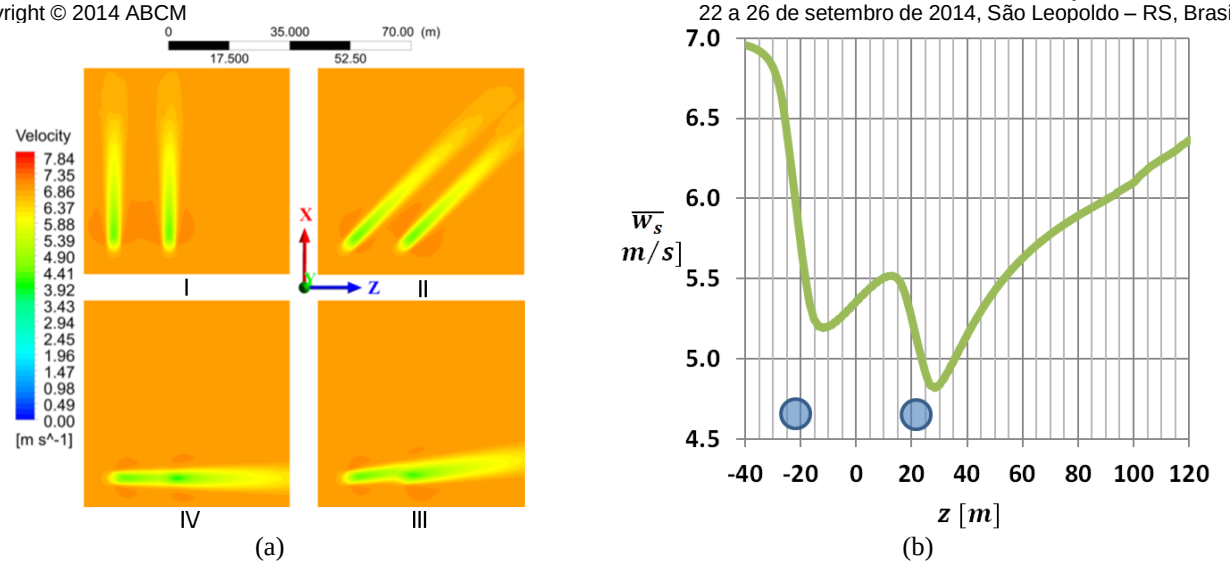

Figura 9. (a) Campos de velocidade para duas esferas adjacentes com vento vindo de quatro direções diferentes e (b) perfil de velocidade $\overline{w_s}$ para o caso IV da Fig. 6.7a. Os círculos azuis representam a dimensão e a posição das esferas sobre o eixo z.

7. CONCLUSÃO

Os objetivos propostos foram atingidos com sucesso. Como pôde ser visto na Fig. 8, ao contrário dos trabalhos até então publicados e citados no Capítulo 3, o modelo de esfera atuadora desenvolvido é capaz de calcular de maneira dinâmica a velocidade de corrente livre média incidente sobre cada máquina, bem como seus respectivos coeficientes de potência. Os resultados mostrados na Fig. 9 e na Tab. 1 indicam que a substituição do disco por uma esfera atuadora oferece ao modelo a capacidade de lidar com ventos vindos de qualquer direção, destacando-se que não é necessária a modificação da malha para se adaptar às diferentes direções de vento incidente sobre cada máquina.

Os testes do modelo de esfera atuadora, apresentados neste trabalho pela primeira vez, ainda resultam em fatores de correção e esteira dependentes do software utilizado e, especialmente, da resolução de discretização do domínio (Fig. 7). Suspeita-se que a maior queda de velocidade em malhas refinadas esteja relacionada à modelagem da turbulência. Visando o aprimoramento do modelo, estão em andamento novos estudos com o objetivo de chegar a uma compreensão sobre o problema da discretização do domínio, bem como dos fatores de correção.

8. REFERÊNCIAS BIBLIOGRÁFICAS

ANSYS Inc., 2010, “ANSYS CFX-Solver Theory Guide”, Release 13.0.

ANSYS Inc., 2009, “ANSYS Fluent 12.0 Theory Guide”.

Burton, T., Sharpe, D., Jenkins, N., Bossanyi, E., 2001, “Wind Energy Handbook”, Wiley.

Calaf, M., Meneveau, C., Meyers, J., 2010, “Large Eddy Simulation Study of Fully Developed Wind-Turbine Array Boundary Layers”, Physics of Fluids 22, 015110.

Fleck, G. D., 2012, “Simulação de Grandes Escalas para Análise Numérica da Esteira Aerodinâmica da Turbina Eólica NREL UAE Phase VI”, Dissertação de Mestrado, Universidade Federal do Rio Grande do Sul.

Gómez-Elvira, R., Crespo, A., Migoya E., Manuel, F., Hernández, J., 2005, “Anisotropy of Turbulence in Wind Turbine Wakes”, Journal of Wind Engineering and Industrial Aerodynamics 93, pp. 797 - 814.

Hand, M. M., Simms, D. A., Fingersh, L. J., Jager, D. W., Cotrell, J. R., Schreck, S., Larwood, S. M., 2001, “Unsteady Aerodynamics Experiment Phase VI: Wind Tunnel Test Configurations and Available Data Campaigns”, NREL.

Lovatto, M. L., 2013, “Modelagem Computacional da Esteira Aerodinâmica de Turbinas Eólicas Baseada em Sumidouro de Quantidade de Movimento”, Monografia, Universidade Federal do Rio Grande do Sul.

Norris, S. E., Cater, J. E., Stol, K. A., Unsworth, C. P., 2010, “Wind Turbine Wake Modelling using Large Eddy Simulation”, 17th Australian Fluid Mechanics Conference.

Ribeiro, A. F. P., 2012, “Otimização e Dinâmica dos Fluidos Computacional Aplicadas a Turbinas Eólicas”, Dissertação de Mestrado, Universidade Federal do Rio Grande do Sul.

Sezer-Uzol, N., Long, L. N., 2006, “3-D Time-Accurate CFD Simulations of Wind Turbine Rotor Flow Fields”, AIAA-2006-0394.

Wenzel, G. M., 2010, “Análise Numérica da Esteira de Turbinas Eólicas de Eixo Horizontal: Estudo Comparativo com Modelos Analíticos”, Dissertação de Mestrado, Universidade Federal do Rio Grande do Sul.

9. NOTA DE RESPONSABILIDADE

Os autores são os únicos responsáveis pelo material impresso incluído neste artigo.

INFLUENCE OF RADIATION ON TURBULENCE IN A 2D AXISYMMETRIC TURBULENT FLAME SIMULATION

Felipe Roman Centeno, frcenteno@unisinos.br
Escola Politécnica - Universidade do Vale do Rio dos Sinos (UNISINOS) – Av. Unisinos, n. 950, CEP 93022-000, São Leopoldo, RS, Brazil

Elizaldo Domingues dos Santos, elizaldosantos@furg.br
Escola de Engenharia – Universidade Federal do Rio Grande (FURG) – Av. Itália, km 8, C.P. 474, Rio Grande, RS, Brazil

Cristiano Vitorino da Silva, cristiano@uricer.edu.br
Departamento de Engenharia e Ciências da Computação – Universidade Regional Integrada do Alto Uruguai e das Missões (URI) – Av. Sete de Setembro, n. 1621, CEP 99700-000, Erechim, RS, Brazil

Francis Henrique Ramos França, frfranca@mecanica.ufrgs.br
Departamento de Engenharia Mecânica - Universidade Federal do Rio Grande do Sul (UFRGS) – Rua Sarmento Leite, n. 425, CEP 90050-170, Porto Alegre, RS, Brazil

Abstract. *This paper presents a study of the influence of thermal radiation on turbulence in the simulation of a turbulent, non-premixed methane-air flame. In such a problem, two aspects need to be considered for a precise evaluation of the thermal radiation: the turbulence-radiation interactions (TRI), and the radiative properties of the participating species, which are treated here with the weighted-sum-of-gray-gases (WSGG) model based on recently obtained correlations from HITEMP2010 database. The chemical reactions rates were considered as the minimum values between the Arrhenius and Eddy Break-Up rates. A two-step global reaction mechanism was employed, while the turbulence modeling was considered via standard k–ε model. The source terms of the energy equation consisted of the heat generated in the chemical reaction rates as well as in the radiation exchanges. The discrete ordinates method (DOM) was employed to solve the radiative transfer equation (RTE), including the TRI. Comparisons of simulations with/without radiation demonstrated that radiation influenced turbulent-properties (root mean square of velocity and temperature fluctuations, and turbulent kinetic energy of the velocity fluctuations). Radiation smoothed turbulent-properties fields. The influence of radiation was more important on the temperature fluctuations than on the velocity fluctuations.*

1. INTRODUCTION

Combustion problems involve a number of coupled phenomena, such as fluid mechanics, heat transfer, and chemical kinetics of gaseous species and soot, in which thermal radiation can be the dominant heat transfer mode. Heat transfer directly affects the temperature field and, therefore, chemical kinetics and thermophysical properties (as density, heat capacity, and viscosity).

An important phenomenon to be considered in turbulent combustion simulations is the so-called turbulence-radiation interactions (TRI). Turbulence and radiation are physical phenomena of high complexity even when analyzed independently. In turbulent flow, it is not possible to deal with these phenomena in an independent way, but in a coupled form. In turbulent reactive flows, temperature and species concentration fields can undergo high levels of fluctuations, leading to variations on the radiative field. Since the radiative field is present in the energy conservation equation as a source term, and turbulent fluctuations influence radiative transfer, then turbulence also influences the temperature and density fields. Therefore, since the density field influences the velocity field and so the scalar fluctuations, it can be concluded that turbulence influences radiation and radiation influences turbulence. Few attention has been devoted to investigate the influence of radiation on turbulence. As the authors best knowledge, the only investigation dealing with such influence in high temperature flows is in Soufiani (1991), where it was found that radiation may smooth the intensity of temperature fluctuations. On the other hand, the influence of turbulence on radiation has been received much more attention.

The first coupled calculation of radiative transfer in reactive flow to investigate TRI was reported in Song and Viskanta (1987), in which property functions were prescribed for the combustion gases. The most recent literature has been focused on analyzing the most important TRI correlations (temperature self-correlation, absorption coefficient-temperature correlation, absorption coefficient self-correlation, and absorption coefficient-radiation intensity correlation). Some examples of coupled investigations were reported in Li and Modest (2002a), Habibi et al. (2007a), Poitou et al. (2012) and Gupta et al. (2013). Results pointed that the absorption coefficient-temperature correlation and the temperature self-correlation are the most important TRI terms in reactive flows (Li and Modest, 2002a; Li and Modest, 2002b; Gupta et al., 2013; Habibi et al., 2007b). Furthermore, it was found in Gupta et al. (2013) and in Modest and Mehta (2006) that the absorption TRI term (correlation between absorption coefficient and radiation intensity fluctuations, which is neglected in *optically thin fluctuation approximation* - OTFA) is important only for optically thick

medium.

An accurate description of radiative heat transfer is of great importance for simulations of combustion systems. Modeling thermal radiation exchanges in combustion gases (such as water vapor and carbon dioxide) is a difficult task due to the highly complex dependence of the absorption coefficient with the wavenumber, which is typically characterized by hundreds of thousands or millions of spectral lines. Thus, the integration of the radiative transfer equation (RTE) over the spectrum would be very expensive or even impossible without the use of spectral or global models. As a first simplification, the RTE is frequently solved with the gray gas (GG) model, where the dependence of the absorption coefficient over the wavenumber is simply neglected. In order to provide realistic results, more refined models are however needed. As one advance to the GG model, the weighted-sum-of-gray-gases (WSGG) (Hottel and Sarofim, 1967) makes perhaps the best compromise between accuracy and computation demand, especially in global simulation of combustion processes in which the RTE is solved together with fluid flow, chemical kinetics and energy equation. In the WSGG model the entire spectrum is represented by a few bands having uniform absorption coefficients, each band corresponding to a gray gas. The weighting coefficients account for the contribution of each gray gas, and can be interpreted as the fractions of the blackbody energy in the spectrum region where the gray gases are located. In practice, those coefficients are obtained from fitting total emittances computed from experimental-gas-data, such as those presented in Smith et al. (1982) and Smith et al. (1987). In a recent study, Demarco et al. (2011) assessed several radiative models, such as the narrow band, wide band, GG and global models such as the WSGG and spectral-line-based WSGG (SLW). According to the authors, the WSGG is very efficient from a computational point of view, and can yield accurate predictions, although significant discrepancies can appear in high soot loadings. Simplified radiative property models, such as the WSGG or GG models, are often used in computational fluid dynamics (CFD) to simulate combustion problems. The main reason is that implementing more sophisticated models may become excessively time consuming when fluid flow/combustion/radiative heat transfer are coupled.

This study presents a numerical RANS (Reynolds Average Navier-Stokes) simulation of a turbulent non-premixed methane-air flame in a cylindrical combustion chamber taking into account radiation effect of non-gray gases by means WSGG correlations (Dorigon et al., 2013) generated from HITEMP 2010 database (Rothman et al., 2010) and including TRI (Snegirev, 2004), with the objective of evaluating the influence of radiation on turbulence, since such influence has been received much less attention in the literature than the influence of turbulence on radiation.

2. PROBLEM STATEMENT

The physical system consists of the natural gas combustion chamber described in Garréton and Simonin (1994), which presents several challenges for thermal modeling in the sense that the flame is turbulent, and with highly non-isothermal, non-homogeneous medium.

Keeping the same conditions as described in Garréton and Simonin (1994), the cylindrical chamber has length and diameter of 1.7 m and 0.5 m, respectively, as shown in Fig. 1. Natural gas is injected into the chamber by a duct aligned with the chamber centerline, leading to a non-swirling flame. The burner provides the necessary amount of air and natural gas as required by the process. In all cases a fuel excess of 5% (equivalence ratio of 1.05) was prescribed. For a fuel mass flow rate of 0.01453 kg/s at a temperature of 313.15 K, this requires an air mass flow rate of 0.1988 kg/s, at a temperature of 323.15 K. The fuel enters the chamber through a cylindrical duct having 0.06 m diameter, while air enters the chamber through a centered annular duct having a spacing of 0.02 m. For such mass flow rates, the fuel and air velocities are 7.23 and 36.29 m/s, respectively. The Reynolds number at the entrance, approximately 1.8×10^4, points that the flow is turbulent. The inlet air is composed of oxygen (23% in mass fraction), nitrogen (76%) and water vapor (1%), while the fuel is composed of 90% of methane and 10% of nitrogen. The burner power is about 600 kW. The fan and the other external components are not included in the computational domain, although their effects are taken into account through the inlet flow conditions. Buoyancy effects are neglected due to the high velocities that are provided by the burner. To complement the boundary conditions, Figure 1 depicts the thermal boundary conditions of the cylindrical chamber: symmetry in the centerline, and prescribed temperature on the walls, equal to 393.15 K. In addition, impermeability and no-slip conditions were assumed on the walls. In the symmetry line, it was assumed that both radial velocity and velocity gradient were null. The same procedure was adopted for the turbulent kinetic energy and its dissipation rate, enthalpy, and species concentrations in the symmetry line. In the outlet, null diffusive fluxes were assumed for all variables, the axial velocity component was corrected by a factor to satisfy mass conservation, and the radial velocity was imposed to be null. For radiation modeling, both chamber walls, inlet and the outlet ducts were modeled as black surfaces. The temperature at the inlet duct was prescribed at the fuel and the oxidant temperatures, while the temperature at the outlet duct was equal to the outlet flow bulk temperature.

In addition, in the inlet, the velocity and concentration profiles were assumed uniform in the axial direction, while the turbulent kinetic energy was computed as $k = \tfrac{3}{2}(u_{in}i)^2$, where i is the turbulence intensity (prescribed as 6% and 10% for the air and for the fuel streams, respectively) and u_{in} is the inlet axial mean velocity, and for the turbulent kinetic energy dissipation rate, the relation $\varepsilon = \left(C_\mu^{3/4}k^{3/2}\right)/l$ was employed, where l is the turbulence characteristic length scale (taken as 0.04 m and 0.03 m for the air and the fuel streams, respectively). For both energy and momentum

conservation equations, standard wall functions were applied for the combustor walls treatment which take into account the viscous layer dominated by molecular diffusion close to the walls (Patankar, 1980).

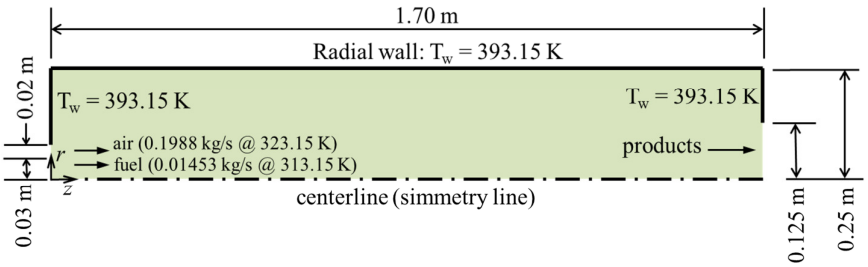

Figure 1. Combustion chamber geometry

3. MATHEMATICAL FORMULATION

The proposed work is stated as: considering a steady turbulent non-premixed methane-air flame in a cylindrical chamber, compute the temperature, species concentrations and velocity fields, and verify the influence of radiation on turbulence main parameters, taking into account the WSGG model based on HITEMP 2010 data (Dorigon et al., 2010) and TRI effects (Snegirev, 2004).

3.1. Governing equations

Conservation equations for mass, momentum in the axial and radial directions, k-ε turbulence model, energy, and chemical species (CH_4, O_2, CO_2, CO, H_2O) for steady low-Mach flow in 2D axisymmetric coordinates are solved. Detailed information about governing equations can be found in Centeno et al. (2014).

3.2. Combustion kinetics

As a basic assumption, it is considered that the combustion process occurs at finite rates with methane oxidation taking two global steps:

$$2CH_4^{(16)} + 3\left(O_2^{(32)} + 3.76N_2^{(28)}\right) \rightarrow 2CO^{(28)} + 4H_2O^{(18)} + 11.28N_2^{(28)}$$
$$2CO^{(28)} + 1\left(O_2^{(32)} + 3.76N_2^{(28)}\right) \rightarrow 2CO_2^{(44)} + 3.76N_2^{(28)}$$

The rate of formation or consumption, $R_{\alpha,c}$, of each α-th species in each c-th reaction (there are two reactions in the present study, so c = 2) is obtained by the Arrhenius-Magnussen's model (Eaton et al., 1999; Turns, 2000; Fluent, 2009), in which the rate of formation or consumption of the chemical species are taken as the smallest one between the values obtained from Arrhenius kinetics or from Magnussen's equations (Eddy Break-Up) (Magnussen and Hjertager, 1977). The investigation in Silva et al. (2007), which considered the same combustion chamber, provided the relative importance of the combustion kinetics by computing the Damköhler number, and found that the combustion process is governed by Arrhenius rates in the flame core and by Magnussen's rates in all the other regions. This formulation was also successfully employed in Silva et al. (2007), Nieckele et al. (2001), Centeno et al. (2013), and Centeno et al. (2014).

The average volumetric rates of formation or consumption of the α-th chemical species, R_α, which appears in both energy and species conservation equations, are then computed from the summation of the volumetric rates of formation or consumption in all the c-th reactions where the α–th species is present, i.e., $R_\alpha = \sum_c R_{\alpha,c}$.

3.3. The weighted-sum-of-gray-gases (WSGG) model

The original formulation of the WSGG model (Hottel and Sarofim, 1967) consists of expressing the total gas emittance by weighted-sum-of-gray-gas emittances. The emission weighted factors, $a_j(T)$, and the absorption coefficients, κ_j, for the j^{th} gray gas are in general determined from the best fit of the total emittance with the constraint that the a_j must sum to 1. From a more general point of view, the WSGG model can be applied as a non-gray gas model (Modest, 1991), solving the radiative transfer equation (RTE) for the N_G (number of gray gases) plus one (j = 0, representing spectral windows where H_2O and CO_2 are transparent to radiation) for a clear gas:

$$\frac{dI_j}{ds} = -\kappa_j I_j + \kappa_j a_j(T) I_{b,j}(T) \tag{1}$$

in which the emission weighted factor $a_j(T)$ is given by,

$$a_j(T) = \sum_{i=1}^{5} b_{j,i} T^{i-1} \tag{2}$$

with j varying from 0 to N_G, and $I = \sum_{j=0}^{N_G} I_j$ .The functional dependence of the weighted factors with temperature is generally fitted by polynomials, Eq. (2), where the polynomial coefficients ($b_{j,i}$) as well as the absorption coefficients for each gray gas can be tabulated. For H_2O/CO_2 mixtures, these coefficients are generally established for particular ratios of the partial pressure, p_{H2O}/p_{CO2}, which could limit the application of the method. In the present study the weighted factors polynomial coefficients and absorption coefficients were taken from Dorigon et al. (2013) for $p_{H2O}/p_{CO2} = 2$. Such WSGG correlations were fitted from HITEMP 2010 (Rothman et al., 2010), which is the most recent molecular spectroscopic database for high temperatures. In the same study, Dorigon et al. (2013) compared results obtained with the new coefficients against line-by-line (LBL) benchmark calculations for one-dimensional non-isothermal and non-homogeneous problems, finding consistently satisfactory agreement between the LBL and WSGG solutions, with maximum and average errors of about 5% and 2% for different test cases. Centeno et al. (2013) tested the coefficients presented in Dorigon et al. (2013) against old ones presented in Smith et al. (1982) for an axisymmetric cylindrical combustion chamber, and found that the new coefficients provided better agreement with experimental data. It is assumed here that the contribution from other radiating species, such as CO e CH_4, is negligible. The contribution from CO in the combustion gases is negligible, since its molar concentration is not expected to exceed 0.1%, while the contribution from CH_4 is even lower (Coelho et al., 2003).

3.4. Turbulence-radiation interactions

The radiative transfer equation (RTE) is applicable to instant quantities that fluctuate in a turbulent flow, while the RANS turbulence model can only provide time-averaged (mean) quantities and, possibly, their mean square fluctuations. Considering the spectrally integrated form of the RTE, and time averaging it, results in:

$$\frac{d\bar{I}}{ds} = -\overline{\kappa I} + \overline{\kappa I_b} \tag{3}$$

The absorption coefficient-radiation intensity correlation, i.e., the first term in the right hand of Eq. (3), is expressed as $\overline{\kappa I} = \bar{\kappa}\bar{I} + \overline{\kappa' I'}$. Several studies have neglected the second term on the right hand side of this expression ($\overline{\kappa' I'}$) based on arguments of Kabashnikov and Kmit (1979), known as the optically thin fluctuation approximation (OTFA), which relies on the assumption that the absorption coefficient fluctuations are weakly correlated with the radiation intensity fluctuations, i.e., $\overline{\kappa' I'} \approx 0$, if the mean free path for radiation is much larger than turbulence integral length scale.

In the second term in the right hand of Eq. (3), which is proportional to $\overline{\kappa T^4}$, the instant values of κ and T correlate in a turbulent flow. In the present study, it is applied the approximation proposed in Snegirev (2004), in which both the absorption coefficient-temperature correlation and the temperature self-correlation are considered. These two TRI correlations were found to be the most important in reactive flows (Li and Modest, 2002a; Li and Modest, 2002b; Habibi et al., 2007b; Gupta et al., 2013). Decomposition of temperature and absorption coefficient into average and fluctuating components, $T = \bar{T} + T'$ and $\kappa = \bar{\kappa} + \kappa'$, followed by time averaging, and neglecting higher order terms, $\overline{\kappa T^4}$ can be written as (Snegirev, 2004):

$$\overline{\kappa T^4} = \bar{\kappa} \cdot \bar{T}^4 \left(1 + C_{TRI}\, 6 \frac{\overline{T'^2}}{\bar{T}^2} + 4 \frac{\overline{T'^2}}{\bar{\kappa} \cdot \bar{T}} \frac{\partial \kappa}{\partial T}\bigg|_{\bar{T}} \right) \tag{4}$$

which allows the consideration of the absorption coefficient-temperature correlation and the temperature self-correlation. The value for C_{TRI} was initially suggested by Snegirev (2004) from data fitting for $\overline{T^4}/\bar{T}^4$ and $\overline{T'^2}/\bar{T}^2$ as presented in Burns (1999), followed by an adjustment leading to a value of 2.5 for C_{TRI}.

To evaluate $\overline{T'^2}$, required for Eq. (4), an additional transport equation for temperature fluctuation variance is solved.

4. RESULTS AND DISCUSSIONS

The set of equations were solved using the finite volume method (Patankar, 1980) by means of a Fortran code. The power-law was applied as the diffusive-advective interpolation function on the faces of the control volumes. The pressure-velocity coupling was made by the SIMPLE method. The resulting system of algebraic equations was solved by the TDMA algorithm, with block correction in all equations except the equations for k and ε. A grid with 140 volumes in the axial direction and 48 volumes in the radial direction was used. The numerical accuracy was checked through the grid convergence index (GCI) method (Roache, 1994; Celik et al., 2008) comparing predicted results calculated using this grid with results obtained using coarser grids. As found, the 140×48 grid provided grid independent results, and required reasonable computational effort. The grid is uniformly spaced in both radial and axial directions. The radiative transfer calculations were performed with the discrete ordinates method using the same spatial grid and S_6 quadrature. Convergence criteria were based on the imposition that the normalized residual mass in the SIMPLE method was 10^{-8}. For the other equations the maximum relative variation between iterations was 10^{-6}.

In order to study the effect of the gas radiation heat transfer inside the combustion chamber, allowing to analyze its influence on turbulence, two different scenarios were considered. In the first scenario, radiation was completely ignored, while in the second scenario, radiation was completely considered, including TRI. Comparisons were made to verify how the different radiative scenarios affect some turbulence-related parameters, as the root mean square (RMS) of the temperature fluctuations and the turbulent kinetic energy of the velocity fluctuations.

Figures 2 and 3 present fields of the turbulent kinetic energy of the velocity fluctuations and the root mean square of the temperature fluctuations (computed from the temperature fluctuation variance square root: $T'_{rms} = \sqrt{\overline{T'^2}}$), respectively, computed in both scenarios – neglecting radiation calculations and considering them. These two turbulence-related properties were selected to verify the influence of radiation on turbulence. As observed, the different radiative scenarios investigated in the present work did not affect importantly those turbulent properties. However, the turbulent fields were smoothed when comparing results obtained without radiation (fields "a" in Figures 2 and 3) against those results obtained with radiation (fields "b" in Figures 2 and 3), in agreement with the findings in Soufiani (1991).

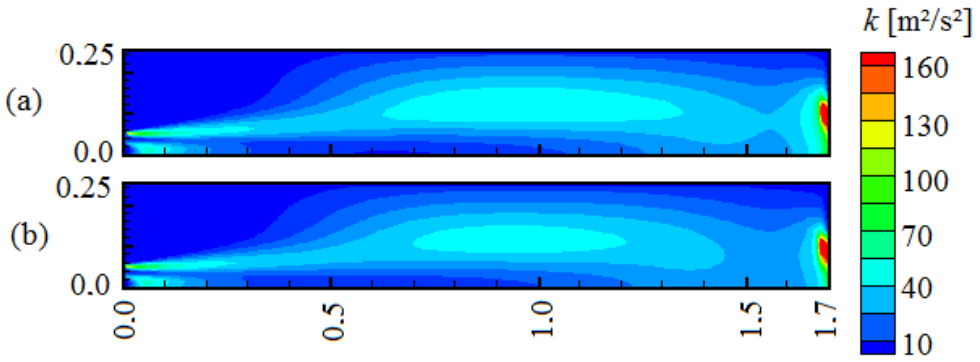

Figure 2. Turbulent kinetic energy fields of the velocity fluctuations: (a) radiation neglected; (b) radiation computed.

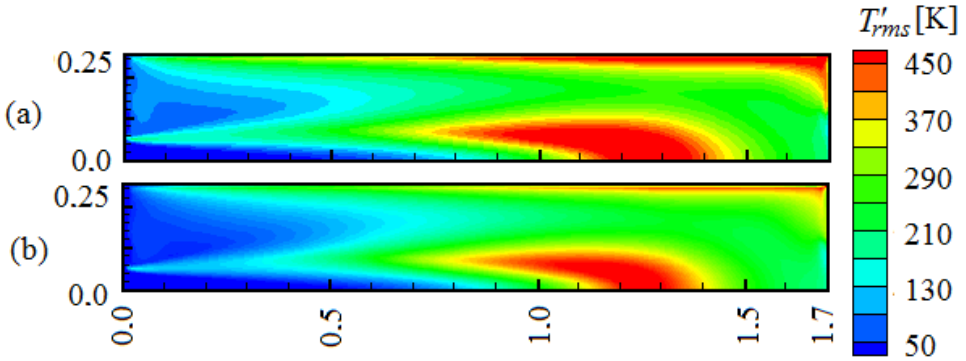

Figure 3. RMS of the temperature fluctuation fields: (a) radiation neglected; (b) radiation computed.

Additionally, Figures 4 and 5 present profiles of the root mean square of the temperature fluctuations and of the root mean square of the velocity fluctuations (considering fully developed isotropic turbulence, RMS of the velocity

fluctuations can be computed as the square root of the turbulent kinetic energy of the velocity fluctuations: $v'_{rms} = \sqrt{k}$). In such figures, profiles are shown for the axial direction at the chamber symmetry-line and for the radial direction at axial position z = 1.3 m. It can be observed that the influence of radiation on those turbulence-related properties was small but it was not negligible (for example, a difference of nearly 70 K for the rms temperature fluctuation was noticed for r = 0.0 m at z = 1.3 m). Radiation tended to smooth turbulent fluctuations of temperature and velocity. Besides, the influence of radiation was more pronounced on the temperature fluctuations than on the velocity fluctuations; such behavior can be especially important for consideration in problems involving transition from laminar to turbulent flows, which in general are determined considering isothermal flows.

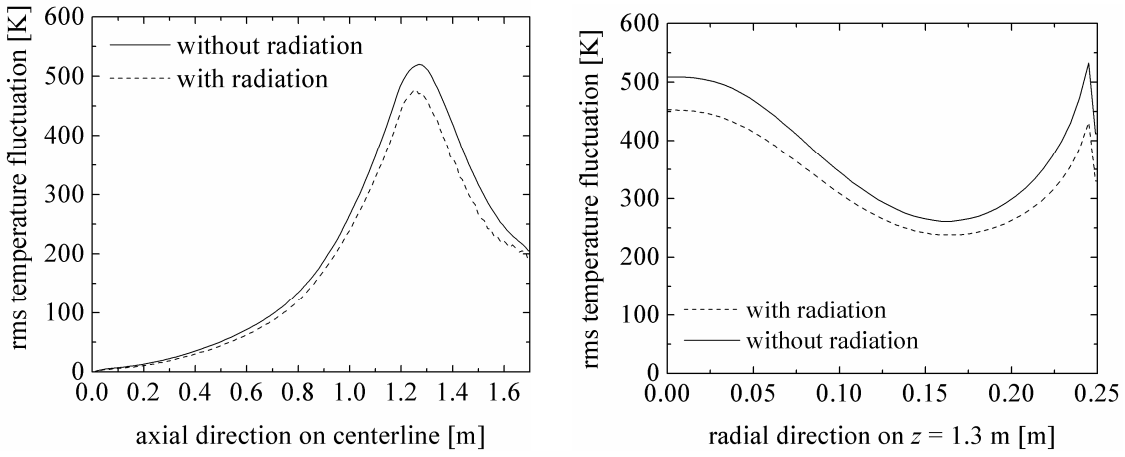

Figure 4. RMS of the temperature fluctuations: profiles at chamber symmetry-line (axial direction) and at z = 1.3 m (radial direction).

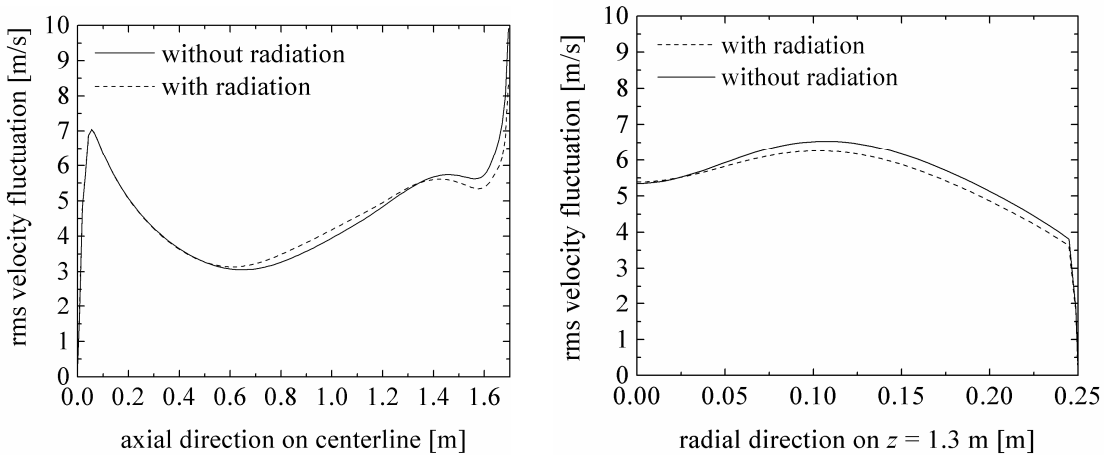

Figure 5. RMS of the velocity fluctuations: profiles at chamber symmetry-line (axial direction) and at z = 1.3 m (radial direction).

5. CONCLUSIONS

This study presented an analysis of the influence of thermal radiation on the turbulence in a turbulent non-premixed methane–air flame in a cylindrical combustion chamber. The radiation field was computed with the WSGG model using recently obtained correlations (Dorigon et al., 2013) based on the up-to-date HITEMP2010 and considering TRI effects (Snegirev, 2004). A two-step global reaction mechanism was used and turbulence modeling was considered via standard k-ε model. The RTE was solved employing the discrete ordinates method. This work showed the influence of radiation on turbulence in a combustion problem by means of two scenarios: radiation neglected from calculations, and radiation included into calculations. Comparison of the results obtained from the different radiative scenarios showed that radiation did not importantly influence the turbulence-related properties (root mean square of the temperature fluctuations and of the velocity fluctuations, and the turbulent kinetic energy of the velocity fluctuations), but such

influence, despite small, was not negligible. Radiation tended to smooth turbulent fields, in agreement with results reported in the literature for high temperature flows. The influence of radiation on temperature fluctuations was more important than its influence on velocity fluctuations. Some possible future advances in the radiation-turbulence analysis are testing different turbulence models (other than standard k-ε) and performing simulations with different turbulence methodology (other than RANS).

6. REFERENCES

Celik, I.B., Ghia, U., Roache, P.J., Freitas, C.J., Coleman, H., Raad, P.E., 2008, "Procedure for estimation and reporting of uncertainty due to discretization in CFD applications", ASME Journal of Fluid Engineering, Vol. 130, pp. 078001-1 - 078001-4.

Centeno, F.R., Silva, C.V., França, F.H.R., 2014, "The influence of gas radiation on the thermal behavior of a 2D axisymmetric turbulent non-premixed methane-air flame", Energy Conversion and Management, Vol. 79, pp. 405-414.

Centeno, F.R., Cassol, F., Vielmo, H.A., França, F.H.R., Silva, C.V., 2013, "Comparison of different WSGG correlations in the computation of thermal radiation in a 2D axisymmetric turbulent non-premixed methane-air flame", Journal of the Brazilian Society of Mechanical Sciences and Engineering, Vol. 35, pp. 419-430.

Demarco, R., Consalvi, J.L., Fuentes, A., Melis, S., 2011, "Assessment of radiative property models in non-gray sooting media", International Journal of Thermal Sciences, Vol. 50, pp. 1672-1684.

Dorigon, L.J., Duciak, G., Brittes, R., Cassol, F., Galarça, M., França, F.H.R., 2013, "WSGG correlations based on HITEMP 2010 for computation of thermal radiation in non-isothermal, non-homogeneous H_2O/CO_2 mixtures", International Journal of Heat and Mass Transfer, Vol. 64, pp. 863-873.

Eaton, A.M., Smoot, L.D., Hill, S.C., Eatough, C.N., 1999, "Components, formulations, solutions, evaluations and applications of comprehensive combustion models", Progress in Energy and Combustion Sciences, Vol. 25, pp. 387-436.

Fluent Incorporated. FLUENT Theory Guide, 2009.

Garréton, D., Simonin, O., 1994, "Final results", Proceedings of the 1th workshop of aerodynamics of steady state combustion chambers and furnaces, Vol. 25, pp. 29-35.

Gupta, A., Haworth, D.C., Modest, M.F., 2013, "Turbulence-radiation interactions in large-eddy simulations of luminous and nonluminous non-premixed flames", Proceedings of the Combustion Institute, Vol. 34, pp. 1281-88.

Habibi, A., Merci, B., Roekaerts, D., 2007a, "Turbulence radiation interaction in Reynolds-averaged Navier-Stokes simulations of nonpremixed piloted turbulent laboratory-scale flames", Combustion and Flame, Vol. 151, pp. 303-320.

Habibi, A., Merci, B., Roekaerts, D., 2007b, "The importance of Turbulence-Radiation Interaction in RANS simulations of a turbulent non-premixed laboratory-scale bluff-body flame", Proceedings of the 3rd European combustion meeting.

Hottel, H.C., Sarofim, A.F., 1967, "Radiative Transfer", McGraw-Hill Book Company.

Li, G., Modest, M.F., 2002a, "Application of composition PDF methods in the investigation of turbulence-radiation interactions", Journal of Quantitative Spectroscopy and Radiative Transfer, Vol. 73, pp. 461-472.

Li, G., Modest, M.F., 2002b, "Importance of Turbulence-Radiation Interactions in turbulent reacting flows", Proceedings of 2002 ASME IMECE.

Magnussen, B.F., Hjertager, B.H., 1977, "On mathematical models of turbulent combustion with special emphasis on soot formation and combustion", Proceedings of the 16th symposium (international) on combustion – The Combustion Institute, pp. 719-729.

Modest, M.F., Mehta, R.S., 2006, "Modeling absorption TRI in optically thick eddies", Proceedings of the Eurotherm 78 – computational thermal radiation in participating media II.

Nieckele, A.O., Naccache, M.F., Gomes, M.S.P., Carneiro, J.E., Serfaty, R., 2001, "Models evaluations of combustion process in a cylindrical furnace", Proceedings of 2001 ASME IMECE.

Patankar, S.V., 1980, "Numerical heat transfer and fluid flow", Hemisphere, Washington, DC.

Poitou, D., Amaya, J., El Hafi, M., Cuénot, B., 2012, "Analysis of the interaction between turbulent combustion and thermal radiation using unsteady coupled LES/DOM simulations", Combustion and Flame, vol. 159, pp. 1605-18.

Roache, P.J., 1994, "Perspective: a method for uniform reporting of grid refinement studies", ASME Journal of Fluid Engineering, Vol. 116, pp. 405-413.

Rothman, L.S., Gordon, I.E., Barber, R.J., Dothe, H., Gamache, R.R., Goldman, A., Perevalov, V.I., Tashkun, S.A., Tennyson, J., 2010, "HITEMP, the high-temperature molecular spectroscopic database", Journal of Quantitative Spectroscopy and Radiative Transfer, Vol. 111, pp. 2130-2150.

Silva, C.V., França, F.H.R., Vielmo, H.A., 2007, "Analysis of the turbulent, non-premixed combustion of natural gas in a cylindrical chamber with and without thermal radiation", Combustion Science and Technology, Vol. 179, pp. 1605-30.

Smith, T.F., Al-Turki, A.M., Byun, K.H., Kim, T.K., 1987, "Radiative and Conductive Transfer for a Gas/Soot Mixture

Between Diffuse Parallel Plates", Journal of Thermophysics Heat Transfer, Vol. 1, pp. 50-55.
Smith, T.F., Shen, Z.F., Friedman, J.N., 1982, "Evaluation of Coefficients for the Weighted Sum of Gray Gases Model", Journal of Heat Transfer, Vol. 104, pp. 602-608.
Snegirev, A.Y., 2004, "Statistical modeling of thermal radiation transfer in buoyant turbulent diffusion flames", Combustion and Flame, Vol. 136, pp. 51-71.
Song, T.H., Viskanta, R., 1987, "Interaction of radiation with turbulence: application to a combustion system", Journal of Thermophysics, Vol. 1, No. 1, pp. 56-62.
Soufiani, A., 1991, "Temperature Turbulence Spectrum for High-Temperature Radiating Gases", Journal of Thermophysics, Vol. 5, pp. 489-494.
Turns, S.R., 2000, "An introduction to combustion: concepts and applications", McGraw-Hill.

7. RESPONSIBILITY NOTICE

The authors are the only responsible for the printed material included in this paper.

DIRECT NUMERICAL SIMULATION OF BI-DISPERSE PARTICLE-LADEN GRAVITY CURRENTS

Ezequiel P. Francisco, ezequielpf@gmail.com
Luis F. R. Espath, espath@gmail.com
Jorge H. Silvestrini, jorgehs@pucrs.br
Faculdade de Engenharia, Pontifícia Universidade Católica do Rio Grande do Sul

Abstract. *A numerical investigation of bi-disperse particle-laden gravity currents is presented in the lock-exchange configuration. Results of previous studies, based on numerical simulation and laboratory experiments, are used to establish a set of comparisons. The present discussion is focused on explaning how the presence of more than one type of particles influences the main features of the flow, such as deposit profile, front location evolution and suspended mass. Complete energy budget for bi-disperse flows is undertaken without simplified assumptions. In this context it is shown that the addition of coarse particles has a damping effect over turbulence, thus the dissipation term related to strain rate is decreased. It is also noted that the dissipation term arising from the drag force over each particle increases.*

Keywords: *Particle-driven gravity current, Energy budget, Deposition of Particles, Direct Numerical Simulation*

1. INTRODUCTION

The physical process called gravity current is an example of a stratified system and can be observed when two fluids, with different densities, collide one against the other. The collision starts a horizontal relative movement in both fluids, so that the heavier fluid flows under the lighter one (Ungarish, 2006). In the case where the density excess is caused by particles diluted in the fluid, gravity currents move due to the gravitational force acting on dispersed sediments (Middleton, 1993). The focus of this numerical study is on gravity currents with negative-buoyancy effects, where its dynamics play a central role in the formation of hydrocarbon reservoirs (Meiburg and Kneller, 2010).

In nature, gravity currents occurrence is quite frequent. The movement between warm and cold air masses, which can give rise to storms, is a good example. Other examples are sand storms, which transport enormous quantities of particles, and oceanic currents which are caused by difference in temperature and in saline concentrations. At smaller scales, it is possible to observe gravity currents in industrial environment during the manufacturing process of sheet glass, when the molten glass flows across a horizontal surface, for example (Huppert, 2006). For engineering and geology, the understanding of gravity currents dynamics is very relevant due to its depositional, erosive and destructive behaviour. Gravity currents are the most common way of sediment transport to deeper regions of the oceans, and these sediments, after deposited, can give rise to hydrocarbon reservoirs (Kneller and Buckee, 2000). In the engineering context, these flows are extremely dangerous as they can destroy seafloor equipments like pipes and cables (Meiburg and Kneller, 2010).

Because its importance, this phenomenon has been studied by many researchers in the last thirty years, most commonly by laboratory experiments and numerical simulations on lock exchange configuration. Rooij and Dalziel (2001) describe deposit profile taking into account a mono-disperse flow, i.e., a flow in which all the suspended particles have the same diameter. Blanchette et al. (2006) and Gray, Alexander and Leeder (2005) performed a variation of the lock exchange case including a complex geometry in bottom domain. Necker et al. (2002), Necker et al. (2005) and Espath et al. (2013) present the energy budget of a mono-disperse gravity current, demonstrating the relationship between potential energy and kinetic energy with their respective dissipative terms. Others global quantities like front position, suspended mass and final deposit profile are also investigated. Gladstone, Phillips and Sparks (1998) and Nasr-Azadani, Hall and Meiburg (2013) performed studies with a bi-disperse flow, showing that its features are strongly affected by mixture of different initial particle fractions. Simplified theoretical approaches (Rottman and Simpson (1983); Bradford and Katapodes (1999); Bonnecaze, Huppert and Lister (1993)) are also used to predict the behaviour of the flow.

In the present work, a typical lock-exchange configuration is employed in order to investigate a bi-disperse dilute suspension particle-laden flow, i.e., the initial concentration of diluted particles is below 1%, also the sedimentation process is taking into account. In order to investigate the features of a bi-disperse flow, two high resolution numerical simulations are carried out, one in 2D and the other in 3D. Both cases are composed, initially, by 50% of coarse and 50% of fine particle factions. Special attention is given to the complete energy budget of the flow considering that there is no theoretical or numerical evidences about the temporal evolution of this global quantity in bi-disperse flows. Other issues addressed are the variations in the final deposit profile and the temporal evolution of the front. The main characteristics of a gravity currents are also related with the amount of suspended material as well as its sedimentation rate.

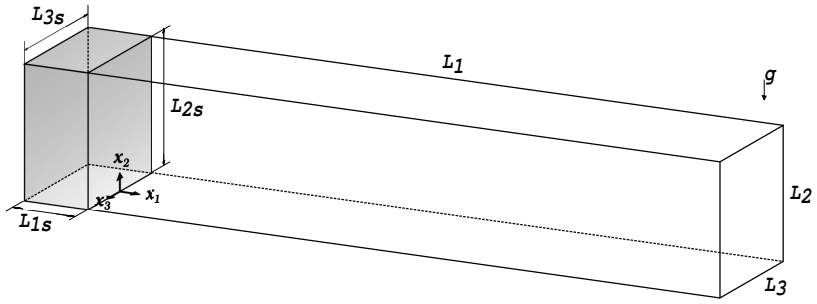

Figure 1. Initial set-up of lock-exchange case. The calculation domain has length L_1, height L_2 and width L_3.

2. FLOW CONFIGURATION AND GOVERNING EQUATIONS

The numerical simulations carried out here are based on the lock-exchange configuration (Fig. 1). This arrangement consists on an initial homogeneous mixture of sediment particles and clear fluid, trapped in a sub-volume of the domain with dimensions L_{1s} x L_{2s} x L_{3s}, separated from clear fluid by a gate. The gate is suddenly removed, and due to gravity action, the mixture of particle and fluid flows under the clear fluid. There are two mechanisms governing the motion: the first one is occasioned by transformation of the potential energy in kinetic energy, an advective motion, and the second is the diffusivity motion, which proportionates the mixing, that occurs by the potential difference between heavy- and clear-fluid.

As previously mentioned, the low initial volume fraction of suspended sediment allows to neglect variations in the mixture viscosity, as well as the influence of particle inertia. It is considered a dilute approach where the initial concentration at the lock is well below 1 %. Thus, this work is focused on diluted incompressible fluid laden with small bi-disperse particles whose their densities are significantly higher than in the clear fluid. In order to mathematically describe the flow, dimensionless incompressible Navier-Stokes equations under Boussinesq assumptions are employed. To make equations dimensionless, it is chosen $\tilde{h} = \tilde{L}_2/2$ (the tilde represents a dimensional quantity) and the buoyancy velocity $\tilde{u}_b$ as the characteristic length and velocity scales, respectively, stated as

$$\tilde{u}_b = \sqrt{\tilde{g}\frac{(\tilde{\rho}_p - \tilde{\rho}_0)\tilde{C}_r}{\tilde{\rho}_0}\tilde{h}}, \tag{1}$$

where, $\tilde{\rho}_p$ denotes the particle density of different fractions, $\tilde{\rho}_0$ is density of clear fluid and $\tilde{g}$ is the gravitational acceleration. $\tilde{C}_r$ is the total initial volume fraction of particles in the lock and it is also used as a characteristic scale. The dimensionless mass and momentum equations can be written as

$$\frac{\partial u_i}{\partial x_i} = 0, \tag{2}$$

$$\frac{\partial u_i}{\partial t} + u_j\frac{\partial u_i}{\partial x_j} = -\frac{\partial p}{\partial x_i} + \frac{1}{Re}\frac{\partial^2 u_i}{\partial x_j \partial x_j} + c_t e_i^g, \tag{3}$$

where $e_i^g = (0, -1, 0)$ is the unit vector acting in gravity direction, as well as u_i, p and c_t represent the velocity field, pressure and total particle concentration, respectively.

The dimensionless Reynolds number is defined as

$$Re = \frac{\tilde{u}_b\tilde{h}}{\tilde{\nu}}, \tag{4}$$

and $\tilde{\nu}$ denotes de kinematic viscosity of the fluid. In order to evaluate the behaviour of the suspended material, it is necessary to determine the particles concentration fields for the N different fractions present in the flow, which are governed by

$$\frac{\partial c_l}{\partial t} + (u_j + u_l^s e_j^g)\frac{\partial c_l}{\partial x_j} = \frac{1}{Sc_l Re}\frac{\partial^2 c_l}{\partial x_j \partial x_j}, \qquad l = 1, \ldots, N. \qquad \text{(no sum on } l\text{)} \tag{5}$$

Here, c_l and u_l^s are the concentration field and settling velocity associated to each particle fraction, respectively. The dimensionless Schmidt number is introduced and expressed as

$$Sc_l = \frac{\tilde{\nu}}{\tilde{k}_l}, \tag{6}$$

where $\tilde{k}_l$ is the mass diffusivity coefficient of the l-th concentration field. The particle settling velocity can be related to its diameter by the Stokes settling velocity law. This law agrees closely with small particles diameters ($d_p < 0,1mm$) (Julien, 1998). However, Gladstone, Phillips and Sparks (1998) suggests that variations of this value may occur due to irregularities in particle shapes, leading to a larger drag coefficient.

Relative to the momentum equation (Eq. 3), the total particle concentration c_t is obtained as follows,

$$c_t = \sum_{l=1}^{N} c_l. \tag{7}$$

Regarding the boundary conditions for the velocity field, no-slip conditions are enforced at top and bottom of the domain whereas, on the side walls, free-slip conditions are chosen. Concerning the concentration fields, no-flux boundary conditions are imposed at the vertical walls and at the top. At the bottom, it is necessary to ensure that the particles leave the domain after deposition, which represents an outflow. To this end, the following boundary condition is employed

$$\frac{\partial c_l}{\partial t} + u_l^s e_2^g \frac{\partial c_l}{\partial x_2} = 0, \qquad l = 1, \ldots, N, \tag{8}$$

in order to assume that the layer of sedimented particles is sufficiently thin so that the bottom of the domain remains flat, this means that re-suspension and erosion are neglected. This boundary condition is used by Necker et al. (2002), Necker et al. (2005) and Espath et al. (2014).

To numerically solve the incompressible Navier-Stokes under Bussinesq assumption and scalar transport equations, the `Incompact3D` code is used. This code is based on sixth-order compact finite difference method for spacial derivatives. The advance in time is performed by the Adams-Bashforth schemes so that, for two-dimensional case the accuracy is second-order and for three-dimensional it is third-order. A spectral method is employed to solve Poisson equation (more details in Laizet and Lamballais (2009)).

3. ENERGY BUDGET OF THE FLOW

As previously stated in section 1, the simplest way to understand a gravity current is to consider it as the conversion of potential energy into kinetic energy. The initial potential energy of the mixture fluid-particle, resting in the lock, is converted into kinetic energy after the release of the gate. For the gravity currents with suspended particles, the kinetic energy, associated with the fluid motion, is dissipated by the macroscopic velocity field and microscopic Stokes flow around each particle.

In their previous work, Necker et al. (2005) evaluate the temporal evolution of the energy components, neglecting the mass diffusivity and introducing simplified assumptions in the dissipation term related to the microscopic scales. For this work, based on Espath et al. (2014), full budget equations are taken into account, without simplifications, in order to accurately estimate all terms of energy for different particle fractions.

The inner product between the momentum equation (3) and the velocity vector field u_i yields to the time derivative of the kinetic energy equation, stated as

$$\frac{D(\frac{1}{2}u_i u_i)}{Dt} = -\frac{\partial p u_i}{\partial x_i} + \frac{2}{Re}\frac{\partial (s_{ij} u_i)}{\partial x_j} - \frac{2}{Re} s_{ij} s_{ij} - u_2 c_t. \tag{9}$$

where, $\frac{D(\cdot)}{Dt}$ denotes the material derivative, while s_{ij} is the strain rate tensor, defined as the symmetric part of the velocity gradient

$$s_{ij} = \frac{1}{2}\left(\frac{\partial u_i}{\partial x_j} + \frac{\partial u_j}{\partial x_i}\right). \tag{10}$$

Integrating the kinetic energy equation (9) over the entire domain Ω, the following expression is obtained:

$$\frac{dk}{dt} = -\int_\Omega \frac{2}{Re} s_{ij} s_{ij} d\Omega - \int_\Omega u_2 c_t d\Omega, \tag{11}$$

the kinetic energy is defined as

$$k(t) = \int_\Omega \frac{1}{2} u_i u_i d\Omega. \tag{12}$$

It is worth noting that, from divergence Gauss theorem, the first and second term of the right side of Equation (9) vanish when the integration over the domain is performed, once there is no transport in the velocity field across the boundary.

The potential energy, related to each particle fraction, is integrated over the entire domain according to the following expression

$$Ep_l(t) = \int_\Omega c_l x_2 d\Omega, \tag{13}$$

$$Ep_t(t) = \sum_{l=1}^{N} Ep_l, \tag{14}$$

where Ep_l and Ep_t are the potential energy associated to each particle mixture and the total potential energy, respectively.

Multiplying the equation of concentration field (5) by x_2 and, after some algebra, it is found the time derivative of potential energy for the l-th particle

$$\frac{dEp_l}{dt} = \int_\Omega \left(x_2 \frac{1}{Sc_l Re} \frac{\partial^2 c_l}{\partial x_2 \partial x_2} + x_2 u_l^s \frac{\partial c_l}{\partial x_2} \right) d\Omega + \int_\Omega u_2 c_l d\Omega. \tag{15}$$

Considering that the total mechanical energy of the flow is equal to the sum of its total kinetic and potential energies, it is evaluated the time variation of the mechanical energy by summing equations (11) and (15)

$$\frac{d(k + Ep_t)}{dt} = -\int_\Omega \frac{2}{Re} s_{ij} s_{ij} d\Omega + \sum_{l=1}^{N} \left[\int_\Omega \left(x_2 \frac{1}{Sc_l Re} \frac{\partial^2 c_l}{\partial x_2 \partial x_2} + x_2 u_l^s \frac{\partial c_l}{\partial x_2} \right) d\Omega \right] = -\epsilon - \sum_{l=1}^{N} \epsilon_{s_l}. \tag{16}$$

From this equation, the losses in energy can be divided into macroscopic E_d and microscopic E_{s_t} dissipations, as follows

$$E_d(t) = \int_0^t \epsilon(\tau) d\tau, \tag{17}$$

$$E_{s_t}(t) = \sum_{l=1}^{N} E_{s_l}(t) = \sum_{l=1}^{N} \left[\int_0^t \epsilon_{s_l}(\tau) d\tau \right]. \tag{18}$$

Therefore the energy budget is established as

$$k + Ep_t + E_d + E_{s_t} = E_{t_0}. \tag{19}$$

where E_{t_0} is the initial total energy.

4. RESULTS

4.1 Validation

In order to demonstrate the ability of the `Incompact3D` code to reproduce a gravity current, it is established some comparison with experimental and computational bi-disperse results provided by Gladstone, Phillips and Sparks (1998) and by Nasr-Azadani, Hall and Meiburg (2013), respectively. Here, the settling velocities for coarse (C) and fine (F) fractions are $u_1^s = 0,03$ and $u_2^s = 0,004$, respectively, according with Gladstone, Phillips and Sparks (1998). The experimental work suggests that the u^s is approximately one-third smaller than the direct Stokes value. Figure 2 shows the comparison between final deposit profile.

There are a general good agreement between results, highlighting the peaks present in numerical results, possibly caused by the great vortex that can carry particle to bottom of the domain. Figures 2(a) and 2(b) show that our results are underestimated probably by the fact that the reference data has a longer simulation time than ours.

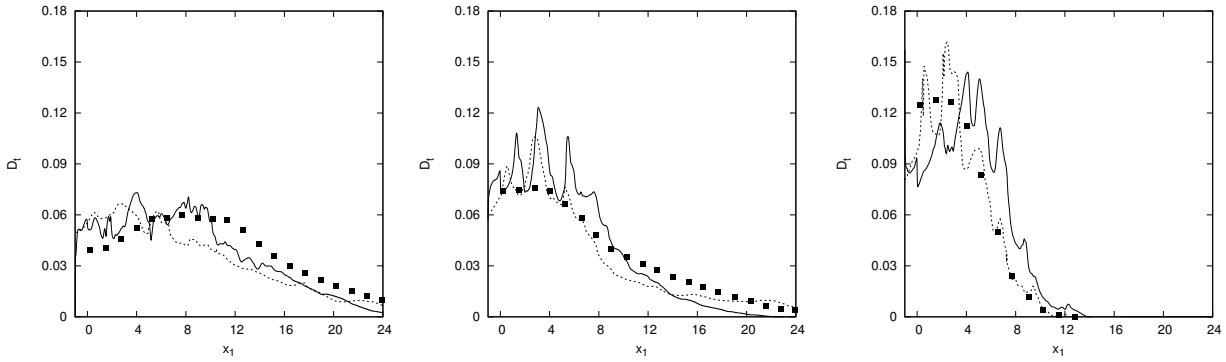

Figure 2. Final deposit profiles for: (a) $0\%C/100\%F$; (b) $50\%C/50\%F$; (c) $100\%C/0\%F$. Solid lines: present work; dashed lines: Nasr-Azadani, Hall and Meiburg (2013); ■: Gladstone, Phillips and Sparks (1998).

Table 1. Parameters for $2D/3D$ simulations.

Re	$\%C/\%F$	Sc	u_1^s	u_2^s		n_1, n_2, n_3	L_1, L_2, L_3	Δt
4000	50/50	1	0.047	0.006	$2D$	1441, 641	28, 2	2 x 10^{-4}
					$3D$	1441, 641, 101	28, 2, 1	

4.2 Comparison 2D X 3D

This section will establish some comparisons between 2D and 3D cases. The parameters for both simulations, in a domain with mesh nodes (n_1,n_2,n_3), are present in Table 1. Here, it is assumed that the settling velocities of the particles are obtained directly by relation of the Stokes law, leading to $u_1^s = 0,047$ and $u_2^s = 0,006$ for coarse and fine fractions, respectively.

Initially, will be presented some instantaneous visualisations where is possible to observe the turbulent structures. In Figure 3, iso-values for the concentration field are shown. Here, it is possible to see that, at the first times after the instantaneous release of the mixture particle-fluid, the current remains two-dimensional, transitioning to a three-dimensional motion according its streamwise propagation, both for coarse and for fine particle. Espath et al. (2014) suggests that this initial two-dimensionality occurs due to small amount of kinetic energy at first stages of the current and he shows that the initial amount of kinetic energy can be related to the Reynolds number. Observing iso-surfaces for $t = 8$, the well-know lobe-and-cleft structures, identified by Simpson (1972), are present in the front of the current.

Following the head, the body of the current develops with intense turbulence allowing the visualization of spanwise vortices, already referred as Kelvin-Helmholtz vortices. At $t = 12$, more turbulent structures are spotted for a finer fraction due the fact that fine particle remains in suspension for longer times than coarse particle. This intense turbulence and vortical structures can be better observed using the Q-criterion which, according to Dubief and Delcayre (2000), captures more details in regions with high accumulation of vortices. In Figure 4, it is possible to see structures like "worms" (see detail for $t = 16$) representing agglomerations of vortices, both in spanwise as in streamwise direction. At $t = 4$ are shown longitudinal vortices, behind lobe-and-cleft structures, close to bottom, formed by sets of two pairs of counter rotating vortices (red is positive and blue negative).

Comparing snapshots of the $2D$ and $3D$ simulations for the same non-dimensional time $t = 14$, the first aspect that can be highlighted is the difference between turbulent structures (see Figure 5).

The main discrepancies are related to the development of larger vortices in $2D$ simulation than in $3D$, contributing to the particles which remain in suspension for longer times. This difference is due to the fact that, in $3D$, kinetic energy of the flow can be dissipated into three dimensions, contrary to two dimensions in $2D$ case. It is noticed that for both, coarse and fine particles, high levels of concentration are trapped within the vortices in $2D$ case, differently from $3D$ case where it accumulates higher concentrations at bottom of the domain. This statement can be confirmed by Figure 6 where the suspended material is given by

$$m_{p_l}(t) = \int_\Omega c_l dV, \tag{20}$$

In $3D$, the total suspended mass, at final time, is about 18% whereas for $2D$ this value is approximately 26%, representing a difference of approximately 30% between simulations. At $t \approx 35$, it seems that coarse particles are totally deposited for tri-dimensional case, which does not occur in bi-dimensional case.

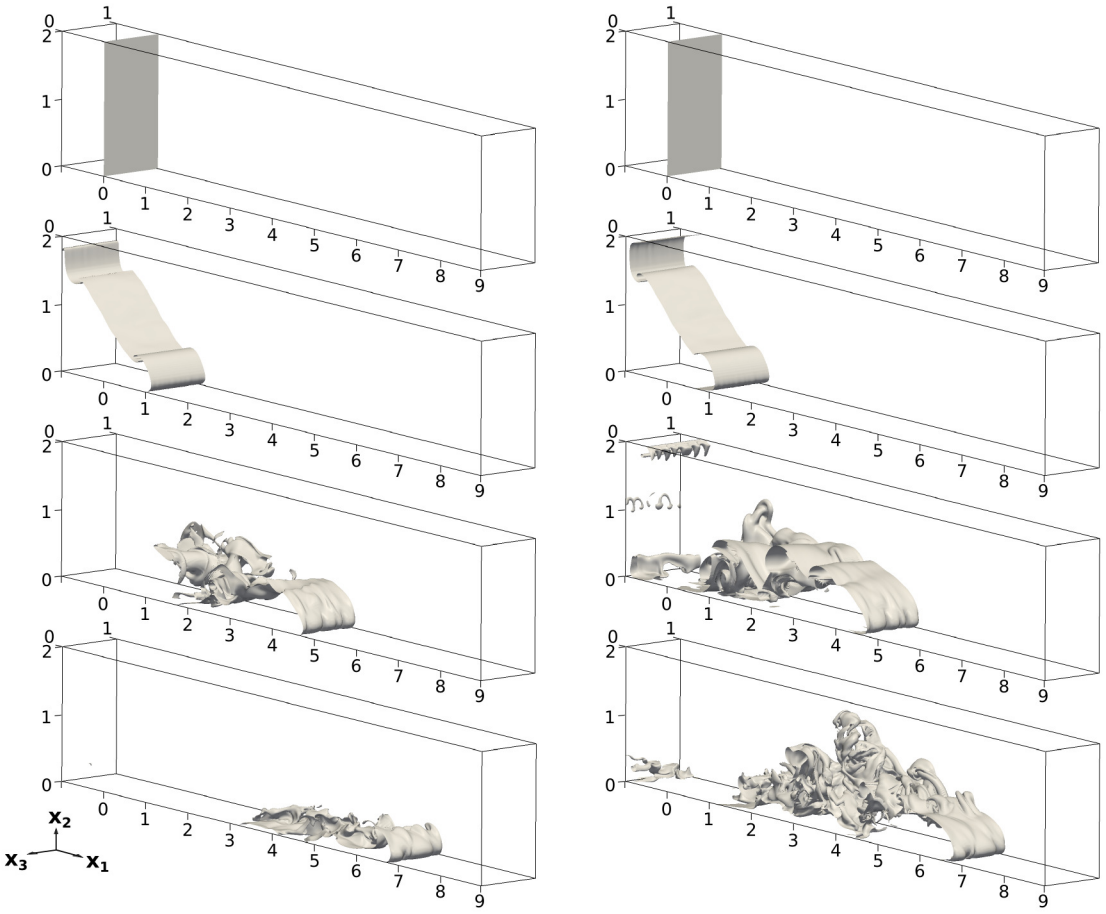

Figure 3. Iso-surfaces for concentration field taking $c = 0.25$. On the left are coarse fraction and on the right are fine. From top to bottom: $t = 0, 2, 8$ and 12.

Figure 7 shows the front evolution of the flow. Both currents have same constant velocity for $2D$ and $3D$ up to about $t \approx 10$, but in $t \approx 15$ there is a divergence between the curves, where tri-dimensional and two-dimensional simulations, at non-dimensional final time, approximately reach distances of 18.5 and 15, respectively.

A comparison between the final sediment layer of two- and three-dimensional simulations with experimental result of Gladstone, Phillips and Sparks (1998) is shown by Figure 8, being defined by

$$D_t(x_1, t) = \frac{1}{L_1 L_3} \sum_{l=0}^{N} \left[\int_0^t < c_{w_l}(x_1, \tau) >_{x_3} u_l^s d\tau \right]. \tag{21}$$

Here, c_{w_l} refers to l-th particle concentration at the bottom, and $< \cdot >_{x_3}$ is an average in spanwise direction for $3D$ simulation. It is possible to see that peaks in $2D$ reach higher values than in $3D$, possibly caused by the large vortices (see Fig. 5) that can carry high levels of concentration trapped within themselves, yielding to a faster sedimentation process. The difference, with respect to experimental result, seems to lie in the fact that the experiment was carried out for longer time and with $Re = 24000$.

In order to investigate the energy budget of a gravity current, it is necessary to examine the temporal evolution of its energy and how the dissipation losses impact the conversion of potential energy into kinetic energy.

Looking at Figure 9, it is possible to observe that, in $2D$ and $3D$, at time $t = 0$, the potential energy E_p is maximum for each particle fraction (according its initial proportion), dropping to around 60 and to 70% of its total initial value, for fine and coarse fractions, respectively, at the first 2-3 time units, as soon as the gate is released. After the sudden drop,

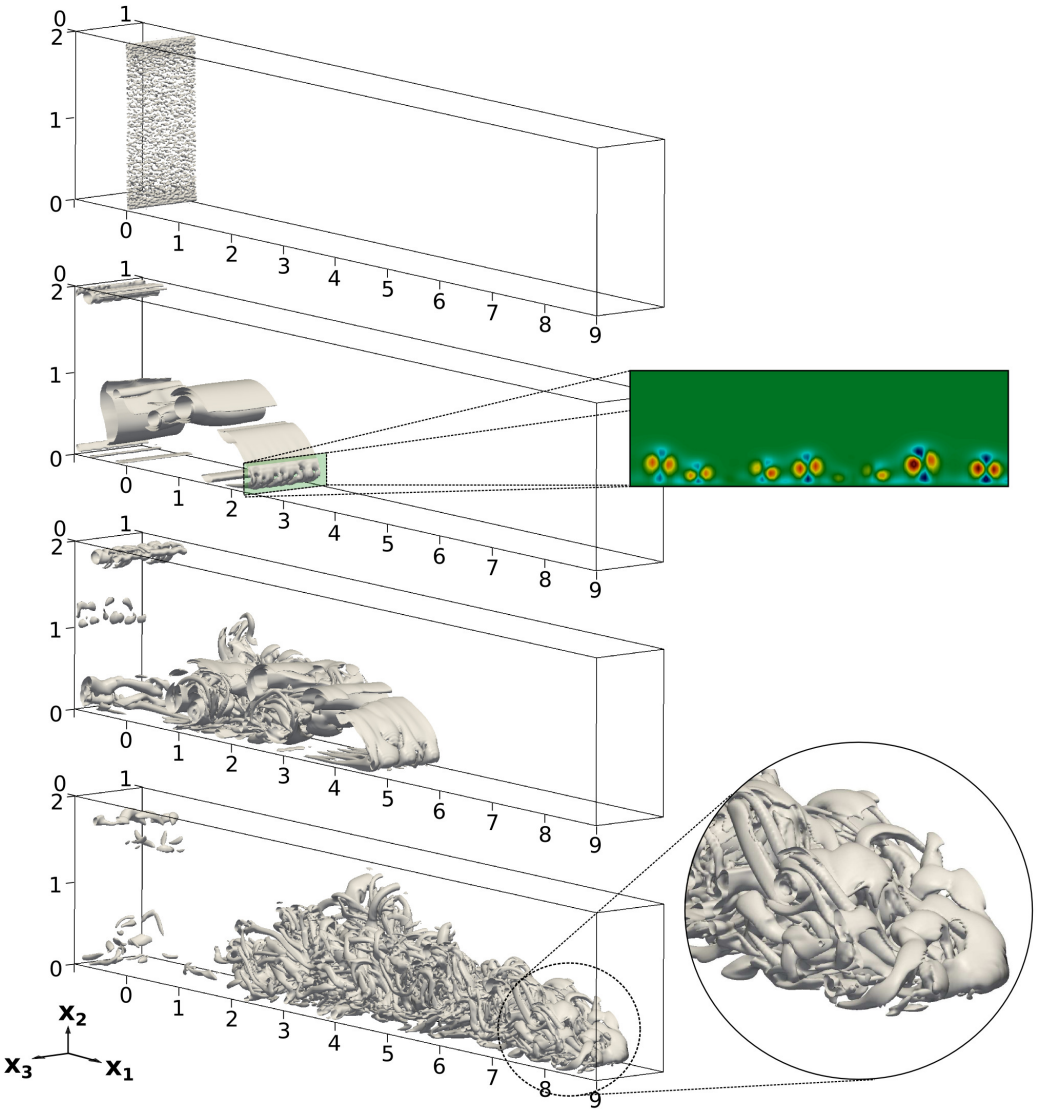

Figure 4. Q-criterion for iso-surfaces with $Q = 1$. Turbulent structures depicted for $t = 0.2, 4, 8$ and 16, from top to bottom.

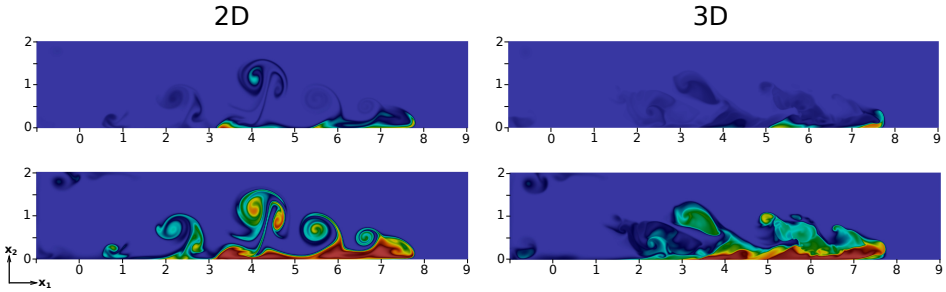

Figure 5. Turbulent structures for $2D$ and $3D$ cases at $t = 14$ in a middle-plane at $x_3 = 0$. From top to bottom: coarse and fine particles. All images ware taken for $0 < c_i < 1$.

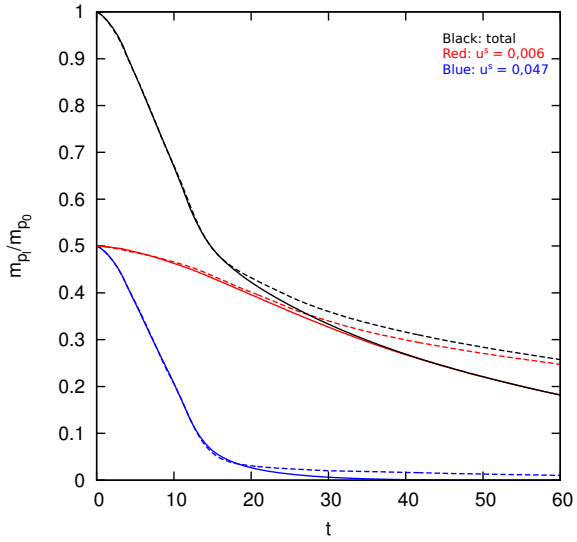

Figure 6. Temporal evolution of suspended particles. Solid lines refers to $3D$ simulation and dashed lines are $2D$ simulation. All curves are normalized with total initial suspended mass (m_{p_0}).

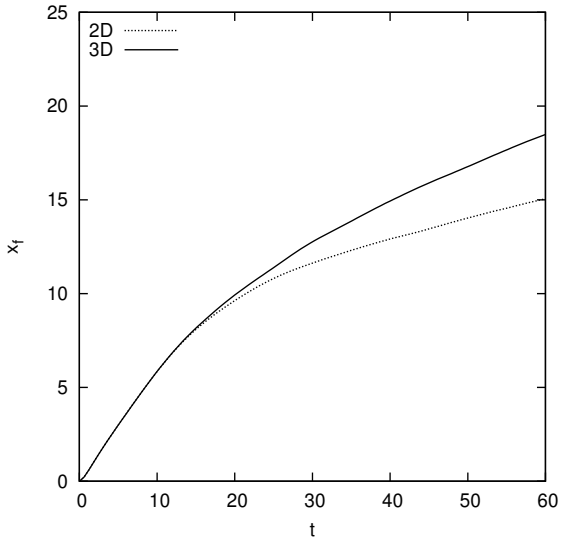

Figure 7. Time evolution of the current front location.

the fine faction has a smoothly decrease, that is more pronounced in the $3D$ simulation. On the other hand, for coarse fraction, after the sudden drop, it is noted, in both simulations, the occurrence of a second drop at $t \approx 3$ up to $t \approx 10$, not as abrupt as the first one, but that leads to a decrease by about 50% of its potential energy still remaining, tending its value to zero, which is firstly reached in $3D$ case.

Looking at the kinetic energy k for all cases, after having reached the peak value of about 56% at $t = 3.2$, the kinetic energy is followed by a decay strongly influenced by the macro (E_d) and micro (E_s) dissipative losses. The final values of E_d and E_s show that convective fluid motion dissipate more energy than particle settling. This behaviour is more evident for $3D$ simulation due to three-dimensional turbulent motion, leading to a macro dissipation $\approx 38\%$ greater than in two-dimensional case. The curves representing E_s highlight the influence of settling velocity (u_l^s) on energy budget. This dissipation term is rapidly increased as the u_l^s increases. Comparing the simulations, we found that the dissipative losses (E_d+E_s) represent $\approx 71\%$ and $\approx 86\%$ of the total final energy, in $2D$ and $3D$ respectively.

5. CONCLUSION

DNS is applied, for $2D$ and $3D$ configurations, to research how the mainly features of a gravity current are affected when two initial fraction of particles are present, as well as how the three-dimensionality influences its dynamics. Related issues to final deposit profile, evolution of front position, suspended mass and complete energy budget are analysed, resulting in a good agreement between them.

The first implication observed is that the formation of large vortices in $2D$ simulation hold the particles in suspension

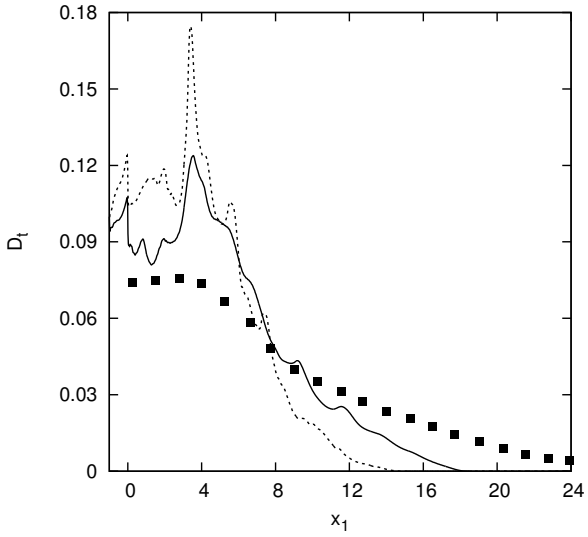

Figure 8. Final deposit profile for $2D$ and $3D$ bi-disperse simulations. Dashed line: $2D$ result; solid line: $3D$ result; ■: Gladstone et al. (1998).

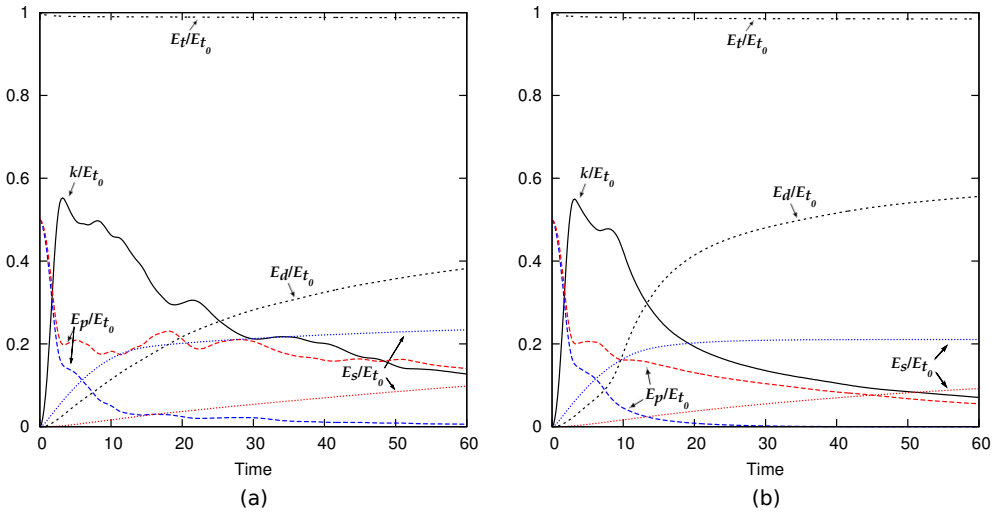

Figure 9. Temporal evolution of energy budget. (a) $2D$ and (b) $3D$. Red lines refer to fine particles, blue to coarse and in black are global quantities of the flow. All curves are normalized with total initial energy.

for longer times compared with $3D$ simulation. With respect to the front position, both $2D$ and $3D$ cases propagate with same velocity up to $t \approx 15$ when the $2D$ decelerates faster than $3D$.

Energy budget shows that the coarser particle dissipates its potential energy into micro dissipation faster than finer particle, due difference in settling velocity. But, the most important result is the inability of $2D$ to reproduce the main features present in $3D$. The unrealistic large vortices that affect the dynamics of settling process and two-dimensionality of the turbulence introduce an error that may be important on reproducing the physical phenomenon. Taking as an example, comparing the final values of E_d, we have 0.38 and 0.55 for $2D$ and $3D$, respectively, corresponding to a difference of about 31%.

6. ACKNOWLEDGEMENTS

The authors are grateful to Petrobras for support and to High Performance Laboratory at Pontifical Catholic University of Rio Grande do Sul (LAD-PUCRS).

7. REFERENCES

Blanchette, F., Piche, V., Meiburg, E. and Strauss, M., 2006, "Evaluation of a simplified approach for simulating gravity currents over slopes of varying angles", Computers and fluids, Vol. 35, pp. 492-500.

Bonnecaze, R. T., Hupper, H. E. and Lister, J. R., 1993, "Particle-driven gravity currents", J. Fluid Mech., Vol. 250, pp. 339-369.

Bradford, S. F., Katapodes, N. D., 1999, "Hydrodinamics of turbid underflows. 1: Formulation and numerical analysis", J. Hydraulic Engineering., Vol. 125, pp. 1006-1015.

Dubief, Y. and Delcayre, F., 2000, "On coherent-vortex identification in turbulence", Journal of Turbulence, Vol. 1, pp. 22.

Espath, L. F. R., Pinto L. C., Laizet, S. and Silvestrini J. H., 2014, "Two- and three-dimensional direct numerical simulation of particle-laden gravity currents", Computers and Geosciences, Vol. 63, pp. 9-16.

Gladstone, C., Phillips, J. and Sparks, R., 1998, "Experiments on bidisperse, constant-volume gravity currents: propagation and sediment deposition", Sedimentology, Vol. 45, pp. 833-843.

Gray, T. E., Alexander, J. and Leeder, M. R., 2005, "Quantifying velocity and turbulence structure in depositing sustained turbidity currents across breaks in slope", Sedimentology, Vol. 52, pp. 467-488.

Huppert, H. E., 2006, "Gravity currents: a personal perspecitve", J. Fluid Mech., Vol. 554, pp. 299-322.

Julien, P. Y., 1998, "Erosion and Sedimentation", Cambridge University Press, 280 p.

Kneller, B. and Buckee, C., 2000, "The structure and fluid mechanics of turbidity currents: a review of some recent studies and their geological implications", Sedimentology, Vol. 47, pp. 62-94.

Laizet, S. and Lamballais, E., 2009, "High-order compact schemes for incompressible flows: A simple and efficient method with quasi-spectral accuracy", Journal of Computational Physics, Vol. 228, pp. 5989-6015.

Meiburg, E. and Kneller, B., 2010, "Turbidity currents and their deposits", Annu. Rev. Fluid Mech., Vol. 42, pp. 135-156.

Middleton, G. V., 1993, "Sediment deposition from turbidity currents", Annual Review of Earth and Planetary Sciences, Vol. 21, pp. 89-114.

Nasr-Azadani, M. M., Hall, B. and Meiburg, E., 2013, "Polydisperse turbidity currents propagating over complex topography: Comparison of experimental and depth-resolved simulation results", Computers and Geosciences, Vol. 53, pp. 141-153.

Necker, F., Härtel, C., Kleiser, L. and Meiburg, E., 2002, "High-resolution simulations of particle-driven gravity currents", J. Multiphase Flow, Vol. 28, pp. 279-300.

Necker, F., Härtel, C., Kleiser, L. and Meiburg, E., 2005, "Mixing and dissipation in particle-driven gravity currents", J. Fluid Mech., Vol. 545, pp. 339-372.

Rooij, F. D. and Dalziel, S. B., 2001, "Time-and space-resolved measurements of deposition under turbidity currents", Special publication of the international association of Sedimentologists, Vol. 31, pp. 207-215.

Rottman, J. W. and Simpson, J. E., 1983, "Gravity current produced by instantaneous releases of a heavy fluid in a rectangular channel", J. Fluid Mech, Vol. 135, pp. 95-110.

Simpson, J., 1972, "Effects of the lower boundary on the head of a gravity current", J. Fluid Mech, Vol. 53, pp. 759-768.

Ungarish, M., 2006, "Energy balances for propagating gravity currents: homogeneous and stratified ambients", J. Fluid Mech, Vol. 565, pp. 363-380.

ON THE DIFFERENT RELAXATION TIME SCALES IN THE COMPRESSIBLE HEAT TRANSFER WITHIN A SUPERCRITICAL FLUID

Leonardo S. de B. Alves, leonardo.alves@mec.uff.br
Universidade Federal Fluminense, Departamento de Engenharia Mecânica, Rua Passo da Pátria 156, Niterói, RJ 24210-240, Brazil.

Abstract. *An approximate solution of the original thermodynamic model for compressible heat transfer of a supercritical fluid under microgravity led to the well-known piston effect relaxation time $t_{PE} = t_D/(\gamma - 1)^2$, where t_D is the thermal diffusion relaxation time and γ is the ratio between specific heats. Although more accurate models, based on the Navier-Stokes equations and an appropriate equation of state, are nowadays used to simulate such a phenomenon, this classical expression is still considered correct. We present the exact analytical solution for the same thermodynamic model to demonstrate that it yields only two characteristic times, but this classical expression is not among them. They are t_D and t_D/γ, which means the latter is the correct definition for t_{PE} according to the original thermodynamic model. This novel expression still predicts a critical speeding-up, since γ diverges faster than t_D, but it shows that temperature equilibration is not as fast as implied by the classical expression. An accuracy and consistency analysis is carried out for verification purposes.*

1. INTRODUCTION

All fluids are subject to an universal divergence of their thermodynamic properties as their critical points are approached. For instance, thermal diffusivity vanishes near the critical point because specific heat at constant pressure diverges faster than thermal conductivity while density remains bounded. Hence, a critical slowing-down of temperature equilibration was expected due to a diverging thermal diffusion relaxation time $t_D = l^2/\alpha$. However, very fast temperature equilibration was still observed in enclosed samples on ground-based experiments (Dahl and Moldover, 1972). Gravity induced buoyancy was assumed responsible for this effect until 25 years ago, when low gravity experiments in orbiting rockets yielded similar results (Nitsche and Straub, 1987). Such a critical speeding-up was explained from a thermodynamic standpoint (Boukari *et al.*, 1990; Onuki *et al.*, 1990) and using the Navier-Stokes equations with a van der Waals equation of state (Zappoli *et al.*, 1990) soon afterwards. It is caused by the ability of small temperature perturbations to create severe compression in near-critical fluids, which, in turn, generates thermo-acoustic waves. When entrapped within cavity walls, their propagation and reflection induces a rapid heating of the entire fluid, resulting in a homogeneous increase of its bulk temperature. Such an understanding of this fast temperature relaxation phenomenon, known today as piston effect, has been validated by theoretical, numerical and experimental studies in the literature (Zappoli, 2003; Barmatz *et al.*, 2007; Carlès, 2010).

The original thermodynamic model of supercritical heat transfer in microgravity proposed to study this phenomenon (Boukari *et al.*, 1990; Onuki *et al.*, 1990) is essentially the heat conduction equation with a source term proportional to the bulk temperature time derivative. This source term models the adiabatic compression mechanism responsible for the piston effect. It becomes dominant whenever $\gamma \gg 1$, i.e., closer to the critical point. On the other hand, it vanishes in the incompressible limit, where $\gamma = 1$. A solution to this equation was first obtained with an approximate Fourier transformation procedure (Onuki *et al.*, 1990), where a detailed derivation is provided elsewhere (Onuki and Ferrell, 1990). The currently accepted definition for the piston effect relaxation time, given by $t_{PE} = t_D/(\gamma - 1)^2$, naturally appears in the analytical solution derived for the bulk temperature in these two studies. This expression indicates a few interesting trends worth noting. It shows that $t_{PE} \ll t_D$ close to the critical point but $t_{PE} \gg t_D$ close to the incompressible limit, consistent with the importance of the adiabatic compressible source term in the governing equation. Furthermore, these deviations from t_D are inversely proportional to γ squared and they are separated by a critical specific heat ratio of $\gamma_c = 2$, where $t_{PE} = t_D$. Although these original studies of the classical thermodynamic model considered steady heating at the boundaries, they were extended towards pulsed (Ferrell and Hao, 1993) and unsteady (Garrabos *et al.*, 1998) heating as well. A similar solution procedure was employed and led to the same expression for t_{PE}. The former study also considered a conjugate problem, coupling the thermodynamic model with the heat transfer within solid walls of a composite material. In doing so, they were able to generalize the piston effect relaxation time by replacing the characteristic length in t_D with an effective one including impedance ratios between consecutive materials. This study was extended to include curvature effects introduced by cylindrical container walls (Carlès *et al.*, 2005), where separation of variables and Laplace transform with numerical inversion were employed. However, they propose expression $t_{PE} = t_D/\gamma^2$ instead, with t_D based on the cylinder diameter as characteristic length. It is consistent with the adiabatic compression source term as well and has the added benefit that $t_{PE} \geqslant t_D$ for any γ. Hence, density never relaxes towards steady-state faster than temperature according to this expression.

Despite all these extensions yielding essentially the same expression for t_{PE}, a closer look at the dimensionless bulk temperature solution that led to the classical expression for the piston effect relaxation time (Onuki *et al.*, 1990), given

by $\Theta_b(t) = 1 - \exp[\,t/t_{PE}\,]\ \mathrm{erfc}[\,\mathrm{sqrt}[\,t/t_{PE}\,]\,]$, reveals an important discrepancy. It is possible to obtain an estimate t_E for t_{PE} by assuming t_E is the time it takes the dimensionless bulk temperature to reach 99% of its steady-state, i.e., $\Theta_b(t_E) = 0.99$, an approach commonly used in boundary layer theory (Schlichting, 1986). This procedure should yield $t_E/t_{PE} \sim O(1)$, but one finds $t_E/t_{PE} \simeq 3182.1$ instead, a number more than three orders of magnitude higher than expected. Hence, there is a clear inconsistency between the classical expression for t_{PE} and the very solution that provided its definition. In the present study, a new definition for t_{PE} is obtained and shown to be consistent with the solution it was derived from, which required no additional approximations to be generated.

2. MATHEMATICAL MODEL

In order to establish an appropriate framework for comparison purposes, the same model problem solved in the original study that put forth the current definition for t_{PE} is considered here (Onuki *et al.*, 1990; Onuki and Ferrell, 1990). It is a one-dimensional impermeable cavity of length l filled with a supercritical fluid at a constant initial temperature T_0 and pressure P_0 close to their critical values. Maximum temperature differences are kept small enough so that all thermodynamic properties can be considered constant. In this scenario, temperature is obtained from the conservation of energy for compressible fluids

$$\rho_0\, C_P^{(0)}\, \frac{\partial T}{\partial t} \;-\; \rho_0 \left(C_P^{(0)} - C_V^{(0)}\right) \frac{\kappa_T^{(0)}}{\alpha_P^{(0)}}\, \frac{dP}{dt} \;=\; k_0\, \frac{\partial^2 T}{\partial x^2}\,, \tag{1}$$

where ρ is the density, x and t are the spatial and temporal coordinates, C_P and C_V are the specific heats and constant pressure and volume, k is the thermal conductivity and κ_T and α_P are the isothermal compressibility and volumetric thermal expansion coefficients, defined as

$$\kappa_T \;=\; \frac{1}{\rho}\, \frac{\partial \rho}{\partial P}\bigg|_T \qquad \text{and} \qquad \alpha_P \;=\; -\,\frac{1}{\rho}\, \frac{\partial \rho}{\partial T}\bigg|_P\,, \tag{2}$$

respectively. It should be noted that pressure is assumed time dependent only, i.e., spatial gradients are negligible, because this is a very low Mach number flow.

On the other hand, density is extracted from its total differential, written as

$$\frac{\partial \rho}{\partial t} \;=\; \rho_0\, \kappa_T^{(0)}\, \frac{dP}{dt} \;-\; \rho_0\, \alpha_P^{(0)}\, \frac{\partial T}{\partial t}\,, \tag{3}$$

where pressure dependence on temperature is extracted by integrating equation (3) over the constant mass cavity volume, generating

$$\frac{dP}{dt} \;=\; \frac{\alpha_P^{(0)}}{\kappa_T^{(0)}}\, \frac{dT_b}{dt}\,, \tag{4}$$

with the bulk temperature defined as

$$T_b(t) \;=\; \frac{1}{l} \int_0^l T\, dx\,. \tag{5}$$

Equations (1) and (4) can be combined to generate a single integral-differential equation for temperature in the form

$$\frac{\partial T}{\partial t} \;-\; \left(1 - \frac{1}{\gamma_0}\right) \frac{dT_b}{dt} \;=\; \alpha_0\, \frac{\partial^2 T}{\partial x^2}\,, \tag{6}$$

where $\gamma = C_P/C_V$ is the ratio between specific heats and α is the thermal diffusivity. This equation is subject to boundary and initial conditions

$$T(0,t) = T_1 \quad , \quad T(l,t) = T_1 \quad \text{and} \quad T(x,0) = T_0\,, \tag{7}$$

with T_1 representing the prescribed temperature at both walls. Using tranformation

$$\tau \;=\; \frac{t}{t_D} \quad , \quad \xi \;=\; \frac{x}{l} \quad \text{and} \quad \Theta = \frac{T - T_0}{T_1 - T_0}\,, \tag{8}$$

the system of equations can be re-written in the dimensionless form

$$\frac{\partial \Theta}{\partial \tau} \;-\; \left(1 - \frac{1}{\gamma_0}\right) \frac{d\Theta_b}{d\tau} \;=\; \frac{\partial^2 \Theta}{\partial \xi^2}\,, \tag{9}$$

where the dimensionless bulk temperature is given by

$$\Theta_b(\tau) \;=\; \int_0^1 \Theta(\xi,\tau)\, d\xi\,, \tag{10}$$

and the boundary and initial conditions are written as

$$\Theta(0,\tau) = 1 \quad , \quad \Theta(1,\tau) = 1 \quad \text{and} \quad \Theta(\xi,0) = 0\,. \tag{11}$$

3. SOLUTION METHODOLOGY

An exact solution for the system of equations (9) to (11) can be constructed by first extracting from it the steady-state solution $\Theta(\xi,\infty) = 1$ using

$$\Theta(\xi,\tau) = 1 + \theta(\xi,\tau)\,, \tag{12}$$

where $\theta(\xi,t)$ represents the unsteady behavior of this system. Substituting relation (12) into governing equation (9) leads to equation

$$\frac{\partial\theta}{\partial\tau} \;-\; \left(1 - \frac{1}{\gamma_0}\right)\frac{d\theta_b}{d\tau} \;=\; \frac{\partial^2\theta}{\partial\xi^2}\,, \tag{13}$$

with the unsteady bulk temperature given by

$$\theta_b(\tau) \;=\; \int_0^1 \theta(\xi,\tau)\, d\xi\,, \tag{14}$$

which is subject to boundary and initial conditions

$$\theta(0,\tau) = 0 \quad , \quad \theta(1,\tau) = 0 \quad \text{and} \quad \theta(\xi,0) = -1\,, \tag{15}$$

obtained by substituting relation (12) into respective conditions in (11).

Now, spatial and temporal dependences of the model problem unsteady representation are separated by proposing a solution of (9) in the form

$$\theta(\xi,\tau) \;=\; \sum_{i=1}^{\infty} \tilde{\psi}_i(\xi)\, \bar{\theta}_i(\tau)\,, \tag{16}$$

where the eigenfunction is provided by eigensystem

$$\frac{d^2\psi_i}{d\xi^2} \;+\; \beta_i^2\, \psi_i(\xi) \;=\; 0 \tag{17}$$

with boundary conditions

$$\psi_i(0) \;=\; 0 \quad \text{and} \quad \psi_i(1) \;=\; 0\,, \tag{18}$$

which yield the eigenfunctions and eigenvalues

$$\psi_i(\xi) \;=\; \sin[\,\beta_i\,\xi\,] \quad \text{and} \quad \beta_i \;=\; i\,\pi\,, \tag{19}$$

respectively, where $i = 1\,,\, 2\,,\, \ldots\,,\, \infty$. Since these eigenfunctions are orthogonal, the integral transformed temperature can be defined according to relation

$$\bar{\theta}_i(\tau) \;=\; \int_0^1 \tilde{\psi}_i(\xi)\, \theta(\xi,\tau)\, d\xi\,, \tag{20}$$

based on the above eigensystem (Özisik, 1993), where the norm

$$N_i \;=\; \int_0^1 \psi_i(\xi)^2\, d\xi \;=\; \frac{1}{2}\,, \tag{21}$$

is used by the normalized eigenfunctions $\tilde{\psi}_i = \psi_i/\sqrt{N_i}$.

Multiplying equation (13) by $\tilde{\psi}_i$, integrating the result over the dimensionless cavity length and applying transformation (20) to the time derivative term yields

$$\frac{d\bar{\theta}_i}{d\tau} - \eta_i \left(1 - \frac{1}{\gamma_0}\right) \frac{d\theta_b}{d\tau} \;=\; \int_0^1 \tilde{\psi}_i(\xi)\, \frac{\partial^2 \theta}{\partial \xi^2}\, d\xi \,, \tag{22}$$

where integral transform coefficient

$$\eta_i \;=\; \int_0^1 \tilde{\psi}_i(\xi)\, d\xi \;=\; \sqrt{2}\, \left(\frac{1 - \cos[\,\beta_i\,]}{\beta_i} \right) \,, \tag{23}$$

is defined for simplicity. Integrating the r.h.s. of equation (22) by parts, applying boundary conditions in (15) and (18), substituting equation (17) and then integral transform definition (20) into the result yields

$$\int_0^1 \tilde{\psi}_i(\xi)\, \frac{\partial^2 \theta}{\partial \xi^2}\, d\xi \;=\; \int_0^1 \frac{d^2 \tilde{\psi}_i}{d\xi^2}\, \theta(\xi,\tau)\, d\xi \;=\; -\,\beta_i^2 \int_0^1 \tilde{\psi}_i(\xi)\, \theta(\xi,\tau)\, d\xi \;=\; -\,\beta_i^2\, \bar{\theta}_i(\tau) \,, \tag{24}$$

which can be substituted into equation (22), using inverse definition (16) in the non-transformed bulk temperature term, to generate

$$\frac{d\bar{\theta}_i}{d\tau} \;-\; \left(1 - \frac{1}{\gamma_0}\right) \sum_{j=1}^{\infty} \eta_i\, \eta_j\, \frac{d\bar{\theta}_j}{d\tau} \;+\; \beta_i^2\, \bar{\theta}_i(\tau) \;=\; 0 \,, \tag{25}$$

for $i = 1\,,\, 2\,,\, \ldots\,,\, \infty$, or, in a more compact form,

$$\sum_{j=1}^{\infty} A_{i,j}\, \frac{d\bar{\theta}_j}{d\tau} \;+\; \beta_i^2\, \bar{\theta}_i(\tau) \;=\; 0 \,, \tag{26}$$

where the integral transform matrix coefficients are

$$A_{i,j} \;=\; \delta_{i,j} \;-\; \left(1 - \frac{1}{\gamma_0}\right) \eta_i\, \eta_j \,, \tag{27}$$

which is subject to transformed initial condition

$$\bar{\theta}_i(0) \;=\; -\int_0^1 \tilde{\psi}_i(\xi)\, d\xi \;=\; -\,\eta_i \,, \tag{28}$$

obtained by transforming initial condition in (15), with $\delta_{i,j}$ representing the Kronecker delta. After solving equations (26) to (28) for the transformed temperatures $\bar{\theta}_i$, the exact solution is obtained by combining them with relations (12) and (16) to generate

$$\Theta(\xi,\tau) \;=\; 1 \;+ \sum_{i=1}^{\infty} \tilde{\psi}_i(\xi)\, \bar{\theta}_i(\tau) \,, \tag{29}$$

where its bulk value defined in (10) becomes

$$\Theta_b(\tau) \;=\; 1 \;+ \sum_{i=1}^{\infty} \eta_i\, \bar{\theta}_i(\tau) \,. \tag{30}$$

Equations (26) to (28) govern the entire unsteady response of the thermodynamic model (9) to (11) through the transformed temperatures $\bar{\theta}_i(\tau)$. Because the eigensystem chosen in (17) to (19) belongs to the Sturm-Liouville class, the infinite summation series solution (16) is convergent (Cotta, 1993). Hence, it can be truncated at a high enough number, named N here, in order to guarantee a predetermined user-defined tolerance. Truncated version of system (26) to (28) is then solved analytically with a matrix exponential (Moler and Loan, 2003) using the software *Mathematica* (Wolfram, 2003).

4. RESULTS AND DISCUSSION

4.1 Solution Verification

Before attempting to evaluate the behaviour of the current results, it is important to verify their numerical accuracy. Figure 1 presents the dimensionless temperature absolute error $\delta\Theta = \Theta - \Theta_R$ calculated with $N_T = 50, 100, \ldots, 300$ and 350 terms. Reference solution Θ_R obtained with $N = 400$ was used for error estimations. Results are presented across the entire cavity length at dimensionless time $\gamma_0\,\tau = 0.001$, with data obtained from the near-critical flow conditions in reference (Shen and Zhang, 2010). Convergence tests at early simulation times are very conservative for this solution in particular because the strongest temporal gradient occurs at $\tau = 0$ but only a steady-state filter is employed in (12). They indicate that $N = 250$ is an adequate choice to maintain absolute errors smaller than 1% as long as the analysis is restricted to $\tau > 0.001$ for $\gamma_0 = 16.2652$. Simulations using higher values of γ_0 require a larger number of terms N to achieve similar errors because the early bulk temperature gradients in time become stronger, i.e., system of equations (26) becomes stiffer. In fact, stiffness is theoretically defined as the ratio between largest and smallest eigenvalues and, hence, is given by γ_0. For this reason, N was selected large enough to guarantee graphical convergence when increasing γ_0 for the results presented in the next figures.

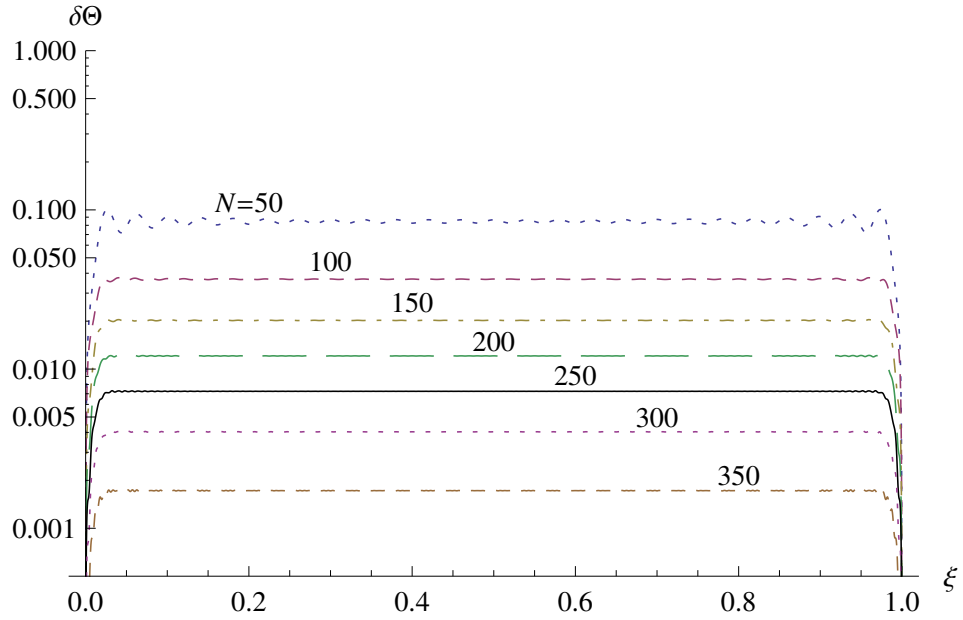

Figure 1. Dimensionless temperature absolute error $\delta\Theta$ versus dimensionless position ξ at dimensionless time $\gamma_0\,\tau = 0.001$ under flow conditions in Shen and Zhang (2010).

4.2 Piston Effect Relaxation Time

Bulk temperature behaviour for $\gamma_0 = 50$ is shown in Figure 2, where a pure thermal diffusion case, artificially generated by setting $\gamma_0 = 1$, is also provided for reference purposes. The latter is included to highlight the bulk temperature increase induced by the piston effect, which is quite prominent as expected. This figure shows that the traditional solution, written out in the introduction, is different from solution (30), confirming the former is only an approximation. Nevertheless, they are qualitatively similar, which explains why the functional form of the traditional solution has been successfully used to fit near critical experimental data for the bulk temperature in a cavity subject to pulsed heating (Garrabos *et al.*, 1998). This figure also highlights an important feature, which is the fact that bulk temperature seems to relax towards steady-state approximately within $1 \lesssim \gamma_0\,\tau \lesssim 2$. On the other hand, the traditional solution bulk temperature has just passed 0.9 and its value is increasing very slowly at this point due to the asymptotic nature of the problem evolution at later times. Furthermore, $\gamma_0\,\tau = 2$ is equivalent to $\gamma_0^2\,\tau = 100$, which means that the traditional bulk temperature is relaxing at a time much larger than predicted by its traditional relaxation time. Hence, a new expression for the piston effect relaxation time is $t_{PE} = t_D/\gamma_0$.

An additional analysis, similar to boundary-layer thickness estimation (Schlichting, 1986), can be performed to confirm this result. It is possible to estimate the piston effect relaxation time from Figure 2 because this dimensionless characteristic time is supposed to represent the time τ_E it takes the bulk temperature to reach 99% of its steady-state

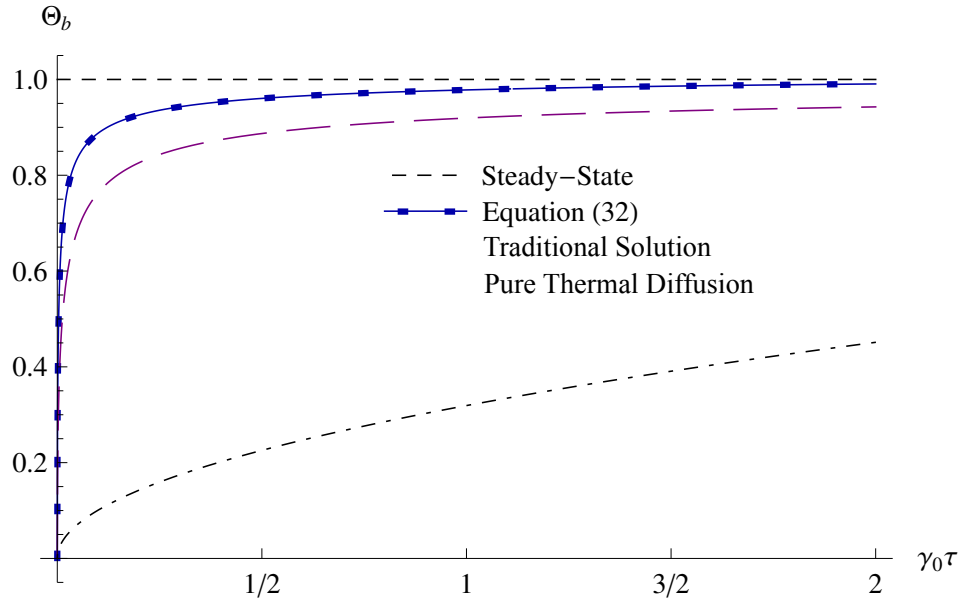

Figure 2. Dimensionless bulk temperature Θ_b with $\gamma_0 = 50$ versus dimensionless time $\gamma_0\,\tau$.

value. In other words, τ_E is defined as the equilibration time

$$\Theta_b(\tau_E) \simeq 0.99\,, \tag{31}$$

where the bulk temperature is obtained from solution (30). If expression t_D/γ_0 is the piston effect relaxation time t_{PE}, equation (31) must yield

$$\gamma_0\,\tau_E \sim O(1)\,, \tag{32}$$

which is equivalent to $0.1 \ll \gamma_0\,\tau_E \ll 10$. Figure 3 proves this to be the case by presenting the normalized equilibration time estimate $\gamma_0\,\tau_E^\infty$ versus γ_0, since it shows that $0.5 \lesssim \gamma_0\,\tau_E^\infty \lesssim 2.0$ for a wide range of γ_0 values between $1 \leqslant \gamma_0 \leqslant 1000$. On the other hand, the traditional expression for the bulk temperature relaxation time yields 3182.1 for all γ_0.

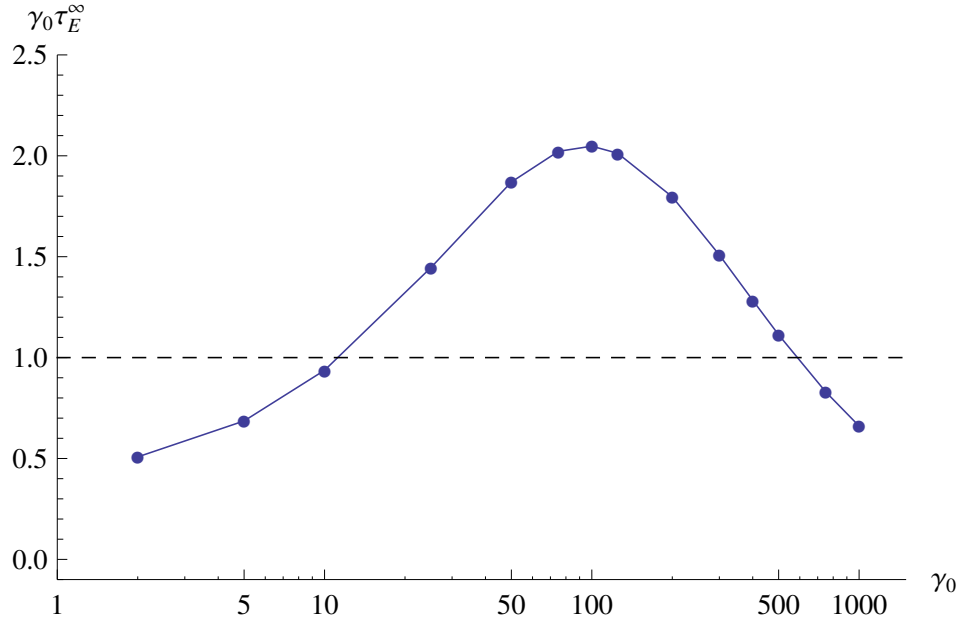

Figure 3. Estimated equilibration time τ_E^∞ normalized by γ_0 versus specific heat ratio γ_0. Dashed line represents new estimate given by $\gamma_0\,\tau = 1$ or, in other words, $t_{PE} = t_D/\gamma_0$.

5. CONCLUSIONS

The piston effect relaxation time $t_{PE} = t_D/(\gamma - 1)^2$ was implicitly defined from the bulk temperature obtained as an approximate solution for the classical piston effect thermodynamic model by an approximate Fourier transform procedure. It was proposed in 1990 and has been widely used in the literature since then, sometimes with the alternative form $t_{PE} = t_D/\gamma^2$, even by experimental studies and simulations employing improved models based on the Navier-Stokes equations and an appropriate equation of state. However, the present work obtains the exact solution of this same model using a generalized Fourier transform and extracts its characteristic times to demonstrate that these expressions are incorrect and should be replaced by $t_{PE} = t_D/\gamma$.

6. ACKNOWLEDGEMENTS

The author would like to acknowledge the financial support of CNPq through grant MCT/CNPq14 - 481072/2012-8 and FAPERJ through grant E-26/111.670/2012.

7. REFERENCES

Barmatz, M., Hahn, I., Lipa, J. A., and Duncan, R. V. (2007). Critical phenomena in microgravity: Past, present and future. *Reviews of Modern Physics*, **79**, 1–52.

Boukari, H., Shaumeyer, J. N., Briggs, M. E., and Gammon, R. W. (1990). Critical speeding up in pure fluids. *Physical Review A*, **41**(4), 2260–2263.

Carlès, P. (2010). A brief review of the thermophysical properties of supercritical fluids. *The Journal of Supercritical Fluids*, **53**, 2–11.

Carlès, P., Zhong, F., Weilert, M., and Barmatz, M. (2005). Temperature and density relaxation close to the liquid-gas critical point: An analytical solution for cylindrical cells. *Physical Review E*, **71**, 041201.

Cotta, R. M. (1993). *Integral Transforms in Computational Heat and Fluid Flow*. CRC Press, Boca Raton, FL.

Dahl, D. and Moldover, M. R. (1972). Thermal relaxation near the critical point. *Physical Review A*, **6**(5), 1915–1920.

Ferrell, R. A. and Hao, H. (1993). Adiabatic temperature changes in a one-component fluid near the liquid-vapor critical point. *Physica A*, **197**, 23–46.

Garrabos, Y., Bonetti, M., Beysens, D., Perrot, F., Fröhlich, T., Carlès, P., and Zappoli, B. (1998). Relaxation of a supercritical fluid after a heat pulse in the absence of gravity effects: Theory and experiments. *Physical Review E*, **57**(5), 5665–5681.

Moler, C. and Loan, C. V. (2003). Nineteen dubious ways to compute the exponential of a matrix, twenty-five years later. *SIAM Review*, **45**(1), 1–46.

Nitsche, K. and Straub, J. (1987). The critical hump of cv under microgravity, results from d-spacelab experiment. In *Proceedings of the 6th European Symposium on Material Sciences under Microgravity Conditions*, ESA SP-256.

Onuki, A. and Ferrell, R. A. (1990). Adiabatic heating effect near the gas-liquid critical point. *Physica A*, **164**, 245–264.

Onuki, A., Hao, H., and Ferrell, R. A. (1990). Fast adiabatic equilibration in a single-component fluid near the liquid-vapor critical point. *Physical Review A*, **41**(4), 2256–2259.

Özisik, M. N. (1993). *Heat Conduction*. Wiley Interscience, New York, 2nd edition.

Schlichting, H. (1986). *Boundary-Layer Theory*. MacGraw Hill, Inc., New York, 7th edition.

Shen, B. and Zhang, P. (2010). On the transition from thermoacoustic convection to diffusion in a near-critical fluid. *International Journal of Heat and Mass Transfer*, **53**, 4832–4843.

Wolfram, S. (2003). *The Mathematica Book*. Wolfram Media. Cambridge University Press, New York, 5th edition.

Zappoli, B. (2003). Near-critical fluid hydrodynamics. *Comptes Rendus Mecanique*, **331**, 713–726.

Zappoli, B., Bailly, D., Garrabos, Y., Neindre, B. L., Guenoun, P., and Beysens, D. (1990). Anomalous heat transport by the piston effect in supercritical fluids under zero gravity. *Physical Review A*, **41**(4), 2264–2267.

8. Responsibility notice

The author(s) is (are) the only responsible for the printed material included in this paper

NUMERICAL STUDY OF NON-REACTIVE TURBULENT JET FLOW WITH COMBINED CONVECTIVE AND RADIATIVE HEAT TRANSFER IN OPTICALLY THIN PARTICIPANT MEDIUM

Elizaldo Domingues dos Santos, elizaldosantos@furg.br
Liércio André Isoldi, liercioisoldi@furg.br
School of Engineering - Universidade Federal do Rio Grande (FURG) – Av. Itália, km 8 – C.P. 474 – Rio Grande – RS

Felipe Roman Centeno, frcenteno@unisinos.br
Escola Politécnica - Universidade do Vale do Rio dos Sinos – Av. Unisinos, n. 950, CEP 93022-000, São Leopoldo, RS, Brazil

Luiz Alberto Oliveira Rocha, luizrocha@mecanica.ufrgs.br
Adriane Prisco Petry, adrianep@mecanica.ufrgs.br
Francis Henrique Ramos França, frfranca@mecanica.ufrgs.br
Department of Mechanical Engineering - Universidade Federal do Rio Grande do Sul (UFRGS) – Rua Sarmento Leite, 425 – Porto Alegre – RS

Abstract. *The present work exhibits a numerical study of turbulent jet flow in cylindrical cavity with combined convective and radiative heat transfer in optically thin participant medium by means of large eddy simulation (LES) and Reynolds averaged Navier-Stokes (RANS) with the k – ε model. The main purpose is to evaluate the validity of the employment of traditional modeling (RANS) for prediction of time-averaged parameters of turbulent non-reactive jet flows with combined convective and radiative transfer, i.e., investigating the influence of Turbulence-Radiation Interactions (TRI) for a free turbulent shear flow. Both studied cases are investigated with fixed Reynolds and Prandtl numbers (Re_D = 22000 and Pr = 0.71) and for an optical thickness of τ_0 = 0.1. Results for time-averaged profiles of temperature and divergence of radiative flux obtained with LES and RANS along the azimuthal axis of the cylindrical cavity present local differences. In spite of this fact, the employment of the different methods (LES with TRI and RANS without TRI) led to similar predictions for time-averaged radiative flux on the cylindrical cavity surfaces. The highest difference achieved between RANS and LES is nearly 5.0 %. Results obtained here showed the non-relevance of TRI for non-reactive free turbulent shear flows in optically thin participant media, similarly to previous observations of non-relevance of TRI for channel flows.*

1. INTRODUCTION

The study of combined convection-radiation heat transfer in turbulent flows is of considerable relevance to several applications as industrial furnaces, gas combustors, flames, fires and high temperature heat exchangers. Concerning the non-reactive flows, high-temperature exhaust gases from several industrial processes, such as production of glass, stainless steel, aluminum and steam generators, have been used for energy savings (Siegel and Howell, 2002; Coelho, 2007).

Turbulent flows generate fluctuations of scalar fields, temperature and species concentration, which in turn cause fluctuations in other physical quantities, such as the Planck emission function and the incident radiation intensity. These fluctuations in the thermal radiation field modify the energy sources that influence the fluid dynamics and the thermal behavior of turbulent flows, due to the coupled nature of the problem. These interactions are named Turbulence-Radiation Interactions (TRI) and its importance has long been recognized (Mazumder and Modest, 1999; Li and Modest, 2003; Coelho, 2007).

Turbulence-Radiation Interactions have a strong non-linear nature and the approach of this phenomenon is extremely difficult. Even when treated separately, turbulence and thermal radiation in participant media are highly complex phenomena (Siegel and Howell, 2002; Pope, 2008). In this sense, the traditional modeling of turbulent flows with combined thermal radiation and convection heat transfer has generally ignored TRI effects (Viskanta, 1998). This approach (RANS without TRI) does not take into account any turbulence closure modeling for the radiative transfer equation.

Turbulence-Radiation Interactions have been mainly investigated in the framework of RANS simulations, where the Reynolds or Frave decomposition is applied to the governing equations, and all fluctuations on the mean quantities must be modeled (Mazumder and Modest, 1999; Li and Modest, 2003; Wang et al., 2008). In the last years, direct numerical simulation (DNS) has been employed for the simulation of conservation equations of mass, momentum, energy and the radiative transfer equation (RTE) (Deshmukh et al., 2008; Roger et al., 2009). However, DNS is still out of reach for practical industrial configurations due to the enormous computational effort required. In this sense, this method has been mainly employed to guide the modeling of TRI for LES or RANS.

Concerning the employment of LES to TRI, few studies has been presented in literature (Jones and Paul, 2005; Gonçalves dos Santos et al., 2008; Coelho, 2009; Gupta et al., 2009; Dos Santos et al., 2014). Most of those studies are devoted to simulation of reactive flows, with exception of the works of Gupta et al. (2009) and Dos Santos et al.

(2014) which evaluated the importance of TRI for non-reactive flows for several optical thicknesses. Coelho (2009) investigated the relevance of TRI considering the subgrid-scale model for radiation. It was observed that the errors resulting from neglecting the sub-grid scales terms in LES for the solution of RTE are much lower than those found in RANS calculations, especially for flows with turbulence intensity lower than 20%, which is commonly found for non-reactive flows. Afterwards, Roger et al. (2010, 2011) supported the previous findings of Coelho (2009) using a comparison between DNS and LES simulations.

For non-reactive flows, the previous study of Mazumder and Modest (1999) noticed that TRI effects can be neglected for optically thin media by means of comparison of two simulations in the RANS framework, one with TRI (where a turbulence model was adopted for the RTE) and another without TRI (classical or traditional modeling). Gupta et al. (2009) used LES to evaluate the influence of TRI in a turbulent non-reactive channel flow for a range of optical thicknesses ($0.01 \leq \tau_0 \leq 1250$) and concluded that, in the absence of chemical reactions, radiation significantly modified the mean temperature fields, but TRI emission and absorption were found to be negligible. In the work of Dos Santos et al. (2014) it was investigated the validity of the employment of classical modeling (RANS without TRI) for the simulation of non-reactive turbulent channel flows (parietal flow) with combined convective-radiative heat transfer in participant media with several optical thicknesses ($0.01 \leq \tau_0 \leq 100$). This investigation was performed by means of direct comparison between the convective and radiative heat flux computed from averaging the instantaneous convective and radiative heat flux with the LES method (which naturally takes into account TRI) and the radiative heat flux computed from average quantities of the RANS (without TRI). Results obtained by the authors showed that for media with thin optical thicknesses TRI can be neglected for the simulation of non-reactive turbulent flows, as previously found in Mazumder and Modest (1999) and Gupta et al. (2009). For optically thick media ($\tau_0 \geq 10.0$), results showed that RANS with $k - \varepsilon$ model is not recommended for achievement of time-averaged radiative fluxes in the channel surfaces. In this sense, results showed the relevance of TRI for non-reactive flows in optically thick media.

In the present work, it is evaluated the validity of the employment of classical modeling (RANS without TRI) for the simulation of non-reactive free turbulent shear flows with combined convective and radiative transfer in optically thin participant medium. More precisely, it has been simulated a turbulent jet flow in a cylindrical cavity. The main purpose is to investigate whether other kind of flow (in this case a free turbulent shear flow) requires the consideration of TRI for correct prediction of non-reactive flows in optically thin participant media. In this study, a comparison between time-averaged radiative flux at the cavity surfaces obtained with LES (with TRI) and RANS (without TRI) is performed. The studied case has the following dimensionless parameters: $Re_D = 22000$, $Pr = 0.71$ and $\tau_0 = 0.1$. The simulations of the present study are performed with FLUENT® (FLUENT, 2007), which is based on the hexahedral finite volume method for solving the conservation equations of mass, momentum and energy (Patankar, 1980; Versteeg and Malalasekera, 2007) and on the discrete ordinates method (DOM) to solve the radiative transfer equation (Kim et al., 2001; Siegel and Howell, 2002). The turbulence is tackled using the dynamic Smagorinsky subgrid-scale (DSSGS) (Germano et al., 1991; Lilly, 1992) for the LES approach and the standard k-ε model (Launder and Spalding, 1972; Wilcox, 2002) for the RANS modeling. The latter closure model is selected based on its higher applicability in the simulations of literature, e.g., Li and Modest (2003) and Wang et al. (2008).

2. MATHEMATICAL MODELING

2.1. Large Eddy Simulation (LES)

The modeling of transient, incompressible, non-isothermal flows is based on the solution of the conservation equations of the problem together with its boundary and initial conditions. In the LES approach, the mass, momentum and energy equations are spatially filtered with a box filter (Findikakis and Street, 1982). These equations can be written by (Lesieur et al., 2005; Sagaut, 2006):

$$\frac{\partial \overline{v}_i}{\partial x_i} = 0 \qquad (i = 1, 2 \text{ and } 3) \text{ in } t \times \Omega \qquad (1)$$

$$\frac{\partial \overline{v}_i}{\partial t} + \frac{\partial \left(\overline{v}_i \overline{v}_j\right)}{\partial x_j} = -\frac{1}{\overline{\rho}} \frac{\partial \overline{p}}{\partial x_j} \delta_{ij} + \frac{\partial}{\partial x_j} \left\{ \upsilon \left(\frac{\partial \overline{v}_i}{\partial x_j} + \frac{\partial \overline{v}_j}{\partial x_i} \right) - \tau_{ij} \right\} \qquad (i, j = 1, 2 \text{ and } 3) \text{ in } t \times \Omega \qquad (2)$$

$$\frac{\partial \overline{T}}{\partial t} + \frac{\partial}{\partial x_j} \left(\overline{v}_j \overline{T} \right) = \frac{\partial}{\partial x_j} \left\{ \alpha \frac{\partial \overline{T}}{\partial x_j} - q_j \right\} - \overline{\nabla \cdot q_r} \qquad (i, j = 1, 2 \text{ and } 3) \text{ in } t \times \Omega \qquad (3)$$

where $\overline{(\,)}$ represents the large (filtered) scales; ρ is the density of the fluid (kg/m^3); υ is the kinematic viscosity (m^2/s); α is the thermal diffusivity (m^2/s); v_i is the velocity in i-direction, i = 1, 2 and 3 (m/s); x_i corresponds to the spatial coordinate, i = 1, 2 and 3 (m); p is the pressure (N/m^2); T is the temperature (K); δ_{ij} is the Kronecker delta, Ω is the spatial domain (m); t represents the time domain (s); is the filtered divergence of the radiative transfer (W/m^3), which is

inserted as a source term in the energy equation. The terms τ_{ij} and q_j that arise in the filtering process of the momentum and energy conservation equation, respectively, need to be modeled and can be written as:

$$\tau_{ij} = \overline{v_i v_j} - \overline{v}_i \overline{v}_j \tag{4}$$

$$q_j = \overline{v_j T} - \overline{v}_j \overline{T} \tag{5}$$

2.1.1. The dynamic Smagorinsky subgrid-scale model (DSSGS)

The DSSGS is based on the hypothesis of Boussinesq's eddy viscosity (Lesieur et al., 2005). For incompressible flows, the turbulent tensor can be written as:

$$\tau_{ij} = \upsilon_{sgs}\left(\frac{\partial \overline{v}_i}{\partial x_j} + \frac{\partial \overline{v}_j}{\partial x_i}\right) - \frac{2}{3}k\delta_{ij} \tag{6}$$

where υ_{sgs} is the kinematic eddy viscosity (m^2/s^1) and k is the turbulent kinetic energy (m^2/s^2). The turbulent transport of the temperature is obtained by an analogy with the subgrid Reynolds tensor (Lesieur et al., 2005; Sagaut, 2006), and is given by:

$$q_j = \alpha_{sgs}\frac{\partial \overline{T}}{\partial x_j} \tag{7}$$

in which α_{sgs} is the thermal eddy diffusivity (m^2/s).

According to the model, the kinematic eddy viscosity and the thermal eddy diffusivity are given by:

$$\upsilon_{sgs} = C(x,t)^2 \overline{\Delta}^2 \left|\overline{S}\right| \tag{8}$$

$$\alpha_{sgs} = \frac{C(x,t)^2}{\mathrm{Pr}_{sgs}(x,t)} \overline{\Delta}^2 \left|\overline{S}\right| \tag{9}$$

where $\overline{\Delta}$ is the subgrid-scale characteristic length (m); $\left|\overline{S}\right|$ is the strain-rate of the filtered field (s^{-1}) and $\overline{S}_{ij}$ is the filtered-field deformation tensor (s^{-1}), which are given by:

$$\overline{\Delta} = \sqrt[3]{\prod_{i=1}^{3} \Delta x_i} \tag{10}$$

$$\left|\overline{S}\right| = \sqrt{2\overline{S}_{ij}\overline{S}_{ij}} \tag{11}$$

$$\overline{S}_{ij} = \frac{1}{2}\left(\frac{\partial \overline{v}_i}{\partial x_j} + \frac{\partial \overline{v}_j}{\partial x_i}\right) \tag{12}$$

The Smagorinsky constant, $C(x,t)$, and the SGS turbulent Prandtl number, $Pr_{sgs}(x,t)$, are dynamically computed based on the approach proposed by Germano et al. (1991) and modified by Lilly (1992). This modeling is based on the use of two spatial filters with different lengths, providing information on the energy transfer between the solved (obtained in the test filtering region) and not solved scales of motion (Lesieur et al., 2005). More details on the SGS model can be found in the works of Germano et al. (1991), Lilly (1992) and Lesieur et al., (2005).

2.2. Reynolds Averaged Navier-Stokes (RANS)

The time-averaged conservation equations of mass, momentum and energy are the same presented before, Eqs. (1) – (3). However, for RANS simulations, $\overline{(\,)}$ represents time-averaged mean variables. For brevity, the conservation equations will not be re-exhibited here.

The time-averaged fields of velocity, pressure and temperature are reached by means of standard two-equation $k - \varepsilon$

model (Launder and Spalding, 1972; Wilcox, 2002). According to this model it is required the solution of two additional equations for the turbulent kinetic energy k and its dissipation rate ε, which can be expressed as follows:

$$\frac{\partial k}{\partial t}+\bar{v}_j\frac{\partial k}{\partial x_j}=\tau_{ij}\frac{\partial \bar{v}_i}{\partial x_j}+\frac{\partial}{\partial x_j}\left[\left(\upsilon+\frac{\upsilon_t}{\sigma_k}\right)\frac{\partial k}{\partial x_j}\right]-\varepsilon \tag{13}$$

$$\frac{\partial \varepsilon}{\partial t}+\bar{v}_j\frac{\partial \varepsilon}{\partial x_j}=\frac{\partial}{\partial x_j}\left[\left(\upsilon+\frac{\upsilon_t}{\sigma_\varepsilon}\right)\frac{\partial \varepsilon}{\partial x_j}\right]+C_{\varepsilon 1}\frac{\varepsilon}{k}\tau_{ij}\frac{\partial \bar{v}_i}{\partial x_j}-C_{\varepsilon 2}\frac{\varepsilon^2}{k} \tag{14}$$

with

$$\upsilon_t=C_\mu\frac{k^2}{\varepsilon} \tag{15}$$

$$\alpha_t=\frac{\upsilon_t}{\mathrm{Pr}_t} \tag{16}$$

The model constants appearing in the governing equations, Eqs. (13) – (16), are given in Tab. 1.

Table 1. Constants appearing in the k - ε model, Eqs. (13-16).

C_μ	$C_{\varepsilon 1}$	$C_{\varepsilon 2}$	σ_k	σ_ε	Pr_t
0.09	1.44	1.92	1.0	1.3	1.0

In order to calculate turbulence quantities accurately in the near-wall region, it is employed an approach named enhanced wall treatment. This is a near-wall modeling method that combines a two-layer model with wall functions. If the near-wall mesh is fine enough to be able to resolve the laminar sublayer (typically $y^+ \leq 5$), then the enhanced wall treatment will be identical to the traditional two-layer zonal model (Chen and Patel, 1988). If the near-wall mesh is coarse, standard wall functions are used. This model, in general, requires near-wall refined meshes in order to solve the laminar sublayer (more than 10 cells inside the inner layer).

2.3. Radiation modeling

For the solution of the thermal radiation field it is necessary to solve the radiative transfer equation (RTE) (Siegel and Howell, 2002). The filtered radiative transfer equation is obtained after the employment of the spatial filtering operation (Jones and Paul, 2005; Gupta et al., 2009). For a gray gas medium this equation can be written by:

$$\frac{d\bar{i}}{ds}=-\overline{\kappa i}+\overline{\kappa i_b} \tag{17}$$

where s is the coordinate along path of radiation (m), κ is the absorption coefficient (m^{-1}), i_b is the total blackbody intensity ($W/(m^2\cdot sr)$) and i is the total radiative intensity ($W/(m^2\cdot sr)$).

For a real gas, the behavior of the absorption coefficient as a function of wavelength is significantly more complex than the gray gas model, which assumes the absorption coefficient to be independent of the wavelength. More advanced models are available for non-gray media. Despite its simplicity, the gas is considered gray to reduce the difficulties and high computational demands regarding the spectral effects. This same aspect leads to other simplification hypotheses, such as the treatment of density and viscosity as constants.

With the purpose to couple the thermal radiation field and the convection heat transfer in the LES framework, it is necessary to take into account the filtered divergence of the radiative flux ($\overline{\nabla\cdot q_r}$), which for a gray medium is given by:

$$\overline{\nabla\cdot q_r}=4\pi\overline{\kappa i_b}-\overline{\int_{4\pi}\kappa i d\Omega} \tag{18}$$

Coelho (2009) and Roger et al. (2010, 2011) noticed that for the simulation of reactive turbulent flows the average errors associated with neglecting the SGS radiative absorption and emission terms are consistently small, especially for flows with low turbulence intensity. It is estimated that for non-reactive flows, where the turbulence intensity is generally lower than that encountered for reactive flows, the errors associated with neglecting the SGS of radiative transfer are even smaller. Then, in the present study, the modeling of SGS radiative absorption and emission terms will be modeled simply by: $\overline{\kappa i}=\bar{\kappa}\bar{i}$, $\overline{\kappa i_b}=\bar{\kappa}\bar{i}_b$. This simplification was previously performed for the simulation of non-reactive

and reactive flows (Gupta et al., 2009). For the RANS solution no modeling is either employed for the solution of radiative transfer equation (RTE), i.e., the classical modeling is used to solve this problem (Viskanta, 1998).

3. NUMERICAL PROCEDURES

Concerning the simulation of turbulent flows, Eqs. (1) to (3) are solved using a CFD package based on hexahedral finite volume method (FLUENT, 2007). The solver is pressure based and all simulations reported with LES were performed with second-order spatial (bounded central differencing) and implicit temporal discretizations, while the second-order upwind advection scheme was employed for RANS simulations. The bounded central differencing scheme employed in the LES simulations consists of a mixture of two advection schemes: central differencing for regions where the flow is diffusive and upwind of second order for regions where advection is dominant (Zhu and Rodi, 1991). The velocity-pressure coupling is performed with SIMPLE method. More details concerned with the FVM can be found in Patankar (1980) and Versteeg and Malalasekera (2007).

The radiative transfer equation, Eq. (17), is solved with the discrete ordinates method (DOM) (Siegel and Howell, 2002; Kim et al., 2001). For the solution, it is employed the approximation (S_4), $n = 4$. For three-dimensional enclosures, the total number of different discrete directions, M, to be considered at each computational node is defined as $M = n(n+2)$. Then, in the present work the number of discrete directions for each computational node is $M = 24$.

The numerical simulations are performed using a computer with two dual-core Intel processors with 2.67 GHz clock and the memory amount of 8 GB. For parallelization it is used the library Message Passing Interface (MPI). The time processing for the simulations combining convection and thermal radiation by means of LES with TRI and RANS without TRI are nearly 5.40×10^6 s and 1.35×10^6 s, respectively.

The calculations are considered converged when the residuals for the mass, momentum, energy and intensity of radiation between two consecutive iterations were less than 10^{-4}, 10^{-6}, 10^{-8} and 10^{-6}, respectively. Moreover, an under-relaxation factor of 0.7 is imposed for all conservation equations.

The verification of the numerical models employed here for simulation of forced convective turbulent channel flows and for solution of the radiative transfer problem into an equilateral triangular enclosure with an absorbing and emitting participant medium was previously performed in the work of Dos Santos et al. (2014). For the sake of brevity this verification was not repeated in the present study.

4. RESULTS AND DISCUSSION

The present simulations investigate whether for a free turbulent shear flow the non-relevance of TRI for prediction of time-averaged radiative flux of combined convective and radiative transfer in optically thin participant media is still valid. It is worthy to mention that in Dos Santos et al. (2014) it was noticed that TRI was not relevant for prediction of convective and radiative fluxes in channels surfaces (parietal turbulent flow) for optically thin media. One additional motivation for the study of this case lies on the fact that turbulent flows with combined convective and radiative heat transfer in participant media represents in a satisfactory way the flow in combustor chamber exhaustions. In this sense, the results reached here can improve the comprehension about this kind of problem.

Figure 1 illustrates the domain of the cylindrical cavity flow studied here. The domain has the following dimensions: $R = D/2 = 5.0 \times 10^{-2}$ m, $R_1 = 12.5 \times 10^{-2}$ m, $R_2 = 25.0 \times 10^{-2}$ m and $L = 1.7$ m. The similarity principle is employed to determine the thermophysical properties of the flow. The convective parameters are defined as $\mathrm{Re}_D = 22000$ and $\mathrm{Pr} = 0.71$. The imposed boundary conditions employed in the present simulations are also presented in Fig. 1. The flow is caused by the imposition of a constant velocity profile ($v_{\mathrm{in}} = 100$ m/s) at the inlet of the cylindrical cavity. In this same surface, it is imposed a temperature of $T_{in} = 2000$ K. At the outlet of cylindrical cavity it is imposed a null tension for the velocity field and null flux for heat transfer (Outflow). For the other surfaces, the velocity field has non-slip and impermeability condition ($v_1 = v_2 = v_3 = 0$ m/s) and for the thermal field a constant temperature of $T_S = 400$ K is imposed. Concerning the radiative problem, all the surfaces are treated as black, and the total emissivity is given by: $\varepsilon_W = 1$. Moreover, the participant medium is treated as a gray gas with an absorption coefficient of $\kappa = 0.4$ m^{-1} to simulate a participant medium with an optical thickness of $\tau_0 = \kappa \bullet R_2 = 0.1$ (which is an optically thin medium).

For this specific case, the domain is discretized with $50 \times 50 \times 65$ discrete volumes in r, θ and z directions for both simulations with LES and RANS. The grid is refined in the radial direction near the lateral surfaces (with 10 cells in $y^+ = 5$) and in the jet region (20 cells with an aspect ratio of AR = 1.05). In θ and z directions, the grid is considered uniform. For the simulations with LES, the minimal cutoff wavenumber is given by 800 m^{-1}. Concerning the temporal discretization, for both simulations performed it is employed a time step of $\Delta t = 3.0 \times 10^{-5}$ s. The simulations are performed until a final time of $t_f = 0.5$ s. The time interval of $0.25 \leq t \leq 0.5$ s where used for determination of time-averaged parameters (temperature and divergence of radiative flux).

Firstly, it is presented a comparison between the temperature fields for a flow with $\mathrm{Re}_D = 22000$, $\mathrm{Pr} = 0.71$ and $\tau_0 = 0.1$ when the flow reaches the steady state. Figures 2(a) and 2(b) show the time-averaged temperature fields obtained with RANS and LES, respectively. In general, the temperature fields obtained with two methods have slight differences. For instance, the turbulent jet obtained with LES has a higher penetration in the axial direction and a lower width than that reached with RANS simulation.

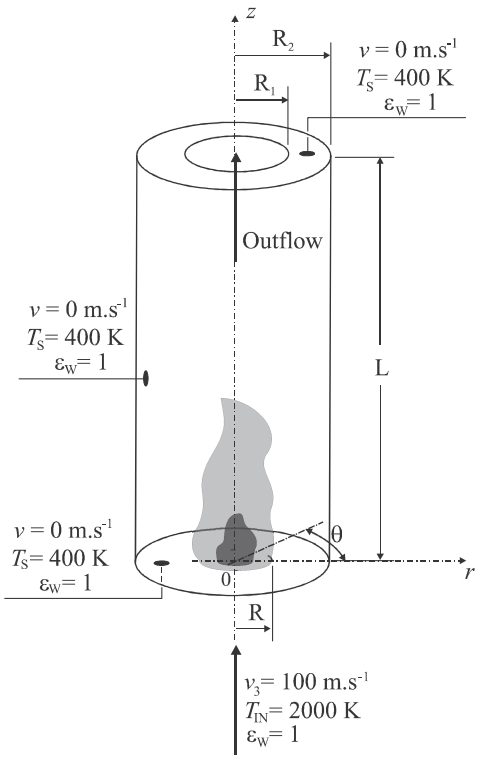

Figure 1. Computational domain for a turbulent jet flow with Re_D = 22000, Pr = 0.71 and τ_0 = 0.1.

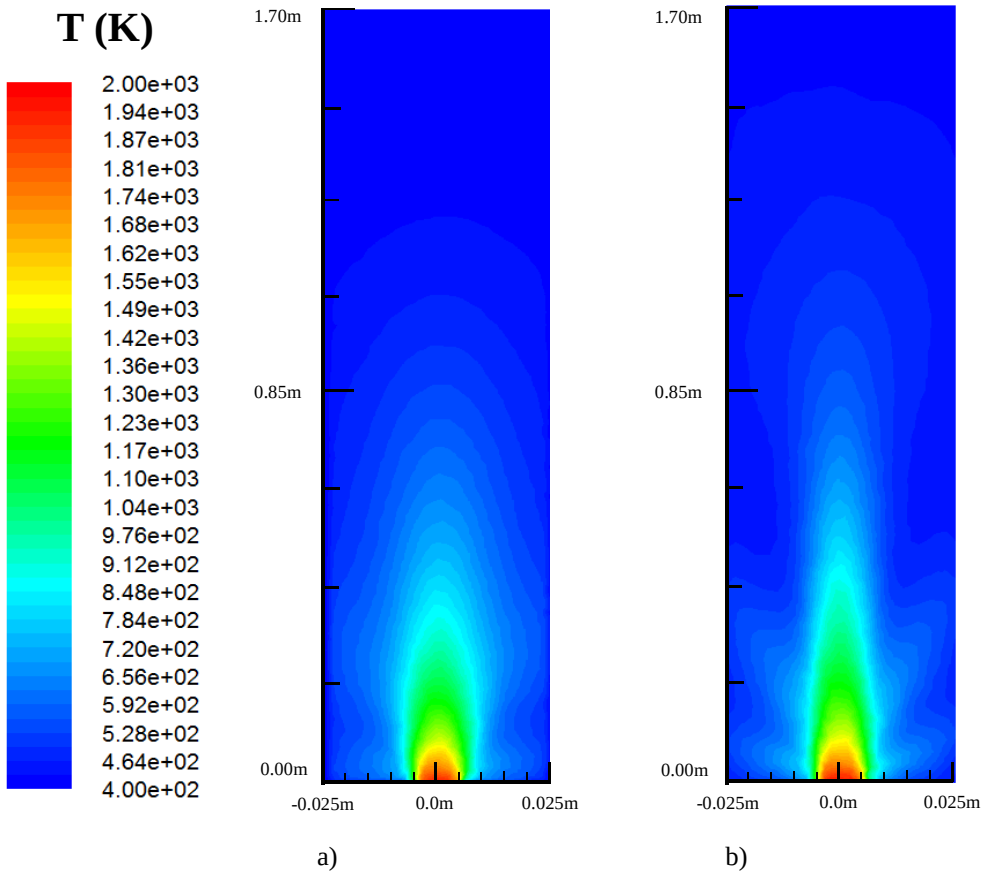

a) b)

Figure 2. Time-averaged temperature fields for the flow with Re_D = 22000, Pr = 0.71 and τ_0 = 0.1 at the steady state: a) RANS (without TRI), (b) LES (with TRI).

In order to perform a quantitative comparison between the time-averaged temperature fields obtained with LES and RANS, temperature profiles as function of radial coordinate (r) for three different positions of azimuth axis (z) are monitored. Figures 3(a), 3(b) and 3(c) present the profiles for the following positions: z = 0.2 m, z = 0.4 m and z = 1.2 m, which represents regions inside, above and far from the jet. In general, the different methods lead to local differences in

prediction of temperature fields. For the monitoring line at z = 0.2 m, Fig. 3(a), the temperature profile obtained with TRI (LES) has a higher magnitude in the central region of cavity (-0.05 m $\leq r \leq$ 0.04 m) than that reached for the flow without TRI (RANS). However, the temperature profile reached with RANS has a higher magnitude than that predicted with LES in the region 0.05 m $\leq r \leq$ 0.13 m. In average, the magnitude of temperature profile obtained with RANS is 0.8 % higher than that reached with LES for z = 0.2 m. It is important to mention that in this region large amount of radiative energy is emitted due to the high temperature of the jet. Then, large discrepancies of temperature field in this region can conduct to large differences in prediction of radiative fluxes in cavity surfaces. For z = 0.4 m, Fig. 3(b), a similar behavior obtained for z = 0.2 m is noticed, i.e., in the central region of the jet (-0.07 m $\leq r \leq$ 0.04 m) the temperature magnitude is higher for simulation with LES than for simulation with RANS, while in peripheral regions the magnitude of temperature reached with RANS is higher than that predicted with LES. The average magnitude of temperature profile obtained with LES is almost 5 % higher than that reached with RANS. For z = 1.2 m, Fig 3(c), the magnitude of temperature profile reached with LES is 6.7 % hotter than that obtained with RANS. This inversion of magnitude between LES and RANS at this region is concerned with the higher penetration of jet in the cavity domain for the LES predictions. It is also noticed that differences between predictions with LES and RANS increases for regions far from the jet inlet. However, the temperature field magnitudes in these regions are strongly smoothed. As a consequence, this region probably will not cause differences on the radiative fluxes predictions with the different methods.

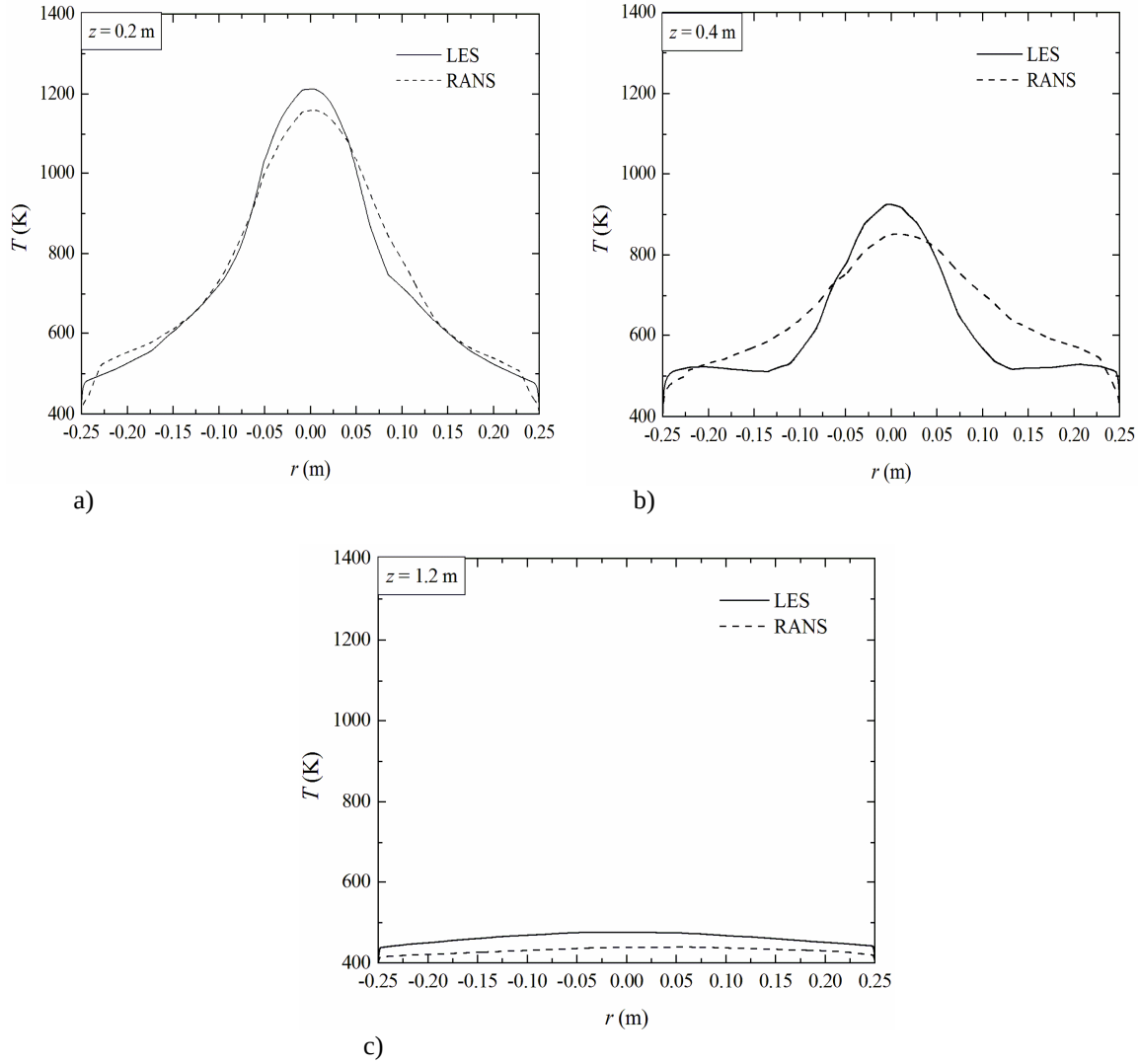

Figure 3. Comparison of time-averaged temperature profiles for the flow Re_D = 22000, Pr = 0.71 and τ_0 = 0.1 at the steady state obtained with LES and RANS for several azimuthal positions: a) z = 0.2 m, b) z = 0.4 m, c) z = 1.2 m.

In order to investigate the influence of differences reached for the temperature fields with different closure models over local radiative thermal field, the time-averaged divergence of radiative flux as a function of radial coordinate is achieved for the same placements where the time-averaged temperature profiles were evaluated: z = 0.2 m, z = 0.4 m and z = 1.2 m. These results are presented in Figs. 4 (a) – (c), respectively. In general, the profiles of time-averaged divergences of radiative flux have a similar behavior to that obtained for temperature profiles. For z = 0.2 m, Fig. 4(a), in spite of higher averaged magnitude of temperature for RANS simulations, the mean magnitude of time-averaged divergence of radiative flux obtained with LES is 6.4 % higher than that achieved for RANS. The higher magnitude of

divergence of radiative flux for the simulation with LES is related with the large influence of the temperature field in the central region of the cylindrical cavity. The emission of radiative energy is proportional of fourth power local temperature and the highest differences of temperature are placed in the central region of the cavity. For z = 0.4 m, Fig. 4(b), the magnitude of divergence of radiative flux is higher for simulations with RANS than that reached for LES, even with the higher magnitude of temperature field in the central region of the cavity obtained with LES simulation. It is also noticed that the mean magnitude of divergence of radiative flux for z = 0.4 m is nearly two times lower than that achieved for z = 0.2 m. This fact is related with the decrease of magnitude of temperature field towards the outlet of cylindrical cavity. For z = 1.2 m, Fig. 4(c), the magnitude of divergence of radiative flux is strongly reduced due to the sensitive decrease of temperature magnitude.

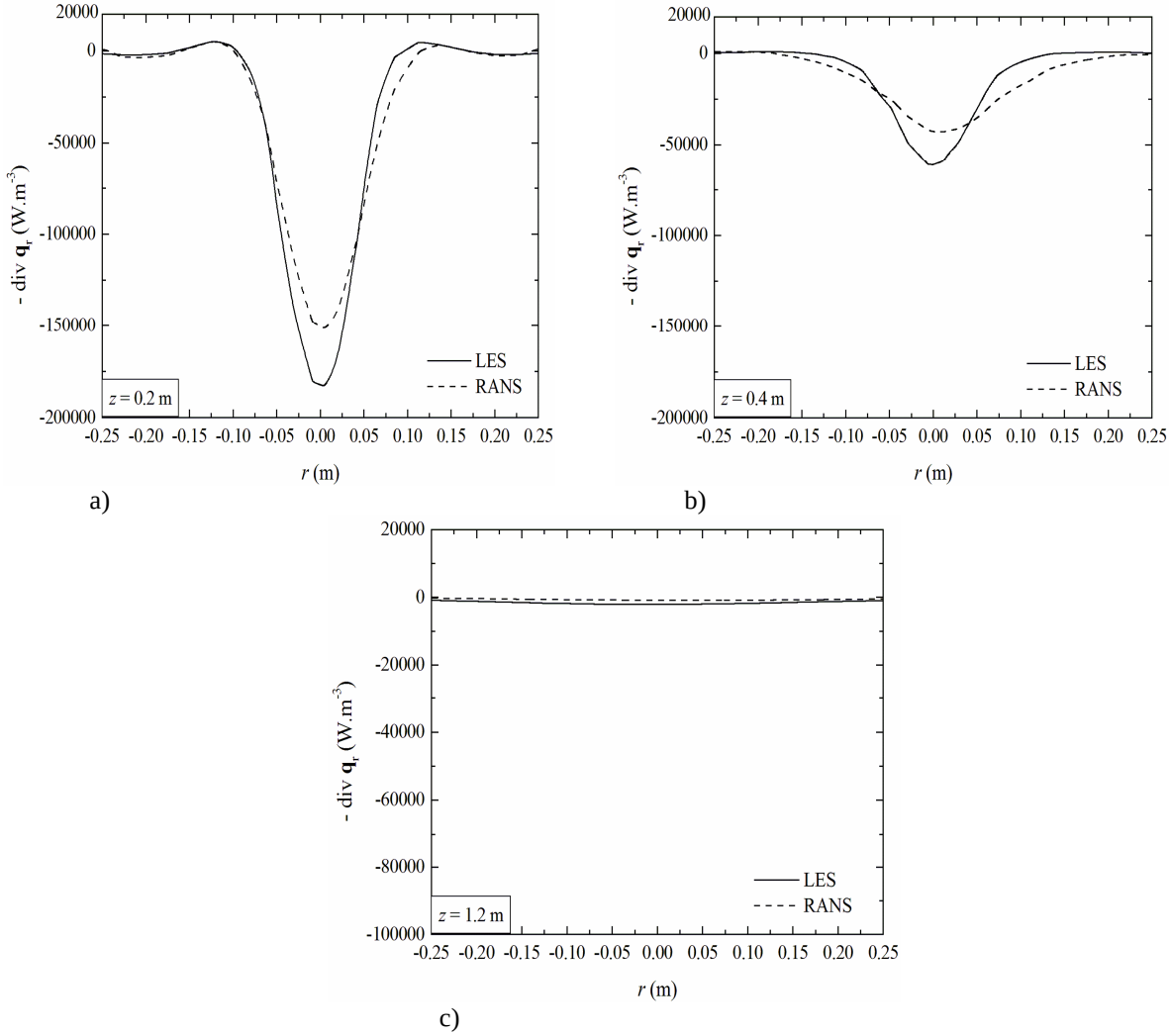

Figure 4. Comparison of time-averaged divergence of radiative flux profiles for the flow Re_D = 22000, Pr = 0.71 and τ_0 = 0.1 at the steady state obtained with LES and RANS for several azimuthal positions: a) z = 0.2 m, b) z = 0.4 m, c) z = 1.2 m.

With the aim to evaluate the effect of differences of temperature and radiative fields over the radiative flux (which is a global parameter of the problem) the time-averaged radiative flux along the cylindrical cavity surface and instantaneous radiative fluxes in two monitoring points Point 1: r = 0.25 m, z = 0.1 m; Point 2: r = 0.25 m, z = 0.5 m) are obtained. These results are depicted in Fig. 5(a) and 5(b), respectively. Figure 5(a) shows that local differences in the temperature and divergence of radiative fluxes does not led to differences in the prediction of radiative fluxes in the cavity surface. Figure 5(a) also shows that in the range near the jet (0.0 m $\leq z \leq$ 0.6 m) the highest difference between the radiative fluxes with TRI (LES) and without TRI (RANS) is lower than 1.0 %, showing that differences caused by the use of different closure models nor TRI effects cause differences in the radiative fluxes. As the value of z increases, the magnitude of radiative flux decreases significantly and differences of predictions with and without TRI increases to nearly 5.0 %. In Fig. 5 (b) can be seen only minor differences between the LES and RANS predictions, even for the instantaneous fluctuations, corroborating the non-relevance of TRI for this kind of flow.

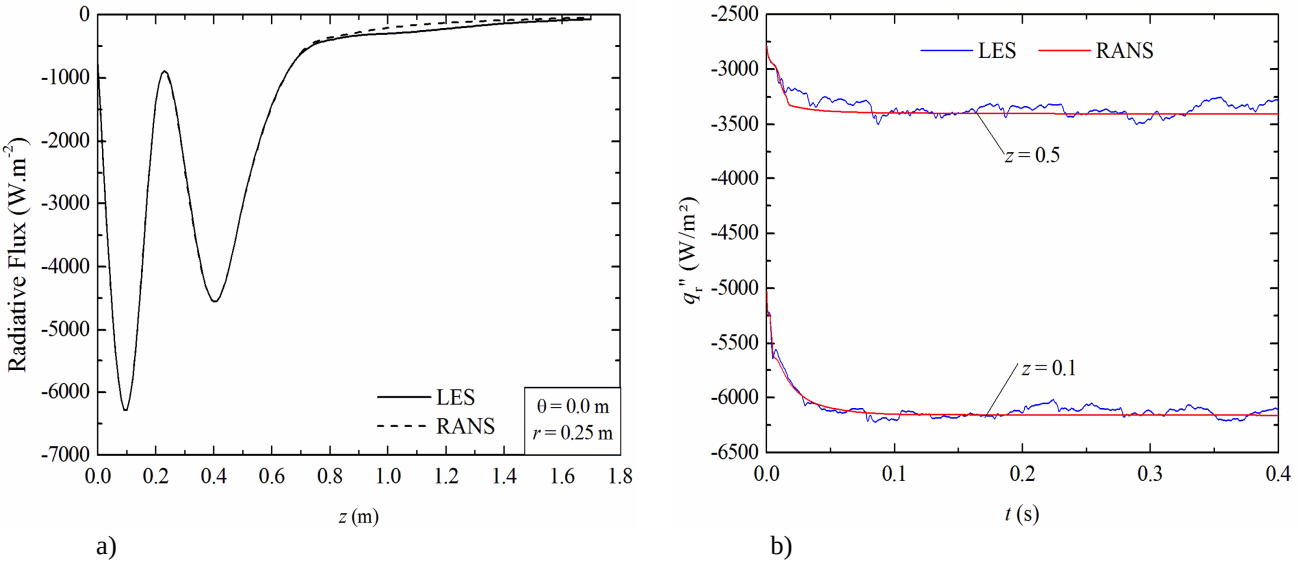

Figure 5. Radiative heat flux obtained with TRI (LES) and without TRI (RANS): a) time-averaged heat flux in cavity surface, b) instantaneous radiative flux in two monitoring points of cylindrical cavity surface.

5. CONCLUSIONS

The present work investigated numerically the validity of the employment of traditional modeling (RANS without TRI) for simulation of combined convective and radiative heat transfer free turbulent shear flows in optically thin participant media. It was simulated a cylindrical cavity turbulent flow comparing the results of time-averaged temperature and divergence of radiative flux along the cavity domain, as well as, the radiative flux in cavity surfaces obtained with TRI (LES) and without TRI (RANS) when the flow reached the steady state. The studied case has the following dimensionless parameters: Re_D = 22000, Pr = 0.71 and τ_0 = 0.1. The simulations of the present study were performed with the finite volume method for solution of conservation equations of mass, momentum and energy (Patankar, 1980; Versteeg and Malalasekera, 2007) and it was used the discrete ordinates method (DOM) to solve the radiative transfer equation (Siegel and Howell, 2002). Both models are implemented in the numerical code FLUENT® (FLUENT, 2007). The turbulene was tackled using dynamic Smagorinsky subgrid-scale (DSSGS) (Germano et al., 1991; Lilly, 1992) for the LES approach and the standard k-ε model (Launder and Spalding, 1972; Wilcox, 2002) for the RANS modeling and the participant media is treated as a gray gas.

Time-averaged profiles of temperature along the cavity domain were measured showing that the use of different methods, with TRI (LES) and without TRI (RANS) led to local slight differences of temperature fields. Similar differences were obtained for the time-averaged divergence of radiative flux as a reflection of deviations in the temperature field. These differences are probably related with the use of different closure models for turbulence. In order to investigate this fact, simulations of purely forced convective flows for the same domain comparing LES and RANS with different methods (k – ε, k – ω and Reynolds Stress Model) are in progress. Other aspect that deserves investigation is the use of the adjusted constants employed for the k – ε model.

In spite of local deviations for time-averaged temperature and divergence of radiative fluxes along the cylindrical cavity domain, as well as, the consideration of temperature fluctuations for LES simulations, the radiative fluxes in the cylindrical cavity surface obtained with TRI and without TRI were in excellent agreement. In other words, results showed the non-relevance of TRI for non-reactive shear turbulent flows in optically thin participant media, similarly to previous observations in the simulation of channel (parietal) flows.

6. ACKNOWLEDGEMENTS

E. D. dos Santos thanks FAPERGS for financial support (Process: 12/1418-4), L. A. O. Rocha and F. H. R. França thanks CNPq for research grant.

7. REFERENCES

Chen, H. C. and Patel, V. C., 1988, “Near-wall turbulence models for complex flows including separation”, AIAA Journal, 6, Vol. 26,, pp. 641–648.

Coelho, P.J., 2007, “Numerical simulation of the interaction between turbulence and radiation in reactive flows”, Progress in Energy and Combustion Science, Vol. 33, No. 4, pp. 311–383.

Coelho, P.J., 2009, “Approximate solutions of the filtered radiative transfer equation in large eddy simulations of turbulent reactive flows”, Combustion and Flame, Vol. 156, No. 5, pp. 1099–1110.

Deshmukh, K.V., Modest, M.F. and Haworth, D.C., 2008, “Direct numerical simulation of turbulence–radiation interactions in a statistically one-dimensional nonpremixed system”, Journal of Quantitative Spectroscopy and Radiative Transfer, Vol. 109, No. 14, pp. 2391–2400.

Dos Santos, E.D., Isoldi, L.A., Petry, A.P. and França, F.H.R., 2014, “A numerical study of combined convective and radiative heat transfer in non-reactive turbulent channel flows with several optical thicknesses: a comparison between LES and RANS”, Journal of the Brazilian Society of Mechanical Sciences and Engineering, Vol. 36, No. 1, pp. 207–219.

Findikakis, A. N. and Street, R. L., 1982, “Mathematical description of turbulent flows”, Journal of Hydraulic Division-ASCE, Vol. 108,, pp. 887 – 903.

FLUENT., 2007, “Documentation Manual – FLUENT 6.3.16”, Ansys, Inc.

Gonçalves dos Santos, R., Lecanu, M., Ducruix, S., Gicquel, O., Iacona, E. and Veynante, D., 2008, “Coupled large eddy simulations of turbulent combustion and radiative heat transfer”, Combustion and Flame, Vol. 152, No. 3, pp. 387–400.

Gupta, A., Modest, M.F. and Haworth, D.C., 2009, “Large-Eddy Simulation of Turbulence-Radiation Interactions in a Turbulent Planar Channel Flow”, Journal of Heat Transfer, Vol. 131, No. 6, p. 061704.

Jones, W.P. and Paul, M.C., 2005, “Combination of DOM with LES in a gas turbine combustor”, International Journal of Engineering Science, Vol. 43, No. 5-6, pp. 379–397.

Kim, Man Young, Baek, Seung Wook and Park, Jae Hyun., 2001, “Unstructured finite-volume method for radiative heat transfer in a complex two-dimensional geometry with obstacles”, Numerical Heat Transfer - Part B Applications, Vol. 39,, pp. 617–635.

Launder, B. E. and Spalding, D. B., 1972, "Lectures in mathematical models of turbulence", Academic Press, London, England.

Lesieur, M., Métais, O. and Comte, P., 2005, "Large-eddy simulations of turbulence", New York, USA.

Li, G. and Modest, M.F., 2003, “Importance of Turbulence-Radiation Interactions in Turbulent Diffusion Jet Flames”, Journal of Heat Transfer, Vol. 125, No. 5, p. 831.

Lilly, D. K., 1992, “A proposal modification of the Germano subgrid-scale closure method”, Physics of Fluids A, Vol. 4,, pp. 633–635.

Mazumder, S. and Modest, M.F., 1999, “A probability density function approach to modeling turbulence_radiation interactions in nonluminous flames”, International Journal of Heat and Mass Transfer, Vol. 42,, pp. 971–991.

Patankar, S. V., 1980, "Numerical heat transfer and fluid flow", McGraw Hill, New York, USA.

Pope, S.B., 2008, "Turbulent Flows", Cambridge University Press.

Roger, M., Coelho, P.J. and da Silva, C.B., 2010, “The influence of the non-resolved scales of thermal radiation in large eddy simulation of turbulent flows: A fundamental study”, International Journal of Heat and Mass Transfer, Vol. 53, No. 13-14, pp. 2897–2907.

Roger, M., Coelho, P.J. and da Silva, C.B., 2011, “Relevance of the subgrid-scales for large eddy simulations of turbulence–radiation interactions in a turbulent plane jet”, Journal of Quantitative Spectroscopy and Radiative Transfer, Vol. 112, No. 7, pp. 1250–1256.

Roger, M., Da Silva, C.B. and Coelho, P.J., 2009, “Analysis of the turbulence–radiation interactions for large eddy simulations of turbulent flows”, International Journal of Heat and Mass Transfer, Vol. 52, No. 9-10, pp. 2243–2254.

Sagaut, P., 2006, Large eddy simulation for incompressible flows, an introduction, Springer Berlin Heidelberg, Berlin, Germany.

Siegel, R. and Howell, J. R., 2002, "Thermal radiation heat transfer", Taylor & Francis, New York, USA, 4thed.

Versteeg, Henk Kaarle and Malalasekera, Weeratunge., 2007, An Introduction to Computational Fluid Dynamics: The Finite Volume Method, Pearson.

Viskanta, R., 1998, “Overview of convection and radiation in high temperature gas flows”, International Journal of Engineering Science, 36, pp. 1677–1699.

Wang, A., Modest, M.F., Haworth, D.C. and Wang, L., 2008, “Monte Carlo simulation of radiative heat transfer and turbulence interactions in methane/air jet flames”, Journal of Quantitative Spectroscopy and Radiative Transfer, Vol. 109, No. 2, pp. 269–279.

Wilcox, D. C., 2002, Turbulence modeling for CFD, DCW Industries, La Canada, USA, 2nded.

Zhu, J. and Rodi, W., 1991, “A Low Dispersion and Bounded Convection Scheme”, Computater Methods in Applied Mechanics and Engineering, Vol. 92, pp. 225–232.

7. RESPONSIBILITY NOTICE

The author(s) is (are) the only responsible for the printed material included in this paper.

NUMERICAL MODELLING OF SWIRLING FLOW IN A COMBUSTION CHAMBER

José Luis Potrich Anapolski, zeanapolski@gmail.com
Thamy Cristina Hayashi, thamy.hayashi@mecanica.ufrgs.br
Universidade Federal do Rio Grande do Sul_UFRGS. Sarmento Leite, 425; Cep: 90.050-170; Porto Alegre; Rio Grande do Sul

Abstract. *The purpose of the present work is an pure numerical investigation of the field flow in a cylindrical combustor using air as fluid. Aerodynamic effects are analyzed, mainly swirl number base on the field flow. The geometry and numerical solution are provided by ANSYS Fluent software applications. The standard k-ε and k-ω SST turbulence models are used and discussed about your models and solutions. After execution of this simulations was possible mentioning that the swirl number affected the characteristics of the flow when the rate of axial and tangential velocity components* changed.

1. INTRODUCTION

Swirling flows are observed in natural flows, such as tornadoes and typhoons, and have been widely used in technical applications, such as aeronautics, heat exchange, spray drying, separation, combustion, more specifically, boilers, aero craft engines, cyclones equipment's, industrial burners, gas combustors, etc. Studies have been development around efficiency burners with low NOx which based on chemical kinetic of Nitrogen and flow of combustors analysis; it can be reached when the flame is stabilized. The flame stabilization can be achieved with swirl induction by a burner when a reverse and rotating flow is formed creating an central recirculation zone (CRZ) that diminishes the dispersion of flame that occur by convective effects according to (Bourgouin et al., 2013). With these information's is possible see that the aerodynamics knowledge is an important part to study before entering in combustion processes as (Mafra, 2000), to anchoring it, namely an instability flame is responsible to generate a heat loss in combustion region caused by dispersion flame which leave the temperature decay and the CO formation passing to occur. In this way a field flow compound by CRZ is one form to control the emissions according to experimental work of (Lenço, 2004) where state that the length of CRZ induces a high or minor NOx formation when a swirl number is optimized. A typical CRZ is shown as following Fig. 1.

As researchers extensively publishing and according to (Negro and O'Doherty, 2000) at low swirl level there may be significant radial pressure gradient at some axial position in order to generate a centrifugal effects, but not strong due to cause axial recirculation. Whenever, when increasing the swirl level, a strong coupling with tangential and axial velocity components develops, forming a highly defined internal circulation, to more exactly, this stage is reached when the adverse pressure gradient along the flow axis cannot be maintain the kinetic energy of the fluid particles which flowing in the axial direction, then a recirculation zone forms in the central portion of the flow. This zone (CRZ) is kind of vortex breakdown acting such an aerodynamic blockage in order to stabilize the flame.

The point of view of present work is analyzing the different effects on field isothermal flow when swirl number is varying using k-ε and k-ω SST turbulence models into cylindrical combustor by ANSYS Fluent commercial application.

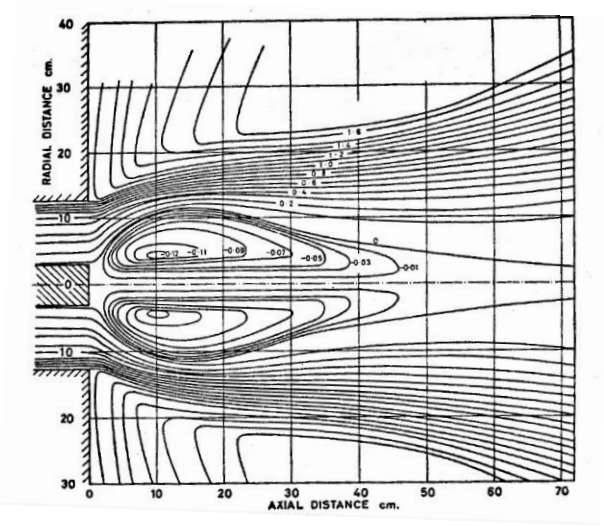

Figure 1. Stream lines of typical central recirculation zone (CRZ).

1.1 Experimental and Numerical Works

The experimental works of (Bizzo, 1997) and (Lenço, 2004) consisted in predict the pollutions on cylindrical combustors using different fuels showing that the emissions occurring when high temperature fluctuations and oxygen are available on combustors. Another important result obtained was the emissions decreasing when the swirl number was increased at certain excess air.

As paper of (Shih et al., 1997) a rotating pipe flow and also swirling flow with recirculation, was found that standard k-ε equations had a numerically simple and robust when applied in aircraft engine combustors.

On work of (Jakirlic et al., 2002) a computationally studied several types of rotating and swirling flows for a range of swirl numbers was obtained. It was found that the Reynolds stress model (RSM) was superior to other models tested. The major advantage of the RSM model was its ability to capture the stress anisotropy in the near-wall region, presenting a major advantage on k-ε models, moreover around complex geometries. Whenever, RNG (Re-normalization Group) k-ε models capture the effect of curvature suited to rotating flows as preliminary results.

At the paper of (Escue A., and Cui, J., 2009) two (RANS-Reynolds Average Navier-Stokes) type turbulence models were used and compared using commercial Fluent code: the RNG k-ε model and the Reynolds stress model (RSM). Velocity and turbulence profiles obtained downstream were compared the experimental results. For lower swirl numbers (too less than 1.00), the RNG k-ε model was found to be superior to the RSM. As the swirl number is increased (too than 2.00), neither model is seen to outperform the other.

Whenever, according to (Menter F.R., 2004) k-ω SST is more suited when complex geometries are applied, rotating flow is dominant into the domain caused by swirl induction, and better performing on the wall effect, moreover k-ε equations is normally applied based on yours quickly convergences in order to previously analysis.

2. TURBULENCE MODELS AND GOVERNING EQUATIONS

The full scales of the turbulence flow has a heavy equations to solve and consequently high computational costs, whenever the minor scales information's were important to analysis, but in many situations is sufficiently treat the flow as an average. The Reynolds Stress concept introduced by (Reynolds, 1895) which describe the flow at the same form being a start way of turbulence models studies. According this concept any property of the flow can be writing with average by the long indefinably time. When a temporal variations of the flow, nothing associates to the turbulence, occurring by the too higher time scales than the largest vortices, then an time average from variables turns suitable to describe the turbulence flow as the following Eq. (1).

$$\overline{U} = \frac{1}{T}\int_{to-T/2}^{to+T/2} U dt \tag{1}$$

The Reynolds Average Navier Stokes Equations (RANS) which was implemented at the present work are basis on the same principle that results into a method to determine the Reynolds stress. The models considered are originally derive from turbulent viscosity propose by (Boussinesq, 1877) which getting the turbulent relations in the momentum transfer by the Reynolds stress of the mean flow, the Eqs. (2-8) below represent the mass conservation, momentum, k-ε and k-ω SST turbulence models respectively (Wilcox, 1993). The terms presenting at the next equations $\rho, t, x_i, \bar{u}_i, p, \mu, \delta_{ij}, \overline{\rho u_i' u_j'}, k, \varepsilon, \omega, \mu_T$ respectively are: density, time, position, mean unidirectional velocity, pressure, molecular viscosity, strain-rate tensor, Reynolds stress, turbulence kinetic energy, dissipation of turbulence kinetic energy, dissipation per unit turbulence kinetic energy, and turbulent viscosity. Closure coefficients are: $\sigma_k, c_{\varepsilon 1}, c_{\varepsilon 2}, \sigma_\varepsilon, \beta^*, \sigma^*, \alpha, \beta, \sigma$.

$$\frac{\partial \rho}{\partial t} + \frac{\partial}{\partial x_i}(\rho \bar{u}_i) = 0 \tag{2}$$

$$\frac{\partial}{\partial t}(\rho \bar{u}_i) + \frac{\partial}{\partial x_i}(\rho \bar{u}_i \bar{u}_j) = -\frac{\partial p}{\partial x_j} + \frac{\partial}{\partial x_j}\left[\mu\left(\frac{\partial \bar{u}_i}{\partial x_j} + \frac{\partial \bar{u}_j}{\partial x_i} - \frac{2}{3}\delta_{ij}\frac{\partial \bar{u}_j}{\partial x_i}\right)\right] + \frac{\partial}{\partial x_j}\left(-\overline{\rho u_i' u_j'}\right) \tag{3}$$

$$\tau_{ij} = -\overline{\rho u_i' u_j'} \tag{4}$$

$$\frac{\partial k}{\partial t} + \bar{u}_j \frac{\partial k}{\partial x_j} = \tau_{ij}\frac{\partial \bar{u}_i}{\partial x_j} - \varepsilon + \frac{\partial}{\partial x_j}\left[\left(\mu + \mu_T / \sigma_k\right)\frac{\partial k}{\partial x_j}\right] \tag{5}$$

$$\frac{\partial \varepsilon}{\partial t}+\bar{u}_j\frac{\partial \varepsilon}{\partial x_j}=C_{\varepsilon 1}\frac{\varepsilon}{k}\tau_{ij}\frac{\partial \bar{u}_i}{\partial x_j}-C_{\varepsilon 2}\frac{\varepsilon^2}{k}+\frac{\partial}{\partial x_j}\left[\left(\mu+{\mu_T}/{\sigma_\varepsilon}\right)\frac{\partial \varepsilon}{\partial x_j}\right] \tag{6}$$

$$\frac{\partial k}{\partial t}+\bar{u}_j\frac{\partial k}{\partial x_j}=\tau_{ij}\frac{\partial \bar{u}_i}{\partial x_j}-\beta^* k\omega+\frac{\partial}{\partial x_j}\left[\left(\mu+\sigma^*\mu_T\right)\frac{\partial k}{\partial x_j}\right] \tag{7}$$

$$\frac{\partial \omega}{\partial t}+\bar{u}_j\frac{\partial \omega}{\partial x_j}=\alpha\frac{\omega}{k}\tau_{ij}\frac{\partial \bar{u}_i}{\partial x_j}-\beta\omega^2+\frac{\partial}{\partial x_j}\left[\left(\mu+\sigma\mu_T\right)\frac{\partial \omega}{\partial x_j}\right] \tag{8}$$

3. PROBLEM DESCRIPTION

3.1 Physical Domain

An cylindrical combustor was modeled with same principle of swirler as following Fig. 2 where axial and tangential inlet air is injected which the velocity components form an rotational flow occurring an particular swirl number depending the velocity components arrangement. The physical domain is express by Fig. 3 below where the combustor length have 0.8m, minor and higher swirler diameter respectively are 0.02m and 0.06m based on paper (Eldrainy Y.A. et. al., 2009).

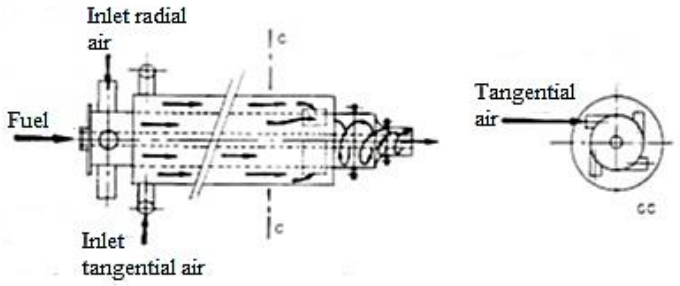

Figure 2. Swirler with axial and tangential inlet air.

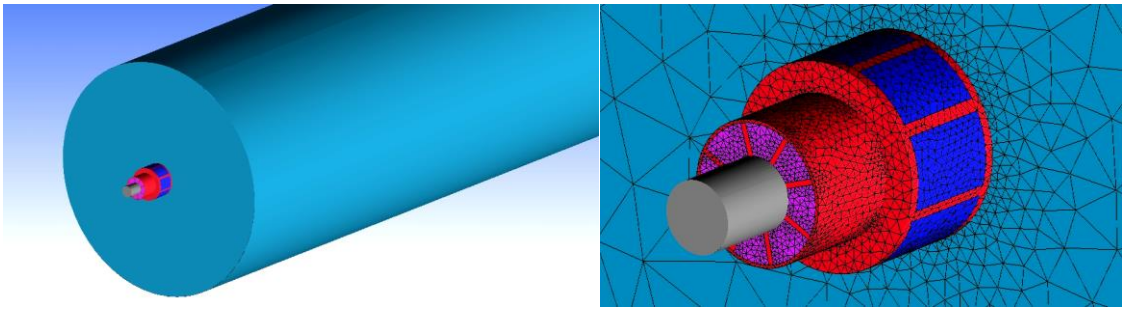

Figure 3. Combustor and swirler domain. Tetraedric mesh 1,626,140 elements. Boundary conditions: axial and tangential mass flow rate (pink and blue surfaces respectively), pressure outlet at the end of combustor surface.

The swirl number according to (Beér and Chigier, 1972) is determined by the dimensionless parameter, *S* as Eq. (9) below, where *U* and *W* are the axial and tangential velocity components respectively and *R* is the swirler radius. After Beér and Chigier a study related that the pressure term can be negligence as (Beltagui e Maccallum, 1976). The range of swirl number, implemented on the present work, as three numerical cases as Tab. 1 below.

$$S=\frac{\int_0^R \rho UWr^2 dr}{R\int_0^R \rho U^2 r dr} \tag{9}$$

Table 1. Swirl parameters modeled. Three cases.

Case	a	b	c
Tangential mass flow rate (1)	0.05	0.075	0.1
Axial mass flow rate (1)	0.15	0.125	0.1
Swirl number	0.586	0.801	1.220

(1) : initial pressure 101325 Pa

3.2 Numerical Scheme

By the commercial software fluent code and applying both turbulence models on geometry as last Fig. 3, it was possible comparing the results provided for each case in Tab. 1. For all cases simulations a steady-state and pressure based solver was modeled which solves the governing equations. The semi implicit method for pressure linked equations (SIMPLE) algorithm was used for pressure velocity coupling. This algorithm satisfies the mass conservation equation by using a relationship between velocity and pressure corrections. As spatial discretization scheme was used: second order for pressure, turbulent kinetic energy, turbulent dissipation rate and first order for momentum.

4. RESULTS AND DISCUSSION

Before starting simulations a mesh independency was analyzed using the static pressure as a parameter (knowing that this is a strong characteristic to form recirculation zones) running four mesh size by k-ω SST as Tab. 2. In this way the mesh III was better describe than others when comparing the data with (Eldrainy Y.A. et. al., 2009) such as Fig. 4.

Table 2. Mesh independency. Four mesh tested.

Tetrahedric mesh tested(1)	I	II	III	IV
Tetrahedric mesh elements(1)	839,734	1,106,558	1,626,140	2,258,294

(1) : k-ω SST case b.

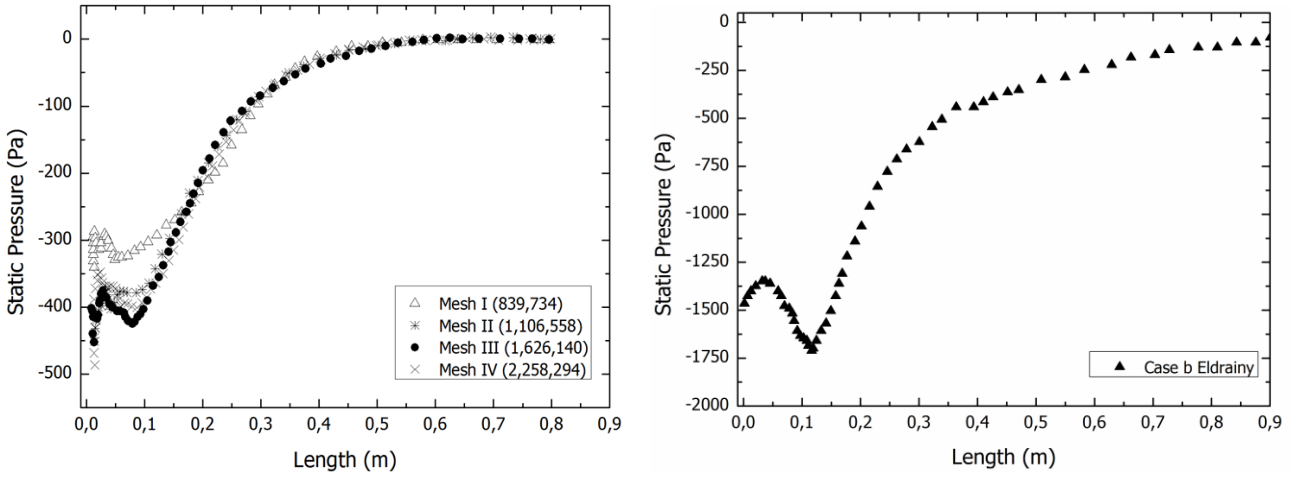

Figure 4. Mesh independency: Meshes I, II, II and IV. Center line data. Initial pressure 101325 Pascal.

Modeling three cases applied in turbulence models (k-ε and k-ω SST) was possible analyzing the field flow and static pressure which both parameters affected by axial and tangential velocity components, in other words, swirl number. The results can be seen on the following Fig. 5-6.

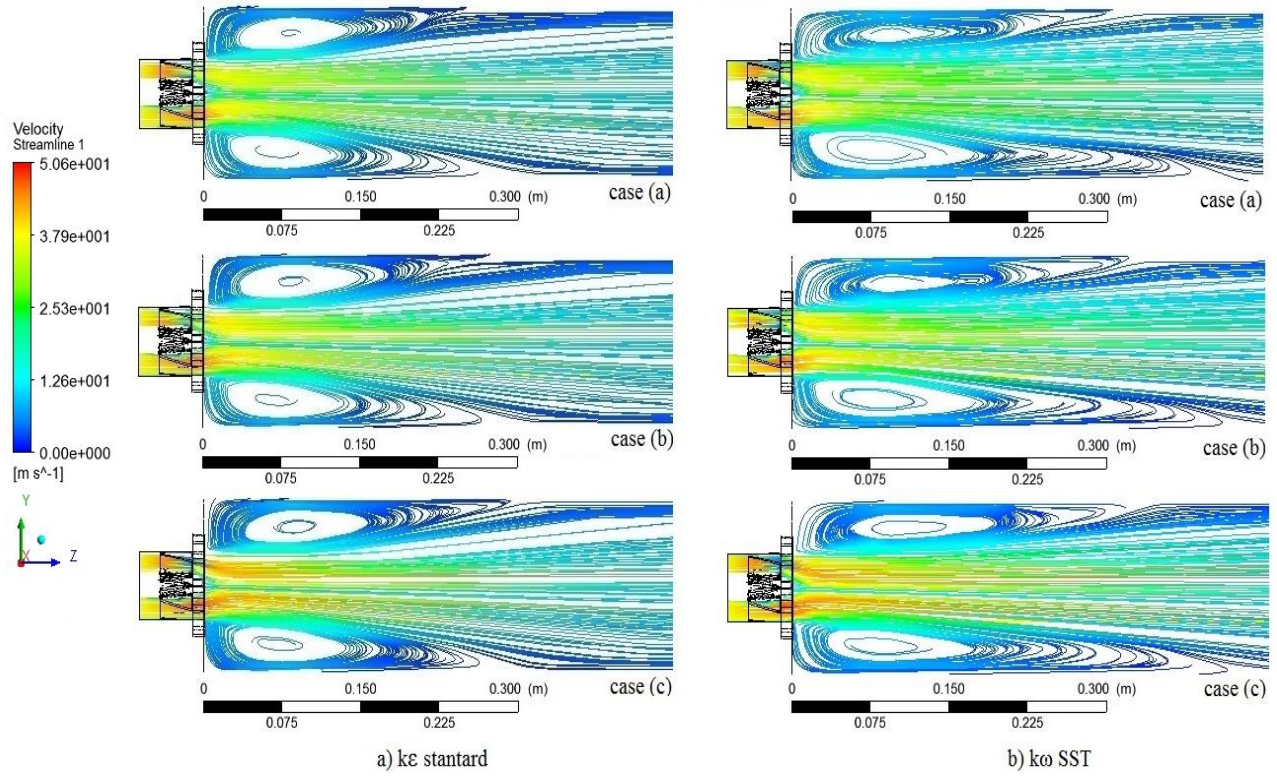

Figure 5. Field flow and CRZ. Cases a, b, c. Middle plane data.

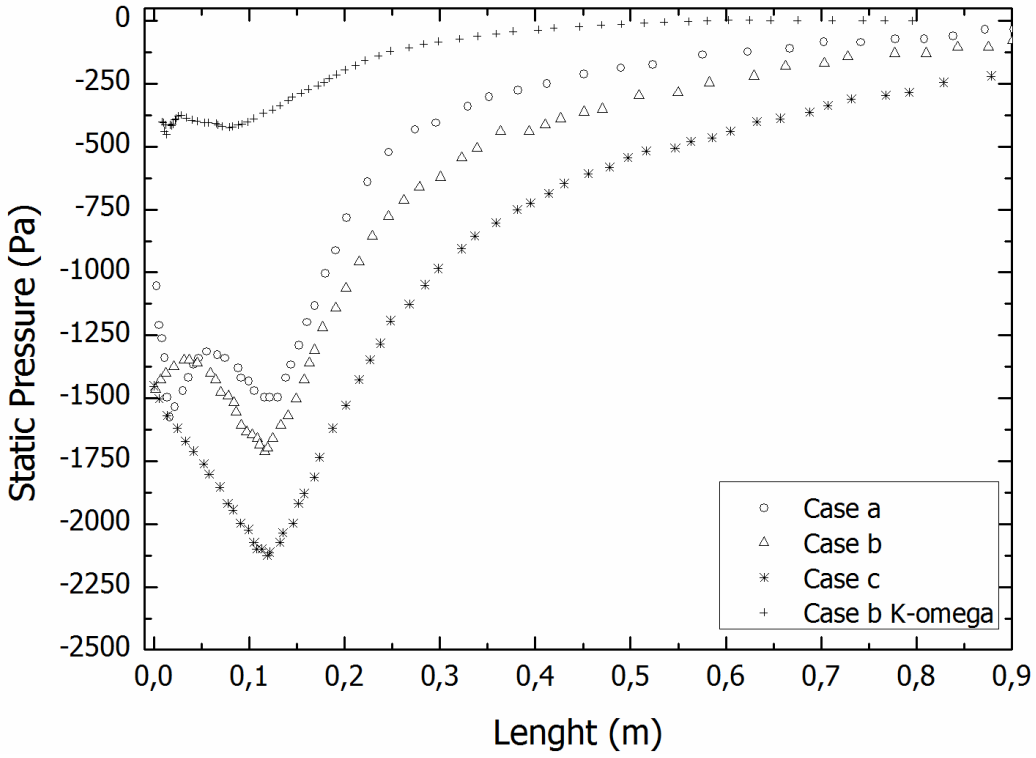

Figure 6. Static pressure for k-ω SST. Case b. Center line data. Initial pressure 101325 Pascal.

It was found that the swirl number affected by the arrangements of velocity components where the recirculation zone at the near wall were higher defined when a specific swirl number was sited occurring for all turbulence models. Ascertaining the field flow on the Fig. 5, the data agreement with data on the Fig. 6 knowing that the inside of combustor, the swirling flow propagates as it moves, and the centrifugal force generates a low pressure region in the center of the flow which, in a certain point downstream, this low pressure region causes the vortex to collapse inwards entering in a process known as vortex breakdown. This phenomenon creates a CRZ, normally, in the center of the flow, which is essential to provide sufficient time, temperature and turbulence for a complete combustion according to (Wang

et al., 2004). The Fig. 7 shows the dark blue regions correspond to reversed flow at the outlet of the burner, forming CRZ, and Fig. 8 shows a 3D view of the rotating flow near the outlet plane of the burner.

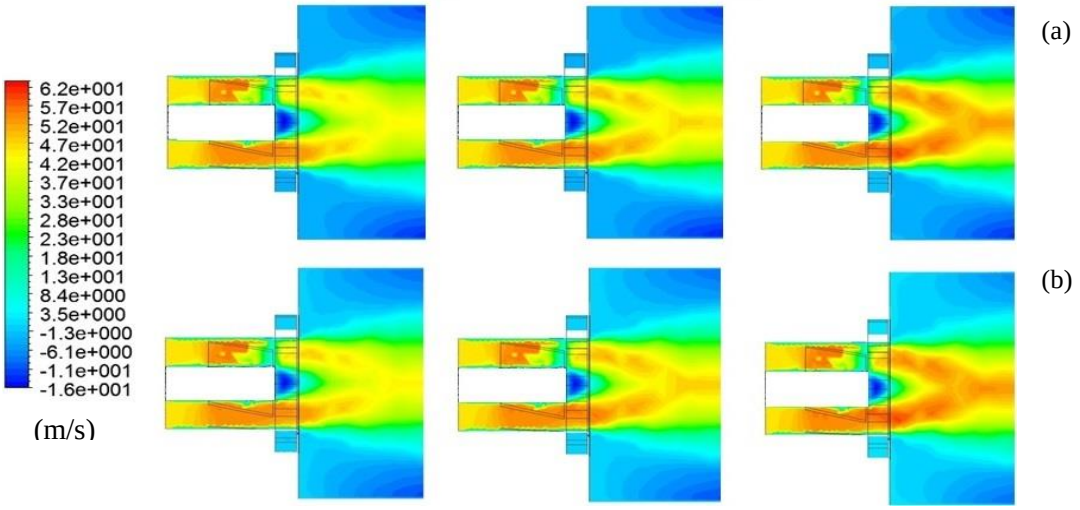

Figure 7. Axial velocity (a) kε (b) kω SST. Dark blue region means CRZ. Middle plane data.

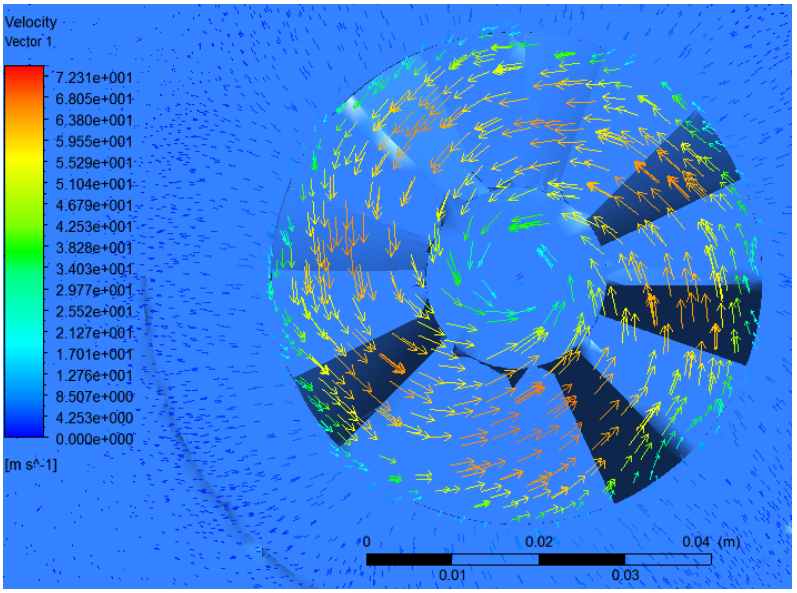

Figure 8. Toroidal vortex core. Exit plane burner of data.

It is observed that the length of the central recirculation zone appears to be not sensitive to the increase of the degree of swirl. However, this effect of the swirl on the length of the toroidal vortex core, defined as the distance of the burner exit to the point of the reversal of the flow direction, is expected to be observable as far as the jet of fuel is included in the model. With this counterpoint, the paper of (Negro and O'Doherty, 2000) which a review of process breakdown related that have many breakdown forms. Based on experimental work (Sarpkaya, 1971a) and (Sarpkaya, 1971b) a cylindrical tube was investigated three types: double helix, spiral, and axisymmetric (bubble) breakdowns. These are among seven different forms of this phenomenon that (Leibovich, 1978) reached in experimental study varying the Reynolds Number (Re) and swirl number accounted the vane angles. Whenever, breakdown types 3-6 are less commonly observed than the others and occur mainly with low Re and for high Re the only types visualized are the bubble and spiral break down's. At present work as Fig. 5 shows the field flow of breakdown is more similar to axisymmetric bubble and strong similar to (Béer and Chigier, 1972) such as first Fig. 1.

The convergence criteria based on residuals were improvement when a k-ω SST turbulence model were applied with comparing from k-ε model, whenever nothing a single parameter to guarantee the numerical robust, since the features of CRZ is a key parameter to close the model purposed as discussed at last items.

5. CONCLUSIONS

The mesh independency was based on qualitative results once comparing with numerical work, the mesh III presented a better discretization, in addition a local refinement on mesh III will be adequate to show particular phenomena.

The CRZ were not to be sensitive changes as the axial and tangential velocity components as increased, in other words, the swirl number, furthermore the recirculation zones were governing the field flow with strong toroidal features. Believes this fact can be adjustment on the vane angles, in addition, some geometry parameters of burner were unavailable going in some hypothesis. At last argument can be explaining the different data of static pressure.

By comparison of simulation results found in the literature for a cylindrical chamber equipped with a fixed-block type burner, it is observed that the k-ε Standard model is able to capture well the main features of the rotating flow in the central recirculation zone. Along with the fact that this model is better suited for the coupling in the modeling of combustion, these results favor the application of this turbulence model in the continuation of the study of the effect of the swirl in a similar combustion chamber fuelled with LPG.

For future works should be interesting that an unsteady state model simulation applied, comparing the RSM and RANS models, based on the anisotropy and isotropy of turbulence effects on the field flow with emissions interactions.

4. REFERENCES

Beér, M. J., Chigier, N. A., 1972. Combustion Aerodynamics, London, Applied Science Publishers LTD, pp.102.

Bizzo, W.A.,1997. Emissão de monóxido de carbono e hidrocarbonetos totais em câmara de incineração – efeito do número de rotação e composição do combustível. Doctor thesis, Universidade Estadual de Campinas, São Paulo, Campinas, Brazil.

Bourgouin, J.F. and Moeck, J. and Durox, D. and Schuller, T. Candel, S., 2013. "Sensitivity of swirling flows to small changes in the swirler geometry". Comptes Rendus Mecanique Acdémie des Science, Vol.341, pp. 211-219.

Eldrainy Y.A., Saqr K.M., Aly H.S., Jaafar M.N., 2009. CFD insight of the flow dynamics in a novel swirler for gas turbine combustors. International Communications on Heat and Mass Transfer, Vol. 36, pp. 936-941.

Jakirlic S., Hanjalic K., Tropea C., 2002. "Modeling rotating and swirling turbulent flows: a perpetual challenge". AIAA J. 40 (10) 1984–1996.

Leibovich, S., 1978. The structure of vortex breakdown, Annual Reviews Fluid Mechanics., pp:10:221-246.

Leibovich, S., 1984. Vortex stability and breakdown: survey and extension, AIAA Journal, pp: 22:1192-206.

Lenço, P.C., 2004. Estudo experimental da formação e emissão do NOx na combustão do etanol e glp em uma câmara de combustão cilíndrica. Master dissertation, Universidade Estadual de Campinas. São Paulo, Campinas, Brazil.

Mafra, M.R., 2000. Estudos da influência do número de rotação na formação do NOx em uma câmara de combustão cilíndrica. Master dissertation, Universidade Estadual de Campinas, São Paulo, Campinas, Brazil.

Menter F. R., 1994. Two-Equation Eddy-Viscosity Turbulence Models for Engineering Applications. AIAA Journal, 32(8), pp.1598–1605.

Najafi A., Sadeghipour M., Saidi M., Souhar M., 2003. Boundary Layer Solution for the Turbulent Swirling Decay Flow Through a Fixed Pipe. SBR at the Inlet,vol. 259, American Society of Mechanical Engineers, Fluids Engineering Division (Publication) FED, pp. 449–456.

Negro, O.L. and O'Doherty, T., 2000, "Vortex Breakdown: a review", Progress in Energy and Combustion Sciences, Vol.27, pp.431-481.

[a]Sarpkaya, T., 1971. On stationary and travelling vortex breakdowns, Journal Fluid Mechanics., pp: 45(3):545-59.

[b]Sarpkaya, T., 1971. Vortex breakdown in swirling conical flows, AIAA Journal, pp: 9(9): 1792-9.

Shih T., Zhu J., Liou W., Chen K., Liu N., Lumley J., 1997. Modeling of turbulent swirling flows". NASA Technical Memorandum, N. 113112, 54pp.

Wang Y., Yang V., Yetter R.A., 2004. Numerical study on swirling flow in an cylindrical chamber, 42nd AIAA Aerospace Sciences Meeting, Reno, Nevada.

Wilcox,C. D., 1993. Turbulence Modeling for CFD, California, DCW Industries Inc., pp.84-.87

Simulação numérica de escoamentos estratificados por partículas em suspensão e salinidade

F. N. Schuch, felipe.schuch@acad.pucrs.br
L. C. Pinto, leandroconp@gmail.com
J. H. Silvestrini, jorgehs@pucrs.br
Faculdade de Engenharia, Pontifícia Universidade Católica do Rio Grande do Sul, Av. Ipiranga 6681, 90619-900 Porto Alegre - RS, Brasil

Resumo. *O presente trabalho tem como objetivo analisar o comportamento do escoamento estratificado por partículas em suspensão e salinidade através de Simulação Numérica Direta (DNS). Para tanto, utilizou-se o código computacional Incompact3D, baseado na solução das equações governantes do escoamento assumindo a hipótese de Boussinesq para fluidos incompressíveis. Os efeitos de estratificação devem-se a diferenças na concentração de partículas suspensas e a salinidade dissolvida no escoamento. As simulações numéricas foram realizadas nas configurações bi- e tri-dimensionais de um canal contendo um fluido com salinidade dissolvida onde há a entrada de outro fluido com partículas em suspensão. A fim de observar a relação do tamanho dos sedimentos bem como a sua influência na coluna de água, foram realizadas doze simulações com a variação destes parâmetros, considerando três diferentes números de Richardson e três diferentes velocidades de queda de partículas. Outras três simulações numéricas são apresentadas, com a finalidade de estudar diferentes condições iniciais e de entrada do problema. Os resultados mostram que o escoamento apresenta maior sensibilidade com relação à variação da velocidade de queda enquanto o número de Richardson da partícula é pouco influente. Observa-se ainda que as condições iniciais influenciam no tempo necessário para que o escoamento se torne estatisticamente estacionário.*

Palavras-chave: *DNS, estratificação, pluma turbulenta, salinidade, sedimentação.*

1. Introdução

Muitos são os processos naturais que definem o destino de partículas em plataformas continentais, e o entendimento destes processos é fundamental para compreender como são transportados cerca de 10×10^9 metros cúbicos por ano de sedimentos transportados pelos rios até o oceano [McCool and Parsons, 2004]. A água salgada é normalmente mais densa que a água doce carregada de sedimentos, de modo que a pluma fluvial flutua na superfície transportando as partículas por uma grande distância horizontal. Este escoamento com flutuação positiva é conhecido como pluma turbulenta hipopicnal. De acordo com [Henniger and Kleiser, 2012], as partículas são mantidas em suspensão unicamente pelos efeitos da turbulência nos fluidos, de modo que as limitações na distância de transporte estão associadas à diminuição da velocidade horizontal, à decantação dos sedimentos e à mistura dos fluidos.

Neste trabalho são apresentadas simulações numéricas de escoamento turbulento estratificado em um canal nas configurações bi- e tri-dimensionais. O transporte de sedimentos por corrente de densidade é o principal mecanismo formador das bacias sedimentares oceânicas, provocando a deposição, erosão e ressuspensão das partículas ao longo da plataforma continental [Meiburg and Kneller, 2010]. Destaca-se a importância deste estudo para a melhor compreensão dos mecanismos formadores das bacias sedimentares oceânicas.

Com o objetivo de analisar o comportamento da concentração de partículas, seu transporte e sedimentação e testar as possíveis condições iniciais e de contorno do problema, utilizou-se o código computacional `incompact3d` para simular o escoamento [Laizet and Lamballais, 2009].

2. Metodologia

2.1 Equações Governantes

No equacionamento do fluido considera-se que as partículas diluídas possuem menos de 1% do volume total, assim as interações entre partículas, a sua inércia e a variação da viscosidade do fluido em função das partículas são desprezadas [Necker et al., 2002]. As equações governantes adimensionais para o escoamento em consideração são descritas a seguir:

$$\frac{\partial u_j}{\partial x_j} = 0, \tag{1}$$

$$\frac{\partial u_i}{\partial t} = -u_j\frac{\partial u_i}{\partial x_j} - \frac{\partial p}{\partial x_i} + \frac{1}{Re}\frac{\partial^2 u_i}{\partial x_j \partial x_j} + e_i^g(Ri_p c_p + Ri_s c_s), \tag{2}$$

$$\frac{\partial c_p}{\partial t} = -(u_j + u_p^s e_j^g)\frac{\partial c_p}{\partial x_j} + \frac{1}{ReSc_p}\frac{\partial^2 c_p}{\partial x_j \partial x_j}, \tag{3}$$

$$\frac{\partial c_s}{\partial t} = -u_j\frac{\partial c_s}{\partial x_j} + \frac{1}{ReSc_s}\frac{\partial^2 c_s}{\partial x_j \partial x_j}. \tag{4}$$

Nas equações acima, x_i representa os eixos de coordenadas, u_i as componentes da velocidade, p a pressão, $e_i^g = (0, -1, 0)$ o vetor unitário atuando na direção da aceleração gravitacional, u_p^s a velocidade de queda de Stokes e c_p e c_s as respectivas concentrações de partícula e salinidade. O escoamento é parametrizado por cinco números adimensionais: número de Reynolds Re, número de Richardson associado à concentração de partículas e de salinidade, Ri_p, Ri_s e o número de Schmidt associado à difusão de concentração de partículas e de salinidade, Sc_p e Sc_s. Os números adimensionais são calculados da seguinte forma:

$$Re = \frac{Uh}{\nu}, \tag{5}$$

$$u_p^s = \frac{2}{9}\frac{r_p^2 g_p^r}{\nu U \phi_p^V}, \tag{6}$$

$$Ri_k = \frac{g_k^r h}{U^2},\ k \in \{\text{partícula, salinidade}\}, \tag{7}$$

$$Sc_k = \frac{\nu}{D_k},\ k \in \{\text{partícula, salinidade}\}. \tag{8}$$

No equacionamento destes parâmetros, utilizam-se a viscosidade cinemática ν, a difusividade de partículas e salinidade considerada como sendo igual a unidade ($D_p = D_s = 1$), velocidade de entrada de fluido U, altura da entrada h, massas específicas da água ϱ, da partícula ϱ_p e da água salgada ϱ_s, aceleração gravitacional reduzida para partículas $g_p^r = [\frac{\varrho_p}{\varrho} - 1]g\phi_p^V$ e para a salinidade $g_s^r = [\frac{\varrho_s}{\varrho} - 1]g$, raio da partícula r_p e a máxima fração volumétrica de partículas $\phi_p^V = 0.01$, considerando 1% das partículas diluídas no volume total.

O método de Simulação Numérica Direta (DNS) é empregado, onde não se utiliza nenhum modelo de turbulência e a equação de Navier-Stokes é totalmente resolvida para toda escala do tempo e do espaço em uma malha cartesiana uniforme. Para resolver numericamente as equações governantes (1,2,3,4), utiliza-se o código computacional `incompact3d`. O código se baseia em um esquema compacto de diferenças finitas de sexta ordem para a diferenciação espacial e um esquema de terceira ordem de Adams-Bashforth para a integração do tempo. Para a solução do campo de pressões, a equação de Poisson é resolvida no espaço espectral com o uso de transformada rápida de Fourier (para mais informações sobre o código, ver [Laizet and Lamballais, 2009];[Laizet and Li, 2011]).

2.2 Condições iniciais e de Contorno

As condições iniciais e de contorno são definidas a seguir para os campos de velocidade u_i, concentração de partículas c_p e concentração de salinidade c_s. Na figura 1 são apresentadas de forma esquemática estas condições.

Condição de entrada (A): A condição na entrada do escoamento é prescrita por condições de contorno de Dirichlet, ou seja, são especificados os valores sobre o contorno do domínio. A função F é utilizada para impor o perfil de entrada:

$$F = \frac{1}{2}\left[1 + \tanh\left\{\frac{\sqrt{\pi}}{\delta h}(x_2 - x_2^{if}(t))\right\}\right]. \tag{9}$$

Nesta equação, $x_2^{if}(t)$ é a posição vertical da interface entre a água com partículas em suspensão e a água salgada, e δh é a espessura da camada cisalhante. Com a finalidade de acelerar a instabilidade da camada de mistura o escoamento é perturbado através do movimento vertical da posição da interface $x_2^{if} = x_2^{if,av} + x_2^{if,rand}(t)$, sendo $x_2^{if,av} = (L_2 - h)$ a posição média da interface e $x_2^{if,rand}(t)$ uma perturbação senoidal ao longo do tempo.

Condição de entrada (B): A segunda condição de entrada (B) é similar a condição (A), porém com alterações na função F dada por:

$$F = \begin{cases} \tanh\left\{\dfrac{\sqrt{\pi}}{\delta h}(x_2 - x_2^{if}(t))\right\} & \text{se} \quad x_2 \geq (L_2 - h) \\ 0 & \text{se} \quad x_2 < (L_2 - h) \end{cases} \tag{10}$$

Condição de saída: Na fronteira de saída são utilizadas equações de convecção para os três campos, onde $U^{b,1}$ é a velocidade de convecção normal ao contorno para os campos de concentração de partículas e de salinidade, enquanto $U_j^{b,u}$ é a velocidade de convecção associada ao transporte dos vórtices para fora do domínio computacional. Em todas as simulações foram consideradas $U^{b,1} = U_j^{b,u} = 1$.

Fronteira superior: Condição de fluxo nulo no campo de concentração de partículas e salinidade e de deslizamento livre para a velocidade.

Fronteira inferior: Uma equação de convecção na direção x_2 é imposta para c_p de forma a simular a condição de depósito de partículas. Neste caso a velocidade de convecção é igual a velocidade de queda das partículas u_p^s. A condição de fluxo nulo é imposta para o campo de salinidade, uma vez que a salinidade permanece dissolvida no escoamento, sem se depositar.

Condição inicial (I): Foi considerado que o domínio possui um volume inicial de partículas e as equações impostas sobre este domínio para cada variável são apresentadas na figura 1. Nestes caso F é definida pela equação (9), imposta ao longo de x_1.

Condição inicial (II): Considerou-se o domínio livre de partículas suspensas com F agora definido pela eq.(10).

Condição inicial (III): O escoamento teve início sem partículas suspensas no domínio e na condição de entrada, até atingir o regime estável, que ocorre no instante $t = 250$, segundo [Henniger et al., 2010]. Somente a partir deste tempo a concentração de partículas é introduzida no domínio.

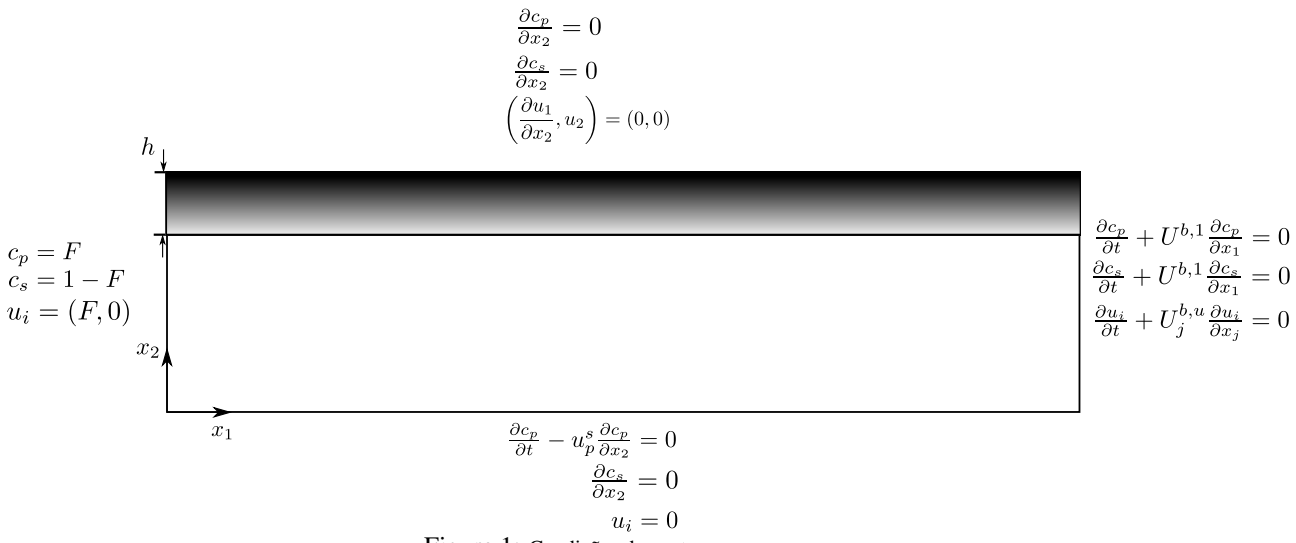

Figure 1: Condições de contorno para u_i, c_p e c_s.

3. Resultados e Discussões

3.1 Simulações bi-dimensionais

Foram realizadas um total de quinze simulações numéricas reunidas em dois grupos, o primeiro para a avaliação da sensibilidade dos parâmetros u_p^s e Ri_p e o segundo para avaliação das diferentes condições iniciais e de contorno.

Foram adotadas as dimensões do canal $(L_1, L_2) = (80h, 4h)$, o número de Reynolds $Re = 1500$ e o número de Richardson da salinidade $Ri_s = 0,5$. Todas as simulações foram rodadas com o intervalo de tempo Δt de acordo com a tabela 1, atingindo o tempo final de 1000 unidades adimensionais. Na Tabela 1 se encontram os demais parâmetros das

Granulometria	$d_p[\mu m]$	u_p^s	Ri_p	n_1	n_2	Δt	CC/CI
Silte médio	21,5	0,005	0,05	3073	193	0,005	A/I
			0,10	3073	193	0,003	
			0,20	3073	193	0,003	
	30,5	0,01	0,05	3073	193	0,005	
			0,10	3073	193	0,005	
			0,20	3073	401	0,002	
Silte grosso	43,5	0,02	0,05	3073	193	0,003	B/I
			0,05	3073	193	0,003	B/II
			0,05	3073	193	0,002	B/III
			0,05	3073	193	0,005	A/I
			0,10	3073	301	0,0025	
			0,20	3073	551	0,001	
	52,8	0,03	0,05	3073	193	0,005	
			0,10	3073	301	0,0025	
			0,20	3073	551	0,001	

Table 1: Parâmetros das simulações numéricas bi-dimensionais. Granulometria, diâmetro da partícula d_p, velocidade de queda u_p^s, número de Richardson da partícula Ri_p, pontos na malha n_1 e n_2 e passo de tempo Δt.

quinze simulações, como a granulometria e diâmetro da partícula d_p, número de pontos da malha n_1 e n_2, passo de tempo Δt e as condições de contorno e iniciais.

Para a comparação das condições iniciais e de entrada, nas configurações B/I, B/II, e B/III, o número de Richardson das partículas foi fixado em $Ri_p = 0,05$. A velocidade de sedimentação $u_p^s = 0,02$ foi usada por ser a que melhor se adapta às dimensões do domínio, diminuindo a perda de sedimento pela condição de saída e também não depositando tão rápido quanto nos casos de velocidades de queda maiores.

Para efeito de comparação dos resultados, são apresentadas curvas do material suspenso m_p, que representa a quantidade de partículas contidas no domínio computacional para cada instante de tempo, determinada conforme a equação:

$$m_p(t) = \int_\Omega c_p(x_1, x_2, t) d\Omega. \tag{11}$$

A sedimentação D_t representa a quantidade de material depositado, e é função do tempo e da posição ao longo do fundo do canal [Necker et al., 2002], conforme equação:

$$D_t(x_1, t) = \int_0^t c_p(x_1, x_2 = 0, \tau) u_p^s d\tau. \tag{12}$$

A taxa de sedimentação $\dot{m}_s$ é a variação de sedimentação com o tempo, demonstrando a variação na quantidade de depósito em função do tempo [Henniger et al., 2010]. O cálculo deste parâmetro é feito conforme a equação:

$$\dot{m}_s(t) = \frac{dm_s(t)}{dt} = \int_0^{L_1} c_p(x_1, x_2 = 0, t) u_p^s dx_1. \tag{13}$$

3.1.1 Avaliação dos parâmetros u_s e Ri

Nesta seção são apresentados os resultados das simulações com condições de contorno e iniciais A/I, onde foi avaliada a influência do número de Richardson $Ri_p = (0,05; 0,10; 0,20)$ e da velocidade de queda $u_p^s = (0,005; 0,01; 0,02; 0,03)$.

Na Figura 2 são apresentados os campos de concentração de partículas para quatro tempos característicos da simulação com $Ri_p = 0,2$ e $u_p^s = 0,02$. Percebe-se a formação de diferentes formas de instabilidade ao longo do tempo e espaço. Em $t = 25$, nota-se a formação da instabilidade de *Kelvin-Helmholtz*, típica na interface de separação de fluidos com diferentes velocidades. Em $t = 50$, ocorre a formação de outra instabilidade denominada *dedilhados* na separação dos fluidos, seguido pela mistura entre eles em $t = 100$. Em $t = 1000$ se percebe grande turbulência e novamente se formam os vórtices de *Kelvin-Helmholtz*.

Na Figura 3 são apresentados campos de concentração de partículas, desta vez para um mesmo tempo e mesma velocidade de queda u_p^s, mas para os três diferentes números de Richardson Ri_p. Analisando-se as três imagens, pode-se notar diferenças nos efeitos de turbulência observados para um dado tempo $t = 100$. Para $Ri_p = 0,05$ se percebe a instabilidade de *Kelvin-Helmholtz*, em $Ri_p = 0,10$ a formação de *dedilhados* e para $Ri_p = 0,20$ observa-se uma mistura

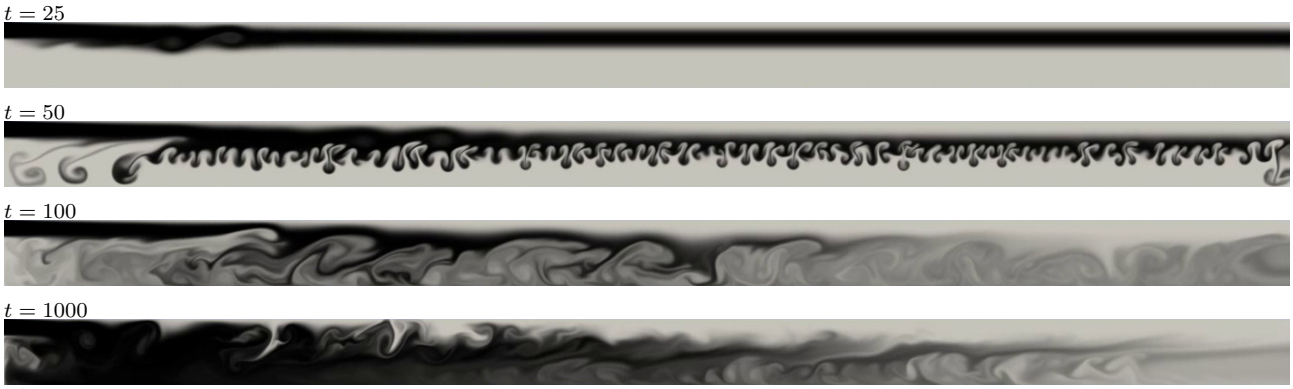

Figure 2: Campo de concentração de partículas c_p, para $Ri_p = 0, 2$, $u_p^s = 0, 02$ e $t = 25, 50, 100, 1000$. A cor preta indica $c_p = 100\%$ e a branca $c_p = 0\%$.

entre os dois fluidos, devido ao escoamento turbulento. Retomando a definição do número de Richardon na equação (7), pode-se melhor compreender as diferenças observadas. Tendo em vista que os parâmetros velocidade U e altura h da entrada são iguais em todos os casos, um maior Richardson implica uma maior aceleração gravitacional reduzida g_p^r. Como a relação de densidade da partícula e da água $\frac{\varrho_p}{\varrho}$ depende apenas do material da partícula, esse não se altera, acarretando então um incremento na máxima fração volumétrica de partículas ϕ_p^V. Deste modo os escoamentos com maior Ri_p alcançam o fundo do canal em um menor tempo.

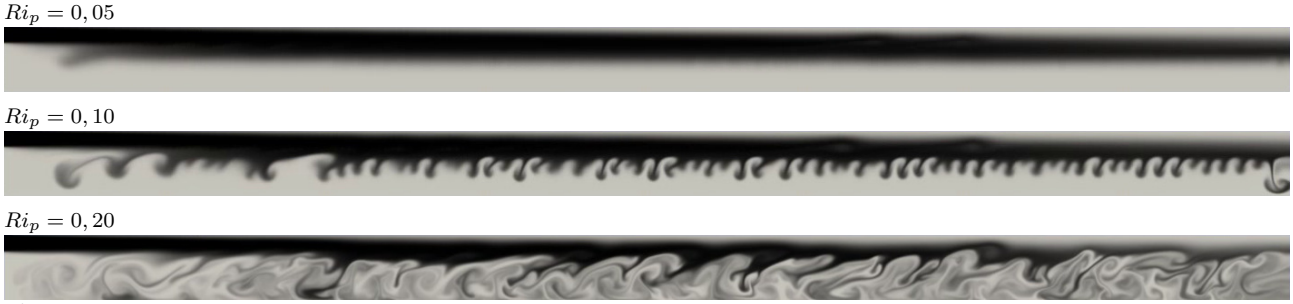

Figure 3: Campo de concentração de partículas c_p, para $Ri_p = 0, 05; 0, 2; 0, 1$, $u_p^s = 0, 02$ e $t = 100$. A cor preta indica $c_p = 100\%$ e a branca $c_p = 0\%$.

Os efeitos na velocidade de queda u_p^s são apresentados na Figura 4. Nas simulações com maiores velocidades de queda u_p^s os sedimentos precipitam na parte inicial do domínio, em uma menor distância horizontal.

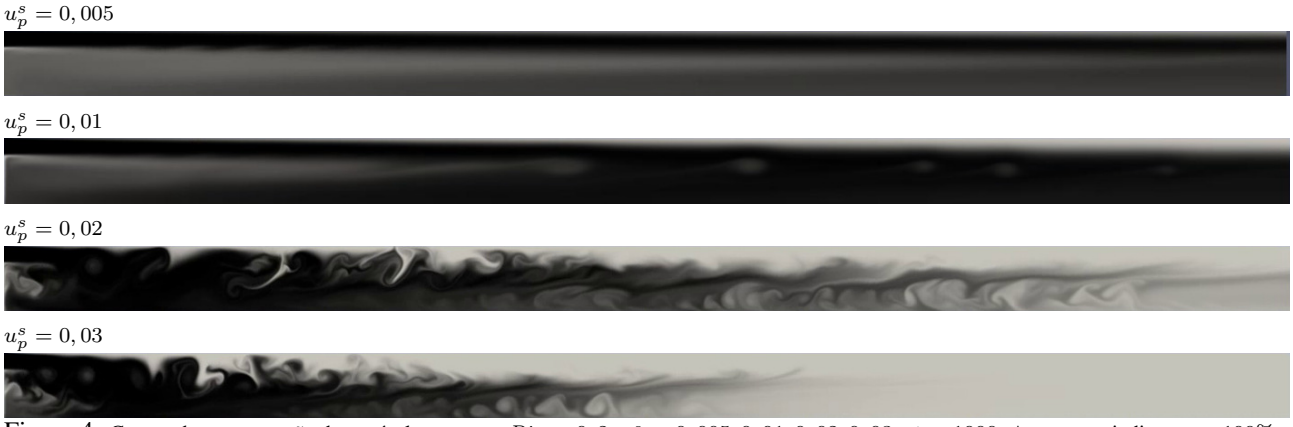

Figure 4: Campo de concentração de partículas c_p, para $Ri_p = 0, 2$, $u_p^s = 0, 005; 0, 01; 0, 02; 0, 03$ e $t = 1000$. A cor preta indica $c_p = 100\%$ e a branca $c_p = 0\%$

A taxa de sedimentação $\dot{m}_s$ em função do tempo é apresentada na Figura 5 (a esquerda), enquanto a massa suspensa m_p, a qual é dividida pela massa suspensa inicial $m_{p0} = 80$, é mostrada na Figura 5 (a direita).

Previsivelmente as partículas com maior diâmetro e consequentemente maior velocidade de sedimentação apresentam maior taxa de deposição. Notam-se mudanças significativas por volta de $t = 100$ para as velocidades $u_p^s = (0, 02; 0, 03)$ decorrentes da massa inicial de partículas atingindo o fundo do canal. Posteriormente, a quantidade de material suspenso se mantem estável e a taxa de sedimentação se iguala para as duas velocidades de deposição. Por volta de $t = 500$ para

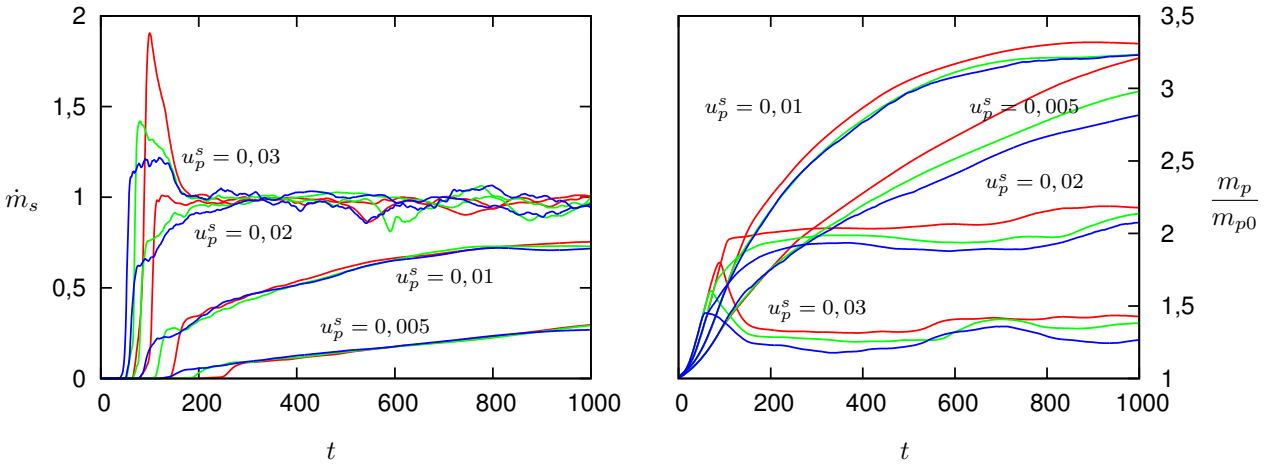

Figure 5: Taxa de deposição $\dot{m}_s$ em função do tempo (a esquerda) e massa suspensa m_p em função do tempo para as doze simulações, adimensionalizada pela massa suspensa inicial m_{p0} (A cor vermelha indica $Ri_p = 0,05$, verde para $Ri_p = 0,1$ e azul para $Ri_p = 0,2$).

$u_p^s = 0,03$ e $t = 700$ para $u_p^s = 0,02$ se percebem alterações nos gráficos, com ligeiro aumento na massa suspensa que por final voltam a se estabilizar.

Para as velocidades $u_p^s = (0,005; 0,01)$ não se evidencia o mesmo comportamento. A quantidade de material suspenso aumenta gradativamente até $t = 800$ para $u_p^s = 0,01$, quando atinge a estabilidade. Não é possível afirmar que as simulações numéricas com $u_p^s = 0,005$ tenham atingido condições de escoamento estatisticamente estacionário até $t = 1000$. Nota-se que a maior influência nos resultados se deve à velocidade de queda u_p^s, e não ao Ri_p. Uma maior diferença em função do Ri_p é percebida somente para $u_p^s = 0,005$.

O depósito D_t em função do tempo e da posição no fundo do canal x_1, é apresentado para os tempos 500 e 1000 na Figura 6.

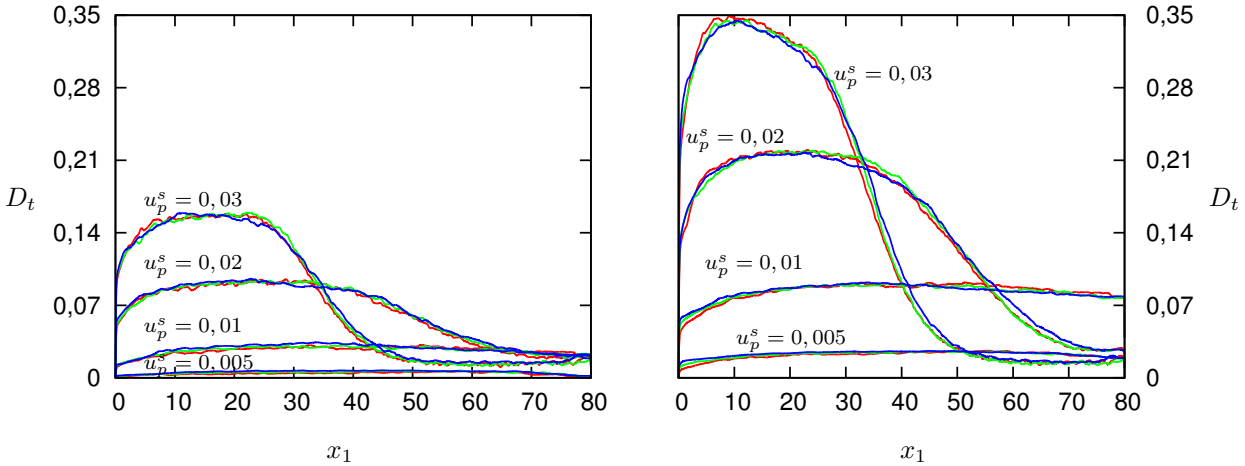

Figure 6: Perfil de depósito $D_t(x_1, t)$ ao longo do fundo do canal para $t = 500$ a esquerda e $t = 1000$ a direita. Mesma descrição de cores da Fig. 5.

A distância horizontal pela qual as partículas são transportadas até se depositarem no fundo do canal está fortemente relacionada com a velocidade de queda. Para $u_p^s = 0,03$ o depósito se concentra principalmente na primeira metade do canal enquanto que para $u_p^s = 0,02$ o depósito se estende até $x_1 = 60$. No caso de $u_p^s = (0,01; 0,005)$ há uma grande perda de material pelo contorno de saída. Para esses casos seria apropriado o uso do canal com maior dimensão horizontal, ao custo do aumento no tempo de processamento.

3.1.2 Avaliação das condições iniciais e de contorno

Nesta seção são apresentados os resultados comparativos para quatro simulações com $Ri_p = 0,05$ e $u_p^s = 0,02$ a fim de avaliar a influência de diferentes condições iniciais e de contorno. São mostrados resultados para condição de entrada A e B e condições iniciais I, II e III.

Na Figura 7 estão os campos de concentração de partículas c_p das quatro simulações para $t = 30$, evidenciando

Figure 7: Campo de concentração de partículas c_p, para $Ri_p = 0,2$, $u_p^s = 0,02$, $t = 30$ para as 4 condições analisadas. A cor preta indica $c_p = 100\%$ e a branca $c_p = 0\%$

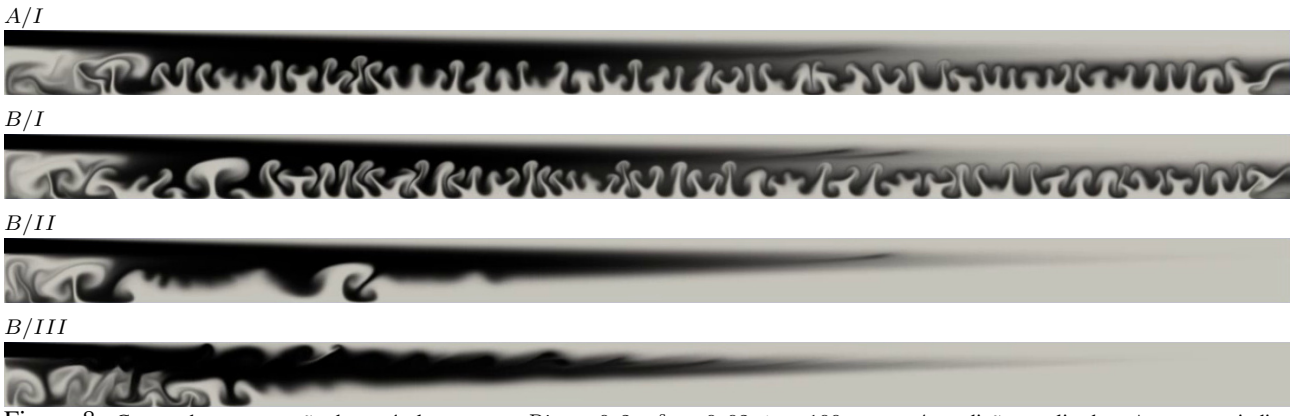

Figure 8: Campo de concentração de partículas c_p, para $Ri_p = 0,2$, $u_p^s = 0,02$, $t = 100$ para as 4 condições analisadas. A cor preta indica $c_p = 100\%$ e a branca $c_p = 0\%$

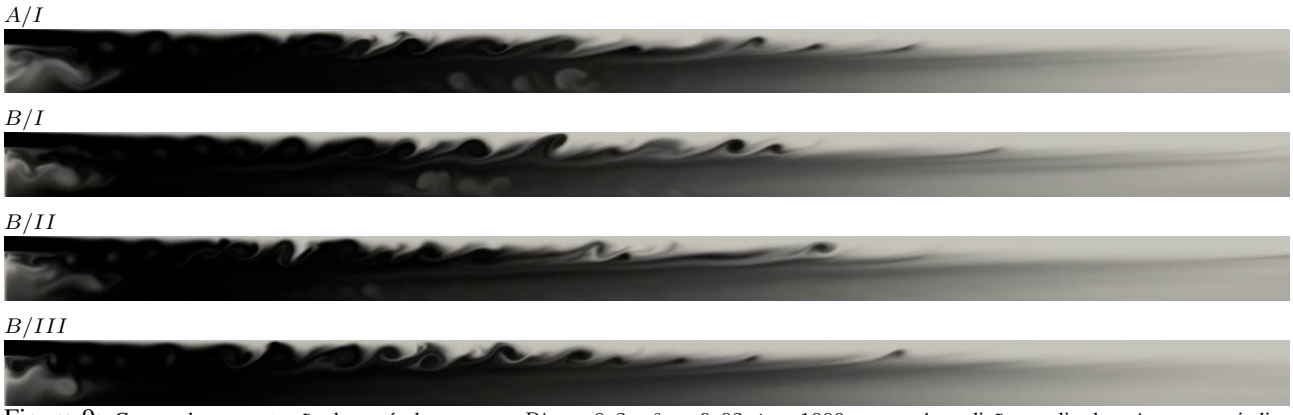

Figure 9: Campo de concentração de partículas c_p, para $Ri_p = 0,2$, $u_p^s = 0,02$, $t = 1000$ para as 4 condições analisadas. A cor preta indica $c_p = 100\%$ e a branca $c_p = 0\%$

o efeito da turbulência inicial de B/III. Para $t = 100$, na Figura 8, é notável apenas a diferença devido a faixa de alta concentração na parte superior do domínio, devido as condições iniciais. Em $t = 1000$ não há visualmente como diferenciá-las, conforme Figura 9.

A taxa de sedimentação $\dot{m}_s$ em função do tempo é apresentada na Figura 10 (a esquerda), enquanto a massa suspensa m_p em função do tempo está na Figura 10 (a direita). Adota-se a divisão pela massa suspensa inicial $m_{p0} = 80$ mesmo para as condições II e III, onde não há massa suspensa inicialmente, a fim de se ter o mesmo padrão para comparação. O depósito D_t em função do tempo e da posição no fundo do canal x_1 são apresentados para os tempos 500 e 1000 na Figura 11.

Três diferenças básicas são evidentemente causadas pela condição inicial sem partículas suspensas nas configurações B/II e B/III. A curva de massa suspensa m_p inicia-se no ponto zero, não há o aumento abrupto na taxa de sedimentação $\dot{m}_s$ por volta de $t = 100$ e um menor número de sedimentos depositados para $x_1 > 30$. As quatro simulações numéricas apresentam valores muito próximos para $\dot{m}_s$ e m_p em $t = 1000$, mostrando que diferentes condições iniciais não tem

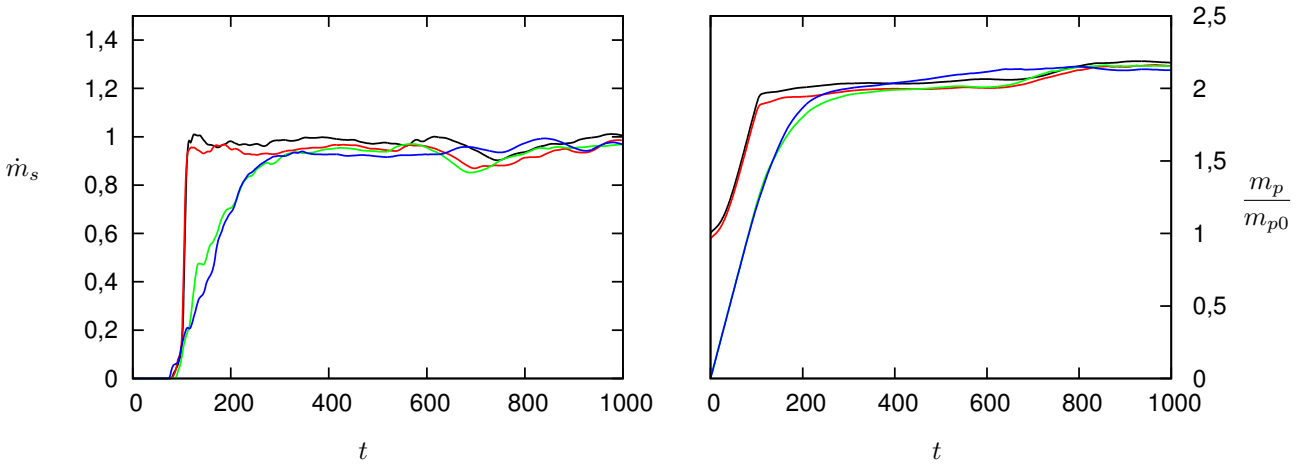

Figure 10: Taxa de deposição $\dot{m}_s$ (esquerda) e massa suspensa m_p adimensionalizada pela massa suspensa inicial m_{p0} (direita) em função do tempo para as quatro simulações. A cor preta incida A/I, vermelha para B/I, verde para B/II e azul para B/III. $Ri_p = 0,05$, $u_p^s = 0,02$.

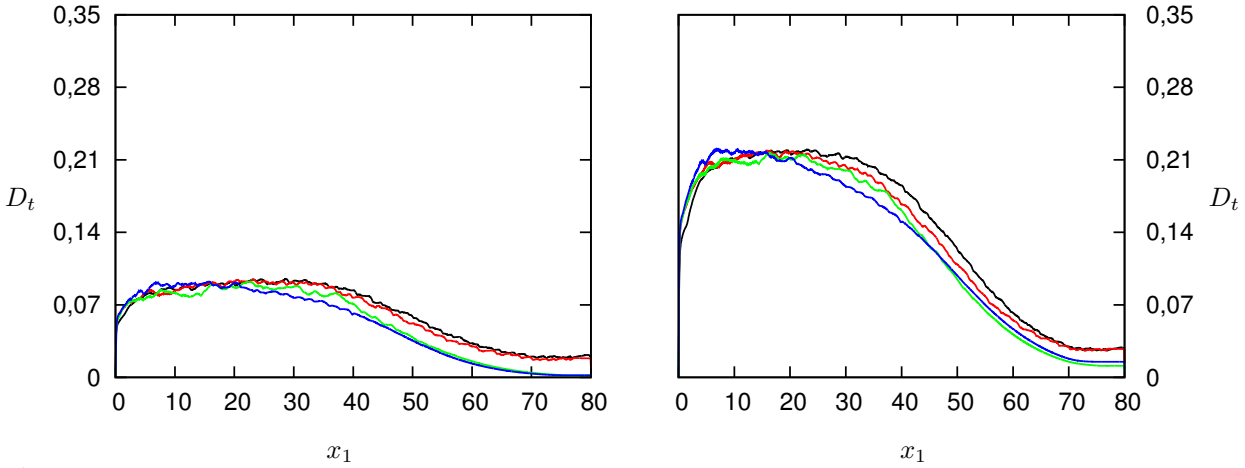

Figure 11: Perfil de depósito $D_t(x_1, t)$ ao longo do fundo do canal para $t = 500$ a esquerda e $t = 1000$ a direita. Mesma descrição de cores da Fig. 10.

influência após o escoamento atingir o regime estatisticamente estacionário.

Realizando uma análise sobre o período transiente, a simulação numérica B/III se destaca por mais rápido alcançar o regime estatisticamente estacionário. Em contra partida é a mais custosa computacionalmente entre as quatro simulações numéricas testadas.

3.2 Simulações tri-dimensionais

Com base nos resultados das simulações da seção anterior foram realizadas mais duas simulações para uma configuração de domínio tri-dimensional. Os seguintes parâmetros foram usados: $L_1, L_2, L_3 = 60, 4, 4$; $n_1, n_2, n_3 = 2305, 193, 193$; $Ri_p = 0,05$; $Ri_s = 0,5$. O número de Reynolds foi mantido constante em $Re = 1500$ e a velocidade de queda foi variada em $u_s = 0,01$ e $0,02$. Estas simulações foram realizadas até o tempo adimensional $t = 1400$, com um intervalo de tempo $\Delta t = 0,004$. Foi considerada a condição inicial I de forma que a massa suspensa inicial é dada por $m_{p0} = 60h \times 4h \times 1h \times c_p = 240c_p$.

As variações temporais de m_p e $\dot{m}_s$ são apresentadas na figura 12. Nestes resultados é possível verificar a estabilização do escoamento quando o material suspenso atinge o patamar de valor $m_p \approx 30$ para o caso $u_s = 0,02$. Na simulação com $u_s = 0,01$, o valor de m_p cresce ao longo do tempo até atingir aproximadamente $m_p \approx 40$. Os resultados são ainda comparados com o trabalho realizado por [Henniger et al., 2010] onde foi considerada a condição inicial (II), isto é, condição inicial livre de partículas suspensas e um domínio de cálculo com dimensões $L_1, L_2, L_3 = 80, 4, 4$. Apesar das diferenças no domínio e na condição inicial entre a presente simulação com $u_s = 0,02$ e o trabalho de [Henniger et al., 2010], é possível notar resultados relativamente próximos.

Observando a variação temporal de $\dot{m}_s$ na figura 12 (a esquerda) é possível identificar o exato momento em que as primeiras partículas são depositadas. A simulação com $u_s = 0,01$ apresenta baixos valores de $\dot{m}_s$ se comparado ao caso

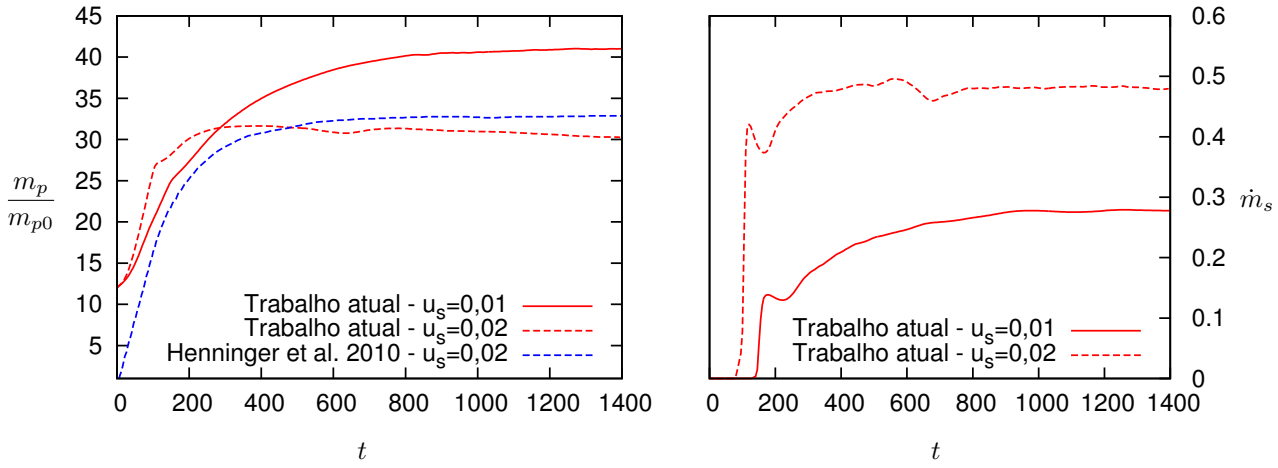

Figure 12: Variação temporal da massa suspensa (m_p, esquerda) e taxa de sedimentação ($\dot{m}_s$, direita) para simulações 3D com $u_s = 0,01; 0,02$.

$u_s = 0,02$. Este resultado mostra a influência da velocidade de queda nas condições de depósito e de material suspenso evidenciando que a lei de conservação das partículas é contemplada pelo modelo.

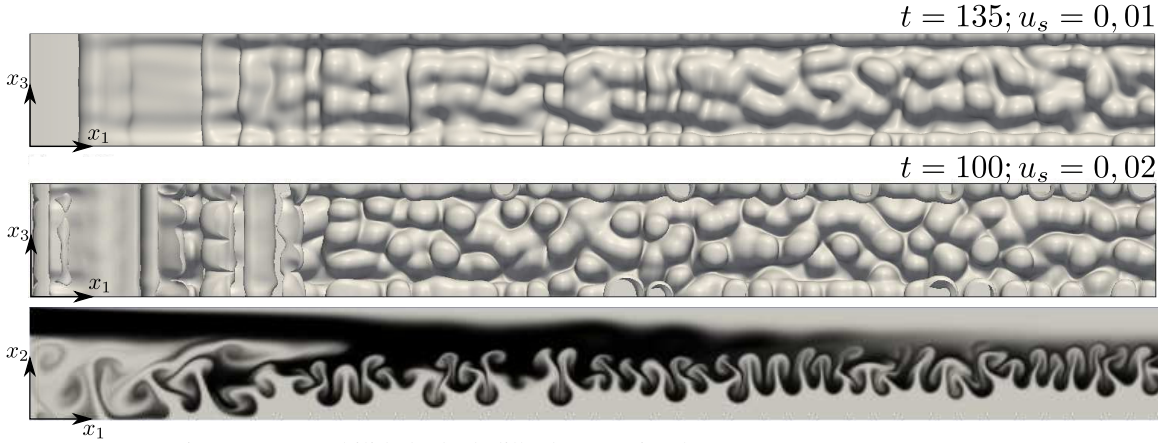

Figure 13: Instabilidade de dedilhados nas simulações $u_s = 0,1$ e $u_s = 0,02$.

Na figura 13 uma vista de fundo da isosuperfície de concentração de partículas ($c_p = 0,25$) das simulações 3D são apresentadas para o início da simulação ($t = 100$ na simulação $u_s = 0,02$ e $t = 135$ na simulação com $u_s = 0,01$). A medida que as partículas são depositadas é possível notar claramente a formação da instabilidade de dedilhados. Os dedilhados são dissipados quando as partículas atingem o fundo do domínio formando as primeiras camadas de depósito.

Após a dissipação dos dedilhados ocorre a formação da instabilidade *K-H* que transiciona à turbulência no instante $t = 600$. Observou-se visualmente que e o escoamento atinge o regime estacionário no instante aproximado $t = 800$. Na figura 14 são apresentados campos do critério Q no tempo $t = 1000$. É possível notar uma pequena redução na espessura da camada de mistura entre as simulações com $u_s = 0,02$ e $u_s = 0,01$. Com relação ao tamanho das estruturas do escoamento não é possível identificar visualmente mudanças significativas.

4. Conclusão

A proposta de análise da influência do número de Richardson Ri_p e da velocidade de queda u_p^s através de doze simulações numéricas demonstra ao final que o escoamento apresenta maior sensibilidade em relação à velocidade de queda. Os resultados se agrupam de acordo com esse último parâmetro e sofrem pequena variação em função do número de Richardson, no modelo testado. Conforme esperado, as partículas com maior velocidade de sedimentação apresentam maior taxa de deposição, se precipitam de forma mais rápida e como consequência, a quantidade de material suspenso diminui. Conclui-se que as partículas de menor diâmetro exigem simulações numéricas com maior duração, e maior dimensão horizontal.

A proposta de análise de condições iniciais e de contorno mostrou que as quatro simulações numéricas se estabilizaram em um mesmo patamar. Aquela que se estabiliza em menos tempo, devido à condição inicial já turbulenta, é também a

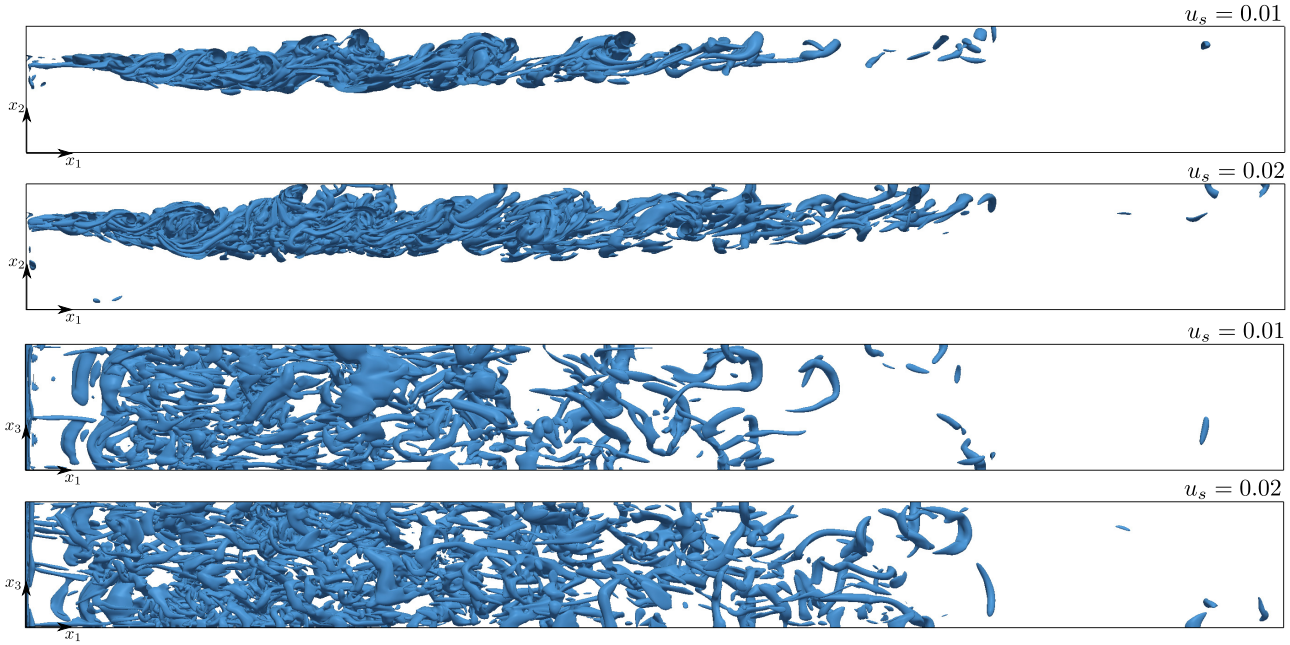

Figure 14: Campo tridimensionais do critério $Q = 0,10$ para as simulações com $u_s = 0,01; 0,02$ no instante $t = 1000$.

que exige mais tempo de cálculo.

Com base nos resultados obtidos pretende-se dar continuidade com os testes de influência dos parâmetros considerados no problema para o caso tri-dimensional, no qual foi demonstrado, através das últimas simulações, ser viável a partir do modelo proposto.

Agradecimentos

Os autores agradecem o apoio da Petrobras e Hewlett-Packard, HP.

5. Referências Bibliográficas

Henniger, R. and Kleiser, L. (2012). Temporal evolution, morphology, and settling of the sediment plume in a model estuary. *Physics of Fluids*, 24:086601.

Henniger, R., Kleiser, L., and Meiburg, E. (2010). Direct numerical simulations of particle transport in a model estuary. *Journal of Turbulence*, (11).

Laizet, S. and Lamballais, E. (2009). High-order compact schemes for incompressible flows: A simple and efficient method with quasi-spectral accuracy. *Journal of Computational Physics*, 228(16):5989–6015.

Laizet, S. and Li, N. (2011). Incompact3d: A powerfull tool to tackle turbulence problems with up to O(10^5) computational cores. **67**:1735–1757.

McCool, W. W. and Parsons, J. D. (2004). Sedimentation from buoyant fine-grained suspensions. *Continental Shelf Research*, 24(10):1129–1142.

Meiburg, E. and Kneller, B. (2010). Turbidity currents and their deposits. *Annual Review of Fluid Mechanics*, 42:135–156.

Necker, F., Härtel, C., Kleiser, L., and Meiburg, E. (2002). High-resolution simulations of particle-driven gravity currents. *International Journal of Multiphase Flow*, 28(2):279–300.

EXPERIMENTAL STUDY OF WIND FEATURES IN THE ALCÂNTARA SPACE LAUNCH CENTER

Ana Cristina Avelar, anacristina.avelar@gmail.com
Gilberto Fisch, fisch.gilberto@gmail.com
Instituto de Aeronáutica e Espaço (IAE), São José dos Campos, SP, 12228-904, Brazil

Amanda Felippe Faria, amanda.felippe.faria@gmail.com
Instituto Tecnológico de Aeronáutica (ITA), São José dos Campos, SP, 1228-900, Brazil

Fabrício L. C. Brasileiro
Universidade do Vale do Paraíba (UNIVAP), São José dos Campos, SP, 12244-000, Brazil

Abstract. *An experimental investigation of the wind flow patterns in the main Brazilian Launching site, the Alcântara Space Launching Center (ASLC), is presented. The focus of the research is to get insights about the wind flow patterns in the neighborhood of the facilities installed in this area. The largest structure in this area is the Mobile Integration Tower (MIT), which is the site where rockets are assembled and prepared for being launched, but there are also others facilities necessary for guaranteeing safe rockets launching operations. This work gives continuation to previous studies about the wind flow pattern in ASLC region, and the incentive for these investigations is that regardless of having several advantageous aspects due to its geographical location, very close to the Equator line, ASLC presents an atypical topography, with a coastal cliff occurrence, which in certain meteorological conditions of wind speed and direction may modify the characteristics of the atmospheric boundary layer and as well influence the space vehicles launching operations, since the LPA is located around 200m from the sea border. The Wind tunnel measurements were conducted using the technique of Particle Image Velocimetry (PIV). The measurements, conducted in planes parallel to the wind tunnel floor, were carried out for three different wind incidence angles, as well as three cliff slope angle and Reynolds number (Re_l) values based on the cliff height, l, of $5.4x10^5$, $1.4x10^6$ and $2.0x10^6$.*

1. INTRODUCTION

Physical phenomena related to wind incidence on buildings are very complex since it is related to the existence of large vortical structures formed from the body shear layer and shed downstream, which differentiates these flows from the flow over streamlined bodies. On the other side, understanding the wind environment associated with planned or existing buildings is of great importance in wind engineering for different reasons, among many others applications, for estimation of wind loads imposed on a structure, for studying pollutants dispersion from rockets, and dispersal of smoke and fumes from building's central heating plant, for estimating how much people will be buffeted by the wind outside the building, on the ground or on aerial walkways, among others applications.

A great amount of studies about wind incidence on buildings, or on bluff bodies, can be encountered in the literature in the latest 50 years, several of them with the purpose of characterizing the generated wakes, as in the investigation conducted by Woo *et al*. (1977), who carried out a comprehensive experimental analysis on this issue. The turbulence in wakes of buildings was analyzed with the purpose of guaranteeing the operational safety of small aircrafts at airfields, which are very susceptible to turbulence and quick changes in wind speed. Wind tunnel measurements on buildings of various sizes and aspect ratios in a simulated atmospheric boundary layer were conducted, and detailed information on mean longitudinal velocity and turbulence intensity were obtained. More recently, Neofytou *et al*. (2006) investigated the impact of a large airport terminal building on the wind flow over a runway located nearby was investigated. The authors presented a prediction of the steady-state velocity field in the vicinity of terminal building for different incident-wind directions, which was compared with available experimental field results. Kwon *et al*. (2003) carried out wind tunnel experiments with the purpose of studying the atmospheric conditions at the Oenaro-Do Island, where the South Corea Naro Space Center was built. In fact, insights about wind characteristics, as its profile, are very import for safe space vehicle launching operations since the rockets are projected for resisting loads which are imposed by the wind. In addition, rockets trajectory, control and guidance are determined by the wind profile on the ground (Pires, 2009).

In the last few years, the wind flow patterns at *Alcântara Launching Center* (ASLC) have been well investigated by researchers of the *Instituto de Aeronáutica e Espaço* (IAE), in São José dos Campos, sometimes in collaborations with researches from different institutions, as for example the *Universidade Federal do Rio Grande do Sul* (Wittwer, et al., 2012) and USP-São Carlos (Pires *et al*., 2009). These studies have been conducted based on field measurement (Fisch, 1999), Roballo and Fisch (2008), Marciotto et al. (2012) on numerical simulations (Pires et al., 2009) and also on wind tunnel tests experiments (Pires *et al*., 2009, Pires *et al*., 2010, Avelar *et al*. 2012, Avelar *et al*. 2014). The ASLC is the site from where most of the Brazilian rockets are launched, and it has some advantages in comparison to others Rocket Launch sites around the world due its privileged location. It is located in the Atlantic Coast, outside of

São Luis, state of *Maranhão*, close to the Equator line, a privilege shared just with the Guiana Space Centre. In addition, a stable climate provides to the researchers reliability in scheduling the launching operations. Nonetheless, in spite of all helpful aspects, ASLC has in its topology a coastal cliff of about 40m high at the edge of the sea land, which modify the atmospheric boundary layer characteristics, and in determined conditions may influence the safety of launching operations once the rockets launch pad and the Integration Mobile Tower (IMT), the building where the space vehicles are assembled, are located around 150 – 200 m from the sea border, respectively. In Fig 1a. it is shown the region of ASLC considered in the present study, the Launching Pad Area (LPA), and the facilities installed in this area. Numbered from 1 to 5 in Fig. 1b and in Fig. 1c, one can observe the TMI building (1), The Brazilian Satellite Launch Vehicles (2), the VLS, the umbilical tower (3), which raised close to the rocket is a means of ready access to all its important levels, the emergency exit tower (4), which allows safety leaves in case of accident and in Fig. 1b, the lightning rods (5), which protects the whole system, rocket, TMI and emergency exit tunnel, against electrical discharges through a Faraday shield. Once assembled and prepared for launching at TMI, this structure moves backward, around 55m, and the space vehicle blast-off. Important concerns regarding the study of the wind flow pattern in ASLC is the short period of time that the rockets standstill waiting for being launched and its first moments in air.

(a) (b)

Figure 1. LPA region in the Alcântara Space Launching Center.

As a continuation of previous studies, especially of the last publication by the same authors, Avelar *et al*. (2014), in the present work a wind tunnel investigation about the wind flow patterns at ASLC is conducted with the purpose of looking at the flow patterns in horizontal planes, in three different heights, considering the predominant wind angles of incidence at ASLC, α, and also different coastal cliff slope angles, β. This last parameter was considered with the purpose of investigating the influence of the coastal cliff irregular structure, which can be observed in Fig. 2. A model representing real irregular shape of cliff will be considered in further studies.

Figure 2. Coastal Cliff irregular structure.

According to the flow field results obtained up to now, the coastal cliff slope angles has a significant effect in flow features around the TMI (Avelar, *et al*., 2013). All configurations of wind incidence and coastal cliff slope angle were investigated for Reynolds number values, Re_l, of 5.4×10^5, 1.4×10^6 and 2.0×10^6. The PIV mean velocity and vorticity contours obtained up to now indicate that the air flow has complex features in the ASLC region and that all the parameters investigated play a significant role in the flow features in the LPA region since the dimensions of the recirculation bubble, in case of flow separation, as well as the vorticity intensity at the cliff edge, over and behind the MIT can be quite different depending on these parameters.

2. DESCRIPTION OF THE EXPERIMENTS

The PIV measurements were conducted in a subsonic facility of the *Instituto de Aeronáutica e Espaço*, the TA-2 aeronautic wind tunnel. The maximum mean velocity value through the wind tunnel test section, of 2.1 m high and 3.0 width, is 120 m/s. Since TA-2 is an aeronautic tunnel, with a short boundary layer thickness, a procedure for increasing the boundary layer thickness, simulating the atmospheric boundary layer in ASLC was conducted. A combination of artificial devices, spires, a barrier, and bottom wall surface roughness was used for accelerating the growth of the boundary layer. The methodology used for simulating the atmospheric boundary layer is well explained by Loredo-Souza *et al*., (2004), and the procedures used for the boundary layer formation in the TA-2 are described by Avelar *et al*. (2012). Several arrangements were tried for obtaining a suitable profile, which was obtained using the Power Law equation defined by,

$$\frac{U(y_r)}{U(y_n)} = \left(\frac{y_r}{y_n}\right)^{\alpha} \tag{1}$$

where $U(y_n)$ and $U(y_r)$ are the mean velocities correspondent to a height y_n and a reference height y_r. The y_r value is assumed to be 10m, which is the height suggested by the World Meteorology Organization to represent the horizontal wind surface. The exponent α is characteristic of the type of terrain, and varies from 0.11 for smooth surface as lakes and the ocean to 0.34 for cities with a high density of buildings. For the ocean surface some studies consider α between 0.11 and 0.15 (Barbosa *et al*. (2002), Hsu *et al*. (1999), Bresmann (1973)). In the present study the value 0.11 was assumed. The turbulence intensity values measured in the simulated boundary layer were in conformity with turbulence field measurement intensities carried out at ASLC region (Marciotto *et al*., 1999). The boundary layer obtained was 1 m high. The turbulence intensity, measured with hot-wire anemometer varied from 10%, close to the wind tunnel bottom wall to 4%, close to boundary layer border.

Images of the ASLC model installed in TA-2 test section are presented in Fig. 3a and Fig. 3b. The model was painted in flat black to minimize laser reflections. Figure 3b was included to show that the wind tunnel model was built in a way to reproduce a high level of details of the facilities in CLA.

(a) (b) (c)

Figure 3. The ASLC model installed in TA-2 test section – (a) LPA model – (b) Wind Tunnel test section.

The model was built in a scale 1:120, and it was installed over a wooden platform, which simulates the coastal cliff. The setup allowed the variation of the cliff slope angle, β, and also of the wind incidence angle, α, as represented in Fig. 4, in which top and frontal view of the wind tunnel model, with dimensions, is shown. In the present study it was investigated the values of β equal 45º, 70º and 90º and of α equal to 0º, 35º, and 45º. For each value of α and β, the velocity values of 8m/s, 20m/s and 30m/s, corresponding to Reynolds number (Re_l) of $5.4\text{x}10^5$, $1.4\text{x}10^6$ and $2.0\text{x}10^6$, were considered.

The mean flow velocity fields were measured using a Dantec Dynamics two-dimensional PIV system. The system is a double-cavity pulsed laser, Nd:Yag, 15 Hz, with an output power of 200 mJ per pulse at the wave length of 532 nm (New Wave Research, Inc.) and two HiSense 4M CCD camera, built by Hamamatsu Photonics, Inc. with acquisition rate of 11 Hz, spatial resolution of 2048 × 2048 pixels, and 7.4 μm pixel pitch. A Nikon f# 2.8 lenses with 105 mm of focal length was used. The laser sheet created was parallel to the wind tunnel bottom wall, as shown in Fig. 5. In both cases the model was positioned in the middle of the test section to avoid wall interferences. The flow was seeded with theatrical fog (polyethylene glycol water-solution) generated by a Rosco Fog Generator placed inside the wind tunnel diffuser. The images were processed using the adaptive correlation option of the commercial software Dynamic Studio,

developed by Dantec Dynamics. A 32×32-pixel interrogation window with 50% overlap and moving average validation was used.

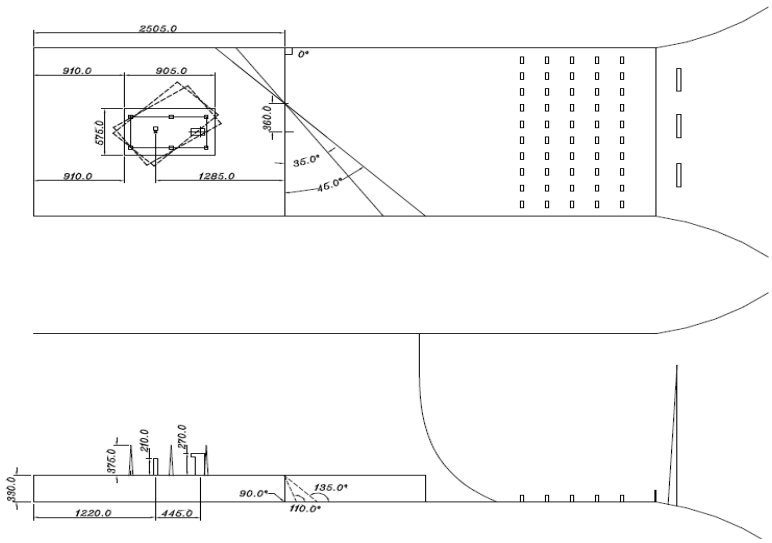

Figure 4. Schematic representation of ASLC model with dimensions – (a) Top view – (b) Frontal view.

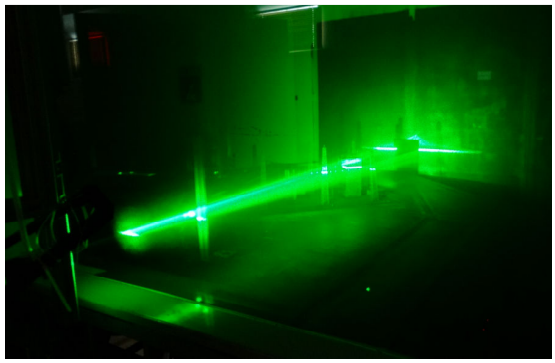

Figure 5. PIV setup for measurements in horizontal.

Three vertical positions, 77mm (P1 and P6), 185mm (P2 and P5), and 255mm (P3 and P4), corresponding to the aspect ratio, *y/L*, equal to 0.29, 0.68 and 0.94, respectively were considered, being *L* the height of TMI model, 270 mm. The laser light sheet was positioned in a way allow velocity field measurements in the wake of TMI as well as in the wake of VLS, as indicated in Fig. 6 by C-1 and C-2.

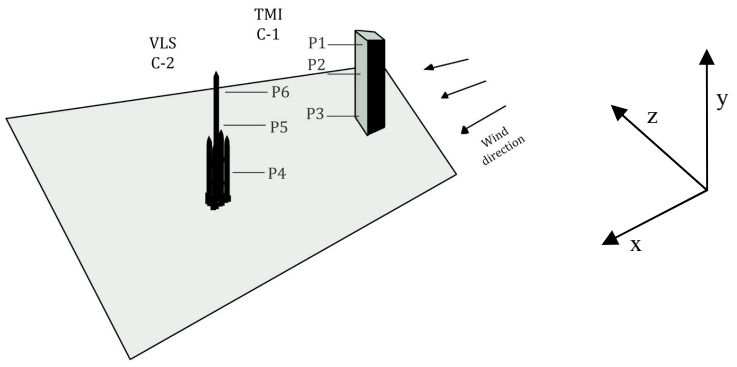

Figure 6. Representation of the regions where measurements were conducted with PIV.

3. RESULTS AND DISCUSSIONS

Preliminary results of velocity and vorticity fields as well as some velocity profiles are presented in this section, giving idea how the parameters investigated in the present analysis affects the wind flow patterns in CLA.

In Fig. 7 PIV flow maps, vorticity contours and velocity vectors, are presented for free-stream velocity of 20 m/s, wind incidence angle, α, of 0°, 35° and 45° and cliff slope angle, β, of 45°, 70° and 90°. These results are presented for y/L equal to 0.95, the highest position around the TMI.

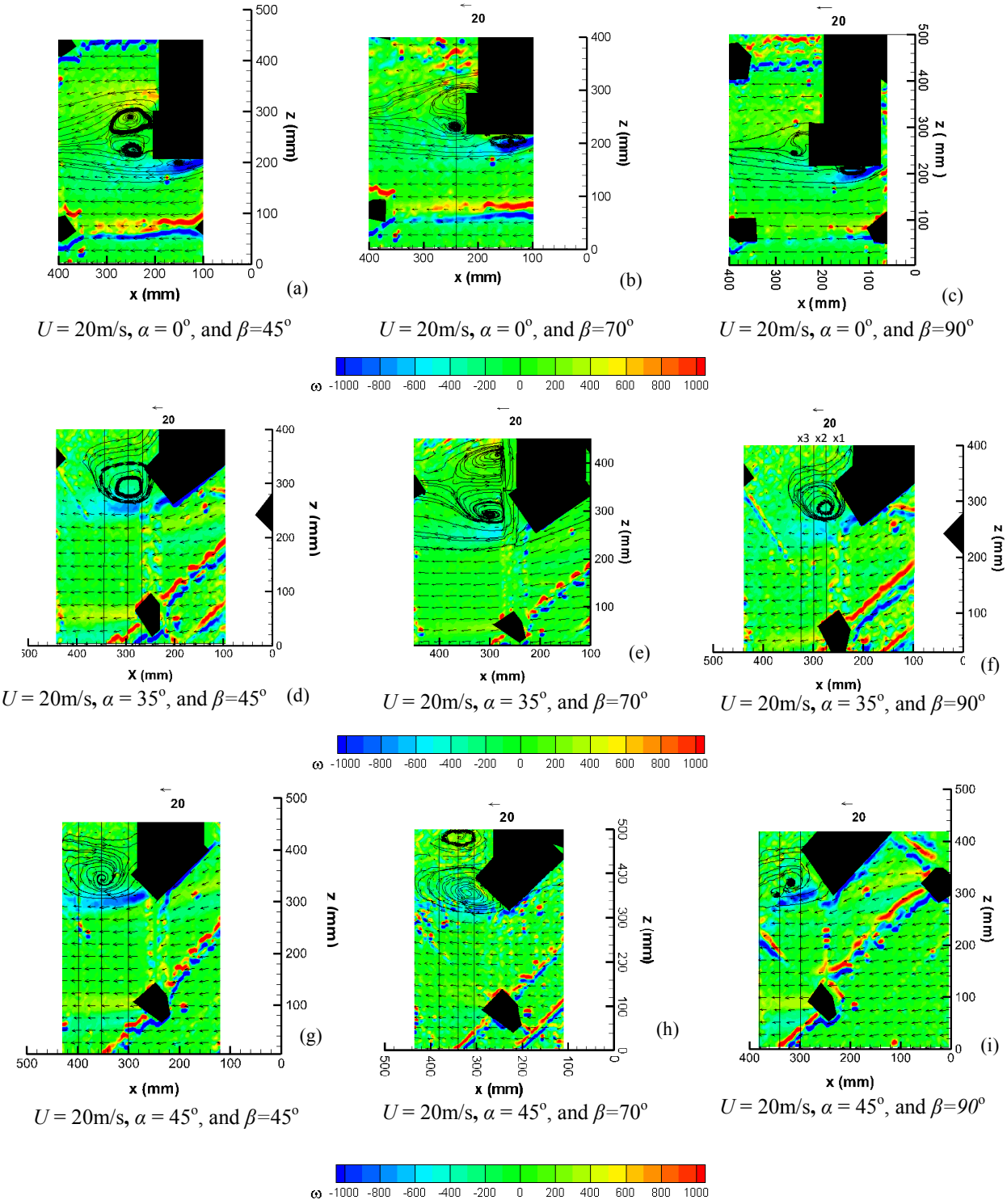

U = 20m/s, α = 0°, and β=45° U = 20m/s, α = 0°, and β=70° U = 20m/s, α = 0°, and β=90°

U = 20m/s, α = 35°, and β=45° U = 20m/s, α = 35°, and β=70° U = 20m/s, α = 35°, and β=90°

U = 20m/s, α = 45°, and β=45° U = 20m/s, α = 45°, and β=70° U = 20m/s, α = 45°, and β=90°

Figure 7. PIV flow maps for different Wind incidence angles and different coastal Cliff slope angle, for mean velocity wind tunnel velocity through the test section of 20 m/s and y\L equal to 0.95.

Observing Fig. 7a to Fig. 7i, different flow patterns behind the TMI can be noticed as the coastal cliff slope angle or the wind angle of incidence are varied. The flow features are very complex and both parameters investigated, wind incidence and cliff slope angle has both a significant effect in the wake created behind the TMI. Recirculation zones behind the MIT, with well defined vortexes can be observed in all configurations investigated. It seems that for cliff slope angles of 45° and 70° stronger recirculation regions are formed. It can be observed also high vorticity, positive and negative values, in the region of the wires connecting the lightning rods.

Velocity profiles behind the TMI for α = 35° and β=90, extracted from Fig. 7f are presented in Fig. 8. The positions x from where the velocity profiles were extracted are indicated by the vertical lines in Fig. 8a

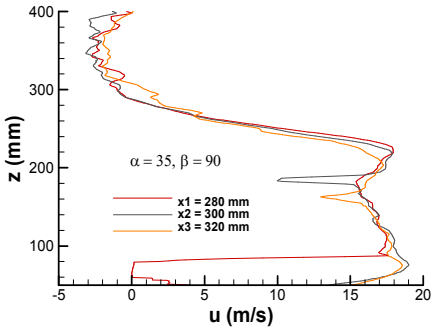

Figure 8. Velocity profiles in MIT wake, extracted from Fig. 7f.

From the velocity profiles shown in Fig. 8, it can be identified regions of velocity deficit, most probably induced by the lightning rods. Reversal flow appears just in the regions where recirculation regions where formed.

In Fig. 9, vorticity contours and velocity vector obtained in the vertical positions considered, aspect rations, y/L, of 0.29, 0.68 and 0.94, are compared for the mean velocity of 20 m/s, α equal to 45° and β equal to 90°.

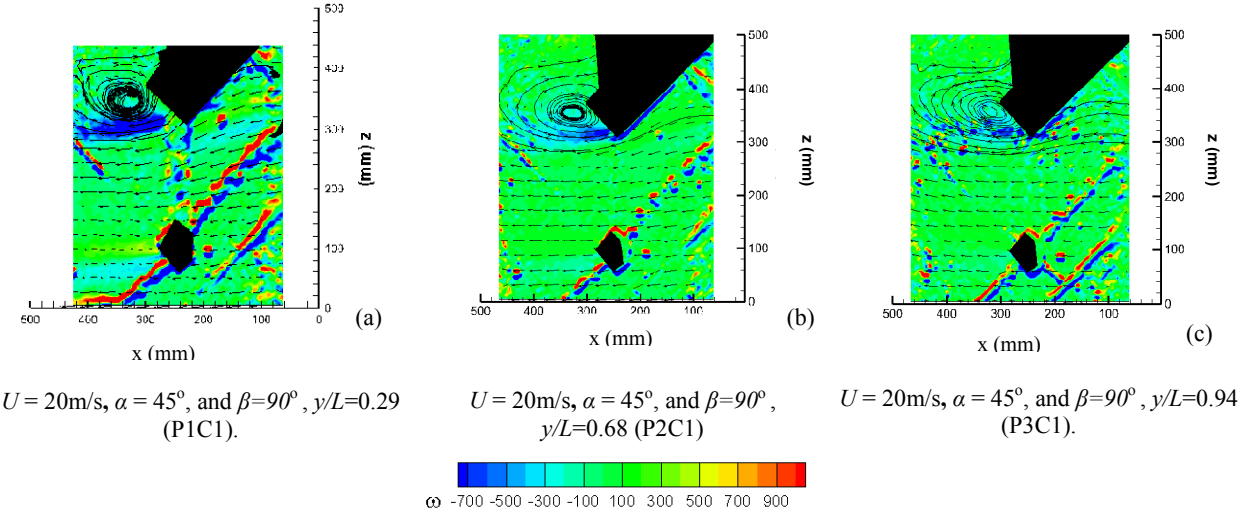

U = 20m/s, α = 45°, and β=90° , y/L=0.29 (P1C1).

U = 20m/s, α = 45°, and β=90° , y/L=0.68 (P2C1)

U = 20m/s, α = 45°, and β=90° , y/L=0.94 (P3C1).

Figure 9. Vorticity contours and velocity vector for different values of aspect ratio.

Comparing Fig. 9a, Fig. 9b and Fig. 9c, it seems that, although similar, the vortex formed behind the TMI seems stronger in the highest position, y/L equal to 0.94, where the highest vorticity values are observed.

In Fig. 10 PIV flow maps are presented in the neighborhood of VLS for the velocity of 20m/s, in the highest vertical position, y/L=0.94, vectors in the VLS region, and free-stream velocity of 20 m/s.

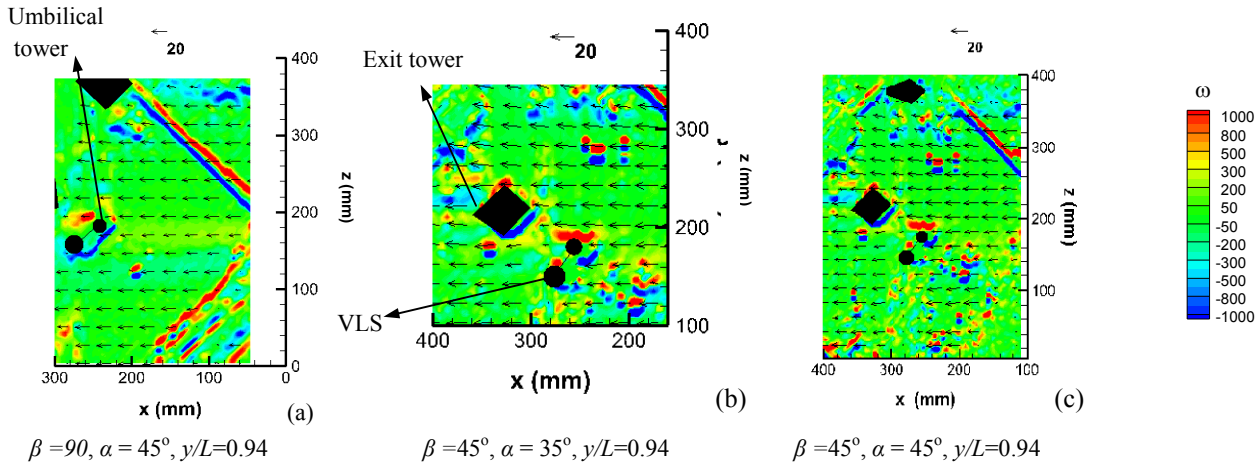

β =90, α = 45°, *y/L*=0.94 β =45°, α = 35°, *y/L*=0.94 β =45°, α = 45°, *y/L*=0.94

Figure 10. Velocity vectors and vorticity contours in the VLS neighborhood.

From the results presented in Fig. 10a, Fig. 10b and Fig. 10c, it seems that no strong recirculation zones appear in the neighborhood of the VLS. However, high vorticity levels are observed close to the emergency exit tower and to the VLS, as well as in region of the wires connecting the lightning rods, which is going to be investigated further.

Fig. 11a and Fig. 11b show velocity profiles extracted from velocity fields behind the TMI and behind the VLS for the velocity values of u = 8m/s, u = 20m/s and u=30m/s, and *y/L* equal to 0.94.

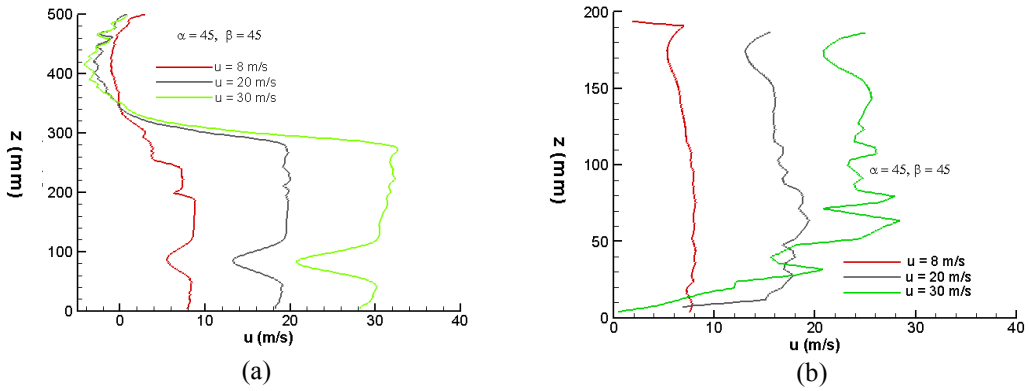

Figure 11. Velocity profiles for the three velocity values considered, u = 8m/s, u = 20m/s and *U*=30m/s, cases 4C and 4D - β = 45°, α = 45°.

From the velocity profiles plotted in Fig. 11a it can be clearly noticed that a deficit in velocity at *y* equal to 100mm, which coincides with the wake of a lightning rod. This effect cannot be noticed when the measurements are conducted in a vertical plane in the middle of the wind tunnel test section, which was observed in Avelar *et al*. (2014). In fact, the current investigation confirms that the wind flow patterns in ASLC, at the LPA, is really complex and that measurements in horizontal planes are of great importance to a better understanding of wake structures created by the facilities installed in this area. There are still a lot of data being processed from the last wind tunnel test, which will be presented further.

4. CONCLUSIONS

A 1/120 scaled model of the ASLC region was used for a wind tunnel investigation using the technique of Particle Image Velocimetry (PIV) to get insights about the flow patterns in LPA area of the Alcantara Space Launching Center. The measurements, conducted mainly in planes parallel to wind tunnel floor, were carried out for two different wind incidence angles, and wind speed through the test section of 8 m/s, 20 m/s and 30 m/s, corresponding to Reynolds number (Re_l) values based on the cliff height, l, of 5.4×10^5, 1.4×10^6 and 2.0×10^6. The results obtained confirms that the wind flow patterns in the ASLC region is very complex, and that the parameters investigated has significant influence in the flow features in this region. The results from PIV measurements in horizontal planes were of great importance in order to complement the information obtained from the measurements carried out in a vertical plane in the centre of the wind tunnel test section in previous investigations.

5. ACKNOWLEDGEMENTS

The authors would like to thank the technicians José Rogério Banhara and Wellington dos Santos for their valuable help to this research. The authors thank also Agencia Espacial Brasileira (AEB), Conselho Nacional de Desenvolvimento Científico e Tecnológico (CNPq) under the Grants 559949/2010-3, PQ 303720/2010-7 (Fisch), Universal, and Fundação de Amparo à Pesquisa do Estado de São Paulo (2014/06790-6) for the financial support.

6. REFERENCES

Avelar, A. C., Fisch, G., Faria, A. F., 2014, "Wind Tunnel Study of Wind Flow Patterns in the Alcantara Space Launching Center", Proceeding *of the* 44th AIAA Fluid Dynamics Conference, AIAA Aviation and Aeronautics Forum and Exposition 2014, Atlanta, Georgia.

Avelar, A. C.,Fisch, G., Marciotto, E.R., 2012, "Wind Tunnel Simulation of the Atmospheric Boundary Layer for Studying the Wind Pattern at *Centro de Lançamento de Alcântara*", Journal of Aerospace Technology and Management, Vol. 04, No.4, pp. 463-473.

Barbosa, P. H. A., Cataldi, M., Freire, A. P. S., 2002, "Wind Tunnel Simulation of Atmospheric Boundary Layer Flows", Journal of the Brazilian Society of Mechanical Science, Vol. 24, No. 3.

Blessmann, J., 1973, "Simulação da estrutura do vento natural em um túnel de vento aerodinâmico", Tese (Doutor em Ciências). Instituto Tecnológico da Aeronaútica – ITA, São José dos Campos, Brazil.

Hsu, A. S., Meindl, E.A., Gilhousen, D.B., 1994, "Determining the Power-Law Wind-Profile Exponent under Near-Neutral Stability Conditions at Sea", Journal of Applied Meteorology, Vol.33, No.6, pp.757-765.

Fisch, G., 1999, "Características do Perfil Vertical do Vento no Centro de Lançamento de Foguetes de Alcântara (ASLC)", *Revista Brasileira de Meteorologia*, Vol.14, No. 1, pp. 11-21.

Kwon K. J., Lee J. Y, Sung B., 2004, "PIV Measurements on the boundary layer flow around Naro Space Center", International Symposium on Particle Image Velocimetry, Busan, Korea, Sept. 2003, p.22-24. PIV'03 Paper 3121.

Loredo-Souza A.C, Schettini, E.B.C., Paluch M.J., 004. "Simulação da Camada Limite Atmosférica em Túnel de Vento", *Turbulência 4*, PP. 137-160.

Marciotto, E.R., Fisch, G., Medeiros, L. E., 2012, "Characterization of Surface Level Wind at the Centro de Lançamento de Alcântara for Use in Rocket Structure Loading and Dispersion Studies", Journal of Aerospace Technology and Management, Vol. 04, No.1, pp. 69-79.

Neofytou, P., Venetsanos, A, G., Vlachogiannis, D., Bartzis, J. G., Scaperdas A., 2006, "CFD Simulations of the wind environment around an airport terminal building", Enviromental Modelling and Software, Vol. 21, pp. 521-524.

Pires, L. B. M., 2009, "Estudo da Camada Limite Interna Desenvolvida em Falésias com Aplicação para o Centro de Lançamento de Alcântara", 150f. Tese (Doutorado em Meteorologia) – National Institute for Space Research, São José dos Campos.

Wittwer, A. R., Loredo-Souza, A. M., Fisch, G., 2012, "Avaliação Experimental do Escoamento Atmosférico no Centro Espacial de Alcântara Usando Modelos Topográficos em Escala Reduzida", VIII Escola de Primavera de Transição e Turbulência, 24-28 September, São Paulo, Brazil.

Woo, H. G. C., Peterka, J. A., Cermak, J. E., 1977, "Wind Tunnel Measurements in the Wakes of Structures". Washington, National Aeronautics and Space Administration, 243 p.

7. RESPONSIBILITY NOTICE

The author are the only responsible for the printed material included in this paper.

CONTROL OF VORTEX SHEDDING OF A CIRCULAR CYLINDER WITH TWO AND FOUR SMALL ROTATING CYLINDERS

Mariana Silva Ortega, silva.mariana@usp.br
Reinaldo M. Orselli, reiorselli@gmail.com
Gustavo R. S. Assi, g.assi@usp.br

NDF, Escola Politécnica, University of São Paulo

Abstract. *Recent achievements in controlling the boundary layer by moving surfaces have been encouraging the development and investigation of passive suppressors of vortex-induced vibration. Within this context, the main purpose of the present work is to evaluate the suppression of vortex shedding of a plain cylinder surrounded by two and four smaller control cylinders. The gap between the main cylinder and the control cylinders is g/D=0.75, where D is the diameter of the main cylinder. A numerical approach is employed to simulate the laminar flow at a laminar Reynolds number of 100. The governing equations are discretized by the finite volume method for a two-dimensional computational domain. In all the cases, a significant reduction in the overall drag coefficient and the unsteady hydrodynamic forces acting on the main cylinder are observed. A stable wake without alternating vortices was achieved for both configurations depending on the rotation of the control cylinders. The case with four cylinders required less rotation speed than the case with only two cylinders in order to stabilize the wake.*

1. INTRODUCTION

Over the past decades, offshore oil exploration reached the so-called ultra-deep waters. At reservoir locations where oil transport through pipeline systems becomes an unviable solution appeared the need to develop new floating platforms such as Spar, semi-submersible, tension-leg, FPSO and monocolumn floating unit. Most of them have circular cross sections being susceptible to vortex-induced vibrations (VIV).

Vortex shedding behind a bluff body can be altered, suppressed or controlled over a limited range of Reynolds numbers. Various flow-control techniques, which results in reduction of drag and unsteady forces, have been suggested and tested in simple geometries. Zdravkovich (1981) presents control techniques that can be classified into three categories: surface protrusions, shrouds and near wake stabilizers. He also investigated the relative effectiveness of the various means of flow control by applying them to the same test model including multi-cylinder arrangements. In an effort to study a passive control device, Strykowski and Sreenivasan (1990) have reported that the vortex shedding past a circular cylinder can be controlled over a limited range of Reynolds number by the proper placement of a smaller control cylinder close to the main cylinder. Mittal and Raghuvanshi (2000) have verified this phenomenon using a numerical approach and observed that the control cylinder provides a local favorable pressure gradient in the wake region, thereby locally stabilizing the shear layer. Gad-el Hak and Bushnell (1991) review various techniques that are employed for separation control, including the moving-surface boundary layer control (MSBC) in which rotating cylinders are employed to inject momentum into the already existing boundary layer.

The numerical simulations performed by Mittal (2001) showed promising results in the use of MSBC to control the flow around a static cylinder and smooth reduction of drag and lift forces. Korkischko (2011) performed an experiment employing MSBC to suppress VIV of an isolated cylinder mounted on an elastic base with one degree of freedom in the transverse direction. Hence, MSBC has already been tested as a means to suppress vortex shedding of static cylinders as well as VIV of oscillating bodies. The smaller control rotating cylinders inject angular momentum in the boundary layer of the main cylinder leading to vortex suppression and consequently drag decrease as well as reduction of the transverse velocity fluctuations in the wake.

2. METHODS

In the present work, the flow control past a circular cylinder is analyzed by means of rotating cylinders of smaller diameter positioned about the main circular cylinder. The rotating control cylinders generate circulation and inject momentum from the outer flow into the wake of the main cylinder. The investigation on the effect of the gap between the bluff body and control cylinders from Mittal (2001) is also considered in the present study. To this extent, computations are carried out considering two cases, one with two and other with four rotating cylinders as illustrated in Fig. 1. The first case is directly comparable with the previous results obtained by Mittal (2000). Based on the main geometrical parameters identified by Korkischko (2011), their values are: the ratio $D/d_c = 20$, between the diameter of the main cylinder (D) and the

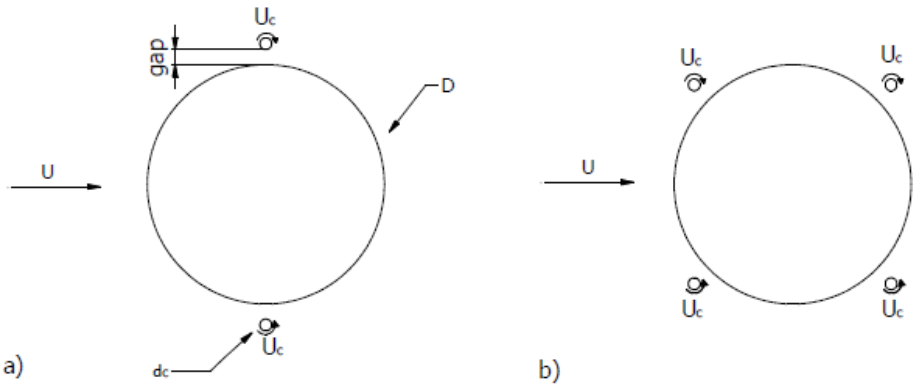

Figure 1. Tested configurations: main cylinder with (a) two and (b) four rotating control cylinders.

diameter of the control cylinders (d_c); the gap spacing g/D=0.075, between the main and the smaller cylinders, the Reynolds number Re=100 and the speed ratio U_c/U= from 0 to 5 m/s, where U_c is the tip speed of the smaller cylinders and U is the free-stream flow speed. Reynolds number is based on the diameter of the main cylinder, free-stream velocity and the kinematic viscosity of the fluid.

2.1. Numerical simulations

All the simulations reported in the present work were carried out using the commercial code ANSYS Fluent (version 13.0). The flow is governed by the Navier-Stokes equations, which are considered here as incompressible and two-dimensional. The unsteady non-dimensional Navier-Stokes equations for the conservation of mass and momentum in the integral form are given by:

$$\int_S \vec{u}.\vec{n}dS = 0 \tag{1}$$

$$\int_\Omega \frac{\partial \vec{u}}{\partial t} d\Omega + \int_S \vec{u}(\vec{u}.\vec{n})dS = -\int_\Omega \vec{\nabla} p d\Omega + \int_S \frac{1}{\mathrm{Re}} \nabla \vec{u}.\vec{n}dS \,, \tag{2}$$

where u is the flow speed, p the static pressure, t is the time, Ω represents the control volume of the system and S denotes its external surfaces whose outward unit normal is $\vec{n}$. The equations are discretized by a cell-centered Finite Volume Method (Versteeg and Malalasekera, 2007).

The fluid domain is divided into a large number of discrete control volumes by means of a computational mesh. The resulting discretized equations are solved sequentially based on an implicit pressure-based scheme. In order to deal with the pressure-velocity coupling, the pressure-based algorithm PISO is employed due to its efficient iterative method for unsteady problems, such scheme is fully described in Versteeg and Malalasekera (2007). In order to obtain the pressure on the control volume faces, an interpolation scheme based on a "staggered" control volume arrangement is employed, known in Fluent as PRESTO (PREssure STaggering Option). The staggered-grid scheme procedure is described in Versteeg and Malalasekera (2007). An upwind second-order spatial differencing method was applied for the convective terms (Barth and Jespersen, 1989) and the diffusive terms were discretized by a central differencing scheme. The solution is time-advanced using an implicit second-order accurate scheme that employs three time levels incorporated within the PISO algorithm (see Versteeg and Malalasekera, 2007). All the equations were solved iteratively, for a given time-step, until the convergence criteria was met (all residuals for each algebraic equation are at least less than 10^{-4} and 20 internal iterations per time step).

The cylinders were surrounded by a rectangular computation domain with upstream and downstream boundaries located respectively at 8 and 30 cylinder diameters from the center of the main cylinder, as shown in Fig. 2 for two and Fig. 3 for four control cylinders. The computation has been carried out with a mesh containing 50,935 cell volumes for the case with two rotating cylinders, 68,130 cells for the corresponding case with four cylinders and 71,322 volumes for the reference case of a plain cylinder without control cylinders. The no-slip condition is specified for the velocity on the surface of the cylinders and free-stream values are assigned for the velocity at the upstream boundary. On the upper and lower boundaries, the component of velocity normal to and the component of stress vector along these boundaries are prescribed zero value.

At the downstream boundary, an outflow boundary condition is employed which prescribes all variables normal gradient to zero.

The degree of flow control that can be achieved by employing rotating control cylinders depends on a variety of parameters. Some of them are the relative diameters of the main and control cylinders, their relative arrangements, and the rotation rates of the two and four control cylinders. The upper cylinders rotate in the clockwise and the lower ones in the counterclockwise direction. The rotation of the control cylinders will be expressed in terms of the ratio of the tip speed of the rotating cylinders U_c to the free-stream speed U.

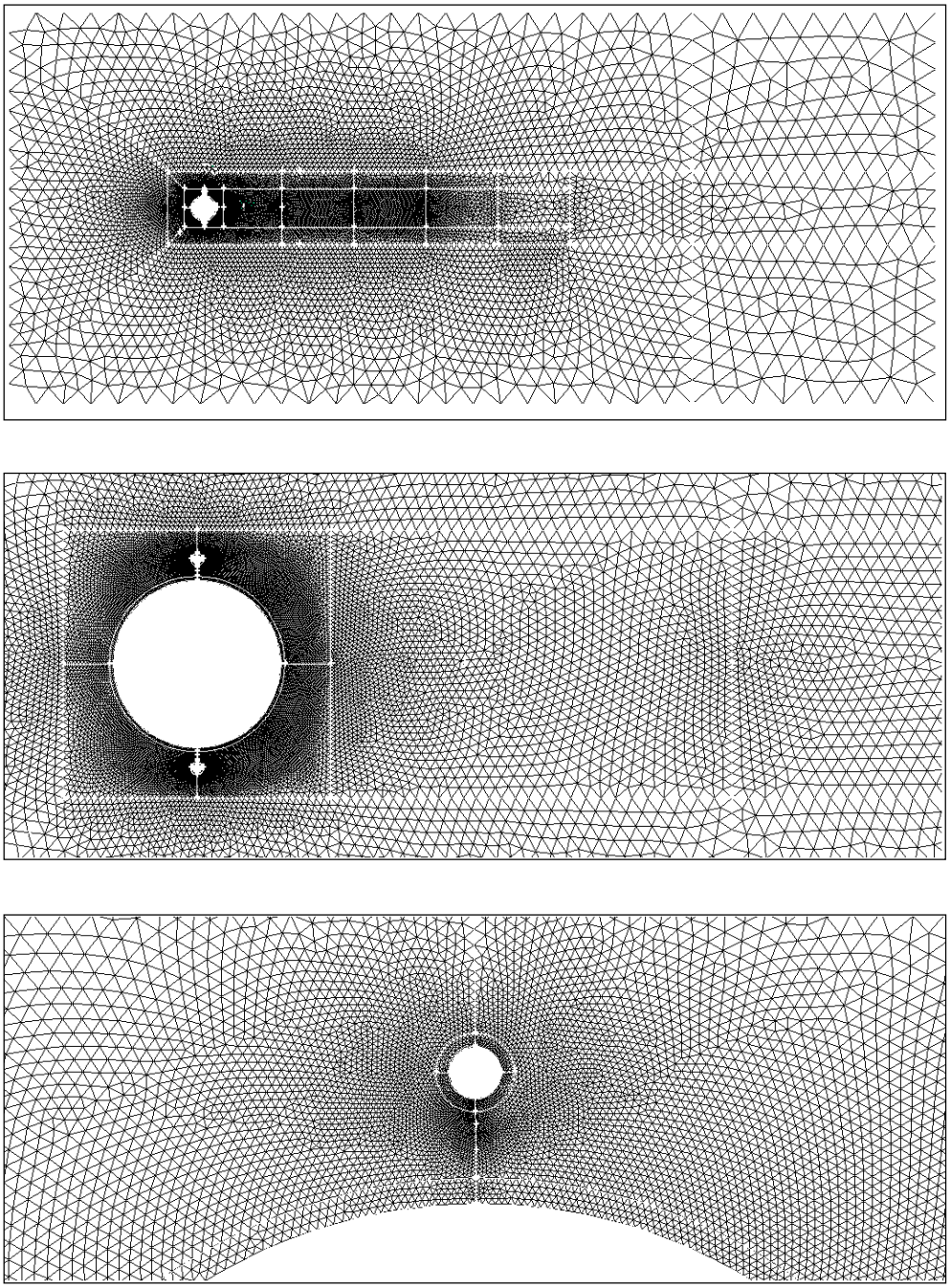

Figure 2. Numerical domain and mesh details around the main cylinder with two control cylinders.

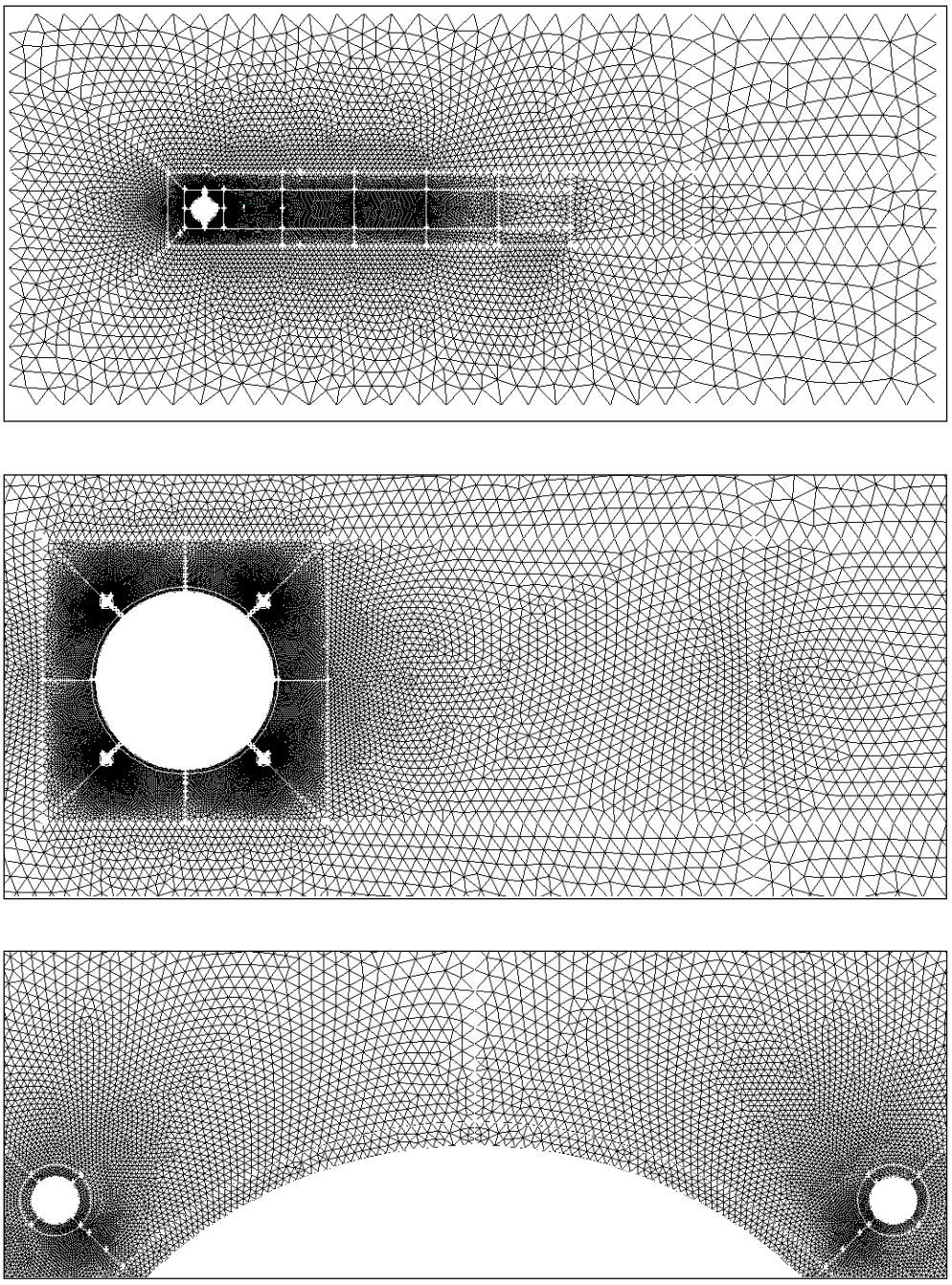

Figure 3. Numerical domain and mesh details around the main cylinder with four control cylinders.

3. RESULTS

3.1. Flow past an isolated cylinder

The flow around an isolated cylinder for Re = 100 was simulated in order to validate the numerical model and the mesh employed. The results also serve as reference for analyzing the effect of two or four control cylinders on the wake of the main cylinder. Fig. 4 presents the development of the drag and lift coefficients as simulation evolves over time. Fig. 5 illustrates the vorticity field for an instant once the periodic regime of vortex shedding has been established, i.e., beyond 70 seconds of simulation time. As expected, a typical von Karman wake is observed to appear downstream of the cylinder with a very clear interaction appearing between the alternating shear layers.

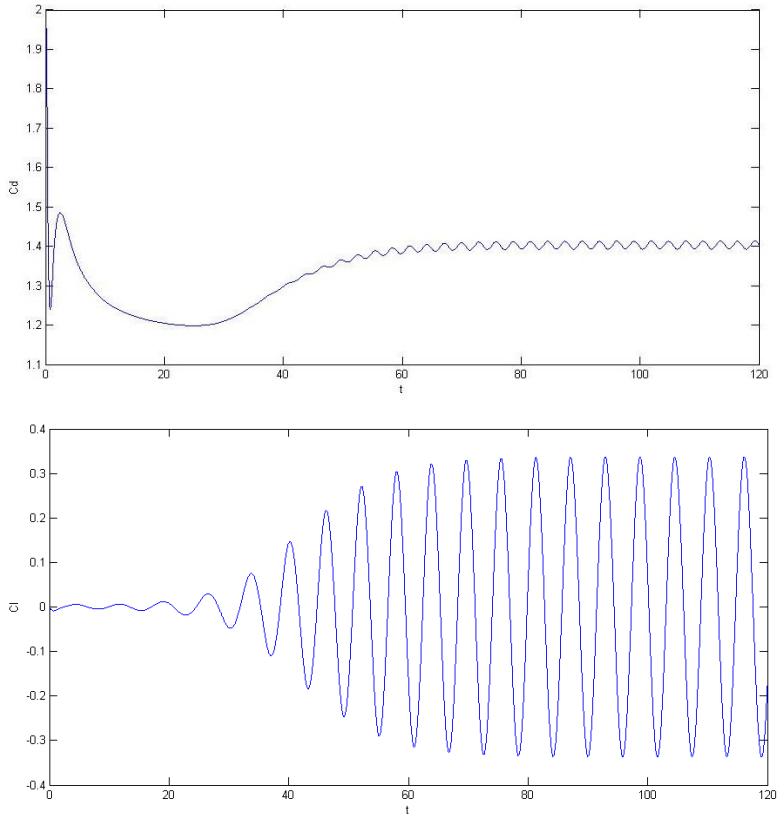

Figure 4. Time histories of (top) drag and (bottom) lift coefficients for a plain cylinder without control cylinder. Re=100

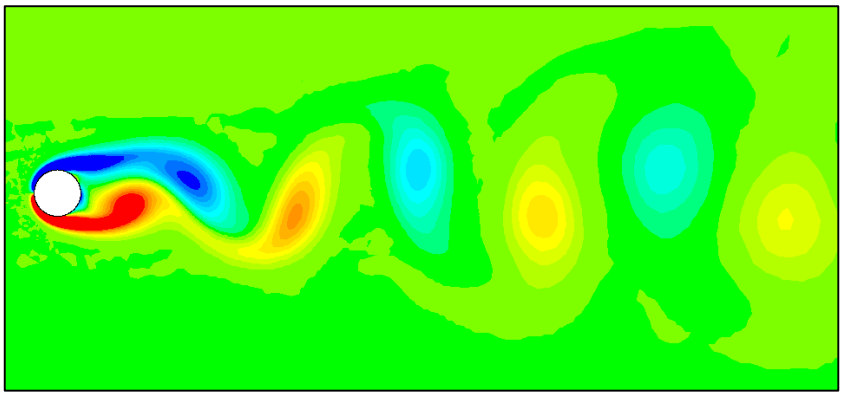

Figure 5. Instantaneous vorticity field for the flow past an isolated cylinder. Re=100.

3.2. Flow past a cylinder with two control cylinders.

For the flow at Re=100 the gap is g/D=0.075 which corresponds to the gap employed by Mittal (2000) in his numerical work. The flow is allowed to evolve until the periodic regime is reached for each one of the six rotation speeds considered from the lowest (U_c/U =0) to the highest rotation considered (U_c/U =5) as shown in Fig. 6. Rotation of the control cylinders was altered subsequently during one single numerical run. At t=0 the simulation starts with static control cylinders (U_c/U =0). At t=146 a rotation of U_c/U=1 was assigned to both cylinders (with a clockwise direction for the upper and a counterclockwise direction for the lower cylinder). At t=244 the rotation is doubled to U_c/U =2 and increased further later in time. Fig. 7 illustrates the development of the simulations highlighting the different plateaus corresponding to each rotation.

Back to Fig 6, the flow pattern for U_c/U=0 looks very similar to that for a single isolated cylinder at the same Reynolds number, as depicted in Fig. 5. The Reynolds number based on the diameter of the control cylinder is 5 which is below the limit value of about 46, the Reynolds number from which shear layer instability should trigger the onset of vortex shedding for the individual control cylinder. Therefore, no independent vortex-shedding is observed from the smaller cylinder. In this case, it can be observed that the vortex shedding is produced by the main and the control cylinders combined as a single body.

As the control cylinders start spinning and the rotation rate is increased, the vortex shedding mechanism is weakened and the coherent vortex structures defining an organized wake are considerably reduced. This is evident from vorticity contours and streamlines presented in Figs. 6a to 6f. Eventually, for U_c/U =5, the interaction between the separated shear layers is so much reduced that no alternating vortex shedding is noticed in the wake. This is also accompanied by a narrowing of the wake. It is shown that two control cylinders rotating at a certain speed are capable of achieving suppression of vortex shedding of a static cylinder.

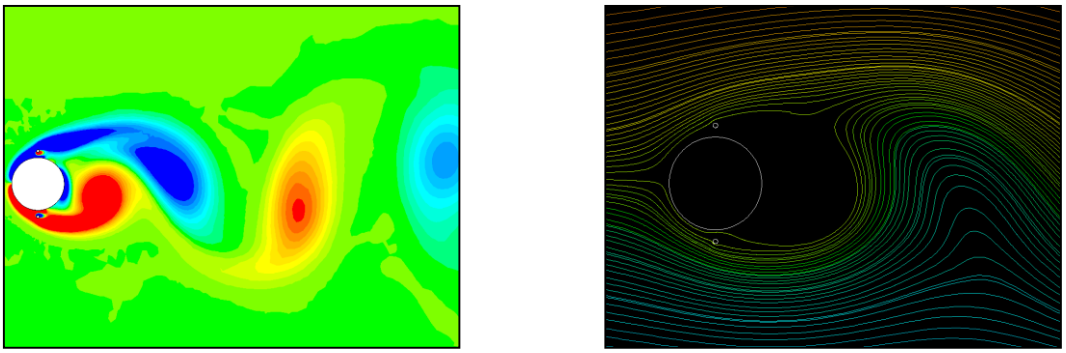

(a) Uc/U =0

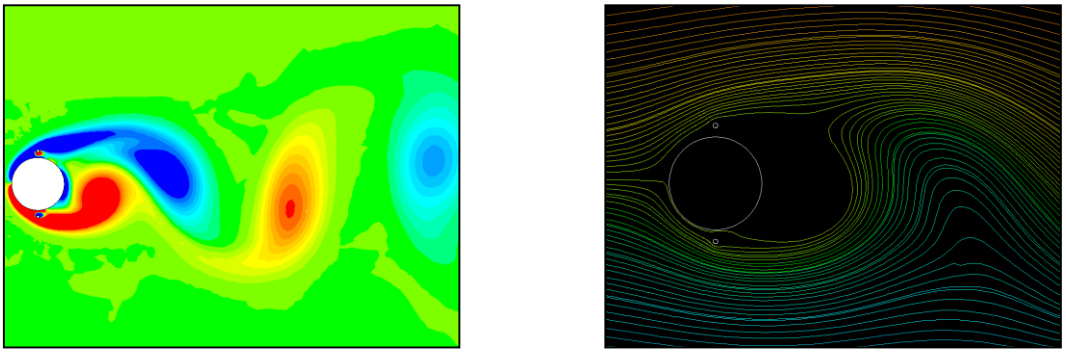

(b) Uc/U =1

Figure 6. (*Key on next page.*)

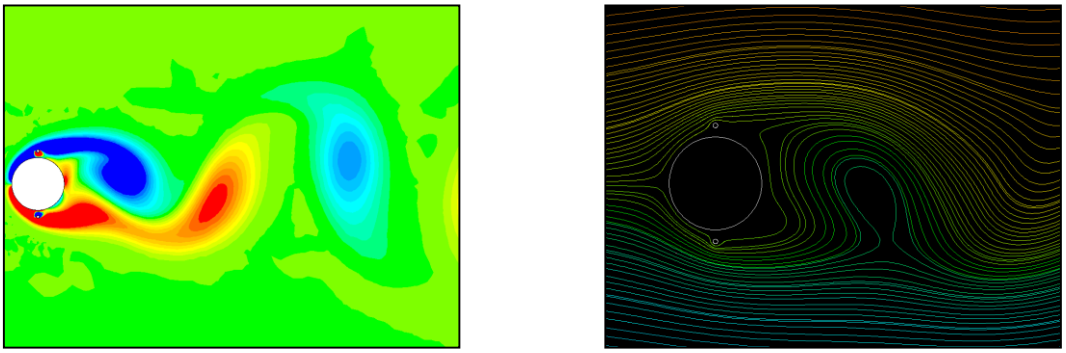

(c) Uc/U =2

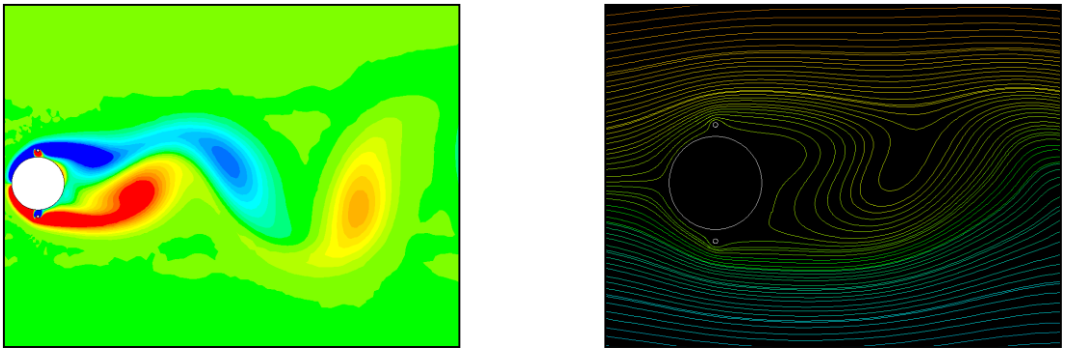

(d) Uc/U =3

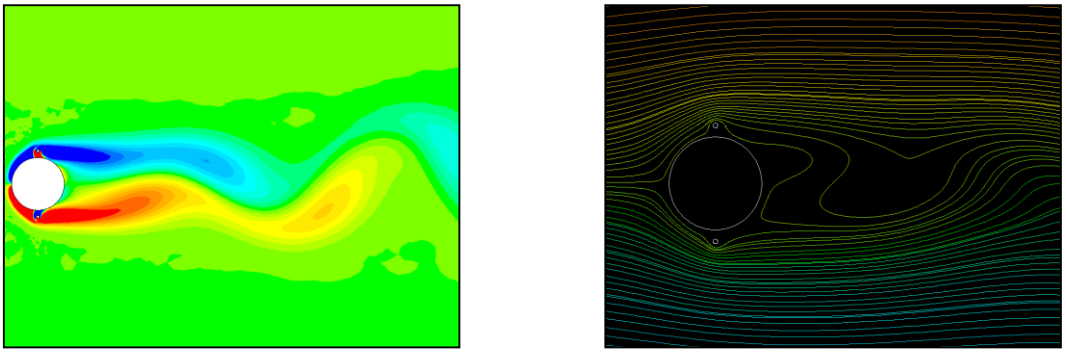

(e) Uc/U =4

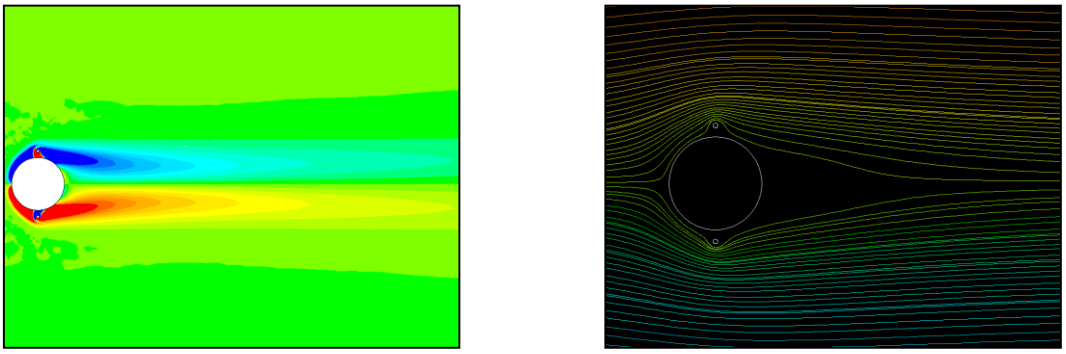

(f) Uc/U =5

Figure 6 (*continued from last page*). Instantaneous vorticity field (left) and details of streamlines in the near wake (right) for the fully developed flow past a cylinder with two control cylinders at different rotations. Re=100.

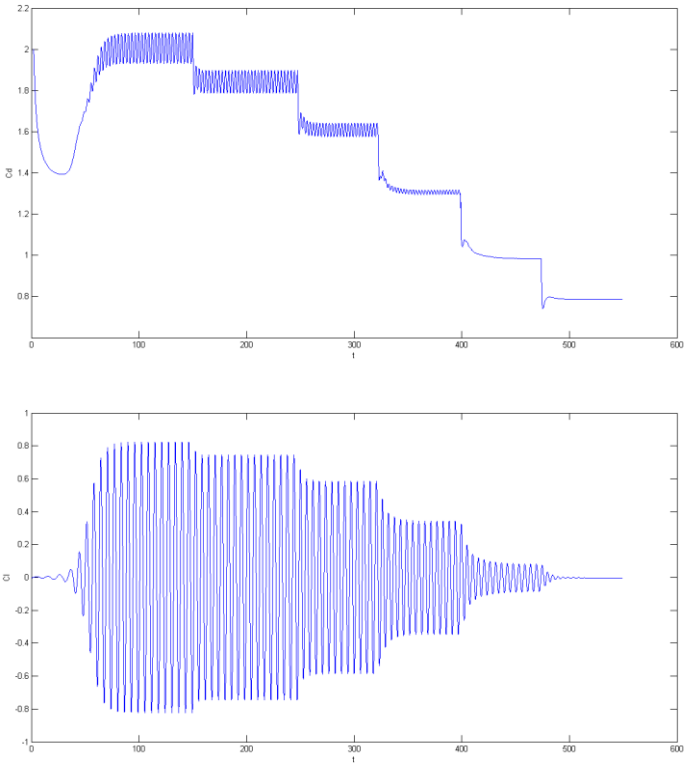

Figure 7. Time histories of the drag (top) and lift (bottom) coefficients for two control smaller cylinders at Re=100.

Fig. 7 shows the time histories of lift and drag coefficients measured by the integration of pressure around the main and the control cylinders. The figure is divided in plateaus, as explained above, each corresponding to a rotation speed of the control cylinders. For U_c/U =0 the drag coefficient of the main cylinder (Cd=2.1) is higher than that experienced by an isolated cylinder, since the presence of the static control cylinders contributes to the enhancement of the wake and increase drag. Likewise, the amplitude of the lift coefficient experienced by the main cylinder (Cl=0.8) is significantly higher than that observed for an isolated cylinder. However, once the control cylinders start to spin, both the drag and lift coefficients drop continually as rotation rate is increased. For U_c/U =5 the drag coefficient for the main cylinder is Cd=0.73 and, since the flow achieves an almost steady state, the lift coefficient is close to zero.

3.3. Flow past a cylinder with four control cylinders.

Similarly to the previous case, the simulation with four control cylinders begins with stationary control cylinders. U_c/U =0; and is gradually changed to 1, 2, 3, 4 and 5 at t=146.5, 244, 399, 474, and 584, respectively. Fig. 8 shows the vorticity field for the fully developed flows at various rotation rates of the control cylinders. As the previous case, the flow for U_c/U =0 looks very similar to that for a single cylinder at the same Reynolds number. The drag coefficient of the main cylinder (Cd=1.35) is close to that experienced by an isolated cylinder and the amplitude of the lift coefficient is also in the expected range (Cl=0.35). For U_c/U =1, 2 and 3 the wake still presents distinct alternating vortices and the width of the wak is not considerably altered. Eventually, U_c/U =3 the unsteadiness in the wake disappears and a steady-state solution is identified. This fairly symmetric but stable wake is sustained for U_c/U =4 and 5.

Fig. 9 shows the time histories of the lift and drag coefficients of the three cylinders. For U_c/U =0 the drag coefficient on the main cylinder (Cd=1.35) is lower than the two cylinder case, but slightly higher than that of an isolated cylinder. For U_c/U =3 the drag coefficient reduces to Cd=1.29. It can be observed that the lift generated by the control cylinders in the present case is smaller than the previous case. Since lift is directly related to the circulation around the control cylinder, it may be concluded that the four control cylinders result in a reduction of circulation generated around the main cylinder. This observation is consistent with our earlier remarks regarding the flow patterns.

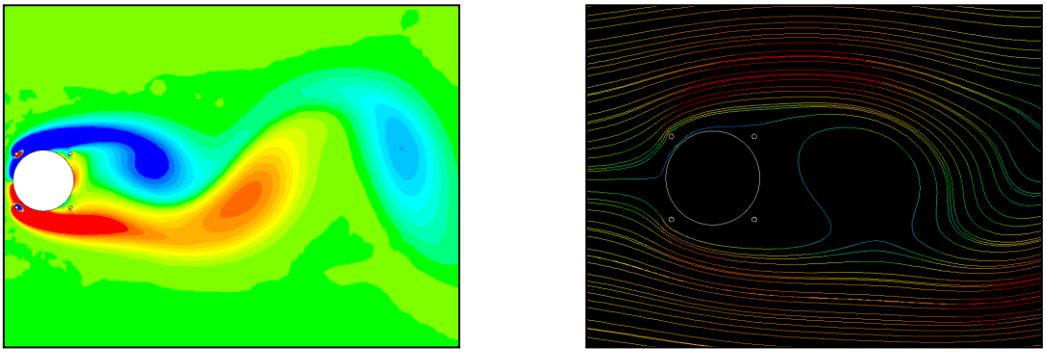

(a) *Uc/U* =0

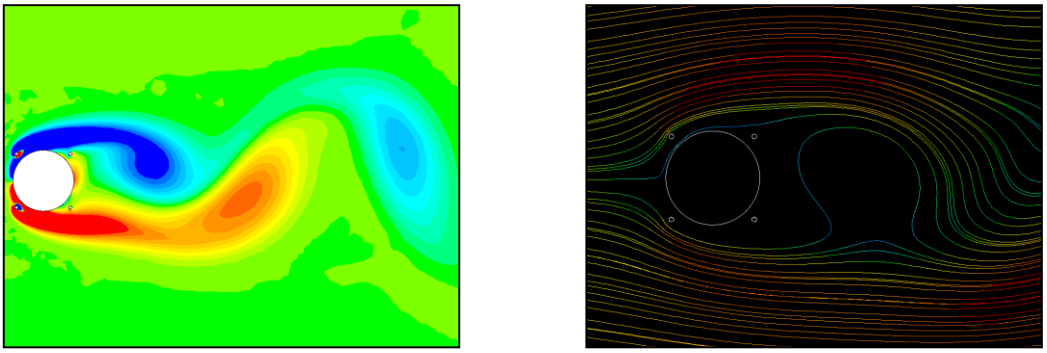

(b) *Uc/U =1*

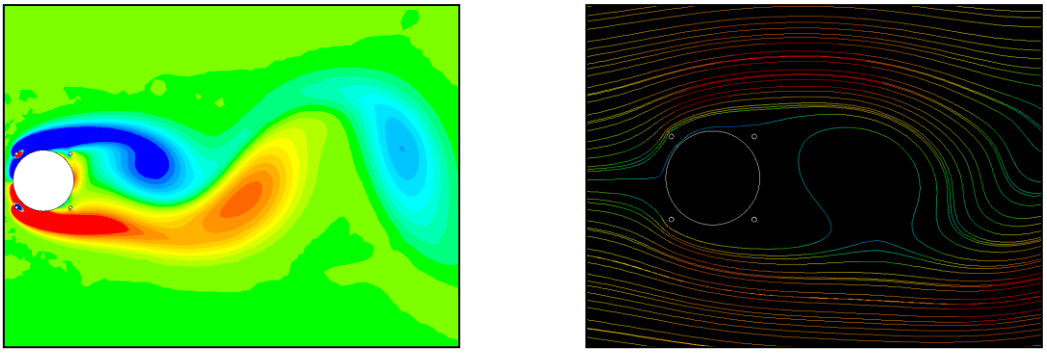

(c) *Uc/U =2*

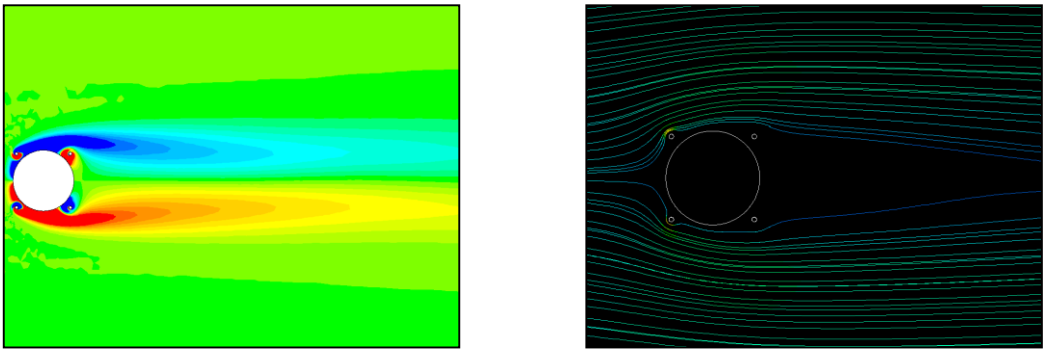

(d) *Uc/U =3*

Figure 8. (*Key on next page.*)

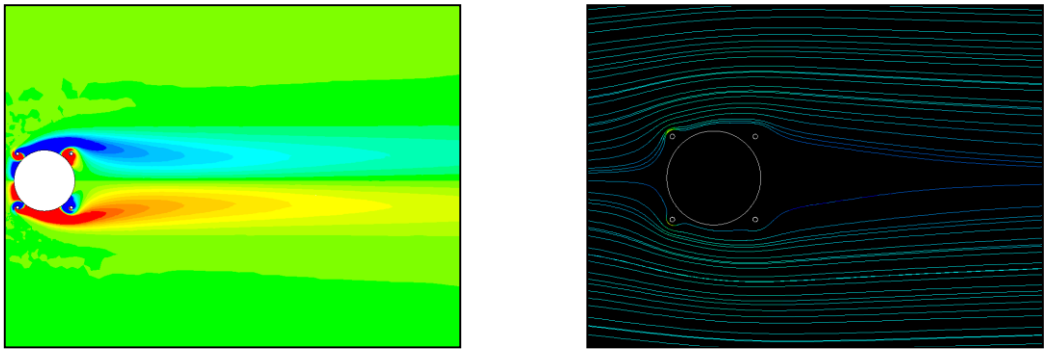

(e) *Uc/U =4*

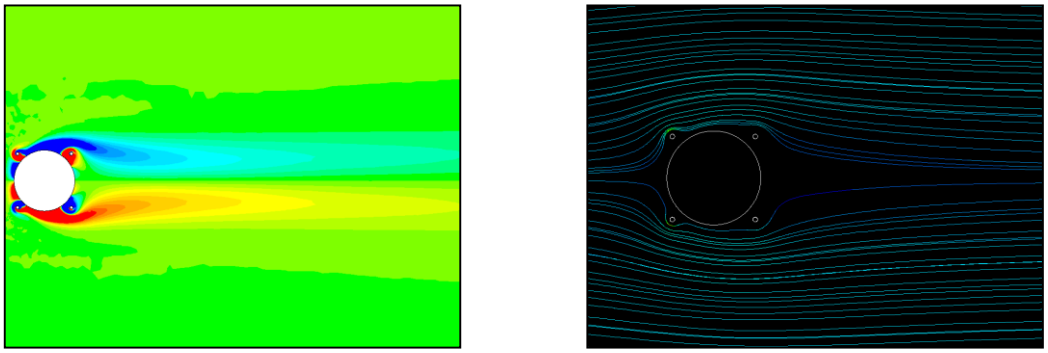

(f) *Uc/U =5*

Figure 8 (*continued from last page*). Instantaneous vorticity field (left) and details of streamlines in the near wake (right) for the fully developed flow past a cylinder with four control cylinders at different rotations. Re=100.

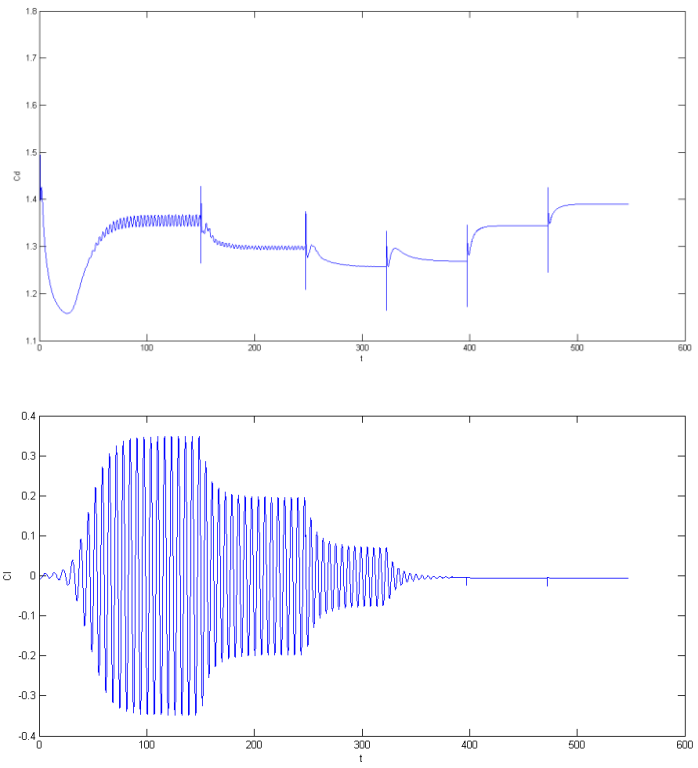

Figure 9. Time histories of the drag (top) and lift (bottom) coefficients for two control smaller cylinders at Re=100.

4. CONCLUSION

In the present work, flow control past a circular cylinder using rotating smaller cylinders has been studied by means of numerical simulations. Firstly, the formulation is employed to study the flow past an isolated cylinder as a reference for comparison of vorticity fields and drag and lift coefficients. A Reynolds number of 100 and a gap of 0.075D between the main and control cylinders were employed for both cases with two and four control cylinders.

In all the cases with Uc/U>1, a significant reduction in the overall drag coefficient and the unsteady hydrodynamic forces acting on the body are observed. For the case with two control cylinders, a steady wake was achieved only with Uc/U=5, while for the case with four control cylinders a stable wake appeared earlier for Uc/U>3. The reduction in unsteady forces may lead to the reduction of the flow-induced vibrations of the body. The effect of four cylinders is found to be more efficient if compared to the case with only two.

The circulation generated by the rotating control cylinders is an important component of this flow-control mechanism. The extension of this effect to flow control using rotating cylinders is another area that needs to be studied. This study can be extended to investigate the effect of the gap, position and number or control rotating cylinders. The 2-D computations set an upper bound on the control effectiveness of the rotating cylinders, and it is expected that the actual behaviour of such control strategies will depend significantly on three-dimensional effects.

ACKNOWLEDGEMENTS

The authors wish to acknowledge the support of FAPESP (2011/00205-6). MSO is in receipt of an MSc scholarship from CAPES Brazilian Ministry of Education. GRSA is grateful to CNPq (308916/2012-3).

REFERENCES

Assi G.R.S., “Estudo Experimental do efeito de Interferência no Escoamento ao Redor de Cilindros Alinhados”, MSc São Paulo EPUSP, 2005.

Assi G.R.S., “Mechanisms for flow-induced vibration of interfering bluff bodies”, PhD London Imperial College, 2009.

Gonçalves, R.T., Matsumoto F.T., Malta E.B., Fujarra A.L.C., Rosetti G.F., Nishimoto K., “Evolution of the MPSO (monocolumn, production, storage and offloading system)”, Marine System & Ocean Technology, December 2009/June 2010, Vol. 5 No.1 pp 43-51.

Mittal S., “Control of flow past bluff bodies using rotating control cylinders”, Journal of fluids and structures 15, 291-326, 2001.

Korkischko I., “Investigação experimental e analítica do escoamento ao redor de cilindro circular com supressores de VIV”, PhD São Paulo EPUSP, 2011.

Zdravkovich M.M, “Review and classification of various aerodynamic and hydrodynamic means for suppressing vortex shedding”, Journal of Wind Engineering and Industrial Aerodynamic, 7, pp.145-189, 1981.

Versteeg, H. K.; Malalasekera, W., “An Introduction to Computational Fluid Dynamics”, The Finite Volume Method. 2 ed. Pearson, 2007.

Barth T.J. and Jespersen D., "The design and application of upwind schemes on unstructured meshes". Technical Report AIAA-89-0366. AIAA 27th Aerospace Sciences Meeting, Reno, Nevada, 1989.

RESPONSIBILITY NOTICE

The authors are the only responsible for the printed material included in this paper

COMPARISON OF VARICOSE AND SINUOUS INSTABILITY DEVELOPMENT IN A GÖRTLER FLOW

Vinicius Malatesta, malatest@icmc.usp.br
Leandro Franco de Souza, lefraso@icmc.usp.br
Department of Applied Mathematics and Statistics, Institute of Mathematics and Computational Sciences, University of São Paulo, Avenida Trabalhador São Carlense, 400, São Paulo, 13566-590, Brazil

Abstract. *The centrifugal instability mechanism for boundary layers over concave surfaces is responsible for the development of counter-rotating vortices, aligned in the streamwise direction, known as Görtler vortices. These vortices create two regions in the spanwise direction: the upwash and the downwash regions. The downwash region is responsible compressing the boundary layer in the direction of the wall. The upwash region does the opposite. The Görtler vortices distort the streamwise velocity profile in the spanwise and the wall-normal directions. These distortions are susceptible to instabilities giving rise to secondary instabilities. The secondary instabilities can be of varicose or sinuous mode. The main objective of the present paper is to analyze the amplification of these modes. The research is carried out by a Spatial Direct Numerical Simulation. The results show that the the varicose predominates over the sinuous mode for the adopted parameters.*

Keywords: *Centrifugal instability, Secondary instability, Varicose and sinuous mode, Spatial direct numerical Simulation*

1. INTRODUCTION

The hydrodynamic instability can occur due to rotation effects on concave surfaces Drazin and Reid [2004]. As examples we have Couette flow, the flow in a curved channel and the boundary layer over a concave surface. This latter is the focus of the present study.

Rayleigh [1917] was the first researcher to study the mechanism of inviscid centrifugal instability, which derived the Rayleigh circulation criterion for instability, furthermore he noted that there is an analogy between the rotational flow stability and stability in a stratified fluid at rest in a gravitational field.

Clauser and Clauser [1937] conducted the first experimental study which showed that the curvature of the wall has a strong effect on boundary layer transition. In the experiment they studied the effects of concave and convex curvature on laminar-turbulent transition. Theoretical analysis was carried out for checking that a flow that is more stable on concave surfaces than convex surfaces and this was confirmed experimentally. Goerlter [1940] showed the existence of centrifugal instability on concave surfaces and defined a dimensionless parameter that carries his name, the Görtler number Go.

One of the Görtler flow characteristics is the change in the streamwise velocity distribution in the spanwise direction, thus two regions are formed, the upwash and the downwash regions. In the upwash region the boundary layer is thrown in the wall normal direction, thus the boundary layer becomes thicker. In the downwash region the opposite occurs, the boundary layer is compressed through to the wall. The streamwise velocity distribution in crosscut planes forms a mushroom-type structure in the nonlinear Görtler development region.

Swearingen and Blackwelder [1987] presented experimental results where the initial boundary layer over a concave wall, quickly becomes three-dimensional with a system of longitudinal vortices and establishes an agreement with the Görtler linear analysis. In this study they showed the mushroom-like structures formed by the streamwise velocity distribution in zy crosscut planes. This latter are generally more complex and is unstable to unsteady disturbances. These new instabilities are known as secondary instabilities.

The secondary instabilities that occur in Görtler flows can be of two types: varicose and sinuous modes Saric [1994], or a medley of them. The varicose mode instability has its origin in the nonlinear Görtler development region, related to the derivative du/dy Li and Malik [1995], and sinuous instability mode has the main feature of the fluctuation of disturbances in the xy plane, as identified in the experiment of Swearingen and Blackwelder [1987].

The nonlinear development of longitudinal vortices appear in the boundary layer over concave walls and reveal that the wavenumbers in the streamwise direction show velocity profiles with inflection point both in the spanwise direction as the direction normal to the wall Swearingen and Blackwelder [1987].

Schmid and Henningson [2001] stated that when the primary disturbance achieve finite amplitude, in which the flow boundary layer is dominated by mushroom-type distribution of the streamwise velocity in a cross plane, often saturates and turns the flow into a new state of equilibrium, which is unstable to secondary instabilities.

Experiments Swearingen and Blackwelder [1987], Inagaki and Aihara [1995], Ito [1985] and Peerhossaini and Wesfreid [1988], analyze the transition of boundary layer over concave walls and provide physical structure and stimulated theoretical studies on the role of longitudinal vortices.

Sabry et al. [1989] was the first to study the cross sections in regions susceptible to secondary instabilities Swearingen and Blackwelder [1987].

According to Mitsudharmadi et al. [2004a] the primary instability (Görtler Vortices) develops inflections in the streamwise velocity component, and these inflections become larger as these instabilities develop downstream. In their experiment, in the region between 500mm and 600mm, the vortices evolve into mushroom distribution of streamwise velocity. The transformation of these vortices in horseshoe type structure is the result of secondary instability over the Görtler vortices. This determines the varicose mode of secondary instability Swearingen and Blackwelder [1987].

Zhang et al. [1995] conducted an experimental study in a wind tunnel in which there was the development of Görtler vortices. The results showed the appearance of horseshoe structures characteristic of the secondary varicose mode. They attributed the formation of these structures to Kelvin-Helmholtz instability.

The aim of this paper is to provide a physical understanding of secondary instability of secondary varicose and sinuous mode of an initially flow disturbed by Görtler Vortices. A simulation code was developed and implemented using spatial direct numerical simulation. These parameters are the same of the experimental study by Mitsudharmadi et al. [2004a,b].

2. Formulation

In this section the governing equations and the numerical methodology are presented. The Navier-Stokes equations, written in the vorticity-velocity formulation, were discretized using high-order finite-differences and spectral approximations for the spatial derivatives. A fourth order Runge-Kutta scheme was adopted for the temporal discretization.

2.1 Governing Equations

The governing equations are the incompressible equations with constant viscosity for a Newtonian fluid. Defining the vorticity as the negative curl of the velocity vector, and using the fact that both the velocity and the vorticity fields are solenoidal, one can obtain the following vorticity transport equation in each direction:

$$\frac{\partial\widetilde{\omega}_x}{\partial t}+\frac{\partial\widetilde{a}}{\partial y}-\frac{\partial\widetilde{b}}{\partial z}+\frac{Go^2}{\sqrt{Re}}\frac{\partial\widetilde{d}}{\partial z}=\frac{1}{Re}\nabla^2\widetilde{\omega}_x, \tag{1}$$

$$\frac{\partial\widetilde{\omega}_y}{\partial t}+\frac{\partial\widetilde{c}}{\partial z}-\frac{\partial\widetilde{a}}{\partial x}=\frac{1}{Re}\nabla^2\widetilde{\omega}_y, \tag{2}$$

$$\frac{\partial\widetilde{\omega}_z}{\partial t}+\frac{\partial\widetilde{b}}{\partial x}-\frac{\partial\widetilde{c}}{\partial y}-\frac{Go^2}{\sqrt{Re}}\frac{\partial\widetilde{d}}{\partial x}=\frac{1}{Re}\nabla^2\widetilde{\omega}_z, \tag{3}$$

where

$$\widetilde{a} = \widetilde{\omega}_x\widetilde{v}-\widetilde{\omega}_y\widetilde{u}, \tag{4}$$

$$\widetilde{b} = \widetilde{\omega}_z\widetilde{u}-\widetilde{\omega}_x\widetilde{w}, \tag{5}$$

$$\widetilde{c} = \widetilde{\omega}_y\widetilde{w}-\widetilde{\omega}_z\widetilde{v}, \tag{6}$$

$$\widetilde{d} = \widetilde{u}^2, \tag{7}$$

are the nonlinear terms resulting from convection, vortex stretching and vortex bending. The variables $(\widetilde{u},\widetilde{v},\widetilde{w},\widetilde{\omega}_x,\widetilde{\omega}_y,\widetilde{\omega}_z)$ are the velocity and vorticity components in the streamwise, wall-normal and spanwise directions respectively; $\widetilde{t}$ is the time. The Laplace operator is:

$$\nabla^2=\left(\frac{\partial^2}{\partial x^2}+\frac{\partial^2}{\partial y^2}+\frac{\partial^2}{\partial z^2}\right). \tag{8}$$

The continuity equation is given by:

$$\frac{\partial\widetilde{u}}{\partial x}+\frac{\partial\widetilde{v}}{\partial y}+\frac{\partial\widetilde{w}}{\partial z}=0. \tag{9}$$

The above equations are presented in a non-dimensional form. The reference length is a plate characteristic length L and the reference velocity is the free stream velocity U_∞. The Reynolds number is given by $Re=U_\infty L/\nu$, where ν is the kinematic viscosity. The Görtler number is given by $Go=(k_c\sqrt{Re})^{1/2}$. The terms $Go^2\frac{\partial\widetilde{d}}{\partial x}/(\sqrt{Re})$ and $Go^2\frac{\partial\widetilde{d}}{\partial z}/(\sqrt{Re})$ are the leading order curvature terms, where $k_c=L/R$ is the wall curvature and R is the curvature radius. The objective of the current study is on the Görtler flow, therefore the simulations were performed with the introduction of steady disturbances only.

Taking the definition of the vorticity and the mass conservation equation, one can obtain Poisson-type equations for each velocity component:

$$\frac{\partial^2\widetilde{u}}{\partial x^2}+\frac{\partial^2\widetilde{u}}{\partial z^2}=-\frac{\partial\widetilde{\omega}_y}{\partial z}-\frac{\partial^2\widetilde{v}}{\partial x\partial y}, \tag{10}$$

$$\frac{\partial^2\widetilde{v}}{\partial x^2}+\frac{\partial^2\widetilde{v}}{\partial y^2}+\frac{\partial^2\widetilde{v}}{\partial z^2}=-\frac{\partial\widetilde{\omega}_z}{\partial x}+\frac{\partial\widetilde{\omega}_x}{\partial z}, \tag{11}$$

$$\frac{\partial^2\widetilde{w}}{\partial x^2}+\frac{\partial^2\widetilde{w}}{\partial z^2}=\frac{\partial\widetilde{\omega}_y}{\partial x}-\frac{\partial^2\widetilde{v}}{\partial y\partial z}. \tag{12}$$

2.2 Disturbance Formulation

A disturbance formulation was adopted in the current study, therefore the flow variables were decomposed in a base flow and a perturbation:

$$\widetilde{f}=f_b+f, \tag{13}$$

where $\widetilde{f}=\{\widetilde{u},\widetilde{v},\widetilde{w},\widetilde{\omega}_x,\widetilde{\omega}_y,\widetilde{\omega}_z\}$ are the total flow variables. The base flow is considered two-dimensional, therefore only u_b, v_b, ω_{z_b} are taken into account, where the index b indicates the base flow.

With such formulation, the stability analysis of any base flow (Blasius, Falkner-Skan, etc.), can be easily performed as the linear and nonlinear terms can be isolated. Some disadvantages of this formulation are the indirect access to the flow variables and a higher memory usage due to the larger number of variables.

Introducing Eq. (13) in the equations (1) – (3), (10) – (12) and subtracting the base quantities, the equations for the perturbations result in:

$$\frac{\partial\omega_x}{\partial t}+\frac{\partial a}{\partial y}-\frac{\partial b}{\partial z}+\frac{Go^2}{\sqrt{Re}}\frac{\partial d}{\partial z}=\frac{1}{Re}\nabla^2\omega_x, \tag{14}$$

$$\frac{\partial\omega_y}{\partial t}+\frac{\partial c}{\partial z}-\frac{\partial a}{\partial x}=\frac{1}{Re}\nabla^2\omega_y, \tag{15}$$

$$\frac{\partial\omega_z}{\partial t}+\frac{\partial b}{\partial x}-\frac{\partial c}{\partial y}-\frac{Go^2}{\sqrt{Re}}\frac{\partial d}{\partial x}=\frac{1}{Re}\nabla^2\omega_z, \tag{16}$$

$$\frac{\partial^2 u}{\partial x^2}+\frac{\partial^2 u}{\partial z^2}=-\frac{\partial\omega_y}{\partial z}-\frac{\partial^2 v}{\partial x\partial y}, \tag{17}$$

$$\frac{\partial^2 v}{\partial x^2}+\frac{\partial^2 v}{\partial y^2}+\frac{\partial^2 v}{\partial z^2}=-\frac{\partial\omega_z}{\partial x}+\frac{\partial\omega_x}{\partial z}, \tag{18}$$

$$\frac{\partial^2 w}{\partial x^2}+\frac{\partial^2 w}{\partial z^2}=\frac{\partial\omega_y}{\partial x}-\frac{\partial^2 v}{\partial y\partial z}, \tag{19}$$

where the nonlinear terms a, b, c, d are:

$$a = \omega_x(v_b+v)-\omega_y(u_b+u), \tag{20}$$

$$b = (\omega_{z_b}+\omega_z)(u_b+u)-\omega_x w, \tag{21}$$

$$c = \omega_y w-(\omega_{z_b}+\omega_z)(v_b+v), \tag{22}$$

$$d = 2u_b u+u^2. \tag{23}$$

3. Numerical Method

In this section the discretization of the adopted equations and the boundary conditions adopted in the simulations are shown. The computational domain is illustrated in Fig. 1.

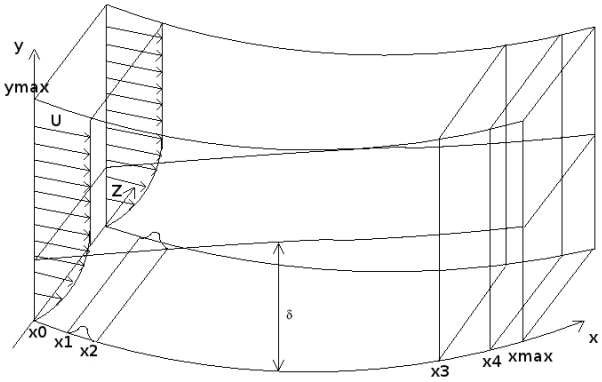

Figure 1: Computational Domain.

3.1 Spectral Approximation

The flow is assumed to be periodic in the spanwise direction. Therefore, the flow field can be expanded in Fourier series with K spanwise Fourier modes:

$$f(x,y,z,t) = \sum_{k=0}^{K} F_k(x,y,t)e^{(i\beta_k z)}, \tag{24}$$

where $f = u, v, w,\ \omega_x, \omega_y, \omega_z,\ a, b, c, d$; $F_k = U_k, V_k, W_k,\ \Omega_{x_k}, \Omega_{y_k}, \Omega_{z_k},\ A_k, B_k, C_k, D_k$ and β_k is the spanwise wavenumber given by $\beta_k = 2\pi k/\lambda_z$, and λ_z is the spanwise wavelength of the fundamental spanwise Fourier mode, and $i = \sqrt{-1}$.

Substituting the Fourier transforms (Eq. 24) in the vorticity transport equations (14 – 16), in the velocity Poisson equations (17 – 19), yield the governing equations in the Fourier space:

$$\frac{\partial \Omega_{x_k}}{\partial t} + \frac{\partial A_k}{\partial y} - \beta_k B_k - \frac{Go^2}{\sqrt{Re}}\beta_k(D_k^2) = \frac{1}{Re}\nabla_k^2 \Omega_{x_k}, \tag{25}$$

$$\frac{\partial \Omega_{y_k}}{\partial t} + \beta_k C_k - \frac{\partial A_k}{\partial x} = \frac{1}{Re}\nabla_k^2 \Omega_{y_k}, \tag{26}$$

$$\frac{\partial \Omega_{z_k}}{\partial t} + \frac{\partial B_k}{\partial x} + \frac{\partial C_k}{\partial y} - \frac{Go^2}{\sqrt{Re}}\frac{\partial (D_k^2)}{\partial x} = \frac{1}{Re}\nabla_k^2 \Omega_{z_k}, \tag{27}$$

$$\frac{\partial^2 U_k}{\partial x^2} - \beta_k^2 U_k = -\beta_k \Omega_{y_k} - \frac{\partial^2 V_k}{\partial x \partial y}, \tag{28}$$

$$\frac{\partial^2 V_k}{\partial x^2} + \frac{\partial^2 V_k}{\partial y^2} - \beta_k^2 V_k = -\frac{\partial \Omega_{z_k}}{\partial x} + \beta_k \Omega_{x_k}, \tag{29}$$

$$\frac{\partial^2 W_k}{\partial x^2} - \beta_k^2 W_k = \frac{\partial \Omega_{y_k}}{\partial x} + \beta_k \frac{\partial V_k}{\partial y}, \tag{30}$$

where $\nabla_k^2 = \left(\frac{\partial^2}{\partial x^2} + \frac{\partial^2}{\partial y^2} - u^2\beta^2\right)$.

The equations (25 – 30) were solved numerically in the domain shown schematically in Fig. 1. The calculations are done on an orthogonal uniform grid, parallel to the wall. The fluid enters the computational domain at $x = x_0$ and exits at the outflow boundary $(x = x_{max})$. Disturbances were introduced into the flow field using spanwise suction and blowing in a disturbance strip at the wall. This strip is located between x_1 and x_2. In the region located between x_3 and x_4 a buffer domain technique Kloker et al. [1993] was implemented in order to avoid wave reflections at the outflow boundary. In these simulations a 2D Navier-Stokes solution, was used as the base flow.

The time derivatives in the vorticity transport equations were discretized with a classical 4^{th} order Runge-Kutta integration scheme Ferziger and Peric [1997]. The spatial derivatives were calculated using a 6^{th} order compact finite difference-scheme Souza et al. [2005], Souza [2003], Lele [1992]. The V-Poisson equation – Eq. (29) – was solved using a multigrid Full Approximation Scheme (FAS) Stuben and Trottenberg [1981]. A V-cycle working with 4 grids was implemented.

3.2 Boundary Conditions

The governing equations are complemented by the specification of boundary conditions. At the wall ($y = 0$), a no-slip condition was imposed for the streamwise (U_k) and the spanwise (W_k) velocity components. The wall-normal velocity component at the wall (V_k) was specified at the suction and blowing strip region between x_1 and x_2, where the disturbances were introduced. Away from the disturbance generator this velocity component was set to zero. The function used for the wall-normal velocity $V_{k=1}$ at the disturbance generator is:

$$\begin{aligned} V_{k=1}(i,0,t) &= A\sin^3(\epsilon) \quad \text{for} \quad l_1 \leq i \leq l_2 \quad \text{and} \\ V_{k=1}(x,0,t) &= 0 \quad \text{for} \quad l < l_1 \quad \text{and} \quad l > l_2, \end{aligned} \tag{31}$$

where $\epsilon = (l - l_1)/(l_2 - l_1)$ and A is a real constant chosen to adjust the amplitude of the disturbance. The variable l indicates the grid point location x_l in the streamwise direction, and points l_1 and l_2 correspond to x_1 and x_2 respectively. For all modes $k \neq 1$ the value of $V_k = 0$ at the wall was settled.

At the inflow boundary ($x = x_0$), the velocity, the vorticity components and the temperature are specified based on the similarity solutions. At the outflow boundary ($x = x_{max}$), the second derivatives with respect to the streamwise direction of the velocity and vorticity components are set to zero. At the upper boundary ($y = y_{max}$) the flow is considered non rotational. This is satisfied by setting all vorticity components and their derivatives to zero. The wall-normal velocity component at the upper boundary was settled according to the condition:

$$\left.\frac{\partial V_k}{\partial y}\right|_{x,y_{max},t} = 0. \tag{32}$$

This condition was imposed in the solution of the U_k velocity in the Poisson equation (Eq.28). The equations used for evaluating the vorticity components at the wall are:

$$\frac{\partial^2 \Omega_{x_k}}{\partial x^2} - \beta_k^2 \Omega_{x_k} = -\frac{\partial^2 \Omega_{y_k}}{\partial x \partial y} - \beta_k \nabla_k^2 V_k \tag{33}$$

$$\frac{\partial \Omega_{z_k}}{\partial x} = \beta_k \Omega_{x_k} - \nabla_k^2 V_k. \tag{34}$$

A damping zone near the outflow boundary was defined in which all the disturbances are gradually damped down to zero Kloker et al. [1993]. This technique is used to avoid reflections in the outflow boundary. Meitz and Fasel [2000] adopted a fifth order polynomial, and the same function was used in the present code. The basic idea is to multiply the vorticity components by a ramp function $f_1(x)$ after each sub-step of the integration method. Using this technique, the vorticity components are taken as:

$$\Omega_k(x,y,t) = f_1(x)\Omega_k^*(x,y,t), \tag{35}$$

where $\Omega_k^*(x,y,t)$ is the disturbance vorticity component that results from the Runge-Kutta integration and $f_1(x)$ is a ramp function that goes smoothly from 1 to 0. The implemented function was:

$$f_1(x) = f(\epsilon) = 1 - 6\epsilon^5 + 15\epsilon^4 - 10\epsilon^3, \tag{36}$$

where $\epsilon = (l - l_3)/(l_4 - l_3)$ for $l_3 \leq l \leq l_4$. The points l_3 and l_4 correspond to the positions x_3 and x_4 in the streamwise direction, respectively. To ensure good numerical results a minimum distance between x_3 and x_4 and between x_4 and the end of the domain x_{max} has to be adopted. In the simulations presented here each zone had 30 grid points.

Another buffer domain, located near the inflow boundary was also implemented in the code. As pointed out by Meitz [1996], in simulations involving streamwise vortices, reflections due to the vortices at the inflow can contaminate the numerical solution. The damping function is similar to the one used for the outflow boundary:

$$f_2(x) = f(\epsilon) = 6\epsilon^5 - 15\epsilon^4 + 10\epsilon^3, \tag{37}$$

where ϵ is $\epsilon = (l - 1)/(l_1 - 1)$ for the range $1 \leq l \leq l_1$. All the vorticity components were multiplied by this function in this region.

4. RESULTS

The parameters adopted in the present paper are: spanwise wavelength $\lambda_z = 15$ mm, free stream velocity U_∞ = 3m/s in a concave wall with radius $R = 2$ m; the Reynolds number was Re = 38336; the Goertler number was Go = 2.385; the distance between two consecutive points in the x and y directions were dx = 0.015 and dy = 0.0006; the number of points in the x and y directions were 857, and 561, respectively; the time step was dt = 0.003; the disturbances were introduced in the region $1.735 \leq x \leq 2.185$, with an amplitude of A = 0.005; in the z direction, 21 Fourier modes were used with 64 points in the physical space.

Figure 2 shows energy development in the streamwise direction, for the steady modes from 1 to 10, and also the mean flow distortion mode (0). Between the Re_x equal 5.0×10^4 until 1.0×10^5 the Görtler vortices show a linear growth. After Re_x = 1.0×10^5, the vortices saturates and almost all modes remains with constant amplitude. This region is known as saturation region, and the difference between the energy amplitude of consecutive modes are almost constant.

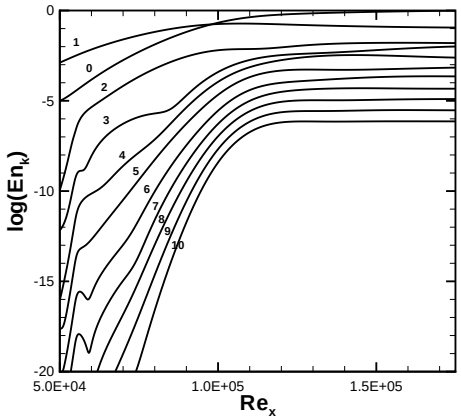

Figure 2: Energy distribution for each mode in the streamwise direction for $\lambda_z = 15$mm.

Figure 3 shows the maximum amplitude of the streamwise disturbance velocity u of each frequency over (z, y) plane in the streamwise direction for varicose mode . The unsteady frequencies introduced range from 18.75 Hz to 300 Hz in steps of 18.75 Hz, aligned in the spanwise direction with the steady disturbances that originated the Görtler vortices. These disturbances were introduced via suction and blowing at the wall in 3 different streamwise positions $Re_x \sim 7.5 \times 10^4$, $Re_x \sim 9.5 \times 10^4$ and $Re_x \sim 1.15 \times 10^5$. Initially all the forced modes exhibit a stable behavior until the streamwise position of $Re_x \sim 1.25 \times 10^5$, where all modes grow due to the onset of secondary instability. The frequencies with the higher values of growth rates in the secondary instability region are $18.75, 112.50, 130.25$ and 141.00 Hz – these frequencies are highlighted in the figure.

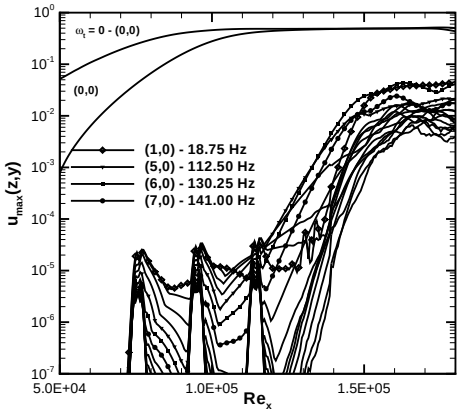

Figure 3: Maximum amplitude of the disturbance streamwise velocity u of each frequency over (z, y) plane in the streamwise direction Re_x for varicose mode.

The sequence in time for the velocity distribution over $z \times y$ slices and the structures obtained in the simulation and the Q isosurfaces are shown in the Fig. 4. Each figure is sequence in time for the t = T/4 apart from the previous figure

giving a complete sequence over one period. The flow is from bottom left to top right. The mushroom structure formed by the thermal boundary layer can be observed in the $z \times y$ slices. The Q isosurfaces show initially the steady Görtler vortices. After a certain streamwise position the secondary instabilities appear and the dominant structures are typical for a varicose mode.

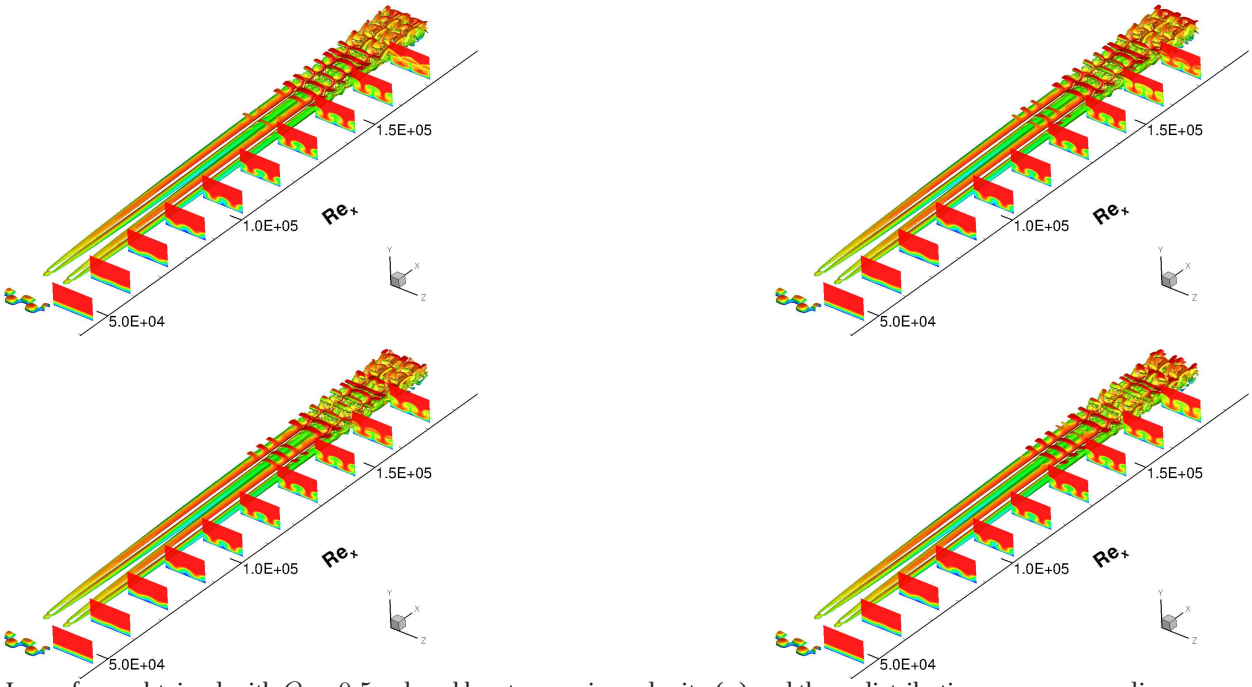

Figure 4: Isosurfaces obtained with $Q = 0.5$ colored by streamwise velocity (u) and the u distribution over a $z \times y$ slices.

Figure 5 shows the maximum amplitude of the streamwise disturbance velocity u of each frequency over (z, y) plane in the streamwise direction for sinuous mode. The unsteady frequencies introduced range from 18.75 Hz to 300 Hz in steps of 18.75 Hz, with a phase shift of 90 degress in the spanwise direction with the steady disturbances that originated the Görtler vortices. These disturbances were introduced via suction and blowing in the same positions of the varicose simulations. Initially all the forced modes exhibit a stable behavior until the streamwise position of $Re_x \sim 1.25 \times 10^5$, where all modes grow due to the onset of secondary instability. The frequencies with the higher values of growth rates in the secondary instability region are $18,75$ Hz, $130,25$ Hz, $141,00$ Hz and $159,75$ Hz Hz – these frequencies are highlighted in the figure.

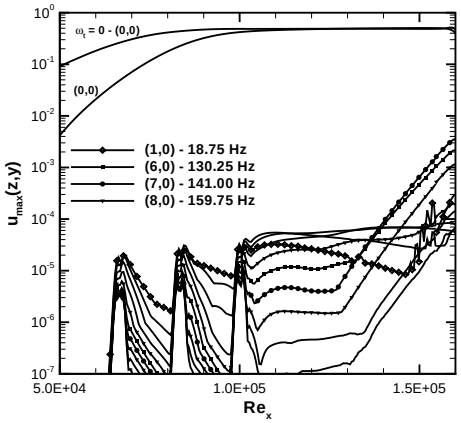

Figure 5: Maximum amplitude of the disturbance streamwise velocity u of each frequency over (z, y) plane in the streamwise direction Re_x for sinuous mode.

The sequence in time for the velocity distribution over $z \times y$ slices and the structures obtained in the simulation and the Q isosurfaces are shown in the Fig. 6. The flow is from bottom left to top right. The mushroom structure formed by the thermal boundary layer can be observed in the $z \times y$ slices. The Q isosurfaces show initially the steady Görtler vortices. After a certain streamwise position the secondary instabilities appear and the dominant structures are typical for

a varicose mode. Although the disturbances were introduced to induce sinuous secondary instability, the results show that the varicose mode dominates and the sinuous mode does not appear, as was also observed experimentally Mitsudharmadi et al. [2004a,b].

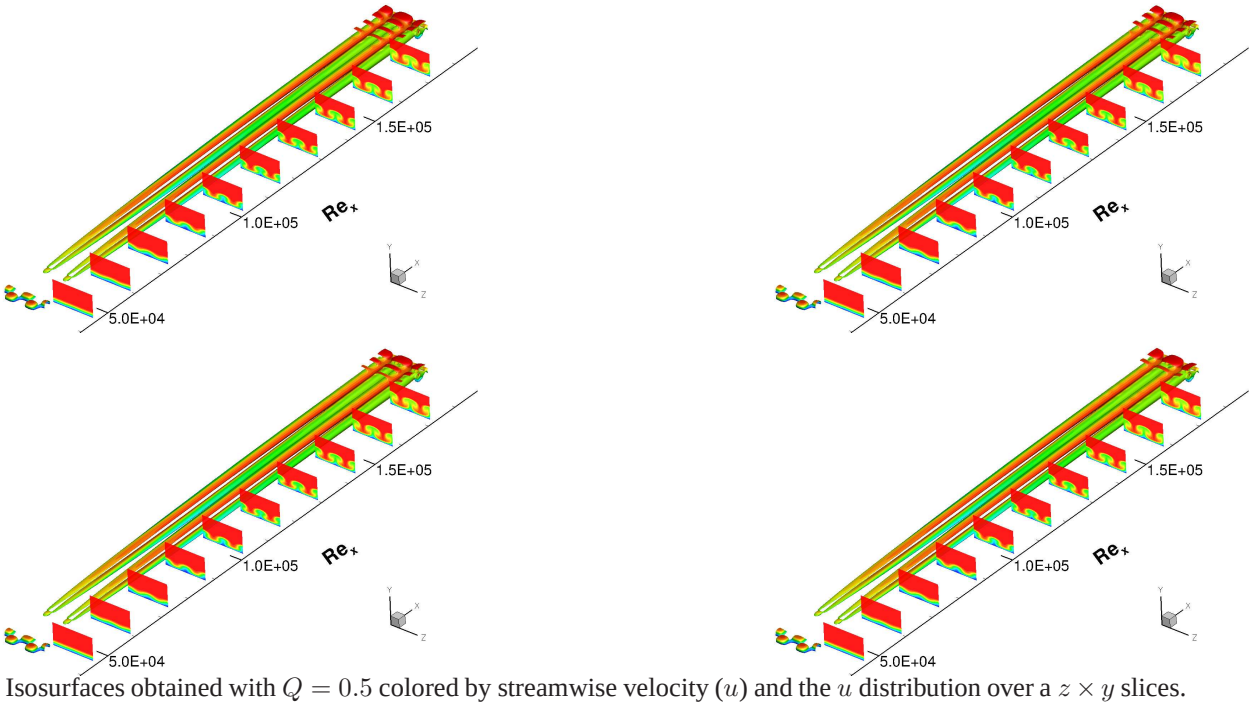

Figure 6: Isosurfaces obtained with $Q = 0.5$ colored by streamwise velocity (u) and the u distribution over a $z \times y$ slices.

5. CONCLUSION

In the present paper the secondary stability of a Görtler flow was analyzed. The parameters adopted were the same of the experimental studies carried out by Winoto and co-workers Mitsudharmadi et al. [2004a,b]. The unsteady disturbances were introduced in the different streamwise positions by suction and blowing at the wall. These disturbances were introduced in two different position in the spanwise direction to give birth to varicose mode (aligned with steady disturbances) or sinuous mode (with a phase shift of 90 degree with the steady disturbances). The results with the adopted parameters, show that the varicose mode dominates the secondary stability region, even when the seeds were introduced to generate sinuous secondary stability.

6. ACKNOWLEDGEMENTS

The authors acknowledge the financial support received from FAPESP under Grant No. 2010/00495-1.

7. REFERENCES

M. Clauser and F. Clauser. The effect of curvature on the transition from laminar to turbulent boundary layer. technical report naca tn-163. *National Advisory Commite of Aeronautics*, 1937.

P. G. Drazin and W. H. Reid. *Hydrodynamic Stability*. Cambridge University Press, 2004.

J. H. Ferziger and M. Peric. *Computational Methods for Fluid Dynamics*. Springer-Verlag Berlin Heidelberg New York, 1997.

H. Goerlter. On the three dimensional instability of laminar boundary layer on concave walls. technical report naca tm-1375. *National Advisory Commite of Aeronautics*, 1940.

K. Inagaki and Y. Aihara. An experimental study of the transition region of the boundary-layer along a concave wall. *European Journal of Mechanics - B/Fluids*, 14:143–168, 1995.

A. Ito. Breakdown structure of longitudinal vortices along a concave wall. *Journal of Japan Society for Aeronautical and Space Sciences*, 166-173:33, 1985.

M. Kloker, U. Konselmann, and H. Fasel. Outflow boundary conditions for spatial navier-stokes simulations of transition boundary layer. *AIAA Journal*, 31:620–628, 1993.

S. K. Lele. Compact finite difference schemes with spectral-like resolution. *Journal of Computational Physics*, 103: 16–42, 1992.

F. Li and M. R. Malik. Fundamental and subharmonic secondary instabilities of gÃűrtler vortices. *Journal of Fluid Mechanics*, 297:77–100, 1995.

H. Meitz and H. Fasel. A compact-difference scheme for the navier-stokes equations in vorticity-velocity formulation. *Journal of Computational Physics*, 157:371–403, 2000.

H. L. Meitz. *Numerical Investigation of Suction in a Trasition Flat-Plate Boundary Layer*. PhD thesis, The University of Arizona, 1996.

H. Mitsudharmadi, S. H. Winoto, and D. A. Shah. Development of boundary-layer flow in the presence of forced wavelength goertler vortices. *Physics of Fluids*, 16, 2004a.

H. Mitsudharmadi, S. H. Winoto, and D. A. Shah. Secondary instability in forced wavelength görlter vortices. *Physics of Fluids*, 16, 2004b.

H. Peerhossaini and J. E. Wesfreid. On the inner structure of streamwise gortler rolls. *International Journal of Heat and Fluid Flow*, 12:9, 1988.

L. Rayleigh. On the dynamics of revolving fluids. *Philosophical Transactions of the Royal Society*, 93:148–154, 1917.

A. S. Sabry, X. Yu, and J. T. C. Liu. Proceedings of the third iutam symposium on laminar-turbulent transition, toulouse, 11-15 september 1989, edited by d. arnal and r. michel (springer-verlag, berlin, in press). 1989.

W. S. Saric. Görtler vortices. *Annu. Rev. Fluid Mech.*, 26:379–409, 1994.

P. J. Schmid and D. S. Henningson. *Stability and Transition in Shear Flows*, volume 142. Springer, New York, 2001.

L. F. Souza. *Instabilidade Centrífuga e Transição para Turbulência em Escoamentos Laminares sobre Superfícies Côncavas*. PhD thesis, Instituto Tecnológico de Aeronáutica, Brazil, 2003.

L. F. Souza, M. T. Mendonça, and M. A. F. Medeiros. The advantages of using high-order finite differences schemes in laminar-turbulent transition studies. *International Journal for Numerical Methods in Fluids*, 48:565–592, 2005.

K. Stuben and U. Trottenberg. *Nonlinear Multigrid Methods, the Full Approximation Scheme*. Koln-Porz, 1981.

J. Swearingen and R. Blackwelder. The growth and breakdown of streamwise vortices in the presence of a wall. *Journal of Fluid Mechanics*, 182:255–290, 1987.

D. H. Zhang, S. H. Winoto, and Y. T. Chew. Measurement in laminar and transitional boundary-layer flows on concave surface. *International Journal of Heat and Fluid Flow*, 16:88–98, 1995.

8. Responsibility notice

The author are the only responsible for the printed material included in this paper

Estudo de turbulência gerada por OGT observada por PIV

Study of turbulence generated by OGT observed by PIV

Amanara Potykytã de Sousa Dias Vieira
Engenheira Sanitarista e Ambiental. Mestre em Hidráulica e Saneamento pela Escola de Engenharia de São Carlos (EESC-USP)

Woodrow Nelson Lopes Roma
Engenheiro Mecânico. Doutor em Hidráulica e Saneamento pela USP. Pós-Doutorado pela Universidade de Minnesota, EUA. Professor Titular da Escola de Engenharia de São Carlos da USP

Resumo
O regime turbulento pode ser definido, simplificadamente, como um movimento aleatório do fluido. Apesar da natureza caótica deste regime, pode-se fazer uso de estudos numéricos em uma tentativa de encontrar uma face determinística do fenômeno.

Neste trabalho foi utilizado OGT (oscillating grid tank) para geração de turbulência e o método PIV (particle imaging velocimeter) para observar e quantificar a turbulência gerada. Os resultados mostraram que o tanque em estudo aproximou-se de condições homogêneas, porém sua isotropia não pôde ser confirmada. O tanque foi eficiente na geração de turbulência, reproduzindo o fenômeno real. O método de velocimetria com o uso de PIV mostrou ser adequado para a observação de campos de velocidades de um escoamento, com limitações quanto à região periférica da área alvo.

Palavras-chave: homogeneidade; isotropia; velocimetria por imagens.

Abstract
Turbulent flow can be defined in a simplified way as a flow with random movement. Although the chaotic behavior of this regime, the researchers can use numerical studies in an attempt to find a deterministic view of the phenomenon.

In this work, it was used a tank with oscillating grid to generate turbulence and the method PIV to observe and quantify the generated turbulence. The results showed that the tank approached homogeneous conditions, but its isotropy cannot be affirmed. The tank with an oscillating grid was efficient in the generation of turbulence, reproducing a real phenomenon. The method PIV showed to be suitable for observation of a flow velocity field with limitations on the peripheral region of the target area.

Key words: homogeneity; isotropy; imaging velocimeter.

1. Introdução e objetivos

O comportamento da água sempre foi de grande interesse do homem, que necessita compreender os fenômenos ao seu redor para então controlá-los ou prevê-los. Dentre os fenômenos relacionados aos fluidos, sempre foi de difícil compreensão o regime turbulento. A turbulência é um regime instável de escoamento, em que as forças de inércia predominam sobre as forças viscosas. O regime turbulento ainda não é um fenômeno completamente compreendido, principalmente devido às dificuldades existentes na sua quantificação.

Com o passar dos anos, o problema de quantificação e equacionamento da turbulência, principalmente na superfície, foi abordado por diversas frentes de estudo. Novas técnicas de instrumentação permitiram que se passasse da observação (visual) com uso de corantes a medições usando sensores, chegando até o desenvolvimento da velocimetria com lasers e câmeras de alta velocidade. Um aspecto importante foi a melhoria na velocidade de processamento dos computadores, facilitando a obtenção de respostas de simulações e de cálculos numéricos.

Em 1984, o termo PIV (velocimetria por imagens de partículas) apareceu pela primeira vez na literatura (Adrian, 2005). O PIV é um método de velocimetria que se utiliza da captura de imagens de partículas inseridas no fluxo em estudo e é muito utilizado atualmente nos estudos de turbulência. O PIV tornou-se muito eficiente com a iluminação por laser pulsado e uso de câmeras de alta velocidade, definindo um processo pelo qual pares de imagens são capturados pelas câmeras, com intervalos de tempo conhecidos. O laser, disparado no momento da captura, ilumina as partículas que se destacam nas fotos. A seção observada é dividida por uma matriz pré-definida, possibilitando a definição do posicionamento das partículas. A partir do deslocamento das partículas observado entre as imagens e do intervalo de tempo entre a obtenção destas, é possível calcular as velocidades. Para adquirir dados tridimensionais é necessário que o sistema possua duas ou mais câmeras, permitindo a tomada de cena, simultaneamente, por dois ou mais pontos de vista distintos.

Visando facilitar o estudo da turbulência, pesquisadores vêm explorando uma alternativa mais simples do regime, a turbulência isotrópica e homogênea. O equacionamento deste tipo de turbulência exige um menor número de parâmetros e relações. Porém, apesar de mais simples, a turbulência isotrópica, assim como a homogênea, possui características comuns a todos os escoamentos turbulentos e sua compreensão permite que se esclareçam questões referentes às formas mais complexas de turbulência (Townsend,1976).

Um equipamento que vem sendo utilizado para a geração de turbulência em laboratório, na tentativa de gerar turbulência isotrópica e homogênea, é o tanque com grade oscilante (*OGT- oscillating grid tank*). O *OGT* é um equipamento composto por um tanque, normalmente de acrílico e uma, ou mais, grade oscilante, além de um sistema mecânico que converte as rotações do motor em oscilações da grade.

Naturalmente o aprimoramento de equipamentos, instrumentos e, consequentemente, a obtenção de dados de maior qualidade, levaram à tentativa de caracterizar e até mesmo equacionar o regime turbulento. Tendo em vista as recentes contribuições existentes na parametrização e equacionamento da turbulência, torna-se evidente a necessidade de validação desses estudos por pesquisadores independentes.

Neste trabalho utilizou-se um tanque com uma grade oscilante para a geração de escoamento em regime turbulento na água. O objetivo foi observar o comportamento da turbulência gerada, atentando-se principalmente para a ocorrência de homogeneidade e isotropia. As velocidades do fluxo gerado foram medidas por um sistema PIV estereoscópico. Outro aspecto observado na pesquisa foi o decaimento da turbulência na seção observada, comparando os resultados com dois modelos de decaimento da turbulência existentes na literatura (Thompson e Turner, 1975; Hopfinger e Toly, 1976).

2. Revisão bibliográfica

2.1. Velocimetria por imagens de partículas (PIV)

A técnica PIV promove uma medição do campo de velocidades, na qual as partículas, referentes a um volume de interesse, terão validados seus vetores velocidade. Deste modo, as grandezas diferenciais em relação às coordenadas espaciais como vorticidade, tensões normais e tensões cisalhantes e também as grandezas integrais, como circulação, fluxo de massa por unidade de profundidade, função do tipo potencial e corrente, dentre outras, passaram a ser possíveis de serem mensuradas (Nunes, 2005).

O sistema PIV é composto por um laser, câmeras, partículas e um computador com o *software* do sistema. Também é necessária uma seção de ensaio, onde o escoamento será observado e medido pelo PIV. A qualidade dos dados adquiridos está fortemente relacionada à iluminação e distribuição das partículas no fluido. Segundo Boillot e Prasad (1996), normalmente o PIV funciona melhor quando a concentração de partículas é baixa, pois isto aumenta a distância entre as partículas, reduzindo erros causados por sobreposição.

Nunes (2005) comenta que as partículas devem preencher dois requisitos: serem capazes de seguir o fluxo sem deslizamento excessivo e serem eficientes espalhadoras de luz do laser, pois quanto menor esta eficiência, mais potente deverá ser o laser ou maior a sensibilidade das câmeras, elevando custos. Nunes (2005) ainda diz que a diferença de densidade entre a partícula e o fluido em escoamento determina que o empuxo e a força gravitacional não sejam iguais, o que prejudica o primeiro requisito citado ou pode causar sedimentação das partículas. Também se observa que quanto menor o diâmetro da partícula, menor será a ação da viscosidade do fluido sobre a sua dinâmica. Logo, quanto menor o diâmetro e quão mais semelhante for sua densidade em relação à do fluido, mais a velocidade da partícula corresponderá à velocidade real do escoamento.

O PIV digital surgiu com o advento de câmeras capazes de gravar duas imagens em rápida sucessão, ou seja, um chip de alta velocidade de gravação é utilizado para armazenar as imagens obtidas pela câmera do sistema. Sobre o método de aquisição e armazenamento das imagens, Boillot e Prasad (1996) afirmam que o filme fotográfico supera os sensores CCD em termos de resolução. Entretanto, o uso dos sensores é mais conveniente, pois desta forma as imagens já são armazenadas em formato digital, necessário para o processamento de imagens. Além disso, os sensores CCD permitem que esse processo ocorra em poucos segundos. Outra vantagem é que a sensibilidade do CCD é maior do que a do filme, possibilitando o uso de laser menos potente.

O laser é amplamente utilizado na velocimetria por imagens de partículas devido a pouca divergência e maior resolução espacial. As fontes de laser podem funcionar de forma contínua ou pulsada, sendo a forma contínua relacionada a aplicações que exigem alta energia e/ ou potência média e o laser pulsado relacionado a aplicações que exigem alta potência instantânea e baixa energia.

Vantagens e limitações

Como instrumento de medida, o PIV apresenta as seguintes vantagens (Adrian, 2005):

1. A interferência do PIV nas medidas é mínima, se comparada a outros métodos, tornando-o pouco intrusivo. A única causa de interferência no fluxo ocorre pela presença das partículas, porém as interferências são minimizadas através de cuidados na escolha dos diâmetros e densidades ideais;

2. Sistemas PIV normalmente possuem filtros de comprimento de onda que minimizam ou eliminam interferências luminosas;
3. O sistema mede o campo de velocidades em uma seção;
4. O PIV fornece as três componentes da velocidade no espaço;
5. Alta velocidade de aquisição de imagens (dados);
6. Os dados podem ser armazenados para uma análise posterior.

Os erros possíveis e limitações são (BOILLOT; PRASAD, 1996):

1. Erros ou imprecisões devido à sobreposição de partículas nas imagens;
2. O deslocamento de uma partícula pode não ser representado por inteiro, caso esta partícula ultrapasse os limites de área em que a imagem está dividida;
3. Partículas com densidades baixas podem deslocar-se exageradamente. No caso oposto, partículas com densidades elevadas podem sedimentar em velocidades mais baixas (Nunes, 2005);
4. Tempo curto de duração do pulso do laser dificulta a observação do deslocamento das partículas. No caso oposto, longa duração do pulso do laser pode causar o efeito conhecido como *blurring*, que causa o aparecimento de estrias nas imagens, ao invés de pontos nítidos.

As Figuras 1 e 2 apresentam, respectivamente, uma imagem obtida por um sistema PIV durante o trabalho de Vieira (2012) e um mapa de vetores bidimensional gerado a partir de um par de imagens.

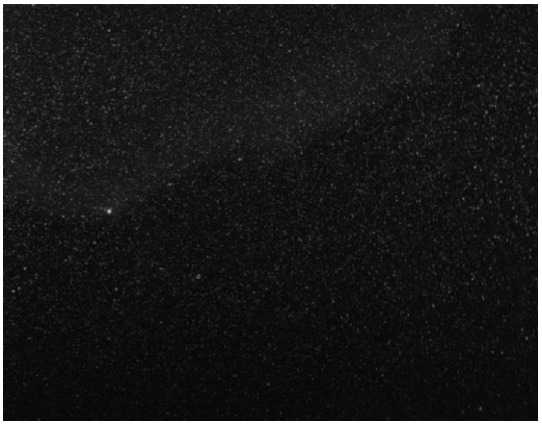

Figura 1: Imagem obtida pelo PIV

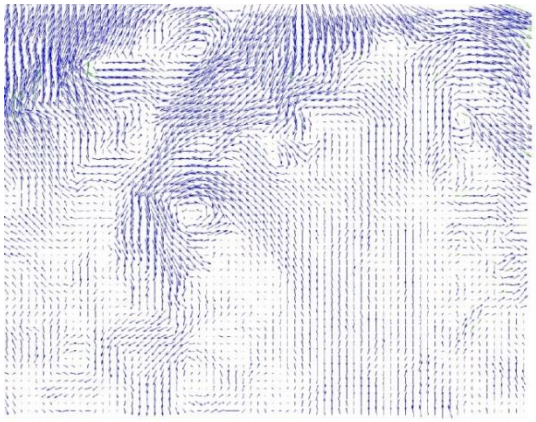

Figura 2: Mapa de vetores 2D (Fonte: Vieira, 2012)

Széliga e Roma (2009) desenvolveram um sistema PIV (equipamento e *software*) e efetuaram medidas na superfície líquida da interface ar / água. O equipamento de medição é similar aos convencionais, porém com características inovadoras e exclusivas, que resultaram na utilização de uma única câmera e um conjunto de espelhos para obtenção de imagens e dados tridimensionais em escoamentos de baixa turbulência. O equipamento foi utilizado na medição de velocidades turbulentas na superfície líquida em um tanque de grades oscilantes que foram correlacionadas com o coeficiente de reaeração do corpo d'água.

No trabalho de Turney e Banerjee (2011), foram propostas novas técnicas denominadas Velocimetria de Imagens de Partículas Interfacial (IPIV) e Tridimensionais IPIV (3D-IPIV) para medir os campos de fluxo próximo à superfície e a morfologia interfacial simultaneamente, aplicados para escoamentos em canais abertos e condições de ondas provocadas pelo vento.

2.2. Tanque com grade oscilante

O tanque com grade oscilante começou a ser usado na década de 60 como equipamento gerador de turbulência em laboratório, assim como na tentativa de geração de turbulência isotrópica e homogênea (Comte-Bellot e Corrsin, 1966; Bouvard e Dumas, 1967; Thompson e Turner, 1975; Hopfinger e Toly, 1976).

As condições de quase isotropia e homogeneidade dependem diretamente das dimensões e posicionamento da grade no interior do tanque, frequência e amplitude das oscilações. Janzen (2003) diz que a turbulência gerada por um OGT tende a possuir propriedades isotrópicas e homogêneas em regiões mais distantes da grade, porém em seu trabalho a isotropia sofreu influência de escoamento secundário. Cheng e Law (2001) afirmam que a homogeneidade só pode ser alcançada a partir de pontos a 3 *mesh* (espaçamento entre as barras) de distância do ponto médio de oscilação da grade. Krogstad e Davidson (2011) investigaram a geração de turbulência por um túnel de vento com grades. A homogeneidade do regime turbulento foi alcançada a alguma distância das grades.

Como foi observado, condições de isotropia e homogeneidade ocorrem a certa distância do centro de oscilação, por isso pesquisadores estudam como se dá a variação da velocidade no espaço. Thompson e Turner (1975) dizem que a velocidade turbulenta gerada em um tanque com grade oscilante varia no espaço obedecendo à Equação 1:

$$\vec{V} = 1{,}4.f.S^{2{,}5}.z^{-1{,}5} \quad (1)$$

Sendo,
$\vec{V}$: velocidade resultante (cm/s);
f: frequência de oscilação da grade (Hz);
S: amplitude de oscilação da grade (cm);
z: distância do ponto de medição da velocidade ao centro de oscilação da grade (cm).

Segundo Hopfinger e Toly (1976), existe influência da geometria da grade na velocidade do decaimento. Os autores modificaram a equação, adicionando um novo parâmetro (Equação 2).

$$\vec{V} = C.S^{\frac{3}{2}}.M^{\frac{1}{2}}.f.z^{-1} \quad (2)$$

Sendo,
C: constante relativa à geometria da grade. Para *Mesh* igual a 5, C vale 0,25;
M: *Mesh*, razão entre distância entre as barras da grade e a espessura da barra.

Além do parâmetro novo, existe divergência entre as duas equações com relação ao expoente de z. Os resultados adquiridos neste trabalho foram comparados às duas equações.

A solidez da grade, relação entre a área horizontal (sólida) ocupada pela grade e a área total da superfície do tanque, é um parâmetro importante e costuma ser o ponto de partida para o dimensionamento de tanques com grade oscilante. Segundo Corrsin (1966), a estrutura de jatos e esteiras formados pela grade fica instável se a solidez da grade for superior a 40%.

Righetto (2008) desenvolveu e calibrou um tanque com grade oscilante. A calibração do tanque foi executada levantando-se o coeficiente de reaeração K_2 para dois tipos de grades.

Janzen et al. (2011) realizaram medidas do fluxo interfacial de oxigênio na água, em tanque no qual a turbulência era produzida por grades oscilantes. O perfil experimental do fluxo turbulento de massa próximo da interface ar/água foi comparado com a predição usando a difusividade turbulenta aproximada por séries de potência em função da distância da interface. O campo de velocidade foi medido usando a técnica PIV.

3. Metodologia

O experimento foi realizado no Laboratório de Fenômenos de Transporte, na Escola de Engenharia de São Carlos (EESC-USP). Um tanque de acrílico prismático, montado por Righetto (2008), com base de 0,5 x 0,5 *m²* e 1 *m* de altura, foi preenchido com água, até uma altura de 55 *cm*. O fluido no interior do tanque era agitado pelas oscilações de uma grade quadrada de 49 *cm* de lado, montada com barras de seção 10 x 10 *mm*, havendo 5 *cm* de espaçamento entre as barras e 27,98% de solidez. A grade estava localizada a 16 *cm* do fundo do tanque e movimentava-se com 10 *cm* de amplitude.

Um conjunto biela-manivela transformava as rotações de um motor, em oscilações da grade. Controlando as rotações do motor, foi possível alterar a quantidade de oscilações por minuto da grade. As frequências adotadas foram: 18,25; 38,00; 57,25; 95,50; 118,00; 135,25; 154,25 e 175,00 *opm (*oscilações por minuto).

A turbulência gerada foi medida com um sistema PIV digital estereoscópico da DANTEC Dynamics. O sistema era composto por duas câmeras digitais CCD SpeedSense 9020, um laser e sua fonte, um microcomputador provido do pacote de *softwares* DynamicStudio, versão 2.30 e partículas revestidas com prata, inseridas na água. A disposição do sistema é mostrada através do esquema na Figura 3.

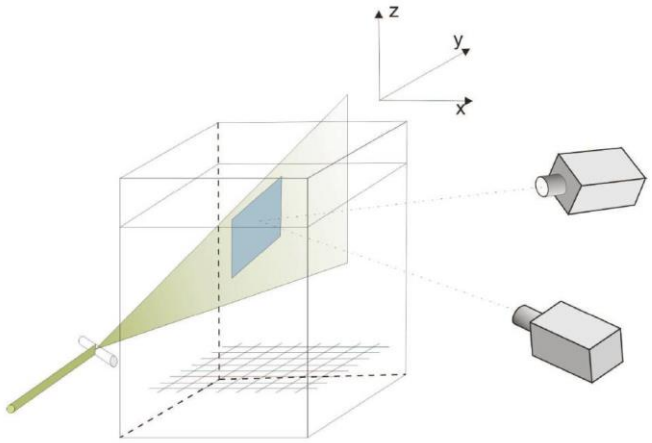

Figura 3: Esquema sistema PIV

A seção selecionada para observação foi uma área de 20 x 20 cm², distante 20 cm do centro de oscilação da grade. As partículas no interior do fluido se movimentavam devido à agitação causada pelas oscilações da grade. O movimento de partículas ocorrido na seção observada era destacado pelo laser e capturado pelas duas câmeras do sistema.

Cada câmera capturava 1024 pares de imagens, com intervalo de tempo entre os pares de 0,001 s, para cada frequência de oscilação da grade estudada. Estas imagens da seção de ensaio eram divididas pelo *software* em uma matriz de 66 linhas por 53 colunas. A partir do deslocamento do grupo de partículas contidas em cada célula desta matriz eram calculadas as velocidades, que aparecem como vetores em mapas bidimensionais. Estes mapas foram gerados para cada par de imagens de uma única câmera, ou seja, foram gerados 1024 mapas bidimensionais por câmera. O mapa de velocidades tridimensional foi gerado com a associação dos mapas bidimensionais das duas câmeras, obtidos no mesmo instante do tempo.

A pesquisa se propôs a investigar a ocorrência de homogeneidade e isotropia na turbulência gerada e também atentar para o decaimento da turbulência. Para isto, foram utilizados os dados dispostos em planilhas, que continham as três componentes das velocidades e a velocidade resultante de cada um dos 3498 pontos dos mapas tridimensionais obtidos para cada frequência. Foram desenvolvidas sub-rotinas, em MatLab, para tratamento dos dados de turbulência e investigação da homogeneidade e isotropia.

A homogeneidade de um escoamento pode ser comprovada quando as médias temporais da velocidade em cada ponto da seção observada se igualam (aproximadamente). Em um regime turbulento, a média temporal considerada deve ser a média quadrática RMS.

$$RMS_{ponto1} \cong RMS_{ponto2} \cong RMS_{ponto3} \cong RMS_{ponton} \quad (3)$$

Essa igualdade entre as médias não é obtida na prática, sendo necessária uma ferramenta estatística para verificar a homogeneidade. Foram utilizados, para este fim, os gráficos de controle de dispersão. Com estes gráficos é possível afirmar a existência de controle de dispersão se 68% das amostras estiverem inseridas no limite de um desvio padrão.

Após a obtenção dos primeiros resultados, observou-se a existência de pontos com velocidades nulas. Visando localizar estes pontos e compreender sua causa, foram elaborados mapas cromáticos. Posteriormente à localização desses pontos e à discussão apresentada nos resultados deste trabalho, optou-se por eliminar os pontos de velocidade nula, resultando uma matriz de 3250 pontos. Todas as sub-rotinas foram aplicadas considerando esta nova matriz.

A isotropia de um escoamento é confirmada quando a razão entre as médias das componentes da velocidade se aproxima de 1 (Equação 4). Neste trabalho impôs-se o limite superior 1,2 e inferior 0,83, seguindo valores propostos por Barra (2002).

$$\frac{RMS_u}{RMS_v} \cong 1$$

$$\frac{RMS_u}{RMS_v} \cong 1 \quad (4)$$

$$\frac{RMS_u}{RMS_v} \cong 1$$

Uma sub-rotina foi desenvolvida para observar como se dá a variação da intensidade turbulenta desde próximo à grade até a superfície da seção observada e comparar os dados observados com os resultados apresentados pelos modelos de decaimento propostos por Thompson e Turner (1975) e Hopfinger e Toly (1976). Para obter uma curva dos dados experimentais, calculou-se o valor RMS da velocidade turbulenta ao longo do

tempo, gerando uma única matriz de valores para cada frequência de oscilação da grade. A partir da matriz, gerou-se uma única coluna de valores, considerando a média resultante de cada linha. Esta coluna, que representa os valores médios das velocidades resultantes no sentido vertical, mostra o decaimento da turbulência no tanque.

4. Resultados e discussões

Nesta seção são apresentados os resultados referentes ao comportamento da turbulência gerada pelo experimento.

4.1. Homogeneidade

O gráfico de controle de dispersão mostrado na figura 4 apresenta no eixo das abscissas os pontos da matriz e no eixo das ordenadas os valores das médias RMS das velocidades resultantes, para uma única frequência de oscilação da grade.

No gráfico, é possível observar a existência de pontos com médias RMS nulas. O mapa cromático, apresentado na figura 5, mostra a localização destes pontos. Observou-se que eles ocorrem nas regiões periféricas da imagem e se devem a uma limitação do PIV, que precisa relacionar a posição anterior e posterior das partículas para obter o deslocamento e, consequentemente, a velocidade. Por causa desta limitação, optou-se pela remoção de uma coluna do lado esquerdo, duas colunas do lado direito e uma linha superior, resultando em uma matriz com 3250 pontos.

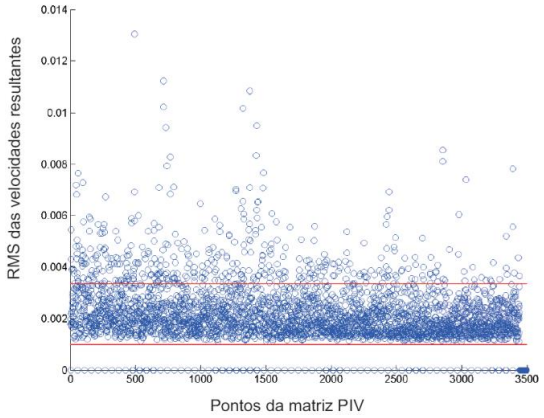

Figura 4: Gráfico de homogeneidade com zeros

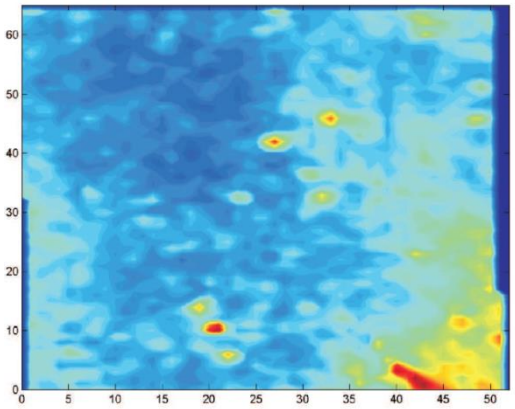

Figura 5: Mapa cromático com zeros

A Tabela 1 apresenta os resultados de homogeneidade em porcentagem. A maior porcentagem de pontos fora dos limites (24%) ocorre quando a grade oscila a 175 opm (oscilações por minuto). A menor porcentagem de pontos fora dos limites ocorre para 18,25 opm. A homogeneidade foi confirmada para todas as frequências de oscilação, já que mais de 68% dos pontos ficam inseridos dentro dos limites em todos os casos.

Tabela 1: Homogeneidade

Oscilações(opm)	Zona	Pontos fora dos limites (3250)	Pontos fora dos limites (%)
18,25	I	154	5
	II	0	0
	III	0	0
38	I	486	15
	II	0	0
	III	0	0
57,25	I	669	21
	II	0	0
	III	0	0
95,5	I	577	18
	II	0	0
	III	0	0
118	I	632	19
	II	0	0
	III	0	0
135,25	I	647	20
	II	0	0
	III	0	0
154,25	I	699	22
	II	0	0
	III	0	0
175	I	772	24
	II	0	0
	III	0	0

4.2. Isotropia

Em todas as rotações, a turbulência gerada no tanque aproximou-se de um comportamento isotrópico nas regiões superficiais e tendeu mais à isotropia em baixas velocidades da grade.

Nos primeiros resultados, foi possível verificar que quando a componente W é inserida nos cálculos, estes valores distanciam-se muito dos limites impostos. Isto ocorre porque a componente *W*, que está na direção *z* (vertical), sofre maior influência com o movimento da grade. Vale ressaltar que a proximidade da superfície e a tensão superficial podem interferir nos valores de W. Isto porque a superfície interfere nas medidas e a tensão superficial causa interferência na própria velocidade.

As medidas realizadas nas três primeiras rotações (18,25; 38,00 e 57,25 opm) apresentaram comportamento mais próximo à isotropia. As razões entre os valores RMS das componentes das intensidades turbulentas para maiores velocidades de oscilação da grade (95,50; 118,00; 135,25; 154,25 e 175,00 opm) ficaram, em sua maioria, fora dos limites impostos, mesmo desconsiderando as razões que envolvam a componente *W*. A quantidade de pontos fora dos limites para a razão entre os valores RMS das componentes *U* e *V* variou de 27% para 57,25 opm (melhor resultado) a 93% dos pontos fora do limite para 175 opm (pior resultado), conforme se vê na Tabela 2.

Tabela 2: Isotropia

Oscilações(opm)	Zona	Pontos fora dos limites (3250)	Pontos fora dos limites (%)
18,25	U e V	1187	37
	U e W	3250	100
	V e W	3250	100
38	U e V	1079	33
	U e W	3250	100
	V e W	3250	100
57,25	U e V	865	27
	U e W	3250	100
	V e W	3250	100
95,5	U e V	2093	64
	U e W	3250	100
	V e W	3250	100
118	U e V	2514	77
	U e W	3250	100
	V e W	3250	100
135,25	U e V	2384	73
	U e W	3250	100
	V e W	3250	100
154,25	U e V	2454	76
	U e W	3250	100
	V e W	3250	100
175	U e V	3025	93
	U e W	3250	100
	V e W	2355	72

4.3. Decaimento da turbulência

Após a obtenção dos resultados experimentais, as velocidades turbulentas obtidas foram comparadas com velocidades resultantes dos modelos de Thompson e Turner (1975) e Hopfinger e Toly (1976).

Conforme esperado, o modelo de Hopfinger e Toly (1976) está mais próximo dos resultados experimentais do que o modelo de Thompson e Turner (1975), devido ao parâmetro de correção *M (Mesh)* existente no primeiro modelo. A constante *C* existente no modelo de Hopfinger e Toly (1976) também está relacionada à geometria da grade.

Os valores obtidos com o modelo de Thompson e Turner (1975) ficaram muito distantes dos resultados experimentais. O grande distanciamento do modelo causa uma atenuação na escala, interferindo na visualização dos dados. Portanto, optou-se pela omissão da curva desse modelo.

Normalizando os resultados e os valores obtidos pelos dois modelos, verificou-se que os modelos seguem a mesma tendência dos resultados experimentais. A figura 6 apresenta os gráficos gerados para duas frequências de oscilação da grade.

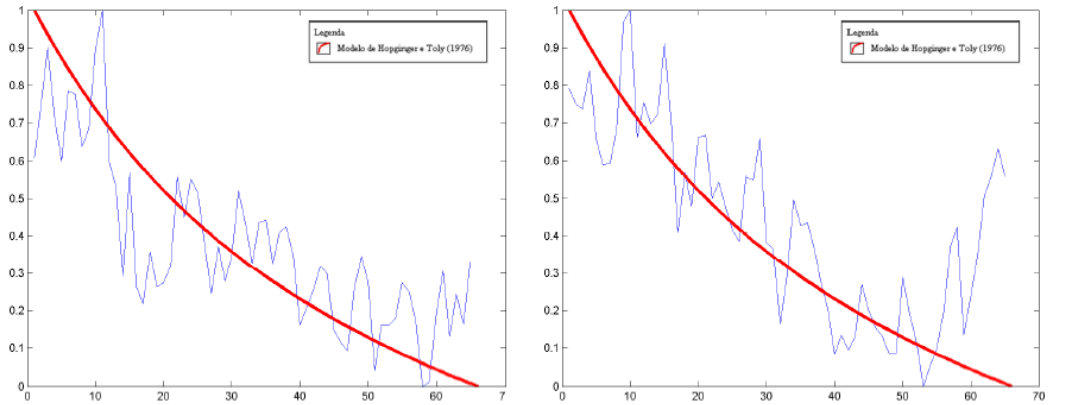

Decaimento da turbulência com 154, 25(a) e 175(b) oscilações da grade por minuto

Figura 6: Decaimento da turbulência

5. Conclusões

A partir da pesquisa realizada e dos resultados experimentais obtidos, pode-se dizer que o tanque de grade oscilante utilizado é um bom equipamento para geração de turbulência em laboratório e consegue produzir regimes turbulentos com características homogêneas. O PIV estereoscópico mostrou ser eficiente na observação de campos de velocidade, apesar de limitações na região periférica.

A turbulência teve comportamento homogêneo em toda a seção observada, ou seja, a intensidade turbulenta apresentou comportamento semelhante em todos os pontos da matriz. Quanto à isotropia, não é possível afirmar que o tanque de grade oscilante utilizado gera uma turbulência isotrópica. A afirmação só seria possível se as três componentes da intensidade turbulenta tivessem apresentado comportamento análogo, o que não ocorre. O módulo da velocidade W varia no espaço entre o centro de oscilação da grade e a superfície. Próximo à grade, a componente W (componente da velocidade no eixo z) é a mais afetada pelas oscilações, ficando com valores muito maiores que os valores das outras duas componentes. Na superfície, a componente W da velocidade é atenuada. Neste trabalho, a área observada estava muito próxima à superfície. Seria interessante, para a observação da isotropia, selecionar mais regiões entre a grade e a superfície para medidas de intensidade turbulenta.

Quanto à velocimetria por imagens de partículas, a concentração ideal de partículas foi controlada visualizando-se a qualidade das imagens. O laser utilizado para iluminar a seção do escoamento era pulsado e o tempo entre os pulsos do laser era definido pelo *software*. Este valor padrão mostrou-se adequado, já que as partículas apareciam como circunferências nítidas nas imagens, sem ocorrência de *blurring.* Foi possível notar que nas regiões periféricas da matriz o funcionamento do PIV fica prejudicado, pois na segunda imagem (considerando o par de imagens) algumas partículas podem estar fora da área observada. A observação da turbulência na superfície continua sendo uma dificuldade, pois esta região é afetada pela tensão superficial e pela superfície.

A turbulência gerada no tanque decai na seção observada (a seção está localizada entre a grade oscilante e a superfície livre da água). Este decaimento segue a mesma tendência que o Modelo de Hopfinger e Toly (1976).

6 Agradecimentos

O autor agradece o CNPq (Conselho Nacional de Desenvolvimento Científico e Tecnológico) e a CAPES (Coordenação de aperfeiçoamento de Pessoal de Nível Superior) pelo apoio financeiro nesta pesquisa.

7 Bibliografia

ADRIAN, R. J. *Twenty years of particle image velocimetry.* Experiments in fluids, 2005;

BARRA, L. *Estudo da estrutura turbulenta em escoamentos gerados por grades oscilantes.* Dissertação (Mestrado) – EESC-USP, 2002;

BOILLOT, A.; PRASAD, A. *Optimization procedure for pulse separation in cross-correlation PIV.* Experiments in fluids, Springer, v. 21, n. 2, p. 87-93, 1996;

CHENG, N. S.; LAW, A. W. K. *Measurements of turbulence generated by oscillating grid.* Journal of Hydraulic engineering, 2001;

CORRSIN, S. *Turbulence: Experiments methods.* Handbuch der physic, Stromungs mechanic, 1963;

DAVIDSON, P. A.; KROGSTAD, P. A. *Freely-Decaying, homogeneous turbulence generated by multi-scale grids.* Journal of Fluid Mech, 2011;

GEORGE, W. K. *The decay of homogeneous turbulence.* In transport phenomena in turbulent flows, 1988;

HOPFINGER, E. J.; TOLY, J. A. *Spatially decaying turbulence and its relation to mixing across density interfaces.* Journal of Fluid Mechanics, 1976;

JANZEN, J. G. *Detalhamento das propriedades turbulentas em água agitada por grades oscilantes.* Dissertação (Mestrado) – EESC-USP, 2003;

JANZEN, J. G.; SCHULZ, H. E.; JIRKA, G. H.(2011) Turbulent gas flux measurements near the air–water interface in an oscillating-grid tank GTWS 2010, Tokio, Japan;

KIEFHABER, D.; ROCHOLZ, R.; GUNTHER, G. B.; JAHNE, B (2011) *Improved Optical Instrument for the Measurement of Water Wave Statistics in the Field* GTWS 2010, Tokio, Japan;

MARKATOS, N. C. *The mathematical modelling of turbulent flows.* Applied mathematical modelling, v. 10, 1986;

MOHAMED, M.; LARUE, J. *The decay power law in grid-generated turbulence.* Journal of Fluid Mechanics, Cambridge Univ Press, v. 219, n. 1, p. 195-214, 1990;

NETO, A. da S. *Turbulência nos fluidos aplicada.* Uberlândia: Universidade Federal de Uberlândia, 2004;

NUNES, R. P. *Projeto e implementação de um sistema de instrumentação eletro-eletrônica para caracterização de escoamentos através de processamento digital de imagens.* Dissertação (Mestrado) – UFRGS, 2005;

RIGHETTO, M. M. *Desenvolvimento e calibração de um tanque de reaeração equipado com grade oscilante.* Dissertação (Mestrado) –EESC-USP, 2008;

RODI, W. *Turbulence models and their application in hidraulics*. Ed. IAHR, Delft, 1980;

SHULZ, H. E.; CHAUDHRY, F. H. *Uma aproximação para turbulência gerada por grades oscilantes.* In: Primeira escola de transição e turbulência. [S.l.;s.n.], 1998;

SHY, S. S.; JANG, R. H. ; TANG. C. Y. *Simulation of turbulent burning velocities using aqueous autocatalytic reactions in a near-homogeneous turbulence.* Combustion and flame, 1996;

SZÉLIGA, M. R.; ROMA, W. N. L. *Estudos de Reaeração com Velocimetria por Imagens de Partículas - Sistema S-PIV-3D*. Revista Engenharia Sanitária e Ambiental, vol.14, n.4, pp. 499-510. ISSN 1413-4152. doi: 10.1590/S1413-41522009000400010, 2009;

THOMPSON, S. M.; TURNER, J. *Mixing across an interface due to turbulence generated by an oscillating grid.* Journal of Fluid Mechanics, 1975;

TOWNSEND, A. A. *The structure of turbulent shear flow.* New York: Cambridge University Press, 1976;

TURNEY, D. and BANERJEE, S. *Near surface turbulence and its relationship to air–water gas transfer rates.* GTWS, Tokio, Japan, 2010;

VIEIRA, A. P. S. D. *Estudo de estrutura turbulenta gerada por tanque de grade oscilante observada por PIV.* Dissertação (Mestrado) –EESC-USP, 2012;

WILLIAMS, S. *3-D Visualization of a Zero-Pressure Gradient Turbulent Boundary Layer*. Tese(Doutorado)— Auburn University, 2010;

YAN, J. et al. *Oscillating-grid turbulence and its applications: a review.* Journal of Hydraulic Research, 2007.

8 Responsibility note

O autor é o único responsável pelo material incluído neste artigo.

ANÁLISE DA INTERAÇÃO ENTRE CORRENTES DE DENSIDADE E ESTRUTURAS CILÍNDRICAS UTILIZANDO SIMULAÇÃO NUMÉRICA DIRETA

Luísa Vieira Lucchese, luisa.lucchese@ufrgs.br
Vitor Souza Viana Silva, vitor.viana@ufrgs.br
Núcleo de Estudos em Transição e Turbulência, Instituto de Pesquisas Hidráulicas, Universidade Federal do Rio Grande do Sul

Jorge Hugo Silvestrini, jorgehs@pucrs.br
Grupo de Estudos em Transição e Turbulência, Pontíficia Universidade Católica do Rio Grande do Sul

Edith Beatriz Camaño Schettini, bcamano@iph.ufrgs.br
Núcleo de Estudos em Transição e Turbulência, Instituto de Pesquisas Hidráulicas, Universidade Federal do Rio Grande do Sul

Abstract. *Submarine conduits can be considered as obstacles for a gravity current that propagates under the sea. It is desirable to know how these natural currents behave in this subaquatic interaction, and how the conduit responds to it (the strain it handles). This work is about the interaction of a gravity current propagating in a channel with an obstacle, which was chosen to be a circular cylinder, because it is the most common shape for a submarine conduit. The research shows the differences on the dynamics of the flow for different Grashof numbers (from* 10^6 *to* $4 \cdot 10^8$*) and different parameters regarding the cylinder, such as size and location. Mainly, the effect of each parameter on the flow was analyzed. The work was fully conducted on a DNS (Direct Numeric Simulation), more accurate than a turbulence model, and finite difference schemes described by Lele were used for spatial discretization; while Adams-Bashfort schemes were used in the temporal discretization. The meshes (spatial and temporal) used for the DNS are listed on this work. The studied interaction can show a number of different phenomena, such as the impact of the current on the cylinder and the Von Kármán vortices in the quasi-steady state, which is a flow state reached when the current head has already passed by the obstacle. One can observe that increasing the Grashof number implies an increase on the number of turbulent eddies and a decrease in its size (dissipative scales become smaller). Changing the size and place of the obstacle affects significantly the flow field: small obstacles (in proportion to the gravity current head) may be passed by with less changes in the gravity current head, but large ones affect the configuration of the current permanently, mixing more the two fluids with different densities involved in the simulation.*

Keywords: *gravity current, DNS, cylinder*

1. INTRODUÇÃO

As correntes de densidade foram descritas por Benjamin (1968) e têm sido estudadas por pesquisadores das áreas de engenharia e geociências. Correntes de densidade são essencialmente formadas por dois fluidos de densidades diferentes, que se propagam um sob o outro. Exemplos são avalanches de neve, deslizamentos de solo e correntes de sedimentos marítimas. Características intrínsecas a este fenômeno são a turbulência e a transição à turbulência, pois inicialmente há dois fluidos estáticos, e, mais tarde, o sistema está em movimento, certas vezes com altas velocidades.

Uma linha de estudos atual, experimental e numérica, na engenharia, é a interação das correntes com obstáculos e anteparos, o que simula a propagação de uma corrente marítima entre tubulações e cabos subaquáticos. Um dos objetivos ao estudar esta interação é aprofundar o conhecimento sobre o comportamento das correntes de densidade e sua propagação, importante para o dimensionamento das estruturas. As velocidades de impacto e a posição da estrutura relativa ao fundo são fatores condicionantes no projeto. Duas das geometrias mais estudadas são o cilindro circular (Ermanyuk e Gavrilov, 2005) e o prisma de seção transversal quadrada (Tokyay et al. 2011). O obstáculo escolhido para a pesquisa é uma estrutura cilíndrica circular, por assemelhar-se à geometria mais comum de uma tubulação a ser instalada no assoalho marinho, como emissários e oleodutos. Estuda-se no presente trabalho a dinâmica da interação entre um conduto cilíndrico e uma corrente de densidade, e como ela se altera com a alteração do tamanho e da localização do obstáculo.

Diversos estudos foram realizados a respeito de interação de obstáculos com correntes de densidade, analisando diferentes aspectos, como a formação da frente da corrente de densidade (Härtel et al., 2000, Neufeld, 2002), a formação das instabilidades de Kelvin-Helmholtz (descritas inicialmente por Thomson em 1871), o impacto da corrente sobre o cilindro (Gonzalez-Juez et al., 2009a), e a formação de uma esteira de vórtices de Von Kármán, ao mesmo tempo que isso gera um estado quase-estável do escoamento. Segundo Gonzalez-Juez et al. (2009b), o escoamento estudado tem três fases: a fase de impacto, quando a corrente encontra o cilindro e as forças hidrodinâmicas verticais chegam a seu máximo, enquanto as horizontais variam bruscamente com alta frequência; a fase transiente, quando as características do escoamento estão transicionando do impacto para o estado quase-estável; e a fase quase-estável, que, para certos espaçamentos entre o

cilindro e o fundo do canal, apresenta uma esteira de vórtices de Von Kármán.

2. METODOLOGIA

Para simular numericamente a interação entre a corrente de densidade e a estrutura cilíndrica, foi escolhida a metodologia de Simulação Numérica Direta (DNS, pela sigla em inglês de *Direct Numeric Simulation*). Esta metodologia permite simular, com alto grau de precisão, todas as escalas de um escoamento turbulento, sem necessidade de recorrer a modelos de turbulência.

A base do que foi utilizado para as simulações é o código *Incompact3d*, desenvolvido por Laizet e Lamballais (2009) e disponibilizado em https://code.google.com/p/incompact3d/. O *Incompact3d* considera adimensionalização em todas as suas variáveis. O código, escrito em Fortran-90, foi modificado para este caso específico: foram adicionadas novas condições de contorno e de configuração do escoamento. Estas modificações fizeram com que o programa fosse capaz de simular correntes de densidade, e, mais recentemente, cilindros imersos em correntes de densidade.

O esquema utilizado para resolução do problema foi bidimensional, considerando um canal hermético em que dois fluidos de densidade diferente estão separados por um obstáculo físico, e no tempo inicial, esse obstáculo é retirado. Isso é uma simulação de corrente de densidade com volume finito, também denominada *lock-exchange*. Uma simulação com volume infinito é normalmente definida como aquela em que não se define as laterais do canal, fazendo apenas com que o fluido menos denso se propague sobre o mais denso e vice-versa, com um eixo de simetria. Na simulação realizada na pesquisa no NETT (Núcleo de Estudos em Transição e Turbulência, IPH, UFRGS), define-se todos os lados do canal, assim como suas condições de contorno e a localização de cada fluido.

2.1 Modelo Matemático

As equações da continuidade, de Navier-Stokes e de transporte e difusão, para descrever o fluxo de uma corrente de densidade, foram adimensionalizadas utilizando a velocidade de flutuabilidade (u_b), o limite da altura do fluido mais denso na condição inicial (h), que normalmente é metade da altura do canal, e a massa específica do fluido mais denso (ρ), indicada pela concentração $C_1 = 1$. A velocidade u_b é uma velocidade que leva em consideração a variação de densidade, e está dada por $u_b = \sqrt{g\Delta\rho/\rho}$.

O número de Reynolds (Re) utilizado no presente trabalho é definido a partir da velocidade u_b:

$$Re = \frac{u_b h}{\nu}, \tag{1}$$

sendo ν a viscosidade cinemática.

Um número adimensional utilizado comumente para classificar e definir as correntes de densidade é o número de Grashof Gr (2), que relaciona as forças de flutuação com as forças viscosas. Considerando a velocidade modificada pela relação de densidades u_b, o número de Grashof Gr pode ser aproximado como o número de Reynolds elevado ao quadrado:

$$Gr = \frac{u_b^2 h^2}{\nu^2} \simeq Re^2. \tag{2}$$

Na equação da continuidade, admitiu-se a aproximação de Boussinesq, ou seja que $\Delta\rho/\rho \ll 1$, e a taxa de deformação volumétrica é invariável. A equação da continuidade fica:

$$\nabla \cdot \vec{u} = 0. \tag{3}$$

A equação de Navier-Stokes é escrita da forma:

$$\frac{\partial \vec{u}}{\partial t} + \vec{u}(\nabla \cdot \vec{u}) = -\nabla p + \rho \vec{e_g} + \frac{1}{\sqrt{Gr}}\nabla^2 \vec{u}, \tag{4}$$

A equação de transporte e difusão é representada da seguinte maneira:

$$\frac{\partial \rho}{\partial t} + \nabla \cdot (\rho \vec{u}) = \frac{1}{\sqrt{Gr}Sc}\nabla^2 \rho. \tag{5}$$

Nestas equações, $\vec{e_g}$ é um versor na direção vertical, dado por $\vec{e_g} = (0, -1, 0)$, $\vec{u}$ representa o campo de velocidades, ρ a massa específica, p o campo de pressões modificado, Gr o número de Grashof, e Sc o número de Schmidt (o qual relaciona a viscosidade cinemática ν e a difusividade molecular k) definido por $Sc = \nu/k$.

2.2 Condições Iniciais e de Contorno

No interior do canal foi localizado, à esquerda, um fluido com concentração adimensional, $C_1 = 1$, dentro do fluido restante, que tem concentração adimensional $C_0 = 0$ (Fig. 1). Esta condição inicial é a que dá origem à corrente de densidade, por efeito gravitacional. Foram implementadas as seguintes condições de contorno: todos os contornos são impermeáveis e na região das fronteiras laterais ($x = 0$ e $x = L_x$) e nas fronteiras superior e inferior ($y = 0$ e $y = L_y$) foi imposta a condição de não-deslizamento (*no-slip*). No cilindro foi imposta a condição de contorno de não-deslizamento na superfície (*no-slip*) e de não-difusão (não há transferência de massa através de sua superfície). A estrutura cilíndrica permaneceu fixa e separada por uma distância constante do fundo durante uma mesma simulação.

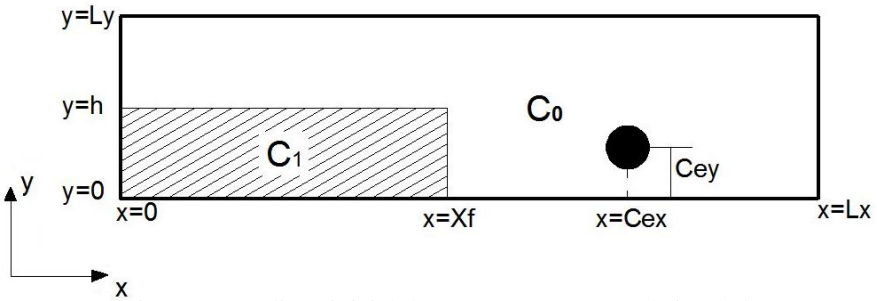

Figura 1. condição inicial do escoamento no canal simulado

O domínio de integração é retangular, de tamanho (L_x, L_y), e o cilindro de diâmetro D está localizado em (Cey, Cex), onde Cey está definido pela relação:

$$Cey = G + \frac{D}{2}, \tag{6}$$

sendo G a distância da parte inferior do obstáculo ao fundo do canal.

2.3 O Código *Incompact3d* e o Esquema Numérico

As equações são resolvidas numericamente empregando o código de cálculo *Incompact3d*, baseado num esquema de diferenças finitas compacto de 6^a ordem, para a discretização espacial, e em um esquema de Adams-Bashforth de 2^a ordem, para a discretização temporal (Laizet e Lamballais, 2009).

A discretização espacial dos termos convectivo-difusivo e de transporte-difusão é feita utilizando um esquema de diferenças finitas centradas, compacto, proposto por Lele (1992). Os esquemas compactos são esquemas implícitos, que relacionam o valor da derivada de uma função em um ponto ao valor da derivada em pontos vizinhos.

Para a discretização espacial, considerando uma malha uniforme, na qual a variável independente para cada nó i da malha é $\xi_i = (i-1)\Delta\xi$, com $1 \leq i \leq N$ e $\xi = x, y$ ou z, os valores da primeira derivada são dados por:

$$\alpha f'_{i-1} + f'_i + \alpha f'_{i+1} = a\frac{f_{i+1} - f_{i-1}}{2\Delta\xi} + b\frac{f_{i+2} - f_{i-2}}{4\Delta\xi}. \tag{7}$$

A segunda derivada é dada por:

$$\alpha f''_{i-1} + f''_i + \alpha f''_{i+1} = a\frac{f_{i+1} - 2f_i + f_{i-1}}{2\Delta\xi^2} + b\frac{f_{i+2} - 2f_i + f_{i-2}}{4\Delta\xi^2}. \tag{8}$$

A aproximação com precisão de sexta ordem é obtida com o conjunto de parâmetros (Lele, 1992), para resolução das equações da primeira e segunda derivada, válidos para todo o domínio e para todas as direções, apresentado na Tab. 1

Tabela 1. Parâmetros utilizados em cada equação do código.

	α	a	b
Eq. 7	1/3	14/9	1/9
Eq. 8	2/11	12/11	3/11

A integração temporal é feita pelo método de Adams-Bashfort, com precisão de segunda ordem. A completa descrição do desenvolvimento matemático dos esquemas de discretização numérica temporal e espacial pode ser encontrada em Lele (1992) e Guerreiro (2000). Os valores da pressão são calculados em pontos escalonados da malha, isto é, no centro da malha. O cilindro foi simulado com o Método de Fronteiras Imersas (Lamballais e Silvestrini, 1999).

A identificação das estruturas coerentes a partir dos resultados de simulações depende, em grande parte, da escolha do método de identificação. Lesieur (1997) define uma estrutura coerente como uma região do espaço de alta concentração de vorticidade, que conserva uma forma definida durante um tempo de vida superior ao seu tempo de rotação, e possui a propriedade de sensibilidade às condições iniciais, ou seja, de imprevisibilidade. Para identificar visualmente estas estruturas, nas simulações realizadas neste trabalho, é utilizada a vorticidade $\vec{\omega} = \vec{\nabla} \times \vec{u}$.

3. RESULTADOS

Foi analisado, no presente trabalho, os três estados da interação estudada, e as influências do número de Grashof e da distância da estrutura cilíndrica ao fundo do canal no escoamento da corrente de densidade.

Os estados do escoamento estudado são, segundo Gonzalez-Juez et al. (2009a) e (2009b): impacto (*impact*), transiente (*transient*) e quase-estável (*quasi-steady*). O primeiro inicia quando o obstáculo é atingido pela corrente de densidade, e é marcado por violentos impactos na estrutura cilíndrica. O estado quase-estável é atingido quando o escoamento se estabiliza, gerando uma situação, de certa forma, semelhante a de um escoamento de fluxo constante passando por um corpo rombudo (Roshko, 1961). Pode-se constatar a semelhança destes casos por meio da análise do campo de vorticidade deles, em que se observa os vórtices de Von Kármán. O estado transiente é o estado em que o escoamento transiciona do estágio de impacto para o quase-estável. Utilizou-se campos de concentração e vetores que indicam a direção e a magnitude da velocidade para analisar e diferenciar os três estados (Fig. 2).

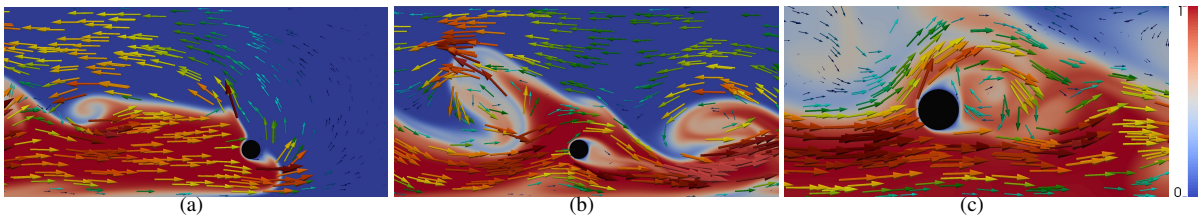

(a) (b) (c)

Figura 2. Visualização dos estágios do escoamento: impacto (a), transiente (b) e quase-estável (c). A figura mostra o campo de concentrações ao fundo, na escala de azul ($C = 0$) a vermelho ($C = 1$), e os vetores indicam a magnitude e direção da velocidade. Esta simulação tem $Gr = 4 \cdot 10^6$

Através da análise de campos de vorticidade e da função de corrente nos três estágios de escoamento (Fig. 3), é possível ver a transição do estágio de impacto (quando a corrente, que pode ser vista impactando no cilindro, tanto no campo de vorticidades quando nas linhas da função corrente) para o estágio quase-estável. Na fase transiente se vê o início da formação de recirculação a jusante do cilindro (através da vorticidade), embora ainda sem o desprendimento de vórtices. No estágio quase-estável, a esteira de vórtices de Von Kármán encontra-se mais desenvolvida, com o desprendimento alternado de vórtices com sentidos rotacionais opostos. As regiões em que não há densidade de linhas de corrente na Fig. 3 são regiões nas quais as linhas da função corrente apresentam comportamento elipsoidal e somente podem ser vistas se a função corrente for definida em uma reta que passe pelo centro dos elipsóides, o que indica que estas regiões do escoamento são de recirculação, apontando a presença do fenômeno das Instabilidades de Kelvin-Helmholtz. A presença destas instabilidades pode ser ratificada pela observação dos campos de concentração desta simulação, mostrados nas Figs. 2 e 4.

As esteiras de vórtices de Von Kármán, que são formadas no estado *quasi-steady* de escoamento, a jusante da estrutura cilíndrica, podem ser observadas mais claramente por meio da análise da vorticidade no campo de escoamento. Pode-se ver, na Fig. 4, o desprendimento de vórtices, semelhante ao que acontece com o cilindro sob escoamento livre.

Foram realizadas simulações para números de Reynolds variando de $Re = 1000$ a $Re = 20000$, correspondentes a $10^6 \leq Gr \leq 4 \cdot 10^8$ Na Tab. 2 são apresentados os parâmetros das simulações correspondentes a estes Gr. A influência destes parâmetros pode ser observada na Fig. 5: quanto maiores são os Gr, mais instabilidades do tipo Kelvin-Helmholtz se desenvolvem na parte posterior à frente da corrente.

Uma análise realizada no presente trabalho foi a interação da corrente de densidade com um obstáculo fixo para baixos e elevados números de Grashof (Eq. 2). A variação deste número adimensional representa diferentes configurações na dinâmica das correntes de densidade. Segundo Härtel et al. (2000), os altos valores do número de Grashof influenciam na velocidade da frente e no aumento do número de turbilhões na camada de mistura, as quais apresentam intensa turbulência (instabilidades de Kelvin-Helmholtz). Observa-se, nas Fig. 6 e Fig. 7, que a passagem da frente da corrente pelo cilindro

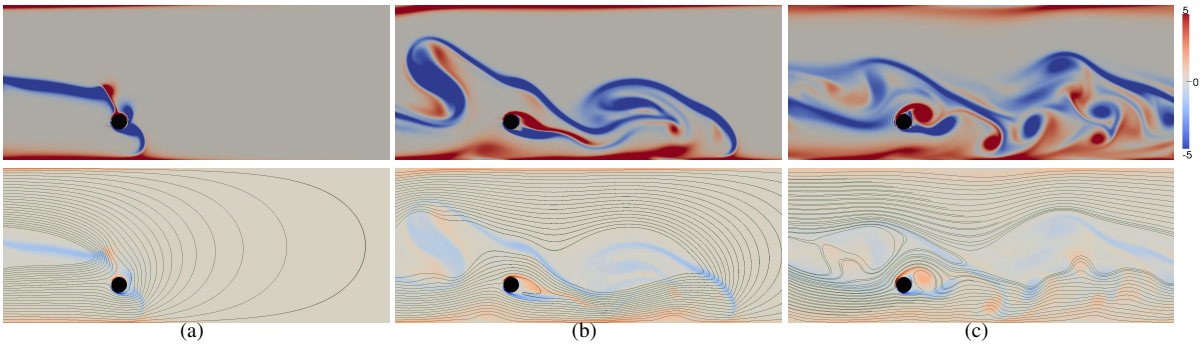

(a) (b) (c)

Figura 3. Campos de vorticidade e função corrente para os estágios de escoamento impacto (a), transiente (b) e quase-estável (c) para $Gr = 4 \cdot 10^6$

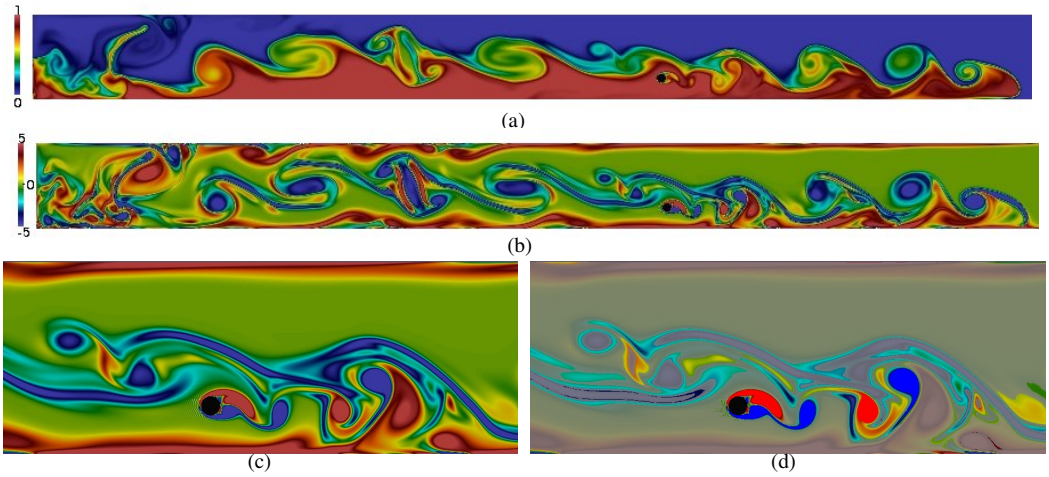

(a)

(b)

(c) (d)

Figura 4. Visualização do campo de concentração (a), e da vorticidade (b), seguidas por um detalhe mais aproximado da imagem da vorticidade (c) e o destaque da esteira de vórtices de Von Kármán (d), no instante $t = 25$, para $Gr = 4 \cdot 10^6$.

Tabela 2. Simulações realizadas variando o número de Grashof

Simulação	Re_h	Gr	L_x	L_y	N_x	N_y	Δx	Δy	Cex	Cey	Δt	D	Inicial	
													X_f	h
I	1000	10^6	12	1	769	101	0,0156	0,0100	7,5	0,25	0,0008	0,1	4,5	1
II	1118	$1,25 \cdot 10^6$	12	1	769	101	0,0156	0,0100	7,5	0,25	0,0008	0,1	4,5	1
III	2000	$4 \cdot 10^6$	12	1	2305	273	0,0052	0,0037	7,5	0,25	0,0008	0,1	4,5	1
IV	3162	10^7	12	1	2305	273	0,0052	0,0037	7,5	0,25	0,0008	0,1	4,5	1
V	10000	10^8	12	1	4097	513	0,0029	0,0019	7,5	0,25	0,0005	0,1	4,5	1
VI	20000	$4 \cdot 10^8$	12	1	4001	401	0,0030	0,0025	7,5	0,25	0,0002	0,1	4,5	1

(a) (b) (c) (d)

Figura 5. Isolinhas de concentração das correntes de densidade, no mesmo instante de tempo, para as simulações I (a), IV (b), V (c) e VI (d)

mostra um efeito de jato, produzido pela parcela que passa por baixo do cilindro. O vórtice superior desenvolve-se claramente, com mesmo sentido de rotação que os da camada de mistura, entanto que o inferior, que gira em sentido contrário, perde intensidade devido à condição de não-deslizamento do fundo do canal.

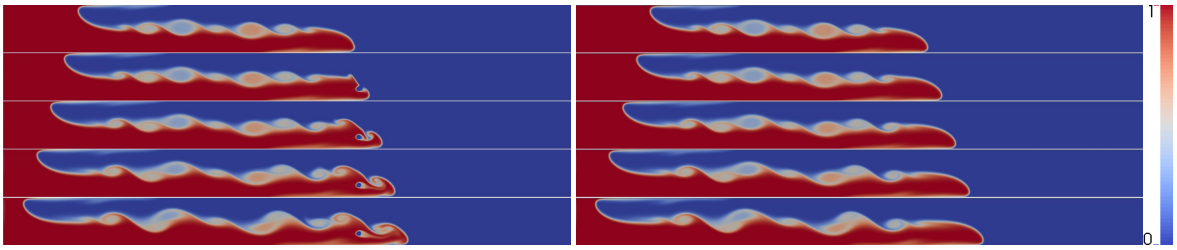

(a) (b)

Figura 6. Choque de uma corrente de densidade com um cilindro a $Gr = 1,25 \cdot 10^6$, na simulação II (a), comparado com uma simulação semelhante à II, mas sem o cilindro (b).

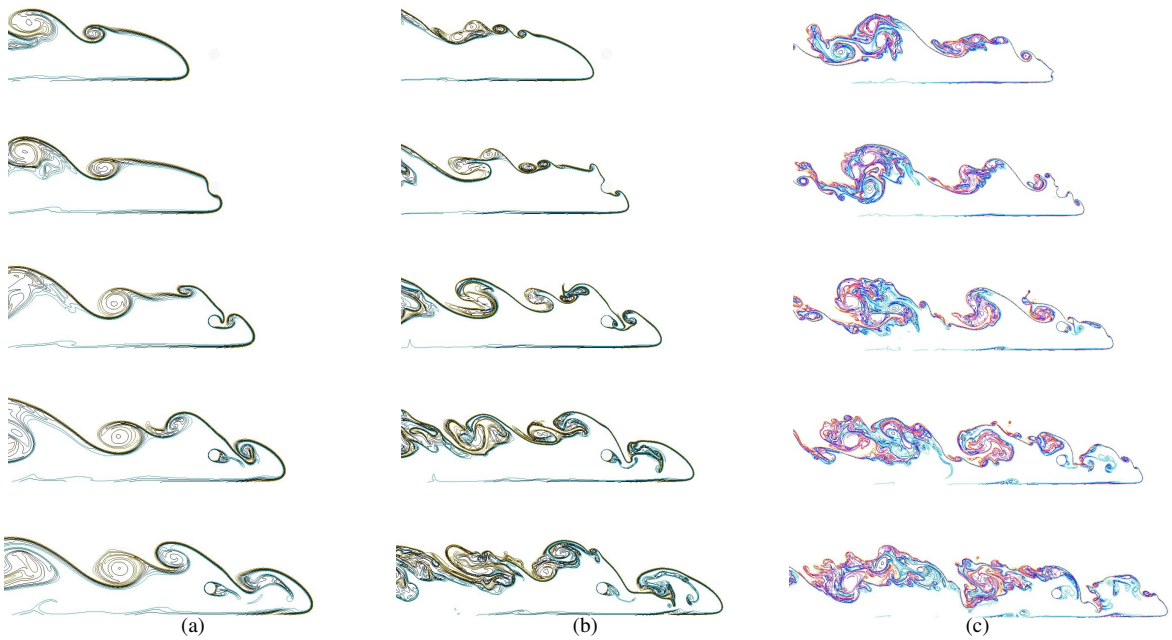

(a) (b) (c)

Figura 7. Isolinhas de concentração mostrando o choque da corrente com a estrutura cilíndrica, para diferentes números de Grashof. Simulações IV (a), V (b) e VI (c).

Tabela 3. Simulações realizadas variando o parâmetro Cey

Simulação	Re_h	Gr	L_x	L_y	N_x	N_y	Δx	Δy	Cex	Cey	Δt	D	Inicial	
													X_f	h
VII	2000	$4 \cdot 10^6$	7,5	1,5	3001	625	0,0025	0,0024	3,6	0,15	0,0008	0,3	2,1	1
VIII	2000	$4 \cdot 10^6$	7,5	1,5	3001	625	0,0025	0,0024	3,6	0,3	0,0008	0,3	2,1	1
IX	2000	$4 \cdot 10^6$	7,5	1,5	3001	625	0,0025	0,0024	3,6	0,45	0,0008	0,3	2,1	1
X	2000	$4 \cdot 10^6$	7,5	1,5	3001	625	0,0025	0,0024	3,6	0,6	0,0008	0,3	2,1	1

Com a finalidade de verificar a influência da distância entre o cilindro e o fundo, foi simulado um cilindro de diâmetro $D = 0,3$, diferente do utilizado nos casos anteriores. Variou-se a distância Cey entre o obstáculo e o fundo do canal, como consta na Tab. 3.

Se o cilindro está posicionado relativamente longe do fundo, mas a uma altura inferior à da cabeça da corrente, os vórtices desprendidos pela cabeça da corrente impactam com o mesmo, causando uma retenção do fluido de maior concentração. Ou seja, o cilindro produz um efeito de retenção, do tipo comporta, fazendo com que a altura da frente diminua

durante um certo período, até o desprendimento do vórtice gerado pelo jato a jusante do cilindro ($Cey = 0,45$, Fig. 8). Após a passagem pelo obstáculo, a corrente tende a recuperar sua forma.

Quando a estrutura cilíndrica é posicionada em uma coordenada $Cey = 0,3$ (Fig. 8), a corrente colide frontalmente com o obstáculo, produzindo uma retenção e posterior espalhamento do fluido mais denso. A corrente se separa em dois escoamentos, mostrando comportamentos típicos dos escoamentos sob comporta e sobre vertedor. Neste caso, a frente da corrente fica completamente descaracterizada e com grande nível de turbulência.

No último caso simulado, o cilindro está apoiado no fundo do canal ($Cey = 0,15$, Fig. 8) e atua como vertedor, produzindo um jato superior de fluido mais denso que imediatamente mergulha devido à ação da gravidade. A corrente fica ainda mais descaracterizada que no caso anterior, apresentado uma intensa mistura.

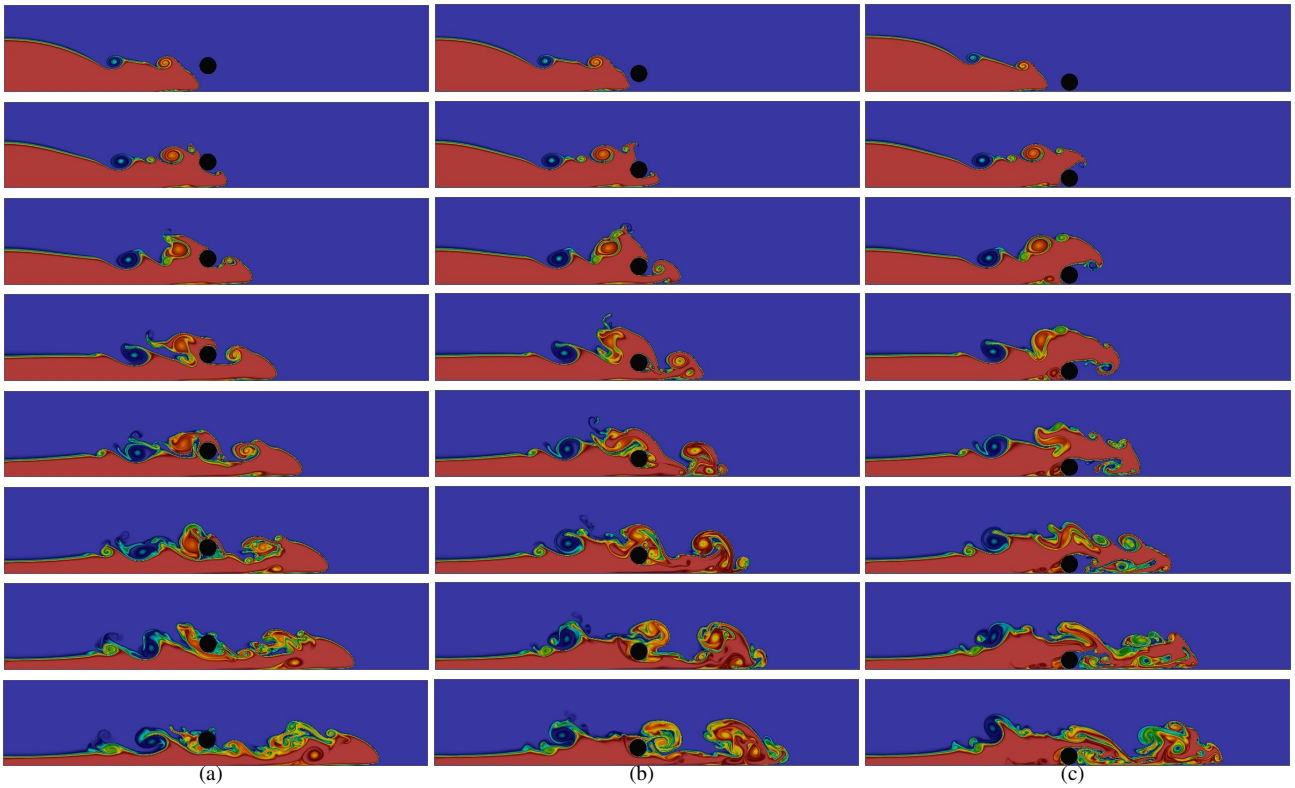

Figura 8. Evolução da propagação da corrente de densidade com $Gr = 4{\cdot}10^6$, e sua interação com um cilindro posicionado em $Cey = 0,45$ (a), $Cey = 0,30$ (b) e $Cey = 0,15$ (c). Simulações VII, VIII e IX.

4. CONCLUSÕES

O presente trabalho estuda, por meio de simulações numéricas, a interação entre correntes de densidade e obstáculos fixos cilíndricos, paralelos ao fundo do canal. Foi feita análise da influência da variação de diferentes parâmetros da configuração do escoamento, como número de Grashof da correnrte, distância entre o cilindro e o fundo do canal. A metodologia utilizada é a da Simulação Numérica Direta (DNS), com esquema em diferenças finitas compacto de sexta ordem, aplicados a uma malha cartesiana. A presença do cilindro foi simulada com o Método de Fronteiras Imersas.

Nos casos estudados, a corrente modificou sua forma após o impacto com a estrutura cilíndrica. Os resultados numéricos indicam que o número de Grashof (Gr) tem grande influência sobre a dinâmica da interação estudada. A variação do tamanho e da localização do cilindro altera os fenômenos envolvidos e o escoamento em torno do obstáculo.

Nas simulações feitas, podem-se observar as três fases do escoamento por meio de campos de concentração, velocidade, vorticidade e função de corrente. Através da análise das linhas de corrente, é possível identificar o comportamento das instabilidades de Kelvin-Helmholtz, que se localizam na parte superior da frente da corrente de densidade. Além disso, pode-se ver a formação da esteira de vórtices de Von Kármán, característica do estágio quase-estável, através da análise da vorticidade. Os campos de vorticidade encontrados são semelhantes aos campos descritos por outros autores. Neles foi possível observar os fenômenos envolvidos na interação estudada como bastante semelhantes aos que ocorrem na natureza.

5. AGRADECIMENTOS

Os autores agradecem à CAPES e ao CNPq pela concessão das bolsas aos dois primeiros autores.

6. REFERÊNCIAS

Benjamin, T. B., 1968, "Gravity currents and related phenomenon", J.Fluid Mechanics.

Ermanyuk, E. V., Gavrilov, N. V., 2005, "Interaction of an Internal Gravity Current with a Submerged Circular Cylinder", Journal of Applied Mechanics and Technical Physics, Volume 46, Pages 216-223.

Gonzalez-Juez, E., Meiburg, E., Constantinescu, G., 2009, "The interaction of a gravity current with a circular cylinder mounted above a wall: Effect of the gap size", Journal of Fluids and Structures, Volume 25.

Gonzalez-Juez, E., Meiburg, E., Constantinescu, G., 2009, "Gravity currents impinging on bottom-mounted square cylinders: Flow fields and associated forces", Journal of Fluid Mechanics, Volume 631.

Guerreiro, C. B. P., 2000, "Resolução Numérica das equações de Navier-Stokes com esquemas de diferenças finitas de quarta ordem", Universidade Federal do Rio Grande do Sul. Instituto de Matemática. Programa de Pós-Graduação em Matemática Aplicada, Porto Alegre.

Hartel, C., Meiburg, E., Necker, F., 2000, "Analysis and direct numerical simulation of the flow at a gravity-current head. Part 1. Flow topology and front speed for slip and no-slip boundaries", Journal of Fluid Mechanics, Volume 418, Pages 189-212.

Laizet, S., Lamballais, E., 2009, "High-order compact schemes for incompressible flows: A simple and efficient method with quasi-spectral accuracy", J.Comput.Phys., Volume 228, Pages 5989-6015.

Lamballais, E., Silvestrini, J. H., 1999, "Documentação do código Incompact3d", Pages: 24.

Lele, S. K., 1992, "Compact finite difference schemes with spectral-like resolution", J. Comp. Phys., Volume 103, Pages 16-42.

Lesieur, M., 1997, "Turbulence in Fluids" ,Pages 515 , Publisher: Kluwer Academic Publishers.

Neufeld, J., 2002, "Lobe-Cleft Patterns in the Leading Edge of a Gravity Current", Department of Physics, University of Toronto.

Roshko, A., 1961, "Experiments on the flow past a circular cylinder at very high Reynolds number", Journal of Fluid Mechanics, Volume 10.

Thomson, W., 1871, "Hydrokinetic solutions and observations", Philosophical Magazine, Volume 42, Pages 362-377.

Tokyay, T., Constantinescu, G., Gonzalez-Juez, E., Meiburg, E., 2011, "Gravity currents propagating over periodic arrays of blunt obstacles: Effect of the obstacle size", Journal of Fluids and Structures, Volume 27.

Tritton, D. J., 2005, "Physical Fluid Dynamics", Publisher: Clarendon Press.

ANÁLISE PRELIMINAR DO EFEITO DA TURBULÊNCIA SOBRE UM MECANISMO DE RECOLAMENTO DA CAMADA LIMITE

Renan Francisco Soares, renanfranciscosoares@hotmail.com
Francisco José de Souza, fjsouza@mecanica.ufu.br
Universidade Federal de Uberlândia – Av. João Naves de Ávila 2121 - Campus Sta. Mônica | Uberlândia - MG - Brazil

Alexandre Felipe Medina Correa, lexmedina@aero.ufu.br
Universidade Federal de Uberlândia – Av. João Naves de Ávila 2121 - Campus Sta. Mônica | Uberlândia - MG - Brazil

Abstract. Almejando reduzir a esteira turbulenta associada ao descolamento da camada limite em aerofólios, o presente trabalho aborda o papel da energia cinética turbulenta em técnica de controle de escoamento para promover o recolamento da camada limite. Adota-se o método de controle ativo do escoamento através de injeção de quantidade de movimento, através de jato plano, para análise neste trabalho. Estudos experimentais revelam que o perfil NACA 0012 apresenta descolamento da camada limite em AoA=12º e Re=10^5. Tomando esta configuração como *baseline*, um perfil modificado é proposto, sendo resultado da configuração do NACA 0012 com a adição de um canal na posição de meia corda na superfície do extradorso (região de descolamento). Portanto, estuda-se o problema em 5 frentes: comportamento do escoamento para *baseline*; perfil modificado sem injeção de jato; perfil modificado com jato de U_∞; transição do jato de U_∞ para $^1/_2U_\infty$, e de U_∞ para $^3/_2U_\infty$. Os resultados ratificam o aumento da energia cinética turbulenta pelo jato na região de descolamento como agente do recolamento da camada limite. Não obstante, verifica-se que a borda do canal de injeção atua como gerador de vorticidade, alimentando a região com instabilidades. Pelo aspecto de evolução temporal dos jatos conclui-se que a variação da velocidade, tanto para maior quanto para menor intensidade, produz um pulso de energia cinética turbulenta. Este fenômeno intensifica o efeito de recolamento da camada limite até que este adicional de energia ser disperso. Por fim, tal característica dos pulsos de energia leva a concluir que deve-se existir uma frequência ideal de intermitência do jato a qual resulte maior eficiência do mecanismo de recolamento do que jatos contínuos em velocidades ainda maiores. Ou seja, jatos intermitentes teriam potencial uso para fins de aplicações na função de sistema aerodinâmico.

1. INTRODUÇÃO

A geração de vorticidade, assim como descolamento da camada limite e possível turbulência decorrente, ganham importância pela sua relação com as forças de arrasto em aplicações aeronáuticas e no automobilismo, seja a física estudada de forma experimental ou através de técnica de Dinâmica dos Fluidos Computacional (CFD).

Sob olhar do ramo aeronáutico, o fenômeno de descolamento do escoamento reduz o coeficiente de sustentação (C_L) e aumenta o de arrasto (C_D); levando à consequente redução da eficiência (C_L/C_D) de perfis aerodinâmicos, de modo que a perda é excessiva à medida que o corpo em questão se aproxima da condição de *stall*: condição em que a camada limite se descola totalmente levando à perda total de sustentação e difícil retorno à um condição estável (Anderson, 2010).

Na esfera da indústria automotiva comercial, o estudo da formação de regiões turbulentas é focado principalmente na região traseira do veículo, onde geralmente ocorre descolamento da camada limite e, embora seja em relação não-linear, a dimensão da esteira turbulenta é associada à forças de arrasto sobre o veículo (Hucho, 1998).

Outro exemplo está no automobilismo de alta performance, onde foi consultado Martin Schudel (2013) – *Senior Aerodynamicist*, equipe Marussia de Formula 1 – sobre o assunto. Segundo ele, recomenda-se a futuros aerodinamicistas estudar estruturas vorticais, como as formações e coerência entre estruturas do escoamento, pois, na Formula 1, a geração de *downforce* (conhecida também como força de sustentação invertida) é fortemente relacionada a estruturas vorticais. Deste modo, o trabalho de otimização aerodinâmica em escoamentos turbulentos, ou no mínimo, em estado de transição à turbulência, faz parte do desenvolvimento de engenharia aplicada neste setor.

A turbulência ganha seu papel de importância na abordagem e análise de problemas de engenharia, onde seu estudo leva a uma maior compreensão da física do escoamento ao redor de corpos de interesse, como perfis aerodinâmicos, automóveis e aeronaves.

Por fim, a compreensão da física dos escoamentos permite a engenharia firmar seus passos na direção do desenvolvimento tecnológico, alcançando o estado da arte. Assim, este trabalho vislumbra conhecer a influência da energia cinética turbulenta sobre o efeito de recolamento de camada limite.

1.1. Injeção de Quantidade de Movimento

Uma das técnicas que podem ser utilizadas para se aplicar controle de camada limite é o uso de injeção de quantidade de movimento através de pequenos orifícios presentes na superfície do modelo. Os primeiros estudos realizados para melhoria de performance de perfis aerodinâmicos se iniciaram em meados dos anos 1920 pelo Comitê Nacional para Aeronáutica dos EUA (NACA, *National Advisory Committee for Aeronautics*, atual NASA) através dos experimentos realizados por Knight e Bamber (1929). A injeção de fluido para controle da camada limite mostrou-se, através de vários estudos realizados ao longo do século XX e início do século XXI, de grande eficiência para aumento da sustentação gerada em diferentes ângulos de incidência e manutenção do arrasto aerodinâmico em valores inferiores aos encontrados experimentalmente para perfis aerodinâmicos sem uso de técnicas de controle.

O uso de tal técnica também mostra-se eficiente para prevenir a separação da camada limite em atitudes de alta incidência, de modo a levar ao atraso do *stall* sob mesmas condições encontradas em testes com ausência de controle. Desse modo, o uso de injeção garante maior sustentação gerada e mantém o arrasto em condições reduzidas, o que é atingido pelo controle da região turbulenta ao se reduzir a esteira gerada devido à separação da camada limite próximo ao bordo de fuga do aerofólio, conforme estudo realizado por Bamber (1931).

A influência da camada limite na geração de sustentação e arrasto varia com o ângulo de ataque de um perfil aeronáutico. Para pequenas incidências o arrasto aerodinâmico é pequeno, de modo que o mesmo aumenta com a incidência devido ao aumento da região turbulenta próximo ao bordo de fuga no extradorso do aerofólio. O aumento da incidência é acompanhado por rápido aumento da esteira à medida que a incidência de máxima sustentação é alcançada, até a ocorrência da separação da camada limite da superfície do aerofólio. Se a dimensão da esteira turbulenta nessa região fosse mantida pequena em grandes incidências, seria esperado que a sustentação continuaria a aumentar e o arrasto seria mantido a pequenos valores (Bamber, 1931). Isso pode ser atingido através do fornecimento de energia cinética à camada limite, retardando assim o descolamento da mesma em altas incidências. Umas das possíveis técnicas é a injeção de fluidos para reenergizar a camada limite.

Nos experimentos realizados por Millard Bamber (1931) para o perfil NACA 84M, o controle da camada limite fora obtido através do uso de aberturas no extradorso do aerofólio para injeção de jatos de ar sob pressão interna do aerofólio constante. Foram analisadas diferentes posições da abertura (13,1%; 32,5%; 53,9% e 72,5%, posições relativas à corda) e também diferentes dimensões do orifício (0,167%; 0,333%; 0,5% e 0,667%, relativos à dimensão da corda). Estudos realizados por Dannenberg & Weiberg (1952) mostram que orifícios de injeção de dimensões maiores que 2,5% relativos à corda não levam a melhorias consideráveis, de modo que micro-orifícios apresentam excelente performance e baixa energia necessária devido à baixa vazão necessária para controle da camada limite.

O uso de jatos de ar para injeção de quantidade de movimento à camada limite, e consequente injeção de energia à mesma, promove o aumento de sustentação em todas as posições de injeção analisadas, de modo que a posição próxima ao bordo de fuga apresenta melhor performance em comparação à outras posições para pequenos ângulos de ataque. A injeção na região de meia-corda apresenta melhor performance para alcance de sustentação máxima; após condição de máxima sustentação, a injeção próxima ao bordo de ataque apresenta melhor performance para maiores incidências, levando a uma condição de perda de sustentação mais suave, devido ao natural descolamento da camada limite para ângulos de ataque de altos.

1.2. Investigação do Perfil NACA 0012

O trabalho de Sheldahl *et al* (1981) é de grande contribuição quanto ao estudo experimental de perfis aerodinâmicos simétricos. Mesmo que a finalidade seja fornecer informações para uso dos perfis em turbinas eólicas de eixo vertical (VAWT), os resultados do estudo são úteis para várias aplicações. Isto tornam-se de conhecimento os coeficientes de sustentação (C_L) e de arrasto (C_D) para ângulos de ataque (AoA) de 0° a 180° graus, através da análise experimental dos perfis NACA: 0009, 0012, 0012H, 0015 e 0018; e projeção dos resultados para os perfis NACA 0018, 0021 e 0025. Uma vez que os perfis são simétricos, a gama de ângulos é suficiente para uma volta completa; em outras palavras, fornece o conhecimento de C_L e C_D para todas as direções do plano do perfil. Portanto, esta enorme gama de ângulo de ataque para estes perfis é exposta ainda para diferentes números de Reynolds, os quais variam de 1×10^3 a 1×10^7. Tal trabalho é uma fonte clássica e rica em resultados experimentais e usualmente utilizada em outros trabalhos como referência para estudos CFD.

Outra fonte rica em parâmetros para simulação de aerofólios é a dissertação de mestrado de Basha (2006) pela *Concordia University*, Canadá. Em seu trabalho, simulando o perfil NACA 0012 para validação, o autor testa a influência de parâmetros como tipo de malha, modelo de fechamento da turbulência e sensibilidade do refinamento junto ao perfil (influência do y+). Em síntese, Basha (2006) sugere o uso do modelo Spalart-Allmaras com malha altamente refinada ao redor do perfil (y+ menor do que 5) e, de preferência, malha híbrida para melhores resultados ou C-*grid* estruturada para eficiência de processamento.

Sobre a separação da camada limite em escoamento turbulento, Ali *et al* (2011) promove outro estudo sobre o perfil NACA 0012. O modelo *k-ε* é empregado, utilizando o método de solução simples. O escopo do estudo é o descolamento (ou separação) da camada limite, avaliando também a distribuição de pressão e os coeficientes C_L e C_D. Ao final, Ali *et al* (2011) conclui que o modelo *k-ε* obteve bom resultado quanto ao ponto de separação sobre o aerofólio.

Outro relevante trabalho é o publicado por Eleni *et al* (2012). Também fazendo o estudo sobre o perfil NACA 0012, este estuda dois pontos de influência dos resultados: a diferença entre regime de transição laminar-turbulento em relação ao totalmente turbulento, e os modelos de turbulência (Spalart-Allmaras, *Realizable* k-ε e SST k-ω), comparando com três fontes de dados experimentais. Para o cenário em estudo é o ar, em regime permanente, para ângulos de ataque variando de -12° a 20°. Eleni *et al* (2012) concluem o trabalho apontando o modelo SST k-ω como melhor opção, e que o arrasto sobrestimado em seus resultados deve-se ao fato de que o escoamento real é laminar em cerca da metade da corda (onde as simulações consideraram regime totalmente turbulento). Os autores relatam ser possível melhorar os resultados da seguinte forma: determinar o ponto de transição laminar-turbulento, refazer a malha dividindo em duas regiões (uma para cada fenômeno) e simular novamente para a nova malha. De tal forma, segundo eles, os resultados são muito parecidos com os correspondentes valores experimentais.

2. PROCEDIMENTOS

2.1. Tratamento da Geometria

Para o estudo, são avaliados dois perfis: um perfil padrão NACA e um perfil modificado geometricamente para atender o objetivo de injeção. Para o primeiro, utiliza-se do perfil NACA 0012 original, o qual é posicionado com ângulo de ataque de 12 graus. O segundo perfil é resultado da configuração do NACA 0012 com a adição de um canal na posição de meia corda na superfície do extradorso (região de descolamento), com espessura equivalente a 1% da corda e de inclinação de 15 graus em relação a tangente da superfície do perfil na posição descrita. Na figura a seguir é exposto o perfil modificado, com dimensões relativas a unidade de comprimento da corda, assim como a posição final de 12 graus de ângulo de ataque.

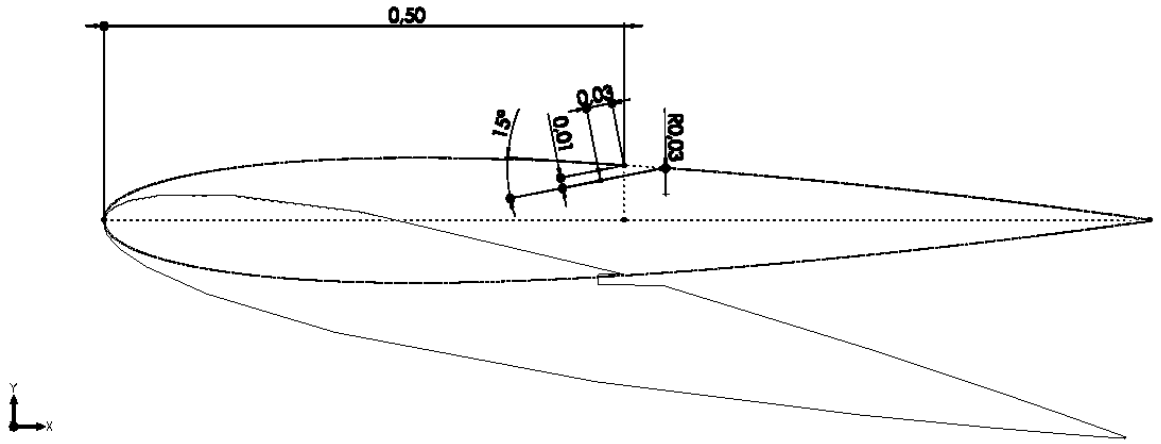

Figura 1. Resultado da modificação do perfil NACA 0012, o qual apresenta canal para injeção.

2.2. Malha Numérica

Devido aos dois perfis de interesse, gera-se uma malha numérica para cada perfil através do software ICEM CFD. Ambas são malhas bloco estruturadas, compostas exclusivamente de volumes hexaédricos. Quanto às dimensões, tomando um ponto do bordo de ataque como referência, o domínio retangular mede 25 cordas a montante, 25 cordas a jusante, 20 cordas acima e 20 cordas abaixo. A partir do plano do perfil, expande-se para um domínio tridimensional, sendo que a terceira dimensão mede 1 unidade de corda.

A distribuição dos elementos a partir das superfícies dos perfis segue distribuição exponencial com razão máxima de 1,1. A primeira camada de volumes tem espessura de cerca de 5.10^{-6} unidade de corda; a fim de manter o parâmetro y+ menor que 1. Na direção perpendicular do perfil é composta por 10 camadas de volumes uniformemente distribuídas.

Ao final desta etapa, a malha para o perfil original possui 998.250 volumes. O perfil modificado resultou em malha numérica de 1.211.920 volumes, com aumento por razão dos refinamentos na região do canal.

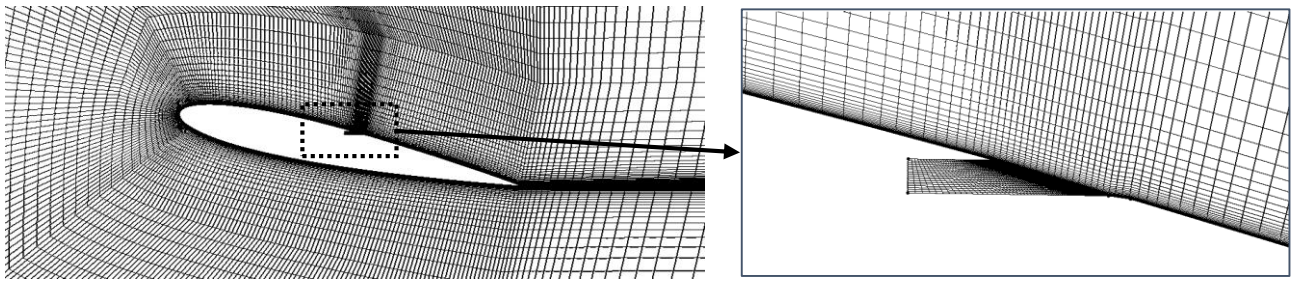

Figura 2. Malha numérica gerada para a geometria modificada, com destaque na região do canal.

2.3. Processo de Solução e Pós-Processamento

As simulações de CFD (*Computational Fluid Dynamics*) empregam o código independente UNSCYFL3D, utilizando-se do modelo de fechamento de turbulência k-epsilon com duas camadas tanto para regimes permanente (RANS) quanto transiente (URANS). O esquema centrado de 2ª ordem é empregado na discretização dos termos do algoritmo SIMPLE. O critério de resíduo adotado é de 10^{-6} para cálculos em regime permanente e 10^{-4} para regime transiente, considerando a conservação de massa e as componentes de velocidade (u, v e w).

No que diz respeito ao código UNSCYFL3D, este apresenta como propósito primordial a análise de escoamentos incompressíveis através da Dinâmica dos Fluidos Computacional. No UNSCYFL3D, as equações de Navier-Stokes na formulação incompressível são resolvidas numericamente através do método de volumes finitos (Ferziger *et al*., 2002) em malhas não-estruturadas, que podem ser compostas por hexaedros, tetraedros, prismas, pirâmides e cunhas. Para o acoplamento pressão-velocidade, o algoritmo SIMPLE (Ferziger *et al*., 2002) é utilizado. Escoamentos em regime permanente e transiente podem ser simulados. Os termos difusivos são discretizados por diferenças centradas de 2ª ordem, para os termos advectivos o esquema Upwind de 1ª ordem e o esquema centrado de 2ª ordem pode ser combinado. Os modelos de turbulência de grandes escalas Smagorinsky, Dinâmico e Yakhot foram implementados e validados. Os modelos DES-SST (Strelets, 2001), SST (Menter, 1994) e RSM também estão disponíveis. Para o avanço no tempo, o esquema de Euler implícito (1ª ordem) e de três níveis no tempo (2ª ordem) podem ser empregados. O código se encontra em constante atualização e implementações para solução em multiprocessadores já estão sendo feitas. Trabalhos de validação e verificação do código foram realizados inclusive para solução de problemas multifásico (Salvo *et al*., 2009, 2013; Souza *et al.*, 2012, 2014).

Todos os casos representam escoamentos em número de Reynolds (Re) de 10^5; onde a massa específica (ρ) é 1 kg/m³, o escoamento livre (U_∞) é de 1 m/s e viscosidade dinâmica (μ) de 10^{-5} N.s/m². Na Tab. 1 apresentam-se as condições de contorno aplicadas sobre o domínio numérico.

Tabela 1. Condições de contorno aplicadas no domínio numérico.

Fronteira	Condição de contorno
Inlet	velocidade imposta = U_∞ intensidade turbulenta = 0,1% comprimento característico = 0,1 m
Outlet	pressão imposta
Top	simetria
Bottom	simetria
Side I e II	simetria
Airfoil	parede
Slot Inlet	velocidade imposta = $0 \sim {}^3/_2 U_\infty$ intensidade turbulenta = 1% comprimento característico = 0,001 m

O software VisIt (*Visualization Tool*), software de fonte aberta, foi escolhido como ferramenta de pós-processamento devido a sua robustez e capacidade de leitura de inúmeros formatos de entrada. Uma vista tridimensional do domínio processado por esta ferramenta é exemplificada na Fig. 3, apresentando o canal da geometria no extradorso e o campo de energia cinética turbulenta nas superfícies laterais.

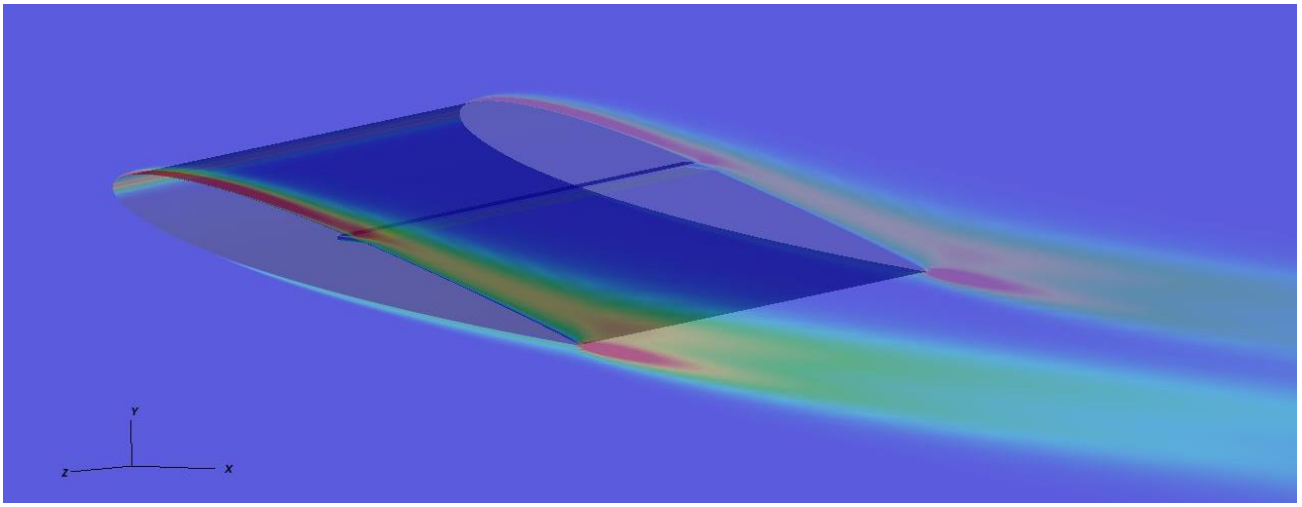

Figura 3. Vista tridimensional da geometria modificada pelo software VisIt, com exposição do campo de energia cinética turbulenta nas superfícies laterais de contorno.

3. ANÁLISE DOS RESULTADOS

3.1. Perfil NACA 0012: regime estacionário do escoamento

As simulações numéricas tiveram como foco a análise da esteira turbulenta do escoamento, com o objetivo de promover o recolamento da camada limite através do uso de injeção de quantidade de movimento. A primeira análise recai sobre o perfil NACA 0012.

Do ponto de vista da simulação, o modelo k-ε em regime permanente (RANS) ou transiente (URANS) pode gerar bons resultados. Entretanto, a convergência em regime permanente foi particularmente impossível, devido ao fato de o escoamento apresentar grandes estruturas coerentes, tanto em evolução temporal quanto espacial.

Logo, esta evidência sugere a presença de estruturas coerentes, em evolução temporal e/ou espacial, que caracterizam o estado de *stall*.

Os resultados da simulação ratificaram a presença de *stall* descrito na literatura nas condições de AoA=12º e Re=10^5 (Sheldahl *et al.*, 1981; Eleni *et al.*, 2002). Na figura 4 é possível visualizar o massivo descolamento da camada limite pelos campos de velocidade e energia cinética turbulenta.

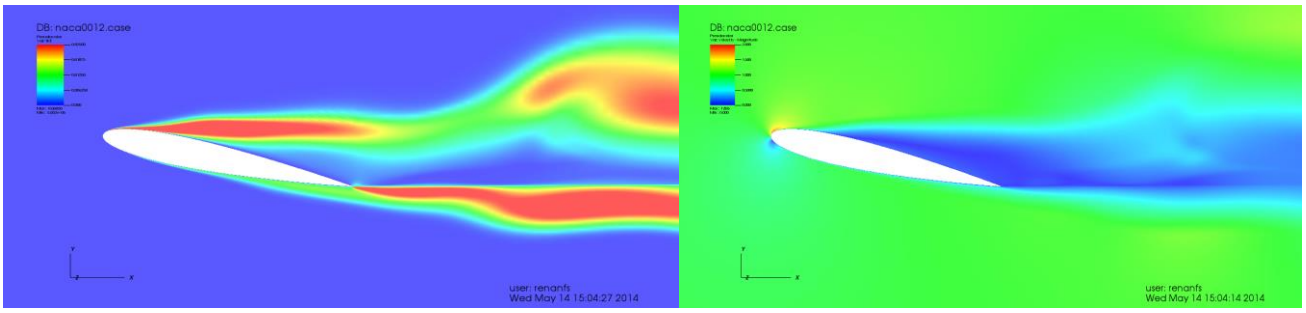

Figura 4. Campos de energia cinética turbulenta (à esquerda) e de velocidade (à direita) para o perfil NACA 0012, para AoA=12º e Re=10^5.

3.2. Perfil Modificado: regime estacionário dos escoamentos

O estudo segue na análise dos escoamentos, considerando o perfil modificado proposto também para AoA=12º e Re=10^5, quando alcançam regime estacionário. Doravante tomando a nomenclatura de velocidade do escoamento livre como U_∞, estuda-se este perfil em quatro condições de aplicação: o primeiro aborda o perfil modificado sem jato; os demais trata do perfil modificado com jato, nas velocidades de $^1/_2U_\infty$, U_∞ e $^3/_2U_\infty$.

A análise dos resultados nesta etapa é feita em instantes onde os escoamentos apresentam estado de estabilidade estatística. Os resultados demonstram que, de fato, alcança-se o recolamento através de injeção de quantidade de movimento. Ainda, o efeito de recolamento responde proporcionalmente (mas em caráter não-linear) à intensidade do jato, como visto na Fig. 5.

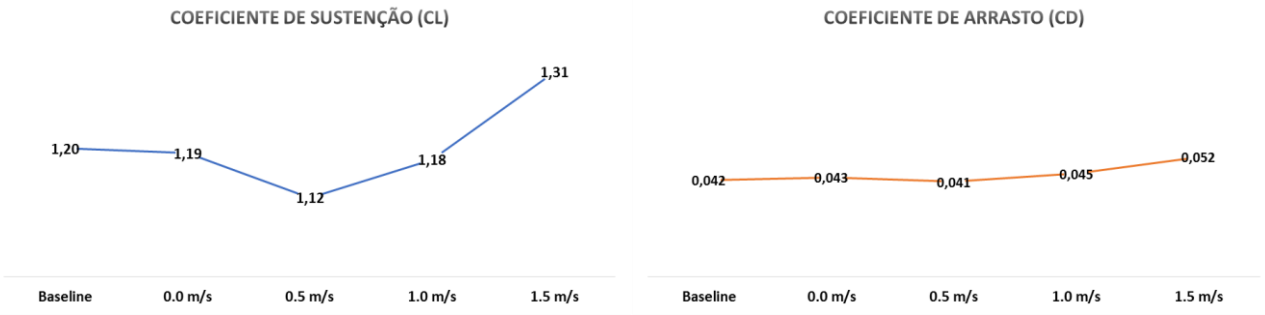

Figura 5. Efeito de recolamento sobre os coeficientes de sustentação (CL) e arrasto (CD) em condição de regime estatisticamente estável.

Verifica-se que a dimensão da esteira é reduzida com o recolamento, apresentando concentração da energia cinética turbulenta em três regiões: na camada limite iniciada no bordo de ataque; após o bordo de fuga, devido ao encontro de escoamentos em velocidades diferentes (efeito de camada de mistura); e na região do canal, onde a geometria coloca o escoamento em estado de geração de perturbações (descolamento pontual escoamento). As Fig.6 a 9 abaixo apresentam os campos de velocidade e energia cinética turbulenta para o perfil modificado, para quatro casos de regime estacionário.

Contudo, a evidência mais enriquecedora é o efeito de recolamento do escoamento sobre o perfil modificado sem

ausência de jato. A própria geometria do canal alimenta esta região do escoamento com perturbações devido ao descolamento pontual na borda do canal, onde espera-se que estruturas de Kelvin-Helmholtz sejam o principal mecanismo de instabilidades.

Logo, tal configuração atua como gerador de vorticidade interno à superfície do extradorso, diferentemente das aplicações comuns na aeronáutica (externa à superfície do extradorso). O efeito é a adição de energia ao escoamento que retarda o descolamento indesejável.

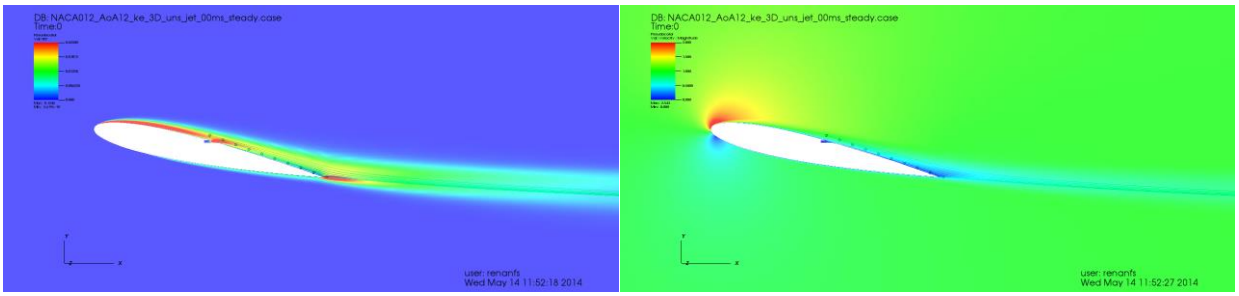

Figura 6. Campos de energia cinética turbulenta (à esquerda) e de velocidade (à direita) para o perfil modificado, sem acionamento do jato.

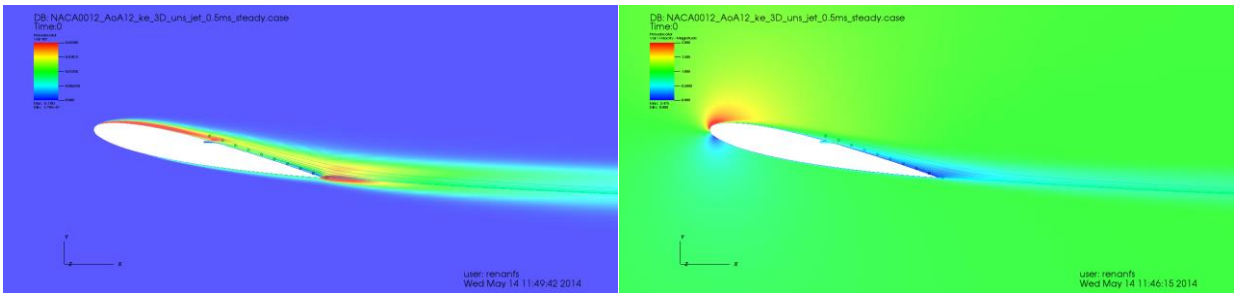

Figura 7. Campos de energia cinética turbulenta (à esquerda) e de velocidade (à direita) para o perfil modificado, para velocidade do jato de $^{1}/_{2}U_{\infty}$.

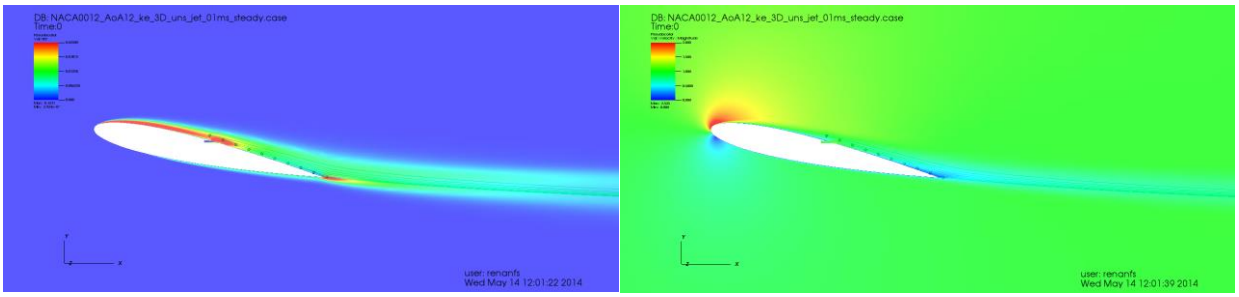

Figura 8. Campos de energia cinética turbulenta (à esquerda) e de velocidade (à direita) para o perfil modificado, para velocidade do jato de U_{∞}.

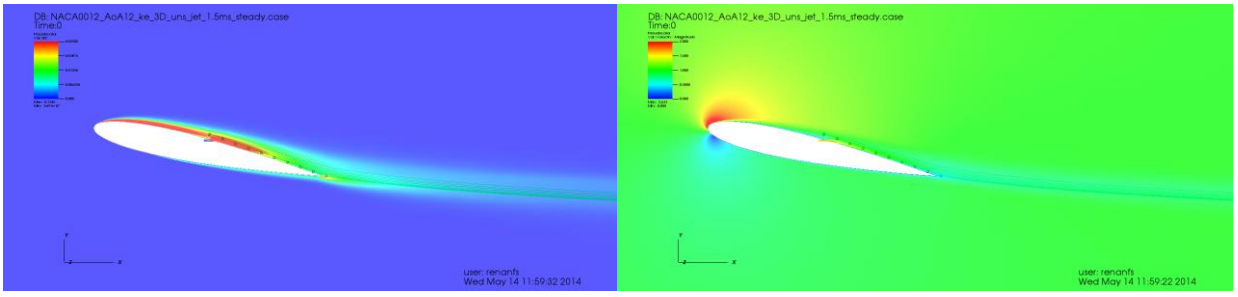

Figura 9. Campos de energia cinética turbulenta (à esquerda) e de velocidade (à direita) para o perfil modificado, para velocidade do jato de $^{3}/_{2}U_{\infty}$;

3.3. Perfil Modificado: evolução temporal dos escoamentos

O segundo ponto de destaque dos resultados é o fenômeno de transição entre velocidades do jato. No tópico anterior, fica evidente que ao aumentar a intensidade do jato, menor será a região de descolamento e a esteira turbulenta associada ao escoamento. Logo, a solução para o problema seria utilizar a maior intensidade possível.

Este tópico do estudo busca analisar a influência da evolução temporal da quantidade de movimento inserida; ou seja, os efeitos da mudança de velocidade de operação do jato. Estudam-se dois escoamentos, a partir de mesmo estado inicial (regime estacionário com jato de U_∞), onde um desacelera o jato de U_∞ para $^1/_2U_\infty$, e o outro acelera de U_∞ para $^3/_2U_\infty$. Na Fig. 10 observa-se a evolução temporal dos escoamentos, sob aspecto da energia cinética turbulenta.

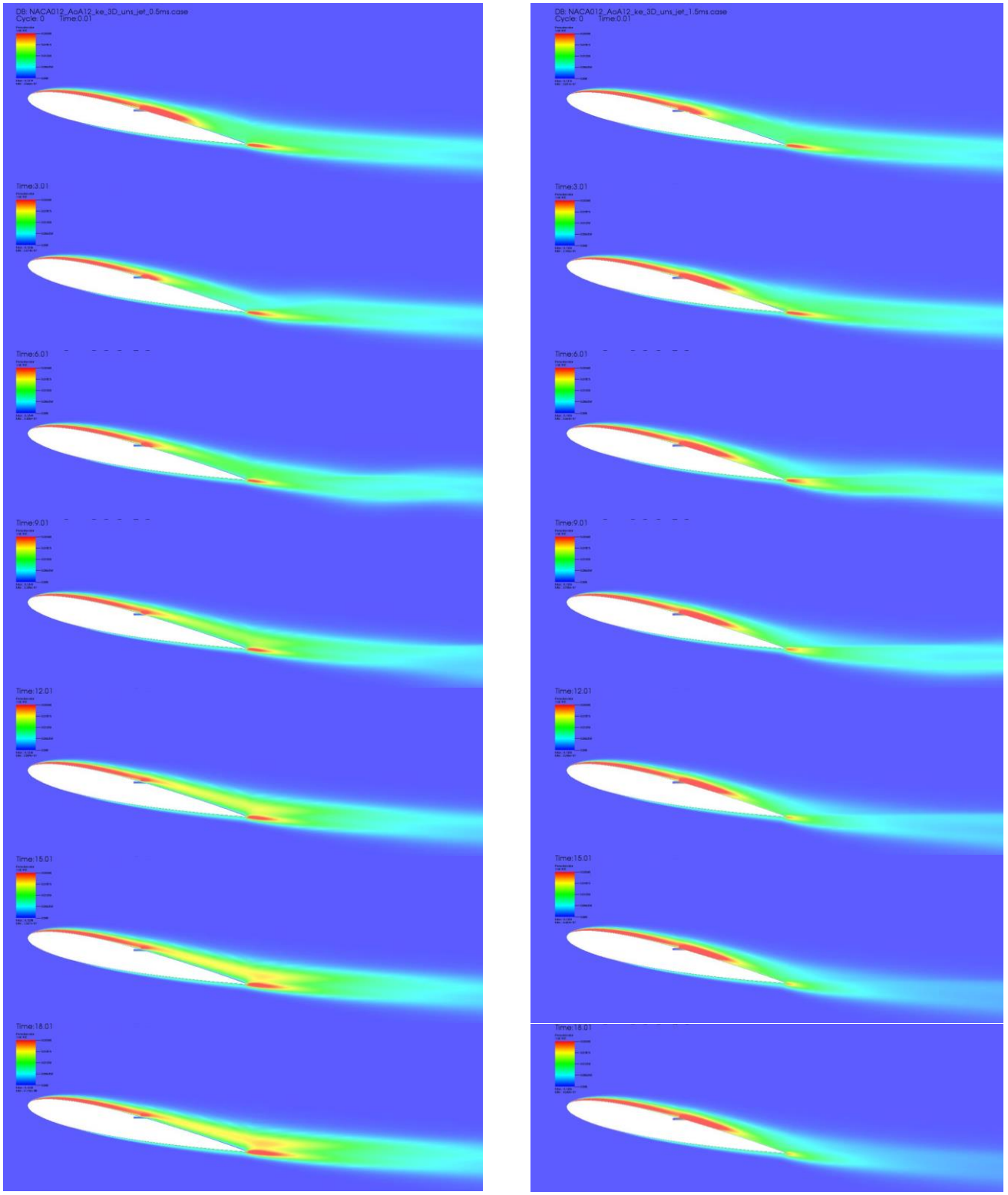

Figura 10. Evolução temporal (de cima para baixo) do campo de energia cinética turbulenta para diminuição para $^1/_2U_\infty$ (coluna à esquerda) e aumento para $^3/_2U_\infty$ (coluna à direita) da intensidade do jato, a partir de U_∞.

O resultado desta abordagem leva a concluir que, ao aumentar a intensidade do jato (aceleração), ocorre geração da energia cinética turbulenta na região do canal. Consequentemente, esta energia adicionada ao escoamento é caracterizada como um pulso, o qual é responsável por iniciar o processo de recolamento da camada limite e estreitamento da camada de energia turbulenta.

Surpreendentemente, ao diminuir a intensidade do jato (desaceleração) o mesmo fenômeno ocorre em um intervalo de tempo inicial. O que difere os escoamentos é o fato de que, após o pulso de estreitamento da esteira turbulenta no escoamento com jato a $^1/_2U_\infty$, a mesma volta a se desenvolver. Isto deve-se pela menor intensidade de energia no escoamento, quando comparado o estado inicial com jato de U_∞.

4. CONCLUSÃO

Os resultados ratificam o aumento da energia cinética turbulenta adicionada pelo jato na região de descolamento como agente do recolamento da camada limite.

Contudo, um ponto importante é a promoção do recolamento não somente pelo método da injeção, mas também pela própria geometria do perfil modificado. Diferentemente dos geradores de vorticidade clássicos (externos ao perfil), a geometria do canal de injeção de fluido atua como gerador de vorticidade internamente ao perfil original. Ou seja, as instabilidades decorrentes do descolamento da borda do canal são promotores de energia cinética turbulenta na região do perfil. Logo, mantém-se o escoamento energizado por um período maior e, assim, retardando seu descolamento.

Tanto processos em regime permanente (RANS) quanto transiente (URANS) apresentam resultados próximos, salvo os resultados para o perfil NACA 0012 original. Ressalta-se que escoamento com presença de grandes estruturas coerentes, em evolução temporal e espacial, dificultam a convergência por método RANS. Tal evidência já comprova que os casos de escoamentos sobre o perfil modificado devem contemplar estruturas vorticais menores, sendo decorrência do maior grau de estabilidade estatística dos escoamentos.

Não menos importante é o aspecto de evolução temporal dos jatos. Conclui-se que a variação da velocidade, tanto para maior quanto para menor intensidade, produz um pulso de energia cinética turbulenta. Este fenômeno intensifica o efeito de recolamento da camada limite até que este adicional de energia ser disperso. Após a dissipação da energia proveniente do pulso, o efeito de recolamento retorna ao patamar de regime estável, pertinente a intensidade do jato.

Por fim, tal característica dos pulsos de energia leva a concluir que deve-se existir uma frequência ideal de intermitência do jato a qual resulte maior eficiência do mecanismo de recolamento do que jatos contínuos em velocidades ainda maiores. Em outras palavras, jatos intermitentes tem potencial de uso maior do que jatos contínuos para fins de aplicações como sistema aerodinâmico.

5. AGRADECIMENTOS

Agradece-se ao Programa de pós-graduação da Faculdade de Engenharia Mecânica (FEMEC), da Universidade Federal de Uberlândia (UFU) e ao Laboratório de Mecânica dos Fluidos (MFLab) pela estrutura disponibilizada para realização das atividades. Agradece-se também ao Conselho Nacional de Desenvolvimento Científico e Tecnológico (CNPq) pelo suporte financeiro para a pesquisa.

6. REFERÊNCIAS

Anderson, J., 2010, "Fundamentals of Aerodynamics", 5th edition.

Bamber, M. J., 1931,"Wind Tunnel Tests on Airfoil Boundary Layer Control using a Backward-Opening Slots", NACA REPORT No. 385, National Advisory Committee for Aeronautics, USA.

Dannenberg, R. E., Weiberg, J. A., 1952, "Section Characteristics of a 10.5-Percent-Thick Airfoil with Area Suction as Affected by Chordwise Distribution of Permeability", DTIC Document.

Eleni, D. C. et al., 2002, "Evaluation of the turbulence models for the simulation of the flow over a National Advisory Committee for Aeronautics (NACA) 0012 airfoil". Journal of Mechanical Engineering Research.

Knight, M., Bamber, M. J., 1929, "Wind Tunnel Tests on Airfoil Boundary Layer Control using a Backward-Opening Slots", NACA Technical Notes No. 323, National Advisory Committee for Aeronautics, USA.

Ferziger, J. H., Peric, M., 2002, "Computational Methods for Fluid Dynamics", Springer, 3rd edition.

Hucho, W-H., 1998, "Aerodynamics of Road Vehicles". Fouth Edition. Society of Automotive Engineers Inc.

Menter, F. R., 1994, "Two-Equation Eddy-Viscosity Turbulence Models for Engineering Applications". AIAA Journal, 32 (8), pp.1598-1605.

Salvo, R. V. et al., 2009. "Large-Eddy Simulation of Single Phase Turbulent Flows in Cyclones". 20nd International Congress of Mechanical Engineering – COBEM, Gramado, Brazil.

Salvo, R. V. et al., 2013. "Effects of Outlet Duct Length and Shape on the Performance of Cyclone Separators". 22nd International Congress of Mechanical Engineering – COBEM, Ribeirão Preto, Brazil.

Schudel, M. Aerodynamics. [mensagem pessoal]. Mensagem recebida por: <renanfranciscosoares@hotmail.com>. em: 12 mar. 2013.

Sheldahl, R. E. et al., 1981, "Aerodynamic Characteristics of Seven Symmetrical Airfoil Sections Through 180-Degree Angle of Attack for Use in Aerodynamic Analysis of Vertical Axis Wind Turbines". Albuquerque, Sandia National

Laboratories.
Souza, F. J., 2012, “Large Eddy Simulation of the gas–particle flow in cyclone separators”. Separation and Purification Technology.
Souza, F. J., 2014, “Four-way coupled simulations of the gas–particle flow in a diffuser”. Powder Technology.
Strelets, M., 2001, “Detached eddy simulation of massively separated flows”. 39th AIAA Aerospace Sciences Meeting and Exhibit, Reno, Nevada.

7. RESPONSIBILITY NOTICE

Os autores são os únicos responsáveis pelo material impresso presente neste artigo.

ON THE TURBULENCE MODULATION BY PARTICLES IN CONFINED GAS-SOLID FLOWS

Jonathan Utzig, jonathanutzigeq@gmail.com
Francisco José de Souza, fjsouza@mecanica.ufu.br
School of Mechanical Engineering - Federal University of Uberlandia
Av. João Naves de Ávila, 2121 Bloco 5P – 38400-902 Uberlandia – Minas Gerais – Brazil

Henry França Meier, meier@furb.br
Chemical Engineering Department - University of Blumenau
R. São Paulo, 3250 I-303 – 89030-000 Blumenau – Santa Catarina – Brazil

Abstract. *Gas-solid flows have many important engineering applications. Such cases disclose a number of intrinsic phenomena related to the fluid phase turbulence. When particles are present, turbulence is modified and this is known as turbulence modulation. Since it is important to understand the modulation effects, special care must be taken regarding the mathematical model adopted. Thus, the goal of this study is to reveal the effects of solids mass loading and particle relaxation time on the carrier phase turbulence. The influence of the particle collision model was also assessed. A horizontal channel dilute gas-solid flow investigated experimentally by Sommerfeld and Kussin (2004) is simulated with the Euler/Lagrange approach. Effects of roughness walls, coupling with the continuous phase and interparticle collision are accounted for. Results show that higher mass loadings attenuate the carrier phase turbulence with small particles and the velocity fields are influenced by the local particle concentration. Particles with larger relaxation times, through its particle wakes, increase the turbulence compared to small particles, but attenuate compared to clean flow.*

1. INTRODUCTION

Turbulence is the most fascinating phenomenon of the fluid mechanics. For over a century studies have been carried out to understand it. In multiphase flows, when particles, droplets and bubbles are present, turbulence is modified and this is known as turbulence modulation. There have been numerous studies, both numerical and material experimentation, on turbulence modulation. Several sources of turbulence in the carrier phase due to particles or droplets have been identified; stream line distortion due to the presence of the particles, the wake generated by particles, the modification of the velocity gradients in the carrier phase and the associated change in turbulence generation and the damping of turbulence motion by the drag force on the particles (Crowe, 2000).

Turbulence modulation by particles is a subject of interest for engineering applications. Since preferential concentrations cause the multiphase flow segregation, mathematical model adopted plays a very important role in the accuracy of the results. The phase-interactions have been studied by several authors, in order to understand the modulation mechanisms (Squires and Eaton, 1990; Elghobashi and Truesdell, 1993; Ljus *et al.*, 2002; Vreman *et al.*, 2009). Notably, in the gas-solid mixtures these phenomena through particle-fluid interactions can be observed, which must be correctly modeled. Our recent works show some examples: the pressure RMS signal and kinetic energy dissipation rate attenuations (Utzig *et al.*, 2012), the turbophoresis effect (Utzig *et al.*, 2014), and the boundary-layer reattachment by particles (Souza *et al.*, 2014).

Studies on particle dynamics, i.e., particle-to-wall and particle-to-particle collisions, are essential. Laín *et al*. (2002), Benson *et al*. (2005) and Laín and Sommerfeld (2012) demonstrated the importance of wall roughness and particle collision models. Mandø *et al*. (2009) proposed a hybrid source term to the turbulence equations, based on the so-called standard and consistent Euler/Lagrange approach. Their new model contains mechanisms for suppression and enhancement of turbulence and, according to the authors, no more terms are needed. Results were compared with experimental measurements and they found that the performance of new model surpasses other models for that range of investigations. Other works deal with frameworks like Euler/Lagrange with probability density function (PDF) methods for particle phase (Meyer, 2012) and the Euler/Euler approach (Hadinoto, 2010) to represent the turbulence modulation.

In this sense, the goal of this study is to reveal the effects of solids mass loading and particle relaxation time on the carrier phase turbulence. The influence of the particle collision model was also assessed. The horizontal channel dilute gas-solid flow investigated by Sommerfeld and Kussin (2004) is simulated in the Euler/Lagrange approach. The following sections present the mathematical model used, the numerical set-up, the validation and main results obtained.

2. MATHEMATICAL MODELS

2.1. Gas-phase model

The Navier-Stokes for a general, incompressible, steady-state flow can be written adopting the tensor notation as:

$$\frac{\partial(\rho u_i)}{\partial x_i} = 0, \tag{1}$$

$$\frac{\partial}{\partial x_j}\left(\rho u_i u_j\right) = -\frac{\partial p}{\partial x_i} + \frac{\partial}{\partial x_j}\left[\mu\left(\frac{\partial u_i}{\partial x_j} + \frac{\partial u_j}{\partial x_i}\right)\right] + \rho g_i + S_{p,Ui}. \tag{2}$$

The conservation equations for the continuity, velocity components and for the turbulence variables in steady state can be written generically as:

$$\frac{\partial}{\partial x_j}\left(\rho u_j \phi\right) = \frac{\partial}{\partial x_j}\left(\Gamma \frac{\partial \phi}{\partial x_j}\right) + S_\phi. \tag{3}$$

By integrating the general conservation equation (3) over the control volume V, we obtain:

$$\oint_A \rho\phi\vec{V}.d\vec{A} = \oint_A \Gamma \mathrm{grad}\phi.d\vec{A} + \int_V S_\phi dV. \tag{4}$$

Note that, for the terms involving surface integrals in Eq. (4), the Gauss Divergence Theorem was applied to convert the volume integrals into surface integrals Ferziger and Peric (2002):

$$\int_V \frac{\partial \phi}{\partial x_i} dV = \oint_A \phi\vec{\imath}_i.d\vec{A}. \tag{5}$$

where $\vec{\imath}_i$ is the unitary vector. For the element L shown in Fig. 1, and located at the LHS of face f, the discretization of Eq. (4) yields:

$$\sum_f J_f \phi_f = \sum_f \mathrm{D}_f + (S_\phi \Delta V)_L, \tag{6}$$

in which J_f is the mass flow rate, $(\rho_f \vec{V}_f.\vec{A}_f)$, across face *f*, Γ_f the diffusion coefficient at the that face and $D_f = \Gamma_f (grad\phi)_f.\vec{A}_f$ is the diffusive flux across face *f*. The summations above apply to all the faces of element L. $\vec{A}_f$ is the normal area vector of face *f*, which is directed from the element L to the element R.

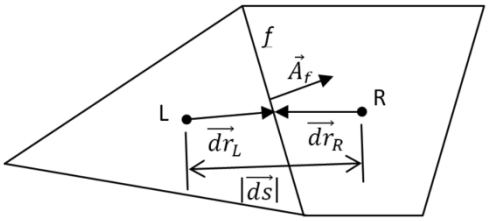

Figure 1. General control volume and nomenclature.

Regarding the advective term in Eq. (6), when the first-order upwind scheme is employed, ϕ_f is assigned the value of the element center at element L if J_f is positive. Otherwise, the value of element R is set to the face. Because first-order schemes are usually very diffusive for many applications of interest, a second-order upwind scheme was used in this work:

$$\phi_f = \phi_L + (grad\phi)_{rL}.\overrightarrow{dr_L} \tag{7}$$

if $J_f > 0$. The vector $\overrightarrow{dr_L}$ is directed from the geometric center of element L to the face *f* center. $(grad\phi)_{rL}$ is the reconstructed gradient at element L, which is again computed by means of the Gauss Divergence Theorem:

$$(grad\phi)_r = \frac{1}{\Delta V}\sum_f \left(\bar{\phi}_f \vec{A}_f\right), \tag{8}$$

where $\bar{\phi}_f$ is the average of ϕ the element centers sharing face *f*.

It can be proven that the diffusive flux for face *f* is given by Mathur and Murthy (1997a),

$$D_f = \Gamma_f \frac{(\phi_R - \phi_L)}{|\vec{ds}|}\frac{\vec{A}_f.\vec{A}_f}{\vec{A}_f.\vec{e}_s} + \Gamma_f\left[\overline{grad\phi}.\vec{A}_f - \overline{grad\phi}.\vec{e}_s\frac{\vec{A}_f.\vec{A}_f}{\vec{A}_f.\vec{e}_s}\right] \tag{9}$$

In Eq.(9), $\vec{e}_s$ is the unit vector connecting the centers of elements R e L, $\vec{e}_s = \frac{\overrightarrow{ds}}{|\vec{ds}|}$. The first term at the RHS of Eq. (14) is treated implicitly, whereas the remaining terms, which represent the secondary diffusion, are calculated explicitly and therefore incorporated into the source-term S in Eq. (6). The secondary diffusion is null for hexahedra for instance, because vectors $\vec{A}_f$ and $\vec{e}_s$ are collinear. The gradient at face *f*, $\overline{grad\phi}$, is calculated as the average of the gradients at the

adjacent elements. The treatment above is equivalent to the application of the second-order, centered differencing scheme in structured meshes and is advantageous in the sense that it does not depend on the element shape.

The numerical solution of the conservation equations for the momentum and turbulence is accomplished by the computational code UNSCYFL3D. This in-house tool is based on the finite volume method in unstructured three-dimensional grids. The SIMPLE (Semi-Implicit Method for Pressure-Linked Equations) algorithm is used to couple the velocity and pressure fields. The collocated arrangement is used for all variables, with the conventional Rhie-Chow interpolation scheme for the computation of the mass flow rate through each volume face. The discretization procedure generates a linear system of equations for ϕ at the element centers. The biconjugate gradient and the algebraic multigrid (AMG) methods are used to efficiently solve the linear system resulting from the discretization of each conserved variable. The main advantage of this modeling is that it does depend on the element shape, as the data structure is based on element faces. For each element face, arrays containing the number of left and right elements sharing it are created. As it be shown subsequently, all operations involved in transferring information from the Eulerian to the Lagrangian frames and vice-versa utilize either face or element center data, and are therefore also irrespective of the number of faces each element contains. For storing the coefficients of the linear systems for the velocity components, pressure correction and turbulence variables, the RCS (Row Compressed Storage) is used. For further information on the method, references Mathur and Murthy (1997b) and Ferziger and Peric (2002) are recommended.

In all the simulations carried out in this work only the steady-state solution for fluid was sought. The second-order upwind scheme was employed for the advective term, whereas the centered differencing scheme was used for the diffusive terms of the momentum equations and turbulence model equations.

The standard k-epsilon model is the most widely known and extensively used two-equation eddy viscosity model. It was originally developed to improve the mixing-length model and to avoid the algebraic prescription of the turbulence length scale in complex flows. Transport equations are solved for two scalar properties of turbulence, the turbulence kinetic energy, k, and the dissipation rate of turbulent kinetic energy, ε:

$$\frac{\partial(\rho u_j k)}{\partial x_j} = \frac{\partial}{\partial x_j}\left[\left(\mu + \frac{\mu_t}{\sigma_k}\right)\frac{\partial k}{\partial x_j}\right] + P - \rho\varepsilon, \tag{10}$$

$$\frac{\partial(\rho u_j \varepsilon)}{\partial x_j} = \frac{\partial}{\partial x_j}\left[\left(\mu + \frac{\mu_t}{\sigma_\varepsilon}\right)\frac{\partial \varepsilon}{\partial x_j}\right] + C_{\varepsilon 1}\frac{\varepsilon}{k}P - C_{\varepsilon 2}\rho\frac{\varepsilon^2}{k}, \tag{11}$$

where P is the production term, given by:

$$P = (\mu_t + \mu)\left[\left(\frac{\partial u_i}{\partial u_j} + \frac{\partial u_j}{\partial u_i}\right)\frac{\partial u_i}{\partial u_j}\right]. \tag{12}$$

The eddy-viscosity in the standard k–epsilon model is defined as a function of the turbulent kinetic energy and the turbulent dissipation rate as:

$$\mu_{t,standard} = C_\mu \rho \frac{k^2}{\varepsilon}. \tag{13}$$

Although widely used, the standard k-epsilon displays some weaknesses, such as the assumption that the flow is fully turbulent. To circumvent this issue, in this work the 2-layer k-epsilon model was employed, as it can handle well both the core flow and the near wall region. Essentially, it consists in solving the standard model for the turbulent flow region and a one-equation model for the region affected by the viscosity. In the one-equation k-epsilon model, the conservation equation for k is retained, whereas ε is computed from:

$$\varepsilon = \frac{k^{3/2}}{l_\varepsilon}. \tag{14}$$

The length scale that appears in Eq. (14) is computed from (Chen and Patel, 1988):

$$l_\varepsilon = yC_l\left(1 - e^{-Re_y/A_\varepsilon}\right). \tag{15}$$

In Eq. (15), Re_y is the turbulent Reynolds number, defined as:

$$Re_y = \frac{\rho y\sqrt{k}}{\mu}, \tag{16}$$

where y is the distance from the wall to the element centers. This number is the demarcation of the two regions, fully turbulent if $Re_y > Re_y{}^*$, $Re_y{}^* = 200$ and viscosity-affected, $Re_y < 200$. For the one-equation model, the turbulent viscosity is computed from:

$$\mu_{t,2layer} = \rho C_\mu l_\mu \sqrt{k}. \tag{17}$$

The length scale in the equation above is computed as below:

$$l_\mu = yC_l\left(1 - e^{-Re_y/A_\mu}\right). \tag{18}$$

The constants in the length scale formulas, Eqs. (15) and (18), are $c_l = 0.4187c_\mu^{-3/4}$, $A_\mu = 70$, $A_\varepsilon = 2c_l$. In UNSCYFL3D, both the standard k-epsilon and the one-equation model described above are solved over the whole domain, and the solutions for the turbulent viscosity and the turbulence kinetic energy dissipation rate provided by both models are smoothly blended:

$$\mu_t = \lambda_\varepsilon \mu_{t,standard} + (1 - \lambda_\varepsilon)\mu_{t,2layer}. \tag{19}$$

A blending function, λ_ε, is defined in such a way that it is equal to unity far from walls and is zero very near walls. The blending function used here is:

$$\lambda_\varepsilon = \frac{1}{2}\left[1 + \tanh\left(\frac{Re_y - Re_y^*}{A}\right)\right]. \tag{20}$$

The constant A determines the width of the blending function:

$$A = \frac{0.20Re_y^*}{\tanh(0.98)}. \tag{21}$$

The purpose of the blending function λ_ε is to prevent solution divergence when the solution from both the standard and the one-equation models do not match. Since no wall-functions are used, it is very important to refine the grid so as to have $y^+ < 1$ in the first element away from the wall to ensure accurate results for the fluid flow.

Finally, the carrier fluid "feels" the presence of particles as an additional source term in the momentum equation. This term is modeled based on Newton's second and third laws:

$$S_{p,Ui} = -n\left\langle m_p\left(\frac{du_{pi}}{dt} - \left(1 - \frac{\rho}{\rho_p}\right)g_i\right)\right\rangle; \tag{22}$$

n is the average number of real particles per unit volume in the control volume, m_p is the particle mass, u_{pi} is the particle velocity, ρ_p is the particle material density, ρ is the fluid density and g_i is the gravity vector. The brackets denote mean values over all particle realizations in that particular control volume. Thus, for each computational particle crossing a control volume, one contribution is added to the source-term above.

2.2. Particle motion model

As mentioned in the previous section, the dispersed phase is treated in a Lagrangian framework, in which each particle is tracked through the domain and its equation of motion is based on Newton's second law. The trajectory, linear momentum and angular momentum conservation equations for a rigid, spherical particle can be written, respectively, as:

$$\frac{dx_{pi}}{dt} = u_{pi}, \tag{23}$$

$$m_p\frac{du_{pi}}{dt} = m_p\frac{3\rho C_D}{4\rho_p d_p}\left(u_i - u_{pi}\right) + F_{si} + F_{ri} + \left(1 - \frac{\rho}{\rho_p}\right)m_p g_i, \tag{24}$$

$$I_p\frac{d\omega_{pi}}{dt} = T_i. \tag{25}$$

In the above equations, $u_i = U_i + u_i'$ are the components of the instantaneous fluid velocity. The average fluid velocity U_i is interpolated from the resolved flow field, whereas the fluctuating component u_i' is calculated according to the Langevin dispersion model. d_p is the particle diameter and $I_p = 0.1m_p d_p^2$ is the moment of inertia for a sphere.

The empirical correlation proposed by Schiller and Naumann (1935) is used to evaluate the drag coefficient past each particle, where Re_p is the particle Reynolds number $Re_p = \rho d_p\left|\vec{u} - \vec{u}_p\right|/\mu$:

$$C_D = 24Re_p^{-1}\left(1 + 0.15Re_p^{0.687}\right) \quad if\ Re_p < 1000,$$
$$C_D = 0.44 \quad if \quad Re_p > 1000. \tag{26}$$

The calculation of the shear-induced lift force is based on the analytical result of Saffman (1965) and extended for higher particle Reynolds numbers according to Mei (1992):

$$\vec{F}_s = 1.615d_p\mu Re_s^{1/2}C_{ls}\left[\left(\vec{u} - \vec{u}_p\right)x\,\vec{\omega}\right], \tag{27}$$

$\vec{\omega}$ is the vorticity, $Re_s = \rho d_p^2 |\vec{\omega}|/\mu$ is the particle Reynolds number of the shear flow and $C_{ls} = F_{ls}/F_{ls,Saff}$ represents the ratio of the extend lift force to the Saffman force:

$$C_{ls} = (1 - 0.3314\beta^{0.5})e^{-0.1Re_p} + 0.3314\beta^{0.5} \quad if\ Re_p < 40,$$
$$C_{ls} = 0.0524\left(\beta Re_p\right)^{0.5} \quad if\ Re_p > 40, \tag{28}$$

β is a parameter $\beta = 0.5Re_s/Re_p (0.005 < \beta < 0.4)$.

The rotation-induced lift is computed based on the relation given by Rubinow and Keller (1961), which was extended to account for the relative motion between particle and fluid:

$$\vec{F}_r = \frac{\pi}{8}\rho d_p^3 \frac{Re_p}{Re_r} C_{lr} \frac{[\vec{\Omega}\, x\, (\vec{u} - \vec{u}_p)\,]}{|\vec{\Omega}|}. \tag{29}$$

In Eq. (30), $\vec{\Omega} = 0.5\vec{\nabla} \times \vec{u} - \overrightarrow{\omega_p}$ and $Re_s = \rho d_p^2 |\vec{\Omega}|/\mu$. The lift coefficient C_{lr} is obtained from the correlation proposed by Lun and Liu (1997):

$$C_{lr} = \frac{Re_r}{Re_p} \quad if\ Re_p < 1,$$
$$C_{lr} = \frac{Re_r}{Re_p}\left(0.178 + 0.822 Re_p^{-0.522}\right) \quad if\ Re_p > 1. \tag{30}$$

Also, the rotating particle experiences torque from the fluid flow. The correlation of Rubinow and Keller (1961) was extended to account for the relative motion between fluid and particle at higher Reynolds number:

$$\vec{T} = C_r \frac{\rho d_p^5}{64} |\vec{\Omega}|\, \vec{\Omega}. \tag{31}$$

The coefficient of rotation, C_r, was obtained from the following correlation, derived from the direct numerical simulations of Dennis *et al.* (1980):

$$C_r = \frac{64\pi}{Re_r} \quad if\ Re_r < 32,$$
$$C_r = \frac{12.9}{\sqrt{Re_r}} + \frac{128.4}{Re_r} \quad if\ Re_r > 32. \tag{32}$$

Forces such as Basset and virtual mass have been neglected. This is a reasonable assumption since the particle material density is over 1000 times the gas density (Crowe, 2006).

The extension of the Euler/Lagrange approach to unstructured meshes requires the use of accurate interpolation schemes, since in the above equations the continuous phase properties must be determined at the particle center. A few interpolation schemes have been tried out, and the best compromise between accuracy and cost was obtained with the Sheppard's scheme. Basically, the velocity and vorticity components at the particle position are calculated by weighing the neighboring element values with their inverse distances from their centers to the particle position.

For integrating the ordinary differential Eqs. (23), (24) and (25), the analytical scheme was used. In order to ensure that only binary collisions occurred, small time steps had to be used. Upon a particle colliding with a wall, the new particle linear and angular velocities after rebound are calculated according to the following conservation equations (Breuer and Alletto, 2012):

Nonsliding collision:

$$\vec{u}_p^{+} = \vec{u}_p^{-} - \frac{2}{7}\vec{u}_{pr}^{-} - (1+e)\left(\vec{u}_p^{-}.\vec{n}\right)\vec{n} \quad \text{and} \quad \vec{\omega}_p^{+} = \vec{\omega}_p^{-} - \frac{10}{7}\frac{\vec{n}}{d_p}\, x\, \vec{u}_{pr}^{-}. \tag{33}$$

Sliding collision:

$$\vec{u}_p^{+} = \vec{u}_p^{-} - (1+e)\left(\vec{u}_p^{-}.\vec{n}\right)\left[\mu_d \frac{\vec{u}_p^{-}}{|\vec{u}_p^{-}|} + \vec{n}\right] \quad \text{and} \quad \vec{\omega}_p^{+} = \vec{\omega}_p^{-} - \frac{5}{d_p}(1+e)\left(\vec{u}_p^{-}.\vec{n}\right)\frac{\mu_d}{|\vec{u}_p^{-}|}\, \vec{n}\, x\, \vec{u}_{pr}^{-}. \tag{34}$$

In the above equations, the superscripts – and + denote values prior to and after the collision, respectively, *e* is the normal restitution coefficient and μ_d is the dynamic friction coefficient. $\vec{n}$ is the normal unit vector pointing outwards of the element face being impacted. $\vec{u}_{pr}$ is the relative velocity at the contact point:

$$\vec{u}_{pr} = \vec{u}_p - \left(\vec{u}_p.\vec{n}\right)\vec{n} + \frac{d_p}{2}\omega_p\, x\, \vec{n}. \tag{35}$$

Numerous experimental studies have shown evidence that wall roughness and interparticle-collisions are important even at low solid loadings. Therefore, their influence must be included in the modeling. As demonstrated by Laín *et al.*

(2008) the wall roughness plays a vital role in the dispersion of particles in pneumatic transport systems. In order to account for such effects, we implemented the model proposed by Sommerfeld and Huber (1999), to represent the effects of surface asperities on the particle flow. Basically, the wall roughness is simulated by assuming that the effective impact angle is composed of the geometric impact angle added to a stochastic contribution due to wall roughness. This stochastic contribution is sampled from a Gaussian distribution with a standard deviation $\Delta\gamma$, which depends on the structure of wall roughness and particle size. Unfortunately, the value of $\Delta\gamma$ must be calibrated so as to provide the best agreement between the experimental and simulated pressure losses. Although the performance of the method is satisfactory, it requires the adjustment of a parameter to correctly reproduce the experimental results. A model which does not depend on such parameter, but instead employs the actual surface topology is under development.

Inter-particle collisions are modeled with a stochastic, hard-sphere model. As described by Oesterlé and Petitjean (1993) for each computational particle, a fictitious collision partner is generated, and the probability of a collision is checked based on an analogy with the kinetic theory of gases. This in turn requires that the average and root mean square (RMS) linear and angular velocities, as well as the particle concentration in each control volume, be sampled and stored every Lagrangian calculation. Although demanding a lot of memory, the method is rather economical and effective, and avoids the use of a deterministic collision model, which is quite expensive computationally. In both interparticle and particle-to-wall collisions, perfectly elastic collisions were assumed ($e = 1$ and $\mu_d = 0.5$).

When a structured grid is used, it is simple to determine the element hosting the particle, as there is a straightforward relationship between the element index and its physical location. Because an unstructured grid is used in this work, there is the need for a specific algorithm to locate the particle after its final position is calculated by the integration of Eq. (23). For that purpose, the particle-localization algorithm proposed by Haselbacher *et al.* (2007) was implemented. This algorithm is based on tracking a particle along its trajectory by computing the intersections of the trajectory and the element faces. Since it does not depend on the element topology, it is very suitable for use in unstructured grids. Furthermore, it was observed to be extremely faster than costly, direct-search algorithms.

The coupled solution of the continuous and particle phases is summarized as follows. First the steady-state solution for the fluid phase without particles is computed. Subsequently, nearly 100,000 computational particles are injected and tracked throughout the domain. For each control volume, the average and RMS linear and angular velocities, the particle concentration and the source-terms for the fluid momentum equations are gathered. After all the particles have left the domain, the fluid flow is solved again, now considering the source-terms sampled during the previous particle calculation. This process is repeated, considering the particle-to-particle collision, until a converged solution for both phases is reached. It is important to bear in mind that the particle statistics must be corrected during each particle calculation. Approximately, from 10,000 time steps, which are necessary for the particles to leave the domain. The particle time step used was 0.0001s. In this study, 100 coupling iterations are carried out, which takes approximately 25 hours on a single processor. It is worth mentioning that the models employed in the UNSCYFL3D code were validated previously (Souza *et al.*, 2012; Souza *et al.*, 2014).

3. RESULTS AND DISCUSSION

In order to validate the Euler/Lagrange approach extension to unstructured grids and assess the turbulence modulation by particles, results for the gas and particulate phases in the flow of air ($\rho = 1.25 kg/m^3$, $\mu = 1.8E-5 Pa.s$) loaded with glass spheres ($d_p = 130\mu m$, $\rho_p = 2450 kg/m^3$) in a horizontal channel have been chosen. The channel length is $6m$ to guarantee that a fully developed profile develops. The channel height and width are $35mm$ and $350mm$, respectively, so that nearly two-dimensional flow is achieved. No-slip conditions are prescribed at both upper and lower walls, while for the side boundaries symmetry boundary conditions are assigned. At the domain outlet, the static pressure is prescribed. Since the flow is nearly two-dimensional, the mesh resolution is as follows: 400 hexahedra in the streamwise direction, 40 elements in the vertical direction and 1 element in the transverse direction. Statistical convergence was achieved for the numerical mesh, computational particles number and coupling iterations. The average uniform inlet velocity is $\boldsymbol{v_g} = 20m/s$, gravity was set $\boldsymbol{g} = 9.8m/s^2$ and the particles were considered to be monodispersed because of their narrow size distribution. The validation case was set with particles at solid mass loading $\eta = 1.0$ like the material experimentation of Sommerfeld and Kussin (2004). Other cases with clean flow and solid mass loadings $\eta = 0.1$ and $\eta = 0.5$ were simulated. The channel wall roughness parameter was set $\Delta\gamma = 1.6°$ for both upper and lower walls. All comparisons are made at $5.8m$, where the flow is known to be fully developed.

Figure 2 shows the validation of the simulated cases and material experimentation for the average gas streamwise velocity, the average particle streamwise velocity, the RMS horizontal and vertical particle velocities and the particle concentration profiles along the channel height, respectively, where symbol sizes represent a measurement error of 3%. It can be seen from Fig. 2 that the results agree well with the experiments. The particle concentration is normalized based on the average particle concentration in the domain. Since the simulation results depend on the correct implementation of a number of models, it can be concluded that the code is validated. As already concluded by Laín *et al.* (2002), the particle concentration is more uniform across the channel height than one would expect. Although gravity tends to create a vertical concentration gradient, the roughness of the upper and lower walls tends to homogenize the particle mass flux by bringing about more collisions. The RMS particle normal-to-wall velocity and the particle concentration are particularly very sensitive to the wall roughness. The overprediction of the particle concentration near the lower wall was also obtained by Laín and Sommerfeld (2012), and was attributed to multiple wall bouncing, currently not included in the model.

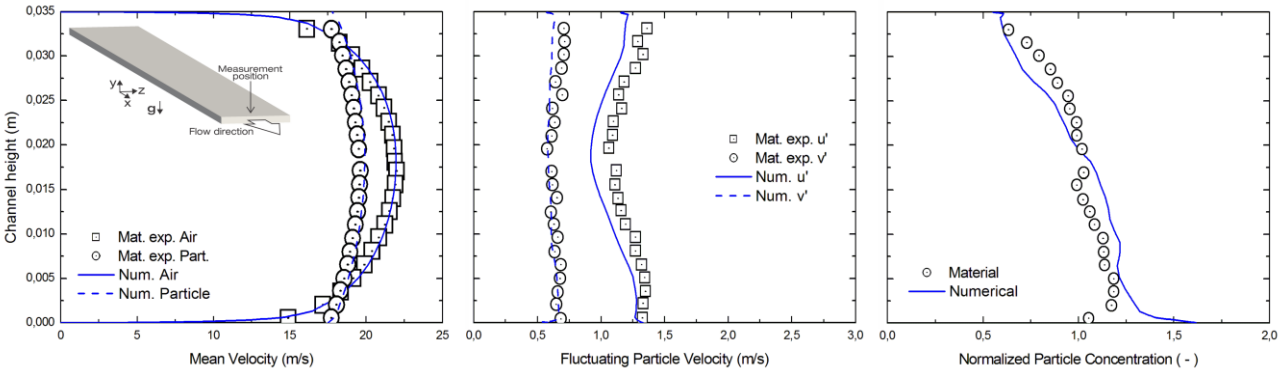

Figure 2. Validation of the numerical results with material experimentation data of Sommerfeld and Kussin (2004); left: streamwise mean velocities; middle: fluctuating particle velocities; right: normalized particle concentration. ($U = 20m/s$, $\Delta\gamma = 1.6°$, $d_p = 130\mu m$, $\eta = 1.0$)

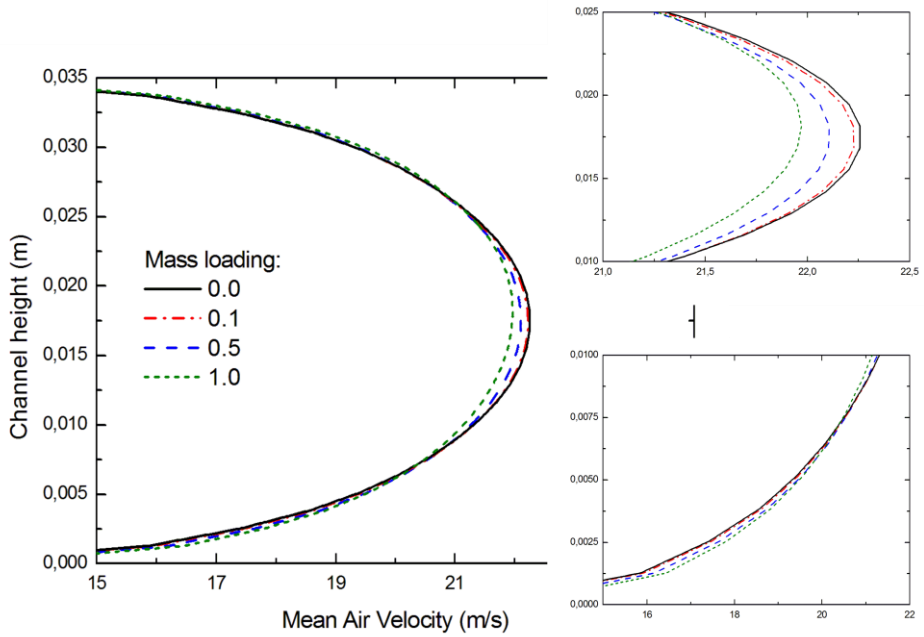

Figure 3. Mean streamwise gas velocities for different mass loadings and details of the modified regions. ($U = 20m/s$, $\Delta\gamma = 1.6°$, $d_p = 130\mu m$)

In order to investigate the solid phase influence on the carrier phase, the channel flow was simulated with lower mass loadings. Gas phase mean velocities are shown in Fig. 3. The clean flow ($\eta = 0.0$) displays the higher velocity in the channel center – height 0.01 to $0.025m$, since it is not influenced by the particles. In the gas-solid flows, lower mean gas velocity in this region is achieved – Fig. 3, upper detail. More particles extract more momentum from the carrier phase through two-way coupling mechanism (Eq. 22). Consequently, by virtue of the gas mass conservation, energy is transferred to near wall regions and the gas phase velocity become higher than that of the clean flow. Therefore, a momentum transfer process occurs from the center region, to the peripheral regions.

The local particle concentration also plays an important role in the turbulence modulation. In the upper half channel, Fig. 4, there are fewer particles whereas in the bottom the concentration is increased due to gravitational particle settling. It can be seen that the lower part has many particles which collide with lower wall and with each other, thus the mean particle velocities are decreased. On the other hand, particles can travel more easily in the upper half and have higher velocity. Fig. 4 (right) also shows the effect of inter-particle collisions on the local particle concentration. At $\eta = 0.1$ the concentration profile increases monotonically while other ones have an inflection in their trends. After rebounding from lower wall, particles collide with each other, pushing them to the central region. Because there are fewer particles when $\eta = 0.1$, this effect is less evident.

Several works have been investigated turbulence modification by particles. Results on the continuous phase turbulence can be less intuitive than expected. According to the Elghobashi's diagram (Elghobashi, 1994), in the present work cases particles would enhance the turbulence dissipation; however, Fig. 5 shows the opposite effect. The turbulence kinetic energy (TKE) and dissipation rate decrease as more particles are present. In fact, one sees a combined correlation between turbulence production, TKE and its dissipation rate. Depending on the particle Reynolds number, turbulence can be suppressed or enhanced. Particularly, these effects are not explicitly considered in our k- and ε-equations through source terms, thus the suppression originates only from the momentum attenuation. As seen in Fig. 3, the particle-laden velocity profiles are flatter than the clear flow one, therefore lower shear occurs. Actually, multiphase flow turbulence has a wide spectrum of important length and time scales and a variety of phase interactions that make

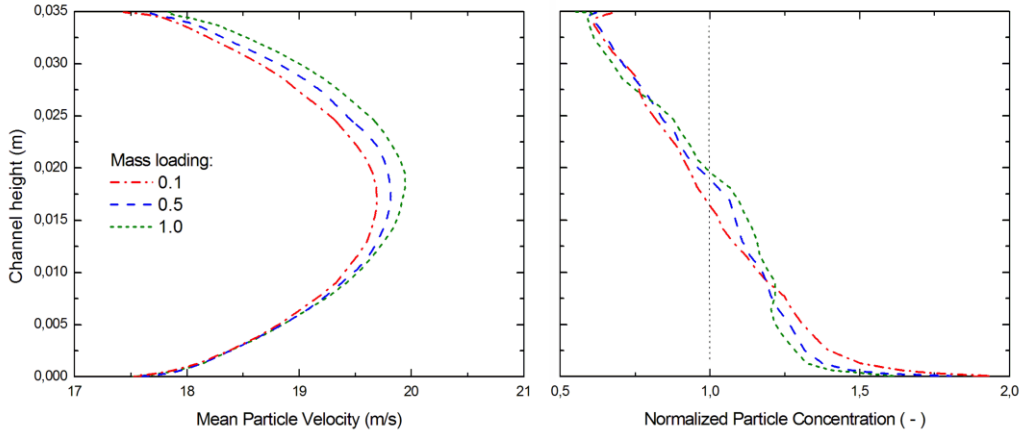

Figure 4. Comparison between different mass loadings; left: mean streamwise particle velocities; right: normalized particle concentration. ($U = 20m/s$, $\Delta\gamma = 1.6°$, $d_p = 130\mu m$)

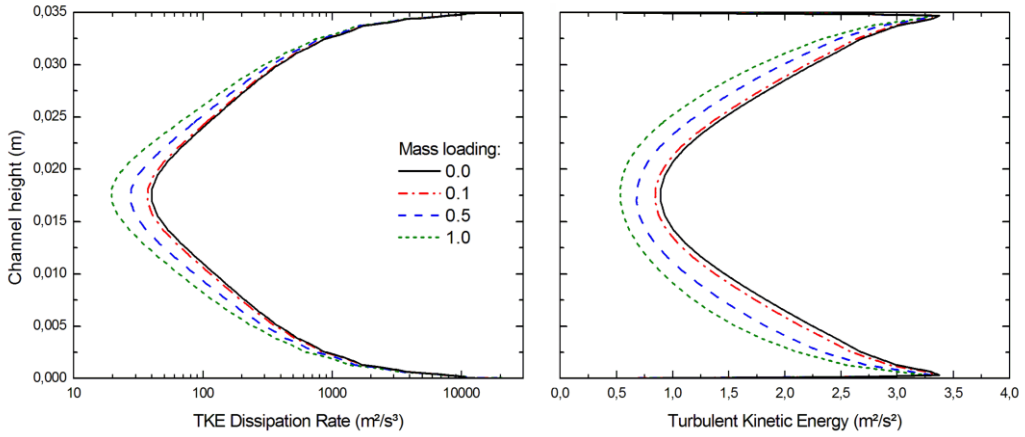

Figure 5. Comparison between different mass loadings; left: turbulence kinetic energy dissipation rates; right: turbulent kinetic energies. ($U = 20m/s$, $\Delta\gamma = 1.6°$, $d_p = 130\mu m$)

the analysis more complex. The Elghobashi's diagram is built assuming a homogeneous spatial distribution of the particles, which does not hold for the present cases and consequences can be quite different.

The particle effects on turbulence modulation can be examined based on the particle relaxation time $\tau_p = \rho_p {d_p}^2/18\mu$, i.e. the required time for a particle at rest to achieve the fluid velocity. Thus, we simulate the channel flow with larger particles, $d_p = 411\mu m$ and same density, resulting in $\tau_p = 1.278s$. The previous case with $\eta = 1.0$ and $d_p = 130\mu m$, yields $\tau_p = 0.1278s$, a relaxation time an order of magnitude lower. Effects on gas phase turbulence are shown in Figs. 6 and 7. Contrary to previous cases, larger particles increase the carrier phase velocity in the central region – Fig. 6 (left); they have greater inertia and the momentum transfer mechanism inverts. The mean particle streamwise velocity – Fig. 6 (middle) – is flatter and the local concentration – Fig. 6 (right) – is more equally distributed. With greater relaxation time, particles respond more slowly to the fluid and due to the wall roughness, particles rebound more frequently between upper and lower walls.

The turbulence kinetic energy and the dissipation rate are increased with larger particles, unlike the previous cases, as shown in Fig. 7 (left and middle). To understand these effects, two mechanisms for the energy transfer of the particles to the fluid phase TKE are illustrated in Fig. 7 (right). First, the turbulence augmentation is related to vortex streets or wakes induced by particles – hence strongly dependent on particle diameter –, which appear as fluid velocity fluctuations. Such mechanism probably occurs with the large particles case, in which TKE and dissipation rate were increased. Second, the turbulence attenuation observed in previous cases can result from interaction between particles and turbulent eddies. When the first mechanism is negligible, even with low relaxation time, particles can cross the turbulence structures and reduce the turbulent intensity. Nevertheless, none of these mechanisms is taken into account in our simulations. The increase in the turbulence kinetic energy and its dissipation rate can be explained based on the increased strain of the mean gas flow in the channel center caused by the larger particles, visible in Fig. 6. The production term for both is then augmented, as the conservation equations reveal. What remains to be better explained is the increase in the air mean velocity: close to the lower boundary layer, where more particles are present, the larger particles extract momentum from the gas phase, which reduces its mean velocity; consequently, the air velocity must to increases in central region.

This particle behavior can be examined by means the Stokes number St. The Stokes number is the main parameter defining the particle dynamics for a given flow field and is defined $St = \tau_p/\tau_e$ – i.e., the ratio particle relaxation time over the characteristic time scale of the carrier fluid $\tau_e = l/u'$, based on the mean fluid fluctuating velocity taken in

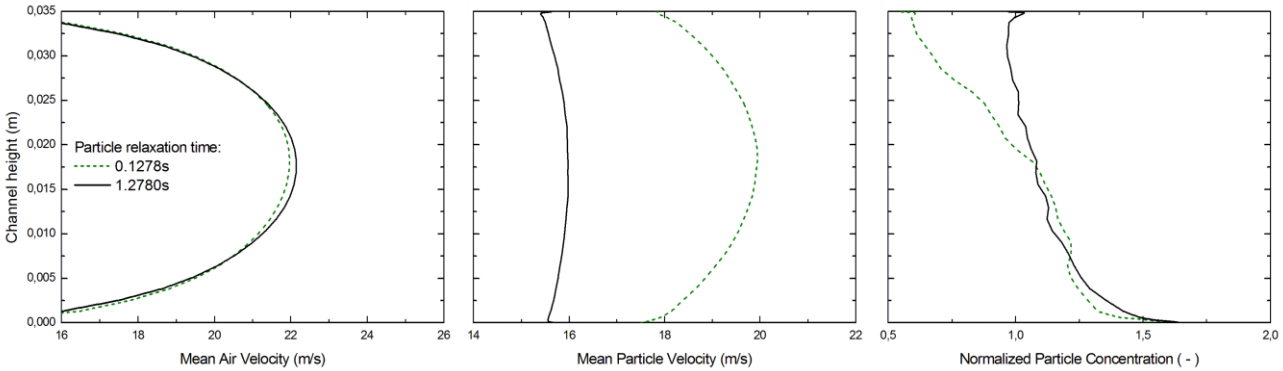

Figure 6. Comparison between two particle relaxation times: $\tau_p = 0.1278s$ ($d_p = 130\mu m$) and $\tau_p = 1.278s$ ($d_p = 411\mu m$); left: mean streamwise air velocities; middle: mean streamwise particle velocities; right: normalized particle concentrations. ($U = 20m/s$, $\Delta\gamma = 1.6°$, $\eta = 1.0$)

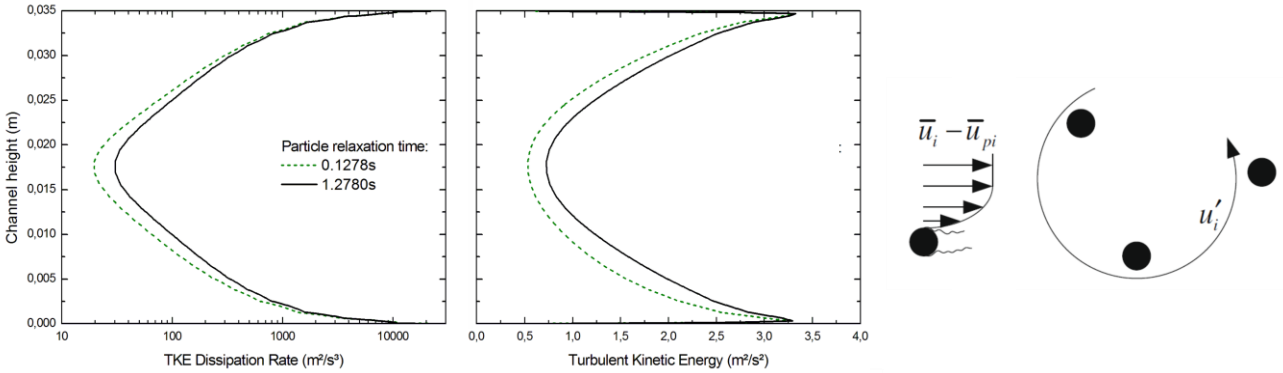

Figure 7. Comparison between two particle relaxation times: $\tau_p = 0.1278s$ ($d_p = 130\mu m$) and $\tau_p = 1.278s$ ($d_p = 411\mu m$); left: turbulence kinetic energy dissipation rate; middle: turbulent kinetic energy. Right: mechanisms for turbulence modulation – adapted from Mandø *et al.* (2009). ($U = 20m/s$, $\Delta\gamma = 1.6°$, $\eta = 1.0$)

channel core and on a typical eddy size, 10% of channel height as spatial scale. For $\tau_p = 0.1278s$, we obtain $St = 18.26$, which indicates that the particles are sufficient large to have a ballistic behavior and cross the eddies. Also, $\tau_p = 1.278s$ yields $St = 182.57$, which attenuates the turbulence compared to the clean flow, but enhances the turbulence production compared to smaller particles.

4. CONCLUSIONS

The turbulent channel gas-solid flow was numerically analyzed in an Euler/Lagrange approach. Effects of particle-wall collision, coupling with the continuous phase and inter-particle collision are accounted for through the two- and four-way coupling concepts.

It was found that higher mass loadings attenuate the carrier phase turbulence with small particles and the velocity fields are influenced by the local particle concentration. Particles with larger relaxation time, through its particle wakes, increase the turbulence compared to small particles, but attenuate compared to clean flow.

The turbulence modulation phenomenon could be verified in this study. Mechanisms of phase-interaction are very complex in multiphase flows, thus the turbulence behavior is modified. Such effects are present in engineering applications and are worth being investigated.

5. ACKNOWLEDGEMENTS

The authors would like to acknowledge the financial support from Petróleo Brasileiro S. A. (PETROBRAS), CAPES and the National Council of Technological and Scientific Development (CNPq). The authors would like to thank Prof. Martin Sommerfeld for useful hints on the implementation of the Euler/Lagrange method.

6. REFERENCES

Bardina, J. E., Huang, P. G. and Coakley, T. J., 1997, "Turbulence Modeling Validation, Testing and Development", NASA TM 110446.

Benson, M., Tanaka, T. and Eaton, J.K., 2005. "Effects of wall roughness on particle velocities in a turbulent channel flow." Trans. ASME J. Fluids Eng., vol. 127, pp. 250–256.

Breuer, M., Alletto, M. and Langfeldt, F., 2012. "Sandgrain roughness model for rough wall within Eulerian-Lagrangian predictions of turbulent flows." Int. J. Multiphase Flow, vol. 43, pp. 157–175.

Breuer, M. and Alletto, M., 2012. "Efficient simulation of particle-laden turbulent flows with high mass loadings using LES." Int. J. Heat and Fluid Flow, vol. 35, pp. 2–12.

Chen, H.C and Patel, V.C., 1988. "Near-wall turbulence models for complex flows including separation", AIAA J., vol. 26, n. 6, pp. 641–648.

Crowe, C.T., Sommerfeld, M. and Tsuji, Y., 1998. "Fundamentals of Gas-Particle and Gas-Droplet Flows." CRC Press.

Crowe, C.T., 2000. "On models for turbulence modulation in fluid-particle flows." Int. J. Multiphase Flow, vol. 26, n. 5, pp. 719–727.

Crowe, C.T., 2006. "Multiphase Flow Handbook." CRC Press Taylor & Francis Group, Boca Raton, USA.

Dennis, S.C.R., Singh, S.N. and Ingham, D.B., 1980. "The steady flow due to a rotating sphere at low and moderate Reynolds numbers." J. Fluid Mech., vol. 101, pp. 257–279.

Ferziger, J. H. and Peric, M., 2002. Computational methods for fluid dynamics, Springer.

Haselbacher, A., Najjar, F. M. and Ferry, J. P., 2007. "An efficient and robust particle-localization algorithm for unstructured grids." Journal of Computational Physics, vol. 225, pp. 2198–2213.

Laín, S. and Sommerfeld, M., 2008. "Euler/Lagrange computations of pneumatic conveying in a horizontal channel with different wall roughness." Powder Technology, vol. 184, pp. 76–88.

Laín, S. and Sommerfeld, M., 2012. "Numerical calculation of pneumatic conveying in horizontal channels and pipes: Detailed analysis of conveying behaviour." Int. J. Multiphase Flow, vol. 39, pp. 105–120.

Laín, S., Sommerfeld, M. and Kussin, J., 2002. "Experimental studies and modelling of four-way coupling in particle-laden horizontal channel flow." Int. J. Heat Fluid Flow, vol. 23, pp. 647–656.

Lun, C. K. K. and Liu, H. S., 1997. "Numerical simulation of dilute turbulent gas-solid flows in horizontal channels." Int. J. Multiphase Flow, vol. 23, n. 3, pp. 575–605.

Mandø, M., Lightstone, M.F., Rosendahl, L., Yin, C. and Sørensen, H. "Turbulence modulation in dilute particle-laden flow." Int, J. Multiphase Flow, vol. 30, p. 331-338.

Mathur, S. R. and Murthy, J. Y., 1997a. "A pressure-based method for unstructured meshes." Numerical Heat Transfer, Part B, vol. 31, pp. 195–215.

Mathur, S. R. and Murthy, J. Y., 1997b. "Pressure boundary conditions for incompressible flow using unstructured meshes." Numerical Heat Transfer, Part B, vol. 32, pp. 283–298.

Mei, R., 1992. "An approximate expression for the shear lift force on a spherical particle at finite Reynolds number." Int. J. Multiphase Flow, vol. 18, pp. 145–147.

Meyer, D.W., 2012, "Modelling of turbulence modulation in particle- or droplet-laden flows." J. Fluid Mech., vol. 706, pp. 251-273.

Oesterlé, B. and Petitjean, A., 1993. "Simulation of particle-to-particle interactions in gas-solid flows." Int. J. Multiphase Flow, vol. 19, pp. 199–211.

Rubinow, S.I. and Keller, J.B., 1961. "The transverse force on a spinning sphere moving in a viscous liquid." J. Fluid Mech., vol. 11, pp. 447–459.

Saffman, P.G., 1965. "The lift on a small sphere in a shear flow." J. Fluid Mech., vol. 22, pp. 385–400.

Schiller, L. and Naumann, A., 1935. "A drag coefficient correlation." Z. Ver. Deutsch. Ing., pp. 77–318.

Sommerfeld, M. and Huber, N., 1999. "Experimental analysis and modelling of particle–wall collision." Int. J. Multiphase Flow, vol. 25, pp. 1457–1489.

Sommerfeld, M. and Kussin, J., 2004. "Wall roughness effects on pneumatic conveying of spherical particles in a narrow horizontal channel." Powder Technology, vol. 142, pp. 180–192.

Souza, F. J., Salvo, R. V. and Martins, D. M. M., 2012. "Large Eddy Simulation of the gas-particle flow in cyclone separators." Separation and Purification Technology, vol. 94, pp. 61–70.

Souza, F. J., Silva, A. L. and Utzig, J., 2014. "Four-way coupled simulations of the gas–particle flow in a diffuser." Powder Technlogy, vol. 253, pp. 496-508.

Utzig, J., Decker, R.K., Noriler, D. and Meier, H.F., 2012. "Análise de interações entre as fases em escoamentos turbulentos multifásicos gás-sólido por experimentação numérica e física." Proceedings of the VIII Escola de Primavera de Transição e Turbulência, vol. 1, São Paulo, Brazil.

Utzig, J., Souza, F.J. and Meier, H.F., 2014. "A numerical analysis of the turbophoresis in a turbulent gas-particle flow." Proceedings of the ASME 2014 4th Joint US-European Fluids Engineering Division Summer Meeting, Chicago, USA.

5. RESPONSIBILITY NOTICE

The authors are the only responsible for the printed material included in this paper.